Damage-associated molecular patterns in necroptosis-dependent skin inflammation

África Fernández Nasarre de Letosa

A thesis submitted to Cardiff University in candidature for the degree of Doctor of Philosophy

April 2022

Acknowledgements

First, I would like to thank my main supervisor, Dr Marion Bonnet for giving me the opportunity of working in such a fascinating project and for always sharing her scientific passion with me. I would also like to thank my co-supervisors, Dr Timothy Hughes and Prof Ernest Choy, for the scientific and moral support during these years. I am also very grateful for my wonderful former colleagues in the lab, Dr Cleo Bonnet and Sudha Arumugam, for their help with experiments but specially for the personal encouragement during the hard times. A special thank you to Dr Amanda Tonks, from the PGR office, for her continuous guidance and assistance, which has allowed me to be writing this today.

A huge thank you to everyone on the 4th floor of HWB, especially my former fellow office members in 4F03 for all the good times. To Dr Teja Rus, who has always supported me and to whom I am extremely grateful to have met during my years in Cardiff. To all the lovely Wellfield people that I have had the pleasure to live with, you have made my experience in Cardiff the best it could be.

To my parents, for never doubting me and pushing me to always do my best and to my sister, Pineta, for all the love and support. To all my friends back home, who have had to deal with the good and the bad, I love you all.

Thank you to everyone who has helped me complete his PhD. It has been a challenging experience, but now, coming to an end, I am grateful and full of love.

Summary

Necroptosis is a regulated form of cell death generally dependent on the activation of receptor interacting serine/threonine kinase 3 (RIPK3) and its substrate mixed lineage kinase domain like pseudokinase (MLKL). MLKL phosphorylation leads to its oligomerisation and translocation to the membrane, where it forms pore that result in homeostasis disruption and cell death. Membrane disruption allows the release of damage-associated molecular patterns (DAMPs) such as interleukin (IL) 33 and high mobility group box protein 1 (HMGB1) to the extracellular space, which act as potent pro-inflammatory molecules alerting the immune system. Specific deletion of Caspase 8 (Casp-8) in epidermal keratinocytes (Casp-8^{EKO}) causes acute necroptosis-dependent psoriasis-like inflammation in the skin. However, the relative contribution of IL-33 and HMGB1 to necroptosis in the skin is poorly understood.

The results reported here indicate that HMGB1 induces phosphorylation of MLKL in normal human epidermal keratinocytes (NHEKs) *in vitro*, which might occur independently of RIPK3. Additionally, deletion of IL-33 or its receptor, suppression of tumorigenicity 2 (ST2), leads to a major rescue of the skin inflammatory phenotype in the $Cap8^{EKO}$ model, identifying IL-33 as an early mediator of necroptosis-dependent skin inflammation. Reduced skin inflammation is associated to a decreased IL-33-mediated recruitment of granulocytes, which might be responsible for mediating inflammation through tumour necrosis factor (TNF) production. In contrast, HMGB1/RAGE signalling does not contribute to inflammation in the necroptosis Casp-8^{EKO} model.

Together, these findings bridge an important gap between DAMPs and extend our knowledge of the molecular mechanisms involved in necroptosis-dependent skin inflammation.

Abbreviations

A/A	Antibiotic-Antimycotic
ACD	Accidental cell death
AD	Atopic dermatitis
AGEs	Advanced glycation endproducts
AKI	Acute kidney injury
ANOVA	Analysis of variation
ATG	Autophagy related
BCA	Bicinchoninic acid
BSA	Bovine Serum Albumin
CAMKII	Calcium/calmodulin-dependent protein kinase II
Casp	Caspase
CBM	Chromatin-binding motif
CD	Cluster of differentiation
CHIP	C-terminus of Hsc70-interacting protein
cIAP	Cellular inhibitor of apoptosis protein
CLE	Cutaneous lupus erythematosus
CLP	Cecal ligation and puncture
CT	Cholera Toxin
CXCL12	C-X-C motif chemokine 12
CXCR4	C-X-C chemokine receptor 4
CYLD	Conserved cylindromatosis
CypD	Cyclophillin D
DAMP	Damage-associated molecular pattern
DAPI	4,6 Diamidino-2-phenylindole
DC	Dendritic cell
DETC	Dendritic epidermal T cell

DISC	Death-inducing signalling complex
DMEM	Dulbecco's Modified Eagle Medium
DMSO	Dimethyl sulfoxide
DNA	Deoxyribonucleic acid
DR	Death receptors
ECL	Enhanced chemiluminescence
ECM	Extracellular matrix
EDGS	EpiLife defined growth supplemented
EGF	Epidermal growth factor
EKO	Epidermal knock-out
ELISA	Enzyme-linked immunosorbent assay
ER	Endoplasmic reticulum
ERK	Extracellular signal-regulated kinase
ESCRT-III	Endosomal sorting complexes required for transport
FADD	Fas Associated Via Death Domain
FCS	Foetal calf serum
FFPE	Formalin fixed paraffin embedded
FIL	Filaggrin
GAPDH	Glyceraldehyde 3-phosphate dehydrogenase
GPX4	Glutathion peroxidase 4
H&E	Haematoxylin and eosin
HC	Hydrocortisone
HEK293	Human embryonic kidney 293 cells
HEV	High endothelial venules
HLA	Human leukocyte antigen
HMGB1	High mobility group box 1 protein
HRP	Horseradish peroxidase
HSA	Human Serum Albumin
ICL2s	Intracellular Loop 2

IFN	Interferon
IFNR	IFN receptor
IHC	Immunohistochemistry
IKK	Inhibitory-κB kinase
IL	Interleukin
IL-1RAcP	IL-1 receptor accessory protein
ILC2	Group 2 innate lymphoid cell
IMQ	Imiquimod
iNKT	Invariant natural killer
IP	Immunoprecipitation
IRAK1	Interleukin 1 Receptor Associated Kinase 1
IRF	Interferon regulatory factors
IRI	Ischemia-reperfusion injury
IVC	Individually ventilated caging
JAK	Janus activated kinase
JBIOS	Joint Biological Services Facilities
JNK	c-Jun N-terminal kinase
KI	Knock in
KO	Knock out
KRT	Keratin
LC	Langerhans cell
LDH	Lactate dehydrogenase
LM	Light microscopy
LT	Leukotriene
LOR	Loricrin
LP	Lichen Planus
LPS	Lipopolysaccharides
LUBAC	Linear ubiquitin chain assembly complex
MAPK	Mitogen-activated protein kinase

MCMV	Murine cytomegalovirus
MD-2	Myeloid Differentiation factor 2
MEK1	Mitogen-activated protein kinase
MIP-2	Macrophage inflammatory protein 2
MLKL	Mixed lineage kinase domain-like pseudokinase
MPT	Mitochondrial permeability transition
mTOR	Mechanistic target of rapamycin
MyD88	Myeloid differentiation primary response 88
NADH	Nicotinamide adenine dinucleotide
NEMO	NF-κB essential modulator
NET	Neutrophil cellular traps
NF-κB	Nuclear Factor Kappa Beta
NFDM	Non-fat dry milk
NHEK	Normal human epidermal keratinocytes
NK	Natural killer cells
NKT	NKT cells
NLR	Nod-like receptors
NLRP3	NLR protein 3
NLS	Nuclear localisation sequence
NOX	NADPH oxidase
NSA	Necrosulfamide
OCT	Optimal cutting temperature
OVA	Ovalbumin
P	Postnatal day
PAGE	Polyacrylamide gel electrophoresis
PARP	Poly-(ADP ribose)-polymerase
PBS	Phosphate buffered saline
PCR	Polymerase chain reaction
PFA	Paraformaldehyde

PGD	Prostaglandin
PI	Propidium iodide
PI3K	Phosphatidylinositol 3-kinase
PKR	Protein kinase RNA-activated
PMK	Primary mouse epidermal keratinocytes
PP	Pustular psoriasis
PPL	Project licence
PRR	Pattern-recognition receptors
PsA	Psoriatic arthritis
PV	Psoriasis vulgaris
PVDF	Polyvinylidene difluoride
RA	Rheumatoid arthritis
RAGE	Receptor for advanced glycation endproducts
RCD	Regulated cell death
RHIM	RIP homotypic interaction motif
RIPA	Radioimmunoprecipitation assay buffer
RIPK	Receptor-interacting serine/threonine-protein kinase
RNA	Ribonucleic acid
RS	Reductase system
SCAR	Severe adverse drug reaction
SDS	Sodium Dodecyl Sulfate
SEB	Staphylococcal enterotoxin B
SJS	Stevens-Johnson Syndrome, a SCAR
SLE	Systemic lupus erythematosus
ST2	Suppressor of tumorigenicity
STAT	Signal transducer and activator of transcription
TAK1	Transforming growth factor beta-activated kinase 1
TBSA	Total body surface area
TEN	Toxic epidermal necrolysis

Th	T-helper
TIM	T-cell immunoglobulin and mucin-domain containing
TIR	Toll/Interleukin-1 receptor
TLRs	Toll-like receptors
TNF	Tumour necrosis factor
TNFR	TNF-receptor
TPA	Tetradecanoyl phorbol acetate
TRADD	TNFR1-associated death domain protein
TRAF	TNFR-associated factor
TRAIL	TNF-related apoptosis-inducing ligand
TRAILR	TRAIL receptor
TRIF	Toll/interleukin-1 receptor domain-containing adapter-inducing interferon
TS	TNF + Smac mimetic
TSLP	Thymic stromal lymphopoietin
TSZ	TNF+ Smac mimetic + z-VAD-fmk
WR	Working reagent
WST	Water-soluble tetrazolium
ZBP1	Z-DNA-binding protein 1

Table of contents

List of figures

List of tables

Chapter 1

General introduction

1.1 Necroptosis, a new form of cell death

1.1.1 Introduction to regulated cell death

Cell death plays an essential role in the development and homeostasis of multicellular organisms through the elimination of unnecessary or potentially dangerous cells. Homeostasis is maintained as a delicate equilibrium between cell death and proliferation (Vaux & Korsmeyer, 1999). An unbalance in this equilibrium, leading to excess or resistance to cell death is responsible for diseases such as cancer resistance or organ failure. In human adults, around 100 thousand million (10^{11}) cells die and are replaced by new cells every day (Ellis et al., 1991). Absence or malfunction of cell death processes, however, can lead to developmental issues, inflammation, autoimmunity or immunodeficiency (Majno & Joris, 1995).

Historically, three distinct types of cell death have been described according to morphology and phagocytic clearance (Schweichel & Merker, 1973): type I cell death or apoptosis, type II cell death known as autophagy-dependent cell death and type III cell death or necrosis. Apoptosis is executed by caspases and leads to distinguishable morphology features such as cytoplasmic shrinkage, chromatin condensation (pyknosis) and nuclear fragmentation (karyorrhexis). The plasma membrane forms irregular bulges (blebs) without integrity

disruption (Figure 1.1). Apoptosis culminates with the formation of apoptotic bodies, which exhibit phosphatidylserine on the outer leaflet of the plasma membrane that allow to be recognised by macrophages and other phagocytic cells (Figure 1.1) (Kroemer et al., 1998). This leads to the engulfment and clearance of dead cell bodies without eliciting inflammatory responses (Fadok et al., 1992). Apoptosis can be triggered by conditions in the extracellular environment that activate death receptors (extrinsic pathway) or by non-receptor-mediated stimuli that produce intracellular signals leading mitochondrial-initiated events (intrinsic pathway). Each pathway activates its own initiator caspase (Casp), Casp-8 and 9 for extrinsic and intrinsic apoptosis respectively, and both converge in the cleavage and activation of the executioner Casp-3 (Majno & Joris, 1995). (Fadok et al., 1992).

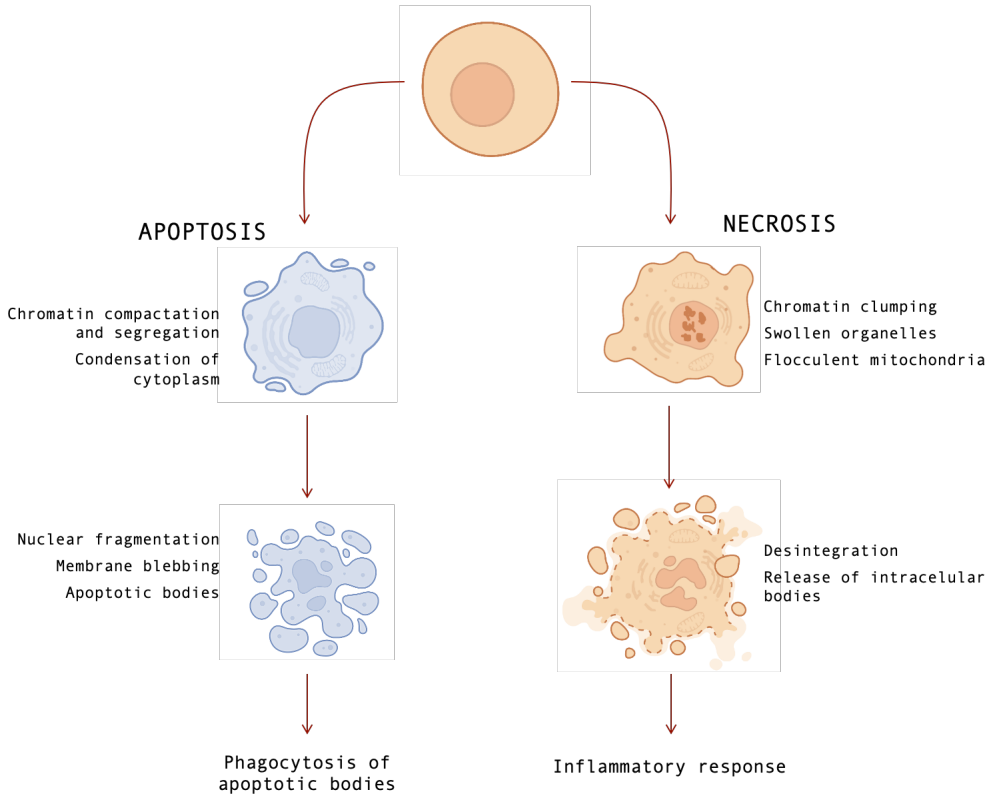

Figure 1.1: Apoptotic versus necrotic morphological features and consequences. Cells that undergo apoptosis are characterised by distinct features when compared to necrosis, some of which are shown in the figure. Furthermore, apoptosis generally leads to the phagocytosis of apoptotic bodies, remaining immunologically silent, while

the release of intracellular content as a consequence of necrosis can trigger an inflammatory response.

Necrotic cell death, on the other hand, displays cellular rounding and swelling, increased cytoplasmic granularity with intact nuclei and, finally, membrane rupture. Membrane permeabilization leads to leak of intracellular content containing damage associated molecular patterns (DAMPs) or alarmins, which can act as pro-inflammatory factors and activate the immune system (Figure 1.1) (Galluzzi et al., 2007). Hence, other than their distinct morphological characteristics, necrosis differs from apoptosis on its capacity to trigger an inflammatory response. Finally, autophagy-dependent cell death exhibits extensive cytoplasmic vacuolisation and phagosome formation resembling autophagic digestion and, similar to apoptosis, results in phagocytic uptake and lysosomal degradation without initiation of an inflammatory response.

Cell death modalities can be differentiated between accidental cell death (ACD)- the instantaneous destruction of cells exposed to severe insults of physical chemical or mechanical nature— and regulated cell death (RCD), which relies on a dedicated molecular machinery, implying that it can be modulated by pharmacological or genetic interventions (Galluzzi et al., 2018). Apoptosis has long been considered as the only form of regulated cell death (Kerr et al., 1972; Majno & Joris, 1995). In contrast to the organised packaging that occurs during apoptosis, necrosis was considered a passive, unregulated form of cell death and was often associated to unfinished apoptosis. It is now known that, under conditions of unpaired efferocytosis, cells can undergo a process of disintegration and release of intracellular content after apoptosis, which is termed secondary necrosis (T. Vanden Berghe et al., 2010).

This view was first challenged by the description of tumour necrosis factor (TNF) as an inducer of a form of cell death that exhibited the morphological

hallmarks of necrosis (Laster et al., 1988). Further studies in the 1990s demonstrated that defective caspase signalling did not prevent cell death but, instead, diverged the pathway to a form of cell death that was non-apoptotic and caspase-independent with similar necrotic morphological features (Grooten et al., 1993; Vercammen et al., 1998). This type of necrotic cell death, which can be blocked by chemical inhibition or knock-out of specific genes was termed necroptosis (Degterev et al., 2005; L. Sun et al., 2012; D.-W. Zhang et al., 2009). Since the characterisation of necroptosis, several other forms of programmed necrosis have been described such as pyroptosis, a Casp-1-dependent process that depends on inflammasome activation; ferroptosis, a form of cell death characterised by iron-dependent lipid peroxidation and metabolic constraints; parthanatos, a cell death modality characterised by the accumulation of poly (ADP) ribose (PAR); or mitochondrial permeability transition (MPT)-driven cell death, characterised by an increase in the permeability of the inner mitochondrial membrane (Figure 1.2) (Galluzzi et al., 2018).

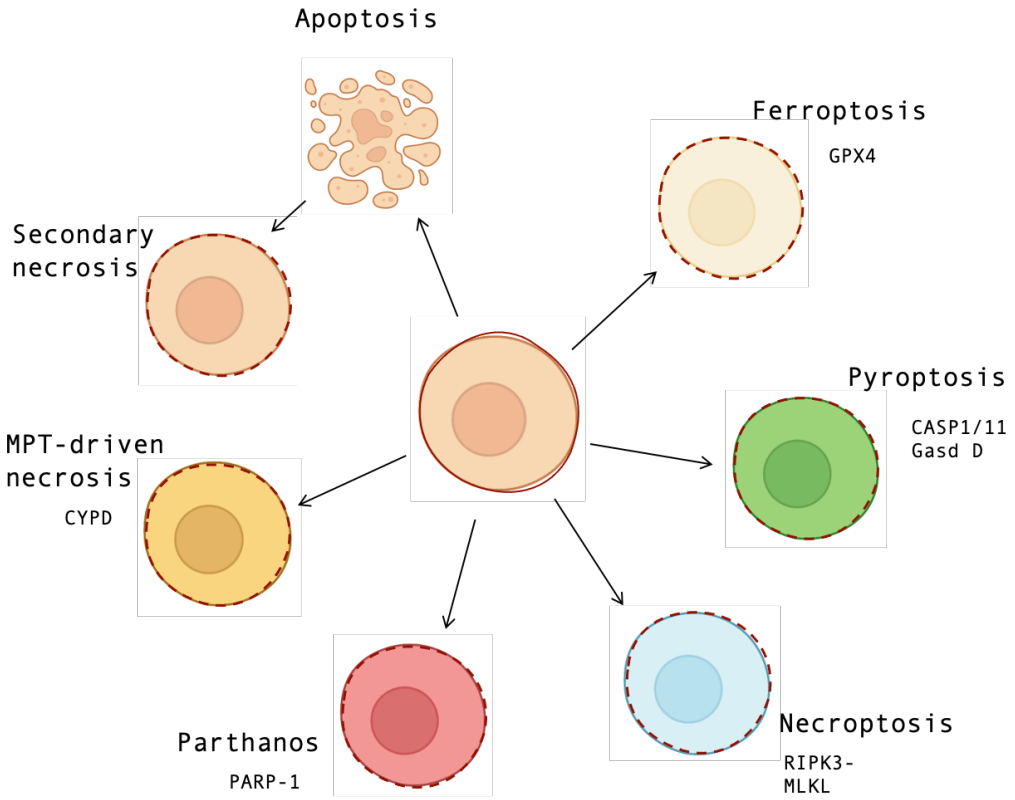

Figure 1.2: Overview of the major regulated forms of regulated cell death, main inducers and executor molecules. Programmed necrotic processes display necrotic morphology characterised by plasma membrane disruption, represented by a dotted line. Apoptosis is characterised by membrane blebbing and can result in secondary necrosis. Ferroptosis is initiated by intracellular oxidative perturbations and is under constitutive control of glutathione peroxidase 4 (GPX4). Pyroptosis depends on Casp-1 activation and plasma membrane pore formation by Gasdermin-D (Gasd-D). Necroptosis can be triggered by several inducers (TNF, LPS or IFN) and is generally dependent on receptor-interacting protein kinase 3 (RIPK3) and mixed lineage kinase domain-like (MLKL) activation. Parthanos is initiated by poly-(ADP ribose)-polymerase 1 hyperactivation; Mitochondrial permeability transition pore (MPT)-driven necrosis can be triggered by perturbations of the intracellular microenvironment and is dependent on cyclophillin D (CYPD).

1.1.2 The necroptosis signalling pathway

Cells undergoing necroptosis exhibit several necrosis-associated morphological features, including cell and organelle swelling, loss of plasma membrane integrity and cell lysis. While the adaptor proteins involved in the execution of necroptosis vary depending on the initial trigger, activation of necroptosis leads to the formation of the necrosome.

The necrosome is an association of specific executioner molecules that can include receptor-interacting serine/threonine-protein kinase 1 (RIPK1) and always includes RIPK3 and mixed lineage kinase domain like pseudokinase (MLKL). Ultimately, a series of phosphorylations and conformational changes leads to the phosphorylation, activation, and oligomerisation of MLKL, which forms pores at the plasma membrane, compromising its integrity (Pasparakis & Vandenabeele, 2015).

Necroptosis can be triggered by the activation of specific death receptors (DR), such as TNF receptor 1 (TNFR1), TNF-related apoptosis-inducing ligand [TRAIL] receptor 1 (TRAILR1, also known as DR4), TRAILR2 (also known as DR5), and Fas (also known as CD95 or APO-1) (Chan et al., 2015). However, insights into the molecular mechanisms of necroptosis have been obtained largely from studies following TNF stimulation of TNFR1. TNFR1 engagement leads to the trimerization of the receptor, which initiates the assembly of a transient molecular complex named complex I, consisting of TNFR1-associated death domain protein (TRADD), TNFR-associated factor 2 (TRAF2), cellular inhibitor of apoptosis proteins 1 and 2 (cIAP1/2) and RIPK1 (reviewed in Pasparakis & Vandenabeele, 2015).

RIPK1 was the first identified protein found to be crucial for necroptosis (Holler et al., 2000). RIPK1 is an integrator of TNFR1 signals and is involved in the activation of pro-survival nuclear factor-κB (NF-κB) and mitogen activated protein kinase (MAPKs), apoptosis and necroptosis. It is formed by an N-terminal kinase domain, an intermediate domain and a C-terminal death domain (Figure 1.3). *Ripk1*$^{-/-}$ animals die perinatally due to increased systemic inflammation (Berger et al., 2014; Kelliher et al., 1998; Rickard, O'Donnell, et al., 2014). Knock-in (KI) of kinase-inactive RIPK1 mutant alleles rescues *Ripk1*$^{-/-}$ lethality (Kaiser et al., 2014; Kelliher et al., 1998; Rickard, O'Donnell, et al., 2014), suggesting that the scaffolding

function of RIPK1 is essential in restricting cell death during development (Holler et al., 2000). However, the kinase function of RIPK1 has been shown to be necessary for both necroptosis and apoptosis given that kinase-dead KI cells are protected from RIPK3-mediated necroptosis and Casp-8 mediated apoptosis (Dillon et al., 2014; Kaiser et al., 2014; Kearney et al., 2014; Rickard, O'Donnell, et al., 2014). RIPK1 also possesses a RIP homotypic interaction motif (RHIM) domain, required for the recruitment of other RHIM-containing proteins such as RIPK3, Toll/interleukin-1 receptor domain-containing adapter-inducing interferon-β (TRIF, an adapter for Toll-like receptor 3 [TLR3] and TLR4) and Z-DNA-binding protein 1 (ZBP1), also known as DNA-dependent activator of interferon-regulatory factors (DAI) (Kaiser & Offermann, 2005; Rebsamen et al., 2009; X. Sun et al., 2002). RIPK3 is a homologous kinase of RIPK1, with a similar RHIM domain and N-terminal kinase domain (Figure 1.3), which has been shown to be essential regulator for necroptosis (Cho et al., 2009; He et al., 2009, 2011; Newton et al., 2004; Upton et al., 2012; D. W. Zhang et al., 2009).

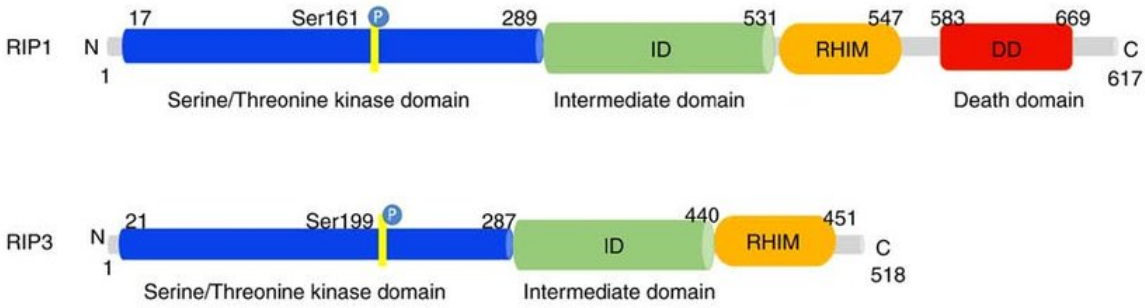

Figure 1.3: Structures of human RIPK1 and RIPK3. RIPK1 (RIP1) and RIPK3 (RIP3) are both formed by a serine/threonine kinase domain, an intermediate domain and a RHIM domain. RIPK1 additionally possesses a death domain in its C-terminus. The main phosphorylation sites necessary for the execution of necroptosis are indicated. Modified from Yuping Liu et al. (2019).

RIPK1 is heavily ubiquitylated in complex I, functioning as a scaffold for the recruitment of NF-κB essential modulator (NEMO) and transforming growth factor beta-activated kinase 1 (TAK1), critical mediators of the TNF-dependent activation of NF-kB and MAPK pathways, respectively (Kelliher et al., 1998; W. Zhou & Yuan, 2014). These signalling pathways generally result in increased cell survival, proliferation, and production of pro-inflammatory cytokines (Figure 1.4). As a result of complex RIPK1 deubiquitylation (described in detail in section 1.1.3), FADD is recruited to join RIPK1 and TRADD. These, in turn, recruit and dimerize Caspase-8 (Casp-8) to form the cytosolic complex IIa or death-inducing signalling complex (DISC), which activates caspase-8 to induce extrinsic apoptosis (Figure 1.4). In contrast to TNFR1 signalling, binding of FAS ligand (FASL) to FAS or of TRAIL to TRAILR1/2 induces the direct assembly of DISC, without formation of a previous pro-survival signalling complex (Grootjans et al., 2017).

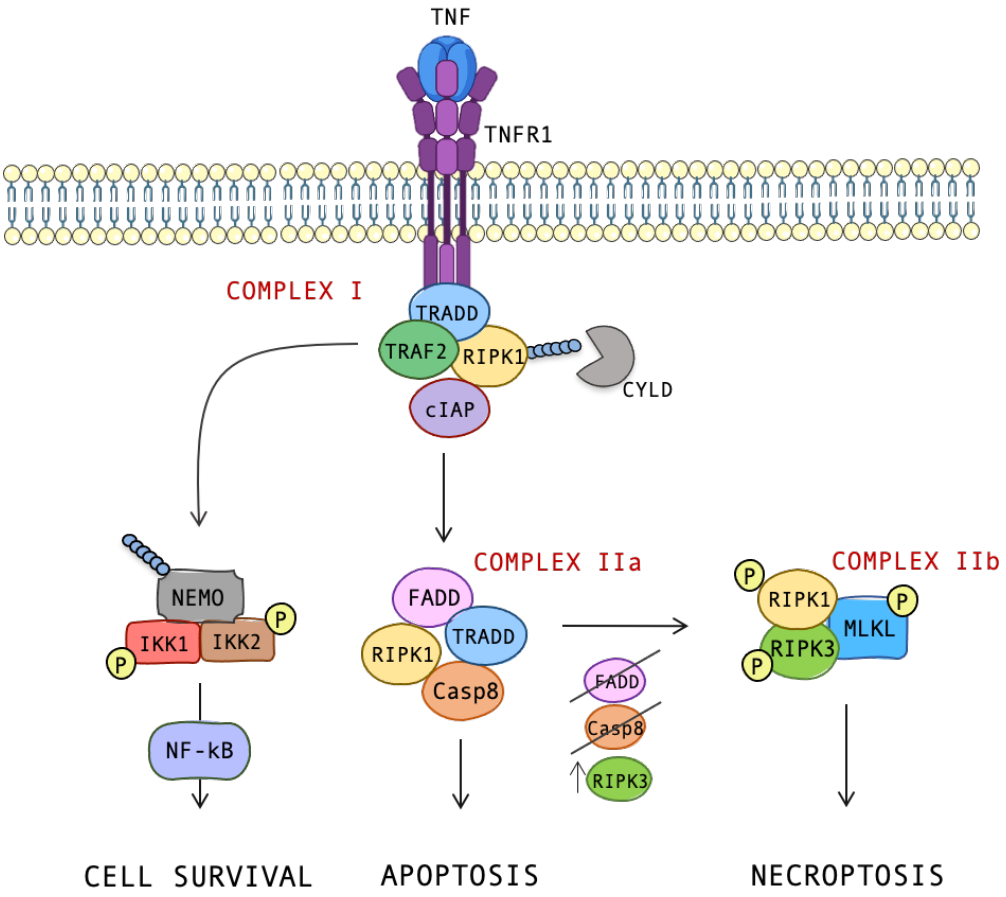

Figure 1.4: Schematic summarised view of consequences of TNFR1 activation. Signalling through TNFR1 leads to the formation of complex I at the plasma membrane, composed of TRADD, TRAF2, RIPK1 and cIAPs which leads to the activation of NF-κB pathway, which promotes pro-inflammatory responses and cell survival. Deubiquitylation of RIPK1 by several enzymes leads to the recruitment of FADD and Casp-8 to form Complex IIa, which activates caspase-dependent extrinsic apoptosis. Absence of Casp-8, FADD or increased RIPK3 leads to the formation of Complex IIb or the necrosome, responsible for the execution of necroptosis.

Absence of Casp-8 activity (either through inhibition or genetic deletion), deletion of FADD, or increased RIPK3 expression, allows deubiquitylated RIPK1 to recruit RIPK3 via RHIM interaction (X.-N. Wu et al., 2014). This facilitates the formation of complex IIb, or what is termed as the canonical necrosome, composed of, RIPK1, RIPK3 and MLKL (Figure 1.4) (Chan et al., 2015). Necrosome assembly leads to the phosphorylation of the RIPK3 activation loop (L. Sun et al., 2012). Although the hypothesis of transphosphorylation between RIPK1 and RIPK3 was initially suggested, later studies indicate that RIPK1 does not, in fact, phosphorylate RIPK3

(Cho et al., 2009). The major substrate of the catalytic activity of RIPK1 is itself (in the RIPK1 kinase domain), through autophosphorylation. Similarly, the only reported substrates of the RIPK3 catalytic activity are the RIPK3 kinase domain by autophosphorylation and the activation loop of MLKL (J. M. Murphy et al., 2013; Rodriguez et al., 2016; L. Sun et al., 2012). The current proposed theory is that, before activation of necroptosis, RIPK1 exists at a conformation in which its RHIM domain is unavailable. Activation of RIPK1 through diverse mechanisms results in autophosphorylation, which allows the interaction of the RIPK1 and RIPK3 RHIM domains (Dondelinger, Vandenabeele, et al., 2016). This interaction promotes RIPK3 oligomerization, which is required for RIPK3 activation by autophosphorylation. Interestingly, overexpression of RIPK3 or induced dimerization is sufficient to phosphorylate RIPK3 and execute necroptosis (Raju et al., 2018; X.-N. Wu et al., 2014), suggesting that the main function of RIPK1 upstream RIPK3 consists of promoting RIPK3 oligomerization.

Other than death receptors, necroptosis can be triggered by the activation of pathogen recognition receptors (PRRs), including TLR3, TLR4, as well as IFN receptors (IFNRs), (Pasparakis & Vandenabeele, 2015). Engagement of these receptors by different triggers leads to the formation of non-canonical necrosomes (Figure 1.5). In contrast to the RIPK1-dependent recruitment of RIPK3 during TNF-induced necroptosis, binding of LPS or various DAMPs to TLR-4 or TLR-3 leads to the recruitment and activation of RIPK3 through homotypic interaction with TRIF (Figure 1.5) (Dillon et al., 2014; Kaiser, Sridharan, et al., 2013; Polykratis et al., 2014). Similarly, execution of necroptosis in response to ds-DNA viruses depends on the RHIM-mediated recruitment of RIPK3 by ZBP1 (Rebsamen et al., 2009; Upton et al., 2012). Necroptosis has also been suggested to be triggered by type I and II interferons, which activate JAK-STAT signalling. The RNA-activated protein kinase PKR has been suggested to

play a role in IFN-induced necroptosis (Thapa et al., 2013), although contradictory studies have been reported (McComb et al., 2014). Instead, more recent studies report that ZBP1 is required for IFN-induced necroptosis (D. Yang et al., 2020)

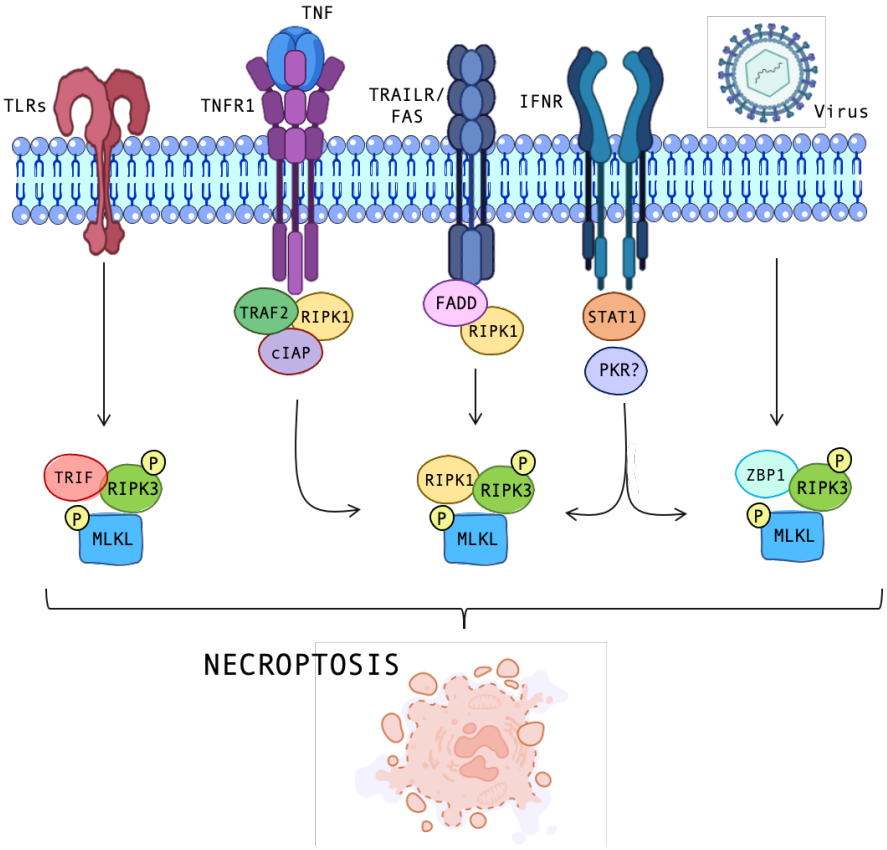

Figure 1.5: Receptor signalling leading to necroptosis. Necroptosis can be triggered by the activation of several receptors, including DRs such as TNFR1, TLRs, TRAILR/Fas, IFNR or interaction with ds-DNA viruses. The necrosome components in response to each trigger varies, and non-canonical necrosomes have been described in following TLR, IFNR1 activation as well as in response to viruses. Non-canonical necrosomes involve RHIM-containing proteins other than RIPK1: TRIF or ZBP1.

Regardless of the upstream stimulus, RIPK3 oligomerization and phosphorylation lead to the recruitment of MLKL, via its pseudokinase domain (Davies et al., 2018; Petrie et al., 2018; L. Sun et al., 2012). MLKL is composed of an N-terminal four-helix bundle domain (4HB) and a C-terminal pseudokinase domain (psKD), connected by a two-helix linker or brace (J. M. Murphy et al., 2013). RIPK3 phosphorylates MLKL at Thr-357

and Ser-358 in humans (L. Sun et al., 2012) and Ser-345, Ser-347 and Thr-349 in mice (J. M. Murphy et al., 2013). Phosphorylation of these residues, present in the activation loop of the psKD, induce a conformational change that uncovers the 4HB domain (Petrie et al., 2018), also termed "killer" domain. Prior to activation, MLKL is believed to exist as a dormant monomeric form (Figure 1.6), in which the 4HB domain is sequestered through engagement with the psKD (Petrie et al., 2018). Phosphorylation of MLKL (ph-MLKL) triggers its oligomerization into trimers in mouse MLKL (Cai et al., 2014; Davies et al., 2018; Hildebrand et al., 2014), while human MLKL forms tetramers *in vitro* (Petrie et al., 2018). Oligomerized ph-MLKL translocates to the membrane (Figure 1.6), where it interacts with phosphatidylinositol lipids or cardiolipin to induce membrane permeabilization resulting in disruption of osmotic homeostasis (Xia et al., 2016). Calcium (Ca^{+2}) influx has been suggested to play a role in the execution of necroptosis, although how critical is that role remains controversial (Cai et al., 2014; Nomura et al., 2014; Ros et al., 2017). Interestingly Ca^{+2}-calmodulin-dependent protein kinase (CaMKII) has been recently described as a substrate of RIPK3, which can mediate myocardial necroptosis independently of RIPK1 and MLKL (Y. Yang et al., 2021; T. Zhang et al., 2016; T. Zhou et al., 2021).

Although oligomerisation plays a key role in MLKL activation, is not sufficient *per se* to induce necroptosis given that a specific mutation of the human MLKL domain α4 helix was able to abolish the deadly function of MLKL without disrupting its capacity to oligomerise (Petrie et al., 2018). Similar observations have been made in mouse MLKL (Hildebrand et al., 2014; Tanzer et al., 2016), supporting necroptosis can also be regulated following necrosome formation, MLKL phosphorylation and oligomerisation (Figure 1.6).

1.1.3 Regulation of necroptosis

Maintaining the correct frequency and balance between different types of cell death, including ensuring neither excessive or inefficient cell death occurs, is crucial to maintain tissue homeostasis and prevent diseases. Multiple mechanisms take place to control the initiation and execution of necroptosis, highlighting the complexity of these and other cell death pathways.

RIPK1 can play opposing roles preventing or promoting cell death due to tight regulation of the balance between its kinase-dependent and -independent functions. Ubiquitination of RIPK1 on lysine 63 (K63), K11, K48 and linear M1 ubiquitin chains prevent the formation of death inducing complexes, promoting its pro-survival role through NF-κB and MAPK pathways (see Figure 1.3). Ubiquitin ligases cIAPs and linear ubiquitin chain assembly complex (LUBAC) both negatively regulate RIPK1-mediated cell death through the K63 ubiquitylation of RIPK1 and linear M1 ubiquitylation of TRADD, respectively (Dondelinger, Darding, et al., 2016). The latter are removed by deubiquitylating enzyme cyclophilin D (CYLD), a necessary step to initiate RIPK1-dependent cell death. A20, on the other hand, is a complex ubiquitin-modifying enzyme that acts both deubiquitinating K63-linked chains from RIPK1 restricting NF-κB activation and ubiquitinating K48-linked ubiquitin chains targeting RIPK1 for proteasomal degradation (Lork et al., 2017; Wertz et al., 2004). A20-deficient mice, mice with impaired LUBAC components and mice bearing RIPK1 with mutations on K63 sites display severe inflammation or embryonic lethality that could be at least partially prevented by deletion of RIPK3, MLKL or Casp-8 (Kumari et al., 2014; E. G. Lee et al., 2000; Peltzer et al., 2014, 2018; Rickard, Anderton, et al., 2014; Yong Tang et al., 2019; Xixi Zhang et al., 2019), making evident the importance and

complexity of RIPK1 ubiquitin regulation. Similarly, ubiquitination of RIPK3 at K5 has been reported to be required for necrosome formation while ubiquitin removal by A20 restricts necroptosis (Onizawa et al., 2015). Ubiquitination by other ubiquitin ligases such as C-terminus of Hsc70-interacting protein (CHIP) and Pellino1 (Peli1) induce RIPK3 degradation and consequently negatively regulates necroptosis (Figure 1.6) (S.-W. Choi et al., 2018; Seo et al., 2016).

Other than ubiquitination, the necroptotic cascade can be highly regulated through phosphorylation. Phosphorylation of RIPK1 on several residues by MK2 or IKK has been shown to restrain its kinase activity (Dondelinger et al., 2017; Jaco et al., 2017; Menon et al., 2017; Daichao Xu et al., 2018), negatively regulating RIPK1-induced cell death. Dephosphorylation of RIPK3 (S277 in humans, T231/S232 in mice) can be catalysed by the Ppm1b phosphatase, negatively regulating necroptosis, and absence of Ppm1b enhances TNF-induced tissue damage (W. Chen et al., 2015). Another key determinant of necroptotic cell death is the cellular levels and availability of RIPK3 in the cell. For example, RIPK3 is not normally expressed in the liver, although its expression can be induced following injury (Dara, 2018).

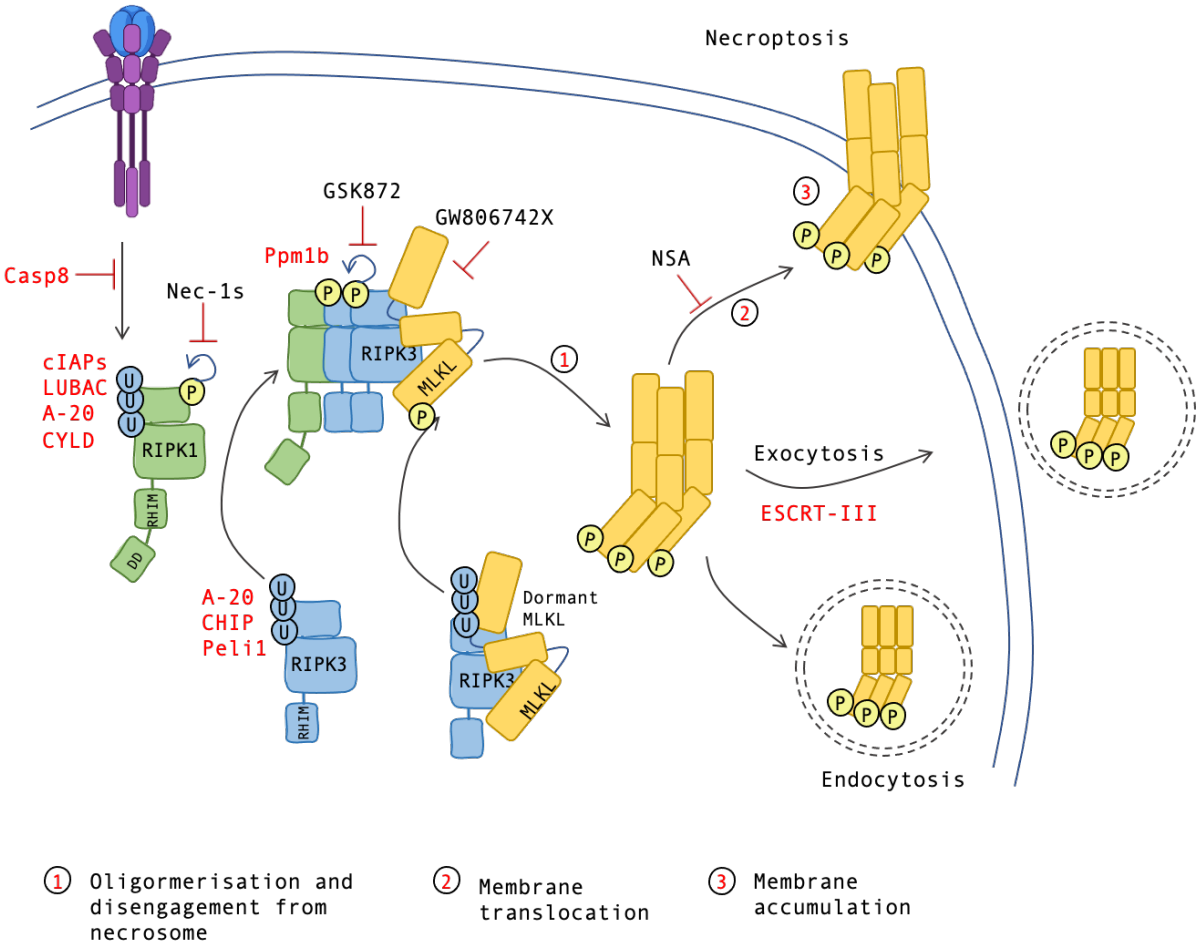

Figure 1.6: The necroptosis pathway is highly regulated through ubiquitination, phosphorylation and other mechanisms. Necroptosis can be initiated through TNFR1 activation at the plasma membrane. Inhibition of Casp-8, as well as deubiquitylation of RIPK1 (cIAPs, LUBAC, A-20, CYLD) is necessary for the initiation of necroptosis. Autophosphorylation of RIPK1 (inhibited by Nec-1s) is necessary for the recruitment of RIPK3 through RHIM domains. RIPK3 can also be targeted for ubiquitylation (A-20, CHIP, Peli1). Its phosphorylation can be targeted by phosphatases (Ppm1b), and its kinase activity inhibited by GSK872 (among many others). Post-necrosomal checkpoints include disengagement from the necrosome, membrane trafficking and accumulation of oligomeric phosphorylated MLKL. Translocation to the membrane can be inhibited by NSA or MB37. Necroptosis can be further regulated through exocytosis (through ESCRT-III machinery) or endocytosis of oligomerised and phosphorylated MLKL.

It is known that Casp-8 can cleave several proteins involved in the regulation of necroptosis including RIPK1, RIPK3, CYLD and cFLIP. Casp-8 is known to negatively regulate necroptosis. In fact, a Casp-8 inhibition is required to induce necroptosis *in vitro,* together with a smac mimetic, that targets IAPs (Grootjans et al., 2017). *Casp-8*$^{-/-}$ mice die in utero

(E10.5) and are completely rescued by deletion of either RIPK3 or MLKL (Alvarez-Diaz et al., 2016; Kaiser et al., 2011; Oberst et al., 2011), which suggests that cleavage of RIPK1 by Casp-8 inhibits necroptosis. Several studies have shown that mice expressing RIPK1 bearing mutations that prevent caspase-8 induced cleavage also die in utero (Lalaoui et al., 2020; Newton et al., 2019; Xixi Zhang et al., 2019) However, this lethality was not fully rescued by the deletion of RIPK3 and MLKL and was only achieved by the combined deletion of FADD/Casp-8, RIPK3 and MLKL, showing that RIPK1 cleavage by Casp-8 acts preventing both apoptosis and necroptosis (Lalaoui et al., 2020; Newton et al., 2019; Xuhua Zhang et al., 2019). In addition, the catalytic activity of Casp-8 is closely controlled by cFLIP and IAPs (Irmler et al., 1997; C. Scaffidi et al., 1999), which regulate RIPK1-induced cell death by extension. Casp-8 cleavage of RIPK3 has also been proposed as a mechanism to restrict necroptosis (S. Feng et al., 2007; Oberst et al., 2011), although the mechanisms remain unclear. Of note, Casp-8 has also been reported to regulate pyroptosis, another form of regulated necrosis (Fritsch et al., 2019).

In addition, several regulating mechanisms downstream MLKL phosphorylation have been described, in an attempt to maintain cell survival. These mechanisms target MLKL oligomerisation, disengagement from the necrosome (Garnish et al., 2021) as well as its translocation to the membrane (Petrie et al., 2020), mediated by the Golgi-/actin-/microtubule-trafficking machinery (Samson et al., 2020). Trafficking and accumulation of MLKL at the plasma membrane has been reported to act as a threshold and control the kinetics of necroptosis (Figure 1.6) (Samson et al., 2020). Indeed, auxiliary proteins HSP-90 or HSP-70 have shown to regulate necroptosis by modulating the stability of MLKL, mediating its oligomerisation and translocation to the membrane (Jacobsen et al., 2016; X. M. Zhao et al., 2016) or facilitating for MLKL polymerization (Johnston

2020), respectively. The endosomal sorting complexes required for transport III (ESCRT-III) machinery, a regulator of endosome trafficking, modulates necroptosis regulating MLKL activity by promoting the formation of extracellular vesicle that remove ph-MLKL from the membrane following MLKL translocation and disruption of the plasma membrane (W. Fan et al., 2019; Y. N. Gong et al., 2017; Yoon et al., 2017). Similarly, the necroptosis-dependent cell membrane damage can be modulated through flotillin-mediated endocytosis of membrane-bound ph-MLKL (Figure 1.6) (W. Fan et al., 2019).

1.1.4 Physiological relevance of necroptosis

The physiological relevance of necroptosis became obvious through the complete rescue of *Casp-8*$^{-/-}$ embryonic lethality by the deletion of RIPK3 (Kaiser et al., 2011). In contrast to the well-defined role of apoptosis, the necroptotic core effectors are not essential to embryonic development. Indeed, whereas mutant mice lacking key components of the apoptotic machinery show severe developmental issues (Cecconi et al., 1998; Kuida et al., 1996, 1998), *Ripk3*$^{-/-}$ and *Mlkl*$^{-/-}$ mice do not exhibit any development consequences or obvious phenotype (Newton et al., 2004; J. Wu et al., 2013). Similarly, kinase-dead knock-in RIPK1 mutant mouse lines (carrying K45A, ΔG26F27 and D138N) show normal development (Yongbo Liu et al., 2017; Polykratis et al., 2014; Shutinoski et al., 2016).

1.1.4.1 *Consequences of membrane disruption*

As a lytic form of cell death, necroptosis releases DAMPs, which mediate inflammation (Kaczmarek et al., 2013). The concept of DAMP was first proposed by P. Matzinger in 1994 in an attempt to explain the strong inflammatory response in the absence of pathogens and their products, termed sterile inflammation (Matzinger, 1994). DAMPs are endogenous

molecules that play diverse non-inflammatory roles during cell homeostasis. In response to stressors, that include physical, chemical, metabolic and infectious factors, DAMPs can be passively released, actively secreted, or exposed in the surface (Aziz et al., 2019; Denning et al., 2019; Krysko et al., 2013). Hence, during necroptosis, the cell environment gains access to previously hidden surfaces that are generally recognised by pattern-recognition receptors (PRRs), such as Toll-like receptors (TLRs) and cytoplasmic Nod-like receptors (NLRs), as well as by non-PRRs such as suppression of tumorigenicity 2 (ST2) or receptor for advanced glycation end products (RAGE). Resident immune cells, as well as non-immune tissue cells, bearing these receptors are crucial initiators of a local inflammatory response. Recognition of DAMPs leads to the recruitment and activation of immune cells which, in turn, express pro-inflammatory genes and secrete cytokines such as TNF or IFNs. These signals, together with released DAMPs, provide feed-forward signals that further reinforce regulated cell death in neighbouring cells (Figure 1.7). If inflammation is not resolved, continuous cell death can lead to damage of local tissue barriers such as the skin, intestine and lung, and the spread of inflammation to a systemic level, which may ultimately lead to organ necrosis and failure (Figure 1.7). Other than activating neighbouring cells, DAMPs can also exit the site of injury to promote inflammation in distal tissues (He & Wang, 2018; Sarhan et al., 2018; Silke et al., 2015).

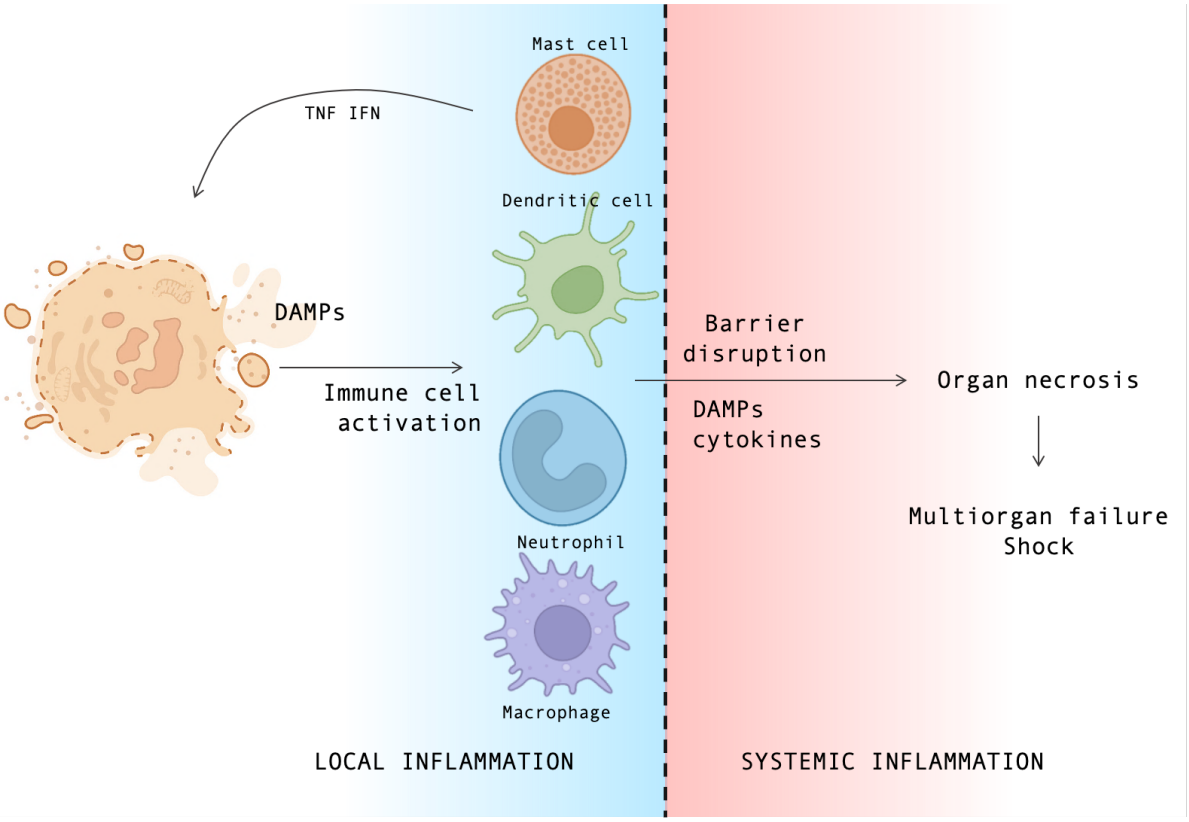

Figure 1.7: Necroptosis leads to inflammation. Release of DAMPs and proinflammatory cytokines from necroptotic cells activate immune cells including dendritic cells, macrophages, mast cells and neutrophils, which provide feed-forward signals reinforcing necroptosis in surrounding cells. Continuing the vicious death cycle can lead to damage of barrier function, the spread of cytokines to a systemic level, which may ultimately cause devastating multi-organ failure

Other than amplifying sterile inflammation, necroptosis can play an immunoregulatory role when triggered by an immunologically harmful event such as infection. It is now known that necroptosis has been conserved in mammals as a pathogen defence mechanism to adapt to viruses or bacteria that have developed mechanisms to evade extrinsic apoptosis (Kaiser, Upton, et al., 2013; Mocarski et al., 2011). *Ripk3*$^{-/-}$ mice fail to initiate a response against vaccina-virus (VV) infection, and show reduced tissue necrosis and inflammation, resulting in highly elevated viral replication and mortality (Cho et al., 2009). Similarly, *Ripk3*$^{-/-}$ mice are highly susceptible to murine cytomegalovirus (MCMV), *Yersinia pestis* and

herpes simplex virus 1 (HSV-1) infections (Nogusa et al., 2016; Upton et al., 2012; Weng et al., 2014).

1.1.4.2 *Studying necroptosis in vitro and in vivo*

Necroptosis is an important mechanism in innate immune responses against pathogens and during sterile injury. Therefore, the necroptotic pathway and its regulatory proteins have been associated with a wide range of diseases including cutaneous, pulmonary, cardiovascular, neurodegenerative, infectious, renal and hepatic diseases and cancer. The potential role of necroptotic signalling in these pathologies has been investigated using numerous animal models of tissue injury and have been extensively reviewed elsewhere (M. E. Choi et al., 2019; Khoury et al., 2020)

The kinase function of RIPK1 can be inhibited using Nec-1s (Figure 1.6), an inhibitor that has been widely used to study the contribution of necroptosis to the pathology of multiple diseases including neurological, cardiovascular, pulmonary, gastrointestinal, renal and infectious disease models (Khoury et al., 2020). However, the kinase function is also necessary for RIPK1-mediated apoptosis, indicating that Nec-1s-dependent protection from cell death should not be taken as definite proof of necroptosis. This highlights that studies using this inhibitor should be supported by further research such as genetic studies targeting RIPK3 or MLKL in animal models of disease. Some of these studies have been reviewed in M. E. Choi et al., (2019) and Tonnus & Linkermann (2017) in detail.

Other than genetic deletion, RIPK3 activity can be targeted through chemical inhibition using GSK'840, 843, and 872 (Figure 1.6), which were essential demonstrating the relevance of RIPK3 kinase function during

necroptosis (Dondelinger et al., 2014; Kaiser, Sridharan, et al., 2013; J.-X. Li et al., 2014; Rodriguez et al., 2016). However, RIPK3 has been associated with necroptosis-independent inflammatory processes such as signalling functions in cytokine production (Armaka et al., 2018), inflammasome activation (Lawlor et al., 2015) and can contribute to apoptosis (N. Khan et al., 2014; Vince et al., 2012). Indeed, a study reported that MLKL-deficient mice are less protected from kidney IRI and inflammation associated with A20 deficiency than mice deficient in RIPK3 or those expressing kinase-dead RIPK1 (Newton et al., 2014), supporting necroptosis-independent roles and RIPK3 in these models.

MLKL inhibitor necrosulfamide (NSA) (Figure 1.6), has been successfully used to block necroptosis *in vitro*. However, NSA does not inhibit murine MLKL, limiting its relevance to human cells or rat *in vivo* models (L. Sun et al., 2012). Nevertheless, *Mlkl*$^{-/-}$ mice might represent the best tool to validate necroptosis contribution to the pathophysiology of diseases *in vivo*. An extensive review of the outcome of the knock-out of MLKL knock-down of MLKL in mice models of disease, including IRI, sterile inflammation, bacterial and viral infection, metabolic, neuromuscular and haematological disease, and neoplasia has been recently published (Crutchfield et al., 2021). Although not described in detail, some necroptosis-independent functions of MLKL have been recently described, including cross-linking with other RCD mediators and translocation to the nucleus to mediate gene expression (C. Zhan et al., 2021).

The association of necroptosis with a large number of animal disease models have led to increasing interest in the involvement of necroptosis in human diseases. Detection of increased expression or upregulation of RIPK1 and RIPK3 is often used as a marker of necroptosis in tissue of different human diseases. However, since the development of phospho-

antibodies against MLKL, detection of this phosphorylated protein constitutes the best method to confirm necroptosis activation in tissue. MLKL phosphorylation has been detected in the skin of several inflammatory diseases (see section 1.2.3.4) as well as in tissue obtained from patients with chronic heart failure, unstable atherosclerosis, multiple sclerosis, several renal diseases (Molnár et al., 2019). Following the extensive evidence of necroptosis in animal models of disease and human diseases, the necroptotic signalling pathway has been established as an attractive target for clinical intervention.

1.2 Introduction to the skin

The work presented in this thesis focuses on investigating necroptosis in the skin. Therefore, a brief introduction to the skin has been included in the following section, attending to its structure, functions, and its immunological role.

1.2.1 Skin structure and functions

The skin is a complex and extensive organ that separates the body from the outside environment. It acts as a physical and chemical barrier, limiting the penetration of exogenous soluble compounds and preventing undesirable water and endogenous fluid loss (Montagna & Parakkal, 1974). Although subject to considerable body areas variations regarding thickness and melanocyte content (Wong et al., 2016), mammalian skin is structured as a stratified tissue, organised into three distinct compartments: epidermis, dermis and hypodermis (Figure 1.8). Each of these layers has unique structure, function and physiology.

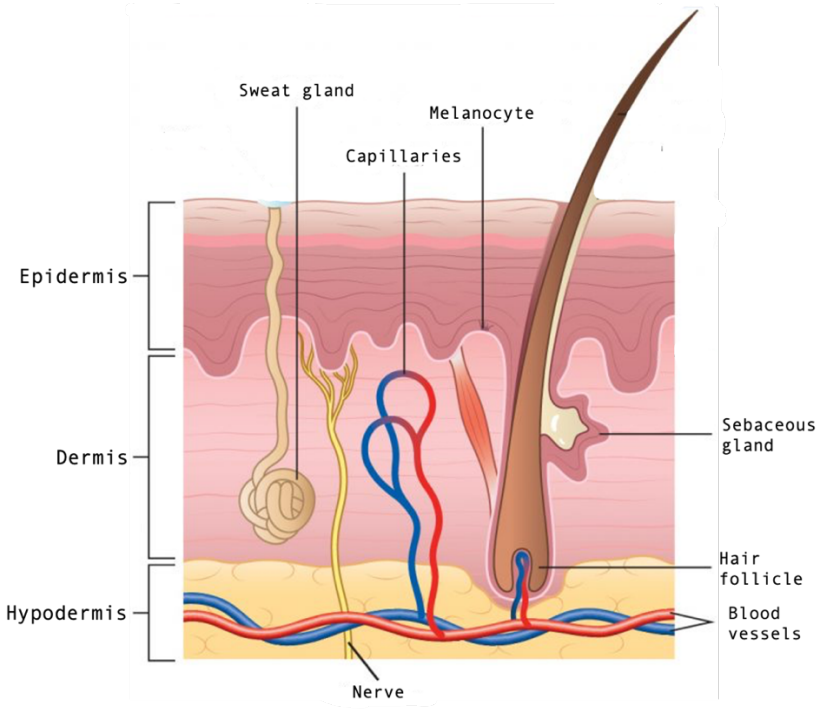

Figure 1.8: General structure of the skin. The skin is structure in three distinct layers: the hypodermis, dermis and epidermis. Blood vessels and capillaries irrigate the skin and can be found in the hypodermis and the dermis respectively. Nervous terminations are also found in the dermis. Sweat and sebaceous glands, as well as hair follicles connect the dermis and the exterior, crossing the epidermis. Adapted from Lawton, S (2019).

The hypodermis or the subcutaneous, mainly consists of loose connective tissue and adipose tissue which acts as an energy reservoir and thermoregulator. The dermis is mainly constituted by extracellular matrix (ECM), composed of collagen, fibronectin and elastin fibres synthesised by fibroblasts. This matrix provides tensile strength and mechanical resistance to the skin, as well as a matrix for immune cell migration (Wong et al., 2016). The dermis is highly vascularised by blood and lymph vessels that are distributed through the ECM, together with mechano- and thermoreceptors (Figure 1.8). During inflammation, postcapillary venules found in the dermis can increase their vascular permeability by loosening endothelial intercellular junctions. This change in permeability allows immunoglobulins, albumin and water to shift into the dermis, leading to

edema (Pasparakis et al., 2014). In addition to fibroblasts, several resident immune cells are present in the dermis (see section 1.2.2).

The outermost layer of the skin is the epidermis, whose main function is to form a physical and biological barrier with the outside environment that protects the organism from mechanical, chemical, and microbial challenges. Physically, this barrier is compromised throughout the skin by appendages such as hair follicles, sebaceous glands and sweat ducts (Figure 1.8). These provide an inside route for small molecules and chemicals as well as an outside route for water loss (Chu & Loomis, 2017). The epidermis is a stratified squamous epithelium primarily formed by tightly connected keratinocytes, organised in four distinct layers as a consequence of the constant regeneration and differentiation of keratinocytes. The specific differentiation process that keratinocytes undergo is known as cornification.. Adhesion between keratinocytes is provided by specialised protein complexes known as desmosomes (Chu & Loomis, 2017). Keratinocytes are further linked through two different types of cell-to-cell junctions: tight junctions block the flow of fluids between keratinocytes, preventing fluid loss, while gap junctions are intercellular channels that allow the passage of water, ions, and small molecules (Bäsler & Brandner, 2017). Other cells found in the epidermis are melanocytes and specific immune cells (described in section 1.2.2). Melanocytes are highly differentiated cells that produce a pigment melanin inside melanosomes, responsible for the skin pigmentation (Montagna & Parakkal, 1974).

1.2.1.1 *Cornification, a regulated form of cell death*

Epidermal keratinocytes undergo a unique form of terminal differentiation and programmed cell death known as cornification. Keratinocytes

progressively differentiate and move from the basal layer to the skin surface, forming several morphologically distinct epidermal strata/layers.

The deepest layer of the epidermis, the basal layer or *stratum basale*, is formed by stem cells which are attached through hemidesmosomes to the basal lamina, an extracellular matrix layer that separates the dermis from the epidermis (Figure 1.9). Stem cells in the skin express keratin 5 (KRT-5) and KRT-14 (Figure 1.9) and are not restricted to the basal layer as they can also be found in hair follicles. Epidermal stem cells can divide symmetrically or asymmetrically by orienting their mitotic spindle in perpendicular or parallel to the underlying basal lamina, respectively. Symmetric division leads to self-renewal of epidermal stem cells, which remain in the basal layer, while asymmetric division give rise to a more differentiated cell that moves towards the following layer. This layer is the suprabasal layer or *stratum spinosum,* where keratinocytes are progressively flattened and express KRT-1 and KRT-10 (Figure 1.9). During the cornification process, the cytoplasm of epidermal keratinocytes forms keratin polypeptides which polymerise into keratin intermediate filaments (tonofilaments) in a process known as keratinisation. The major function of keratin filaments is to provide epithelial cells with mechanical resistance (Eckhart et al., 2013).

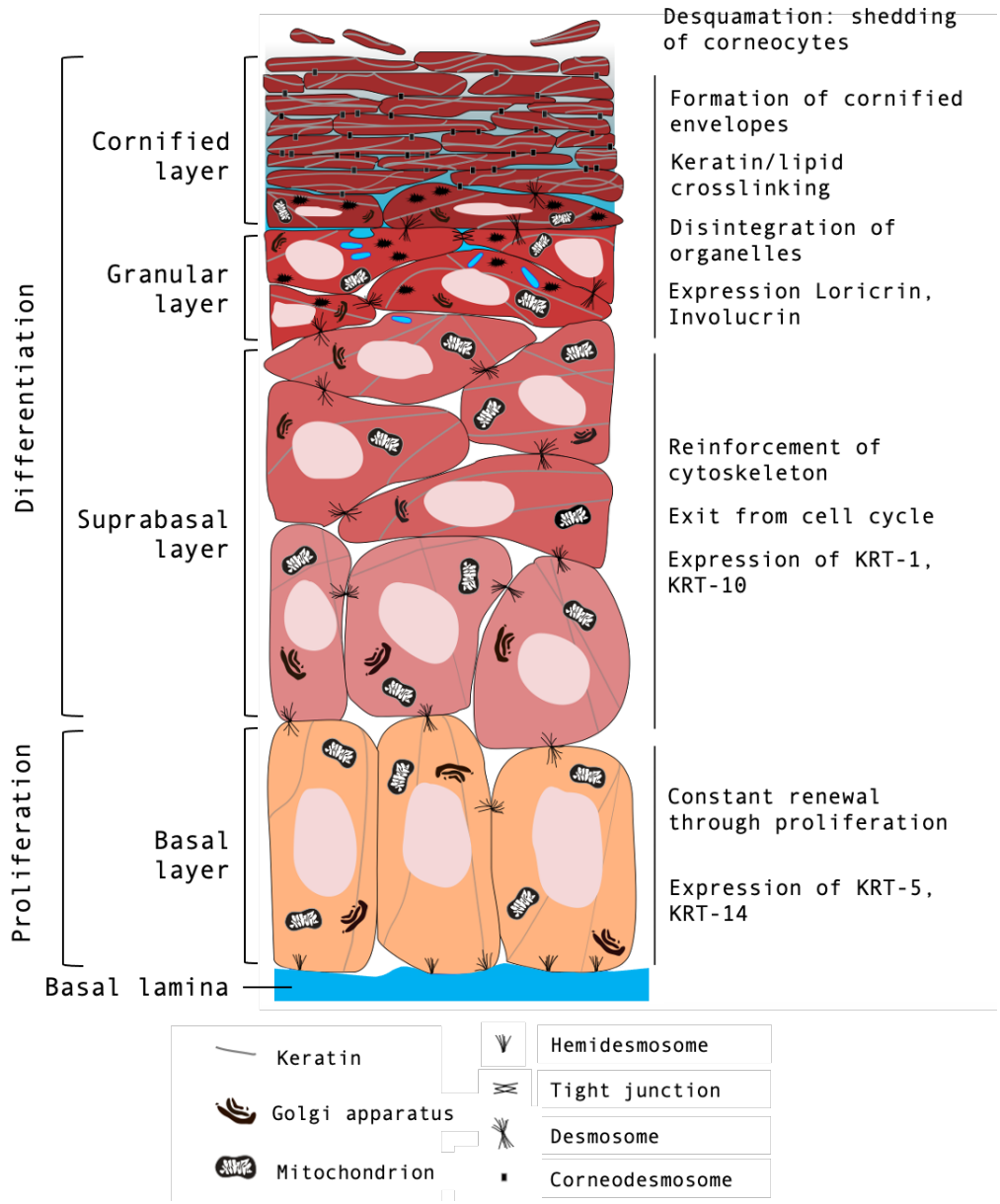

Figure 1.9: Proliferation and terminal differentiation of epidermal keratinocytes forms distinct layers. There are four layers of the epidermis, indicated on the left, which consist of keratinocytes in different stages of differentiation, tightly connected through desmosomes and tight junctions. The different layers express distinct keratins (indicated on the right) that can be used as markers of proliferation, early and late differentiation, The basal layer has the capacity to proliferate and constantly provide the epidermis with new cells. Keratinocytes in the spinous layer do not longer divide. Cells express insoluble proteins, lose their organelles, and flatten to form corneocytes, connected through corneocytes. These eventually degrade leading to desquamation. Adapted from Eckhart et al., (2013).

Superficial to the suprabasal layer is the granular layer or *stratum granulosum*, characterised by the presence of keratohyalin granules in the cytoplasm of keratinocytes. At this stage, keratinocytes shed their

cytoplasmic organelles, lose their metabolic activity and begin to express large numbers of insoluble proteins, such as loricrin and pro-filaggrin, inside keratohyalin granules, and lipids in lamellar bodies (Matsui & Amagai, 2015). These are eventually extruded from the cell and crosslinked by transglutaminases along the exterior to form an insoluble structure, known as the cornified envelope. This compacted and highly hydrophobic keratinous layer is known as the cornified layer or *stratum corneum*. It is the outermost layer of the epidermis and sheds in a process of epidermal turnover called desquamation. The total epidermal renewal time is approximately two months (Eckhart et al., 2013).

1.2.2 The skin as an immune organ

The skin plays an essential role in protecting the host by providing physical, biochemical and immunological barriers. The correct functioning of the skin immune response requires careful collaboration and communication between keratinocytes, fibroblasts, and immune cells. Keratinocytes and fibroblasts express several different patter recognition receptors (PRRs) such as TLRs, NOD-like receptors (NLRs) or Rig-like receptors (RLRs) as well as other non-PRR receptors (Pasparakis et al., 2014). Activation of these receptors can lead to the activation of MAPK or NF-kB pathways, which regulate multiple aspects of innate and adaptative immune functions.

The most prevalent immune cells in human epidermis include Langerhans cells (LCs), which are professional antigen presenting cells (APCs) and CD-8+ tissue-resident memory T (T_{RM}) cells (Figure 1.10), derived from antigen-specific effector T cells which previously infiltrated the tissue during inflammation (Nguyen & Soulika, 2019). CD-8+ T_{RM} cells can act sensing the microenvironment for antigens and travel to the skin draining lymph nodes to promote tolerance during homeostasis or initiate an

adaptative immune responses (Romani, Koide, et al., 1989). Resident T-cells are also distributed through the dermis. αβ T cells (CD-4+ or CD-8+ T_{RM} cells) are the dominant T-cell population in human skin and mainly reside within the hair follicle epithelium in steady state (Kabashima et al., 2019) while γδ T cells are the main subtype of T-cells in murine skin. These can be found within the junctions of the epidermis and act identifying antigens and secreting a range of cytokines that trigger further immune responses (Ho & Kupper, 2019).

Several other immune cells can also be found in the dermis, such as myeloid dendritic cells, macrophages, NK cells and B cells. Dermal dendritic cells (dDCs) have an immune surveillance role and rapidly migrate to lymph nodes to initiate pathogen-specific immune responses. Dermal macrophages have a role in wound healing and, when activated, they can recruit immune cells through production of pro-inflammatory cytokines (Kabashima et al., 2019). Human resident B cells play homeostatic functions in host defence, regulation of microbial communities and wound healing (Debes & McGettigan, 2019). NK cells, which can also reside in the skin, serve as anti- microbial immune sentinels and can contribute to contact hypersensitivity (Kobayashi et al., 2020; Nestle et al., 2009). Mast cells and eosinophils are also dermis-resident immune cells. They contain granules which enclose mediators such as histamine, proteoglycans, tryptase and chymase. They also produce large amounts of prostaglandin D2 (PGD2) and leukotrienes (LTs), lipid-derived inflammatory mediators involved in allergic responses and recruitment of immune cells (Kabashima et al., 2019).

Skin inflammation has been extensively studied in relation to two skin inflammatory diseases, psoriasis and atopic dermatitis (AD), which involve distinct mechanisms and are associated to different types of immune response. Psoriasis is an immune-mediated disease that can affect the skin

and joints. Psoriasis is a systemic immune-mediated disease that can affect the skin and joints. It has a strong genetic predisposition and can be triggered by environmental factors. Genetic analyses have identified many putative associated loci, being HLA-Cw6 named psoriasis susceptibility locus 1 (PSORS1), the most prevalent allele. Other candidates include mutations include IL-36 receptor antagonist (IL-36RN) or caspase recruitment domain family member (CARD14) gain-of-function mutation (Boehncke & Schön, 2015).

There are different forms of the disease: plaque psoriasis is the most common form and is also termed psoriasis vulgaris; other forms include pustular psoriasis (PP), psoriatic arthritis (PsA), as well as eruptive, inversive or erythrodermic psoriasis (Boehncke & Schön, 2015). Histologically, psoriatic hallmark features include epidermal acanthosis (thickening of viable layers), hyperkeratosis (thickened cornified layer), and parakeratosis (cell nuclei present in the cornified layer). Epidermal rete ridges (thickenings that extend down between dermal papillae) are markedly elongated in human psoriasis (Figure 1.10) (Boehncke & Schön, 2015). The immune cell infiltrate recruited to the lesions includes T-lymphocytes, macrophages, mast cells, and neutrophils. The later can accumulate in the epidermis to form Munro's micro-abscesses (Figure 1.10).

Psoriatic skin lesions originate as a result of dysregulated interactions of innate and adaptive components of the immune system with resident cutaneous cell types, which leads to proliferation and cytokine production by epidermal keratinocytes (Boehncke & Schön, 2015). This is a result of multifactorial setting which includes genetics and environmental factors. Inflammation is mainly driven by type-17 (T17) immune responses, and therefore it is dendritic cell and T-cell-mediated disease with complex feedback loops from APCs, neutrophils and keratinocytes. Although

traditionally considered crucial the role of T1 inflammation has been greatly diminished in the last years and Th-1 cells are not considered to drive disease. Differentiation of Th1 and Th17 cells is stimulated by dendritic cells through IL-12 and IL-23, respectively. Immune cells facilitate the inflammatory response through their mediators in the skin and involve the production of TNF, IL-17A/IL17F and IL-23 (Figure 1.10) (Meephansan et al., 2012). A possible role for IL-33 in the pathogenesis of psoriasis has been recently suggested (see section 1.3.1.4) and has been addressed in this thesis.

Atopic dermatitis skin displays crusted or excoriated itchy erythematous plaques, which are histologically characterised by marked intercellular edema (Bieber, 2010). It has a considerable heritability component as its major risk factor is a positive family history with AD. The strongest genetic risk factor is semi-dominant null mutation in FLG, which encodes the epidermal protein filaggrin. Other AD loci contribute to abnormalities in the innate immune signalling and T cell activation as well as Th-2 cell differentiation. AD has also been associated with the role of microbial flora, especially susceptibility to Staphylococcus aureus (*S. aureus*) colonisation. This colonisation is associated to decreased production of the normally produced antimicrobial peptides which act disrupting bacterial membranes and changes in the pH of the skin, which normally prevent pathogenic infections (Geoghegan et al., 2018; Kabashima et al., 2019). *S. aureus* recognition through NLRs activates the NLRP3 inflammasome, which leads to production of IL-1β and IL-18 through caspase-1 activation (Muñoz-Planillo et al., 2009). Impairment of the components of the stratum corneum, such as decreased levels of ceramide content can also contribute to inflammation in atopic dermatitis (Matsui & Amagai, 2015).

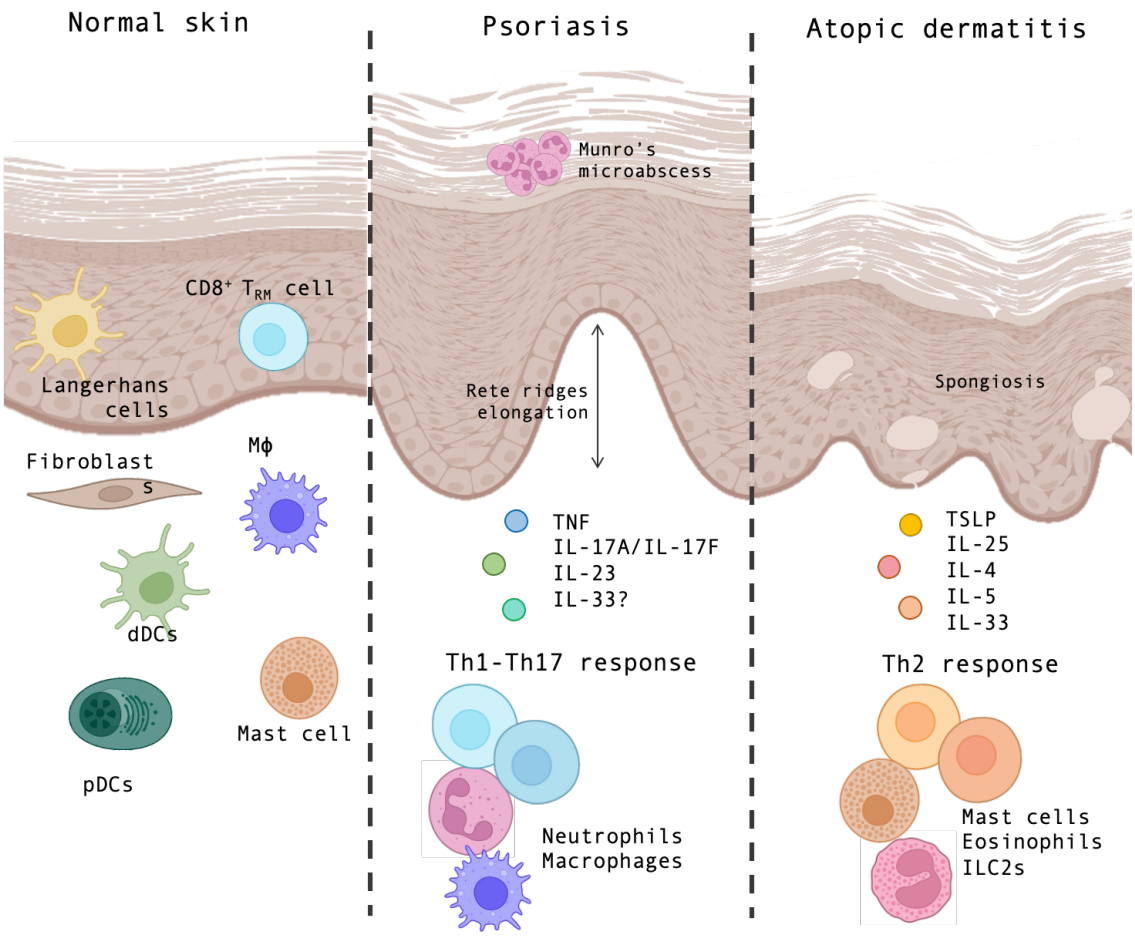

Figure 1.10: Resident cells found in normal skin and inflammation responses induced during psoriasis and atopic dermatitis. Psoriatic inflammation is mediated by Th-1/Th-17 immunity, characterised by the release or secretion of TNF, IL-17A/IL-17F and IL-23, and the recruitment of dendritic cells, macrophages and neutrophils. In contrast, atopic dermatitis is mediated by a Th-2 response, in which are involved TSLP, IL-25, IL-4, IL-5 and IL-33, and activation of Th-2 lymphocytes, mast cells, eosinophils and ILC2s. A role of IL-33 in psoriasis has been suggested.

The immune response in AD is skewed towards T helper 2 (Th-2) cell-mediated pathways. The release of cytokines such as thymic stromal lymphopoietin (TSLP) result in migration of dermal DCs to lymph nodes to induce Th-2 polarization. The inflammatory reaction is conducted by the release of TSLP, IL-25, IL-4, IL-5 and IL-33 by mast cells, eosinophils and group 2 innate lymphoid cells (ILC2s) (Figure 1.10) (Weidinger et al., 2018). ILC2s (also designated natural helper cells, nuocytes or innate helper 2 cells) are a recently described cell type crucial for the allergic

and infectious responses and the production of high amounts of Th2 cytokines (Moro et al., 2010a).

1.2.3 Inflammation in the skin: lessons from animal models

Balance between apoptosis and necroptosis is essential to maintain tissue homeostasis and is closely regulated by the abundance of different signalling effectors of the pathway. Sensitivity to necroptosis can be modulated by the expression levels of necroptosis effectors (see section 1.1.3) and is also inherent of specific cell types in tissues. Studies using mouse models have revealed that skin homeostasis is critically dependent on tight control of cell death pathways and found certain predisposition of the epidermis to necroptosis when compared with other tissues (Dannappel et al., 2014; Takahashi et al., 2014).

Genetic models and, specifically, models that allow tissue-specific gene targeting, provide invaluable information to define the molecular mechanisms and pathways regulating tissue homeostasis and inflammation. In the epidermis, keratinocyte specific expression of proteins can be targeted using promotors such as KRT-14 or KRT-5, which are almost exclusively expressed in basal epidermal keratinocytes (Shetty & Gokul, 2012). Expression of -Cre recombinase under these promoters can be combined with a large number of mouse models carrying loxP-flanked alleles to produce epidermal keratinocyte-specific knock-out mice (also epidermal knock-out, referred hereon as EKO). Generation of mice expressing transgenes in keratinocytes are now indispensable tools to study keratinocyte specific function in cell death and inflammation. This section focuses on some of the most relevant skin inflammation models, including necroptosis-dependent skin inflammation models that will be later used in Part II of this thesis to study the role of DAMPs in necroptosis *in vivo.*

1.2.3.1 *NF-κB pathway in skin homeostasis and inflammation*

The NF-κB pathway controls the expression of pro-inflammatory mediators that orchestrate and sustain the inflammatory response but also plays an important role in the maintenance of physiological immune homeostasis and the prevention of inflammatory diseases in many tissues. NF- κB is composed of five subunits, Rel-A/p65, Rel-B, c-Rel, p50 and p52, and is maintained in a deactivated state through its association with the inhibitory protein of NF-κB (IκB). Upon activation by diverse of stimuli, IκB are phosphorylated by the IκB kinase (IKK) complex, composed of IKK1 (also known as IKKα) and IKK2 (also known as IKKβ) catalytic subunits, and NEMO (also known as IKKγ) regulatory subunit (Figure 1.3) (Wullaert et al., 2011). Phosphorylation of the IκB subunits targets them for polyubiquitination and proteasome degradation, resulting disassociation from NF-κB. Activated NF-κB is then translocated into the nucleus where it binds to specific DNA sequences, activating transcription of target genes such as cytokines chemokines, adhesion molecules, survival and death (Kumari & Pasparakis, 2015)

A role for NF-κB in skin inflammation was first reported in 1995 and 1996, when several studies showed that increasing NF-κB activity through the ubiquitous deletion of IκB-α, a member of the IκB family, resulted in skin inflammation in mice that led to death within 7 to 10 days after birth (Klement et al., 1996), which was partially rescued by the deletion of p50 (Beg et al., 1995). Deletion of IκB–α specifically in epidermal keratinocyte leads to epidermal hyperplasia and dermal immune cell infiltration, although of IκB–α needs to be additionally abolished from T-cells to recapitulate the *Iκb–α*$^{-/-}$ inflammatory phenotype (Rebholz et al., 2007). Targeted deletion of p65 completely rescues the *Iκb–α*$^{-/-}$ inflammatory phenotype, showing that increased NF-κB signalling in keratinocytes drives skin inflammation in this model (Rebholz et al., 2007).

Interestingly, specific inhibition of NF-κB in keratinocytes can also lead to inflammatory skin lesions in mice. Initial studies were performed overexpressing non-degradable IκB-α under the K5 promoter (van Hogerlinden et al., 1999) and were later corroborated by epidermal specific knock-out of IKK2 (Kumari et al., 2013; Pasparakis et al., 2002) and NEMO (Nenci et al., 2006). Similarly, RelA^{EKO} c-Rel^{EKO} mice developed inflammatory skin lesions resembling the phenotype of IKK2^{EKO} mice (Grinberg-Bleyer et al., 2015). Large numbers of apoptotic keratinocytes are detected in early lesions of NEMO^{EKO} mice. Ablation of TNFR1 fully prevented IKK2^{EKO} skin inflammation (Pasparakis et al., 2002) and drastically delayed the development of inflammatory lesions in NEMO^{EKO} animals to 4-6 months of age (Nenci et al., 2006). Finally, mutations disrupting the expression of different LUBAC components trigger a severe proliferative dermatitis phenotype (Seymour et al., 2007; Sundberg et al., 2020; Taraborrelli et al., 2018), which is at least partially dependent on TNFR1 signalling and driven by FADD, TRADD or Casp-8 dependent apoptosis (Berger et al., 2014; Kumari et al., 2014; Laurien et al., 2020; Patel et al., 2020; Taraborrelli et al., 2018)

1.2.3.2 *Necroptosis-dependent skin inflammation models*

Genetic mouse models have provided evidence that Casp-8 and FADD play roles in epidermal keratinocytes that are crucial for maintaining skin homeostasis. Keratinocyte-specific deletion of Casp-8 (Casp-8^{EKO}) in mice triggers a severe skin inflammatory phenotype, first described by Lee et al. in 2009. These animals appeared slightly runted, with flaky skin by postnatal day 10 (P10), which presented increased epidermal thickness and keratinocyte proliferation. They proposed that the inflammatory lesions were caused by a p38-MAPK-mediated production of IL-1α and regulation of NLRP3 by keratinocytes. However, a later study using the Casp-8^{EKO} skin inflammation model showed that IL-1α and IL-1β KO did

not prevent the development of inflammatory lesions (Kovalenko et al., 2009). Instead, they suggested that Casp-8 acts restraining excessive activation of pathways that respond DAMPs or pathogens, such as the RIG-I signalling complex. A role for the RIG-1 pathway in this model, however, could not be confirmed by a later study (Weinlich et al., 2013).

A similarly severe skin inflammation phenotype was described by Bonnet et al., in 2011, through the specific deletion of FADD from epidermal keratinocytes ($FADD^{EKO}$). The complete rescue of the $FADD^{EKO}$ phenotype was successfully accomplished through the deletion of RIPK3. $FADD^{EKO}$ *Ripk3*$^{-/-}$ animals were healthy and have normal skin until adulthood, providing experimental evidence that RIPK3-dependent necroptosis in FADD-deficient keratinocytes was responsible for triggering skin inflammation. Similarly, RIPK3 deficiency was shown to completely rescue the embryonic lethality of *Casp-8*$^{-/-}$ animals (Kaiser et al., 2011; Oberst et al., 2011) and prevent skin lesions caused by inducible Casp-8 knock-out (Weinlich et al., 2013), supporting that keratinocyte necroptosis is be responsible for $Casp\text{-}8^{EKO}$ skin inflammation. Confirmation of necroptosis through the deletion of MLKL in these models has not been performed. However, *Fadd*$^{-/-}$ *Mlkl*$^{-/-}$ and *Casp-8*$^{-/-}$ *Mlkl*$^{-/-}$ animals do not present inflammatory lesions in the skin, suggesting that RIPK3-dependent necroptosis is the trigger of skin inflammation in $FADD^{EKO}$ and $Casp\text{-}8^{EKO}$ animals.

The $Casp\text{-}8^{EKO}$ and $FADD^{EKO}$ models described by Kovalenko et al. and Bonnet et al., respectively, start showing psoriasis-like cutaneous lesions at an early age (P3) and had a more severe inflammatory phenotype than the initial model described by Lee et al. At P3, animals appeared runted, with unevenly thickened and hard skin showing extensive scaling, which led to death by P8. Histologically, the skin of these animals is characterised by marked epidermal hyperplasia and accompanied by

increased expression of KRT-14 and KRT-6, hyperkeratosis, and alteration of keratinocyte differentiation, evident from the loss of suprabasal and granular layers (Bonnet et al., 2011; Kovalenko et al., 2009). Gene expression analysis of Casp-8^{EKO} skin at different times suggested that the skin disease was initiated in the suprabasal layer of the epidermis before birth, point at which cornification starts (Kovalenko et al., 2009). However, epidermal formation, proliferation, or differentiation was not affected in FADD^{EKO} animals at the time of birth (P0). Cell death was detected in the epidermis at P1, followed by an inflammatory reaction and the loss of epidermal differentiation (Bonnet et al., 2011).

Common to these two models is a large infiltration of macrophages, granulocytes, and lymphocytes in the dermis. In contrast to the IKK2^{EKO} model, depletion of macrophages from the dermis by subcutaneous injection of clodronate-containing liposomes did not affect the kinetics or extent of development of skin lesions in Casp-8^{EKO} mice (Kovalenko et al., 2009). The FADD^{EKO} inflammatory phenotype was not affected by the deletion of recombinant activating gene 1 (*RAG-1*), needed for the maturation of B- and T-cells, indicating the adaptative immune response does not play a detrimental role in the inflammatory phenotype (Bonnet et al., 2011). RAG-1 or T-cell antigen receptor α (TCR-α) independence has also been observed in NEMO^{EKO} and IKK2^{EKO} models respectively (Nenci et al., 2006; Pasparakis et al., 2002).

Both FADD^{EKO} and Casp-8^{EKO} skin inflammation were shown to be independent of IL-1 signalling (Bonnet et al., 2011; Kovalenko et al., 2009). As seen with some skin inflammation models associated to activation or inhibition of NF-κB in keratinocytes, deletion of the *Tnf* and *Tnfr1* gene led to a drastic delay in the development of skin lesions and increase of the survival of both FADD^{EKO} and Casp-8^{EKO} animals (Bonnet et al., 2011; Kovalenko et al., 2009). However, the inflammatory phenotype

was not completely rescued, and although gene induction was reduced, there was no evident change in pattern of the induced genes (Kovalenko et al., 2009). Although deletion of TRIF did not affect the rate or extent of development of the skin lesions nor the survival of Casp-8^{EKO} animals (Kovalenko et al., 2009), a mild delay of the FADD^{EKO} skin lesion development was achieved through MyD-88 deficiency (Bonnet et al., 2011), suggesting that activation of TLRs and other MyD-88-related receptors could be implicated in disease development. Similarly, CYLD was shown to contribute to the induction of necroptosis in FADD^{EKO} keratinocytes, as the lack of CYLD catalytic activity resulted in considerable delay of the phenotype (Bonnet et al., 2011)

Recently, the IKK2^{EKO} has been shown to be mainly driven by RIPK3-MLKL-dependent necroptosis. IKK2^{EKO} *Ripk3*$^{-/-}$, IKK2^{EKO} Ripk3^{EKO} and IKK2^{EKO} *Mlkl*$^{-/-}$ mice display strongly ameliorated skin inflammation and only develop mild skin lesions at the age of 2-5 months (Kumari et al., 2021). Similarly, IKK2^{EKO} mice expressing kinase inactive RIPK1 (*Ripk1*$^{D138N/D138N}$) were protected from skin inflammation until 5-9 months of age, indicating that RIPK1-dependent keratinocyte necroptosis and apoptosis trigger the development of IKK2^{EKO} skin lesions (Kumari et al., 2021). Deficiency in RIPK1 kinase activity was also able to rescue skin inflammation triggered through the combined epidermis-specific ablation of the NF-κB subunits RelA and c-Rel, indicating NF-κB inhibition can cause RIPK1-dependent keratinocyte necroptosis and apoptosis (Kumari et al., 2021).

1.2.3.3 *RIPK1 in skin homeostasis and inflammation*

Mice lacking RIPK1 *s*pecifically in epidermal keratinocytes start to develop skin lesions after 1 week of age, characterised by epidermal hyperproliferation, alteration of epidermal differentiation markers and

infiltration of myeloid cells (Dannappel et al., 2014). Constitutive deletion of RIPK3 or MLKL completely prevented the development of RIPK1^{EKO} skin inflammation, indicating that RIPK1 acts preventing the activation of RIPK3 in the skin and that other RHIM-containing proteins must be responsible for RIPK3 activation in the absence of RIPK1. Specific keratinocyte ablation of ZBP1 but not TRIF drastically rescued the skin inflammation of RIPK1^{EKO} animals, (Dannappel et al., 2014). Interestingly, the skin pathology of mice expressing RIPK1 bearing mutations in its RHIM domain (*Ripk1*$^{mRHIM/mRHIM}$), which die perinatally like *Ripk1*$^{-/-}$ mice, is different than that found in the skin of RIPK1^{EKO} and *RIPK1*$^{mRHIM/EKO}$, suggesting that necroptotic death of other cells contributes to the perinatal skin phenotype (J. Lin et al., 2016).

1.2.3.4 *Necroptosis in human skin inflammatory diseases*

Understanding the processes and molecular pathways that maintain skin homeostasis or drive inflammation provides valuable insight in the pathophysiology of human inflammatory skin diseases. Identification of keratinocyte necroptosis as a potent trigger of skin inflammation in mouse models led to investigate whether necroptosis could also be implicated in the pathogenesis of human inflammatory diseases. Indeed, RIPK3 expression and elevated MLKL phosphorylation was found in skin tissue sections from patients suffering toxic epidermal necrolysis (TEN), a life-threatening type of severe cutaneous adverse reaction (SCAR) (S. K. Kim et al., 2015). Other examples of human skin diseases that have been associated with keratinocyte necroptosis include Stevens-Johnson Syndrome (SJS) – another SCAR – (Saito et al., 2014), systemic lupus erythematosus (SLE) and Lichen Planus (LP) (Lauffer et al., 2018). More recently, certain association has been established between necroptosis and psoriasis. Increased expression of RIPK1 phosphorylation, RIPK3 and MLKL has been found in psoriatic biopsies (X. Duan et al., 2020; Honda et

al., 2017). Necroptosis has also been suggested to drive inflammation in IMQ-induced psoriasis-like mouse models, which was strongly reduced by intradermal injection of RIPK1 inhibitor Nec-1s (X. Duan et al., 2020). Although an interesting and promising field of research, the molecular mechanisms and role of necroptosis in psoriasis remain unclear and need to be further studied.

1.3 DAMPs in necroptosis

DAMPs released during necrosis play a critical role activating the immune system and inducing an inflammatory response (Murao et al., 2021). My thesis focuses on the effect of two specific DAMPs, IL-33 and HMGB1, and their receptors ST2 and RAGE, and explores their contribution to necroptosis and necroptosis-dependent inflammation. This section briefly describes these DAMPs and their receptors as well as their implication in skin inflammation.

1.3.1 IL-33

1.3.1.1 *IL-33, a brief introduction*

IL-33 was initially discovered as a nuclear protein abundantly expressed in high endothelial venules (HEVs) and initially called nuclear factor (NF)-HEV (Baekkevold et al., 2003). However, the molecule was later reported to contain a similar three-dimensional structure to that described for IL-1α, IL-1β and IL-18, and to function as a cytokine through activation of ST2, an orphan receptor of the IL-1 receptor superfamily (Schmitz et al., 2005). The C-terminal IL-1-like cytokine domain is separated by a central domain from the N-terminal nuclear domain, which contains a chromatin-binding motif (CBM) (Roussel et al., 2008) and a nuclear localisation

sequence (NLS) (Figure 1.11) (Baekkevold et al., 2003), necessary for its nucleus localisation (Carriere et al., 2007).

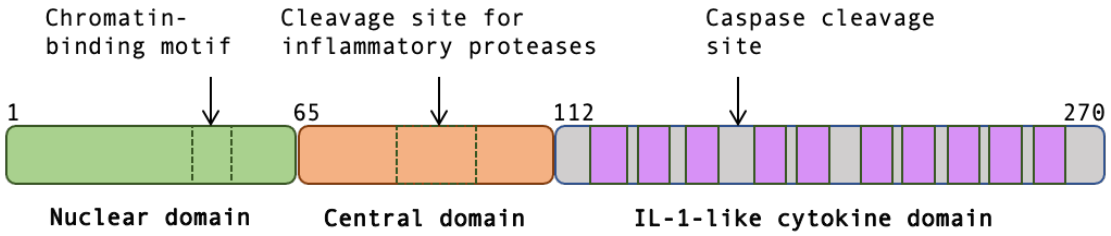

Figure 1.11: Structure of the IL-33: domains, motives, and cleavage sites. IL-33 is structure in a nuclear domain containing a chromatin-binding motif, a central domain, which is the general target for cleavage of inflammatory proteases and a IL-1-like cytokine domain, which can be cleaved by caspases.

Other than endothelial cells, IL-33 is specifically expressed in cells of barrier tissues such as nasal, lung, gut, vagina and skin epitheliums (Moussion et al., 2008). However, IL-33 expression and regulation are subject to strong species differences. In contrast to human endothelium, mouse endothelium does not express IL-33. Several mouse epithelium, like human, express constitutive IL-33, including in skin, stomach, intestine, salivary gland, vagina, and lung (Pichery et al., 2012). IL-33 expression can be increased during inflammation, as reported in the lungs (Byers et al., 2013; Kearley et al., 2015), the gut (Reichenbach et al., 2015) or the skin (Savinko et al., 2012). In addition to epithelial and endothelial cells, activated fibroblasts are important sources of IL-33 during inflammation, particularly in diseases associated with tissue fibrosis (Manetti et al., 2010; Marvie et al., 2010) and wound repair (Gatti et al., 2021).

Initially, IL-33 was described to be a product of tissue cells, passively released by dying cells, rather than a product of activated leukocytes, which is the classical source of proinflammatory cytokines. However, mechanical stress or hypertension in cardiac endothelial cells and fibroblasts can lead to the release of bioactive IL-33 without cell death

(W.-Y. Chen et al., 2015; Kakkar et al., 2012; Sanada et al., 2007), suggesting a controlled secretion of IL-33. In addition, the fact that IL-33 expression and release can be induced in different types of tissue cells and leukocytes (Martin & Martin, 2016), further supports controlled secretion of this cytokine, although additional studies are necessary in order to elucidate the mechanisms of IL-33 secretion.

The accumulation of IL-33 in the nucleus and its association with histones and chromatin (Carriere et al., 2007; Roussel et al., 2008), as well as other transcription factors, suggest a role regulating gene expression. This was backed by the transcriptional repressor properties observed in IL-33 overexpressing HEK293 cells (Roussel et al., 2008). However, studies using a global proteomic approach found that exogenous extracellular IL-33 cytokine, and not endogenous nuclear IL-33, was able to induce the expression of proteins associated with inflammatory responses (Gautier et al., 2016). This study suggested that the main purpose of IL-33 nuclear localisation is the regulation of its extracellular cytokine activity through nuclear sequestration, rather than the regulation of gene or protein expression.

IL-33 is produced as a full-length precursor form (IL-33FL). Contrary to what was initially proposed (Schmitz et al., 2005), this precursor does not require processing for biological activity (Cayrol & Girard, 2009; Lüthi et al., 2009; Talabot-Ayer et al., 2009). Caspases can cleave, and inactivate, IL-33FL through a specific cleavage site in the IL-1-like domain not found in other IL-1 family members (Cayrol & Girard, 2009). This suggests specific regulation of IL-33 during apoptosis, probably related to the high levels of constitutive expression of the cytokine in healthy tissues. The bioactivity of extracellular IL-33 can be regulated by the action of inflammatory proteases, such as neutrophil cathepsin G, elastase and proteinase 3 (PR3), as well as mast cell chymase, tryptase and granzyme

B, which cleave IL-33 to produce shorter N-terminally truncated forms of the cytokine. Some of these truncated forms show increased biological activity (Lefrançais et al., 2012, 2014), while others, such as chymase, inactivate IL-33 and limit the duration of the alarm signal (Roy et al., 2014). The biological activity of extracellular IL-33 can also be rapidly terminated by the formation of two disulphide bridges through oxidation of critical cysteine residues (Cohen et al., 2015). In conclusion, released IL-33 is biologically active but is subject to regulation through caspases, proteases or oxidation that can transiently enhance before termination of its bioactivity.

1.3.1.2 *ST2 signalling and expression*

Once in the extracellular space, IL-33 interacts with its only receptor, ST2 (also known as IL-33R, IL-1R4, T1, DER-4 and Fit-1). Initially identified in fibroblasts (Tominaga, 1989), it remained an orphan receptor until 2005, when IL-33 was identified as its ligand by Schmitz et al. No other ligands have been described to interact with ST2. Like most members of the IL-1/TLR receptor family, the intracellular part of the receptor contains a Toll/Interleukin-1 receptor (TIR) domain. Binding of IL-33 to ST2 allows the latter to undergo a conformational change and interact with IL-1R accessory protein (IL-1RAcP, also known as IL-1R3), a co-receptor shared with other IL-1 family members (Figure 1.12) (Chackerian et al., 2007; Palmer et al., 2008). The ST2/IL-1RAcP complex mediates the heterodimerisation of transmembrane proteins and TIR domains allowing the recruiting of adaptor proteins. MyD88 is recruited to TIR dimers by homotypic protein-protein interaction, leading the N-terminal death domain of MyD88 to oligomerise and recruit the serine-threonine kinases IL-1R-associated kinase 1 and 4 (IRAK1 and 4) and the adaptor protein TNF receptor-associated factor 6 (TRAF6) (Figure 1.12). Activation of the MyD88-IRAK-TRAF6 signalling pathway culminates in the activation of

MAP kinases (JNK, p38 or ERK) and NF-κB transcription factors (Figure 1.12) (T. Liu et al., 2017).

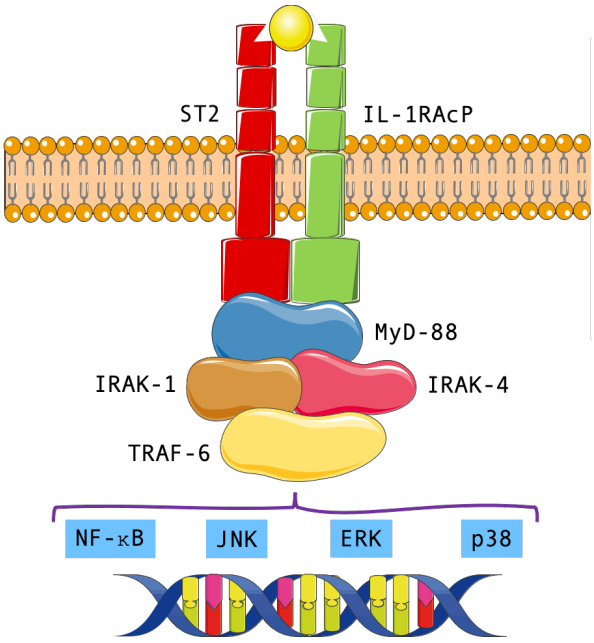

Figure 1.12: Structure and intracellular signalling of ST2. Upon interaction of IL-33 with ST2, co-receptor IL-1RAcP undergoes a conformational change that allows its interaction with ST2. The ST2/ IL-1RAcP complex recruits MyD88 which, in turn, recruits IRAK1 and 4 together with TRAF6 to activate MAPK (JNK, p38 or ERK) and NF-κB transcription factors.

A soluble form of the ST2 receptor (sST2) has also been described. Both forms are generated from a single mRNA through differential expression of two distinct promoters and alternative splicing (Bergers et al., 1994; Yanagisawa et al., 1993). This shorter form is a secreted protein which acts as a decoy receptor to sequester free IL-33, preventing IL-33/ST2 signalling (Hayakawa et al., 2007). Production of sST2 can be enhanced by pro-inflammatory cytokines in vitro (Kumar et al., 1997), and high levels of serum sST2 have been found in several inflammatory diseases (Oshikawa et al., 2001). In fact, sST2 has been shown to predict mortality and clinical outcome in acute myocardial infarction, revealing its importance as a potential biomarker of clinical cardiovascular disease (Shimpo et al., 2004).

ST2 was initially described to be expressed in type 2 helper T (Th2) cells (Löhning et al., 1998; D Xu et al., 1998). Stimulation of Th2 cells by IL-33 promotes cell proliferation and survival, leading to a strong production of type 2 immune mediators (Guo et al., 2009). ST2 has also been described to be constitutively expressed at the surface of ILC2s, which produce high amounts of Th2 cytokines in response to IL-33 (Moro et al., 2010b; Neill et al., 2010) and play a critical role in allergic inflammation and infections (Neill et al., 2010; Stehle et al., 2016). Mast cells also constitutively express ST2 and have reported to be responsive to ST2/IL-33 signalling, which promotes survival, activation and maturation (Allakhverdi et al., 2007; Sabatino et al., 2012), as well as production of type 2 cytokines (Saluja et al., 2015).

To a lesser extent, ST2 can also be constitutively found in regulatory T cells (Tregs), neutrophils, dendritic cells or macrophages. Several animal studies have suggested the ability of IL-33 signalling to increase the immunomodulatory and protective roles of regulatory T-cells, through their expansion (Schiering et al., 2014). ST2/IL-33 signalling can also enhance macrophage activation through upregulation of LPS receptor components such as TLR4, MD2, soluble CD-14 and MyD88 (Espinassous et al., 2009). Additional studies have reported a role of IL-33 in other immune cells such as invariant natural killer T (iNKT) cells, natural killer (NK) cells, T helper 1 (Th1) cells, eosinophils and basophils (reviewed in Griesenauer & Paczesny, 2017).

1.3.1.3 *IL-33/ST2 signalling in health and disease*

The signalling model of IL-33, through ST2, corresponds to a typical DAMP function. Given its increased expression in epithelial and endothelial cells, IL-33 has been proposed to act as a barrier guardian (N. T. Martin & Martin, 2016).

The first evidence for a role of IL-33 in host defence was found in response to a worm infection (Humphreys et al., 2008). Since then, it has been shown that IL-33 signalling is essential for worm elimination (Hung et al., 2013; Yasuda et al., 2012), as well as enhancing clearance of several fungal (Le et al., 2012; Nelson et al., 2011), bacterial (Hazlett et al., 2010) and viral (Bonilla et al., 2012) infections in mice. Release of IL-33 upon breach of barrier activates mast cells, ICL2s, DCs or macrophages and, typically, type 2 proinflammatory cytokines such as IL-4 and IL-5 would be released, favouring the recruitment of eosinophils and basophils to the site of inflammation (Martin & Martin, 2016). Deletion of the N-terminal nuclear domain of IL-33 in a knock-in mouse model resulted in elevated levels of IL-33 in the serum with profound ST2-mediated Th-2-biased inflammation, eosinophilia and fatal multiorgan failure, suggesting an autoregulatory circuit of IL-33 self-production and release (Bessa et al., 2014).

Although most research on ST2/IL-33 signalling has been focused on type 2 signalling, several recent studies have described that type 1- and type 17-mediated responses can also be activated by IL-33. Blocking of IL-33/ST2 signalling ameliorates the severity of murine models of rheumatoid arthritis (Leung et al., 2004; Palmer et al., 2009). Furthermore, high levels of IL-33 in tissue or serum and presence of sST2 in serum have also been reported to be associated with rheumatoid arthritis. Similar observations have been associated with cancer, cardiovascular diseases, obesity or disorders of the central nervous system (reviewed in Griesenauer & Paczesny, 2017; Jiang et al., 2021).

To study IL-33/ST2 signalling in disease, several knock-out mice have been generated to abrogate IL-33 or ST2. *Il-33*$^{-/-}$ (Hardman et al., 2013; Oboki et al., 2010; Pichery et al., 2012) and *St2*$^{-/-}$ mice (Hoshino et al., 1999; Senn et al., 2000; Townsend et al., 2000) develop normally, are

healthy and fertile and show no obvious phenotypic abnormalities under pathogen-free conditions. However, if challenged, mice lacking or unable to respond to IL-33 show differences in immune responses compared to wild-type animals, such as a reduced Th-2-dependent responses and Th-2 cytokine production, as well as reduced CD-8+ T cell responses and antiviral Th-1 lymphocytes (N. T. Martin & Martin, 2016).

1.3.1.4 *IL-33 in the skin*

IL-33 is abundantly expressed in the nucleus of epithelial cells of tissues in contact with the environment, like the skin, where pathogens, allergens and other environmental agents are frequently encountered. The expression pattern is slightly different in humans and mice. While high levels of IL-33 can be detected in normal murine skin, constitutive levels of IL-33 in human epidermis are low but can be strongly induced (Pichery et al., 2012). Furthermore, a significant variability of IL-33 expression in human skin between different cell types and different individuals has been reported (Moussion et al., 2008), suggesting modulation of IL-33 expression by local environmental cues.

As a traditional type 2 cytokine, IL-33 has been associated with Th-2 driven diseases, including AD. Increased IL-33 and ST2 expression have been detected through immunohistochemistry in AD patients skin (Dajnoki et al., 2016; Savinko et al., 2012) and IL-33 and ST2 have been found to be upregulated in AD skin after allergen or staphylococcal enterotoxin B (SEB) exposure (Savinko et al., 2012). Skin lesions of AD patients are enriched with ST2 positive ILC2 cells (Salimi et al., 2013) and serum levels of IL-33 are significantly higher AD patients (Nygaard et al., 2016), which correlates with disease severity (Tamagawa-Mineoka et al., 2014). Increased expression of IL-33 and ST2 or sST2 has also been found in several AD mice models, including BALB/c mice receiving topically applied

OVA, house dust mites, SEB or in filaggrin-deficient BALB/c mice (Savinko et al., 2012). Furthermore, C57BL/6 transgenic mice expressing IL-33 specifically in epidermal keratinocytes develop spontaneous AD-like inflammation. The inflammatory phenotype was shown to be almost fully dependent on ILC2s, partially dependent on basophils and B- and T-cell independent (Imai et al., 2013, 2019). These findings propose IL-33 as a potential biomarker of disease severity. Two different clinical trials have investigated the efficacy of IL-33 targeting biologic in chronic atopic dermatitis (Etokimab from AnaptysBio and REGN3500 from Regeneron Pharmaceuticals). However, although initially promising after relatively successful results of the phase IIa study, Etokimab did not show significant improvement in a phase IIb, randomised, double-blinded, placebo-controlled, multi-dose study. Similarly, REGN3500 failed to significantly alleviate the AD score compared to the placebo group in a phase II study.

In the last few years, the traditional definition of IL-33 as a pure type 2 cytokine has been challenged. The IL-33/ST2 axis has been shown to participate in the Th17 response in allergic airway diseases (Vocca et al., 2015) and several studies have revealed the ability of IL-33 to stimulate type 1 and 17 immune cells, such as Th1 cells, Th17 cells, CD-8+ cells, B cells, NK cells, NKT cells, as well as Treg cells (reviewed in Peine et al., 2016). In line with this, several studies have shown increased IL-33 or ST2 expression in psoriatic skin compared to healthy skin patients (Balato et al., 2012; Duan et al., 2019; Hueber et al., 2011; Zeng et al., 2021, P. di Meglio's lab BSID 2021), although a contradictory result has been reported (Batista et al., 2013). Serum IL-33 levels in patients with PV, PP or PsA have been found to be significantly higher than those in healthy controls (Mitsui et al., 2016). Furthermore, IL-33 levels correlated with serum TNF-α levels and decreased after anti-TNF-α therapy (Mitsui et al., 2016).

Some contradictory results on psoriasis-like mice models have been observed regarding IL-33/ST2 signalling, which are suggested to be due to strain-dependent immune response predisposition. An initial study using Imiquimod (IMQ)-induced psoriasis-like inflammation was shown to develop independently of IL-33 when using C57BL/6 mice (Athari et al., 2016). In contrast, a later study reported IL-33 to be essential and aggravate psoriasis-like lesions in the IMQ-induced model on BALB/c background mice (Y. Duan et al., 2019). A more recent study, however, has shown that IL-33 or ST2 deficiency ameliorated the inflammatory phenotype and markedly decreased number of neutrophils and mast cells the IMQ-induced psoriasis-like model on a C57BL/6 background (Zeng et al., 2021).

Moreover, injection of IL-33 in the ears of BALB/c mice has shown to induce ST2-dependent cutaneous fibrosis (Rankin et al., 2010) and psoriasis-like ST2-dependent inflammation which was shown to be partially dependent on mast cells, and also induced neutrophil infiltration (Axel J. Hueber et al., 2011). In line with these studies, IL-33 has also been reported to induce ST2-dependent psoriasis-like dermatitis, when injected in C57BL/6 mice (Zeng et al., 2021). Furthermore, deficiency of ST2 in BALB/c mice leads to reduced cutaneous inflammatory response compared to WT in a phorbol ester-induced murine model of psoriasis-like skin inflammation (Axel J. Hueber et al., 2011).

IL-33 has also been described to play a role in wound healing responses. Dysregulation of the wound healing process is, in part, responsible for maintaining chronic inflammation and multiple cellular and mechanisms are active during the immune response (Eming et al., 2007). IL-33 is released after cell injury, and therefore is found to be upregulated in incisional wound skin (Yin et al., 2013). Interestingly, *Il-33*$^{-/-}$mice and *St2*$^{-/-}$mice show delayed wound healing (J. S. Lee et al., 2016; Oshio et al., 2017),

which was accompanied by diminished ILC2 responses, and abrogation of these also resulted in impairs in re-epithelization and efficient wound closure (Rak et al., 2016). Similarly, keratinocytes from *Il-33*$^{-/-}$ animals showed delayed wound closure in an *in vitro* scratch wound assay (Oshio et al., 2017).

1.3.2 HMGB1

1.3.2.1 *Expression and release of HMGB1*

HMGB1, also known as HMG1, is a highly conserved DNA-binding protein that has been reported to act as a prototypical DAMP when present in the extracellular environment. HMGB1 is expressed by all cells that contain a nucleus (thus excluding erythrocytes or cornified epithelial cells). As a member of the HMGB family, it contains two DNA-binding domains (Bianchi et al., 1992) (Figure 1.13). It can normally be found in the nucleus due to two nuclear-localisation signals (NLS) but also contains nuclear export signals that allow HMGB1 to exit the nucleus (Bonaldi et al., 2003). In the nucleus, HMGB1 binds to DNA with structure-specificity but not sequence-specificity (S. S. Yu et al., 1977). HMGB1 acts as a chaperone, bending DNA and facilitating binding of regulatory protein complexes (Ferrari et al., 1994; Pasqualini et al., 1989; Prendergast et al., 1994; Stros et al., 2004; C. C. Zhang et al., 1999). HMGB1 is therefore implicated in the regulation of gene transcription, DNA repair, DNA replication, gene delivery and transfer. It is also involved in nucleosome stability and number as well as nuclear catastrophe and telomere homeostasis (R. Kang et al., 2014).

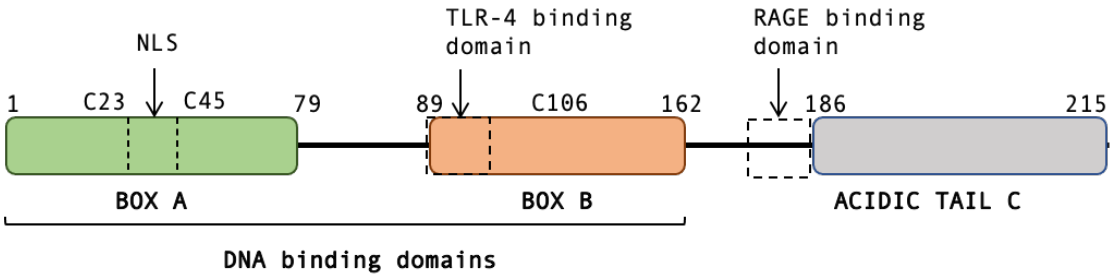

Figure 1.13: Structure or HMGB1: domains and oxidation sites. HMGB1 is composed of two DNA-binding domains (Box A and Box B) and an acidic tail. HMGB1 is susceptible of oxidation in several residues, marked in the figure, together with the binding domains to RAGE and TLR-4.

Even though HMGB1 is mainly localised in the nucleus, several cell types have normal cytosolic HMGB1 expression (Einck et al., 1984; Guillet et al., 1990), which has been linked to autophagy (D. Tang et al., 2010) and unconventional protein secretion (H. Lee et al., 2010). Membrane-bound HMGB1, initially called amphoterin, has been also described and has shown to be involved in neuronal sprouting *in vitro* (Merenmies et al., 1991). Release of HMGB1 into the extracellular space can occur passively, through cell death, or actively, by immune or endothelial cells. As a traditional DAMP, HMGB1 release has been widely associated with necrosis and specific programmed necrotic processes. HMGB1 can be cleaved by Casp-1 and released in response to pyroptosis in immune cells (Kamo et al., 2013; Lu et al., 2012). Necroptosis has also implicated in the release of HMGB1 in response to diverse stimuli (Wen et al., 2017; Yoo et al., 2021; Zemskova et al., 2020).

On the other hand, HMGB1 can be actively secreted by macrophages, mature DCs and activated NK cells (G. Chen et al., 2004; Kalinina et al., 2004). Active release of HMGB1 by macrophages and DCs seems to be controlled by a crucial acetylation step (Bonaldi et al., 2003). Hyperacetylation on lysine residues distributed throughout the molecule occurs in the nucleus and prevents HMGB1 from interacting with nuclear-importer protein complex, which blocks its re-entry to the nucleus

(Bonaldi et al., 2003). HMGB1 lacks the leader peptide that normally determines the classic route to export extracellular proteins via the endoplasmic reticulum (ER)-Golgi pathway. Cytoplasmic HMGB1 is instead packed into specialized non-classical secretory vesicles in response to inflammatory stimuli (Gardella et al., 2002). The kinetic for HMGB1 secretion is delayed in comparison to other pro-inflammatory mediators such as TNF and IL-1 (Milev et al., 1998), prototypical early pro-inflammatory cytokines.

1.3.2.2 *RAGE, a multiligand receptor*

The first identified and main receptor of HMGB1 is the receptor for advanced glycation endproducts (RAGE), also called AGER. RAGE is a transmembrane receptor with a ligand-binding extracellular domain, a short transmembrane domain and a cytoplasmic tail responsible for intracellular signalling transduction (Figure 1.14). Unlike most receptors that recognise DAMPs, RAGE is not a PRR. It recognises tertiary structures rather than amino acid sequences and therefore, has the ability to engage classes of molecules rather than individual ligands (Schmidt et al., 2001; Yan et al., 2003). It was first described to recognise advanced glycation endproducts (AGEs), which are products of nonenzymatic glycation/oxidation of proteins/lipids induced by hyperglycaemia and accumulate in diabetes. The AGE/RAGE axis induces oxidative stress and endothelial cell dysfunction, contributing to vascular hyperpermeability in diabetes (Wautier et al., 1996).

However, RAGE is now known to be a multi-ligand receptor as it can also bind to HMGB1, S100 proteins (S100s), amyloid-β peptide (Aβ) and DNA to regulate multiple physiological and pathological processes. S100s are a family of pro-inflammatory cytokine-like mediators with intracellular and extracellular properties. Generally, they have been shown to promote the

expression of pro-inflammatory genes, as well as cell migration, proliferation and apoptosis (T. Gong et al., 2020). RAGE signalling is very complex and depends not only on the identity of the ligand but also on the cell type. It can initiate multiple signalling pathways, including the PI3K-AKT, MAPK and JAK-STAT pathways that, in turn, activate transcription factors such as NF-kB, activator protein 1 (AP-1) and STAT3 (Figure 1.14) (T. Gong et al., 2020).

RAGE is expressed at low levels in normal tissues and vasculature and it becomes upregulated at sites where its ligands accumulate (Schmidt et al., 2001; Yan et al., 2003). Specifically, extracellular HMGB1 can stimulate RAGE expression in several cell types (Jianfeng Li et al., 1998). HMGB1, AGEs and S100s have been reported to upregulate RAGE expression, suggesting a positive feedback loop in the RAGE-induced inflammatory response (Y. Chen et al., 2015; L. Feng et al., 2005; Tanaka et al., 2000).

1.3.2.3 *HMGB1 signalling*

For many years, numerous and diverse HMGB1 extracellular functions could not be attributed to interaction with RAGE. More recently, several new binding partners have been described: HMGB1 can interact with TLRs, integrins, proteoglycans, CD-24, T-cell immunoglobulin and mucin-domain containing-3 (TIM-3), C-X-C chemokine receptor type 4 (CXCR4, also known as fusin or CD-184), N-methyl-D-aspartate receptor (NMDAR, also known as NMDA) and triggering receptor expressed on myeloid cells 1 (TREM-1).

Which receptor HMGB1 binds to largely depends on whether HMGB1 acts on its own or in complex with partner molecules. HMGB1 is prone to bind other proinflammatory molecules including DNA, RNA, histones, nucleosomes, LPS, C-X-C motif chemokine 12 (CXCL-12), IL-1α and IL-

1β. These complexes act in synergy via cognate receptors to the HMGB1-partner molecules. In fact, many of the receptor systems claimed to perform as HMGB1 receptors are actually receptors for complexes of molecules bound to HMGB1. For example, TLR-9 is mainly responsible for HMGB1-DNA complex-induced nucleotide immunity, which can be enhanced by RAGE (R. Kang et al., 2014). Other HMGB1-interacting molecules include leukocyte integrin Mac-1 (also known as CD-11b/CD-18) which has been reported to mediate neutrophil recruitment through HMGB1 and RAGE (Orlova et al., 2007). Similarly, the proteoglycan heparan sulphate can bind to RAGE and might be essential for HMGB1/RAGE interaction (Ding Xu et al., 2011).

HMGB1 is a redox-sensitive protein: cysteine 23 (C23) and C45, in the A box, can form a disulphide bond, and the unpaired C106, in the B box, is also susceptible of oxidation (Figure 1.14). Notably, the redox state of these cysteines modulates the extracellular activities and determines its binding to different receptors. In a quiescent cell, HMGB1 is always fully reduced, with all three cysteines expressing thiol groups. Extracellularly, the fully reduced form of HMGB1 acts forming a complex with CXCL-12 to interact with CXCR4, which leads to inflammatory cell recruitment to damaged tissues (Schiraldi et al., 2012). Formation of a disulfide bond between C23 and C45 enables HMGB1 to bind to TLR-4/MD-2 complex or RAGE and determines its cytokine activity and proinflammatory function (Figure 1.13) (Ferrara et al., 2020). Finally, further cysteine oxidation by reactive oxygen species abrogates both activities and is associated with the resolution phase of inflammation (Figure 1.14) (Yiting Tang et al., 2016). These redox modifications are reversible processes, which enable HMGB1 to shift from its different forms and activities (Yiting Tang et al., 2016).

Even if the list of reported HMGB1 binding partners is quite extensive, only RAGE and TLR-2 and 4 are fully confirmed to act as established HMGB1 receptors. HMGB1 can interact with TLR-2, TLR-4 to activate the NF-kB and IRF pathways to produce inflammatory cytokines and activate the immune response (Figure 1.13). The disulphide form of HMGB1 activates TLR-4 and binds to MD-2, forcing two TLR-4 chains to form a complex that can bind intracellular signal transduction molecules (H. Yang et al., 2015). MD-2/TLR-4 interaction has been widely described in response to LPS (Shimazu et al., 1999). However, the binding site for HMGB1 on the MD-2 molecule is distinct from that of LPS (H. Yang et al., 2020). Signalling through TLR-2 and TLR-4 induces several responses including tissue injury cell migration and adhesion, and inflammation (R. Kang et al., 2014).

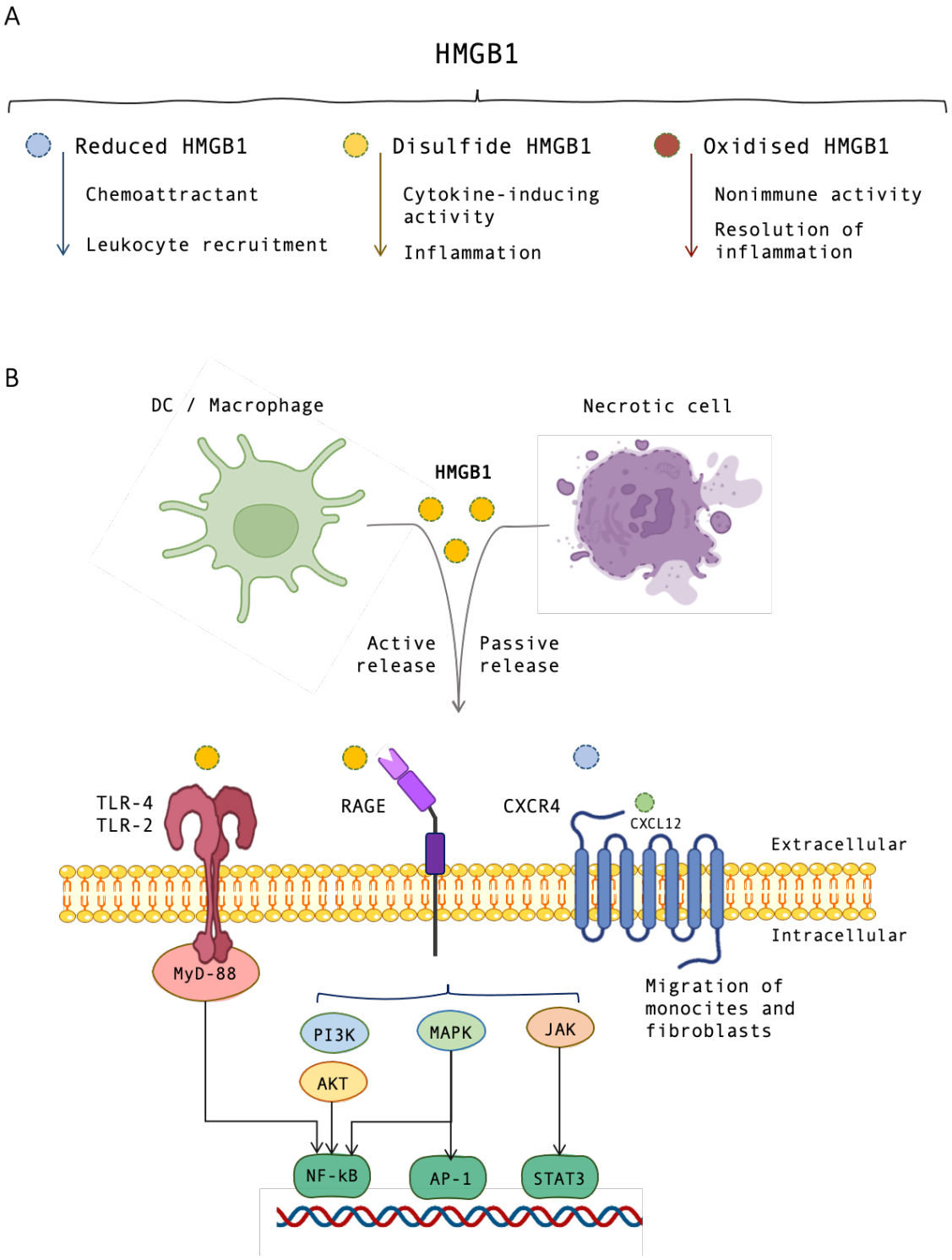

Figure 1.14: HMGB1 redox state determines its signalling function. (A) The three different redox forms of extracellular HMGB1 have distinct functions. These also determine the receptor which HMGB1 interacts with, and the molecular cascade initiated by this interaction.

1.3.2.4 *HMGB1/RAGE signalling in disease*

Since the discovery, almost two decades ago, of the immunogenic properties of HMGB1, numerous studies have focused on investigating its role in the pathophysiology of diseases. Constitutive deletion of HMGB1 in mice leads to lethal hypoglycaemia and late embryonic death (Calogero et al., 1999). Hence, genetic studies designed to investigate the role of HMGB1 in different pathologies target its receptors or HMGB1 specifically in tissues. Alternatively, several HMGB1 antagonists, polyclonal and monoclonal antibodies against HMGB1 or its receptors can be used to inhibit the functions of HMGB1. Studies using these approaches have shown HMGB1 to occupy a central role in the pathogenesis of both infectious and sterile inflammation.

During sepsis, HMGB1 acts as a late mediator of inflammation that can be sustained for several days and correlates with unfavourable prognosis (H Wang et al., 1999). Upon infection, the early release of conventional proinflammatory cytokines (TNFα or IL-1β) is followed by the late release of HMGB1 that often leads to lethality. Treatment with HMGB1 neutralising antibodies or the HMGB1 antagonist, HMGB1 A box, provides protection even if administered several hours after the peak secretion of the early cytokines (Abeyama et al., 2005; Nagato et al., 2009). Signalling through RAGE is known to be at least partially responsible for the development of acute inflammation during sepsis given that genetic ablation of the receptor or anti-RAGE antibodies provides protection from the lethal effects of septic shock caused by cecal ligation and puncture (CLP) (Liliensiek et al., 2004; Lutterloh et al., 2007). In addition to RAGE, the effects of HMGB1 are believed to be also mediated through TLR-4 (H. Yang et al., 2015; Youn et al., 2008).

In contrast to its role during sepsis, HMGB1 acts mediating early inflammatory responses in the context of sterile tissue damage and cell death. High levels of circulating HMGB1 are detected following major events such as stroke, myocardial infarction or haemorrhagic shock, during which ischemia-reperfusion injury leads to passive release of HMGB1 (Bertheloot & Latz, 2017). Indeed, neutralising HMGB1 through polyclonal antibodies has a protective role in animal models of ischemia-reperfusion and haemorrhagic shock (Venereau et al., 2016). Both TLR-4 and RAGE play roles in these settings. HMGB1 also has a central role in the development and aggravation of chronic inflammation. Rheumatoid arthritis (RA) was one of the first setting in which this role was demonstrated convincingly. Increased levels of HMGB1 can be found in blood, synovial tissue and fluid of arthritis patients and arthritis animal models (Harris et al., 2012). In accordance with this, HMGB1 injection leads to destructive arthritis in mice and treatment with agents that antagonise expression or activity leads to disease attenuation in models of disease (Harris et al., 2012).

1.3.2.5 *HMGB1 and RAGE in the skin*

As previously described, extracellular HMGB1 generally functions propagating inflammation, alerting and initiating immune responses. HMGB1 and HMGB1-induced inflammatory factors, such as IL-18, have been shown contribute to the development of IMQ-derived psoriatic inflammatory lesions (W. Zhang et al., 2017). Specifically, keratinocyte-derived HMGB1 is suggested to induce Th-17-type inflammatory factors in an autocrine manner and promote the development of psoriasis in this model (W. Zhang et al., 2017). Furthermore, *in vivo* knock-down of HMGB1 in mice, through subcutaneous injection of a lentivirus containing a small harpin RNA (shRNA) against HMGB1, or specific deletion of HMGB1 from epidermal keratinocytes significantly ameliorates psoriasis severity and

reduces dermal inflammatory cell infiltration in the IMQ-induced psoriasis-like model (Z. Wang et al., 2021). Selective ablation of HMGB1 from DCs, myeloid cells or T-cells (expressing -Cre under *Itgax*, *Lyz2* and *Lck* promoters respectively), did not affect the outcome of IMQ-induced psoriasis-like severity (Z. Wang et al., 2021). This study also associated HMGB1 secretion with keratinocyte autophagy, which was at least partially dependent on crosstalk between keratinocytes and γδT-cells. Furthermore, injection of HMGB1 intradermally in mice leads to epidermal thickening and cell infiltration and induces the expression of psoriasis-associated inflammatory chemokines and anti-microbial peptides as well as cytokines associated with innate immunity and the IL-23-IL-17A axis (Z. Wang et al., 2021).

An association between psoriasis and HMGB1 has also been found in humans. HMGB1 serum levels have been found to be significantly higher in patients with psoriasis compared to healthy controls, which correlate with the severity of the disease (Bergmann et al., 2016; T. Chen et al., 2013). Immunohistochemistry and immunofluorescence stainings, as well as Western blot data, confirmed that HMGB1 was detected in the cytoplasm of keratinocytes found in psoriatic lesions while control skin showed HMGB1 restricted to the nucleus (T. Chen et al., 2013). In line with these results the expression of TLR-2, TR-4 and RAGE is enhanced both in human psoriasis lesions and in skin lesions found in the IMQ-induced psoriasis-like model (W. Zhang et al., 2017).

RAGE signalling has also demonstrated to be key sustaining inflammation in the skin. Although not essential for the initiation of the inflammatory process (Riehl et al., 2010), RAGE is required for the upregulation of pro-inflammatory mediators, maintenance of immune cell infiltration and epidermal hyperplasia following treatment with phorbol ester TPA, a carcinogenic and inflammation inducer (Gebhardt et al., 2008). Several

studies have shown, using this model, that RAGE modulates the strength, maintenance and kinetics of skin inflammation and protects from tumour development in the skin (Gebhardt et al., 2008; Leibold et al., 2013; Riehl et al., 2010). $RAGE^{EKO}$ and wild type animals have similar inflammatory responses up to 24 hours after TPA treatment, but $RAGE^{EKO}$ mice show no signs of inflammation after 48 hours (Leibold et al., 2013), suggesting that specific expression of RAGE in keratinocytes is responsible for the modulation of TPA-induced inflammation. A role of RAGE in the regulating the expression of pro-inflammatory cytokines such as TNF has also been suggested (Leibold et al., 2013; Wolf et al., 2010).

A role for HMGB1 in atopic dermatitis has not been clearly defined: the presence of HMGB1 in serum is contradictory (T. Chen et al., 2013; Cuppari et al., 2016), although HMGB1 expression was detected through Western blot in the cytoplasmic fraction of skin cells (T. Chen et al., 2013). Epidermal keratinocyte-derived HMGB1 has been shown to play a role in chronic inflammation and wound healing by regulating NET formation (Hoste et al., 2015, 2019) and neutralisation of RAGE or TLR-4 in chronic skin inflammation in mice results in enhanced wound healing (Hoste et al., 2019). Moreover, local delivery of HMGB1 derives in marked hypertrophic scar formation in rabbit hypertrophic scar models, while its blockade causes anti-scaring effects (Jingling Zhao et al., 2018). Other studies, however, have reported opposing results showing that inhibition of HMGB1 impairs wound healing in normal mice (Straino et al., 2008).

HMGB1 has also been studied for its role in SLE, a multisystemic autoimmune disease. HMGB1 levels have been found to be increased in the serum and in epidermis and dermis infiltrate of patients with SLE, which correlated with disease activity (Barkauskaite et al., 2007; Popovic et al., 2005). The cellular source of HMGB1 has not been identified and could be result of either activation or the death of keratinocytes or

infiltrating immune cells. A role of RAGE in SLE has also been reported given that sRAGE levels were significantly higher in the skin of patients compared to healthy controls (Nienhuis et al., 2008).

In conclusion, a clear role of HMGB1 in inflammatory skin conditions has been established by signalling through different receptors by itself or in the company of other molecules. RAGE has shown to be essential in sustaining inflammation in the skin and other inflammatory diseases, although other ligands than HMGB1 might contribute to this role. Nevertheless, targeting the HMGB1/RAGE axis is promising experimental strategy to reduce inflammation in the skin.

1.4 Project aims

Necroptosis is an inflammatory form of regulated cell death that has been shown to play a role in pathophysiology of infectious and sterile inflammatory diseases through the release of DAMPs. The role of necroptosis in the skin has been a major focus of interest after the description of several necroptosis-dependent skin inflammation animal models. DAMPs released during necroptosis, such as HMGB1 and IL-33, can trigger an innate immune response, which might contribute to skin inflammation. This thesis focuses on studying the role of HMGB1 and IL-33 in skin necroptosis *in vitro* and *in vivo.*

The first part of this thesis will address the possible role of HMGB1 in inducing keratinocyte necroptosis *in vitro*. The work is based on several previous work that show HMGB1 can induce MLKL phosphorylation in epidermal keratinocytes *in vitro* and *ex vivo* (personal communication, MC Bonnet).

- **Chapter 3** focuses on detecting necroptosis-associated proteins upon HMGB1 treatment of normal human epidermal keratinocytes (NHEKs) and the optimisation of such detection. Furthermore, it investigates the composition of the HMGB1-induced necrosome in NHEKs.
- The aim of **Chapter 4** is to optimise a sensitive and specific method to detect necroptosis in NHEK, which allows the detection of HMGB1-induced cell death.

The second part of this thesis focuses on studying the role of IL-33, ST2 and RAGE signalling in skin necroptosis *in vivo.* The necroptosis-dependent skin inflammation model, Casp-8^{EKO}, is used to study the effect of these DAMPs and receptors:

- **Chapter 5** investigates the role of IL-33/ST2 signalling in Casp-8^{EKO} skin inflammation by studying the skin inflammatory phenotype of Casp-8^{EKO} *Il-33*$^{-/-}$, Casp-8^{EKO} *St2*$^{-/-}$.
- The aim of **Chapter 6** is to study the role of RAGE signalling in Casp-8^{EKO} animals by deleting RAGE constitutively or specifically from epidermal keratinocytes.

the skin inflammatory phenotype and animal survival has been assessed for each line, together with the expression of skin proliferation and differentiation markers, necroptosis and apoptosis markers, immune cell infiltration and cytokine profile.

Chapter 2

Materials and methods

2.1 General information

2.1.1 General laboratory equipment

Information regarding reagent concentrations and suppliers are provided below in the relevant methods sections and can also be found listed in Appendix I. General laboratory plastic-ware was purchased from Grenier Bio-one (tips, filtered tips, microcentrifuge tubes) and Thermo Fisher Scientific (conical centrifuge Falcons). Centrifugation for general molecular biology work was performed using an Eppendorf 5415R refrigerated centrifuge. PCMT Thermoshaker was used as a benchtop incubator to shake and heat samples.

2.1.2 Buffers and stock solutions

RIPA lysis buffer: 150 mM NaCl, 5mM EDTA (pH 8), 50 mM Tris (pH 8), 1% (v/v) NP-40, 0.5% (w/v) sodium deoxycholate (DOC), 0.1% (w/v) SDS. 1X cOmplete ULTRA protease inhibitor cocktail (Roche) and 1X PhosStop phosphatase inhibitor cocktail (Roche).

IP lysis buffer: 20 mM Tris-HCl pH 7.5, 1 mM Na_2EDTA, 1% (v/v) NP-40, 10% (v/v) Glycerol, 1X cOmplete ULTRA protease inhibitor cocktail (Roche) and 1X PhosStop phosphatase inhibitor cocktail (Roche).

LDH storage buffer: 200 mM Tris-HCl (pH 7.3), 10% (v/v) Glycerol, 1% (w/v) BSA.

SDS running buffer (10X): 0.25 M Tris base, 1.9 M Glycine, 0.34 M SDS, 1X solutions were prepared by diluting 10X solutions 1:10 with distilled water.

Glycine transfer buffer: 25 mM Tris base, 192 mM Glycine pH 8.3, 20% (v/v) methanol.

Mild stripping buffer: 0.2 M Glycine, 3.5 mM SDS, 1% (v/v) Tween-20, Adjust pH to 2.2.

DNA lysis buffer: 100 mM Tris-HCl pH 8.5, 5 mM EDTA, 200 mM NaCl, 0.2% (w/v) SDS.

Tris-acetate-EDTA, TAE (10X): 0.4 M Tris Base, 1.15% (v/v) glacial acetic acid, 10 M EDTA (pH 8).

Citrate buffer: 10 mM Tri-sodium citrate, 0.05 % (v/v) Tween-20, Adjust pH to 6.

Preparation of 1X cOmplete ULTRA protease inhibitor and 1X PhosStop phosphatase inhibitor cocktails (both from Roche) were achieved by dissolving one tablet per 10 ml of lysis buffer.

2.1.3 Antibodies

Name	Host	Blocking & concentration	Provider
Anti- RIP3 Polyclonal (ab56164)	Rabbit	(WB) 1:1000 NFDM	Abcam
RIPK1 (BD 610459) (38/RIP)	Mouse	(WB) 1:1000 NFDM (IP) 1:200	BD Biosciences
α-MLKL (phospho S358) (ab187091) (EPR9514)	Rabbit	(WB) 1:1000 BSA (IP) 1:200	Abcam

Human Phospho-MLKL (T357) (MAB9187) (954702)	Mouse	(WB) 1:1000 BSA	R&D Systems
Recombinant MLKL (ab243142) (3H1)	Rat	(WB) 1:1000 NFDM	Abcam
Recombinant anti-GSDMD (ab210070) (EPR19829)	Rabbit	(WB) 1:100 NFDM	Abcam
β-Actin (sc-47778)	Rabbit	(WB) 1:1000 NFDM	Santa Cruz
RIPK3 (NBP2-45592) (OTI1B3)	Mouse	(IP) 1:200	Novus Bio
Human RIPK3 (MAB7604) (780115)	Mouse	(IP) 1:1000 (IHC) 1:1000 GS; Citrate B AR	R&D Systems
Human RIP3 Polyclonal (PA1-41533)	Rabbit	(WB) 1:1000 NFDM (IP) 1:100	Invitrogen
Anti-RIP3 (B-2) (SC-374639)	Rabbit	(IP) 1:200	Santa Cruz
Anti-Mouse HRP Polyclonal	Goat	(WB) 1:1000	Dako
Anti-Rat HRP Polyclonal	Rabbit	(WB) 1:1000	Abcam
Anti-Rabbit HRP Polyclonal	Goat	(WB) 1:1000	Dako
Anti-Mouse RIP3 Polyclonal (ab62344)	Rabbit	(IHC) 1:1000 GS; Citrate B AR	Abcam
Purified mouse keratin 6A Polyclonal (905701)	Rabbit	(IHC) 1:1000 GS Citrate B AR	BioLegend
Keratin 14, LL002 (MS-115-P	Rabbit	(IHC) 1:50 GS Citrate B AR	NeoMarkers
Ki-67 Polyclonal (ab15580)	Rabbit	(IHC) 1:100 GS Citrate B AR	Abcam
Keratin 10 Polyclonal (905401)	Rabbit	(IHC) 1:1000 GS Citrate B AR	BioLegend
Loricrin Polyclonal (905101)	Rabbit	(IHC) 1:100 GS Citrate B AR	BioLegend

Cleaved Casp-3 (AF835)	Rabbit	(IHC) 1:100 GS	R&D Systems
Mouse MLKL (phospho S345) ab196436 (EPR9515)	Rabbit	IHC) 1:100 GS; Trypsin AR	Abcam
Anti-Mouse F4/80 (MCA497GA) (A3-1)	Rat	(IHC) 1:100 GS	AbD Serotec
Anti-Human CD3 (A0452)	Rabbit	(IHC) 1:100 GS	Dako
Anti-Mouse Ly-6G and Ly-6C (557445) (RB6-8C5)	Rat	(IHC) 1:20 FSG	BD Biosciences
Purified anti-Mouse TNF (559064) (MP6-XT22)	Rat	(IHC) 1:25 FSG	BD Biosciences
Mouse IL-33 AF3626	Goat	(IHC) 1:100 FSG	R&D Systems
Anti-Rabbit IgG – Alexa Fluor 488 (Poly4054)	Goat	(IHC) 1:1000	BioLegend
Anti-Rabbit IgG – Alexa Fluor 594 (Poly4054)	Goat	(IHC) 1:1000	BioLegend
Anti-Rat IgG – Alexa Fluor 594 (Poly4054)	Goat	(IHC) 1:1000	BioLegend
Anti-Mouse IgG – Alexa Fluor 594 (Poly4054)	Goat	(IHC) 1:1000	BioLegend

Table 2.1: Information on commercial antibodies including host, provider, concentration and blocking used. For Western blot (WB), the concentration ratio is shown (volume) as well as the blocking solution for the antibody incubation, which can be either 5% (w/v) non-fat dried milk (NFDM) or 5% (w/v) bovine serum albumin (BSA). For immunohistochemistry (IHC), the concentration and blocking used are indicated: goat serum (GS) or fish skin gelatine (FSG). Additionally, the type of antigen retrieval (AR) used is indicated, if necessary. HRP-conjugated and Alexa Fluor secondary antibodies are incubated in the same blocking solution as the primary antibody. For immunoprecipitation (IP), the ratio of antibody per protein (mass) is indicated.

2.1.4 Statistical data analysis

Figures and statistical analysis were made using GraphPad Prism 9 software (GraphPad Software Inc., La Jolla, USA). For *in vitro* data, for which data was generally collected from technical replicates, normal distribution was assumed for sample sizes of 3 replicates (n=3). For larger sample sizes (which were always smaller than 10), the Shapiro–Wilk test was used to test normality as this is a powerful test designed for small sample sizes (n<50). Similarly, data obtained from *in vivo* experiments was also checked for using the Shapiro–Wilk test.

If normally distributed (or if normality is assumed), the one-way ANOVA test was used to determine statistical significance when comparing two or more experimental groups followed by Turkey's multiple comparison test. Two-way ANOVA was used where experimental groups were compared across multiple timepoints, followed by followed by Turkey's multiple comparison test or Sidák's multiple comparison test. If not normally distributed, data was statistically analysed using non-parametric tests: the Mann–Whitney U test was used when comparing two populations while the Kruskal–Wallis test was used when comparing more than two samples. When data was not normally distributed, Dunn's test was used to compare between multiple groups.

2.2 Tissue culture

2.2.1 Equipment and tissue culture plastics

All tissue culture was performed in a MICROFLOW Advanced Bio Safety Cabinet Class II (Bioquell). Cells were incubated in New Brunswick Galaxy 170S CO_2 incubator, Thermo Scientific BB15 CO_2 incubator or Nuaire Autoflow IR CO_2 incubator at 37 °C with 20% O_2 and 5% CO_2. Centrifugation

of cell suspensions was performed using an Eppendorf 5810R refrigerated centrifuge. Culture medium was always warmed to 37 °C before use, using a WB22 Phoenix water bath.

Nunc EasYFlask cell culture T75-175 cm^2 flasks with filtered caps (ThermoFisher) were used to culture HT-29 cells. NHEK cells were cultured in 60-, 100- and 150-mm diameter Falcon Standard tissue culture dishes (Fisher Scientific) coated with collagen. For coating, the total dish surface was covered with a 0.1 mg/mL PureCol® (Advanced Biomatrix) solution diluted in sterile water and kept at 37 °C for a minimum of 8 hours before use.

2.2.2 HT-29 cell line maintenance

Human colon adenocarcinoma cell line HT-29 were a kind gift of Dr. Carmen van den Berg (Cardiff University). HT-29 cells were cultured in DMEM high glucose GlutaMAX growth medium supplemented with 10% (v/v) foetal calf serum (FCS) and antibiotics (100U/mL Penicillin and 100 μg/mL streptomycin). This formulation is herein termed "complete DMEM". Cells were maintained at 40-80% confluency in T75 or T175 culture flasks. For routine maintenance, culture medium was discarded every 2-3 days and renewed with fresh complete DMEM. To passage cells, growth medium was removed, and cells were washed twice with room temperature PBS. Next, cells were incubated with 0.05% (w/v) trypsin-EDTA for 5 minutes at 37 °C. Complete DMEM was then added to neutralise the trypsin and the cell suspension was harvested and centrifuged. Cell pellets were resuspended in complete DMEM and replated at between 1:4 and 1:6 ratios.

For cryopreservation, HT-29 were harvested as described above and, after centrifugation, resuspended in 1 mL of 90% (v/v) complete DMEM and 10% (v/v) dimethyl sulfoxide (DMSO). Cell suspension was transferred to

cryovials and placed in Nalgene Cryogenic freezing container (ThermoFisher) at -80 °C for short-term storage. For long-term storage, vials were transferred to liquid nitrogen containers. Regular mycoplasma testing was undertaken using Mycoplasma PCR ELISA (Sigma Aldrich) following manufacturer's instructions.

2.2.3 NHEK isolation and maintenance

Keratinocytes were cultured using culture medium described by J. G. Rheinwald & Green (1975), and referred herein as "complete keratinocyte culture medium" or "Green's medium". Complete NHEK culture medium was made of 1:4 DMEM high glucose GlutaMAX (Gibco) supplemented with: 2.5% (v/v) FCS, 0.4 μg/mL hydrocortisone (HC), 8.4 ng/mL Cholera toxin (CT), 5 μg/mL insulin, 24 μg/mL adenine, 10 ng/mL human epidermal growth factor (hEGF) and Antimycotic/Antibiotic solution (Gibco) plus 3:4 F-12 Nutrient Mix GlutaMAX (Gibco).

2.2.3.1 *Isolation from human skin samples*

Skin samples were obtained from abdominoplasties and breast reductions of healthy adult donors (various ages) after informed consent (NREC 08/WSE04/17). Information regarding the sex, age or ethnicity of the donors was not accessible as the Ethics Protocol did not allow the recording of details from the surgery patients. Primary keratinocytes were isolated using an adapted methodology described by J. Rheinwald (1989), briefly detailed here. After surgery, skin pieces were placed aseptically in bottles containing DMEM plus Antibiotic-Antimycotic solution (Gibco) to transport immediately from the clinical setting to the research laboratory, where they were processed within 2 hours after surgery. PBS supplemented with Antibiotic-Antimycotic solution (Gibco), hereon referred as PBS + A/A, was used to wash the sample thoroughly. With the aid of fine forceps, scissors and

scalpels, the subcutaneous fat and deeper portion of the dermis were removed from the sample. The cleaned skin was then cut in 1x1 cm portions and placed in 6-well plates containing 1 mL of 2.5% (v/v) Trypsin-EDTA, no phenol red (Gibco). Skin samples were positioned so only the dermis and not the epidermis was in contact with the trypsin. After trypsin incubation at 4 °C for 72 hours, the epidermis was carefully separated from the dermis using fine forceps. The obtained epidermal sheet was then mechanically disrupted using two scalpels and placed in a 1.5 mL centrifugation tube containing complete keratinocyte culture medium. This process was repeated for every 1x1 cm portion of skin. Centrifugation tubes were then placed on a shaker at 1000 rpm at 25 °C for 1 hour to complete mechanical disruption of the tissue. The obtained solution was transferred to a 5 mL centrifuge tube containing 3 mL of complete keratinocyte culture medium and this was passed through a 5 mL polystyrene pipette 10-15 times. The resulting solution was then plated in 60 mm collagen-coated culture dishes. After 24 hours, the supernatant from each culture dish, containing un-attached cells was transferred to new a collagen-coated dish. The initial dish was washed once with PBS + A/A and filled with fresh Green's medium.

2.2.3.2 *Passage and maintenance*

Normal human epidermal keratinocytes (NHEK) were passaged when cells reached 60-70% confluency. Cells were washed twice with room temperature PBS + A/A and incubated with 0.5% (v/v) trypsin-EDTA for 15 minutes at 37 °C. Detachment of the NHEK from the culture plate was confirmed using a light microscope and cells were incubated for longer if needed. When complete detachment was achieved, complete keratinocyte culture medium was added to the cells to neutralise the trypsin activity. NHEK suspension was collected and centrifuged at 300 xg for 5 min, after which the supernatant was carefully discarded. The remaining pellet was washed twice and resuspended in complete keratinocyte culture medium.

After thorough mixing with additional medium, the cells were plated in collagen-coated culture dishes in a 1:2 to 1:3 ratio.

After plating the keratinocytes for the first time after isolation, NHEK can take up to 1 week to attach effectively and grow forming characteristic patches. The growth rate of the keratinocytes was assessed by eye using a light microscope, by which confluency and passage ratio was determined. NHEK were not counted before plating, thus, a trained eye for the growth rate and differentiation stage of the cells was needed to make this assessment. The differentiation stage of the keratinocytes was monitored regularly to ensure differentiated cells were not used for experiments. The growth and differentiation rate, as well as the efficiency of the isolation was dependent on the skin sample obtained.

2.2.4 Commercially obtained NHEK

Commercially obtained NHEK were purchased from PromoCell. NHEK were isolated from adult skin from pooled donors. Cells were received in T25 flasks at high confluency and were immediately passaged and maintained as described above.

2.2.5 Cell count

HT-29 cells were counted using a haemocytometer coupled with Trypan Blue at 0.1% (v/v) to assess viability prior to plating and approximately 10,000 cells per well were plated when using a 96 well plate. As mentioned, NHEK were not counted and the number of cells was assessed by eye depending on the growth rate and differentiation stage of the cells.

2.3 Induction of cell death

HT-29 or NHEK were seeded in appropriate flasks or plates 24-36 hours before stimulation, depending on cell density (HT-29) or the level of differentiation and growth rate of the cells (NHEK). Complete growth medium was changed before stimulation.

Necroptosis was induced in HT-29 and NHEK by the addition of 20 ng/mL human recombinant TNF (PeproTech) in combination with the Smac mimetic, Birinapant (1 μM), and pan-caspase inhibitor Z-VAD-FMK (20 μM) (both from SelleckChem). The combination of these three reagents is abbreviated as TSZ. Apoptosis was induced by the addition of 20 ng/mL human TNF and 1μM Birinapant. Combination of these reagents is abbreviated as TS. The time of incubation depends on the cell type used and the specific experiment performed and is indicated in the results text and figure legends.

Stimulation of NHEK with HMGB1 was performed with endotoxin-free purified disulfide HMGB1 (IBL-Tecan) at 50 μM unless stated otherwise. The time of incubation depends on the specific experiment performed and is clearly indicated in the results text and figure legends.

2.3.1 Necroptosis inhibitors

The necroptotic inhibitors used during this project are: Necrostatin 1s (Nec-1s), Necrosulfonamide (NSA), GSK872 and GW806742X. Their mode of action of each inhibitor, together with the concentration information is detailed in Table 2.2. HT-29 or NHEK were incubated with the indicated inhibitor 1 hour prior to the addition of TSZ, TS or HMGB1.

Inhibitor	Description	Concentration
Necrostatin 1s (Nec-1s)	ATP-competitive allosteric inhibitor of RIPK1. Blocks RIPK1/RIPK3 interaction *in vitro* without affecting TNFR-induced apoptosis	20 μM
Necrosulfonamide (NSA)	Binds to N-terminal MLKL, covalently modifying Cys86 of human MLKL and preventing necrosome from interacting with its downstream effectors	1 μM
GSK-872 (GSK)	Inhibits RIPK3 kinase activity, preventing MLKL phosphorylation and necrosome formation	1 μM
GW806742X (GW)	Inhibits MLKL pseudokinase domain targeting its 4HB domain	5 μM

Table 2.2: Necroptosis inhibitors, target and concentrations used.

2.4 Cell toxicity and viability assays

2.4.1 Materials and equipment

Clear 96-well plates, for LDH and WST-1 assays, were coated with collagen as described in section 2.2.1. White opaque Collagen Type I-coated 96-well plates (Gibco) were used for PI-based assays. Fluorescence, luminescence and absorbance were read using CLARIOstar microplate reader (BMG LABTECH).

2.4.2 PI-based cell death assay

PI is a fluorescent intercalating agent that binds to DNA when taken into the cell. As an impermeant dye, it can only reach DNA when membrane permeability and integrity has been compromised. It is, therefore, a well-

established marker of necrosis and widely used, often together with annexin V negative stain (an apoptosis marker) to detect necrotic processes.

All PI-based experiments were performed using collagen coated 96-well opaque plates. Following compound treatment at 37 °C, cells were stained with 10 μg/mL of PI (Sigma-Aldrich), which consisted in the addition of 1 μL of PI (stock solution at 1 mg/mL) to each well at the end of the stimulation. Prior to PI addition, supernatant was not removed, and cells were not washed to avoid losing detached dead cells. All following steps are performed in the dark and using tin foil to cover the plate at all times. The plate was gently shaken for 1-2 minutes and kept in the incubator at 37 °C for 20-30 minutes, after which fluorescence (520/630 nm) was read using a microplate reader. Next, 10 μL of 10% (v/v) Triton-X100 in complete DMEM were added to each well to achieve total cell lysis. The plate was gently shaken for 5 minutes and incubated for 20-30 minutes at 37 °C. Fluorescence was read, again, to obtain the maximal fluorescence value. Background fluorescence was calculated as an average of the fluorescence obtained from wells containing untreated cells. Percentage of cell death was calculated as follows:

$$100 * \frac{\text{induced fluorescence} - \text{background fluorescence}}{\text{maximal fluorescence} - \text{background fluorescence}}$$

2.4.3 LDH-based cell death assay

LDH is a soluble cytoplasmic enzyme present in many cell types and is rapidly released into extracellular space when the plasma membrane is disrupted. To detect the leakage of LDH into cell culture medium, a tetrazolium salt is used in this assay. In the first step, LDH produces reduced nicotinamide adenine dinucleotide (NADH) when it catalyses the oxidation of lactate to pyruvate. In the second step, a tetrazolium salt is converted to a coloured formazan product using newly synthesized NADH in the presence

of an electron acceptor. The amount of formazan product can be quantified by standard the reading of luminescence.

The LDH-based assay used was LDH-Glo Cytotoxicity Assay (Promega) and was performed following manufacturer instructions. Briefly, 5 μL of supernatant were recovered from each well at the desired timepoints and transferred to a new clear plate. Supernatants were mixed with 45 μL of LDH Storage Buffer (see section 2.1.2). Next, 50 μL of LDH detection reagent (provided with the assay) is added to each well and plate is shaken for 2 minutes in the plate shaker. After 1 hour incubation at room temperature, luminescence is read using a plate reader. The sensibility of assay was unexpectedly high and maximal luminescence (3.5) was reached when cells were incubated with 10% (v/v) Triton-X100 in complete DMEM for total cell lysis. Hence, the percentage of cell death was not calculated considering the total number of cells for each condition and a standardised number was used as maximal luminescence. The formula used in to calculate the percentage of LDH release is:

$$100 * \frac{\text{induced luminescence} - \text{background luminescence}}{3 - \text{background luminescence}}$$

2.4.4 WST-1 cell viability assay

The WST-1 viability assay is based on the cleavage of the tetrazolium salt WST-1 to form formazan dye, which is a slight darker colour. The conversion only occurs in metabolically active cells through the mitochondrial succinate-tetrazolium-reductase system (RS). An expansion in the number of viable cells results in an increase of the overall activity of mitochondrial dehydrogenases, leading to an increase in formazan dye, which can be directly quantified through spectrophotometry in a plate reader.

Cell viability was assessed using the cell proliferation reagent WST-1 (Roche) according to manufacturer's instructions. Briefly, after stimulation of the cells, 20 μL of WST-1 reagent are added to each well, mixed thoroughly and incubated at 37 °C for 1 hour. The plate was shaken for 1-2 minutes on a shaker and absorbance was read using a plate reader at 420 to 480 nm. Background absorbance is calculated through an average of the absorbance measured in wells containing untreated cells. Percentage of death is calculated using this formula:

$$100 * \frac{\text{Induced absorbance}}{\text{background absorbance}}$$

2.4.5 Assessment of morphological changes in NHEK

Assessment of major morphological changes can reveal useful information on the overall health of the cells. Traditionally, morphologic detection of death refers to membrane alterations, alterations of the nucleus, and changes in the cytoplasmic contents (Schweichel & Merker, 1973). Under the experimental conditions used here, cultured keratinocytes associate and grow forming tightly packed patches that spread over the culture plate. Changes in the size of these patches and in the overall confluency of the wells are determinant indicators of overall health of NHEK cells.

2.4.6 Culture medium optimisation

For culture medium optimisation in Chapter 4, preparation of the different mediums was performed progressively, separating batches of medium before adding the proportional amount of the next ingredient. NHEK were passaged as described above, using Green's medium, and were cultured in the "new" medium for at least 24 hours before initiation of the experiment to allow cells to adapt to the new conditions.

2.5 Protein extraction and detection

2.5.1 Protein extraction

Following stimulation or at the end of the experiment, HT-29 or NHEK were washed twice with ice-cold PBS and scraped using CELLTREAT cell scraper (Fisher Scientific) in the appropriate volume of freshly made cell lysis buffer, which differed depending on the protein detection protocol that followed: i) cells were lysed with RIPA buffer (see section 2.1.2) if they were to be used for Western blot analysis, unless stated otherwise; ii) if protein samples were to be used for immunoprecipitation (IP) of proteins, IP lysis buffer was used (see section 2.1.2). The scraped cell suspension was transferred to a 1.5 mL microcentrifuge tube and incubated on ice for 20 minutes during which time the lysates were mixed several times using a vortex. The cell lysate was then cleared by a 20-minute centrifugation at 17700 xg at 4 °C. The supernatant, containing the proteins, was transferred to a new 1.5 mL microcentrifuge tube for determination of protein concentration.

2.5.2 Determination of protein concentration

The protein concentration was determined using Bio-Rad Protein Assay (Bio-Rad) or Pierce BCA Protein Assay Kit (ThermoFisher) according to manufacturer's instructions. Bio-Rad Protein Assay is based on the method of Bradford and involves the addition of an acidic dye, containing Coomassie Blue which binds to basic aromatic amino acid residues. Binding of this dye to proteins shifts the absorbance maximum and allows the subsequent measurement of absorbance at 595 nm with a microplate reader. First, the reagent was diluted 1:5 with dH_20 and 200 µL were added to the desired wells of a 96-well plate. Human Serum Albumin (HSA) protein standard (Sigma) was used to prepare a standard curve of serial concentrations within the linear range of the assay (0.05 to 0.5 mg/mL). Next, 10 µL of each

standard and sample were added to the diluted dye reagent in each well, in duplicate. The plate was briefly mixed using a plate shaker and, after a 10-minute incubation at room temperature, the absorbance was read using a plate reader (595 nm).

Given that some chemical reagents found in the lysis buffers, such as detergents, cause interference in the chemical-protein interaction, BCA Protein Assay Kit was occasionally used to ensure correct quantification of proteins. This assay is a more detergent-compatible option for protein quantification than Bradford assays. It is based on bicinchoninic acid (BCA), which interacts with peptide bonds to form a purple-coloured product that can be quantified through colorimetric detection. The protocol procedure is similar to the Bradford-based assay just described, though the working range of this assay is considerably higher (0.02-2 mg/mL). The protein standard used was Bovine Serum Albumin (BSA), provided with the commercial kit. The working reagent (WR) was prepared by mixing 50 parts of BCA Reagent A with 1 part of BCA Reagent B. In a plate, 200 μL of WR were mixed with 10 μL of the different protein standard concentrations and unknown samples, in duplicates. The plate was briefly mixed in a shaker and incubated at 37º C for 30 minutes. When the plate had cooled down, absorbance was read on a plate reader at 562 nm.

Two dilutions of the samples were always used (ratio depended on the initial cell number), given that protein concentrations obtained were generally high and out of the linear range. Dilutions of the sample, as well as of the protein standard, were made using the same lysis buffer that had been used to obtain the samples. After either of the assays, the average measurement of the blank standard replicates was subtracted from standard and unknown sample replicate measurements. Next, a standard curve is prepared by plotting the absorbance measurement of each protein standard (HSA or BSA) versus its

concentration (μg/mL). The standard curve was used to determine the protein concentration of each unknown sample.

2.5.3 Immunoprecipitation of proteins

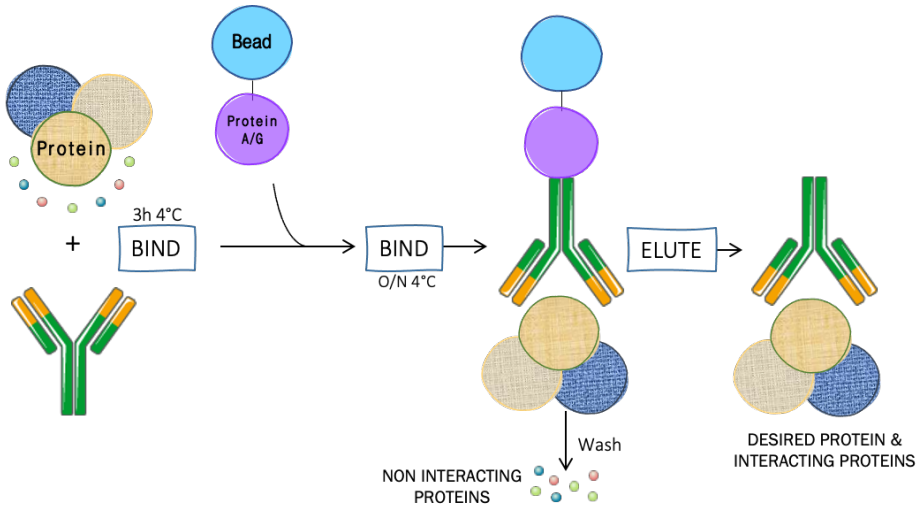

Figure 3.8: Schematic view of the immunoprecipitation protocol. A specific antibody was incubated with the protein lysate for 3 hours at 4 °C. Next, agarose beads were added and incubated overnight at 4 °C. Non-interacting proteins were washed through gentle centrifugation and the desired protein, together with interacting proteins, were eluted from the beads through acidic elution (see section 2.1.2).

For immunoprecipitation of proteins, cells were washed, harvested and protein concentration quantified as described above. During all subsequent steps, samples were kept on ice and all procedures were performed at 4 °C (incubation, centrifugation, etc.). Final volumes of cell lysates were adjusted to obtain the amount of protein for each condition. For each condition studied, 50 μg of extract were set aside to use as a crude control. The remaining lysate was incubated with the desired antibody or correspondent IgG control (see section 2.1.3). Antibody or IgG control concentration depended on the quality of the antibody, although, generally, a ratio of 1 μg antibody per 200 μg of protein extract was used. Incubation was carried out for 2 hours with constant rotation at 4 °C. Next, Sepharose Protein A/G beads (Rockland) or Protein A/G Plus-Agarose immunoprecipitation reagent (Santa Cruz) were added to the sample-antibody solution, generally as 10

μL of beads per 1 μg of antibody. Incubation of the A/G beads with the sample was carried out overnight, with constant rotation at 4 °C. The next day, beads were pelleted by centrifugation at 300 xg (4 °C) and 50 μl of supernatant were set aside to use as supernatant control. Beads were then washed four times with ice-cold IP lysis buffer by gently mixing and centrifugating. After the last wash, supernatant was discarded and the targeted proteins were eluted from the beads through incubation with 50 μL of low pH Glycine buffer (50 mM, pH 2.8) for 40 minutes at room temperature. After gently mixing and centrifugation, the eluates (supernatants) were transferred to new microcentrifuge tubes and 2 μL of 1M Tris pH 8 buffer were added. All eluated samples, together with supernatants and crude controls were then prepared for Western blot analysis as described below.

2.5.4 Preparation of samples for Western blot

The crude cell lysates or immunoprecipitation eluates were mixed with loading buffer containing 20% (v/v) β-Mercaptoethanol and 80% (v/v) NuPAGE LDS Sample Buffer (ThermoFisher), in a 1:4 ratio, and protein concentrations were corrected to the new volume. Samples were mixed using a vortex, boiled at 95 °C for 10 minutes and then briefly centrifuged. Samples were used immediately or kept at -20 °C for later use. Total concentrations of protein vary depending on the size of plate or flask used for the experiment (60-150mm or T175).

2.5.5 SDS polyacrylamide gel electrophoresis (SDS-PAGE)

Gels used for protein separation and Western blotting were either acquired commercially: Bolt 4-12% (w/v) acrylamide (ThermoFisher); or cast in-house: (4% (w/v) acrylamide stacking gel and 10% (w/v) acrylamide resolving gel. Table 2.3 depicts the components and concentrations used for

in-house cast gels. Gels were cast using a Mini-Protean Tetra cell casting stand and clamps (Bio-Rad). Prepared solutions were added between two glass plates to form 1.5 mm thick gels. After polymerisation of the resolving gel, the stacking gel solution was added on top of the resolving gel and a comb was inserted to create the wells. Gels were either used immediately or kept at 4 °C wrapped in wet tissue to prevent them from drying out.

	Resolving gel (20 mL)	Stacking gel (8 mL)
dH_20	7.9 mL	5.5 mL
30% (v/v) Acrylamide/Bis (Bio-Rad)	6.7 mL	1.3 mL
1.5 M Tris-HCl (pH 8.8)	5 mL	1 mL
10% (w/v) SDS	0.2 mL	0.08 mL
10% (w/v) Ammonium persulfate (APS)	0.2 mL	0.08 mL
TEMED (Sigma Aldrich)	0.02 mL	0.008 mL

Table 2.3: Concentrations used to cast SDS polyacrylamide electrophoresis gels

At the time of use, in-house cassettes were placed in a Mini-PROTEAN Tetra vertical electrophoresis tank (Bio-Rad), filled with either Tris/Glycine/SDS running buffer (see section 2.1.2) or Bolt MES SDS running buffer (ThermoFisher). Commercial Bolt gels were placed in Mini Gel Tank (ThermoFisher), filled with Bolt MES SDS running buffer. Samples were boiled 10 minutes at 95 °C and briefly centrifuged before loaded in the gel. The volumes loaded were adapted according to the protein concentration in order to load 30-50 µg of proteins per well. Amersham ECL Rainbow Marker (5 µL) (Sigma Aldrich) or Spectra Multicolor Broad Range (Thermo Fisher) were loaded as protein molecular weight markers. Gels were subjected to electrophoresis using a Powerpac power supply (Bio-Rad) at a constant

voltage of 100 V for 90 minutes or until visualisation of adequate protein marker separation.

2.5.6 Membrane transfer and blocking

Once the SDS-PAGE run was completed, proteins were transferred to a 0.45μm PVDF membrane (ThermoFisher) using either a semidry or wet system. For the semi-dry transfer, two different pieces of equipment were used during the duration of this project: Thermo Scientific Pierce Power Blotter semi-dry station (ThermoFisher) and Trans-Blot SD semi-dry transfer cell (Bio-Rad). The equipment for the wet transfer included a Mini gel holder cassette (Bio-Rad) and a Mini trans-blot cell (Bio-Rad). Two different transfer buffers were used during the optimisation of the different protocols: Glycine transfer buffer (see section 2.1.2) and Pierce 1-step transfer buffer (ThermoFisher). The general steps of these protocols are described below.

PVDF membrane, cut to the same size as the resolving gel, was activated in methanol for 1 minute and then equilibrated in transfer buffer for 5 minutes. In addition, three pieces of Whatman filter paper (Sigma Aldrich) were soaked in transfer buffer. One of these filter papers was placed onto the bottom graphite base electrode of the semidry transfer machine (or closer to the red panel of the cassette for the wet transfer). Next, the PVDF membrane was placed on top of the filter paper ensuring no air bubbles were retained between the two. The SDS-PAGE gel was then carefully removed from the cassette and the stacking gel discarded. The resolving gel was gently rinsed in transfer buffer and placed on top of the PVDF membrane, followed by a last soaked filter paper. Air bubbles were removed from the sandwich by using a roller and electroblotting was carried out. For wet transfers, extra soaked sponges were added before the first and after the last filter papers. The transfer sandwich assembled in the Thermo Scientific

Pierce semi-dry station was run at constant amperage of 1.3 Amps for 20 minutes. The Bio-Rad Trans-Blot SD semi-dry transfer cell was subjected to electrophoretic transfer for 30 minutes at 20-25 V; wet transfer in the Mini trans-blot cell was carried out for 1 hour at 110 V, both using a Powerpac HC power supply (Bio-Rad).

Once the transfer was complete, membranes were briefly washed in PBS and transferred to a 50 mL conical centrifuge tube. Membranes were then incubated with blocking solution (30-50 mL) on a rotator tube roller (Star lab) at room temperature for at least 1 hour to block possible non-specific binding of the primary antibody. Blocking solution was either 5% (w/v) non-fat dry milk (NFDM) (Sigma Aldrich) or BSA (Sigma Aldrich) in 0.05% (v/v) PBS-T (see section 2.1.2).

2.5.7 Immunoblotting of proteins

Following blocking, the membrane was incubated with the primary antibody at 4 °C overnight with constant rotation. A list containing relevant information on the antibodies used, including antibody concentration and the blocking solution used in each case can be found in section 2.1.3. After primary antibody incubation, membranes were washed three times for 5 minutes using 0.05% (v/v) PBS-Tween with constant rotation. The horseradish peroxidase (HRP)-conjugated secondary antibody was chosen according to the animal source of the primary antibody and diluted in the same blocking solution as the primary antibody. Information regarding secondary antibodies, including concentration and source can be found in section 2.1.3. Secondary antibody incubation was performed at room temperature for 1 hour with constant rotation, after which membranes were washed three times for 5 minutes using 0.05% (v/v) PBS-Tween with constant rotation.

Chemiluminescence was performed using luminol/peroxide enhanced chemiluminescence (ECL) Supersignal West Pico or Supersignal West Femto Maximum Sensitivity assay (both from Thermo Fisher). ECL reagent enables the detection of antigen by oxidizing luminol in the presence of HRP and peroxidise. The probed membrane was incubated for 5 minutes with the reagent and the chemiluminescent signal was detected using G:BOX Chemiluminescence and GeneSys software (Syngene).

Re-probing of blots after chemiluminescent detection was performed by washing each membrane for 1-2 hours with 0.05% (v/v) PBS-Tween at room temperature with constant rotation followed by incubation with the new primary antibody and subsequent steps. When proteins with a similar size needed to be analysed on the same membrane, a mild stripping buffer (see section 2.1.2) was used to remove any previously bound primary or secondary antibodies that could confuse interpretation. This was especially the case when some primary antibodies had the same animal source and therefore needed the same secondary antibody. Once all antibodies of interest had been investigated, membranes were incubated with a protein loading control, such as α-actin or α-GAPDH.

2.5.8 Protein quantification

The intensity of the signals (bands) obtained through chemiluminescence were quantified using Radames Software. To compare the expression of proteins of interest, the absolute intensity value of a specific band was obtained using the Radames software and used to generate a ratio relative to the intensity of the loading control for that specific blot. The obtained quantification was analysed graphically using GraphPad.

2.6 Genetically modified animals

2.6.1 Husbandry information

Animals were housed in the Joint Biological Services Facilities (JBIOS) at Heath Park, Cardiff University. An individually ventilated caging (IVC) scantainer system was used, and animals were maintained individually or in small groups (< 5 per cage), with a 12-hour light / 12-hour dark cycle and *ad libitum* access to food and water. All work on animals was carried out in accordance with the United Kingdom Animals (scientific procedures) act (1986) and European Directive EC 86/609, under the authority of UK Home Office experimental project licence P6177CDBB.

2.6.2 Background and general breeding strategy

Casp-8^{EKO} animals were obtained by crossing KRT-14-Cre males with *Casp-8*$^{fl/fl}$ females (kind gift from Pr. Stephen Hedrick, UCSD, USA). *Il-33*$^{-/-}$ animals were obtained from MacLaren J. (Cardiff University) and were also a backcross on C57BL/6J background mice. *St2*$^{-/-}$ animals were a kind gift of Pr. Daniel Pinschewer (U. Basel, Switzerland) and were on a mixed 129sv and C57BL/6J genetic background (Liliensiek et al., 2004; Senn et al., 2000). *Rage*$^{-/-}$ and *Rage*$^{fl/fl}$ animals were mixed 129sv and C57BL/6J background and were a kind gift from Pr. Angelika Bierhaus (DKFZ, Heidelberg, Germany).

Specific epidermal keratinocyte deletion of Casp-8 (Casp-8^{EKO}) was achieved by the expression of floxed alleles under the KRT-14 promotor. Males carrying Cre under the KRT-14 promoter were crossed with females carrying the floxed allele of Casp-8 (*Casp-8*$^{fl/fl}$). This allowed the generation of K14+ *Casp-8*$^{fl/+}$ males that were then crossed with *St2*$^{-/-}$, *Il-33*$^{-/-}$, *Rage*$^{-/-}$ or *Rage*$^{fl/fl}$ animals to obtain the double KO mouse lines of interest (Figure

2.1). The KRT-14-Cre allele must always come from males, as the KRT-14 promoter is active in oocytes and breeding a KRT-14-Cre female would generate animals with a full body deletion of Casp-8, which is lethal at the embryonic level.

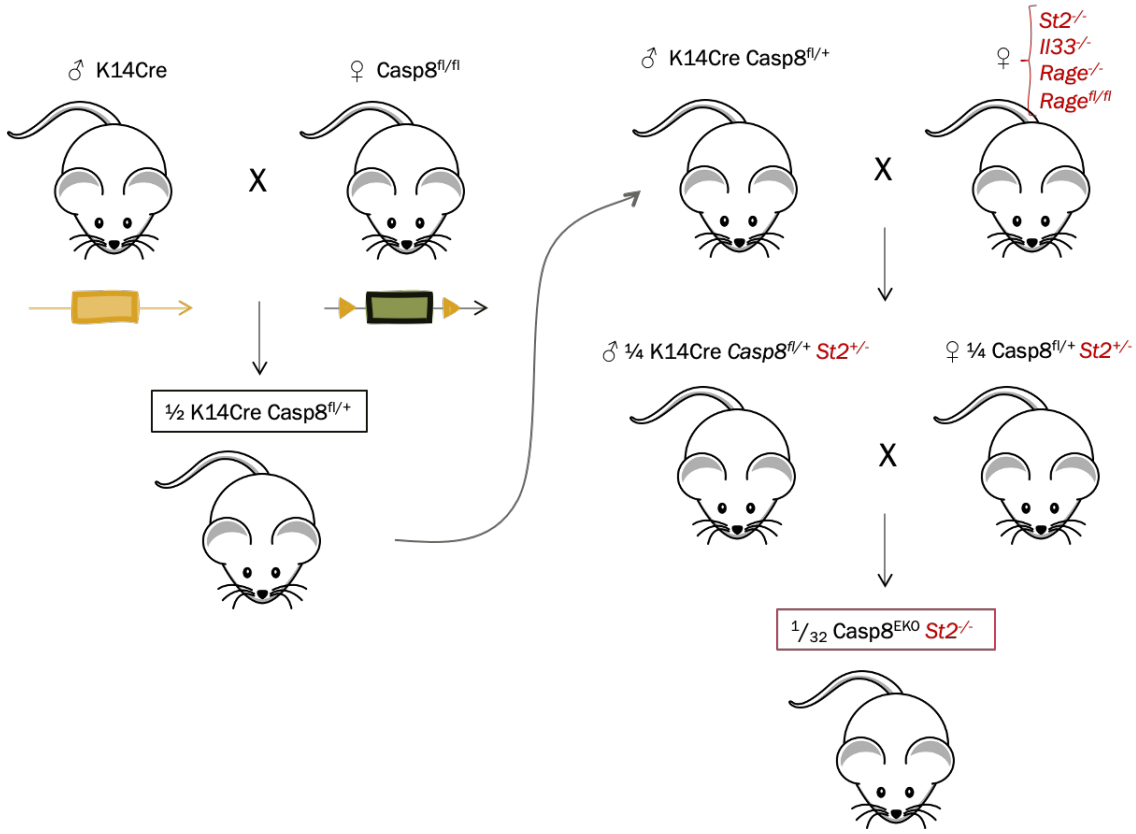

Figure 2.1: General breeding strategy to obtain Casp-8^{EKO} *St2*$^{-/-}$ Casp-8^{EKO} *Il-33*$^{-/-}$ Casp-8^{EKO} *Rage*$^{-/-}$ Casp-8^{EKO} RAGE^{EKO} animals. The strategy is represented for *St2*$^{-/-}$ animals as an example and the same procedure was followed to obtain all other lines.

2.7 Genotyping

2.7.1 DNA extraction

Genomic DNA was purified from ear biopsy tissue. After collection, samples were either kept at -20 °C or immediately incubated for 3 hours or overnight in 500 µL of DNA lysis buffer (see section 2.1.2 plus 15 µL Proteinase K (Roche). All centrifugation steps were carried out at 18900 xg for 5 min at room temperature. Any remaining tissue was pelleted by centrifugation and

the supernatant mixed with 500 µL of isopropanol to precipitate the genomic DNA. Samples were then centrifuged, and the supernatant discarded carefully. The pellet, containing the precipitated DNA, was then washed twice by centrifugation with 70 % (v/v) ethanol. After discarding the supernatant, the centrifugation tubes were left at room temperature for 10 minutes to allow the remaining ethanol to evaporate. Next, 100 µL of purified distilled DNase-free water were used to resuspend the DNA. The obtained DNA was left for 2 hours at room temperature or at 4 °C overnight before being analysed by PCR.

2.7.2 Primer design

The primers for the genotyping of *Rage*$^{+/+}$ *Rage*$^{-/-}$, *Rage*$^{fl/fl}$, *Il-33*$^{-/-}$ *Il-33*$^{+/+}$ *and St2*$^{+/+}$ animals were provided with the animals (see section 2.5.2). Detection of KRT-14-Cre, *Casp-8*$^{fl/fl}$ and wild type alleles was possible thanks to primers designed by Bonnet MC from genomic DNA sequences available through Ensembl and primer design software.

For the design of primers for the genotyping of *St2*$^{-/-}$ animals, the sequence of the murine gene of interest, was obtained from the online-available Ensembl software (https://www.ensembl.org). Although the exact sequence of the disrupted gene was unknown, the *St2* targeting strategy could be accessed (Senn et al., 2000). An analysis of the overall organization of introns and exons showed the presence of a lacZ vector included in exon 2. This allowed the design of a forward primer at the end of exon 2 and a reverse primer at the beginning of the lacZ vector. Primers were designed using Primer3Plus (https://www.primer3plus.com). All primers were purchased from Invitrogen (ThermoFisher), and their sequence and information are included in Appendix II.

2.7.3 Polymerase chain reaction

Polymerase chain reaction (PCR) protocols were used to discriminate between wild type (wt) and null alleles of *Rage*, *Il-33* and *St2*, between wild type and floxed alleles of *Casp-8* and *Rage*, and between wild type and -Cre alleles of *Krt-14*. PCR was performed using KAPA Mouse Genotyping kit (Merck). The KAPA2G Fast Genotyping Mix with dye includes all reagents required, including DNA polymerase. A PCR master mix was prepared according to manufacturer's instructions Table 2.4 shows the general ingredients included in the PCR. Some PCRs were performed using a combination of three primers (see Appendix II)

Component	Per 25 ul reaction	Final concentration
PCR-grade water	Up to 25 ul	N/A
2X KAPA2G Fast Genotyping Mix with dye	12.5 ul	1X
10 μM Forward primer	1.25 uM	0.5uM
10 μM reverse primer	1.25 uM	0.5uM
Template DNA	2 ul	N/A

Table 2.4: General composition of 1X master mix used for PCR.

After mixing thoroughly and centrifugating the tubes briefly, PCR was performed using the cycling protocol described in Table 2.5, with modifications to the annealing temperature, which is listed in Appendix II for each primer combination. In order to determine the optimal annealing temperature, a gradient PCR was sometimes performed using 12 different temperatures with an increase of 0.9 °C per column. After reaction cycling was completed, samples were kept at 4 °C until the time of analysis.

Step	Temp	Duration	Cycles
Initial denaturation	95 °C	3 min	1
Denaturation	95 °C	15 sec	
Annealing	60 °C *	15 sec	35-40
Extension	72 °C	15 sec/kb	
Final extension	72 °C	1 min/kb	1

Table 2.5: General cycling protocol with amplification steps for PCR. Annealing temperature varied depending on the primer pair used, information is included in Appendix II.

2.7.4 Analysis of PCR products by agarose gel electrophoresis

PCR products were analysed by agarose gel electrophoresis. Agarose gels (1,5%) (w/v) were prepared by heating agarose, in Tris-acetate-EDTA (TAE) (see section 2.1.2) using a microwave until fully dissolved. The nucleic acid intercalating stain Ethidium Bromide (20 μM) (Fisher Scientific) was added to the gel prior to setting to allow visualisation of the DNA products under UV light. 10 μL of each PCR product, as well as 100 bp DNA ladder (Invitrogen), were loaded into the gel. Standard horizontal agarose electrophoresis was carried out in electrophoresis tanks connected to a Powerpac power supply (Bio-Rad) at 110 V for 20 min or until samples were resolved sufficiently. MyECL imager (ThermoFisher) was used to visualize the DNA bands under UV light and to acquire images of the results. An example of Casp-8, KRT-14-Cre, IL-33 (wt/KO), RAGE (wt/KO) and ST2 (wt) PCRs is shown in Figure 2.2.

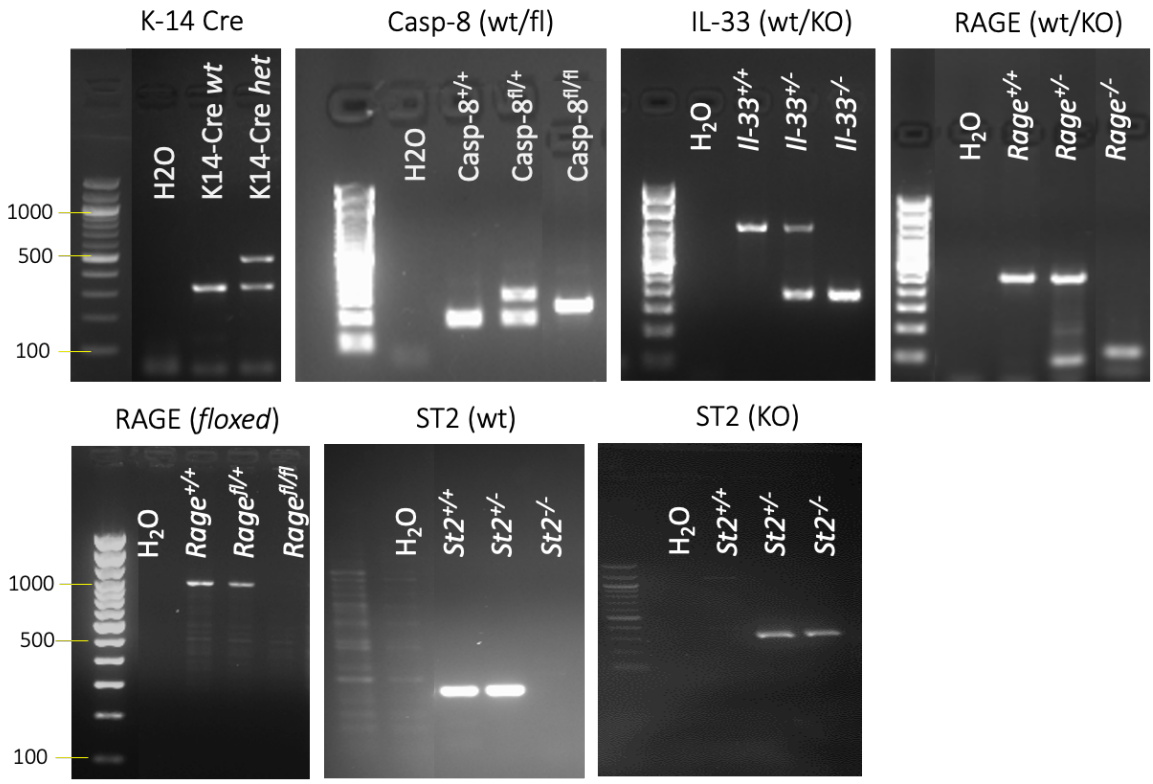

Figure 2.2: Analysis of PCR products for the animal genotyping. Images of PCR products: Casp-8, KRT-14Cre, IL-33 (wt/KO), RAGE (wt/KO), RAGE floxed, IL-33R (wt) and IL-33 (KO) analysed in a 1.5% (w/v) agarose gel.

2.8 Skin lesions assessment

2.8.1 Macroscopical analysis and scoring system

Lesion development in experimental animals was assessed macroscopically daily or every other day depending on the severity of the lesions observed. The evolution of the phenotype was recorded by keeping photographic and written documentation. Animals with lesions were housed individually after weaning age to avoid any interaction with other animals that might affect the lesion areas. Lesions can be present in any area of the body, thus assessment of the back, head and neck, abdominal area and tail was necessary. If animals reached weaning age, their weight was measured weekly using a Ohaus Scout lab scale (Fisher Scientific).

Lesion development was assessed using a scoring system based on the total percentage of skin affected by lesions. Scoring of the animals was performed whenever possible in a blinded fashion, without knowledge of the genotype of the animal. In order to calculate the percentage of skin affected by the lesions, the body surface was divided in two: abdominal surface area (ASA) and back surface area (BSA) which includes back, sides, head, neck and tail. A diagram of the distribution of the total body surface area (TBSA) is represented in Figure 2.2.

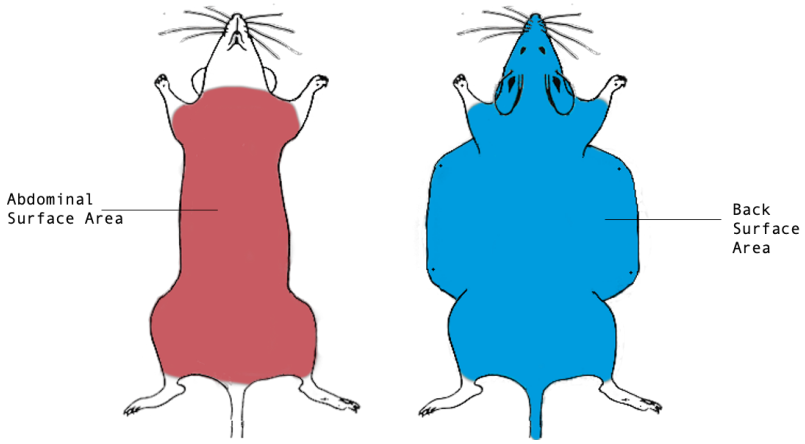

Figure 2.3: Distribution of the TBSA in the body of the animal.

The different parameters taken into account for lesion assessment include (i) the number of lesions present in each area, (ii) the size and (iii) severity of these. The number and size of the lesions can easily be recorded and calculated as the percentage of total body surface affected. Lesion severity, however, could vary from a hairless or scaly patch of skin to a deeper scabbed area. It is crucial to take this parameter into consideration, especially when recording scores in pups and adults. Pups are considerably more vulnerable, and lesions can easily affect their mobility and, consequently, their access to food. This had to be considered when assessing the severity of the phenotype in terms of general animal welfare, and thus, the severity threshold was different when assessing pups and adults. An example of the different severity of the lesions is showed in Figure 2.4.

Another aspect to consider when recording the severity of the lesions was the inevitable access of the adults to scratch the lesion area. It was noticed that lesions affecting the lower neck (under ears) would be persistent and less likely to heal due to scratching and self-grooming. For this reason, keeping track of the development of these lesions as well as comparing them to lesions in other parts of the body was crucial.

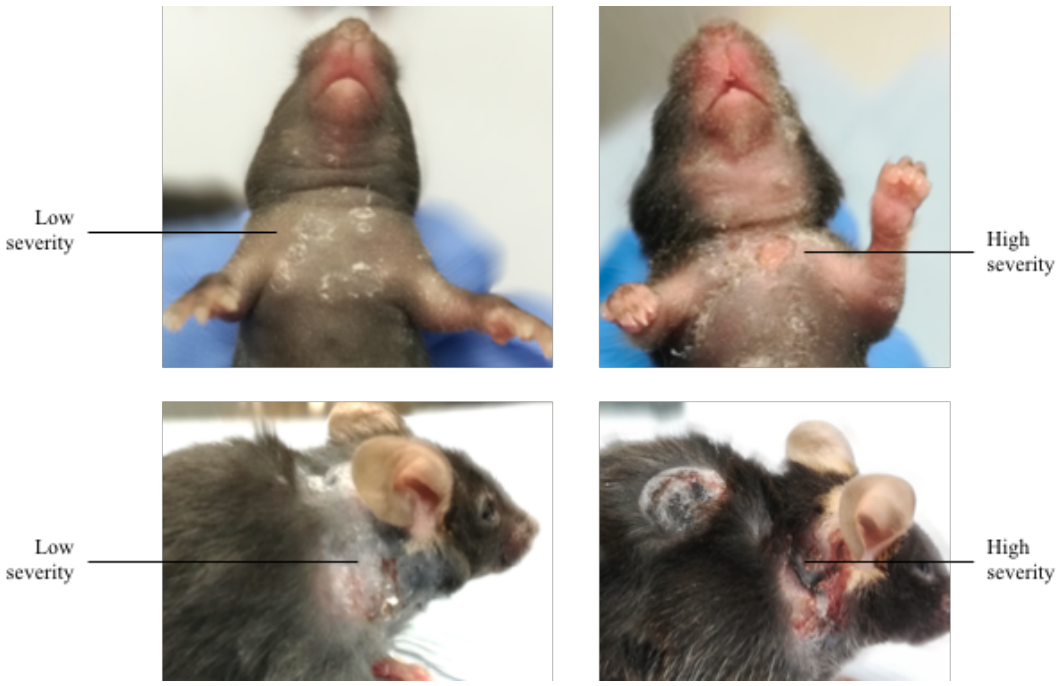

Figure 2.4: Lesion severity examples in pups and adults. Examples of low (left) and high (right) lesion severity in pups (up) and adults (down).

The mentioned parameters were carefully assessed by eye and quantified into a percentage. TBSA percentage was then calculated applying the following equation:

$$TBSA\ \% = 100 \times (0.7 \times BSA) + (0.3 \times ASA)$$

TBSA percentage was then used to determine the score of the lesions for each animal (see Table 2.6). A representative example of each score in P12 animals is in Figure 2.5. The maximum severity in this scoring system (very high) corresponds to the maximum severity specified in the PPL (moderate).

Score	Severity	TBSA %
0	None	0
1	Faint	1 – 10
2	Low	11 – 20
3	Moderate	21 – 35
4	High	36 – 45
5	Very high (endpoint)	46 +

Table 2.6: Scoring system used to quantify the number and severity of lesions.

Figure 2.5: Representative examples of the different Casp-8^{EKO} skin inflammation scores in pups at P12.

2.8.2 Experimental endpoint

All experimental animals were monitored regularly to evaluate skin lesions and general wellbeing. The maximum severity level of the PPL under which the experiments were performed was “moderate” and established animals could only be kept to the point at which lesions covered a maximum of 50% of the body surface. Hence, the experimental endpoint was reached when lesions covered 50% of the total animal body surface. When assessing younger animals, an additional endpoint is reached when these are unable to get back onto their legs by themselves after being placed lying on their back. When either of these endpoints are reached, animals were culled by decapitation (pups only) or schedule 1 method.

2.9 Immunohistochemistry

2.9.1 Collection and preparation of mice skin samples for histology

Skin samples were collected for immunohistochemistry at the endpoint of the experiments. Samples were taken from both the upper back and upper abdominal area of each animal. One half of each sample was fixed in 4% (w/v) paraformaldehyde (PFA) overnight at 4 °C and later transferred to 70% (v/v) ethanol at 4 °C. The second half of the sample was embedded in OCT Embedding Matrix for Frozen Sections (CellPath) using histology molds and stored at −80 C. Formalin fixed samples were later processed and embedded in paraffin using HistoCore PEARL and Arcadia H instruments from Leica Biosystems or externally in the Histology Department in the School of Biosciences (Cardiff University). Serial sections of 7 μm thickness were cut using a Leica RM2235 rotatory microtome. To ensure strong adherence to the glass slides, samples were baked at 60 °C overnight. Frozen samples

were cut using Epredia Cryostar cryostat (Fisher Scientific) into 7 μm sections, placed on SuperFrost microscope slides (ThermoFisher).

2.9.2 Haematoxylin/eosin staining of skin sections

Formalin fixed paraffin embedded (FFPE) samples were dewaxed in three consecutive baths of xylene and rehydrated in decreasing concentrations of absolute ethanol – 100%, 90% and 70% (2 min each) before placing in distilled water. For cryosections, slides were thawed at room temperature, fixed in 4% (w/v) PFA for 15 minutes and placed in distilled water. Both FFPE samples and cryosections were then placed in Mayers Haematoxylin (Fisher Scientific) for 1 minute. Excess stain was removed under running tap water. Slides where next rinsed in 70% (v/v) ethanol and stained with eosin (Sigma Aldrich) for 45 seconds. After staining, sections were dehydrated briefly in 95% (v/v) ethanol and then in two changes of 100% (v/v) ethanol for 2 minutes. Finally, samples were cleared in two changes of xylene and coverslips were placed onto the stained slides using DPX Mounting Medium (Sigma Aldrich).

2.9.3 Epidermal thickness measurement and histological assessment of skin pathology

Tissue sections stained with haematoxylin and eosin (H&E) were used to determine the histological score of each sample. Lesions were easily identifiable throughout the samples due to the characteristic histology of the skin such as the presence of cellular infiltration of the dermis and epidermal thickening. Observation of each sample by brightfield microscopy (LM) allows determination of the percentage of the total sample affected by lesions. This parameter is used for comparison with the macroscopical score of the animals and to determine the representability of the samples. Figure

2.5 shows an example of the histology of a skin sample containing lesional and non-lesional areas.

For epidermal thickness measurement, images of the samples were taken at magnification 5X objective using Zeiss Apotome Axio Observer microscope and stitched using the "tile" option of Zeiss Zen software. This allowed me to visualise the totality of the sample in one go. The freely available Java-based image processing programme ImageJ was used for the analysis of these images using a method described by Turin et al., (2018). Briefly, the method uses the "polygon" function of ImageJ to draw the outline of the epidermis, considering all the different indentations (yellow line, Figure 2.6). To calculate the epidermal thickness, the area of the drawn shape is divided by the length of the epidermal surface included in the shape (blue line, Figure 2.6). The epidermal thickening of non-lesional areas is calculated similarly. However, given that epidermal thickness these areas do not vary substantially, two to three measurements are taken as an average. A weighted average of each section measured defines the total epidermal thickness of the sample.

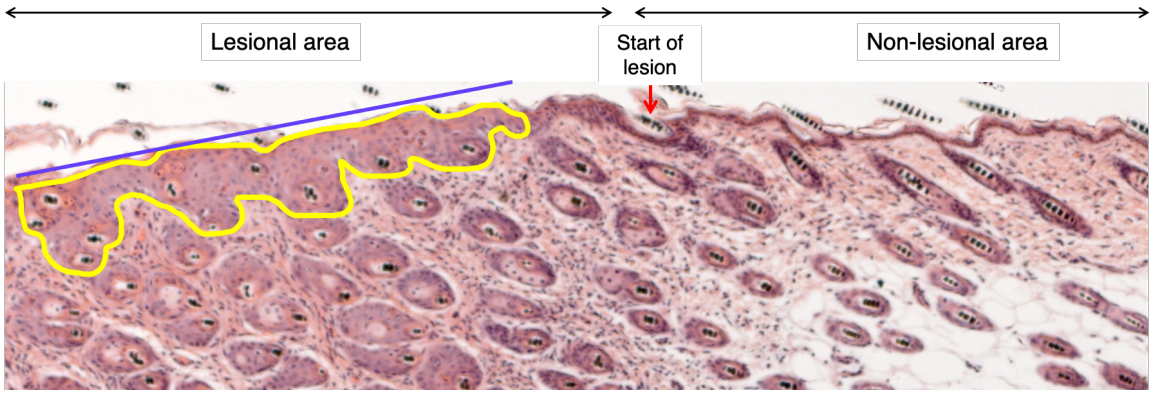

Figure 2.6: Measurement of epidermal thickness. Sample containing a lesion and non-lesional area. A polygon is drawn surrounding the epidermal thickening area (yellow) and its area is divided by the length of its base, which is the extensity of the lesion (blue line). Image obtained using Zeiss Apotome Axio Observer microscope, magnification 5X.

Methods based on ocular micrometres, which take measurements either perpendicular to the base of the membrane or vertically across the epidermis can lead to sampling error. By contrast, this method treats the skin as a folded rectangle and can compensate for the contours in the epidermal/dermal junction responsible for the lack of reliability of other methods. Given that the direction of the object is assumed to be horizontal, if the object is curved, several non-over-lapping areas with small curvature can be assessed in order to reduce the "curvature error" to a minimum. The totality of the sample, including both lesional and non-lesional areas, is considered to calculate epidermal thickness. As a consequence, the standard deviation of these measurements was often very high.

2.9.4 Immunofluorescent staining of skin samples

For immunofluorescence staining, slides containing skin sample cryosections were brought to room temperature and fixated with 4% (w/v) PFA for 15 min followed by three washes in PBS. To facilitate staining with certain antibodies, an antigen retrieval step was required that consisted in incubation of the slides with citrate buffer solution (see section 2.1.3) at 95 °C for 20 minutes with the use of a water bath, after which slides were cooled down and washed twice with PBS. Protein cross-links could also be targeted by antigen retrieval with a trypsin-based solution using Trypsin tablets (Sigma Aldrich), diluted in dH_2O, and used at 1:100 ratio. Information on which antibodies require antigen retrieval is included in section 2.1.3. Next, samples were incubated for 1h at room temperature with blocking reagent: 10% (v/v) goat serum (Sigma Aldrich) in PBS-0.05% (v/v) Tween or 0.02% (v/v) fish skin gelatine (Sigma Aldrich) in PBS-0.05% (v/v) Tween. To facilitate incubation, skin samples were circled with water repellent pen (Dako) that provides a hydrophobic barrier around the sample. After blocking, samples were incubated with the appropriate primary antibody

overnight at 4 °C, diluted in the same blocking reagent as the previous blocking step (see section 2.1.3 for concentrations). The following day, slides were washed three times in PBS-0.05% (v/v) Tween and incubated with the appropriate fluorescent secondary antibody for 1 h at room temperature, protecting the slides from exposure to light. The slides were then washed three times in PBS-0.05% (v/v) Tween and incubated with nuclear counterstain DAPI at 1:1000 in PBS-0.05% (v/v) Tween for 10 min at room temperature, protecting the slides from exposure to light. The counterstain was washed once in PBS and mounted using Thermanox plastic coverslips (ThermoFisher) and Vectashield mounting medium (Vector Laboratories). Slides were sealed using a transparent nail polish, to ensure coverslip immobilisation. Slides were kept at 4 °C, protected from light, for at least 1 hour prior to analysis.

2.9.5 Image acquisition

Imaging was performed on a Zeiss LSM 880 scanning confocal microscope using 405 nm, 488 nm, 647 nm lasers. To obtain the best signal for each specific staining, setup configuration was slightly adjusted, always maintaining pinhole aperture to 1 AU, laser powers calibrated at 0.2-0.4% and 600-800 W gain. All setups remained consistent between experimental replicates. Images were acquired using the Z-stack function of the microscope in order to detect signal from all sample layers or fields of view. Acquired images were then stacked using the "Orthogonal Projection" function of the ZEN software to obtain a clear focused image of the sample. Images were processed and exported for analysis.

Regarding the immunofluorescence stainings of skin samples, whenever possible, images of positive staining were acquired, which in most cases meant selecting an area of the sample that was affected by lesions. As sample size was generally large and the Z-stack function was used (which

is highly time consuming), acquisition of good quality images of the totality of the sample was unattainable. Instead, the areas selected to acquire images were chosen by a trained eye to represent the highlights and main observations made in each sample. However, no specific criteria were selected prior to the acquisition of this images, such as randomised selection or selecting the totality of lesional areas. For that reason, quantification of the stainings has not been performed.

Part I: In vitro analysis of necroptosis in normal human epidermal keratinocytes in response to HMGB1

Introduction and aims

Necroptosis leads to loss of plasma membrane integrity and the release of intracellular DAMPs that can elicit an immune response from neighbouring cells, playing a key role in local amplification of the inflammatory response (Vénéreau et al., 2015). Consequently, necroptosis has been widely implicated in innate immunity and has been suggested to be linked to several human diseases in which tissue damage is associated with inflammation (Petrie et al., 2019).

In the skin, necroptosis has been shown to occur in Toxic Epidermal Necrolysis (TEN), a life threatening severe cutaneous adverse reaction (SCAR) (S. K. Kim et al., 2015). Interestingly, research from Bonnet's lab regarding this condition has revealed increased expression of HMGB1 around infiltrating immune cells in the dermis of non lesional skin samples from TEN patients (Bonnet MC, personal communication), suggesting that the DAMP function of HMGB1 might play a role in the early development of skin lesions. These findings led my group to investigate the possible role of HMGB1 in the regulation of the necroptotic cascade. *Ex-vivo* treatment of human skin explants with increasing doses of HMGB1 induced phosphorylation of MLKL in keratinocytes in the epidermis, detected by immunohistochemistry (Bonnet MC, Bonnet C, personal communication). In line with these results, treatment of cultured primary normal human epidermal keratinocytes (NHEK) with HMGB1 resulted in phosphorylation of MLKL, as detected through Western blot (Figure P1.1). In light of these data, it was hypothesised that HMGB1 could play a role inducing necroptosis in NHEK.

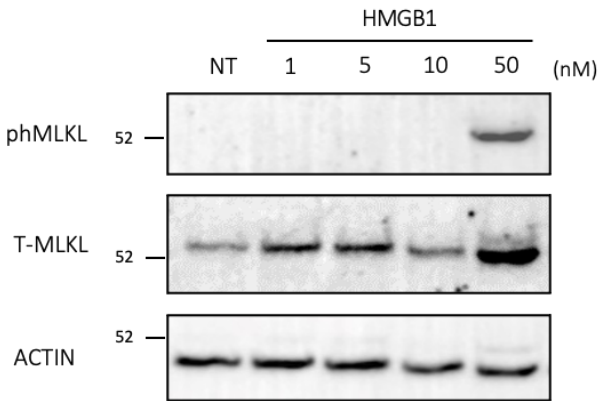

Figure P1.1: Treatment of NHEK with 50 nM HMGB1 results in the phosphorylation of MLKL. detected by Western Blot (courtesy of M. Bonnet). NHEK were treated with 0, 1, 5, 10 and 50 nM of HMGB1 for 4 hours. Western blot analysis of the lysates allowed the detection of MLKL phosphorylation (54 kDa) upon treatment with 50 nM HMGB1. Total MLKL (T-MLKL) expression levels were also shown, together with a loading control (actin).

Ligands of the TNFR family are the best studied necroptosis triggers and, despite other receptors having shown to activate this form of cell death (TLRs, IFNR), most of the information available regarding the necroptotic molecular cascade focuses on TNFR1 activation (Pasparakis & Vandenabeele, 2015). In this regard, little is known about necroptosis signalling following other stimuli and how it might differ from TNF-induced necroptosis. Furthermore, *in vitro* research on necroptosis has been mostly performed using well-described necroptosis-sensitive cell lines such as human HT-29, Caco-2 and Jurkat or mouse L929, which provide us with useful tools to further dissect necroptosis mechanisms.

The first part of this thesis has been divided into two chapters with the aim of achieving a better understanding of the molecular mechanisms induced by HMGB1 treatment of NHEK. In order to test the hypothesis that HMGB1 plays a role inducing NHEK necroptosis, a molecular analysis of necroptotic markers (Chapter 3) and necroptotic cell death (Chapter 4) has been carried out using HMGB1-treated NHEKs. Given that HMGB1-induced necroptosis has not been described before, optimisation of

treatment dosage as well as the kinetic response of the cells to this stimulus has also been assessed.

Chapter 3

Molecular analysis of HMGB1-induced necroptosis

3.1 Background and aims

Necroptosis was initially defined as being dependent on the kinase activity of RIPK1 (Hsu et al., 1995, 1996). However, RIPK1 has been shown to contribute to both apoptosis and necroptosis (Kaiser et al., 2014; Xuhua Zhang et al., 2019). RIPK3 was then identified as the key initiator molecule in this form of programmed cell death (Newton et al., 2014), given that the pathway can be activated in the absence of RIPK1 (Kaiser et al., 2014; Moujalled et al., 2013). Identification of MLKL as a substrate for RIPK3 (L. Sun et al., 2012; Jie Zhao et al., 2012) shone further light on the mechanisms of necroptosis. Trimerization and subsequent translocation of phosphorylated MLKL to the membrane has been shown to be essential for the execution of necroptosis (Cai et al., 2014; Dondelinger et al., 2014; Huayi Wang et al., 2014) and MLKL is now considered a crucial mediator of necroptosis (L. Sun et al., 2012). Based on these findings, the development of specific antibodies that recognise phosphorylated MLKL (ph-MLKL) has been crucial and the use of these is now considered to be an effective method for detecting active necroptosis *in vitro* and *in vivo* (He et al., 2016; X. Liu et al., 2016). For this reason, detection of MKL

phosphorylation upon HMGB1 treatment of NHEK clearly suggests the execution of the necroptotic cascade. This chapter will first focus on reproducing this data and investigating the kinetics in which HMGB1 induces MLKL phosphorylation in NHEK.

Necroptosis following the activation of death receptors leads to the formation of a RIPK1-RIPK3 complex through RHIM-dependent interactions that, together with MLKL, form what is referred to as the canonical necrosome (Tom Vanden Berghe et al., 2016). Non-canonical necrosomes have been described following activation of other receptors such as some TLRs and DNA sensors by LPS, viruses or dsRNA (Grootjans et al., 2017). Signalling through these receptors can activate RIPK1-independent necroptosis which depend on RHIM-mediated recruitment of TRIF (He et al., 2011) or ZBP1 (Upton et al., 2012) to activate RIPK3. Given that HMGB1-induced phosphorylation of MLKL has only been recently described by my group, the molecular cascade and possible necrosome composition following HMGB1 treatment of NHEK is unknown.

Co-immunoprecipitation of proteins is a useful and widely used method for the detection of protein complexes, including the necrosome. Previous knowledge of necrosome composition has been obtained by targeting RIPK1 through immunoprecipitation or by immunoprecipitating over-expressed RIPK3 or MLKL, which had been tagged with an epitope (Ali & Mocarski, 2018; Dillon et al., 2014; Rodriguez et al., 2016; L. Sun et al., 2012). However, although it facilitates the experimental procedure, usage and detection of overexpressed proteins lacks true biological relevance, as these do not recreate physiological conditions. Considering that RIPK1 might not be necessary for the recruitment of the HMGB1-induced necrosome, and with the purpose of investigating the necrosome composition following HMGB1 treatment, endogenous RIPK3 and

phosphorylated MLKL have been immunoprecipitated from HMGB1-treated NHEK.

Post translational modifications, especially phosphorylation events, are crucial signalling switches in the necroptotic cascade (X. Liu et al., 2016). Other than the detection of targeted proteins through Western blot, lysates obtained from HMGB1-treated NHEK can also be used for a variety of large-scale proteomic analysis. Phospho-proteomic analysis of HMGB1-treated NHEK would allow better understanding of the potential changes in protein phosphorylation networks and cell death.

Chapter aims:

I. Confirm the detection, through Western blot, of MLKL phosphorylation upon HMGB1 treatment of NHEK cells at different timepoints.

II. Investigate the expression of necroptosis-associated proteins upon treatment of NHEK with HMGB1.

III. Obtain protein lysates from HMGB1-treated NHEK for mass-spectrometry based phospho-proteomic analysis.

IV. Investigate the HMGB1-induced necrosome by immunoprecipitating endogenous RIPK3 and phosphorylated MLKL upon HMGB1 treatment of NHEK and co-detecting associated proteins.

3.2 Results: Analysis of HMGB1-treated NHEK

3.2.1 Optimisation of ph-MLKL Western blots

The first step in the detection of ph-MLKL was to validate the cell lysis and Western blot protocol that would allow us to identify this necroptotic marker. Necroptosis was induced in necroptosis-sensitive HT-29 cells through stimulation with TNF in combination with the Smac mimetic Birinapant, and the pan-caspase inhibitor Z-VAD-FMK (TSZ) (see section 2.3 for details).

Necroptosis was induced in HT-29 cells by culturing these in presence of TSZ for 0, 2, 4 and 6 hours, as previous studies have shown TSZ-induced MLKL trimerization or phosphorylation after 4 and 8 hours of stimulation (Cai et al., 2014; Huayi Wang et al., 2014). These timepoints are further supported by experiments detailed in Chapter 4. An additional condition included cells stimulated with the RIPK1 inhibitor Nec-1s and TSZ for 6 hours. Protein extracts obtained from these cells were then analysed by Western blot. As shown in Figure 3.1A, TSZ stimulation of HT-29 cells led to the phosphorylation of MLKL, detected at the expected molecular weight (MW) of 54 kDa, 4 and 6 hours after treatment. MLKL phosphorylation was successfully inhibited by the presence of RIPK1 inhibitor, Nec-1s. TSZ stimulation resulted in a decrease in RIPK1 levels from 2 h after treatment, this was blocked by Nec-1s. Total MLKL levels were increased at 4 and 6 hours, while RIPK3 expression levels, on the other hand, were relatively constant throughout the experiment, excepting a slight increase after 4 hours treatment. This initial experiment allowed us to validate the different steps of the protocol and the efficiency of the antibody. Also, it provided us with valuable positive controls of ph-MLKL lysates that would help us optimise this protocol later.

The next step was to optimise this protocol using my cell type of interest, NHEKs. For this purpose, a kinetic experiment using HMGB1 and TSZ was performed. NHEK were treated with 50 nM HMGB1 for 0, 2, 4, 6, 8 and 12 hours, based on the results shown in Figure P1.1, or with TSZ for 0, 8, 18 or 24 hours, based on previous research on TSZ-stimulated NHEK and other keratinocyte cell lines (S. K. Kim et al., 2015; Shlomovitz et al., 2019) and experiments conducted which are detailed in Chapter 4.

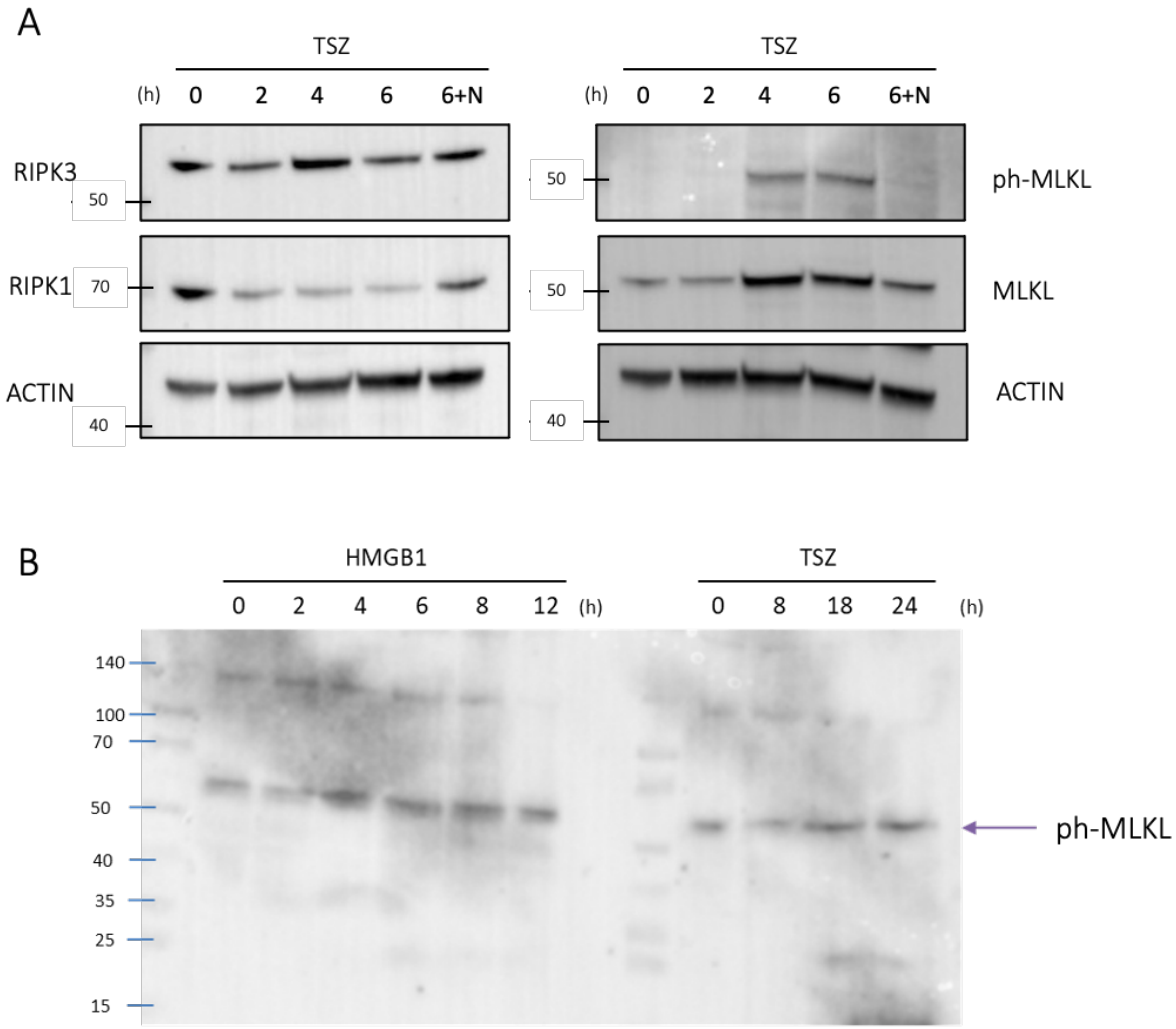

Figure 3.1: Detection of necroptotic markers by Western blot in HT-29 and NHEK. **(A)** HT-29 cells were treated with TSZ for 0, 2, 4, and 6 hours. Additionally, cells were treated with 20 µM Nec-1s for one hour before 6-hour TSZ treatment (6+N). The obtained cell lysates were separated by SDS-PAGE using two 10% (w/v) acrylamide in-house cast gels in parallel. Proteins were transferred to a PVDF membrane using Pierce Power Blotter semi-dry station and Pierce 1-step transfer buffer (both from Thermo Fisher). Membranes were blotted for necroptotic markers

RIPK3 and RIPK1 (left) or ph-MLKL and total MLKL (right) along with ß-actin as loading control. Incubation of the antibodies was done successively, without striping of the membrane. **(B)** NHEK isolated from D1 were treated with 50 nM HMGB1 for 0, 2, 4, 6, 8 and 12 hours or with TSZ for 0, 8, 18 and 24 hours. Whole cell lysates were separated by SDS-PAGE using two 10% (w/v) acrylamide and transferred using Trans-Blot semi-dry Transfer Cell (Bio-Rad) and Tris-Glycine transfer buffer. Ph-MLKL blot was incubated in 5% (w/v) BSA blocking buffer.

Western blot analysis of lysates obtained from TSZ- and HMGB1-stimulated NHEK showed high background and what appeared to be non-specific bands given that both untreated samples (0 hours - HMGB1 and TSZ) displayed an unexpected band at the estimated size of ph-MLKL (Figure 3.1B). Phosphorylation of MLKL should not occur in the absence of stimuli in any cell type, and has not been observed previously in TSZ-stimulated HT-29 (Figure 3.1A) or HMGB1-stimulated NHEKs (Figure P1.1), which led to conclude that the observed bands were non-specific. These results led to an in-depth optimisation of the stimulation and ph-MLKL Western blot protocol. A summary of the different parameters examined during the optimisation is shown on Table 3.1.

Given that the purpose of this optimisation process is to reduce the non-specific background obtained in ph-MLKL blots rather than quantify expression levels of proteins in relation to the total amount of protein, loading controls were not performed. However, total protein concentrations of each sample were always measured through Bradford protein assay and adjusted before Western blot analysis (see section 2.5.2).

Protocol step	Optimisation	Shown in Figure
Cell type	HT-29 vs. NHEK	Fig. 3.3A, 3.5A
NHEK source	NHEK isolated from donors 1-5 (D1-5)	Fig. 3.1B, 3.4A-B
Lysis buffer	IP lysis buffer vs. RIPA lysis buffer	Fig. 3.4A
Transfer method	Semi-dry (Trans-Blot SD, Bio-Rad) vs. wet transfer	Fig. 3.2A
Transfer Buffer	Glycine buffer vs. 1-step Buffer (Thermo Fisher)	Fig. 3.3A
Blocking method	5% (w/v) NFDM in PBS-T vs. 5% (w/v) BSA in PBS-T	Fig. 3.2, 3.3, 3.4
Primary antibody - dilution	1/1000 vs. 1/500	Data not shown
Primary antibody - batches	α-MLKL (phospho S358) (Abcam, ab187091) lot numbers: GR271516-1, GR322706-1, GR212667-35, GR212667-37	Fig. 3.5A
Primary antibody - brand	α-MLKL (phospho S358) (Abcam, ab187091) vs. ph-MLKL (T357) (R&D, MAB9187)	Fig. 3.5B
Secondary antibody - brand	α-rabbit IgG-HRP (Life Sciences) vs α-rabbit IgG-HRP (Jackson Laboratories)	Data not shown

Table 3.1: Summary of steps studied during the optimisation of ph-MLKL Western blot.

3.2.1.1 *Optimisation of running, transfer and blocking method*

The first step of the optimisation focused on the transfer method of the protocol. The successful experiments performed in HT-29 (Figure 3.1A) were performed using a Thermo Scientific Pierce Power Blotter semi-dry station, (which, unfortunately, had to be replaced) together with Pierce Thermo 1-step transfer buffer (Thermo Fisher). Subsequent protocols used a Bio-Rad Trans-Blot SD semi-dry Transfer Cell and Pierce Thermo 1-step (Thermo Fisher) or Tris-Glycine transfer buffer (see section 2.1.2). In order to determine if the transfer method was responsible for the unexpected high background and unspecific bands in the ph-MLKL blots, HMGB1- and TSZ-stimulated samples were run on an SDS-PAGE gel and transferred through wet transfer using Tris-Glycine transfer buffer and maintaining all other protocol steps unchanged (blocking and probing using 5% (w/v) BSA in PBS-T).

The ph-MLKL blot resulting from this experiment displayed a high level of non-specific background (Figure 3.2A), which led us to conclude that the transfer equipment used was not affecting the outcome of the experiment. The membrane from this blot was then stripped with a mild stripping buffer and blocked and probed using 5% (w/v) non-fat dried milk (NFDM) in PBS-T. NFDM blocking successfully got rid of the non-specific background, as seen in Figure 3.2B. However, some strong non-specific bands at 260 kDa were still present. Cutting the membrane underneath these bands achieved the detection of a strong ph-MLKL band, corresponding to the positive control load (TSZ-stimulated HT-29 cells) (Figure 3.2C). A few weaker bands were also noticeable in the lanes corresponding to TSZ-stimulated NHEK for 18 and 24 hours. These results indicated that NFDM blocking was effective blocking non-specific background in ph-MLKL blots.

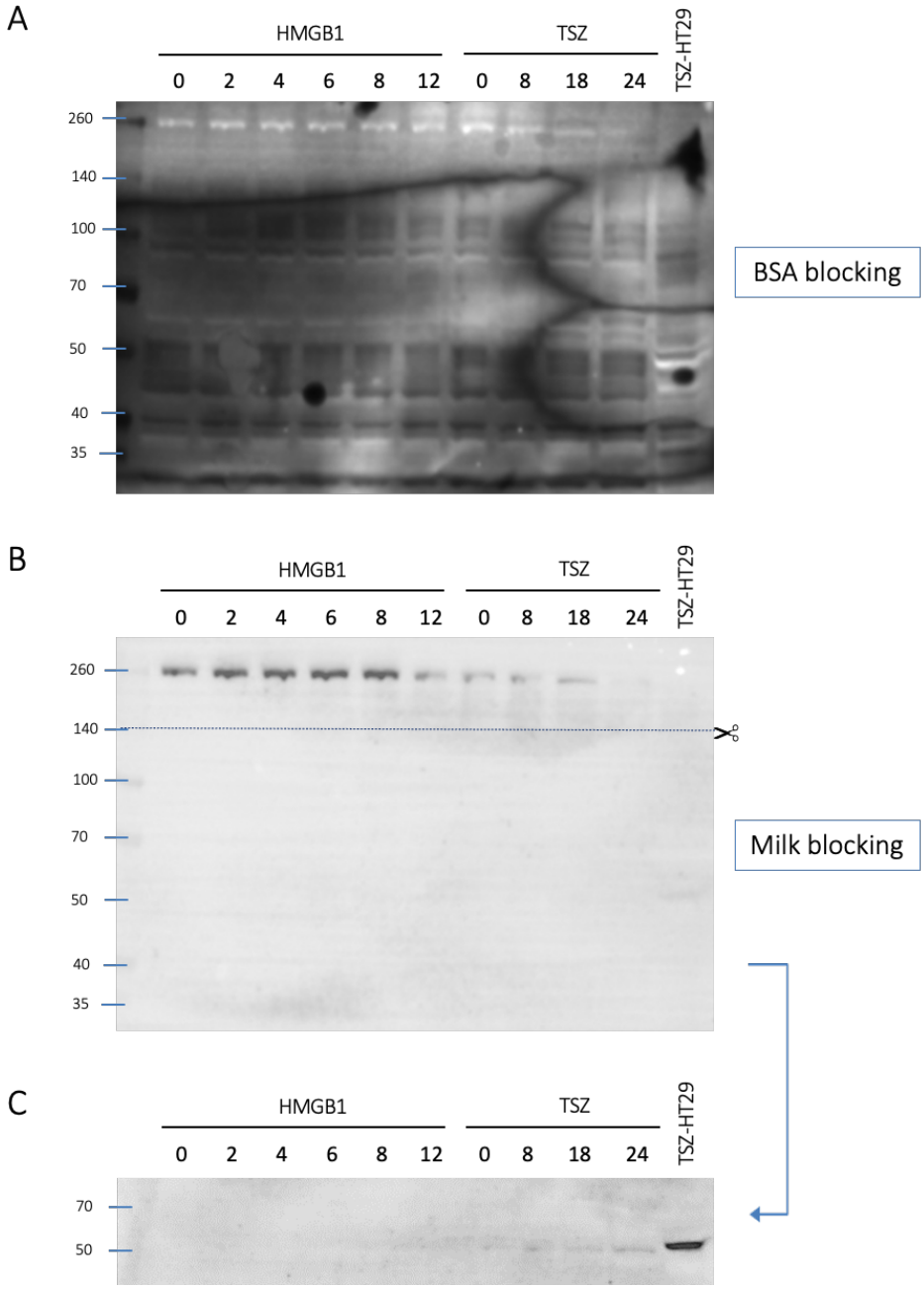

Figure 3.2: Transfer method and blocking optimisation of ph-MLKL blot. NHEK were treated with 50 nM HMGB1 for 0, 2, 4, 6, 8 and 12 hours or with TSZ for 0, 8, 18 and 24 hours. Obtained whole cell lysates, along with a TSZ-treated HT-29 positive control (*TSZ-HT-29*), were separated by SDS-PAGE using 10% (w/v) acrylamide in-house cast gels and transferred to a PVDF membrane by wet transfer in Tris-Glycine transfer buffer. **(A)** The obtained membrane was blocked with 5% (w/v) BSA in PBS-T and blotted for ph-MLKL. **(B)** After visualisation of the results, the membrane was stripped using a mild stripping buffer, blocked with 5% (w/v) NFDM in PBS-T and blotted for ph-MLKL. The dotted line shows the place the membrane was cut in order to eliminate high molecular weight unspecific bands. **(C)** The resulting membrane was re-incubated with chemiluminescent substrate obtain the blot in, where ph-MLKL was successfully detected.

Comparison of BSA and NFDM blocking was performed in another experiment using TSZ-stimulated HT-29 lysates that had previously shown specific ph-MLKL band by Western blot (Figure 3.3A). Membranes blocked with 5% (w/v) BSA (Figure 3.3, panels 2 and 4) displayed higher background than membranes blocked with 5% (w/v) NFDM (Figure 3.3, panels 1 and 3). This same experiment also compared different transfer buffers: no appreciable difference was observed between Tris-Glycine buffer (panels 1 and 2) and Thermo 1-step buffer (panels 3 and 4). However, a considerable reduction of high molecular weight bands was detected in NFDM-blocked membranes that had been transferred using Thermo 1-step transfer buffer (panel 3). For this reason, further experiments were performed using Thermo 1-step transfer buffer.

It was observed that the strength of HMGB1-induced ph-MLK band was considerably weaker than that obtained from TSZ-treated HT-29 cells (highly sensitive to necroptosis). When the lane corresponding to the positive control (TSZ-stimulated HT-29) was cut out of the membrane, a ph-MLKL band was detected at the 8-hour HMGB1-stimulation condition, and very weak bands for 4-hour HMGB1 and 18-hours TSZ timepoints (Figure 3.3B). Despite blots displaying less background after NFDM blocking, the casein present in NFDM can react with phospho-antibodies, weakening or obstructing it completely the signal (Bass et al., 2017). In order to avoid decreasing ever further the HMGB1-induced ph-MLKL signal NFDM blocking was not used in following experiments.

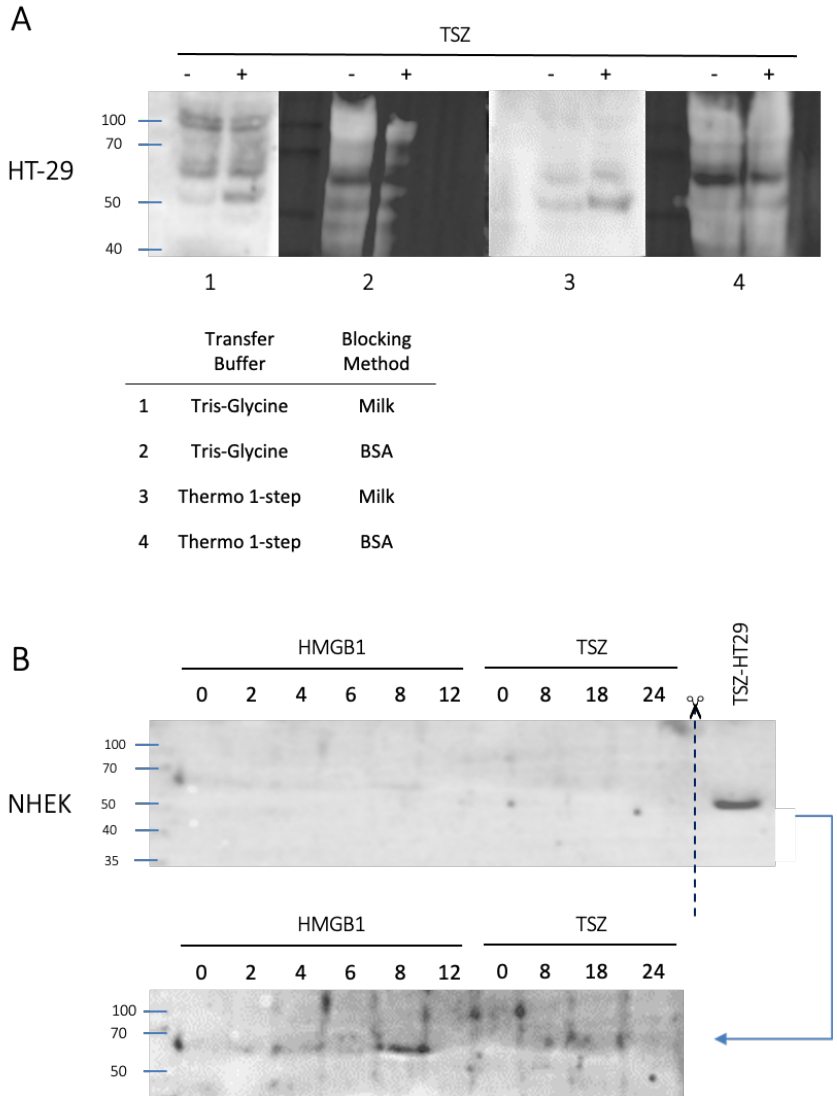

Figure 3.3: Transfer buffer and blocking optimisation of ph-MLKL blot. (A) HT-29 cells were treated with TSZ for 0 or 4 hours. The obtained whole cell lysates were separated through SDS-PAGE and transferred to a PVDF membrane using Trans-Blot semi-dry transfer (Bio-Rad) and Tris-Glycine transfer buffer (panels 1 and 2) or Pierce 1-step transfer buffer (Thermo Fisher) (panels 3 and 4). Next membranes were blocked using 5% (w/v) NFDM in PBS-T (panels 1 and 3) or 5% (w/v) BSA in PBS-T (panels 2 and 4). All membranes were then blotted for ph-MLKL, diluting the antibody in the solution they were blocked in. **(B)** NHEK were treated with 50 nM HMGB1 for 0, 2, 4, 6, 8 and 12 hours or with TSZ for 0, 8, 18 and 24 hours. Obtained whole cell lysates, along with a TSZ-treated HT-29 positive control (*TSZ-HT-29*), were separated by SDS-PAGE using in-house cast gels and transferred to a PVDF membrane using Trans-Blot SD semi-dry transfer (Bio-Rad) and Pierce 1-step transfer buffer (Thermo Fisher). The obtained membrane was blocked with 5% (w/v) NFDM in PBS-T and blotted for ph-MLKL. After visualisation of the results, the membrane was cut by the dotted line in order to eliminate the strong signal generated by the TSZ-HT-29 positive control. The resulting membrane was re-incubated with chemiluminescent substrate obtain the blot in the lower panel, where ph-MLKL was successfully detected after 4 and 8 hours of HMGB1 treatment.

3.2.1.2 *Optimisation of cell source and lysis method*

As described in section 2.2.3, NHEK cells were obtained from skin from healthy donors after plastic surgery. Due to the fast differentiation process of these primary cells once they've been isolated from the tissue, each stimulation was performed using cells from different donors. For this reason, and for a better understanding of how the experiments were designed, stimulations along the chapter are labelled with a number (D1-D5), each letter representing an independent stimulation experiment using cells obtained from a different donor. In order to keep the source of the cells constant, the optimisation process was done using samples from the same stimulation (D1), unless stated otherwise. However, this raised an obvious question: in that was the variability and background found in the ph-MLKL blots specific to the cells used for that specific stimulation. Two additional stimulations with different donors (D2 and D3) were performed, with similar results (Figure 3.4 A and B, respectively). Non-specific ph-MLKL bands were also detected using untreated HT-29 lysates (Figure 3.3A), in contrast with my previously obtained results (Figure 3.1A), which have been extensively reported in the literature by others (Ali & Mocarski, 2018; Rodriguez et al., 2016). These observations indicated that the cell source or cell type was not responsible for the high background observed in ph-MLKL blots.

To investigate whether the lysis buffer used could be determining factor regarding this issue, RIPA lysis buffer was compared to a different lysis buffer, used for immunoprecipitation protocols (IP lysis buffer), both described in section 2.1.2. NHEK cells were stimulated with HMGB1 for 4 and 8 hours and lysed with RIPA lysis buffer or 2, 4, 6 and 8 hours and lysed with IP lysis buffer. The resulting ph-MLKL blot (Figure 3.4A)

displayed high background and unexpected bands at 54 kDa in non-treated samples, in line with previous obtained results.

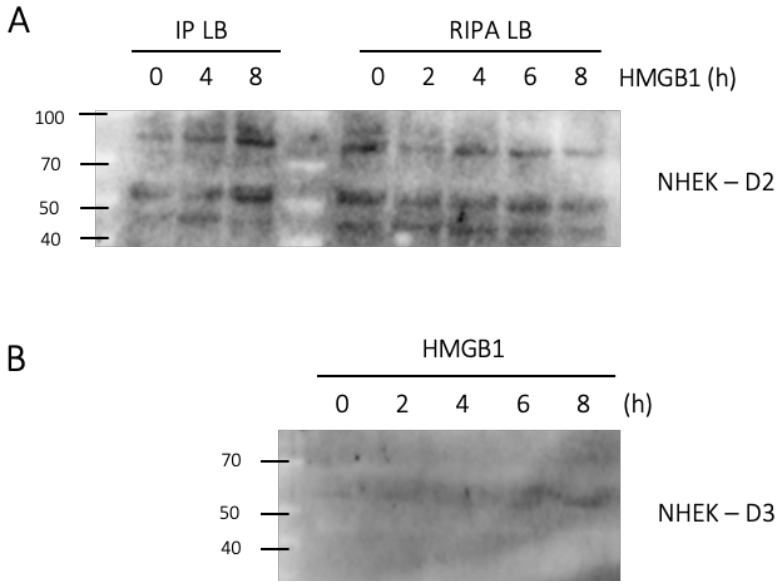

Figure 3.4: Optimisation of lysis method and cell source variability in ph-MLKL blots. NHEK obtained from two different donors (D2 and D3) were treated with 50 nM HMGB1 for 0, 2, 4, 6 and 8 hours or for 0, 4 and 8 hours. Whole cell lysates were obtained straight after stimulation and prepared for SDS-PAGE. SDS-PAGE was performed using in-house cast gels, and proteins were transferred to a PVDF membrane using Trans-Blot SD semi-dry transfer (Bio-Rad) and Pierce 1-step transfer buffer (Thermo Fisher). In **(A)**, cell lysates were obtained using IP lysis buffer or RIPA lysis buffer (see section 2.1.2), both were supplemented with PhoSTOP phosphatase inhibitor cocktail (Sigma Aldrich) and cOmplete ULTRA protease inhibitor cocktail (Roche). After transfer, the resulting membrane was blocked with 5% (w/v) BSA in PBS-T and blotted for ph-MLKL. In **(B)**, cell lysates were obtained using RIPA lysis buffer and, after transfer, the membrane was blocked with 5% (w/v) NFDM in PBS-T and blotted for ph-MLKL.

3.2.1.3 *Optimisation of antibody dilution, batch and brand*

Once all the previous steps in the Western blot protocol had been investigated, we focused in exploring the efficacy of the primary antibody. During the optimisation process, different dilutions of the antibody were tested, both in BSA and NFDM blocking, with no appreciable difference in the results (data not shown). Even though the primary antibody had been previously validated in TSZ-stimulated HT-29 cells (Figure 3.1A), new batches of the antibody had been purchased since that initial experiment.

Four different batches of α-MLKL (phospho S358) (Abcam, ab187091) with lot numbers GR271516-1, GR322706-1, GR212667-35 and GR212667-37 were tested in TSZ-treated and untreated HT-29 samples (previously validated and used as positive and negative controls). As shown in Figure 3.5A, the four blots displayed bands around 54 kDa in the treated and non-treated samples. However, a higher weak band around 60 kDa was present only in the TSZ-treated samples (Figure 3.5A, red arrow), suggesting these antibodies could be detecting both phosphorylated and non-phosphorylated MLKL.

Further optimisable steps of the Western blot protocol included the secondary antibody and the chemiluminescent (ECL) horseradish peroxidase (HRP) substrate. The secondary antibody used for α-MLKL (phospho358) antibody was a donkey α-rabbit IgG HRP-conjugated antibody (Life Sciences, NA934V), which was successfully being used in parallel in Western blot protocols using other primary antibodies. Unfortunately, incubation of a ph-MLKL probed membrane with a different α-Rabbit-HRP conjugated antibody (Jackson Lab) antibody had no effect in the results (Bonnet MC, personal communication). Similarly, the ECL-HRP substrate used to develop the membrane, West Pico PLUS Chemiluminescent Substrate was compared to SuperSignal West Femto substrate (both from Thermo Fisher), with no impact in the previously observed non-specific bands (data not shown).

After studying every step in the protocol, the causes of the high background and non-specific bands were still unclear. A new ph-MLKL antibody, R&D phospho-MLKL (T357), was purchased and used to probe blots of HMGB1-treated NHEK samples from previously tested donors (D3). This new antibody was able to successfully detect a strong ph-MLKL band around 54 kDa after 4 and 8 hours of treatment (Figure 3.5B).

Although non-specific bands at different molecular weights were also present, no bands were detected in untreated samples. This was the expected result, which put an end to the optimisation process.

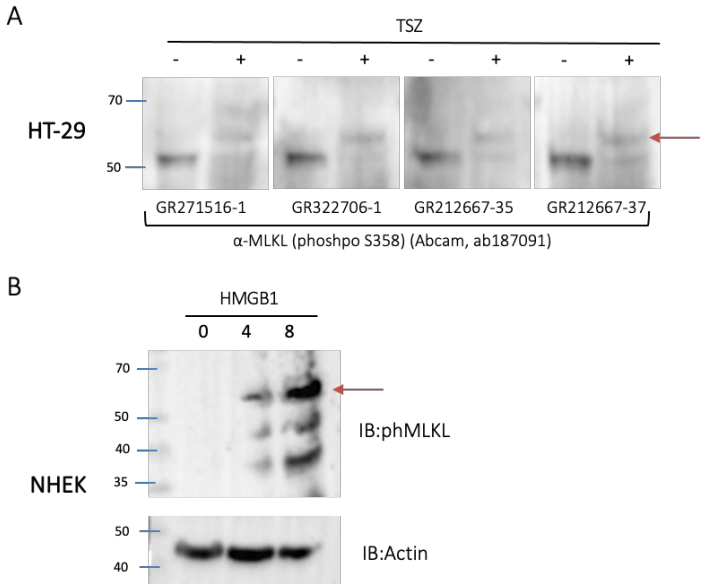

Figure 3.5: ph-MLKL antibody batch and brand optimisation. (A) HT-29 cells were treated with TSZ for 0 or 4 hours. The obtained whole cell lysates were separated by SDS-PAGE and transferred to a PVDF membrane using Trans-Blot semi-dry transfer (Bio-Rad) and Pierce 1-step transfer buffer (Thermo Fisher). Next, membranes were blocked using 5% (w/v) BSA in PBS-T and probed using four different batches of α-MLKL (phospho S358) (Abcam, ab187091): GR271516-1 (1), GR322706-1 (2), GR212667-35 (3), GR212667-37 (4). **(B)** NHEK isolated from D3 were treated with 50 nM HMGB1 for 0, 4 and 8 hours. Obtained whole cell lysates were separated by SDS-PAGE using 10 % (w/v) acrylamide in-house cast gels and transferred to a PVDF membrane using Trans-Blot semi-dry transfer (Bio-Rad) and Pierce 1-step transfer buffer (Thermo Fisher). The obtained membrane was blocked with 5% (w/v) BSA in PBS-T and probed for ph-MLKL using R&D phospho-MLKL (phospho T357) antibody.

3.2.2 Detection of necroptosis-associated proteins

A time course of HMGB1 and TSZ stimulation of NHEK allowed the study of necroptosis-related proteins RIPK1, RIPK3 and MLKL by Western blot (Figure 3.6). Bands corresponding to ph-MLKL after HMGB1 treatment for 4 and 8 hours, and a faint band after 8- and 18-hour treatment with TSZ

were observed. Interestingly, total MLKL levels at 4 and 8-hour HMGB1 treatment were slightly lower compared to other timepoints. In the case of TSZ-stimulated NHEK, MLKL expression is reduced at the 8-hour time point, after which it goes back to normal levels, or increases slightly. On the other hand, RIPK1 and RIPK3 levels are maintained during HMGB1 stimulation, but increased during TSZ stimulation, unlike what has been previously observed upon TSZ-induced necroptosis in HT-29 cells (Figure 3.1A).

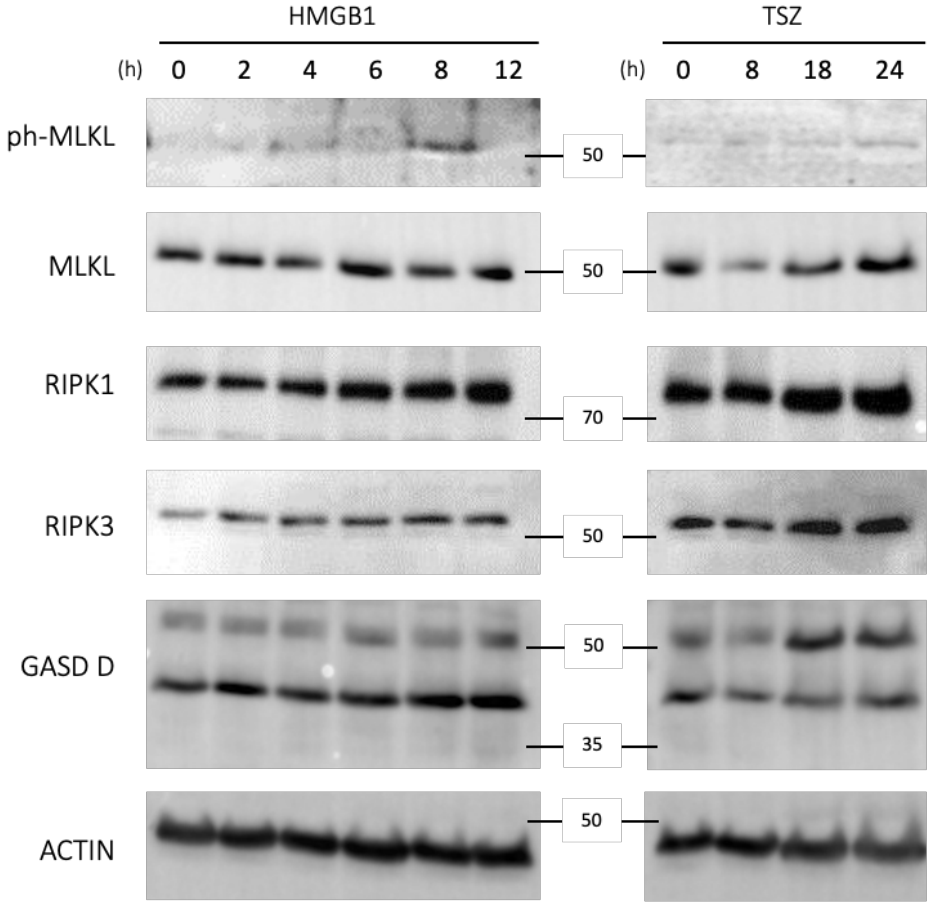

Figure 3.6: Analysis of necroptosis-related proteins by Western blot upon HMGB1 or TSZ stimulation kinetic of HMGB1. NHEK isolated from D1 were treated with 50 nM HMGB1 for 0, 2, 4, 6, 8 and 12 hours or with TSZ for 0, 8, 18 and 24 hours. Obtained whole cell lysates were separated by SDS-PAGE using 10% (w/v) acrylamide in-house cast gels and transferred to a PVDF membrane using Trans-Blot semi-dry transfer (Bio-Rad) and Pierce 1-step transfer buffer (Thermo Fisher). The membrane was blocked with 5% (w/v) BSA in PBS-T and probed for ph-MLKL using α-MLKL (phospho S358) (Abcam, ab187091). After visualisation of the results,

the same was membrane was stripped if necessary and incubated with total MLKL, RIPK3 and RIPK1, Gasdermin-D and β-actin antibodies.

Crosstalk between the different forms of cell death, including necroptosis, apoptosis, pyroptosis and autophagy happens within cells, through integrated molecular pathways (Tom Vanden Berghe, Kaiser, et al., 2015). The relationship between pyroptosis and necroptosis has been recently described and it is based on the ability of RIPK3 and MLKL to promote NLRP3-caspase-1 mediated IL-1β secretion (S. A. Conos et al., 2017; T.-B. Kang et al., 2013; Vince et al., 2012). In order to determine if HMGB1 treatment of NHEK could be activating this cell death pathway, cleavage of Gasdermin D, the pore-forming effector protein of pyroptosis, was studied. Treatment of NHEK with HMGB1 did not impact the expression of Gasdermin D (53 kDa) nor induce its cleavage (30 kDa terminal fragment) . TSZ was also not able to induce the cleavage of Gasdermin D. However, a slight increase in the expression of Gasdermin D is observed after TSZ treatment of NHEK after 18 and 24 hours (Figure 3.6).

3.3 Results: HMGB1-induced necroptosis and donor variability

Once the detection protocol of ph-MLK by Western blot had improved, large quantities of HMGB1-treated NHEK lysates were produced to later perform further large-scale proteomic analysis. NHEK obtained from two different donors (D4 and 5) were treated with HMGB1 for 0, 2, 4, 6 and 8 hours. In order to strengthen the future statistical analysis and provide more robust results, two technical duplicates of the same experiment were performed. Technical duplicates were performed side by side using cells in the same passage in separate culture dishes. Identified targets would be

later validated through Western blot using cells obtained from different donors, giving us an estimate of the consistency of the results.

The obtained lysates were first analysed by Western blot aiming to confirm the presence of ph-MLKL at the expected timepoints. NHEKs obtained from donor 4 and treated with HMGB1 showed an increase in the intensity of the ph-MLKL band 6 and 8 hours after stimulation (Figure 3.7A). This was observed in both of the technical duplicates of the experiment (duplicates 1 and 2, Figure 3.7A). Protein lysates obtained from donor 5, on the other hand, did not show the same consistency between duplicates (Figure 3.7B). There is a substantial increase in the expression of ph-MLKL on duplicate 2 (lower panel), which is not so obvious on duplicate 1 (upper panel). ß-actin was used as loading controls for all blots shown in Figure 3.7. An estimation of the ph-MLKL expression as a ratio relative to the loading control is shown to the side of each blot. The graphs confirm that treatment of NHEK with HMGB1 for 8 hours leads to an increase in MLKL phosphorylation in one of the donors used (donor 4, Figure 3.7A). These results, however, were only observed in one of the duplicates loaded and analysed through Western blot when a different donor was used (donor 5, Figure 3.7B), confirming high variability both between donors and between the response of the NHEK to HMGB1 within technical duplicates. In conclusion, the variability of the assay between different donors as well as between technical duplicates of the same donor led to decide against using these samples for further phospho-proteomic analysis.

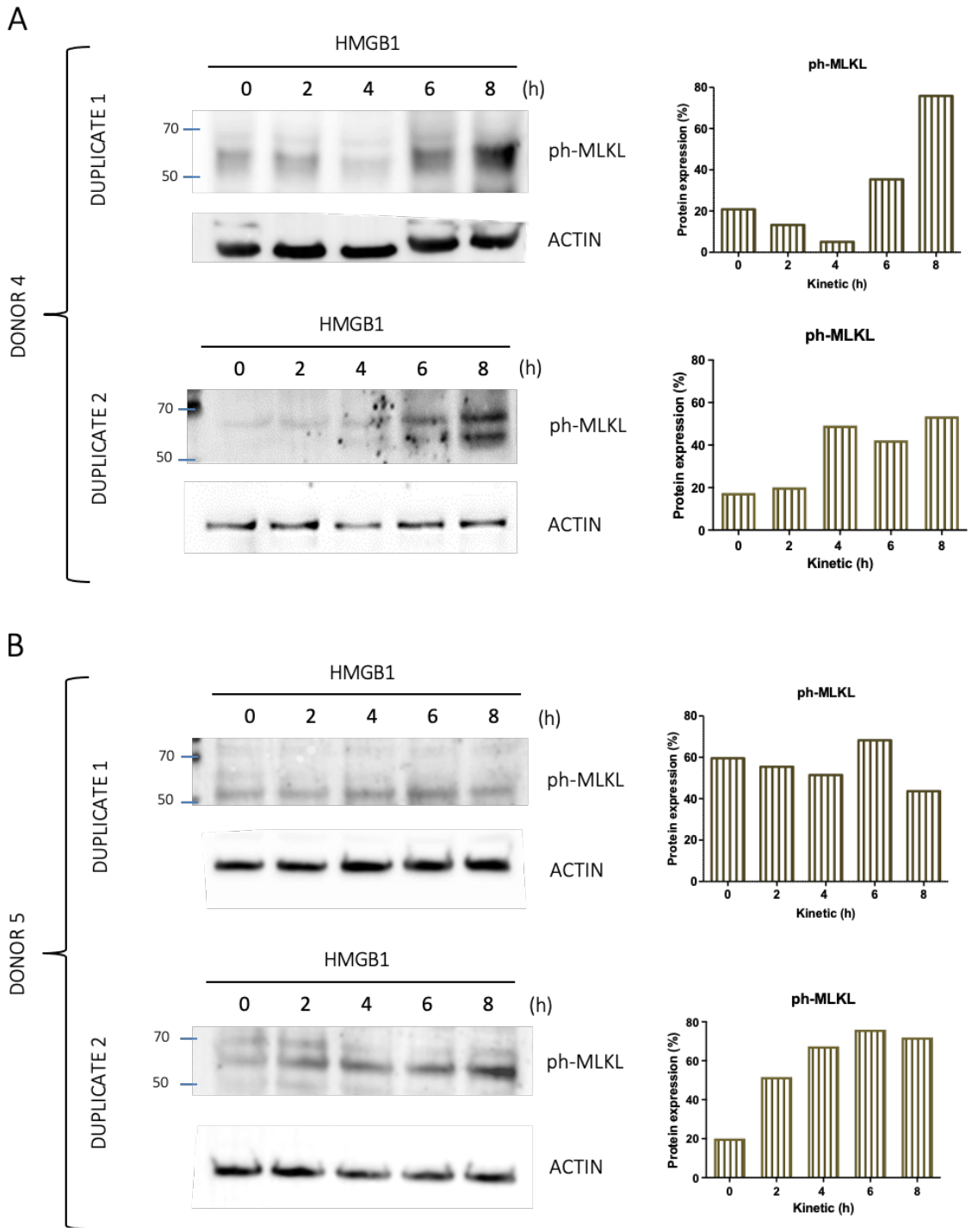

Figure 3.7: Western blot detection and quantification of ph-MLKL in kinetics of HMGB1-treated NHEK. NHEK obtained from two different donors - **(A)** donor 4, **(B)** donor 5 - were treated with 50 nM HMGB1 for 0, 2, 4, 6 and 8 hours. Two technical duplicates of each stimulation were performed side by side for each experiment. Obtained whole cell lysates were separated by SDS-PAGE using 10% (w/v) in-house cast gels and transferred to a PVDF membrane using Trans-Blot SD semi-dry transfer (Bio-Rad) and Pierce 1-step transfer buffer. The obtained membrane was blocked with 5% (w/v) BSA in PBS-T and blotted for ph-MLKL using R&D phospho-MLKL (T357) antibody. A blot with a β-actin loading control, is shown under each

ph-MLKL blot. MLKL phosphorylation levels were quantified in relation to total amount of protein (LC) and are shown in graphs on the right of each blot. Quantifications of the blots were made using Radames software.

3.4 Results: Immunoprecipitation of endogenous HMGB1-induced necrosome

3.4.1 Immunoprecipitation of TSZ-induced necrosome in HT-29

The optimisation of the immunoprecipitation protocol was performed using HT-29 cells and a RIPK1 antibody previously described in the literature (Ermolaeva et al., 2008). 60- or 100-mm dishes with 70% confluent HT-29 cells were lysed using IP lysis buffer (see section 2.1.2) and lysates were incubated with mouse α-RIPK1 antibody and a mouse IgG isotype control with A/G Agarose beads. A ratio of 1 μg antibody per 200 μg of protein was maintained. A fraction of the total cell lysate, before incubation, was always set aside for analysis (crude). After incubation with the RIPK1 antibody or IgG isotype control, a fraction of the supernatant, containing the proteins that have not bound specifically -RIP1 supernatant (Sup) and Ms IgG Sup, respectively- was also set aside for posterior analysis. After elution from the beads, immunoprecipitated proteins, together with the crude and saved supernatants were analysed by Western blot. Confirmation of RIPK1 immunoprecipitation was detected by probing the membrane with RIPK1 antibody (Figure 3.8). No RIPK1 was detected after incubation of cell lysates with the IgG isotype control, proving the immunoprecipitation was specific. Furthermore, incubation of the cell lysates with RIPK1 antibody was able to efficiently retrieve RIPK1 completely (Figure 3.8), confirming the efficacy of the antibody.

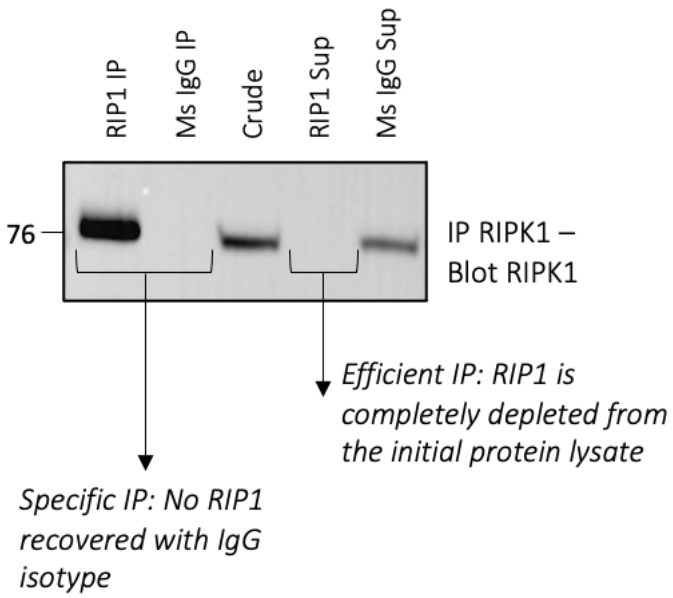

Figure 3.8: Immunoprecipitation of RIPK1 in unstimulated HT-29 cells. Immunoprecipitation using RIPK1 polyclonal mouse antibody (BD 610459) in non-treated HT-29 cells. RIPK1 Western blot of the immunoprecipitation using RIPK1 antibody (RIP1 IP) and an isotype IgG control (Ms IgG IP). The specificity of the immunoprecipitation is based on the absence of RIPK1 in the isotype immunoprecipitation The blot also shows the presence of RIPK1 in the whole cell lysate (crude), and supernatants recovered from the immunoprecipitation using the isotype IgG control antibody (Ms IgG Sup). The absence of RIPK1 in the supernatant recovered after incubation of the lysate with the RIPK1 antibody (RIP1 Sup) shows the immunoprecipitation is highly efficient. IP: immunoprecipitation; Sup: supernatant.

The optimised protocol followed using the RIPK1 antibody (described in detail in section 2.4.3) was used for all subsequent immunoprecipitation experiments. Given that most published literature at the time focused on over-expressed RIPK3 immunoprecipitations, up to six different antibodies had to be tested before successfully immunoprecipitating endogenous RIPK3. Figure 3.9A shows the attempts at immunoprecipitating endogenous RIPK3 with five different antibodies: R&D mouse RIPK3 (MAB7604), Novus Biotechnology rabbit RIPK3 (NBP1-77299), Santa Cruz mouse RIPK3 (SC-374639), Abcam rabbit RIPK3 (ab56164) and Novus Biotechnology mouse RIPK3 (NBP1-45592). Successful immunoprecipitation of endogenous RIPK3 was achieved using

Thermo Fisher RIPK3 (PAI-4533) (Simoes Eugénio et al., 2021) (Figure 3.9B). Incubation of untreated or TSZ-stimulated (4 hours) HT-29 cell lysates with PAI-4533 RIPK3 antibody led to immunoprecipitation of endogenous RIPK3, detected by Western blot (Figure 3.9B).

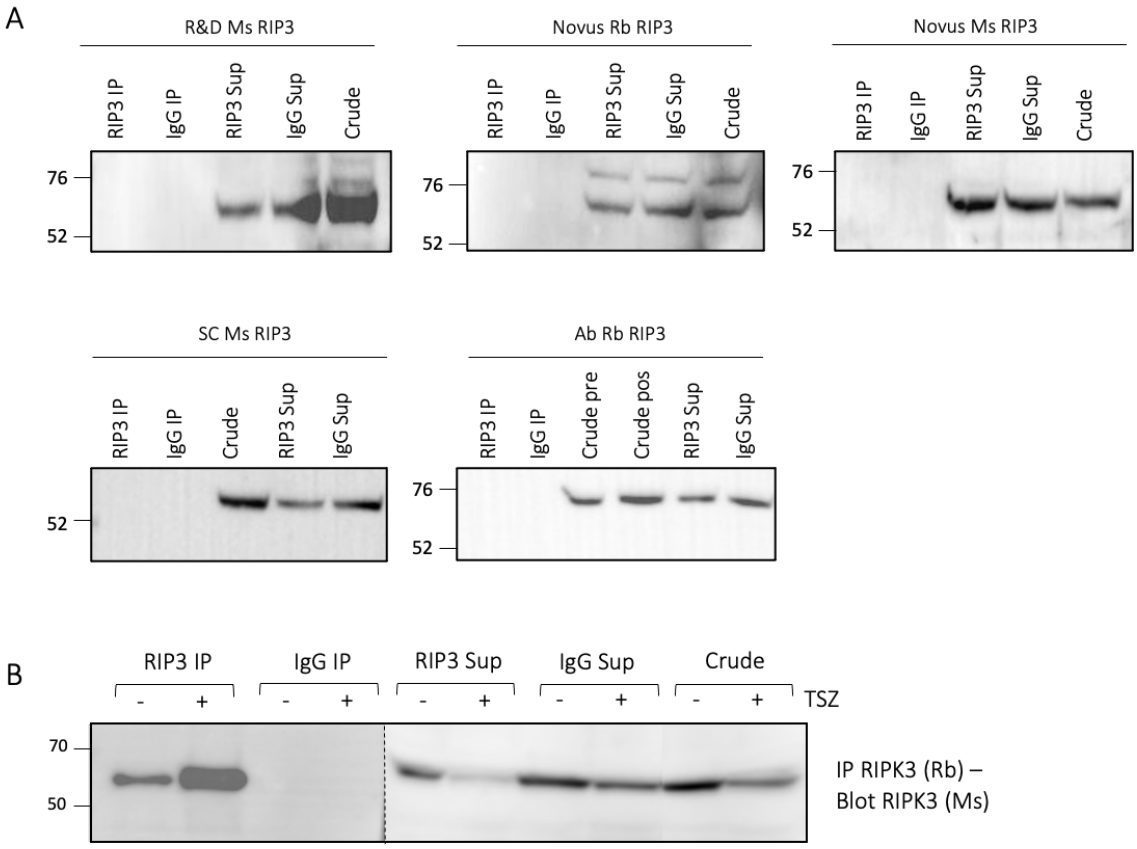

Figure 3.9 Immunoprecipitation of endogenous RIPK3 in HT-29 cells. (A) Endogenous RIPK3 immunoprecipitation in untreated HT-29 was not achieved using five different RIPK3 antibodies: R&D mouse RIPK3 (MAB7604), Novus Biotechnology rabbit RIPK3 (NBP1-77299), Santa Cruz mouse RIPK3 (SC-374639), Abcam rabbit RIPK3 (ab56164) and Novus Biotechnology mouse RIPK3 (NBP1-45592). **(B)** Successful RIPK3 immunoprecipitation of endogenous RIPK3 in untreated and TSZ-stimulated (4 hours) HT-29 cells. Immunoprecipitations, supernatants recovered after antibody incubation and whole cell lysates were loaded and analysed by Western blot using RIPK3 antibodies. IP: immunoprecipitation; Sup: supernatant.

Immunoprecipitation of endogenous RIPK3 in TSZ-stimulated HT-29 cells allowed the co-immunoprecipitation of MLKL and RIPK1 (Figure 3.10), which are known to be part of the TNF-induced necrosome (Pasparakis & Vandenabeele, 2015). Similarly, immunoprecipitation of MLKL pooled

down interacting protein RIPK3 (Figure 3.10). MLKL was not co-immunoprecipitated with RIPK3 and RIPK3 was not co-immunoprecipitated with MLKL when using untreated HT-29 cells (Figure 3.10), validating the co-immunoprecipitation of necrosome components upon necroptosis induction.

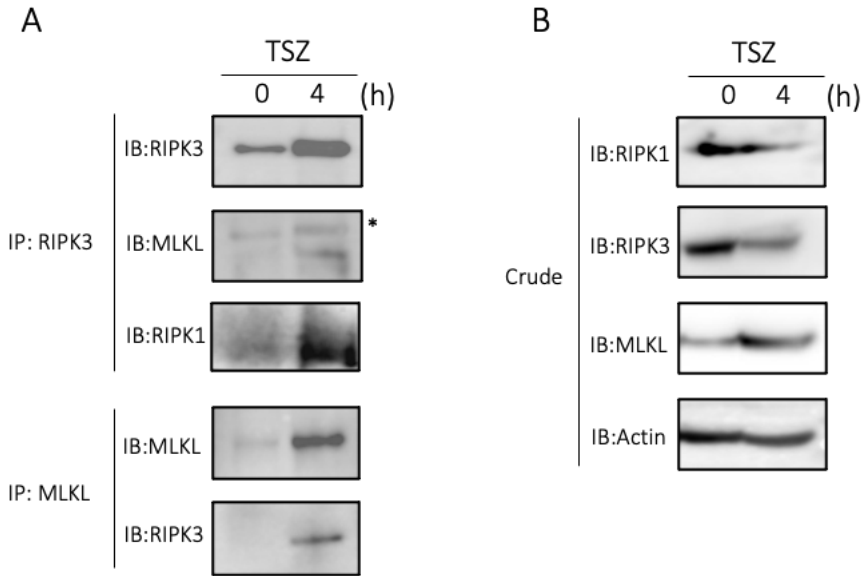

Figure 3.10: Co-immunoprecipitation of necrosome components using RIPK3 and MLKL antibodies in TSZ-treated HT-29 cells. HT-29 cells were stimulated with TSZ for 0 or 4 hours, lysed and incubated with beads and RIPK3 or MLKL. Eluates were analysed by SDS-PAGE followed by Western Blotting with the indicated antibodies. Whole cell lysate extracts (crude) were also loaded and blotted for necroptotic markers RIPK1, RIPK3, MLKL and loading control (actin).

Optimisation of the immunoprecipitation protocol allowed the successful immunoprecipitation of phosphorylated MLKL from TSZ-stimulated HT-29 cells (antibody: α-MLKL ph S358, ab187091) (Figure 3.11). Here, the Clean-blot IP (Thermo Fisher) detection kit was used during the Western blot procedure to facilitate detection of target proteins after immunoprecipitation without interference of antibody fragments. As expected, no ph-MLKL was immunoprecipitated in untreated HT-29 cells, validating the specificity of the antibody for later experiments. A lower band was detected when blotting untreated HT-29 cell lysates (crude) with

the ph-MLKL antibody, in line with results described in the previous section of this chapter (Figure 3.11). However, a higher band, not present in untreated HT-29 cells, was detected in TSZ-stimulated cell lysates. The size of this higher band corresponded to the band detected in the immunoprecipitation product. Blotting for total MLKL confirmed that the lower band corresponded to non-phosphorylated MLKL (Figure 3.10).

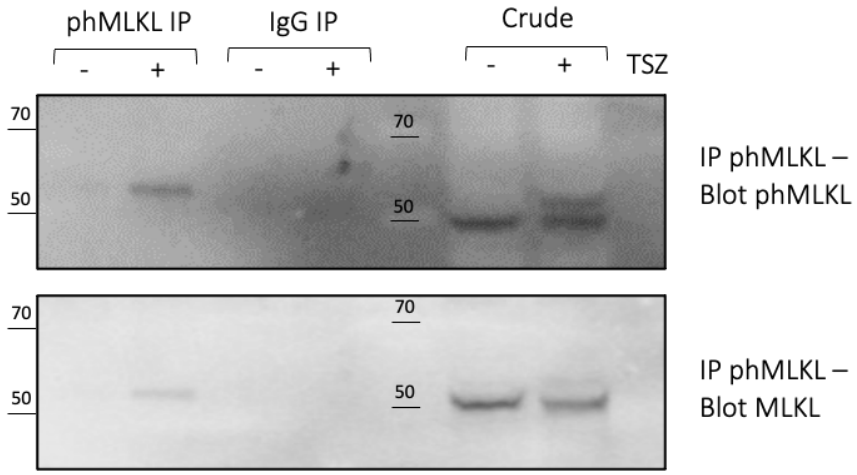

Figure 3.11 Immunoprecipitation of phosphorylated MLKL in TSZ-stimulated HT-29 cells. Lysate obtained from HT-29 cells either untreated or stimulated with TSZ for 4 hours were incubated with ph-MLKL antibody (ab187091) or an isotype control for immunoprecipitation. Crude lysates together with eluates obtained from the immunoprecipitations were subjected to Western blotting and probed with the same ph-MLKL antibody used for the immunoprecipitation using Clean-blot IP detection kit (Thermo Fisher) (upper panel) or with a MLKL antibody (lower panel).

3.3.2 Immunoprecipitation of RIPK3 and ph-MLKL in NHEK

The optimised protocol was next used to immunoprecipitate RIPK1 from NHEK cells (Figure 3.12A). Thermo Fisher RIPK3 (PAI-4533) antibody was also used to immunoprecipitate RIPK3 (Figure 3.12B). A specific band for RIPK3 was detected at the expected size, which was not present in the IgG control (Figure 3.12B). However, incubation of NHEK lysates with the beads and RIPK3 antibody did not result in a decrease of RIPK3 in the supernatant, indicating an inefficient recovery of endogenous RIPK3. In

order to obtain a more efficient immunoprecipitation, increasing concentrations of RIPK3 antibody were used (1, 2 and 5 μg per 200 μg of protein lysate). Figure 3.12C shows an increase in the total amount of immunoprecipitated RIPK3 when higher concentrations of antibody were used. Although total depletion of RIPK3 from total cell lysates (RIP3 Sup) was not achieved, a reduction of RIPK3 protein levels was observed from the supernatant analysis when higher antibody concentrations were used (Figure 3.12C, RIP3 Sup 5).

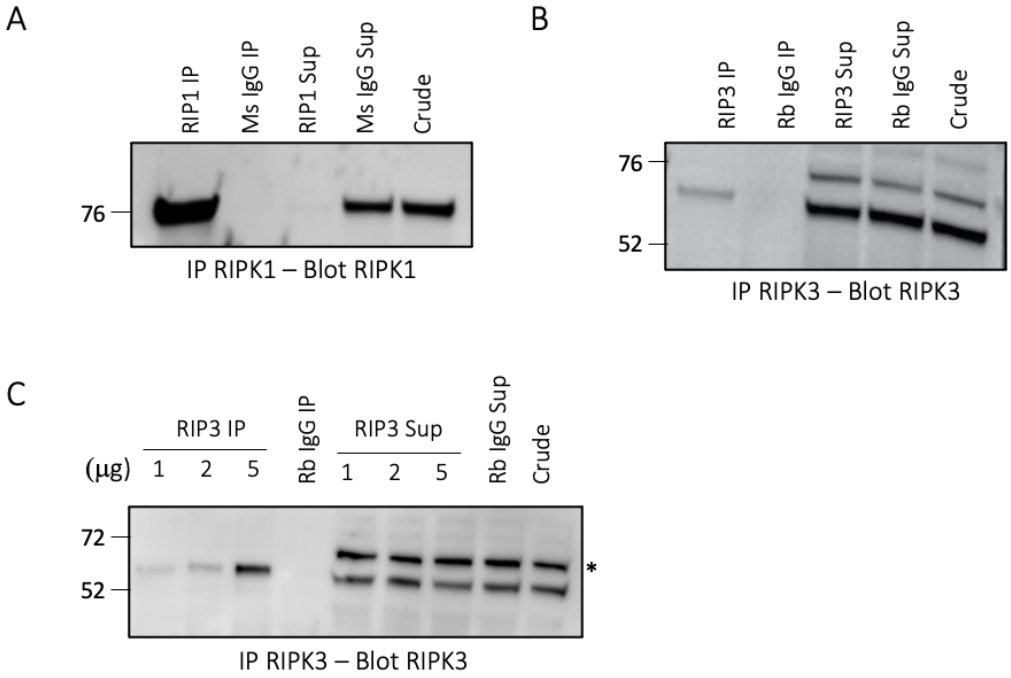

Figure 3.12: Analysis by Western blot of immunoprecipitated RIPK1 and RIPK3 in NHEKs. Elution from immunoprecipitation using **(A)** RIPK1 polyclonal mouse antibody (BD 610459); **(B)** and **(C)** Thermo Fisher rabbit RIPK3 (PAI-4533) antibody. In **(C)**, different concentrations of antibody were used (1, 2 and 5 μg). All immunoprecipitations were performed using an IgG control from the same species as the antibody used. Lanes represent the proteins immunoprecipitated with the antibody or isotype control (IgG IP); whole cell lysate (crude); and supernatants collected after incubation of the lysate with the antibody and beads (Sup).

To investigate the association of the different necroptotic markers in HMGB1-stimulated NHEK, RIPK3 and ph-MLKL immunoprecipitations were carried out after 0-, 4- and 8-hour stimulations with HMGB1. A weak

RIPK1 band was detected by Western blot when RIPK3 was immunoprecipitated in untreated NHEK (Figure 3.13A, IP: RIPK3), suggesting RIPK1-RIPK3 preassembly in NHEK cells. However, HMGB1 stimulation of NHEK did not lead to an increase of RIPK3/RIPK1 association. In addition, MLKL was not co-immunoprecipitated with RIPK3 upon HMGB1 stimulation. (Figure 3.13A, IP: RIPK3). Specific immunoprecipitation of ph-MLKL was achieved after stimulation of NHEK with HMGB1 for 4 and 8 hours (Figure 3.13A, IP: ph-MLKL). In agreement with the RIPK3 immunoprecipitation results, RIPK3 was not co-immunoprecipitated with ph-MLKL, suggesting there is no interaction between these proteins in response to HMGB1.

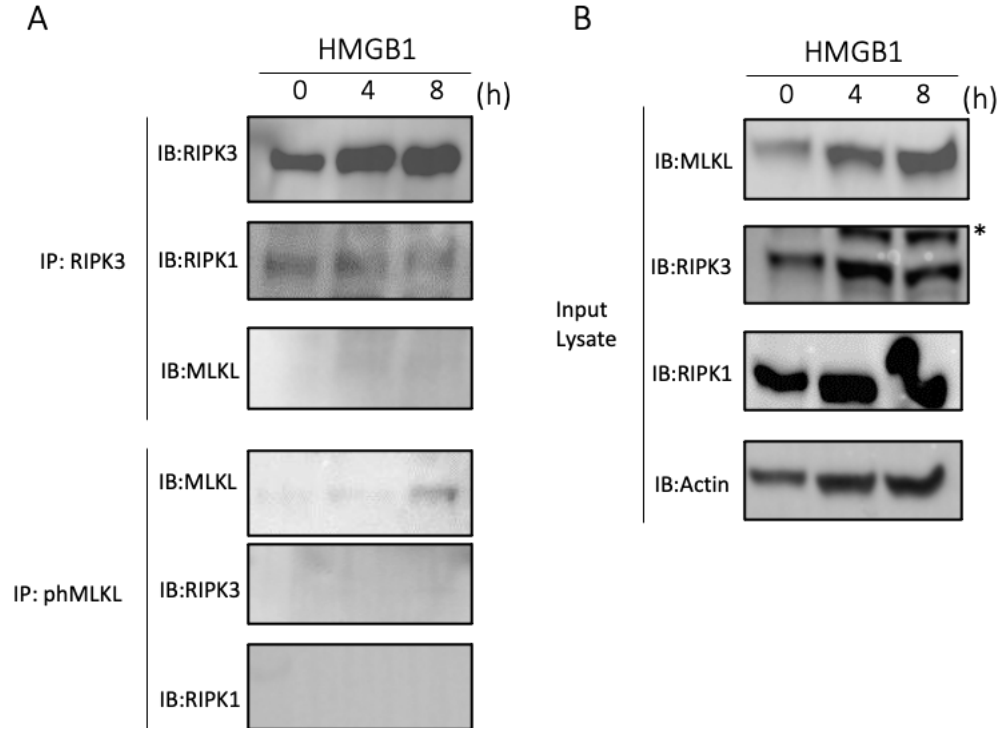

Figure 3.13: Immunoprecipitation of RIPK3 and ph-MLKL on HMGB1-treated NHEK. NHEK cells were treated with HMGB1 for 0, 4 and 8 hours and protein extracts were immunoprecipitated with anti-RIPK3 antibody or anti-ph-MLKL antibody. Eluates and input lysates were analysed by Western blotting alongside using the listed antibodies input lysates.

3.5 Discussion

Increased interest in necroptosis in recent years has led to the identification of different necroptosis triggers including chemicals, toxins or viruses (Tom Vanden Berghe et al., 2016). HMGB1 is a potent DAMP able to stimulate the innate immune system inducing inflammation in the skin (Hoste et al., 2015; Z. Wang et al., 2021). However, ph-MLK is detected upon HMGB1 treatment of NHEK skin explants *ex vivo* (personal communication, MC. Bonnet, C. Bonnet), suggesting that HMGB1 could play a role initiating keratinocyte necroptosis. This chapter investigated HMGB1-induced MLKL phosphorylation and subsequent molecular cascade in NHEKs. An extensive optimisation was carried out throughout the chapter which ultimately led to confirm, through Western blot and immunoprecipitation, that HMGB1 induces MLKL phosphorylation, which

might not associate with RIPK1 and RIPK3 in NHEKs. Detection of ph-MLKL through HMGB1 treatment provides new insight into the extracellular role of HMGB1 given that, to date, there is no research describing a role for HMGB1, or any other DAMP, in necroptosis induction.

A wide range of proteins have been reported to be involved in the necroptotic signalling pathway. MLKL phosphorylation by RIPK3, however, has been described to be essential for the execution of necroptosis, as ph-MLKL ultimately leads to plasma membrane permeabilization (J. M. Murphy et al., 2013; L. Sun et al., 2012). Initially, it proved very difficult to obtain clear definitive results relating to MLKL phosphorylation after HMGB1 treatment of NHEK cells. This appeared to be partly due to high background interference during the Western blot procedure. An extensive optimisation was carried out, during which every step of the protocol was addressed, to try and determine the cause of the poor-quality of the data and improve the outcome. During the optimisation, and whenever possible, each variable of the protocol was progressively altered while maintaining the rest unchanged. Unlike immortalised cell lines, the variability derived from primary cells isolated from donor samples is a major challenge to study cell signalling pathways. The scarce availability of donors made this task even more difficult. The source of NHEK was maintained, whenever possible during the optimisation process to avoid donor variability, except when donor variability itself was tested. HT-29 cells are widely use to study necroptosis, and MLKL phosphorylation can be detected after TSZ treatment (Cai et al., 2014; Huayi Wang et al., 2014). However, similar background interference was observed when trying to reproduce previous experiments performed in my lab regarding TSZ-induced MLKL phosphorylation in HT-29 and HMGB1-induced MLKL phosphorylation in NHEKs. The inability to reproduce results using lysates that had been previously validated by Western blot

by me, confirmed that the source of the problem was not cell type- nor cell-processing method-related.

Differences in transfer efficiency have been shown to result in a two- to four-fold increase or decrease in signal between gel lanes (Taylor et al., 2013). However, both the semi-dry transfer and wet transfer methods evaluated during the optimisation process, as well as the transfer buffers assessed did not improve the highly non-specific display of ph-MLKL blots with bands for ph-MLKL appearing in unstimulated samples. Given the sometimes-weak signal detected in the ph-MLKL blots, it was hypothesised that the levels of HMGB1-induced ph-MLKL would be low. In an attempt to successfully detect the protein, the mass of protein loaded was increased. However, loading too much protein can increase the chance of non-specific binding of antibodies (Gilda et al., 2015). and a number of studies have shown that quantitative analysis of poorly expressed proteins can often be obtained when smaller amounts of protein are loaded (Gilda et al., 2015; R. M. Murphy & Lamb, 2013).

Blocking of the Western blot membrane with NFDM substantially reduced the non-specific background observed in ph-MLKL blots. However, the phospho-proteins present in NFDM, such as casein, could interact with phospho-antibodies, making this a nonpreferred blocking agent for phospho-antibodies (Simpson & Browning, 2017). It has been reported that including phosphatase inhibitors in the blocking solution significantly increases the signal detected by phospho-specific antibodies (Sharma & Carew, 2002). Phosphatase inhibitors, already included in the lysis buffer, could be additionally incorporated during blocking, primary and secondary incubations to obtain clearer ph-MLKL blots.

Analysis of the bands of interest depends on the type of detection imaging system available. Automatic detection of saturation is a standard feature of most imaging software. If oversaturation occurs, it may be possible for the sensitivity of the camera to be reduced, failing to detect weaker signals during the chemiluminescent reaction (J. P. Mollica et al., 2009). The inclusion of a positive control was necessary during the ph-MLKL blot optimisation process. However, it was observed that the high intensity of TSZ-HT-29 samples (positive control) was, in fact, disguising weaker ph-MLKL bands from HMGB1-treated NHEK. To avoid this, membranes had to be carefully cut to exclude high-intensity that could hinder less intense ph-MLKL bands.

Interestingly, it has been reported that commercially available recombinant HMGB1 preparations can contain the reducing agent dithiothreitol which disrupts the crucial disulfide bond (H. Yang et al., 2012). These preparations are unable to stimulate cytokine production and their use in experiments has led to conflicting reports regarding the capacity of HMGB1 to induce inflammation (Ivanov et al., 2007; Rouhiainen et al., 2007; Sha et al., 2008; Tian et al., 2007). However, the same commercial HMGB1 preparation used during the experiments reported here and the following chapter, successfully induced MLKL phosphorylation in skin *ex vivo* explants (personal communication, MC Bonnet, C Bonnet), indicating the commercial HMGB1 preparation was not determinant for the variability of the results observed in NHEKs.

Another key aspect of the optimisation was the specificity and efficacy of the primary antibody. The fact that the antibody had been previously validated in Western blot using a HT-29 cells, dissuaded initial questioning of this step of the protocol. Furthermore, the antibody was being used successfully in IHC experiments by other members of the laboratory.

However, numerous articles report significant reproducibility and quality issues experienced with commercial antibodies (Herrera et al., 2013; W. Yu & Hill, 2013) and there is often variability between different lots or batches of that antibody, which can make it very difficult to reproduce previous work (Baker, 2015). Indeed, different batches of antibody were used during the initial experiments – which showed specific detection of ph-MLKL in TSZ-treated HT-29 and HMGB1-treated NHEKs – and the following experiments displaying non-specific bands due to a considerable time gap between these two events. In this case, working with a phospho-specific antibody only added to the problems with consistency of commercial antibodies. Because of the methodology in the preparation of antibodies, a phospho-specific antibody will have the possibility of bearing some affinity to the non phospho-site (Simpson & Browning, 2017). Thus, when target protein levels are abundant, some binding could conceivably occur, giving a possible explanation of the presence of a weak, similar-size band in ph-MLKL blots of untreated samples.

Ultimately, the acquisition of a different commercial antibody partially solved the problem and put an end to the optimisation process. However, it is worth mentioning that, even after acquiring the new antibody, the variability within each experiment was considerable: following the exact same Western blot protocol and using the same set of samples would occasionally result in different outcomes. These different outcomes were not contradictory but would often include unclear or failed data from which results could not be interpreted due to the presence of non-specific bands. The lack of robust reproducibility regarding ph-MLKL detection dissuaded following further steps to perform large-scale proteomic analysis, given their cost.

Nevertheless, optimised results point towards an increase in the levels of MLKL phosphorylation upon treatment of NHEK with HMGB1 for 4 to 8 hours. In contrast, phosphorylation of MLKL by TSZ-treatment of NHEK was detected at later timepoints (18 and 24 hours). Detection of ph-MLKL as early as 4 hours after HMGB1 treatment of NHEK suggests activation of the necroptotic effector might not a consequence of TNF release by keratinocytes. However, further experiments including anti-TNF antibodies would be necessary to confirm this.

The inflammatory responses elicited by HMGB1 can be driven by the activation of several receptors, including RAGE, TLR-2 and TLR-4 (R. Kang et al., 2014). Interestingly, interaction between RIPK3 and RAGE has been described, and deletion of RAGE has been directly associated with a decrease in necroptotic cell death in vitro (Faust et al., 2020), suggesting a role of this receptor inducing necroptosis. Furthermore, RAGE-mediated endocytosis of HMGB1 has been reported to induce pyroptosis in macrophages. Endosomes containing HMGB1 translocate into lysosomes, which leads to lysosome destabilisation and rupture around 6 hours after HMGB1 stimulation. Lysosomal rupture initiates a cascade of molecular events including Cathepsin B activation and release, pyroptosome formation and caspase-1 activation. (J. Xu et al., 2014). However, neither HMGB1 nor TSZ induced the activation of Gasdermin D by proteolytic cleavage. Since this finding has only been reported in macrophages, it is possible that this phenomenon is cell specific.

Interestingly, initial observations indicated RIPK1 levels were slightly increased upon HMGB1 treatment of NHEK, which could suggest that HMGB1-induced necroptosis is RIPK1-dependent. However, RIPK1-dependent TNF-induced necroptosis in HT-29 show a decrease, not increase, of RIPK1 expression upon induction of necroptosis with TSZ.

Furthermore, RIPK3 immunoprecipitation did not lead to the co-immunoprecipitation of RIPK1 in HMGB1-treated NHEK, suggesting these proteins do not interact after HMGB1 treatment of NHEK. This result was not unexpected given that other RHIM-containing adaptors such as TRIF and ZBP1 can bind and activate RIPK3 independently of RIPK1 in response to necrosome triggers other than TNF (He et al., 2011; Kaiser, Sridharan, et al., 2013; Upton et al., 2012). Initiation of necroptosis through activation of TLR-4 by HMGB1 could involve similar signalling pathways. Treatment of NHEK with HMGB1 in the presence of antibodies targeting RAGE or TLR-4 would help identify the signalling pathway responsible for MLKL phosphorylation upon HMGB1 treatment.

Ph-MLKL also does not associate with RIPK3, in disagreement with the results obtained in HT-29 and studies that reports that RIPK3 and MLKL normally associate in the absence of stimuli (Garnish et al., 2021). This association, however, might be cell-type dependent. This lack of interaction suggests that a different kinase might phosphorylate and associate with MLKL upon HMGB1 treatment of NHEKs. However, given the observed donor variability in previous experiments using NHEK, additional replicates of the experiments are essential to confirm this.

Activation of RIPK3 through autophosphorylation is a prerequisite for the recruitment and phosphorylation of MLKL and it is sufficient to induce necroptosis provided that MLKL is accessible (Jixi Li et al., 2012; Orozco et al., 2014; X.-N. Wu et al., 2014). However, it has been shown that phosphorylated RIPK3 can play a role in cytokine production, independently of MLKL phosphorylation and necroptosis (Lawlor et al., 2015). Nevertheless, further studies could include analysing the expression of RIPK3 phosphorylation in HMGB1-treated NHEK. Furthermore, considering the difficulties encountered when using

phospho-antibodies by Western blot, and being aware that the ph-MLKL (ab187091, Abcam) antibody is successfully used in IHC experiments, future work could focus on the detection of HMGB1-induced ph-MLKL by immunostaining. This will also allow us to confirm the localisation of ph-MLKL in the cell as well as to study the colocalization with other necroptosis markers.

Phosphorylation of MLKL in keratinocyte raises several possibilities concerning the possible source of HMGB1 *in vivo*. HMGB1 could be secreted by immune cells resulting in necroptosis activation of surrounding cells, which could explain the presence of HMGB1 in infiltrating immune cells in the dermis of TEN prelesional skin before detection of MLKL phosphorylation in the epidermis (personal communication, Bonnet MC). Additionally, necrotic keratinocytes can release HMGB1 (W. Zhang et al., 2017), which, in turn, could re-enforce necroptotic cell death in neighbouring keratinocytes. Extensive further research would be necessary to investigate this hypothesis and the physiological source on HMGB1 *in vivo.*

In conclusion, further research is necessary to stablish the molecular signalling downstream of HMGB1 stimulation in NHEK. The results reported here show that treatment of NHEK with HMGB1 leads to the phosphorylation of MLKL, the primary mediator of necroptosis. The receptor for HMGB1 on NHEK has not been investigated and will require further research. HMGB1 induction of MLKL phosphorylation could be a RAGE-mediated event, as is the case in HMGB1 induced pyroptosis (J. Xu et al., 2014), or act by interaction with other receptors such as TLR-2 or TLR-4. Interestingly, association of RIPK1-RIPK3-MLKL in response to HMGB1 was not observed, although more experiments are needed to confirm this. The use of established inhibitors of RIPK1 (Nec-1s), RIPK3

(GSK872) or MLKL (NSA, GW806742X) would allow us to better understand the role of these proteins in HMGB1-treated keratinocytes. The results reported here raise questions around a necroptosis-independent role of HMGB1-induced ph-MLKL, which are addressed in the following chapter.

Chapter 4

Necroptosis in NHEKs

4.1 Background and aims

Until the discovery of different regulated forms of necrosis, cell death was generally classified into apoptosis, which is programmed and regulated, and necrosis, which established thinking said was largely unregulated and due to either external effectors such as pathogens, toxins, trauma or unrestrained inflammation. These forms of death have easily distinguishable morphological features, characterised by cytoplasmic shrinkage, chromatin condensation, nuclear fragmentation and plasma membrane blebbing versus cellular swelling, increased cytoplasmic granularity, intact nuclei and membrane rupture (Schweichel & Merker, 1973). Apoptosis can be detected through identification of well-established markers such as nuclear fragmentation or Casp-3 cleavage (Tom Vanden Berghe et al., 2013). However, over the past decade, the field of regulated necrosis has continued to expand, and the complexity of the mechanisms make it important to distinguish the different types of programmed necrosis. Necroptosis, as with any other necrotic process, leads to rapid loss of membrane integrity and the release of cellular content (Tom Vanden Berghe et al., 2014). Hence, although detection of membrane permeabilization can exclude apoptotic cell death, it does not distinguish between necroptosis, pyroptosis, ferroptosis, NETosis, and other forms of regulated necrosis. As a regulated form of cell death, necroptosis can be blocked by numerous small molecule inhibitors

targeting different key effector steps of the necroptotic pathway (Zhuang & Chen, 2020). Therefore, blocking of cell death with the use of these inhibitors is an efficient confirmation of necroptosis.

As described in the previous chapter, MLKL phosphorylation can be detected in response to HMGB1 stimulation of NHEK. Although ph-MLKL is a well-established marker of necroptosis, confirmation of actual cell death is needed. This chapter aims to test the previously stated hypothesis, that HMGB1 induces NHEK necroptosis, by assessing NHEK cell death in response to HMGB1 stimulation. In order to investigate this hypothesis, an optimisation of the experimental assays and conditions to measure NHEK necroptosis has been performed using TSZ (TNF, Smac mimetic and z-VAD-fmk) as a necroptosis positive control, and TS (TNF and Smac mimetic) for apoptosis induction as described in section 2.3. Cell toxicity has been studied using two different methods, the first based on the differential uptake of membrane impermeable DNA binding dye propidium iodide (PI) and a second method based on the leakage of intracellular LDH through impaired plasma membrane. The necroptosis-sensitive cell line, HT-29, has been used to optimise the cell death assay protocols. Additionally, overall health of NHEK cells has also been explored using a cell viability assay (WST-1) and through microscopical examination of NHEK cell morphology and confluency status. Along this optimisation, specific inhibitors have been used to confirm necroptotic cell death.

With the purpose of finding the best conditions in which to measure NHEK cell death, the different additives and supplements included in the complete keratinocyte medium (Green's medium) have been investigated. These include Ham's Nutrient Mixture F-12, insulin, hEGF, cholera toxin, hydrocortisone, adenine and FCS (see section 2.2.3 for details). Additionally, the potential effect of calcium in NHEK necroptosis has also

been assessed. Although still controversial, Calcium has been shown to play a role downstream necroptosis, with increases of calcium found as a consequence of necrosome formation (Nomura et al., 2014). Additionally, it has been suggested that elevated cytosolic Ca^{+2} can drive the necroptotic mode of cell death (Nomura et al., 2014), making it an interesting variable when studying necroptosis.

4.2 Results: PI-based assays

4.2.1 Optimisation in HT-29

Treatment of HT-29 with TSZ led to an increase in PI-positive cells over time, as seen in Figure 4.1. TSZ-induced cell death after 2, 4, 6 and 8 hours was significantly higher than TS-induced death at those timepoints (*p=0.0347 at 2 h, *p=0.0335 at 4 h, *p=0.0329 at 6 h and **p= 0.0072 at 8 h). Low levels of PI uptake were detected upon TS treatment of NHEK cells, especially after longer periods of exposure, due to secondary necrosis. Cells treated with TSZ and RIPK1 inhibitor Nec-1s showed reduced PI uptake, which was significant at 6 and 8 hours (*p= 0.0267 and **p=0.0027, respectively) (Figure 4.1A). This result is in agreement with those described in Chapter 3, where MLKL phosphorylation was detected 4 and 6 hours after TSZ treatment of HT-29 and inhibited by pre-treatment with Nec-1s (Figure 3.1A).

HT-29 cells were also used to validate the commercially available necroptosis inhibitors shown in Table 4.1. The use of Nec-1s and MLKL inhibitors NSA and GW806742X (GW) led to a significant decrease of necroptotic cell death induced by TSZ. Surprisingly, treatment with RIPK3 inhibitor GSK872 did not inhibit TSZ-induced cell death, suggesting an optimisation of the concentration used was necessary (Figure 4.1B). These

inhibitors, particularly Nec-1s and NSA were regularly used in further experiments to confirm necroptotic cell death.

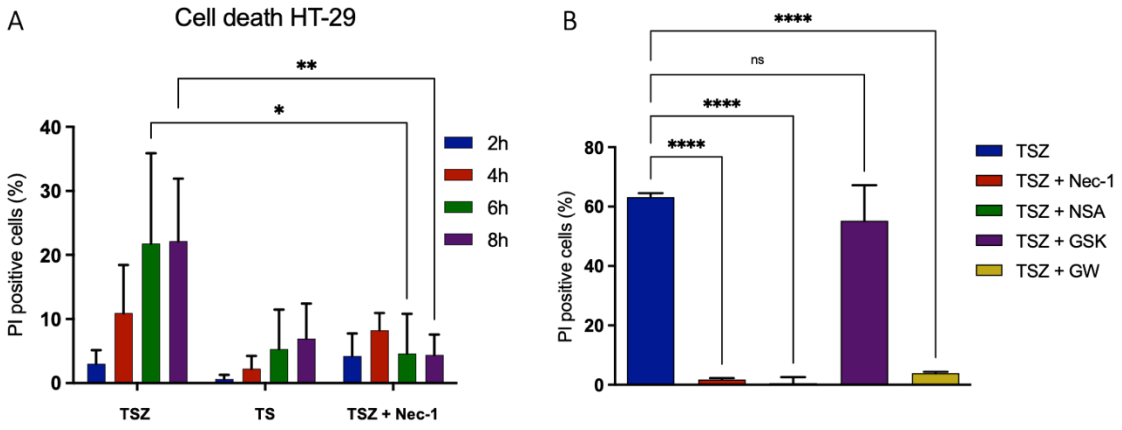

Figure 4.1: Optimisation of PI-based cell death assay using TSZ-treated HT-29 cells and necroptosis inhibitors. (A) HT-29 were treated with TSZ, TS or TSZ + Nec-1s during 2, 4, 6 and 8 hours. **(B)** HT-29 were treated with TSZ for 6 hours and inhibitors Nec-1s (20 μM), NSA (1 μM), GSK-872 (GSK, 1 μM) or GW806742X (GW, 5 μM). PI (10 μg/mL) was added to each well and intake percentage was calculated according to the total number of cells and normalised to non-treated values. Data shown was calculated from (A) three independent experiments using triplicates, (B) one experiment using triplicates. Graphs show mean values in columns and standard deviation (SD). The statistical analysis performed was two-way ANOVA (*p=0.0267, **p=0.0027) for (A) and ordinary one-way ANOVA (****p<0.0001) for (B), followed by Turkey's multiple comparison test.

4.2.2 Detecting necroptosis in NHEK cells

PI uptake through membrane permeabilization of NHEK was successfully detected in a time dependent manner in response to TSZ stimulation. Cell death after TS treatment due to secondary necrosis was detected only at later time points (Figure 4.2). The ability of HMGB1 to induce cell death was also investigated. The timepoints used (4, 6 and 8 hours) were decided upon after consideration of the results obtained in Chapter 3. Cell death was not detected after treatment of NHEKs with HMGB1 at any of these timepoints (Figure 4.2).

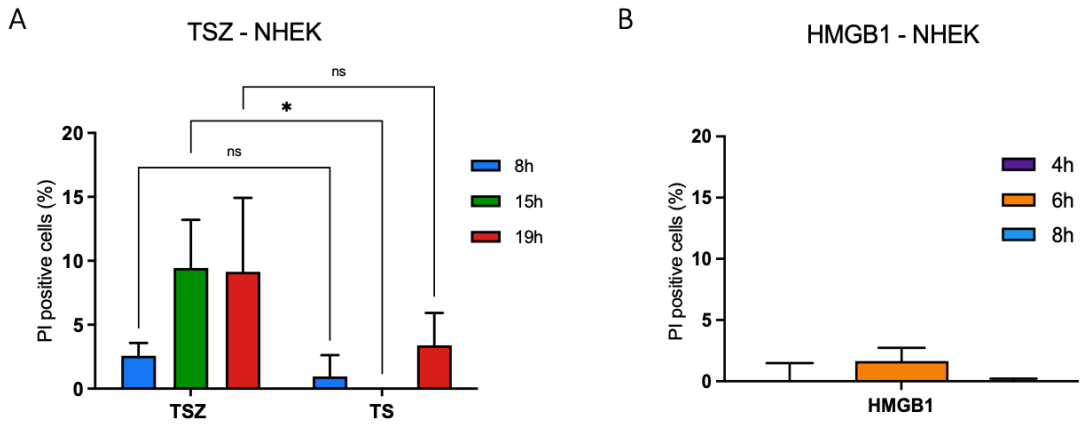

Figure 4.2: Detection of HMGB1- and TSZ-induced necroptosis through PI uptake in NHEKs. (A) NHEKs were treated with TSZ or TS for 8, 15 and 19 hours or **(B)** 50 nM HMGB1 for 4, 6 and 8 hours. PI (10 μg/mL) was added to each well and uptake percentage was calculated according to the total number of cells and normalised to non-treated values. Data shown was calculated from a single experiment with triplicates. Graphs show mean ± SD. The statistical analysis performed for (A) was two-way ANOVA (*p=0.0174) followed by Šídák's multiple comparison test.

4.2.3 Optimisation of the NHEK culture conditions

Despite a substantial increase in cell death achieved through TSZ treatment, the percentage of necroptotic NHEKs was lower than expected, only reaching 10-15%. Previous optimisation of the protocol using the necroptosis-sensitive HT-29 cells suggested that the sensitivity of the PI-based experimental assay was not very high (Figure 4.1A). Given that percentages in NHEK were even lower, concern was raised on whether the keratinocyte culture conditions could be preventing cell death, and, in that case, hindering the detection of HMGB1-induced necroptosis.

4.2.3.1 *Culture Medium*

Homemade complete keratinocyte medium (Green's medium) was compared to commercial EpiLife defined growth supplemented (EDGS) medium (GIBCO, Thermo Fisher), a commercially available medium specifically designed for the culture of human epidermal keratinocytes.

The percentage of PI-positive cells following 19 hours of TSZ treatment was higher when NHEK cells were cultured in Epilife medium (Figure 4.3). However, NHEK death could not be inhibited by pre-treatment with inhibitor Nec-1s, which as expected, resulted in a strong decrease in cell death in NHEK cultured in Green's medium (Figure 4.3A). Given that PI the uptake observed following TSZ treatment of NHEK cultured in Epilife medium could not be inhibited by Nec-1s, this medium was not used in further experiments.

4.2.3.2 *Calcium*

In order to assess the possible role of Ca^{+2} in NHEK necroptosis, cells were cultured in Green's medium (control) with increasing concentrations of Ca^{+2}. The basal concentration of Ca^{+2} in Green's medium is approximately 1.2 mM (being DMEM, Ham nutrient mixture F12 and FCS the sources of Ca^{+2}). By adding Ca^{+2} to the culture medium ($CaCl_2$), increasing concentrations of Ca^{+2} were studied: 1,18 mM, 1,35 mM, 1,55 mM and 1,7 mM. NHEK stimulated with TSZ or HMGB1 for 19 hours were protected from cell death with increasing Ca^{+2} concentrations, as PI uptake decreased (Figure 4.3B).

4.2.3.3 *Growth Factors*

The role of growth factors included in Green's medium, insulin and hEGF, was next assessed. Culture medium with decreasing and increasing concentrations of hEGF and insulin – 500 ng/ml, 2 µg/ml, 5µg/ml (control), 20 µg/ml and 50µg/ml – were prepared. NHEK cultured with lower concentrations of insulin were more sensitive to cell death induced by both TSZ and HMGB1 (19 hours), while higher concentrations had a protective effect on cell death (Figure 4.3C). Similarly, lower concentrations of hEGF also allowed NHEK to die in response to TSZ and HMGB1 than higher

concentrations of this growth factor (Figure 4.3D). This provided preliminary evidence that growth factors included in the NHEK culture medium inhibit cell death.

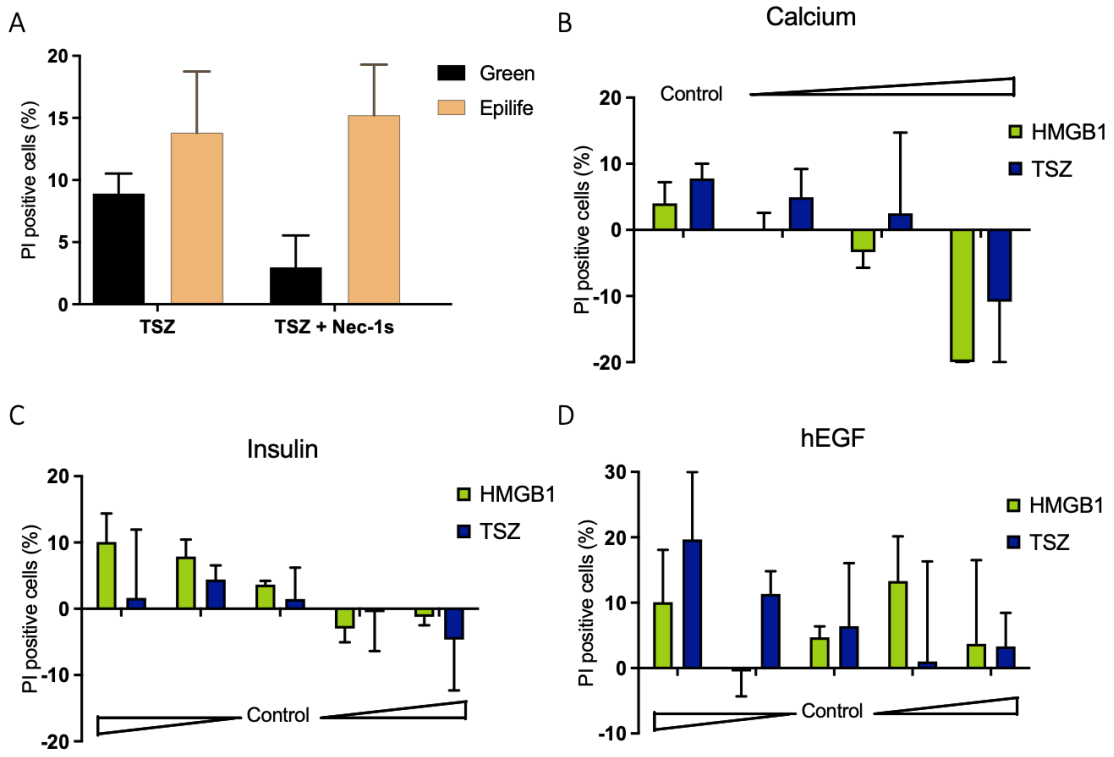

Figure 4.3: Cell death assays using different culture media conditions (A) Cell death after 19 hours treatment of TSZ or TSZ + Nec-1s was determined through PI uptake in NHEK that had been cultured in homemade Green's medium or EpiLife culture medium. HMGB1 and TSZ-induced cell death (19 hours) was also assessed using different concentrations of **(B)** Calcium, by adding increasing concentrations of $CaCl_2$ to the medium (up to a maximum of 1,7 mM); **(C)** hEGF and **(D)** insulin: 500 ng/ml, 2 µg/ml, 5 µg/ml (control), 20 µg/ml and 50 µg/ml. NHEK were grown in the different culture media during and 24 hours prior to stimulation. All values are normalised to readings from non-treated conditions and percentages are calculated considering the total amount of cells. Data shown was obtained from one experiment with triplicates. All graphs show the mean ± SD for each condition.

4.2.3.4 *Combinations*

In order to further address the role of all ingredients included in Green's NHEK culture medium, fifteen different combinations of media were generated, and TSZ-induced cell death was assessed after 19 hours through PI uptake. Figure 4.4A shows the ingredients of each formula, labelled from the letter A (which corresponds to Green's medium) to the letter O. Green's medium showed to be, again, one of the conditions in which NHEK were most protected from cell death (less than 10%), (Figure 4.4B, letter A). By contrast, NHEK cultured in media formulas with low serum (1% v/v FCS) were more sensitive to death (Figure 4.4A, formulas G-O). In line with previous results, the absence of insulin and hEGF (Figure 4.4A, formula H) proved to be determinant for NHEK death. Of all the conditions tested, low-serum DMEM showed to be one of the best conditions in which to assess NHEK cell death (Figure 4.4A, formula N).

A

	A	B	C	D	E	F	G	H	I	J	K	L	M	N	O
Ins	+	-	+	+	+	+	+	-	-	-	-	-	+	-	-
hEGF	+	+	-	+	+	+	+	-	-	-	-	-	+	-	-
CT	+	+	+	-	+	+	+	+	+	-	+	-	-	-	-
HC	+	+	+	+	-	+	+	+	+	+	-	-	-	-	-
Ade	+	+	+	+	+	-	+	+	+	+	+	+	+	-	-
FCS	↑	↑	↑	↑	↑	↑	↓	↓	↓	↓	↓	↓	↓	↓	↓
F12	+	+	+	+	+	+	+	+	-	+	+	+	+	-	+

B

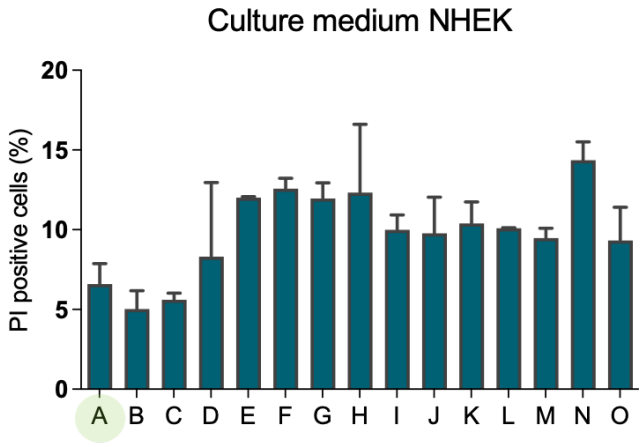

Figure 4.4: PI-based cell death assay in TSZ-treated keratinocytes cultured in different media. (A) Different formulas of NHEK culture medium, which are modifications of Green's medium (A, highlighted in green). The table shows the presence (+) or absence (-) of different ingredients: insulin (ins), hEGF, cholera toxin (TC), hydrocortisone (HC), Adenine (Ade) or Ham nutrient mixture F12 (F12), and indicates low (1%, down arrow) or high (2,5%, up arrow) concentrations of added FCS. **(B)** NHEKs were grown in the different culture mediums during and 24 hours prior to being treated with TSZ for 19 hours. Cell death was calculated according to the percentage of PI-positive cells. All values are normalised to readings from non-treated conditions and percentages are calculated considering the total amount of cells. Data shown was obtained from one experiment with triplicates The graph shows the mean ± SD for each condition.

4.2.3.5 *Evaluation of NHEK morphology*

The morphology and plate confluency of NHEK cells were, whenever possible, assessed microscopically to detect any possible changes induced by the different culture mediums studied, as well as by the effect of TSZ and HMGB1. NHEK cells were cultured in clear plates and grown using medium formulas containing different growth factors (see formulas in Figure 4.5B). After stimulation with TSZ or HMGB1 for 19 hours, the shape, number and morphology of the cells were recorded microscopically. NHEK cells grown in Green's medium form characteristic patches that can be observed in Figure 4.5A, NT column, row A. Observing some round yellow cells, corresponding to detached NHEK, is normal. Non treated cells of all conditions (Figure 4.5A, NT column, rows B-F) had similar morphology and growth pattern, except serum-free DMEM (Figure 4.5A, NT column, row G). Cells grown in Green's medium showed no substantial changes after HMGB1 or TSZ stimulation (Figure 4.5A, row A). However, the confluency state of the well, which indicates overall health of NHEKs, was drastically decreased after 19h treatment with TSZ when cells were grown in low serum conditions (Figure 4.5A, TSZ column, rows B-F). Among all of them, NHEKs seemed to be more affected by TSZ treatment when they were grown in the absence of Ham's F12 Nutrient Mixture (F-

12) (Figure 4.5A, TSZ column, rows D–F). These results further confirmed that the presence of growth factors in the culture medium can limit NHEK death. Consequently, and considering the medium optimisation results obtained using the PI-based assay (previous section), DMEM + 1% (v/v) FCS (hereon referred as low serum DMEM) was chosen as the preferred condition to detect NHEK death. However, and in line with previous results, no differences in NHEK confluency or morphology were observed this or any other culture condition after stimulation with HMGB1 (Figure 4.5A, HMGB1 column).

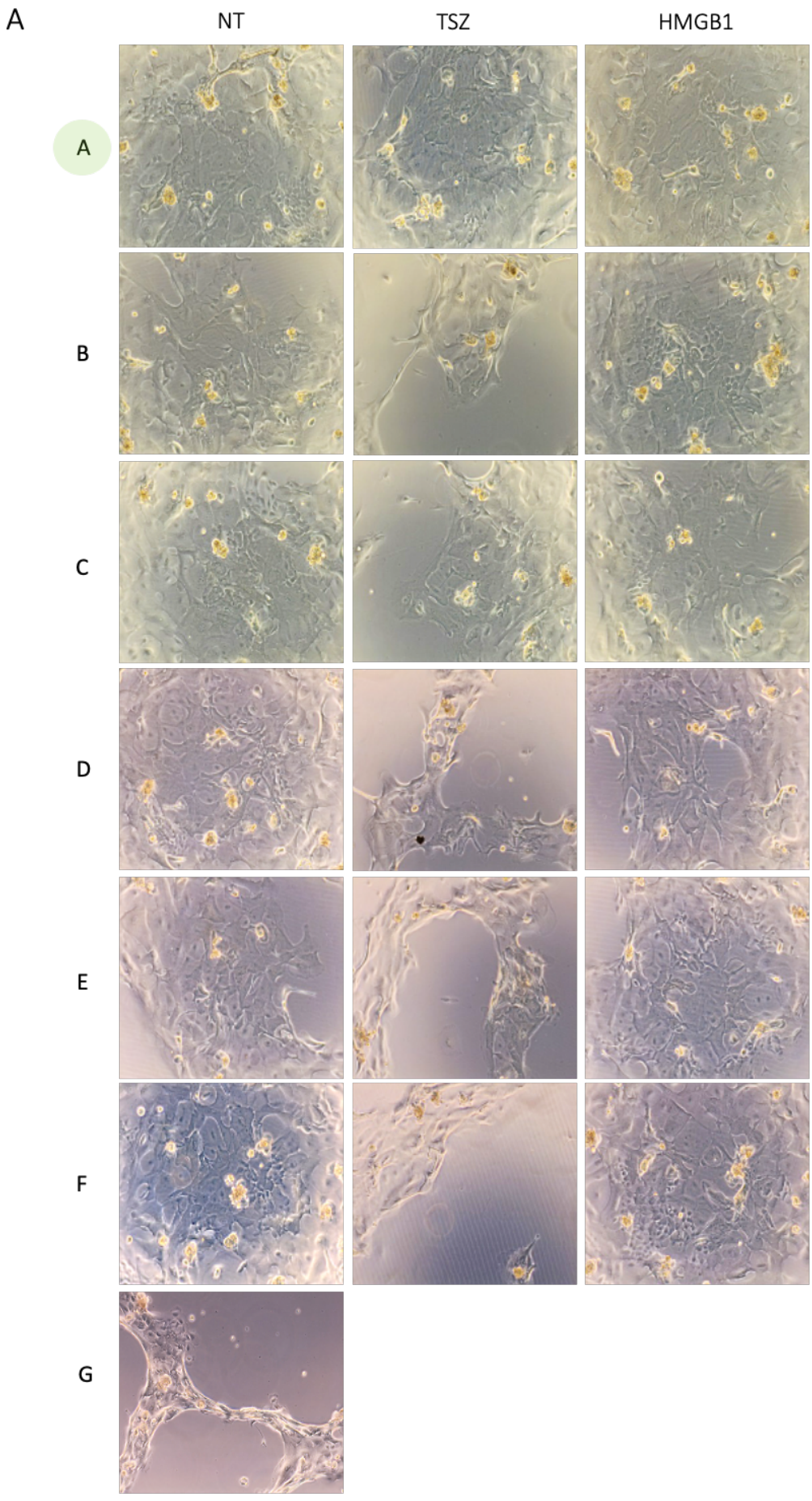
A
NT
TSZ
HMGB1
A
B
C
D
E
F
G

B

	A	B	C	D	E	F	G
Insulin	+	+	-	+	-	-	-
hEGF	+	+	-	+	-	-	-
CT	+	+	+	+	+	-	-
HC	+	+	+	+	+	-	-
Ade	+	+	+	+	+	-	-
FCS	↑	↓	↓	↓	↓	↓	-
F12	+	+	+	-	-	-	-

Figure 4.5: Documentation of morphological changes in NHEK growth and morphology when cultured in different mediums and in response to 19 hours of TSZ or HMGB1. (A) Representative images of non-treated NHEKs (NT) and 19-hour treated NHEKs. Rows represent the different culture conditions of NHEK (A-G), which are detailed in (B). NHEK were grown in the different culture mediums during and 24 hours prior to stimulation. Representative images have been chosen from a single experiment with duplicates **(B)** Different formulas of NHEK culture medium, which are modifications of Green's medium (A, highlighted in green). The table shows the presence (+) or absence (-) of different ingredients: insulin (ins), hEGF, cholera toxin (TC), hydrocortisone (HC), Adenine (Ade) or Ham nutrient mixture F12 (F12), and indicates low (1%, down arrow) or high (2,5%, up arrow) concentrations of added FCS.

4.3 Results: LDH-based cell death assays

4.3.1 Optimisation in HT-29 cells

TSZ treatment of HT-29 cells led to the release of LDH after 2, 4 and 6 hours (Figure 4.5). The sensitivity of this assay was higher than initially expected and maximum fluorescence was reached only after 4 hours of TSZ treatment. Further optimisation of cell concentration and protocol was performed to avoid this. Quantification and statistical analysis of these data was not performed (n=1), and cell death percentage is relative and must be interpreted at a qualitative level only. With these caveats, the results were similar to those found with PI. Secondary necrosis was detectable

after 4- and 6-hour treatments of TS, and Nec-1s was able to inhibit cell death successfully at all timepoints (Figure 4.1).

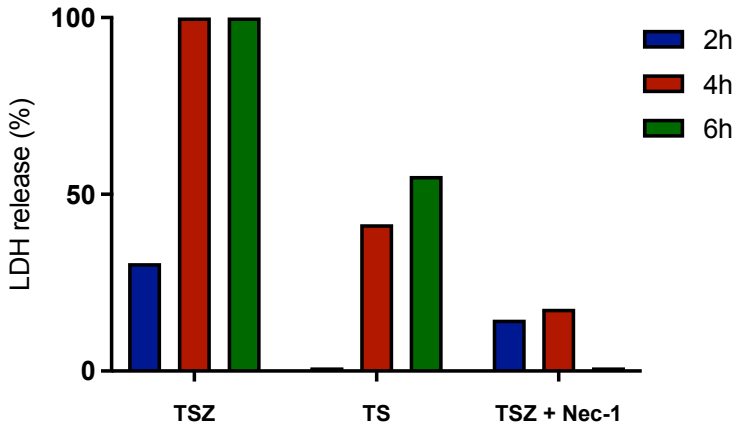

Figure 4.6: LDH-based cell death assay of TSZ-treated HT -29. HT-29 cells were treated with TSZ, TS or TSZ + Nec-1s (20 μM) during 2, 4, 6 hours. Total LDH release was measured after each timepoint. All values are normalised to non-treated readings. Data shown was calculated from one experiment without duplicates.

4.3.2 Detecting necroptosis in NHEK cells

TSZ stimulation of NHEK led to LDH release after 6 hours and up to 32 hours (Figure 4.7A), confirming the efficiency of the assay in measuring NHEK cell death. As observed with HT-29 cells, the sensitivity of LDH was higher than that seen in PI based assays, with maximal luminescence (saturated readings) achieved after 12 hours of TSZ stimulation. To avoid reaching maximal luminescence, a reduction of the initial seeded cell number and the volume of supernatant recovered for the assay was carried out in following experiments. As confirmation of TSZ-induced NHEK death had been achieved in the previous experiment, the time-course kinetic was not repeated after protocol optimisation to avoid luminescence saturation. Further experiments (Figures 7.4B and C), however, always include TSZ-treated NHEK data alongside, as positive controls of necroptotic cell death.

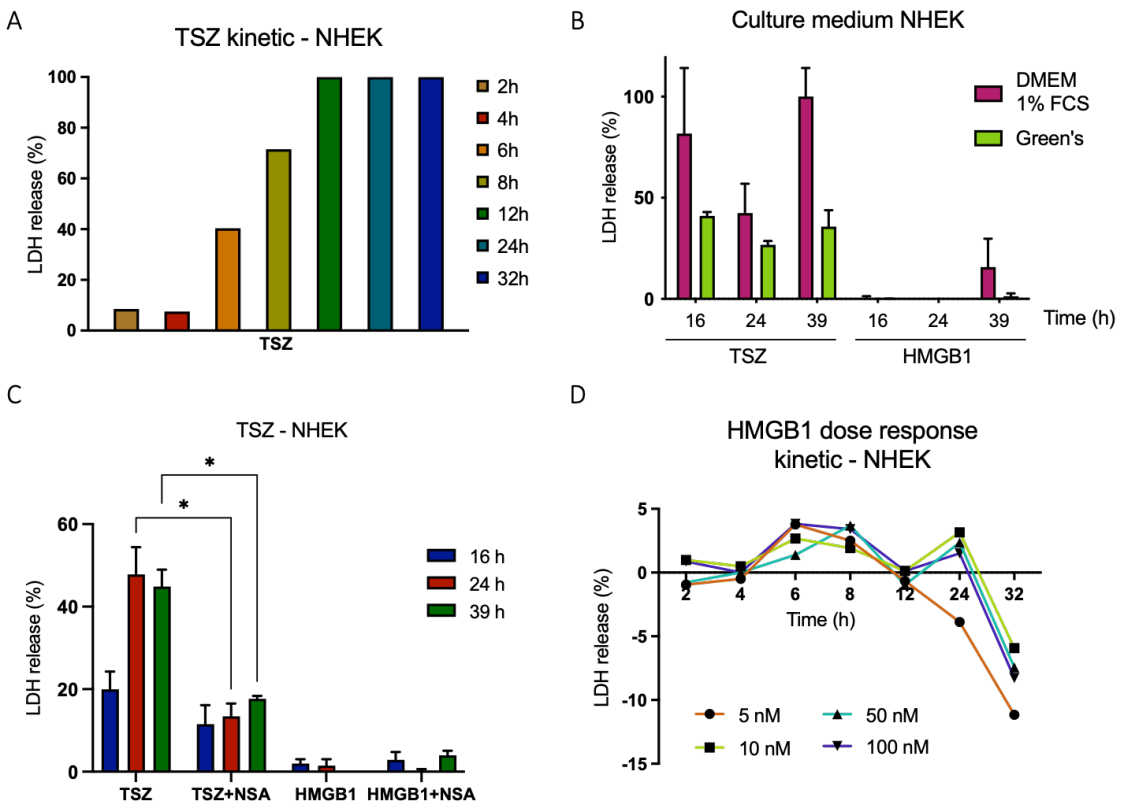

Figure 4.7: Detection of HMGB1 and TSZ-induced necroptosis through LDH release in NHEK. Cell death was assessed through LDH release in NHEKs cultured in low serum DMEM (1% FCS) and stimulated with **(A)** TSZ during 2, 4, 6, 8, 12, 24 and 32 hours or **(C)** TSZ or 50 nM HMGB1 plus inhibitor NSA (1 μM) for 16, 24 and 39 hours. **(B)** NHEKs cultured in Green's medium or low serum DMEM (1% FCS) were stimulated with TSZ or 50 nM HMGB1 and LDH release was measured after 16, 24 and 39 hours. **(D)** NHEKs cultured in low serum DMEM were treated with increasing concentrations of concentrations of HMGB1 (5, 10, 50 and 100 nM) and LDH release was measured after 2, 4, 6, 8, 12, 24 and 32 hours. NHEKs were grown in the different culture media during and 24 hours prior to stimulation. All values are normalised to readings from non-treated conditions. Data shown in (A) and (D) was obtained from a single experiment (no duplicates); data from (B) and (C) was obtained from one experiment with triplicates and the graphs show the mean ± SD for each condition. The statistical analysis performed and shown in (C) was two-way ANOVA, followed by Turkey's multiple comparison test. *p=0.0137 (24 h TSZ – TSZ+ NSA), *p=0.0162 (39 h TSZ – TSZ+ NSA).

Given the previous results indicating the ingredients in Green's medium can limit cell death, the effect of TSZ and HMGB1 was assessed in NHEKs cultured in low serum DMEM and Green's medium. As expected, culture of NHEK in DMEM + 1% FCS led to a higher LDH release than Green's medium upon TSZ treatment at 16, 24 and 39 hours (Figure 4.6B).

Culturing NHEK in low serum DMEM did not lead to a higher LDH release upon HMGB1 stimulation at 16 or 24 hours. However, a slight increase in LDH release was observed after 39 hours (Figure 4.6C). To investigate this possible HMGB1-induced cell death, the previous experiment was repeated including necroptosis inhibitors. NHEK cultured in low serum DMEM were treated with HMGB1 for 16, 24 and 39 hours in the presence of MLKL inhibitor NSA. In agreement with the previous experiments, TSZ induced necroptosis successfully at these timepoints (Figure 4.6C) and was effectively inhibited by NSA at 24 and 39 hours. HMGB1, on the other hand, was unable to induce death of NHEK at any of these timepoints (Figure 4.6C). The role of HMGB1 was further explored using NHEK cells cultured in low serum DMEM and stimulated with increasing concentrations of HMGB1 (5, 10, 50 and 100 nM) over time (2, 4, 6, 8, 12, 24 and 32 hours). Again, NHEK cell death was not detected in any of these conditions and the highest estimate of death was under 4% (Figure 4.6D).

4.4 Results: WST-1 cell viability assay

The viability of TSZ- and HMGB1-stimulated NHEKs was next assessed using a WST-1 cell proliferation assay. Cell proliferation was measured after 24 hours of stimulation with either TSZ or HMGB1 cultured either in Green's medium or in DMEM + 1% FCS. Results showed a decrease in NHEK cell number upon TSZ treatment, which, as expected, was more pronounced in cells grown in DMEM + 1% FCS culture medium (Figure 4.7). Treatment of NHEK with HMGB1, on the other hand, did not affect the proliferation status of the cells. HMGB1 treatment of NHEK cultured in DMEM + 1% FCS led to a slight decrease in cell viability, which could be further studied.

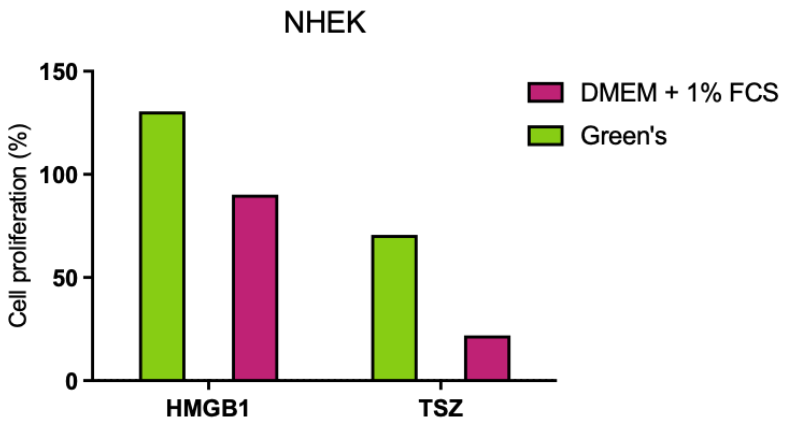

Figure 4.8: Cell viability measurements in TSZ and HMGB1-treated NHEKs. NHEKs were cultured in either low serum (1% FCS) or Green's medium and stimulated with TSZ or 50 nM HMGB1 for 19 hours. WST-1 proliferation assay was used to measure cell viability under each condition. Data shown was obtained from a single experiment (no duplicates).

4.5 Discussion

HMGB1 is a multifunctional protein with regulatory functions inside the nuclei that also acts as a prototypical DAMP when secreted or released from cells. Necrotic cells can release HMGB1 to promote inflammation in neighbouring cells (P. Scaffidi et al., 2002) by interacting with receptors such as RAGE or TLRs and inducing the production of pro-inflammatory cytokines. (R. Kang et al., 2014). However, results from my group have shown a new role of HMGB1 inducing MLKL phosphorylation in NHEK (Chapter 3, personal communication, MC Bonnet). With the purpose of investigating whether HMGB1 can induce necroptosis, cell death in response to HMGB1 treatment has been assessed along this chapter. Specific necroptotic NHEK death was achieved through TSZ treatment, which was inhibited by Nec-1s or NSA. An extensive optimisation of NHEK culture media was performed in order to find the ideal conditions for NHEK necroptosis induction. However, and regardless of culture conditions, the data reported here indicate that HMGB1 does not lead to NHEK necroptosis *in vitro*.

The main measurable difference between apoptotic and necrotic death relays on the loss of plasma membrane integrity during necrotic processes. Using appropriate measuring techniques to specifically detect different types of cell death is crucial to study different cell death inducers. For many years, TdT-mediated dUTP-biotin nick end-labelling (TUNEL) assays were considered to measure apoptosis. However, it is now known that TUNEL-positivity can be caused by any type of cell death (Grasl-Kraupp et al., 1995), highlighting the importance of the specificity of the cell death measuring kits and the use of specific inhibitors. Necroptosis and other forms of programmed necrosis have only been described in the past decade, which means gold standard methods to detect them have not yet been established. When analysing the literature, a commonly used protocol to identify necroptotic cell death is based on the use of Annexin V and PI in flow cytometry (Cummings et al., 2004; Hu et al., 2021). Annexin V binds to phosphatidylserine (PS), which is exposed from the inner to the outer leaflet of the membrane during apoptosis. Necrotic cells can also stain for Annexin V, but these will also be positive for PI, which, in turn, is excluded from apoptotic cells (Pietkiewicz et al., 2015). The main advantage of using this double staining through flow cytometry is that it allows the analysis of both the marker expression and the cell number, making it an efficient quantitative method to measure cell death. Unfortunately, flow cytometry is not as useful for adherent cells, especially when membrane markers are to be analysed. The preparation of cells for flow cytometry can cause damage to the original morphology or membrane markers expressed in dying adherent cells, especially during the detachment from their substrate, if enzymes such as trypsin are used (Nowak-Terpiłowska et al., 2021). Hence, alternative methods to study cell death in adherent cells had to be sought and optimised.

As mentioned, the use of PI is a useful tool to measure loss of membrane integrity during cell death. Using this dye alone, and measuring fluorescence values with a plate reader, was a potentially good strategy to study keratinocyte necroptosis. However, some limitations were found during the execution of this assay. Contrary to cultured cell lines (such as HT-29), NHEK growth rate can be inconsistent, leading to irregular/uneven confluency between wells due to poor attachment or proliferation. One of the limitations of the PI-based cell death assay was the fact that NHEKs had to be plated in opaque plates in order to allow the correct measurement of fluorescence in the plate reader. These plates, however, impeded microscopical observation for confluency and morphology assessment of NHEK cells before and during the stimulation process. An additional clear limitation of this assay, under the experimental conditions used here, was that the maximum percentage of cell death calculated was generally low, even when using the positive control TSZ, suggesting that the assay was of low sensitivity. Keratinocyte cornification, which also occurs in NHEKs *in vitro,* leads, among other events, to the loss of nuclear content through DNA degradation (Julie Henry Eve Toulza, 2012; Kypriotou et al., 2012). The absence of DNA for PI to interact with, due to differentiation of keratinocytes, constitutes a clear limitation of PI-based cell death assays to study NHEK necroptosis. This observation was also evident when NHEKs cultured with increasing concentrations of Ca^{+2}, a major regulator of keratinocyte differentiation *in vivo* and *in vitro* (Bikle et al., 2012), led to low PI readings.

Fluorescence emitted by PI drops around 6 hours after binding to DNA, which was found to be a limitation when longer timepoints of the same condition wanted to be studied. This meant that different technical conditions had to be prepared for each timepoint, which translated in a great number of cells having to be used. Furthermore, considering the

mentioned irregular proliferation of NHEK cells, increasing the number of conditions led to variability during the experiments. By contrast, LDH-based assays allowed the collection of a fraction of the supernatant from the same well at different timepoints, ensuring that parameters such as initial confluency were consistent and facilitating comparison between timepoints. This was one of the major advantages observed when using LDH-based cell death assays. In addition, as this method is based in a luminescent measurement, opaque plates to culture NHEK were not necessary. Microscopical observation of the NHEK cells allowed the documentation of the confluency status prior to the initiation of the experiment as well as the assessment morphology and overall health at the different timepoints of study.

LDH-based assays were found to be highly sensitive, which was initially considered a great advantage, especially by comparison with the sensitivity achieved by the PI-based assay. However, maximal luminescence readings were easily reached, especially when total lysis of the cells was achieved through Triton-X100. Hence, the higher sensitivity of the assay, while very useful, required additional technical optimisation of cell confluency and supernatant recovered during the experiments. Given that total cell lysis readings were repeatedly saturated, calculations to determine total cell death had to be adapted. As described earlier in this chapter (section 4.2.3), all maximal luminescence values were substituted by an invariable value, preventing accurate measurement of the total cell death percentage. Table 4.2 shows a summary of advantages and limitations, found under the experimental conditions used here, of the PI and LDH assays when studying necrotic cell death in NHEK.

	PI	LDH
Quantification based on the total number of cells	✓	×
Measurements at different timepoints from the same well	×	✓
Sensitivity	↓	↑
Allows observation of cell confluency and morphology	×	✓

Table 4.1: Advantages and disadvantages of PI and LDH-based cell death assays.

Similar advantages and limitations to the ones found with the LDH-based assay were observed when using WST-1 viability assay. For example, it permitted the use of clear plates that allows the observation of the cells, but kinetic experiments could not be performed using a single well in the plate. This method was, however, considerably less explored than the ones previously described and further experiments would be needed to discuss its own limitations. Nevertheless, and looking at the overall optimisation, the experimental data showed that measurement of LDH release provided the most sensitive assay. Provided that technical optimisation of the assay was performed to avoid luminescence saturation, this would be the preferred method to study NHEK cell death. However, considering the variability observed between assays in this experimental set up, relying in a singular marker of cell death could lead to inaccurate conclusions. Hence, combination of the LDH assay with an additional assay (either using PI or WST-1) would be ideal.

Notwithstanding the type of assay chosen to study cell death, common difficulties were consistently encountered while handling NHEK. As mentioned, NHEK confluency and growth rate were irregular, creating additional variables to consider when comparing conditions and experiments. Furthermore, as discussed in the previous chapter, as primary cells, NHEK response can vary widely depending on the donor and the differentiation state of the cells at the time of the experiment

(passage). Taking into consideration the time necessary to perform each experiment (NHEK must be seeded at least 24 hours before stimulation to ensure attachment) and the fact that NHEK can differentiate rapidly, confirmation of a given result using the same donor and cell passage was often very difficult. This sometimes led to variability between experiments, decreasing the robustness of the conclusions made.

These practical difficulties in handling NHEK may well be part of the reason for the lack of studies and references to NHEK necroptosis in the literature. A single reference was found regarding NHEK necroptosis *in vitro*: Kim et al., (2015) showed that NHEKs are provided with necroptotic machinery, as detected by endogenous expression of RIPK3. Furthermore, they showed NHEKs are capable of dying by canonical, TNF-induced necroptosis, similar to what is seen using the standard necroptosis-sensitive cell line, HT-29. The mentioned work is, to my knowledge, is the only evidence of NHEK necroptotic death *in vitro*, given that other claims of necroptosis in NHEKs have only been claimed through the detection of MLKL phosphorylation (Lauffer et al., 2018). The work presented in this chapter confirms NHEKs can undergo TSZ-induced necroptosis, which can be inhibited through Nec-1s, NSA and GW806742X. In contrast, most knowledge on skin necroptosis has been provided by necroptosis-dependent skin inflammation models Casp-8^{EKO} and $FADD^{EKO}$ (Bonnet et al., 2011; Kovalenko et al., 2009; Wallach et al., 2014). Keratinocytes obtained from $FADD^{EKO}$ model die *in vitro* easily upon TNF treatment (Bonnet et al., 2011). Other than primary mouse epidermal keratinocytes (PMK) from skin-inflammation models, additional research on necroptosis has been performed in the immortalised human keratinocyte cell line HaCat (X. Duan et al., 2020; Murai et al., 2018).

Invariably, across the literature, the study of necroptosis in NHEKs, PMKs or HaCat cells is performed through cell viability assays (either WST-1 or

MTT assays) (Bonnet et al., 2011; X. Duan et al., 2020; S. K. Kim et al., 2015; Kovalenko et al., 2009; Murai et al., 2018; Taraborrelli et al., 2018) or LDH-based assay (S. K. Kim et al., 2015). Viability assays were originally not the preferred method to study necroptosis given that they measure overall cell health through alterations in the cellular metabolism, which can be caused by several diverse factors such as proliferation, death or metabolic activity (Wright Muelas et al., 2018). In contrast, for this study, assays based upon membrane integrity were preferred, as disruption of the plasma membrane is a direct consequence of necrotic cell death. Nevertheless ,TSZ-induced NHEK death was confirmed through all the methods investigated here: PI uptake, LDH release and viability assay (WST-1). The data in this chapter represents the first described use of a PI-based cell death assay to assess NHEK necroptosis.

To my knowledge, it is also the first time that the effect of culture conditions of NHEK in cell death has been investigated. The purpose of the culture media optimisation was to establish the conditions for NHEK optimal response to necroptotic stimuli. It was found that the concentrations of Ca^{+2}, insulin, hEGF and FCS were relevant in NHEK necroptosis. Indeed, insulin or growth factors such as EGF promote cell proliferation and can protect against death (Gibson et al., 1999). Ca^{+2}, on the other hand, is known to affect keratinocyte differentiation *in vitro* (Bikle et al., 2012), and it was therefore not surprising to see reduced cell death upon increase in Ca^{+2} concentrations. Further investigation of the effect of the different ingredients included in the medium might uncover useful information regarding NHEK viability and responsiveness. The commercially available Epilife keratinocyte culture medium (60 μM Ca^{+2}, Gibco), supplemented with human keratinocyte growth medium (Gibco), did not lead to specific NHEK necroptosis under my experimental conditions, in contrast to a previous study reporting TSZ-induced

necroptosis in NHEKs using this culture medium (S. K. Kim et al., 2015). However, considering that the presence of serum in the culture media protected NHEKs from cell death and that Ca^{+2} concentrations in Green's medium are considerably higher than those recommended to avoid NHEK differentiation (Yamada, 2004), it would be interesting to investigate more in depth how NHEKs respond to HMGB1 in EpiLife medium.

My results show that stimulation of NHEKs with HMGB1 did not lead to an increase of the PI uptake or LDH release. Similarly, cell viability through WST-1 and keratinocyte morphology and confluency were not affected after incubation with HMGB1. Several studies have shown some delay between the detection of MLKL phosphorylation and the loss of plasma membrane integrity that leads to cell death (Y. N. Gong et al., 2017; Zargarian et al., 2017). Hence, other than the timepoints during which MLKL phosphorylation had been detected (4-8 hours), NHEK death was studied after longer stimulations (16-39 hours). No cell death was detected under any of these conditions. Even the deprivation from growth factors from the NHEK culture medium did not allow to detect potential HMGB1-induced necroptosis. This was difficult to understand, considering that MLKL phosphorylation upon HMGB1 treatment had been detected in NHEK cultured with growth factors. Given some of the difficulties and variability observed during the experimental procedure, one might hypothesise that further optimisation of the cell death protocols would be required to adequately detect HMGB1-induced necroptosis. Indeed, further work including the study of cell viability (WST-1) following HMGB1 treatment during shorter time periods (4-8 hours) and using NHEK cells at different stages of differentiation would possibly prove informative. However, a great number of experiments have been performed to study HMGB1-induced death, some of which have not been included in this report to avoid redundancy. HMGB1 failed to induce cell

death in all of these experiments, even when the experimental conditions proved high sensitivity of the assay.

A possible explanation for the absence of cell death in HMGB1-treated NHEKs could be supported by the recent description of several regulatory checkpoints of necroptosis downstream MLKL phosphorylation. These checkpoints include the oligomerisation and disengagement of ph-MLKL from the necrosome (Garnish et al., 2021), as well as trafficking via the Golgi/actin/microtubule trafficking machinery (Samson et al., 2020). These checkpoints can be targeted to prevent necroptosis and are thought to be highly regulated. For example, HSP-90 and HSP-70 positively regulate necroptosis by modulating the oligomerisation of MLKL, or by facilitating its accumulation at plasma membrane, respectively (Jacobsen et al., 2016; Johnston et al., 2020). Furthermore, oligomerised and phosphorylated MLKL can reach the plasma membrane but not conclude on cell death due to the externalisation of the pore forming structures in bubbles, mediated by the ESCRT-III machinery (Y. N. Gong et al., 2017). This machinery is responsible for the shedding of ph-MLKL-targeted plasma membrane, which leads to preserve cell survival (Y. N. Gong et al., 2017; Yoon et al., 2017). Part of this intricate regulation of necroptosis could be preventing ph-MLKL from inducing NHEK cell death upon HMGB1 treatment. This hypothesis is reinforced by the fact that HMGB1 induces the phosphorylation of MLKL in S358 and T357, which have been principally linked to the necroptotic cascade (Huayi Wang et al., 2014). A recent study has shown that Listeria infection-induced MLKL activation did not lead to its oligomerisation and translocation to the plasma membrane, hence preventing its permeabilization (Sai et al., 2019). To determine if similar conditions are induced by HMGB1 treatment of NHEK, analysis of MLKL expression under non-reducing conditions could be performed to detect its possible oligomerisation.

However, considering the lack of association between RIPK3 and MLKL upon HMGB1 treatment reported Chapter 3, it is also possible that HMGB1-induced ph-MLKL has a necroptosis-independent function in NHEKs. Since the discovery of MLKL as the main effector molecule of necroptotic cell death, extensive description of this role has been reported. However, several necroptosis-independent functions of MLKL have been described more recently. These include roles derived from the crosstalk, generally from synergistic relationships, between regulated necrotic processes (D'Cruz et al., 2018; Schreiber et al., 2017) and inflammasome activation (S. a. Conos et al., 2017; T.-B. Kang et al., 2013). Nevertheless, these ultimately lead to cell death through membrane permeabilization, which was not a consequence of HMGB1 treatment of NHEK. Furthermore, MLKL has been shown to translocate to the nucleus before necroptotic cell death (Yoon et al., 2017), where it can interact with RNA-binding motif proteins to promote the expression of adhesion molecules (J. Dai et al., 2020). Although noteworthy, roles for MLKL regulating gene expression have been linked to the non-phosphorylated form of MLKL.

Further studies have linked non-necroptotic functions of ph-MLKL with insulin resistance (H. Xu et al., 2019), fatty liver disease (X. Wu et al., 2020), demyelisation and multiple sclerosis (Ying et al., 2018; S. Zhang et al., 2019) as well as carcinoma events (Dong et al., 2019). Activated MLKL has also been recently shown to modulate autophagic flux (Frank et al., 2019; C. Zhan et al., 2021). Phosphorylated MLKL leads to attenuation of autophagic flux, following its translocation to intracellular membranes, in a RIPK3-dependent (Frank et al., 2019) and independent (X. Wu et al., 2020) manner. Inhibition of autophagy, however, is necroptosis-dependent, given that it occurs under necroptotic conditions. In contrast, CAMKII-dependent phosphorylation of MLKL in response to serum and

amino acid deprivation facilitates autophagic flux and is RIPK3-independent (Q. Zhan et al., 2021). These findings suggest that MLKL exerts opposite functions depending on how it is activated, which, in turn, depends on cell stimulus. Under nutrient-deprived conditions, CAMKII activates MLKL to support survival (Q. Zhan et al., 2021), while, under stress conditions such as necroptosis (Frank et al., 2019) or high-fat-induced endoplasmic reticulum stress (X. Wu et al., 2020), MLKL activation triggers necrosome formation and cell death.

Recent studies have demonstrated that terminal differentiation of keratinocyte cultures is accompanied by the targeted autophagic degradation of nuclear material (Akinduro et al., 2016), implying that degradative autophagy is involved in the physiological mechanisms of keratinocytes. Interestingly, extracellular HMGB1, through RAGE, has been shown to provide protection against keratinocyte UV-induced death, through promotion of autophagy (Mou et al., 2017). A role for HMGB1-induced ph-MLKL modulating autophagy and keratinocyte differentiation is possible. In conclusion, it must be highlighted that alternative mechanisms to necroptosis control MLKL function, probably in a stimulus-specific and cell type-specific manner, which are not fully understood yet and would need to be characterised in the future.

The data presented in this chapter confirms the susceptibility of NHEK to TSZ-induced necroptosis and describes three distinct experimental procedures in which it can be measured. These procedures were not able to detect changes in NHEK cell cytotoxicity or viability after HMGB1 stimulation, in spite of HMGB1 being able to induce MLKL phosphorylation. More studies are necessary to determine whether the downstream regulation of ph-MLKL could be preventing NHEK cell death or ph-MLKL plays necroptosis-independent functions in NHEKs *in vitro.*

Part II: In vivo role of DAMPs in necroptosis-dependent model of skin inflammation

Introduction and aims

The first necroptosis skin models were described in 2009 by Lee et al. and Kovalenko et al. These animals were obtained through epidermis specific Casp-8 knock-outs by crossing mice carrying floxed Casp-8 alleles and mice expressing Cre the under the keratin 14 (KRT-14) or keratin 5 (KRT5) promotors (Kovalenko et al., 2009; P. Lee et al., 2009, respectively). The resultant animals, Casp-8 epidermal knock-out (Casp-8^{EKO}) mice, display altered skin phenotype with flaky skin. Neither of these publications, however, identified necroptosis as the reason of the phenotype. It wasn't until 2011 that this link was made, when Bonnet et al. described that the deletion of RIPK3 achieved a complete rescue of the skin inflammatory phenotype caused by epidermal specific deletion of FADD, Casp-8 apoptotic adaptor protein. That same year, RIPK3 was shown to completely rescue the embryonic lethality of Casp-8 full body KO animals (Kaiser et al. 2011, Oberst al., 2011).

These findings confirmed previous knowledge from *in vitro* studies that Casp-8 plays an essential role in the transition between apoptosis and necroptosis. Furthermore, they are proof of necroptotic processes in the skin and described for the first time the necroptotic skin phenotype. Casp-8^{EKO} animals described by Lee et al. appeared slightly runted and with flaky skin by postnatal day 10 (P10). The observed epidermal thickness and keratinocyte proliferation linked the interaction of keratinocytes, fibroblasts and leukocytes to IL-1α, induced by a p38-MAPK-mediated regulation of NLRP3. Later studies refuted this theory and showed that phenotype severity and survival of $FADD^{EKO}$ or Casp-8^{EKO} animals was not affected by the deletion of IL-1β and IL-1R1, or IL-1α respectively (Bonnet et al., 2011; Kovalenko et al., 2009).

The Casp-8^{EKO} model described by Kovalenko et al. and the FADD^{EKO} model described by Bonnet et al. start showing cutaneous lesions at an early stage (P3) and have a more severe inflammatory phenotype than the one described by Lee et al. Kovalenko et al. and Bonnet et al. Both showed, in Casp-8^{EKO} and FADD^{EKO} models respectively, that TNF and TNFR-1 deletion from these animals strongly delayed, but not prevented, the inflammatory phenotype. However, while Kovalenko et al. suggested that skin disease was initiated in the suprabasal layer of the epidermis before birth, Bonnet et al showed that epidermal formation, proliferation or differentiation was not affected in FADD^{EKO} animals at the time of birth (P0). Furthermore, Kovalenko et. al. reported that MyD-88 or TRIF deletion did not affect the rate or extent of development of inflammation. In contrast, FADD^{EKO} *Myd-88*$^{-/-}$ animals showed a slight delay in skin lesion development compared to FADD^{EKO} mice, which suggested that activation of TLR signalling by DAMPs, along with other signalling, could be implicated in inducing skin inflammation. These papers provide the scientific insight and support for the evaluation of a necroptosis-dependent skin inflammation model.

The second part of this thesis explore the effect of two DAMPs, IL-33 and HMGB1, in necroptosis-dependent skin inflammation *in vivo.* This has been investigated through a genetic approach using the Casp-8^{EKO} skin necroptosis model. The potential role of IL-33 has been investigated by the deletion of IL-33 or its receptor ST2 (Chapter 5), while the effect of HMGB1 has been studied through the constitutive or epidermal keratinocyte-specific deletion of RAGE from Casp-8^{EKO} animals (Chapter 6). In total, five different mouse lines have been produced: Casp-8^{EKO}, Casp-8^{EKO} *Il-33*$^{-/-}$, Casp-8^{EKO} *St2*$^{-/-}$, Casp-8^{EKO} *Rage*$^{-/-}$ *and* Casp-8^{EKO} RAGE^{EKO}. Breeding to obtain the four double knock-out lines of interest is described in Chapter 2.6.2. All animals have been closely monitored in

order to investigate their skin inflammatory phenotype and compare it to Casp-8^{EKO} littermates. Overall, the aim was to determine what role these DAMPs play in the necroptotic skin inflammation by studying any changes in the Casp-8^{EKO} phenotype produced by the deletion of IL-33, ST2 and RAGE.

Chapter 5 and 6 aims:

V. Through cross breeding obtain and closely monitor the following animals: Casp-8^{EKO}, Casp-8^{EKO} *St2*$^{-/-}$, Casp-8^{EKO} *Il-33*$^{-/-}$, and control littermates (Chapter 5) or Casp-8^{EKO}, Casp-8^{EKO} *Rage*$^{-/-}$, Casp-8^{EKO} RAGE^{EKO}, and control littermates (Chapter 6). Identify possible skin lesions and determine the experimental endpoints of each line.

VI. Documentation, comparison, and analysis at different timepoints of the different skin inflammatory phenotypes macroscopically using a lesion score system (Chapter 2.81).

VII. Histological analysis of the skin samples to detect any changes between the different phenotypes and obtention of overall epidermal thickness measurements.

VIII. Analysis of epidermal proliferation (KRT-6, KRT-14), early and late differentiation markers (KRT-10 and LOR respectively) as well as stem cell markers (Ki-67) through immunostaining.

IX. Immunostaining of the skin samples collected for each line for necroptosis markers ph-MLKL and RIPK3, as well as the apoptosis marker, cleaved Casp-3.

X. Investigation of the immune cell infiltrate present in the skin lesions of the obtained lines by immunostaining the collected samples for T-cells (CD3), macrophages (F4-80) and granulocytes (Gr-1).

XI. Analysis of the presence necroptosis-associated cytokine TNF and the DAMP IL-33 in the skin of the different animals, aiming to detect any distinct changes caused by the deletion of IL-33, ST2 or RAGE

A brief characterisation of the Casp-8^{EKO} skin inflammation phenotype and skin histology can be found in Appendix III. This supplementary information aims to facilitate the reader's familiarisation with the Casp-8^{EKO} skin inflammation model, as well as report phenotypical differences observed in Casp-8^{EKO} animals during the development of the experiments.

Chapter 5

IL-33 and ST2 signalling in the Casp-8^{EKO} skin inflammation model

5.1 Background and aims

IL-33 is a tissue-derived cytokine of the IL-1 family, mostly expressed in endothelial and epithelial cells (Cayrol & Girard, 2018). It is normally stored in the nucleus but can be released upon cell injury or necrosis acting as a damage-associated molecular pattern (DAMP) or alarmin (N. T. Martin & Martin, 2016). It acts through binding to its receptor ST2 (Schmitz et al., 2005), a member of the IL-1R family, which belongs to the TIR superfamily. The major targets of IL-33 *in vivo* are tissue-resident immune cells such as ILC2s and mast cells, but also non-immune cells such as ST2-expressing endothelial or epithelial cells, fibroblasts, astrocytes and neurons. IL-33 plays important roles in tissue homeostasis through regulation of immune responses in allergic, fibrotic, infectious and chronic inflammatory diseases. Binding of IL-33 to its receptor ST2 has been described to shape both innate and adaptative immune responses (Cayrol & Girard, 2018).

IL-33 is constitutively expressed by epithelial cells, including murine keratinocytes (Sundnes et al., 2015). It has been reported to be implicated in skin inflammatory diseases such as AD as serum levels of IL-33 are elevated in some AD patients, and these levels correlate with disease severity (Dajnoki et al., 2016; Tamagawa-Mineoka et al., 2014). Furthermore, AD patients and mice with AD-like dermatitis have increased expression of IL-33 and ST2 levels in tissue (Savinko et al., 2012; Shimizu et al., 2005). Alterations of IL-33 serum levels in psoriatic patients, however, are controversial (Athari et al., 2016; Mitsui et al., 2016; Zeng et al., 2021). Intradermal injection of IL-33 can induce psoriasis-like dermatitis in mice and IL-33 or ST2 deficiency ameliorate the phenotype of the IMQ-induced psoriasiform model (Zeng et al., 2021). However, neither IL-33 nor ST2 knock-out had any effect in the well-stablished Calcipotriol-induced model of AD (Pietka et al., 2020).

Nevertheless, IL-33 is expressed during necroptosis-dependent skin inflammation. A dramatic increase in IL-33 mRNA level was found in the epidermis of Casp-8^{EKO} and FADD^{EKO} mice (Kovalenko et al., 2009; personal communication, Bonnet MC). IL-33 was also found to be highly expressed in the tissue of skin lesions found in Casp-8^{EKO} animals (Kovalenko et al., 2009). The aim of the work described in this chapter is to explore the role of this cytokine in Casp-8^{EKO} mice. In order to do so, Casp-8^{EKO} animals were crossed with *Il-33*$^{-/-}$ and *St2*$^{-/-}$ animals to obtain two double knock-out mouse lines: Casp-8^{EKO} *Il-33*$^{-/-}$ and Casp-8^{EKO} *St2*$^{-/-}$ animals. *Il-33*$^{-/-}$ and *St2*$^{-/-}$ mice have been described previously and are healthy and fertile (Hardman et al., 2013; Townsend et al., 2000, respectively). The animals generated from these crosses were carefully monitored, and their skin lesion development was scored both macroscopically and by immunohistochemistry (see section 2.8.1 and 2.9.3). Three different timepoints have been studied, for which skin

biopsies were collected. The expression of different epidermal proliferation and differentiation makers was analysed in the collected samples aiming to study how IL-33 signalling might affect the epidermal alterations observed in Casp-8^{EKO} mice. Furthermore, cell death markers were studied in the cutaneous lesions, including necroptotic markers RIPK3 and ph-MLKL and apoptotic marker cleaved Casp-3. The presence of immune cell infiltrate in lesions developed in each line was also investigated, together with the presence of other necroptosis-related cytokines such as TNF and IL-33.

5.2 Results

5.2.1 Casp-8^{EKO} *Il-33*$^{-/-}$ and Casp-8^{EKO} *St2*$^{-/-}$ animals show reduced number and severity of skin lesions

All Casp-8^{EKO} were macroscopically indistinguishable from their control littermates until around postnatal day 5 (P5). After this point, small, faint lesions could be observed in the skin of Casp-8^{EKO} animals (Figure 5.1A). Hence, P6 was established as the first timepoint to study the evolution of the phenotype. Casp-8^{EKO} *Il-33*$^{-/-}$ and Casp-8^{EKO} *St2*$^{-/-}$ pups at P6 showed very few or no lesions in their skin, as shown in Figure 5.1B and 6.1C. Contrary to most Casp-8^{EKO} pups at this age, which could easily be identified macroscopically due to the presence of lesions, double KO pups from both lines were almost undistinguishable from control littermates, making genotyping necessary identify them. This indicated that lesion development was delayed by the deletion of either IL-33 or ST2 from Casp-8^{EKO} animals. Not only were number of lesions reduced, but their severity and morphology also seemed distinct. Unlike the blister-looking lesions found in Casp-8^{EKO}, the few lesions that could be detected in the

skin of Casp-8^{EKO} *Il-33*$^{-/-}$ and Casp-8^{EKO} *St2*$^{-/-}$ pups were only less pigmentated patches of skin (see red arrows in Figure 5.1).

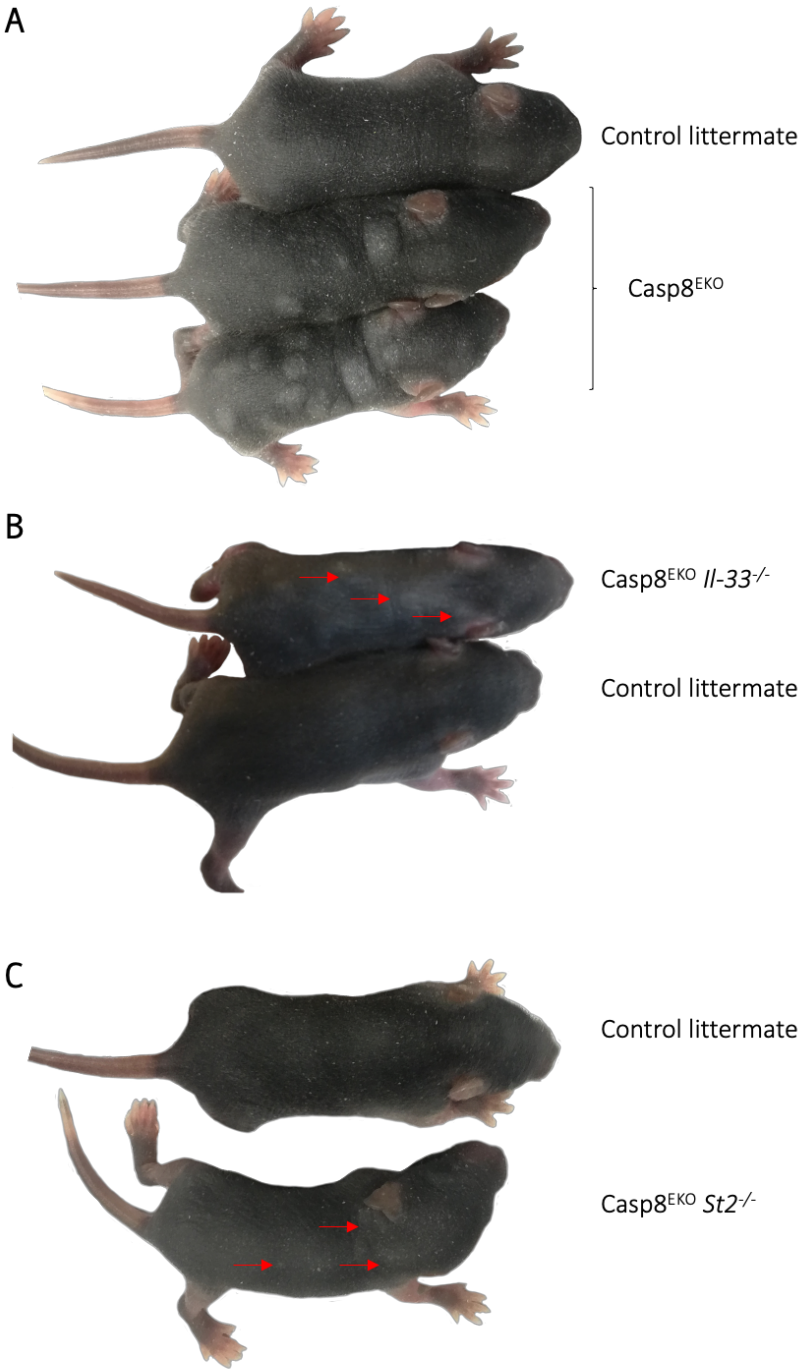

Figure 5.1: Phenotypes of Casp-8^{EKO}, Casp-8^{EKO} *Il-33*$^{-/-}$, Casp-8^{EKO} *St2*$^{-/-}$ mice and control littermates at P6. Representative images showing back area of **(A)** two Casp-8^{EKO} mice and a littermate control, **(B)** Casp-8^{EKO} *Il-33*$^{-/-}$ animal and a littermate control and **(C)** Casp-8^{EKO}*St2*$^{-/-}$ animal and a littermate control. Number of animals analysed: Casp-8^{EKO} *St2*$^{-/-}$ n=14; Casp-8^{EKO} *Il-33*$^{-/-}$ n=11; Casp-8^{EKO} n=10.

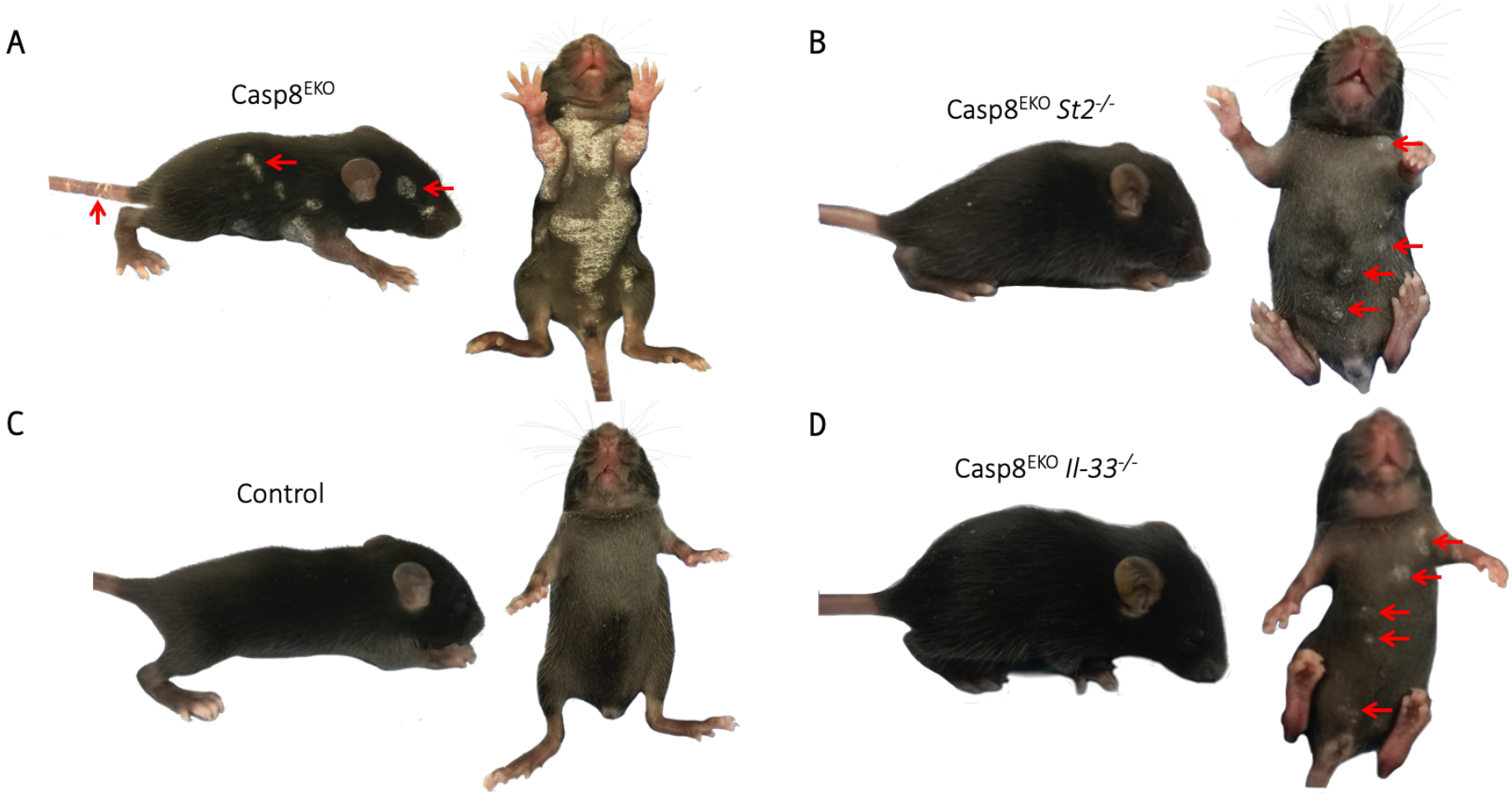

Figure 5.2: Phenotypes of Casp-8^{EKO}, Casp-8^{EKO} *Il-33*$^{-/-}$, Casp-8^{EKO} *St2*$^{-/-}$ mice and control littermates at P12. Representative images of lateral and abdominal areas of **(A)** Casp-8^{EKO}, **(B)** Casp-8^{EKO} *St2*$^{-/-}$, **(C)** Casp-8^{EKO} *Il-33*$^{-/-}$, and **(D)** littermate control animals. Red arrows point to small skin lesions found in these animals. Number of animals analysed: C8^{EKO} *St2*$^{-/-}$ n=21; C8^{EKO} *Il-33*$^{-/-}$ n=18; C8^{EKO} n=30.

Casp-8^{EKO} pups displayed extensive skin lesions before they reached two weeks of age, and most had to be culled shortly after postnatal day 12 (P12) as they were then about to reach their experimental endpoint (see section 2.7.2). P12 was therefore selected as the standard experimental endpoint, and thus the second timepoint used to study the phenotype. Lesions in Casp-8^{EKO} animals at this stage were distributed in patches across the skin and characterised by flaky skin and thickening of the epidermis that resulted in scally, slightly scabbed-looking lesions (Figure 5.2A). Hence, these animals were clearly identifiable due to the presence of large lesions covering both the back and abdominal areas (Figure 5.2A). In contrast, lesions in Casp-8^{EKO}*St2*$^{-/-}$ and Casp-8^{EKO} *Il-33*$^{-/-}$ animals were limited, and only a few were detectable in the abdominal area (Figure 5.1B and 6.1D).

As seen in Figure 5.3A (left graph), the scores of Casp-8^{EKO} *St2*$^{-/-}$ pups (mean: 0,57) and Casp-8^{EKO} *Il-33*$^{-/-}$ pups (mean: 1,09) at P6 were significantly different ($p<0,0001$) than Casp-8^{EKO} animals (mean: 2,4). The score of Casp-8^{EKO} *St2*$^{-/-}$ pups was not significantly different from the score of control littermates or Casp-8^{EKO} *Il-33*$^{-/-}$ animals. Casp-8^{EKO} *Il-33*$^{-/-}$ P6 pups' score, however, was significantly higher than control littermates ($p=0,0004$) (Figure 5.3A, left graph). Similarly, the score of both Casp-8^{EKO} *St2*$^{-/-}$ and Casp-8^{EKO} *Il-33*$^{-/-}$ animals at P12 was significantly lower ($p<0.0001$) than the score achieved by Casp-8^{EKO} littermates (Fig 6.3A, right graph). Again, at this timepoint, there was no significant difference between the double knock-out groups, but both Casp-8^{EKO} *St2*$^{-/-}$ and Casp-8^{EKO} *Il-33*$^{-/-}$ scores were now significantly higher from control littermates ($p=0,0048$ and $p=0,0002$ respectively). This data confirms that the deletion of either IL-33 or ST2 from Casp-8^{EKO} animals leads to a partial rescue of the inflammatory phenotype, evidenced by a reduced number and severity of lesions in the skin.

Regular monitoring of the animals between the two timepoints revealed that the skin inflammation phenotype in Casp-8^{EKO} *Il-33*$^{-/-}$ and Casp-8^{EKO}*St2*$^{-/-}$ animals developed at a slower rate than in Casp-8^{EKO} animals. Figure 5.3B shows a summary of the data presented in Figure 5.3A, organised by line. Statistical analysis shows that there were no significant changes in lesion scores between P6 and P12 timepoints for Casp-8^{EKO} *Il-33*$^{-/-}$ or Casp-8^{EKO} *St2*$^{-/-}$ animals but the lesion growth between this timepoints was significant for Casp-8^{EKO} mice (p=0.0001). These results indicate that, in addition to a delay in the appearance of the inflammatory phenotype, IL-33 and ST2 deletion leads to a slower development of given phenotype.

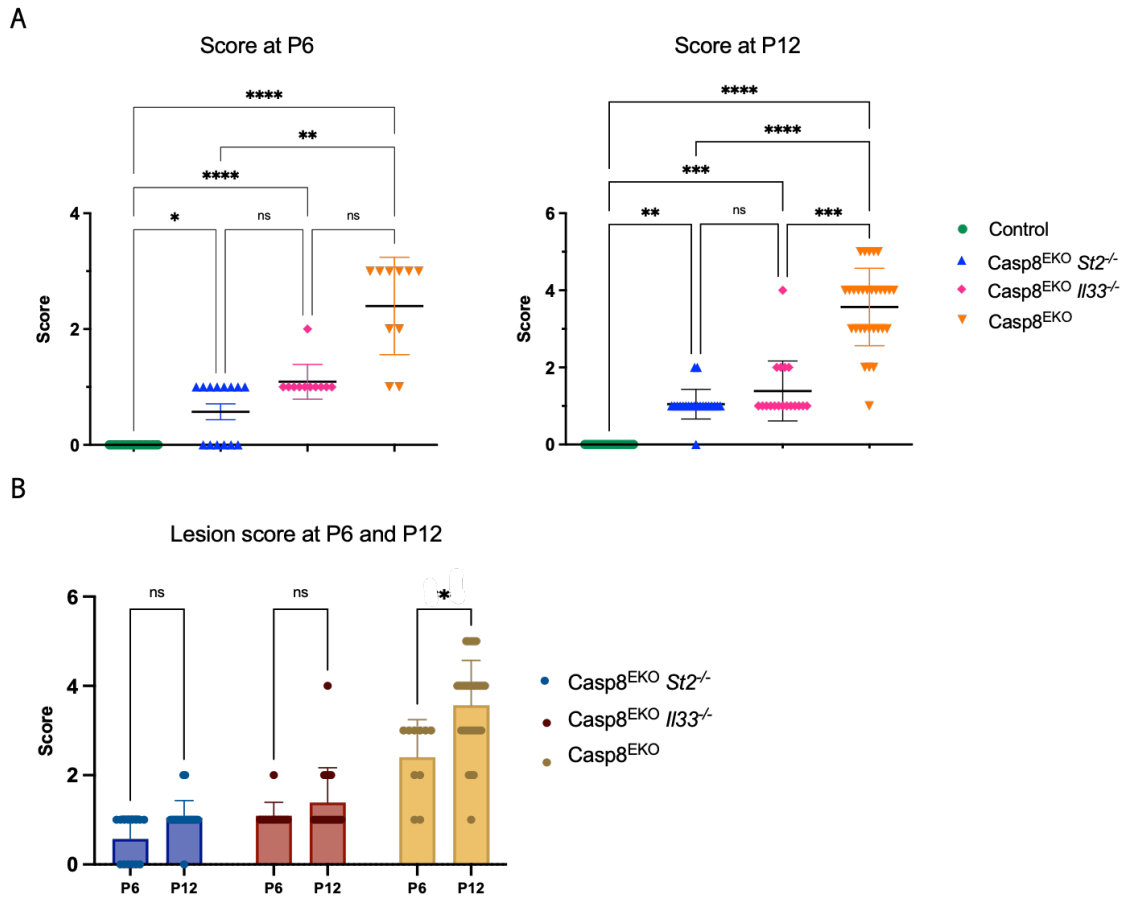

Figure 5.3: Lesion score of Casp-8^{EKO}, Casp-8^{EKO} *Il-33*$^{-/-}$, Casp-8^{EKO} *St2*$^{-/-}$ mice and control littermates at P6 and P12. Number and severity of skin lesions were assessed macroscopically through a scoring system (described in Chapter 2.8.1). Casp-8^{EKO}, Casp-8^{EKO} IL-33, Casp-8^{EKO} *St2*$^{-/-}$ and littermate control animals were assessed at

(A) P6, left panel and P12, right panel. **(B)** shows a summary of P6 and P12 data, organised by line. All graphs show individual values, mean ± SD. Statistical analysis used in **(A)** is Kruskal-Wallis test followed by Dunn's multiple comparison test. Left panel: ****p<0.0001, **p=0.0029, *p=0.0395; Right panel, ****p<0.0001, ***p=0.0004 (A-C), ***p=0.0005 (C-D), **p=0.0049. For **(B)**, multiple Kolmogorov-Smirnov tests were performed using Holm-Sídák's multiple comparison method, *p=0.016. Number of animals analysed: C8^{EKO} *St2*$^{-/-}$ P6 n=14, P12 n=21; C8^{EKO} *Il-33*$^{-/-}$ P6 n=11, P12 n=18; C8^{EKO} P6 n=10, P12 n=30.

5.2.2 Deletion of IL-33 or ST2 improves Casp-8^{EKO} survival

Unlike most Casp-8^{EKO} animals, which reached the maximum score by P12, most Casp-8^{EKO} *Il-33*$^{-/-}$ and Casp-8^{EKO} *St2*$^{-/-}$ animals reached young adulthood (over 6 weeks). Lesions start appearing in the back of the animals around weaning age (3 weeks), at which point they were housed individually. As animals grew older, lesions turned to a more chronic appearance as many evolved into hardened scab-looking patches compared to the scaly skin lesions observed in younger animals. Patches of alopecia were also commonly found affecting the animals' body. Since deletion of IL-33 or ST2 from Casp-8^{EKO} mice allowed animals to survive to young adulthood, a third timepoint was established to study their phenotype at P60 (8-9 weeks). Figure 5.4A and B show representative images of Casp-8^{EKO} *Il-33*$^{-/-}$ and Casp-8^{EKO} *St2*$^{-/-}$ animals at 8 weeks of age, respectively.

Amelioration of the inflammatory phenotype led to a significant increase in the survival of Casp-8^{EKO} *St2*$^{-/-}$ (p=0.005) and Casp-8^{EKO} *Il-33*$^{-/-}$ animals (p<0.0001) compared to Casp-8^{EKO} animals (Fig 6.4C). No differences in animal survival were observed between male and female Casp-8^{EKO} *St2*$^{-/-}$ mice (Figure 5.4E, upper panel). Casp-8^{EKO} *Il-33*$^{-/-}$ and Casp-8^{EKO} *St2*$^{-/-}$ adults were the same size as littermate controls (Figure 5.4A), their weight was always maintained in healthy levels for their age (Figure 5.4E, lower panel), and males were able to breed normally. This

data confirms that, even though the inflammatory phenotype continues developing in adults, the deletion of either IL-33 or ST2 had a significant impact on animal survival.

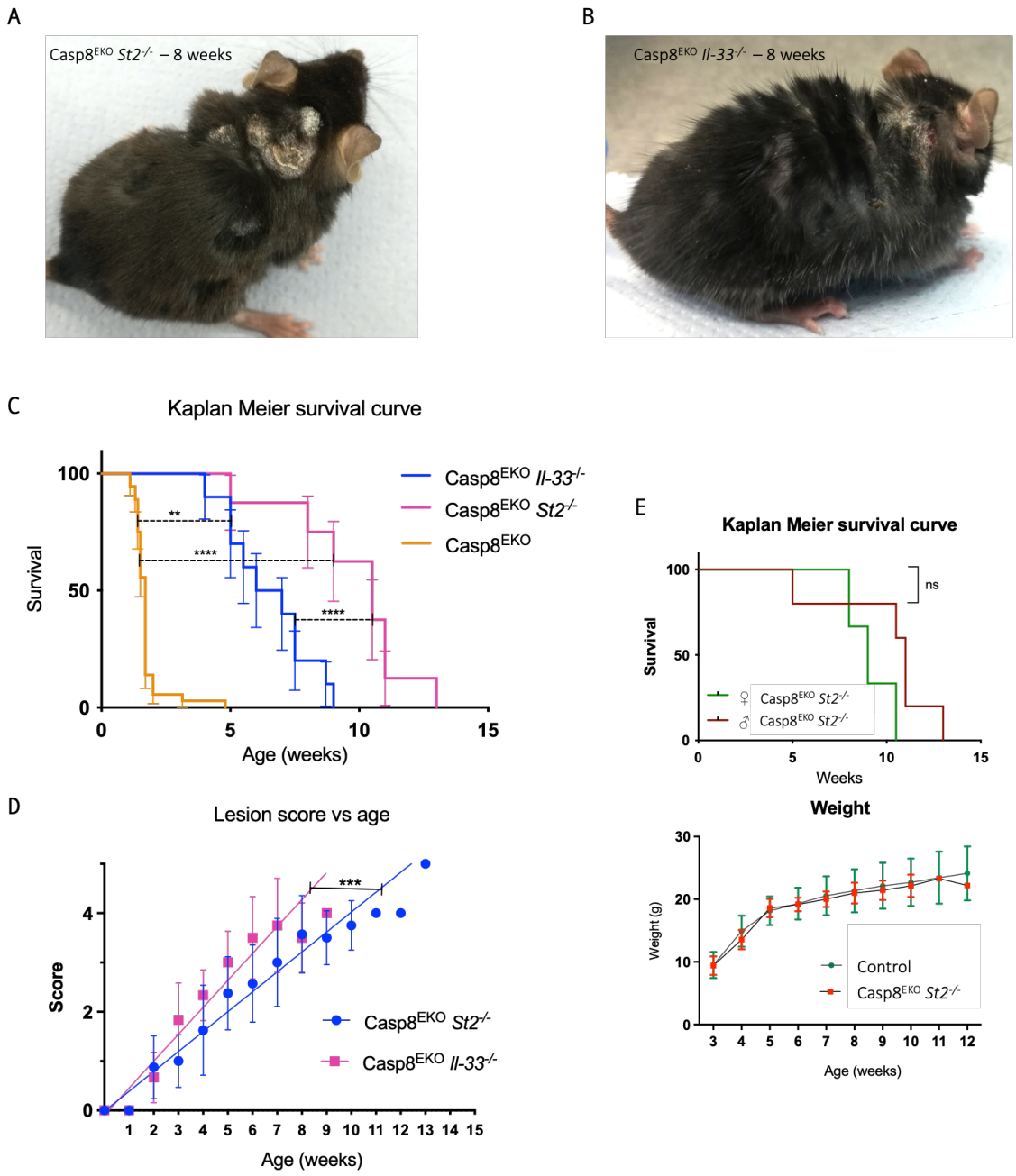

Figure 5.4: Lesion score and survival of Casp-8^{EKO} *Il-33*$^{-/-}$ and Casp-8^{EKO} *St2*$^{-/-}$ skin during adulthood. Images of 8-weeks-old **(A)** Casp-8^{EKO} *St2*$^{-/-}$ and **(B)** Casp-8^{EKO} *Il-33*$^{-/-}$ animals with clear lesions in neck and back. **(C)** Kaplan Meier survival curve of Casp-8^{EKO}, Casp-8^{EKO} *Il-33*$^{-/-}$ and Casp-8^{EKO} *St2*$^{-/-}$ animals. Error bars represent SD. Number of animals analysed: Casp-8^{EKO} *Il-33*$^{-/-}$ n=10, Casp-8^{EKO} *St2*$^{-/-}$ n=8, Casp-8^{EKO} n=26. **(D)** Lesion score evolution of Casp-8^{EKO} *Il-33*$^{-/-}$ (n=7) and Casp-8^{EKO} *St2*$^{-/-}$ (n=8) animals over time (weeks). Each point represents the mean score

for that age ± SD. Each set of data was fit with a simple linear regression line. Simple linear regression comparison was performed using Graphpad, **p=0.0009. **(E)** Upper panel, Kaplan Meier survival curve of Casp-8^{EKO} *St2*$^{-/-}$ males (red, n=5) and females (green, n=4). Lower panel, weight of Casp-8^{EKO} *St2*$^{-/-}$ animals (red) and stablished average weight for C57BL/6N mice (green) (The Jackson Laboratory). Animals analysed: Casp-8^{EKO} *St2*$^{-/-}$ n=6. Each point represents the mean weight for that age ± SD. Statistical analysis for Kaplan Meier curve comparison (panels C and E) was the Gehan-Breslow- Wilcoxon test.

The difference in survival between Casp-8^{EKO} *Il-33*$^{-/-}$ and Casp-8^{EKO} *St2*$^{-/-}$ mice, however, was also significant (p=0.014) (Figure 5.4C). The median survival for Casp-8^{EKO} *Il-33*$^{-/-}$ animals was 7 weeks whereas for Casp-8^{EKO} *St2*$^{-/-}$ animals this rose to 10.5 weeks. A mild difference in the inflammatory phenotype between the two double knock-out groups was noticeable at an earlier age, but this was not significant (Figure 5.3B and 6.3C). As animals grew older, this difference becames more obvious. The average lesion score of double knock-out animals was determined every week and is shown in Figure 5.4D. This analysis revealed that, although the severity of the phenotype at early stages was very similar for both double knock-out lines, lesions in Casp-8^{EKO} *Il-33*$^{-/-}$ animals developed at a faster rate than in Casp-8^{EKO} *St2*$^{-/-}$ animals. This change in the lesion development was found to be significant when comparing the slopes of the simple linear regression models. This data shows that Casp-8^{EKO} *Il-33*$^{-/-}$ adults were significantly more affected by the inflammatory phenotype than Casp-8^{EKO} *St2*$^{-/-}$ adults, exhibiting for the first time a significant difference between the double knock-out groups.

5.2.3 Histological analysis of skin samples

When animals were assessed macroscopically, it was observed that the abdominal area was significantly more affected by lesions than the back area (Figure 5.2). The overall score of each animal, based on the total body surface affected by lesions, considered the totality of the animal skin (see section 2.8.1). Skin sections were collected from the back-neck and

abdominal areas of animals at either P6 or P12, independently of the presence or absence of lesions in this area. As showed previously (Figure 5.1 and 6.2), animals were only partially covered by lesions, creating some variability within the samples collected. To verify if samples were consistent with the macroscopical observations (overall animal score) and therefore representative of the phenotype, the number and extensity of lesions in skin samples collected at P12 from Casp-8^{EKO} and Casp-8^{EKO} *St2*$^{-/-}$ animals were quantified. Skin samples were stained with haematoxylin and eosin and analysed to calculate the percentage area of sample affected by lesions, attending to epidermal thickening and dermal cell infiltration (see section 2.9.3). Indeed, as observed macroscopically, this quantification showed that samples collected from the abdominal area were more affected by lesions than those collected from the back area of the animals (Figure 5.5A). In addition, the quantification revealed a higher variability in the extent of lesions when samples were collected from the abdominal area compared to samples compared from the back area (Figure 5.5A).

Next, the phenotypical score of each individual animal at the time of sample collection (Y axis) was compared to the lesional percentage calculated for that collected sample (X axis). This comparison was performed for samples collected both from back and abdominal areas (Figure 5.5B and C respectively). The analysis revealed that samples obtained from the back area of animals with lower macroscopical scores also had lower number of lesions per sample, while higher phenotype scores are linked to higher percentages of lesions per sample (Figure 5.5B, left panel). Samples collected from the abdominal areas of the animal, however, showed less consistency between the macroscopic score and the percentage of sample affected by lesions, as sections from animals with low score had high percentages of lesions per sample (Figure 5.5B, right

panel). This meant that the samples collected from the back area of both Casp-8^{EKO} and Casp-8^{EKO} *St2*$^{-/-}$ animals were more representative of the direct lesion observations than those collected from the abdominal area of these animals. Consequently, it was decided that, in order to maintain the accuracy of further studies, only samples collected from the back area would be used for histological analysis. This was applied to all other mouse lines in this and the following chapter.

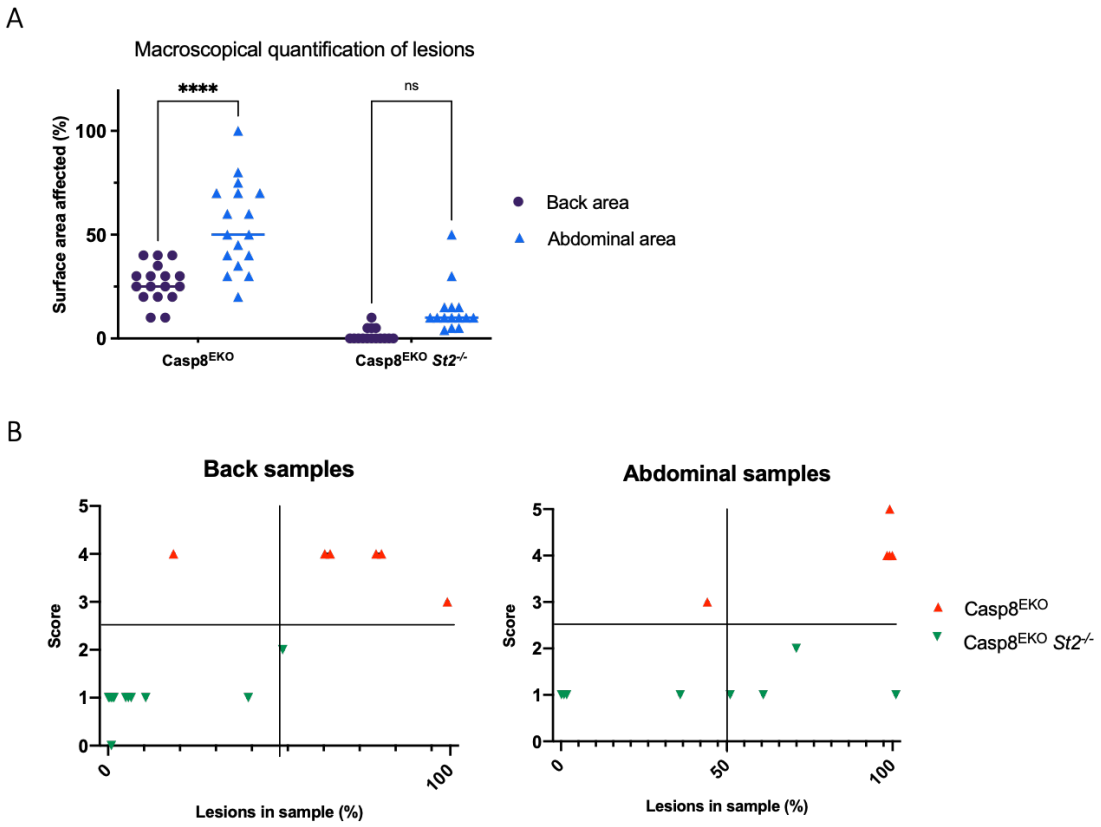

Figure 5.5: Analysis of the phenotype representativeness of the samples collected from the back and abdominal area of the animals. (A) Quantification of the percentage of skin sample affected by lesions (hyperplasia) of Casp-8^{EKO}, Casp-8^{EKO} *Il-33*$^{-/-}$ or Casp-8^{EKO} *St2*$^{-/-}$ animals collected from back and abdominal areas. Each point represents an individual animal and bars show mean ± SD. The statistical analysis performed is two-way ANOVA followed by Sidák's multiple comparisons test, ****p<0.0001. Number of animals analysed: Casp-8^{EKO} n=17; Casp-8^{EKO} *St2*$^{-/-}$ n=15. **(B)** Graphs representing the phenotypical score (Y axis) versus the total sample area affected by lesions (%). Left panel shows data from skin sections collected from the back area; right panel represents abdominal sections. Each point represents an individual animal. Number of animals analysed: : Casp-8^{EKO} back n=6, abdominal n=6; Casp-8^{EKO} *St2*$^{-/-}$ back n=12, abdominal n=8.

Histological analysis, through H&E staining of skin samples collected from 6-day-old Casp-8^{EKO}, Casp-8^{EKO} *Il-33*$^{-/-}$ and Casp-8^{EKO} *St2*$^{-/-}$ animals, showed mostly normal-looking skin, identical to that collected from control littermates (Figure 5.6A, upper panel). Similar to what was observed macroscopically, only a few lesions in Casp-8^{EKO} samples were noticeable, although these were not enough to significantly increase the overall epidermal thickness of the animals when compared to control littermate controls (Figure 5.6B, left panel). In fact, as shown in Figure 5.6B (left graph), there were no significant differences in the epidermal thickness between any of the different groups, showing that even though lesions could be detected in the samples, these did not contribute to increase epidermal thickness significantly. Indeed, when the extent of the lesions affecting each sample was assessed, it was found that, on average, only 20% of the total sample collected from P6 Casp-8^{EKO} animals was affected by lesions, compared to 7.5 and 7.6% of P6 Casp-8^{EKO} *Il-33*$^{-/-}$ and Casp-8^{EKO} *St2*$^{-/-}$ respectively (Figure 5.6C. right panel).

Histological analysis of Casp-8^{EKO} skin samples collected at P12 revealed the presence extensive lesions, while skin was mostly non-lesional in Casp-8^{EKO} *Il-33*$^{-/-}$ and Casp-8^{EKO} *St2*$^{-/-}$ samples (Figure 5.6A, lower panel). Consequently, the overall epidermal thickness of Casp-8^{EKO} animals was significantly higher than control littermates ($p<0,0001$), but also Casp-8^{EKO} *Il-33*$^{-/-}$ ($p=0.0009$) and Casp-8^{EKO} *St2*$^{-/-}$ animals ($p<0.0001$) (Figure 5.6B). At this stage, inflammatory patches in Casp-8^{EKO} *Il-33*$^{-/-}$ and Casp-8^{EKO} *St2*$^{-/-}$ samples were more common and extensive, but this did not translate to a significant difference between epidermal thickness of control littermates and the two double knock-out groups (Figure 5.6B). The same observation could be made when the percentage of lesions per sample was quantified for each line (Figure 5.6C, right panel). When looking at this data organised by line (Figure 5.6C, left panel),

it is confirmed that Casp-8^{EKO}, but not Casp-8^{EKO} *Il-33*$^{-/-}$ or Casp-8^{EKO} *St2*$^{-/-}$ samples show significant increase in the number of lesions between the two timepoints (P6 and P12), indicating a faster development rate of the inflammatory phenotype. Lesions found in Casp-8^{EKO} *Il-33*$^{-/-}$ and Casp-8^{EKO} *St2*$^{-/-}$skin at P12 had similar histological characteristics than those found in Casp-8^{EKO} skin. As previously reported in the literature, and described in Appendix III, histological characteristics included acanthosis, loss of granular layer (hypogranulosis) and hyperkeratosis with retained nuclei in the cornified layer (parakeratosis), a sign of delayed keratinocyte terminal differentiation or cornification (Figure 5.6A).

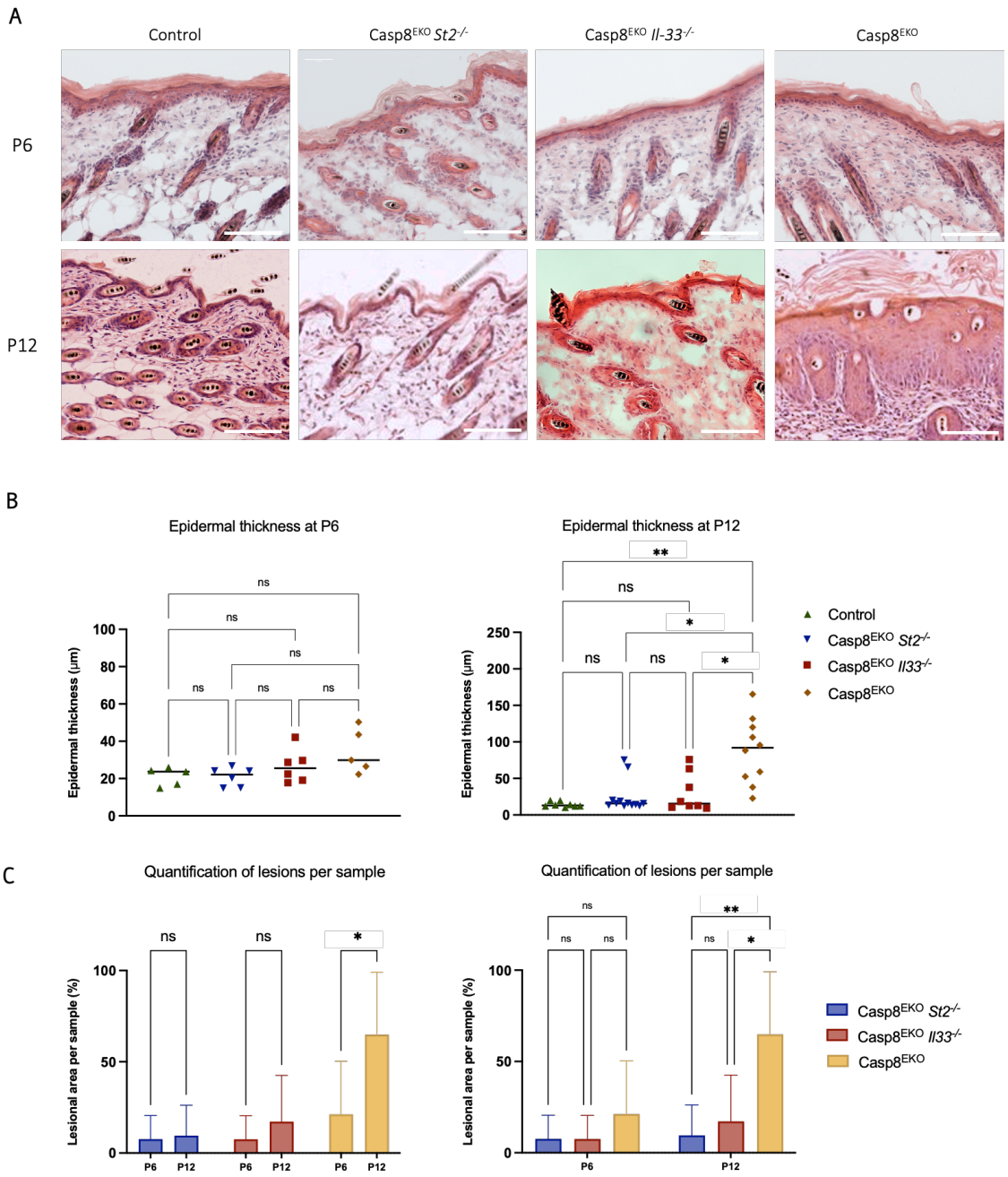

Figure 5.6: Skin histology and quantification of epidermal thickness and lesion evolution of Casp-8^{EKO}, Casp-8^{EKO} *Il-33*$^{-/-}$, Casp-8^{EKO} *St2*$^{-/-}$ and control littermates skin samples. (A) Representative images of skin histology from Casp-8^{EKO}, Casp-8^{EKO} *Il-33*$^{-/-}$ and Casp-8^{EKO} *St2*$^{-/-}$ and control littermates. Skin samples collected at P6 (upper panel) and P12 (lower panel) from were fixed and stained for haematoxylin and eosin. Images obtained using Zeiss Apotome Axio Observer microscope, magnification 40X. Scale bar represents 50 µm. **(B)** Epidermal thickness quantification of samples collected from Casp-8^{EKO}, Casp-8^{EKO} *Il-33*$^{-/-}$ and Casp-8^{EKO} *St2*$^{-/-}$ and control littermates at P6 (left) and P12 (right). Graph shows individual values and their mean. The statistical analysis performed was Kruskal-Wallis test followed by Dunn's multiple comparisons test. *p=0.0142 (B-D), *p=0.0163 (C-D), ***p=0.0004. **(C)** Histological quantification of lesions found in skin sections collected from Casp-

8^{EKO}, Casp-8^{EKO} *Il-33*$^{-/-}$ and Casp-8^{EKO} *St2*$^{-/-}$ animals at P6 and P12. Values are expressed as mean ± SD. Left panel organises data per line; multiple Mann-Whitney tests were performed for statistical analysis using the Holm-Sídák method. *p=0.013. Right panel organises data by timepoint; statistical analysis performed was Kruskal-Wallis test followed by Dunn's multiple comparison test, **p=0.0011, *p=0.014. Number of animals analysed for (B) and (C): Casp-8^{EKO} P6 n=6, P12 n=12; Casp-8^{EKO} *Il-33*$^{-/-}$ P6 n=7, P12 n=9; Casp-8^{EKO} *St2*$^{-/-}$ P6 n=6, P12 n=12; Control P6 n=5, P12 n=8.

Histological analysis of skin samples collected from adult mice (P60) showed skin was almost completely covered by lesions, characterised by epidermal hyperplasia, parakeratosis and marked hyperkeratosis (Figure 5.7A and B). The increased proliferation of the epidermal layers and thickening of the cornified layer, which coincides with the scabby lesions observed macroscopically, led to the formation of numerous small epidermoid or inclusion cysts. Figure 8B shows an example of how the cornified layer goes through the epidermis (red arrow labelled 1) creating small compartments (red arrows labelled 2) that eventually detach from the epidermis (yellow arrow). These structures, containing all the epidermal layers, can then be found in the dermis (red arrows labelled 3).

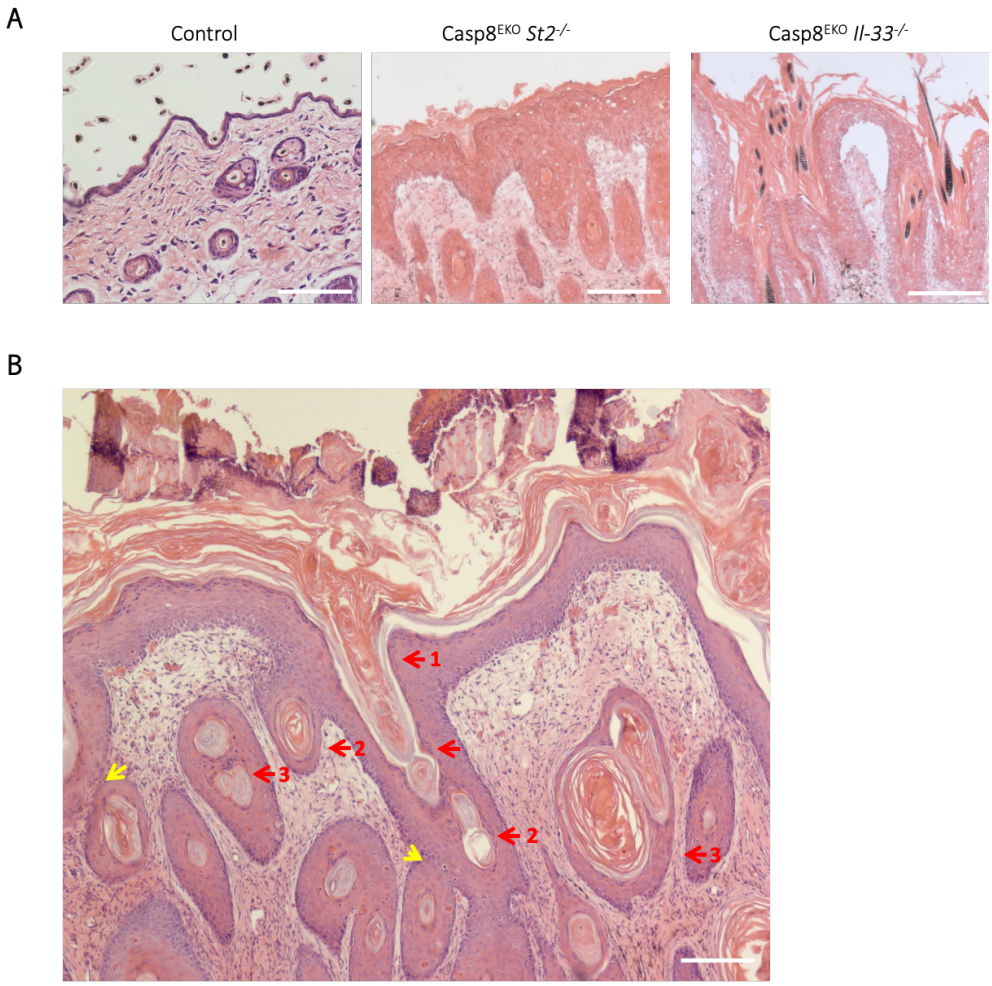

Figure 5.7: Histological analysis of lesional areas found in Casp-8^{EKO} *Il-33*$^{-/-}$, Casp-8^{EKO} *St2*$^{-/-}$ and control littermates young adult skin samples. Skin samples collected from adult Casp-8^{EKO} *Il-33*$^{-/-}$, Casp-8^{EKO} *St2*$^{-/-}$ and control littermates were fixed and stained with haematoxylin and eosin. **(A)** shows representative images of each line. Scale bars represent 50 μm **(B)** shows a representation of epidermoid cyst formation found in some 9-week-old Casp-8^{EKO} *St2*$^{-/-}$ animals due to hyperproliferation. Images shows a representation of this process. Outer layers of the epidermis travel inside (red arrow 1) creating cysts that contain all epidermal layers (red arrow 2). These eventually break free from the epidermis and can be found in the dermis. Scale bar represents 25 μm. Images obtained using Zeiss Apotome Axio Observer microscope, (A) magnification 40X, (B) magnification 5X.

5.2.4 Immunohistological analysis of proliferation and differentiation markers in the skin

Different subtypes of keratins are expressed specifically in the distinct epidermal layers (see Figure 1.9) and are commonly used as epidermal proliferation and differentiation markers including for skin diseases diagnostics. The following figures (Figures 6.8-12) show representative images of Casp-8^{EKO}, Casp-8^{EKO} *Il-33*$^{-/-}$ and Casp-8^{EKO} *St2*$^{-/-}$ skin at P6 (non-lesional) and at P60 (lesional). At the P12 timepoint, both non-lesional and lesional have been included, in order to facilitate lesion-to-lesion comparison of the different markers. However, it is important to highlight that the skin of Casp-8^{EKO} *Il-33*$^{-/-}$ and Casp-8^{EKO} *St2*$^{-/-}$ at P12 is mainly non-lesional, while the lesional images chosen correspond to sporadic lesions found in the skin of these animals.

Keratin 6 (KRT-6) is an epidermal stem cell marker and its expression in normal mice skin is restricted to hair follicles epidermal stem cells. This pattern was found in skin collected from control littermates, as well as non-hyperplastic skin patches found in Casp-8^{EKO}, Casp-8^{EKO} *Il-33*$^{-/-}$ and Casp-8^{EKO} *St2*$^{-/-}$ both at P6 and P12 (Figure 5.8A). KRT-6 was very strongly expressed by epidermal keratinocytes throughout lesions found in Casp-8^{EKO}, Casp-8^{EKO} *Il-33*$^{-/-}$ and Casp-8^{EKO} *St2*$^{-/-}$ skin at P12, a characteristic feature of an ongoing repair process in the epidermis. This increased expression of KRT-6 was maintained in time, as it was observed throughout the lesions found in adult skin of both lesion-presenting animals (P60).

KRT-14 is a marker of basal proliferating keratinocytes and, therefore, a hallmark of basal keratinocytes. Control and non-lesional skin found in Casp-8^{EKO}, Casp-8^{EKO} *Il-33*$^{-/-}$ and Casp-8^{EKO} *St2*$^{-/-}$ at P6 and P12 show KRT-14 expression in hair follicles and the basal layer of the epidermis

(Figure 5.8B). KRT-14, however, was highly expressed throughout hyperplastic epidermal areas at P12. Similarly, the expression of proliferation marker Ki-67, was highly increased in lesional areas found in Casp-8^{EKO}, Casp-8^{EKO} *Il-33*$^{-/-}$ and Casp-8^{EKO} *St2*$^{-/-}$ at P12 (Figure 5.8C). Positive Ki-67 cells could be found covering the basal layer of hyperplastic areas as well as in some areas of suprabasal layers making evident an abnormal proliferation of keratinocytes. Samples collected at P60 from Casp-8^{EKO} *Il-33*$^{-/-}$ and Casp-8^{EKO} *St2*$^{-/-}$ animals showed a similar KRT-14 and Ki-67 pattern indicating that cell proliferation is still remarkably active in adult skin lesions.

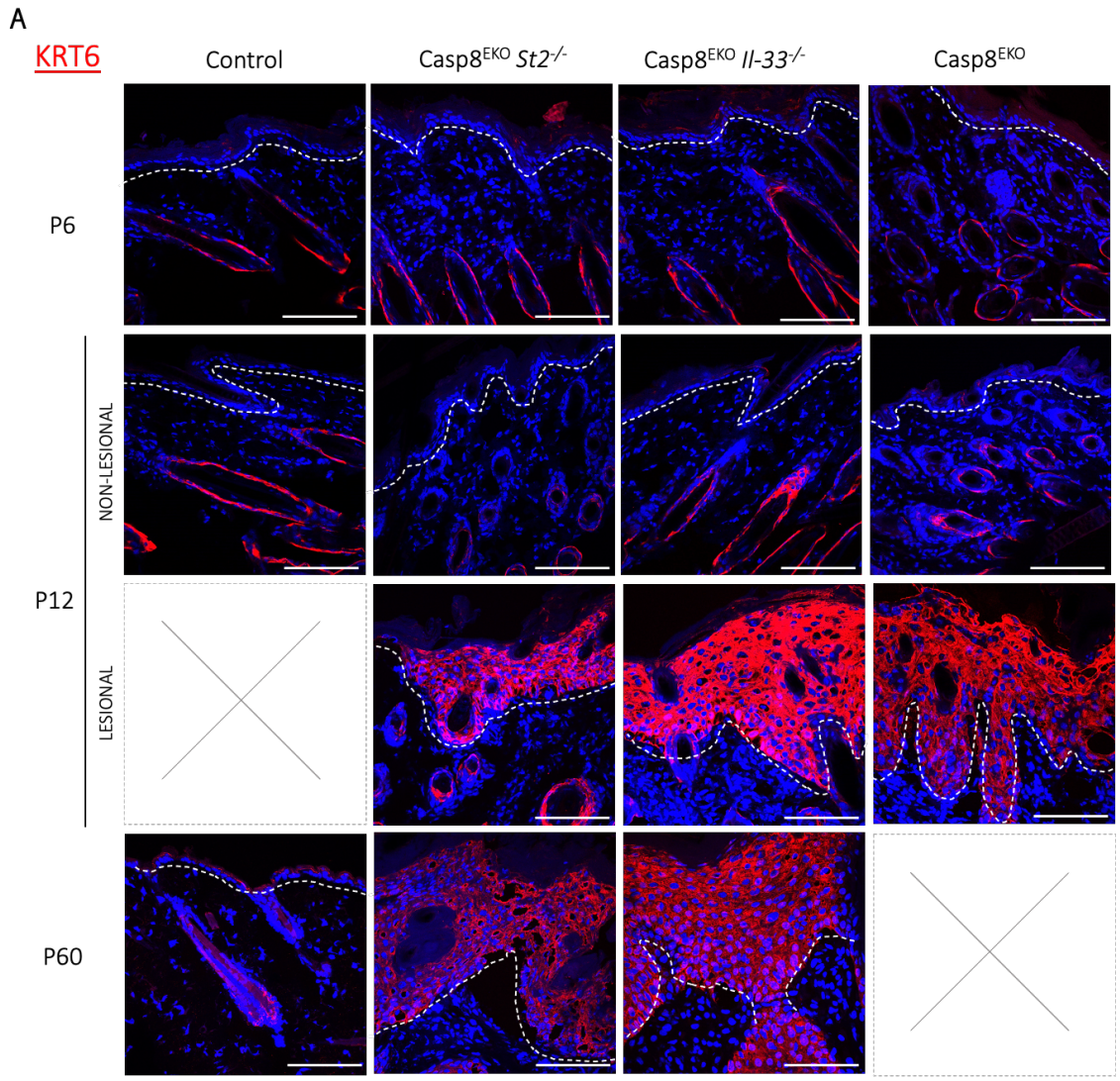

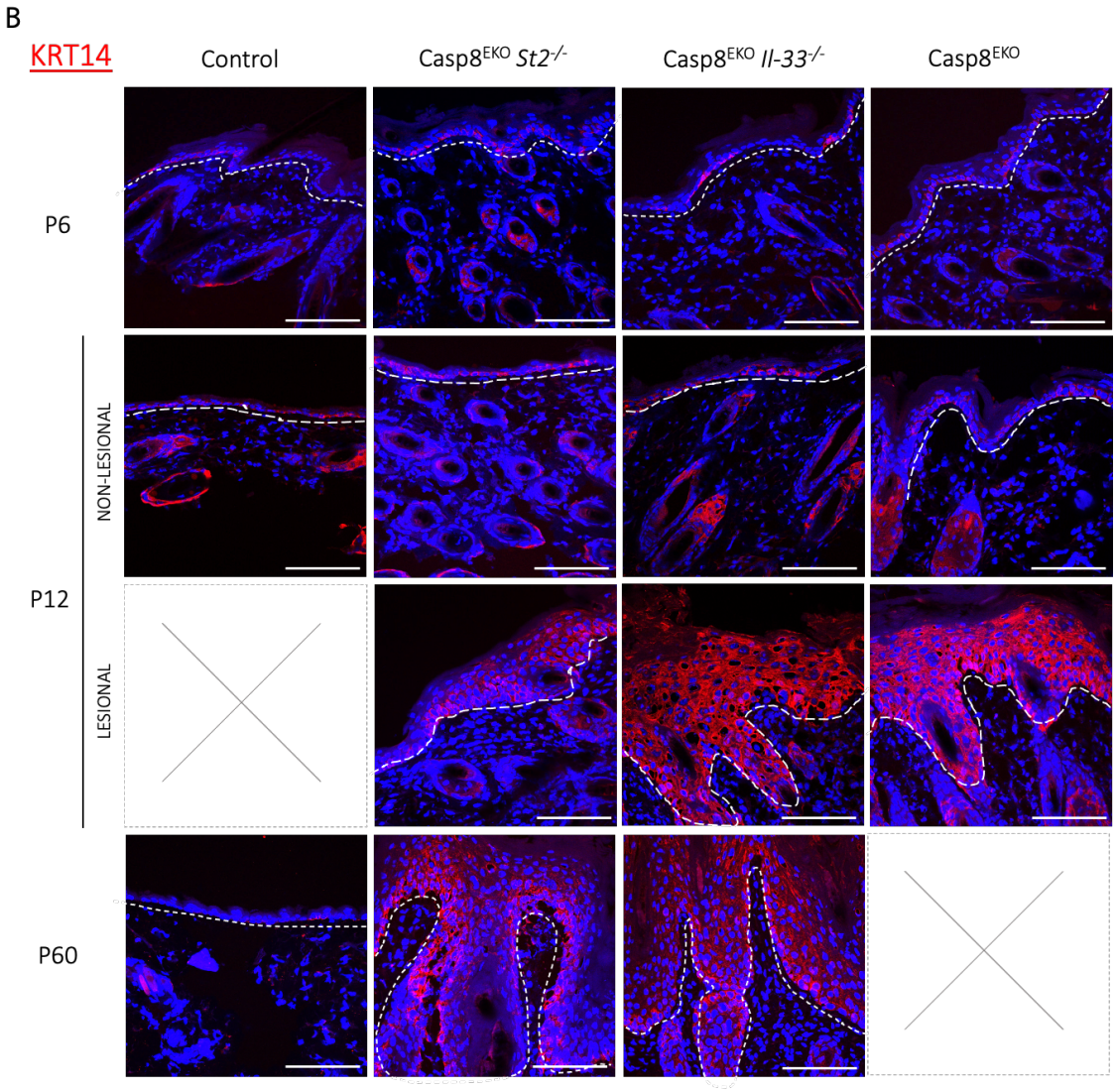
B
KRT14
Control
Casp8EKO St2-/-
Casp8EKO Il-33-/-
Casp8EKO
P6
P12
NON-LESIONAL
LESIONAL
P60

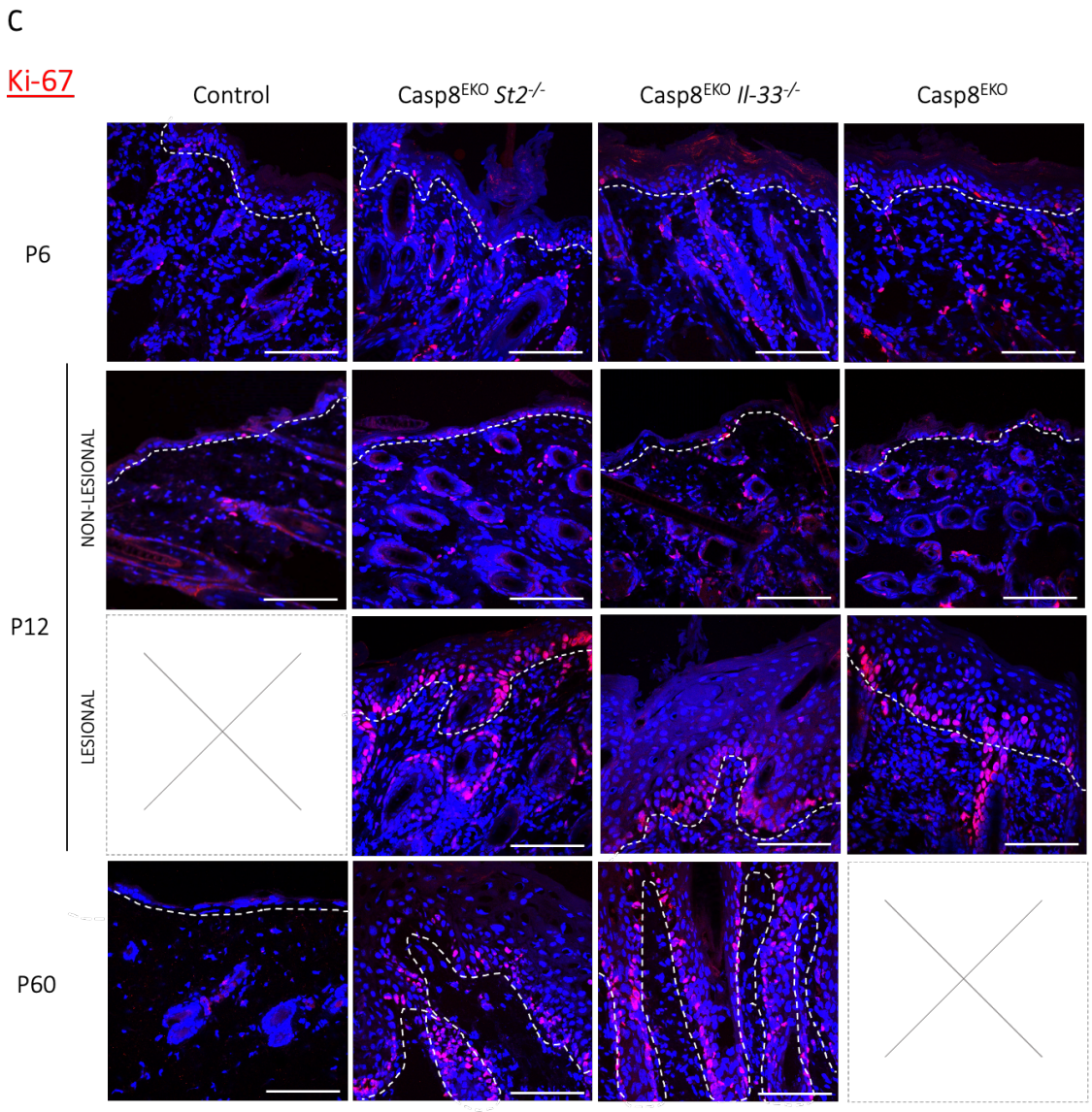

Figure 5.8: Immunohistological analysis of proliferation and differentiation markers in Casp-8^{EKO}, Casp-8^{EKO} *Il-33*$^{-/-}$ and Casp-8^{EKO} *St2*$^{-/-}$ skin samples. Skin samples were collected at different timepoints (P6, P12 and P60) from Casp-8^{EKO}, Casp-8^{EKO} *Il-33*$^{-/-}$, Casp-8^{EKO} *St2*$^{-/-}$ and control littermates. Sections were fixed and immunostained (red) for **(A)** stem cell marker KRT-6, **(B)** KRT-14 and **(C)** proliferation marker Ki-67. Nuclei were stained with DAPI (blue). To facilitate lesion to lesion comparison with Casp8^{EKO} skin, sporadic lesional areas found in Casp-8^{EKO} *Il-33*$^{-/-}$ and Casp-8^{EKO} *St2*$^{-/-}$ skin at P12 are shown but are not representative of the phenotypes. Images were obtained using Zeiss LSM 880 scanning confocal microscope using a Z-stack function at magnification 63X. Scale bar represents 50 µm. Mice analysed for each genotype: KRT-6: C8^{EKO} P6 n= 4, P12 n=5; C8^{EKO} *Il-33*$^{-/-}$ P6 n=5, P12 n=4, P60 n=5; C8^{EKO} *St2*$^{-/-}$ P6 n=6, P12 n=5, P60 n=6; Control P6 n=3, P12 n=2, P60 n=6. KRT-14: C8^{EKO} P6 n=5, P12 n=8; C8^{EKO} *Il-33*$^{-/-}$ P6 n=7, P12 n=5, P60 n=5; C8^{EKO} *St2*$^{-/-}$ P6 n= 5, P12 n=4, P60 n=6; Control P6 n=3, P12 n=3, P60 n=2. Ki-67: C8^{EKO} P6 n=5, P12 n=8; C8^{EKO} *Il-33*$^{-/-}$ P6 n=7, P12 n=5, P60 n=5;

C8^{EKO}
St2$^{-/-}$ P6 n= 5, P12 n=4, P60 n=6; Control P6 n=3, P12 n=3, P60 n=3.

Next, the differentiation state of the keratinocytes was assessed through immunostaining of KRT-10 and Loricrin (LOR). During the cornification process, keratinocytes move from the single epidermal basal layer upward to the suprabasal layer, where they express KRT-10. Hence, the expression of KRT-10 reflects an early differentiation stage of keratinocytes. As keratinocytes in the spinous layer differentiate further, they move to the granular layer and express late differentiation markers such as LOR.

As expected, KRT-10 and LOR were expressed in the spinous and granular layers, respectively, in control skin as well as non-hyperplastic skin from Casp-8^{EKO}, Casp-8^{EKO} *Il-33*$^{-/-}$ and Casp-8^{EKO} *St2*$^{-/-}$ animals (Figure 5.9A and 6.9B). KRT-10 was almost completely lost in P6 and P12 Casp-8^{EKO} lesions. Casp-8^{EKO} *Il-33*$^{-/-}$ and Casp-8^{EKO} *St2*$^{-/-}$ skin, however, showed patched but strong KRT-10 staining throughout the lesion. Similarly, the expression of LOR was completely lost in hyperplastic areas in Casp-8^{EKO} skin but was noticeable in lesions found in Casp-8^{EKO} *Il-33*$^{-/-}$ and Casp-8^{EKO} *St2*$^{-/-}$ both at P6 and P12 (Figure 5.9B). Interestingly, KRT-10 expression at P60 was partially restored in the suprabasal layers, and the LOR staining was almost entirely restricted to the cornified layer, its normal localisation (Figure 5.9B), indicating less alteration of the differentiation pattern. Both skin markers were also present in the epidermoid cysts found along the dermis, as they are formed directly from epidermal structures. This data shows that the keratinocyte differentiation process is less affected following the deletion of IL-33 or ST2 from Casp-8^{EKO} animals.

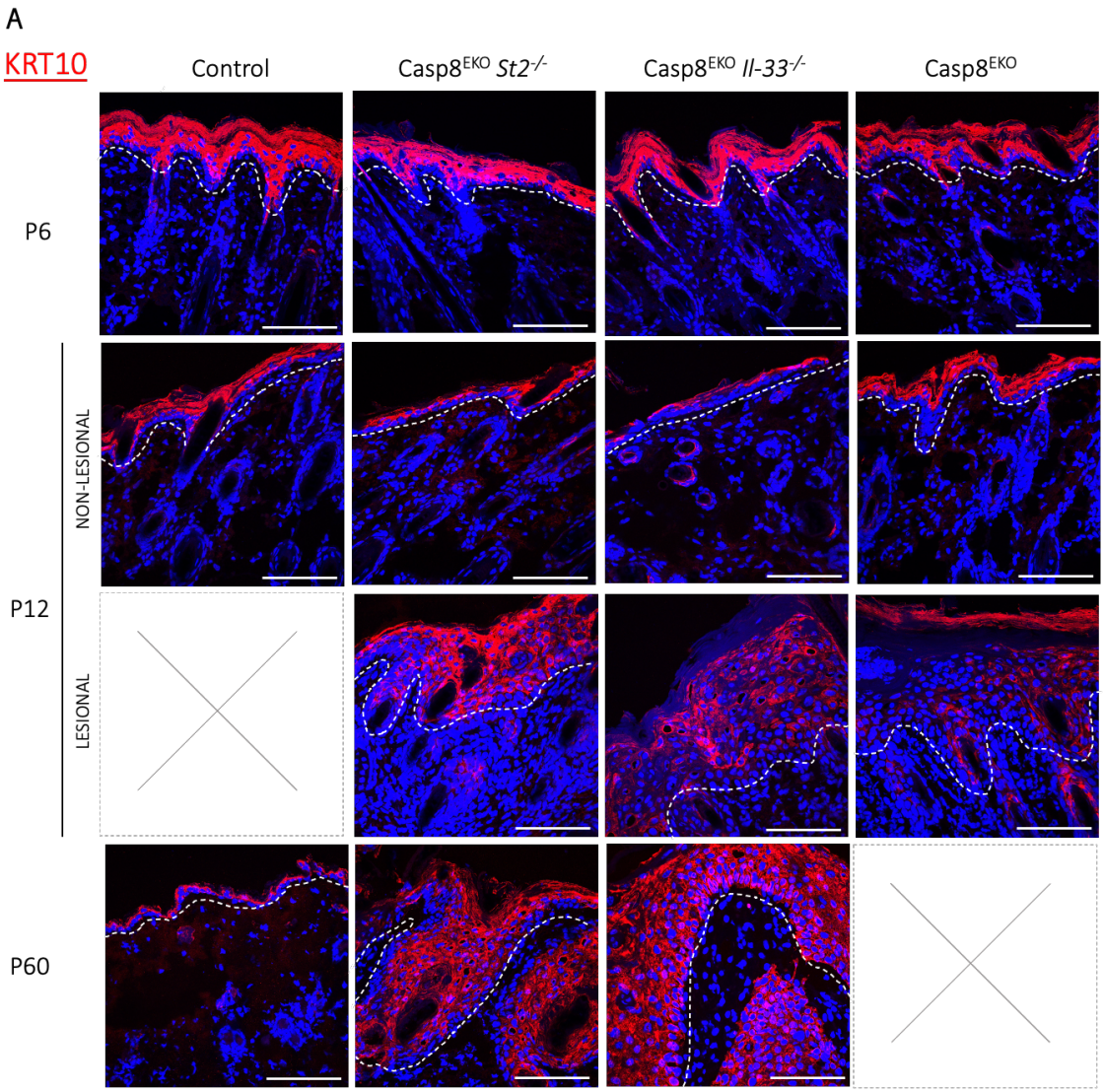
A
KRT10
Control
Casp8EKO St2-/-
Casp8EKO Il-33-/-
Casp8EKO
P6
P12
P60
NON-LESIONAL
LESIONAL

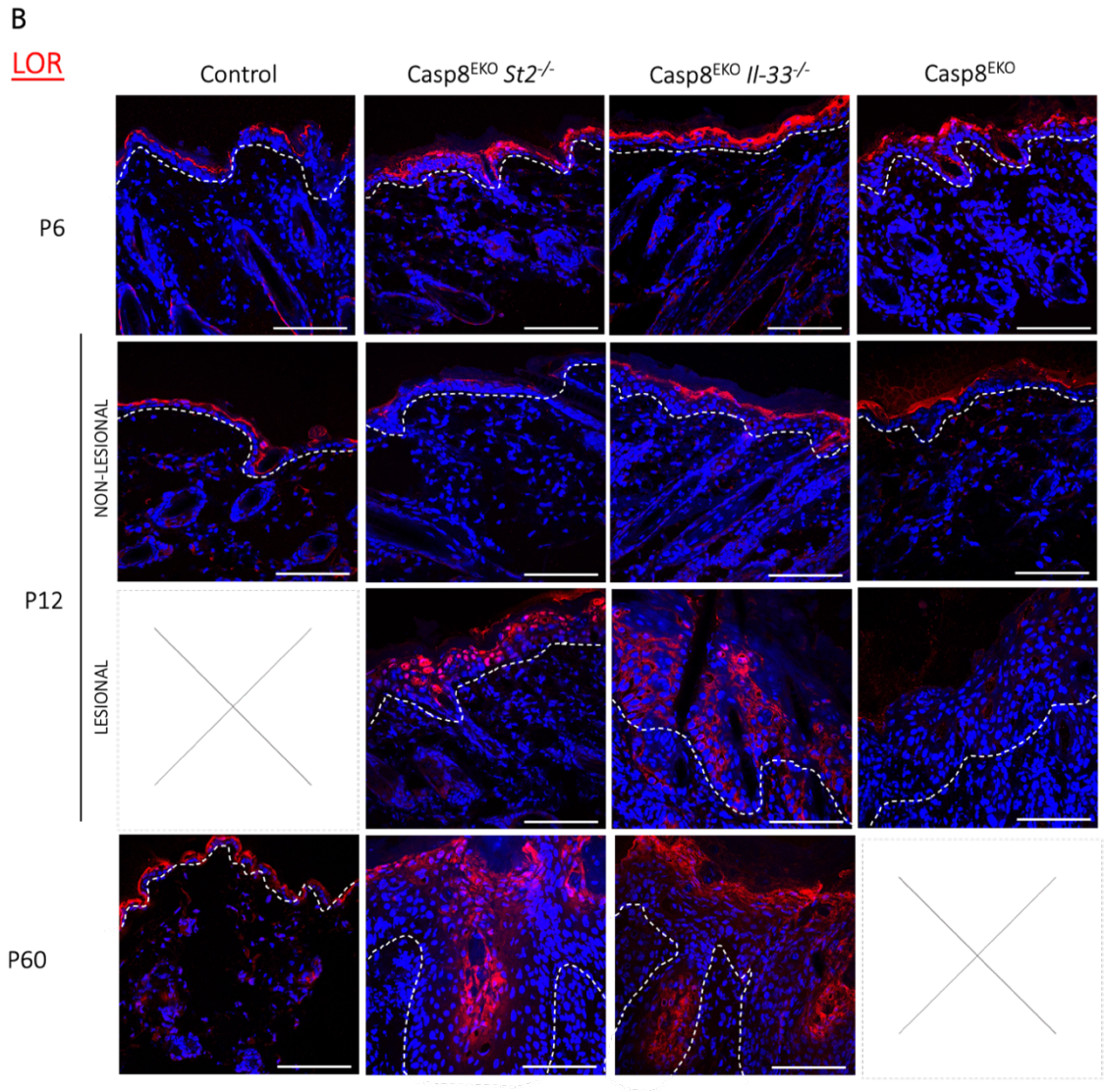

Figure 5.9: Immunohistological analysis of early and late keratinocyte differentiation markers in Casp-8^{EKO}, Casp-8^{EKO} *Il-33*$^{-/-}$ and Casp-8^{EKO} *St2*$^{-/-}$ skin samples Skin samples collected at different timepoints (P6, P12 and P60) from Casp-8^{EKO}, Casp-8^{EKO} *Il-33*$^{-/-}$ and Casp-8^{EKO} *St2*$^{-/-}$ and control littermates. Sections were fixed and immunostained (red) for **(A)** suprabasal marker KRT-10 and **(B)** granular layer marker LOR. Nuclei were stained with DAPI (blue). To facilitate lesion to lesion comparison with Casp8^{EKO} skin, sporadic lesional areas found in Casp-8^{EKO} *Il-33*$^{-/-}$ and Casp-8^{EKO} *St2*$^{-/-}$ skin at P12 are shown but are not representative of the phenotypes. Images were obtained using Zeiss LSM 880 scanning confocal microscope using a Z-stack function at magnification 63X. Scale bar represents 50 μm. Mice analysed for each genotype: KRT-10, C8^{EKO} P6 n=5, P12 n=6; C8^{EKO} *Il-33*$^{-/-}$ P6 n=5, P12 n=5, P60 n=4; C8^{EKO} *St2*$^{-/-}$ P6 n= 4, P12 n=6, P60 n=3; Control P6 n=5, P12 n=5, P60 n=2. LOR, C8^{EKO} P6 n=4, P12 n=5; C8^{EKO} *Il-33*$^{-/-}$ P6 n=7, P12 n=7, P60 n=4; C8^{EKO} *St2*$^{-/-}$ P6 n= 4, P12 n=4, P60 n=3; Control P6 n=4, P12 n=6, P60 n=2.

5.2.5 Immunohistological analysis of necroptotic and apoptotic markers

RIPK3 is an essential component of the necrosome, and it has been shown to play an essential role in activating necroptosis by phosphorylating its substrate, MLKL (Weber et al., 2018). Phosphorylated MLKL (ph-MLKL) is the main effector of necroptosis as it initiates plasma membrane rupture (Cai et al., 2014). In order to confirm ongoing necroptosis in the epidermis of Casp-8^{EKO} animals and assess to what extent it was active in the considered phenotypes, immunostaining for RIPK3 and ph-MLKL were performed. Immunohistochemistry analysis revealed the presence of RIPK3 positive cells throughout the epidermis of hyperplastic skin patches found in Casp-8^{EKO}, Casp-8^{EKO} *Il-33*$^{-/-}$ and Casp-8^{EKO} *St2*$^{-/-}$ skin at P12 (Figure 5.10A). Non-hyperplastic patches and control skin showed unspecific staining of the cornified layer.

Necroptotic death at inflammation sites was confirmed through membrane localised staining of ph-MLKL throughout lesions found in Casp-8^{EKO} *Il-33*$^{-/-}$ and Casp-8^{EKO} *St2*$^{-/-}$ animals at P12 (Figure 5.10B). Positive ph-MLKL staining was also observed in the scarce hyperplastic skin patches found in Casp-8^{EKO} samples at P6. As expected, no phosphorylated MLKL could be found in control skin at any of the studied timepoints (Figure 5.10B). Casp-8^{EKO}, Casp-8^{EKO} *Il-33*$^{-/-}$ and Casp-8^{EKO} *St2*$^{-/-}$ non-hyperplastic skin patches, showed some ph-MLKL positive cells (Figure 5.10B), showing active necroptosis at early stages of lesion development. MLKL phosphorylation was still present in P60 skin samples both in Casp-8^{EKO} *Il-33*$^{-/-}$ and Casp-8^{EKO} *St2*$^{-/-}$ animals, showing necroptosis is maintained and contributes to inflammation even at later stages.

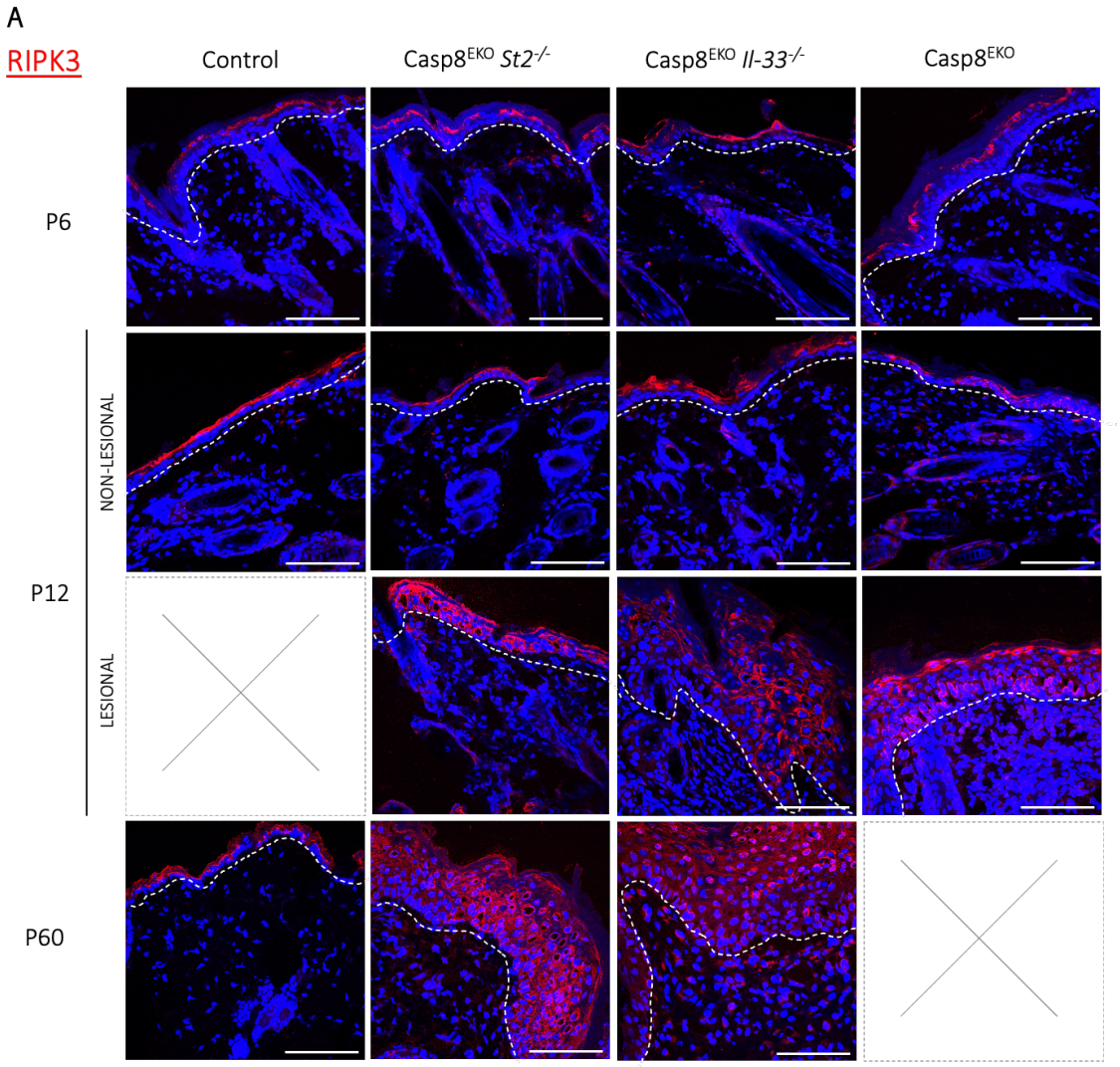
A
RIPK3
Control
Casp8EKO St2-/-
Casp8EKO Il-33-/-
Casp8EKO
P6
P12
P60
NON-LESIONAL
LESIONAL

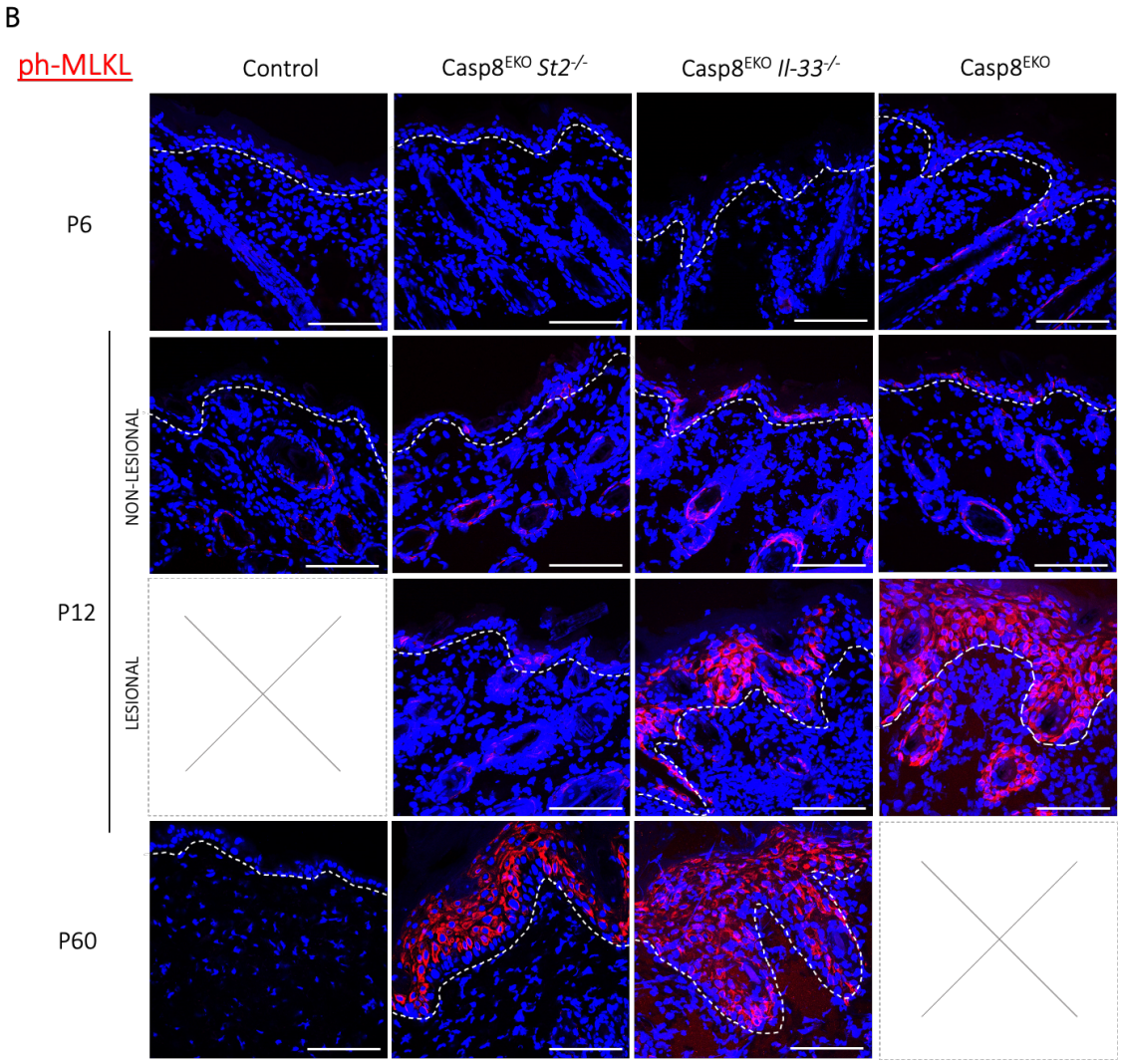

Figure 5.10: Immunohistological analysis of necroptotic markers RIPK3 and ph-MLKL in Casp-8^{EKO}, Casp-8^{EKO} *Il-33*$^{-/-}$ and Casp-8^{EKO} *St2*$^{-/-}$ skin samples. Skin samples collected at different timepoints (P6, P12 and P60) from Casp-8^{EKO}, Casp-8^{EKO} *Il-33*$^{-/-}$ and Casp-8^{EKO} *St2*$^{-/-}$ and control littermates. Sections were fixed and immunostained (red) for **(A)** RIPK3 and **(B)** ph-MLKL. Nuclei were stained with DAPI (blue). To facilitate lesion to lesion comparison with Casp8^{EKO} skin, sporadic lesional areas found in Casp-8^{EKO} *Il-33*$^{-/-}$ and Casp-8^{EKO} *St2*$^{-/-}$ skin at P12 are shown but are not representative of the phenotypes. Images were obtained using Zeiss LSM 880 scanning confocal microscope using a Z-stack function at magnification 63X. Scale bar represents 50 μm. Mice analysed for each genotype: RIPK3, C8^{EKO} P6 n=4, P12 n=6; C8^{EKO} *Il-33*$^{-/-}$ P6 n=6, P12 n=5, P60 n=4; C8^{EKO} *St2*$^{-/-}$ P6 n= 5, P12 n=7, P60 n=4; Control P6 n=4, P12 n=5, P60 n=2. Ph-MLKL, C8^{EKO} P6 n=4, P12 n=5; C8^{EKO} *Il-33*$^{-/-}$ P6 n=6, P12 n=5, P60 n=4; C8^{EKO} *St2*$^{-/-}$ P6 n= 4, P12 n=4, P60 n=4; Control P6 n=3, P12 n=3, P60 n=2.

To confirm ongoing apoptosis was not present in the Casp-8^{EKO} model in the model described here, cleaved Caspase-3 (c-Casp-3)

immunohistochemistry was performed in skin samples collected. As shown in Figure 5.11, cleaved Casp3 was not detected in the lesions found in Casp-8^{EKO}, Casp-8^{EKO} *Il-33*$^{-/-}$ or Casp-8^{EKO} *St2*$^{-/-}$ skin at P6 or P12, confirming keratinocyte death is apoptosis-independent. As a positive control for this staining, a human skin explant treated with apoptotic inducer (TNF plus SMAC mimetic) was stained with the same antibody, which had been shown previously to work both in mouse and human cleaved Caspase-3.

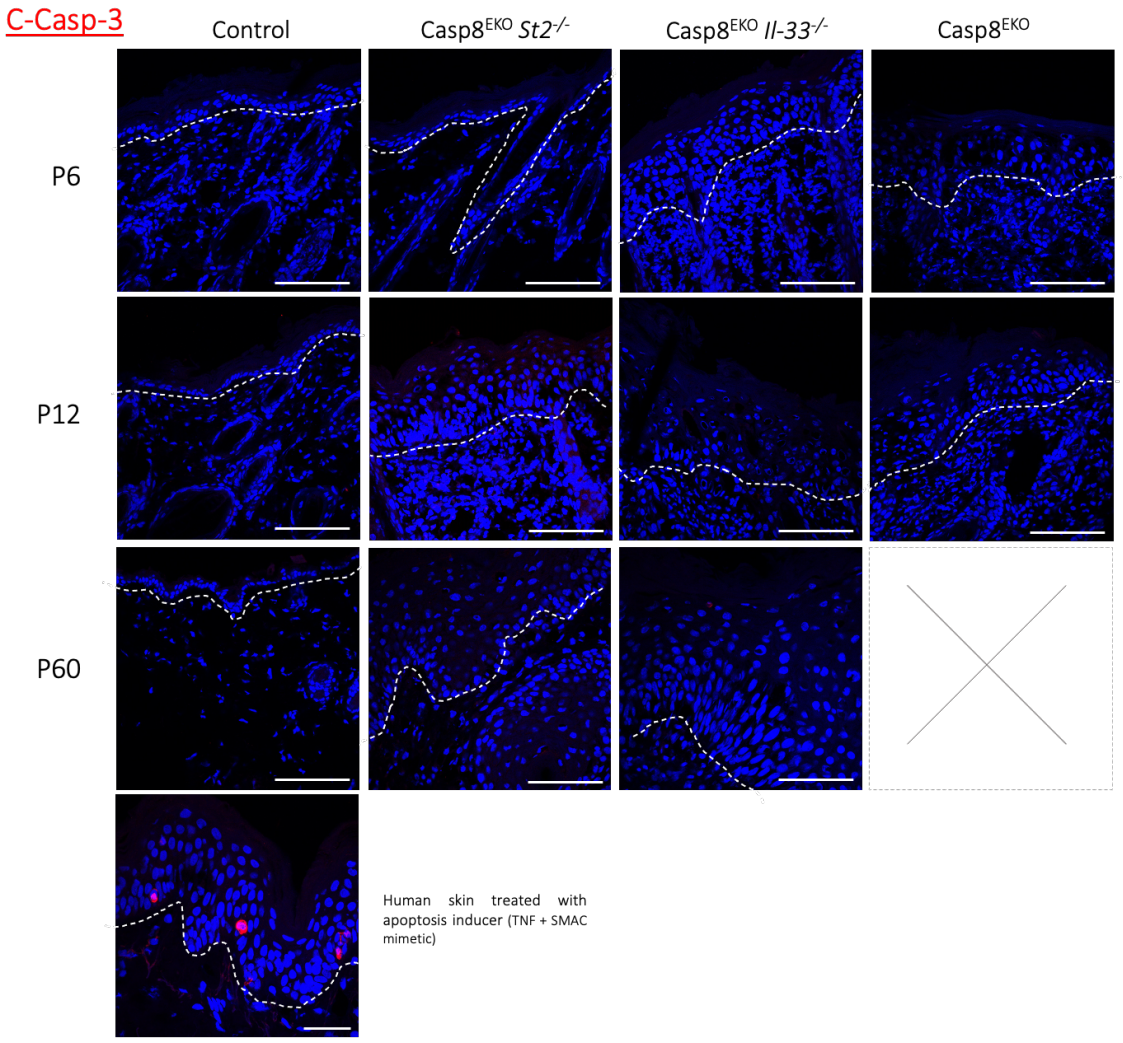

Figure 5.11: Immunohistological analysis of apoptotic marker, cleaved Casp-3 in Casp-8^{EKO}, Casp-8^{EKO} *Il-33*$^{-/-}$ and Casp-8^{EKO} *St2*$^{-/-}$ skin samples. Skin samples collected at different timepoints (P6, P12 and P60) from Casp-8^{EKO}, Casp-8^{EKO} *Il-33*$^{-/-}$ and Casp-8^{EKO} *St2*$^{-/-}$ and control littermates. Sections were fixed and immunostained (red) for cleaved Casp-3 (C-Casp-3) and nuclei were stained with

DAPI (blue). To facilitate lesion to lesion comparison, images of lesional areas have been included whenever possible, even if not representative of the phenotype. Last row shows a positive control for this immunostaining: human skin treated with apoptotic inducer (TNF + SMAC mimetic). Images were obtained using Zeiss LSM 880 scanning confocal microscope using a Z-stack function at magnification 63X. Scale bar represents 50 μm, except for the lowest row (TS-treated skin), where scale bar represents 20 μm. Mice analysed for each genotype: C8^{EKO} P6 n=6, P12 n=7; C8^{EKO} *Il-33*$^{-/-}$ P6 n=6, P12 n=5, P60 n=4; C8^{EKO} *St2*$^{-/-}$ P6 n= 7, P12 n=6, P60 n=4; Control P6 n=4, P12 n=5, P60 n=3.

5.2.6 Immunohistological analysis of inflammatory immune cells

Hyperplastic areas found in Casp-8^{EKO} as well as Casp-8^{EKO} *Il-33*$^{-/-}$ and Casp-8^{EKO} *St2*$^{-/-}$ skin were associated with increased inflammatory cell infiltrate of the dermis. To help define the profile of these inflammatory immune cells, skin sections were stained for T-cells (CD3), macrophages (F4/80) and granulocytes (Gr-1).

As seen in macroscopical and histological analysis, Casp-8^{EKO} *Il-33*$^{-/-}$ and Casp-8^{EKO} *St2*$^{-/-}$ lesional patches were less frequent and extensive than those found in Casp-8^{EKO} skin samples. When comparing immune cell infiltration, the overall observation was a drastically reduced presence of F480, CD3 and Gr-1 positive cells in Casp-8^{EKO} *Il-33*$^{-/-}$ and Casp-8^{EKO} *St2*$^{-/-}$ samples, due to the reduced number of lesions found per sample. It is important to remember that representative skin all animals at P6 and from double KO animals at P12 (see Fig 6.6C) is non lesional. In the following figures (6.12 and 6.13), and unlike in the previous ones, non-lesional images of P12 animals have been omitted. Instead, and to facilitate lesion to lesion comparison analysis, images of sporadic lesions found in P6 and P12 timepoints are shown, although these are not representative of the overall phenotype.

Recruitment of T-cells was unaffected by IL-33 or ST2 deletion (Figure 5.12A). A CD3+ cell subset with clear dendritic morphology corresponding to dendritic epidermal T cells (DETC) could be found in the epidermis and around hair follicles of healthy skin. As lesions start developing, these cells start disappearing from the epidermis and are substituted by dermis-infiltrating T cells, of smaller and rounder morphology (Figure 5.12A). T-cell infiltrate could be found in early stages of the inflammation phenotype (P6) and was maintained throughout lesion development (P12 and P60) (Figure 5.12A). The CD3 staining corresponding to Casp8^{EKO} *St2*$^{-/-}$ skin at P12 was performed using a green secondary antibody due to protocol modifications not relevant to the samples.

Macrophages were commonly found in control skin, which suggested the presence of a tissue resident macrophage population in the skin (Figure 5.12B). F4/80+ cells infiltrated early lesions found at P6, characterised by small cell clusters, indicated an early recruitment of these cells to the inflammation site. Their presence was increased and maintained as inflammation develops and lesions become hyperplastic, as observed in P12 and P60 skin samples. Visual comparison of lesion-to-lesion areas showed that deletion of IL-33 or ST2 had no effect in macrophage recruitment at early or late timepoints (Figure 5.12A).

Granulocyte recruitment was easily identifiable associated to Casp-8^{EKO} lesional skin (Fig 6.12C). Gr-1+ cells were, however, hardly present in early stages of Casp-8^{EKO} *Il-33*$^{-/-}$ or Casp-8^{EKO} *St2*$^{-/-}$ phenotype. In fact, no granulocyte infiltrate was found in P6 Casp-8^{EKO} *St2*$^{-/-}$ samples, and only a few cells were stained for Gr-1 in Casp-8^{EKO} *Il-33*$^{-/-}$ skin (Fig 6.12C), suggesting that IL-33/ST2 signalling plays a role in granulocyte recruitment. Casp-8^{EKO} *Il-33*$^{-/-}$ lesions at P12 showed granulocyte infiltrate associated with lesions but Gr-1+ cells were generally hard to find in Casp-8^{EKO} *St2*$^{-/-}$ samples compared to Casp-8^{EKO} lesions (Fig

6.12C). Gr-1 staining of older animals (P60) showed that granulocyte infiltration is present at the inflammation site in later stages of the phenotype (Fig 6.12C). This data suggests that granulocyte recruitment at the inflammation site might be delayed by the deletion of IL-33 or ST2.

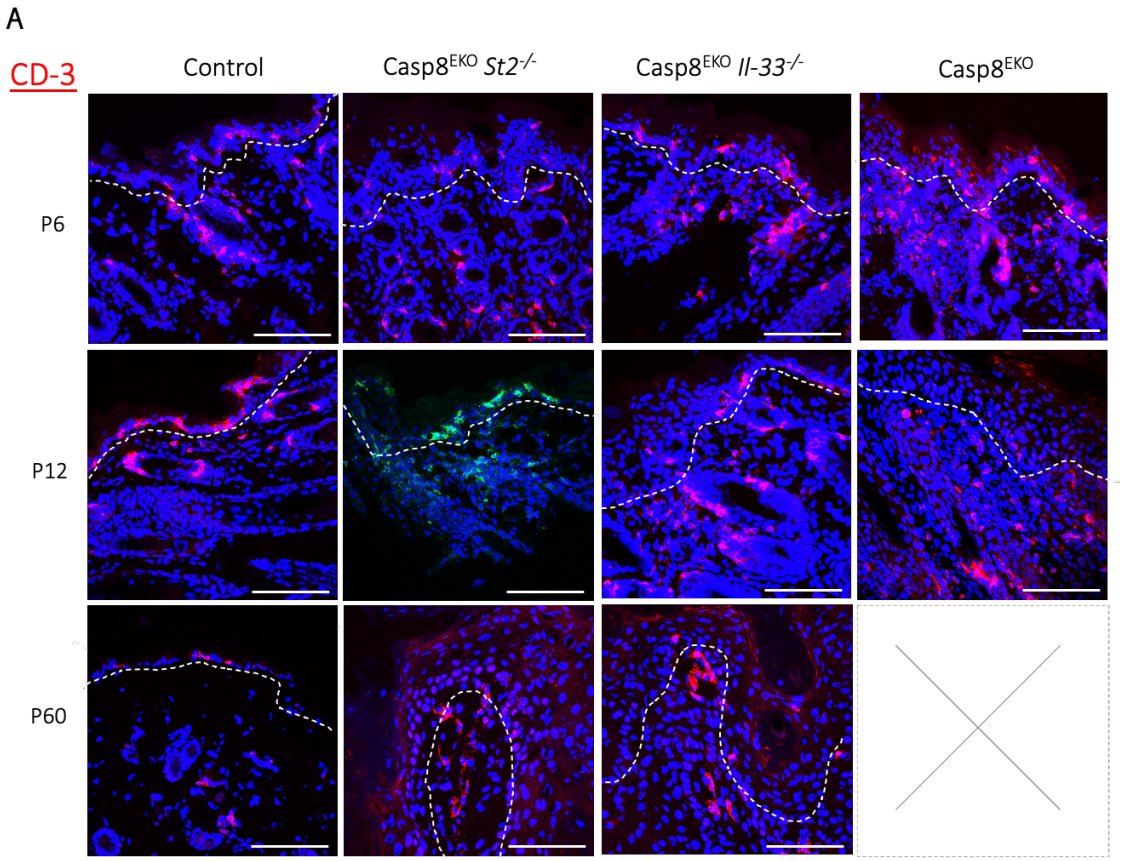

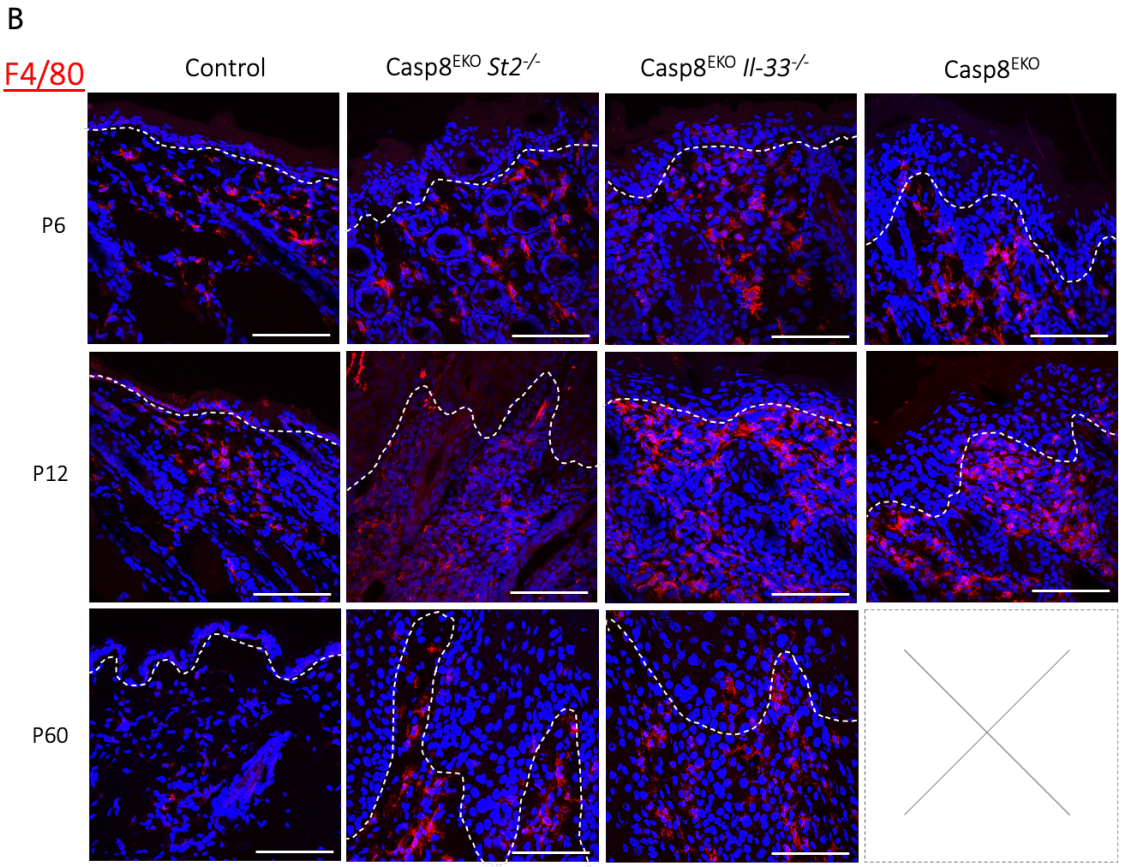
B
F4/80
Control
Casp8EKO St2-/-
Casp8EKO Il-33-/-
Casp8EKO
P6
P12
P60

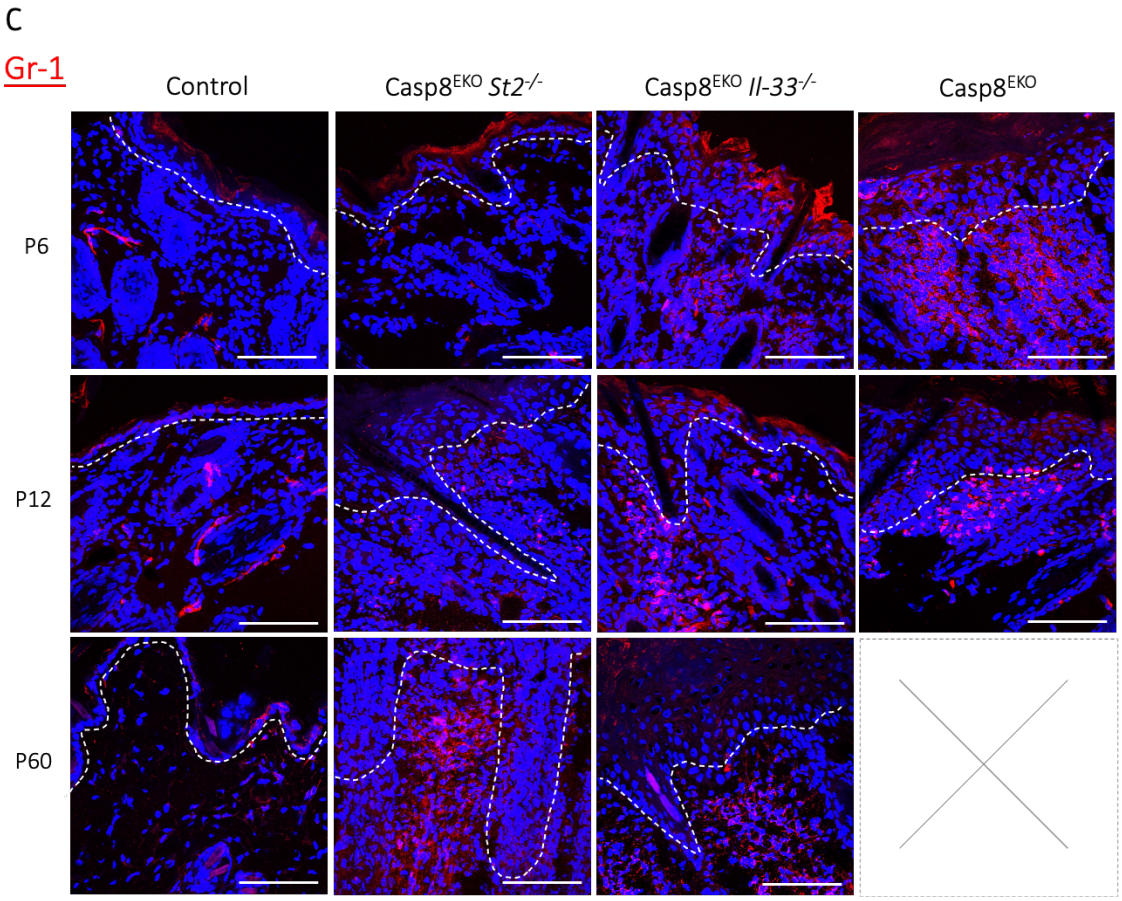
C
Gr-1
Control
Casp8EKO St2-/-
Casp8EKO Il-33-/-
Casp8EKO
P6
P12
P60

Figure 5.12: Immunohistological analysis of immune cell infiltrate in Casp-8^{EKO}, Casp-8^{EKO} *Il-33*$^{-/-}$ and Casp-8^{EKO} *St2*$^{-/-}$ skin samples. Skin samples were collected at different timepoints (P6, P12 and P60) from Casp-8^{EKO}, Casp-8^{EKO} *Il-33*$^{-/-}$ and Casp-8^{EKO} *St2*$^{-/-}$ and control littermates. Sections were fixed and immunostained (red) for **(A)** CD3, **(B)** F4/80 and **(C)** Gr-1. CD3 staining of P12 Casp-8^{EKO} skin was performed using the same protocol as the others but with a green secondary antibody. Nuclei were stained with DAPI (blue). To facilitate lesion to lesion comparison, images of lesional areas have been included whenever possible, even if not representative of the phenotype. Images were obtained using Zeiss LSM 880 scanning confocal microscope using a Z-stack function at magnification 63X. Scale bar represents 50 μm. Mice analysed for each genotype: F4/80, P6 C8^{EKO} n=5 P12 n=7; C8^{EKO} *Il-33*$^{-/-}$ P6 n=7, P12 & 60 n=5; C8^{EKO} *St2*$^{-/-}$ P6 & P12 n= 5, P60 n=7; Control P6 & P12 n=3, P60 n=6. CD3: C8^{EKO} P6 n=4, P12 =6; C8^{EKO} *Il-33*$^{-/-}$ P6 & P12 n=5, P60 n=4; C8^{EKO} *St2*$^{-/-}$ P6 n= 6, P12 n=5, P60 n=4; Control P6 n=3, P12 n=4, P60 n=7. Gr-1, C8^{EKO} P6 & P12 n=5; C8^{EKO} *Il-33*$^{-/-}$ P6 & P12 n=7, P60 n=5; C8^{EKO} *St2*$^{-/-}$ P6 n= 4, P12 n=10, P60 n=7; Control P6 n=3, P12 n=3, P60 n=2.

5.2.7 Immunohistological analysis of inflammatory cytokines

The pro-inflammatory cytokine TNF has been shown to play a determinant role in the inflammation phenotype of necroptosis-dependent skin models, since the deletion of TNF and TNFR1 from Casp-8^{EKO} and FADD^{EKO} animals led to a partial rescue of the skin inflammatory phenotype (Bonnet et al., 2011; Kovalenko et al., 2009). In order to elucidate the effect of IL-33 and ST2 in TNF production, skin sections collected at different timepoints were stained using an anti-TNF antibody. Some nonspecific staining can be seen in skin from control littermates, corresponding to fibres found in the dermis but not associated with cells. TNF expression was not abundant in skin sections collected at P6 from Casp-8^{EKO} *Il-33*$^{-/-}$ or Casp-8^{EKO} *St2*$^{-/-}$ animals and was only noticeable in infiltrates associated to larger lesions found in Casp-8^{EKO} samples (Figure 5.13A). At P12, lesion-associated staining of TNF could be found in hyperplastic patches found in Casp-8^{EKO}, Casp-8^{EKO} *Il-33*$^{-/-}$ and Casp-8^{EKO} *St2*$^{-/-}$ skin. Similarly, lesion-associated TNF was also present in the infiltrates of older Casp-8^{EKO} *Il-33*$^{-/-}$ and Casp-8^{EKO} *St2*$^{-/-}$ animals (P60) (Figure 5.13A).

As described previously, IL-33 localised in the nucleus under normal conditions and can be released after cell injury or death and act as a proinflammatory signal, an alarmin (Moussion et al., 2008). In order to evaluate IL-33 expression in the Casp-8^{EKO} model, skin sections were stained to detect extracellular (pro-inflammatory) IL-33. By avoiding permeabilization of the sections, I was able to observe an increase of IL-33 expression associated to skin inflammation, as previously described (Kovalenko et al., 2009). IL-33 staining of Casp-8^{EKO} *Il-33*$^{-/-}$ samples was negative at all timepoints (P6, P12 and P60), confirming the specificity of the staining (Figure 5.13B). Casp-8^{EKO} skin showed strong IL-33 expression at P6 and P12. Prelesional skin found in P6 Casp-8^{EKO} *St2*$^{-/-}$ samples showed some IL-33 staining in the epidermis in a similar pattern to that seen for necroptotic markers (RIPK3 and ph-MLKL) at this timepoint (Figure 5.10A and B). IL-33 expression was also observed at late stages of the inflammatory phenotype, as seen in adult Casp-8^{EKO} *St2*$^{-/-}$ skin (P60) (Figure 5.13B).

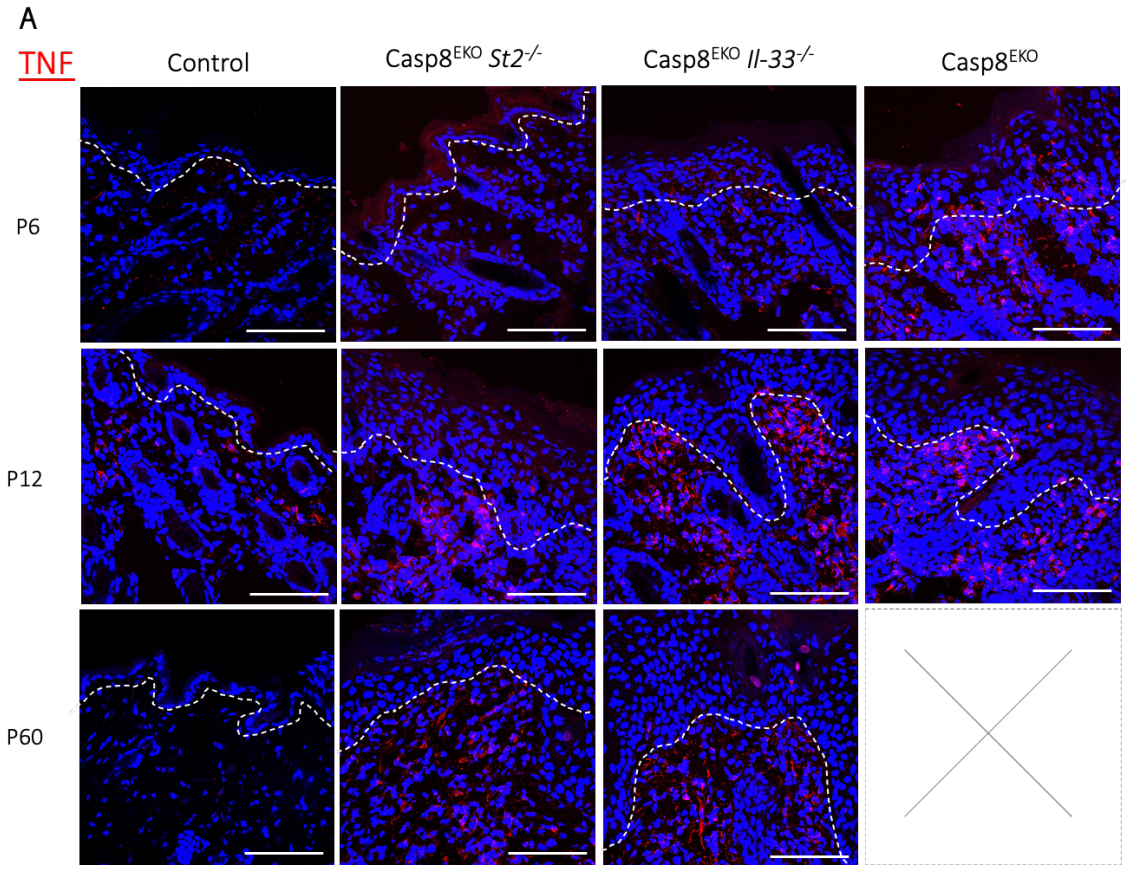
A
TNF
Control
Casp8EKO St2-/-
Casp8EKO Il-33-/-
Casp8EKO
P6
P12
P60

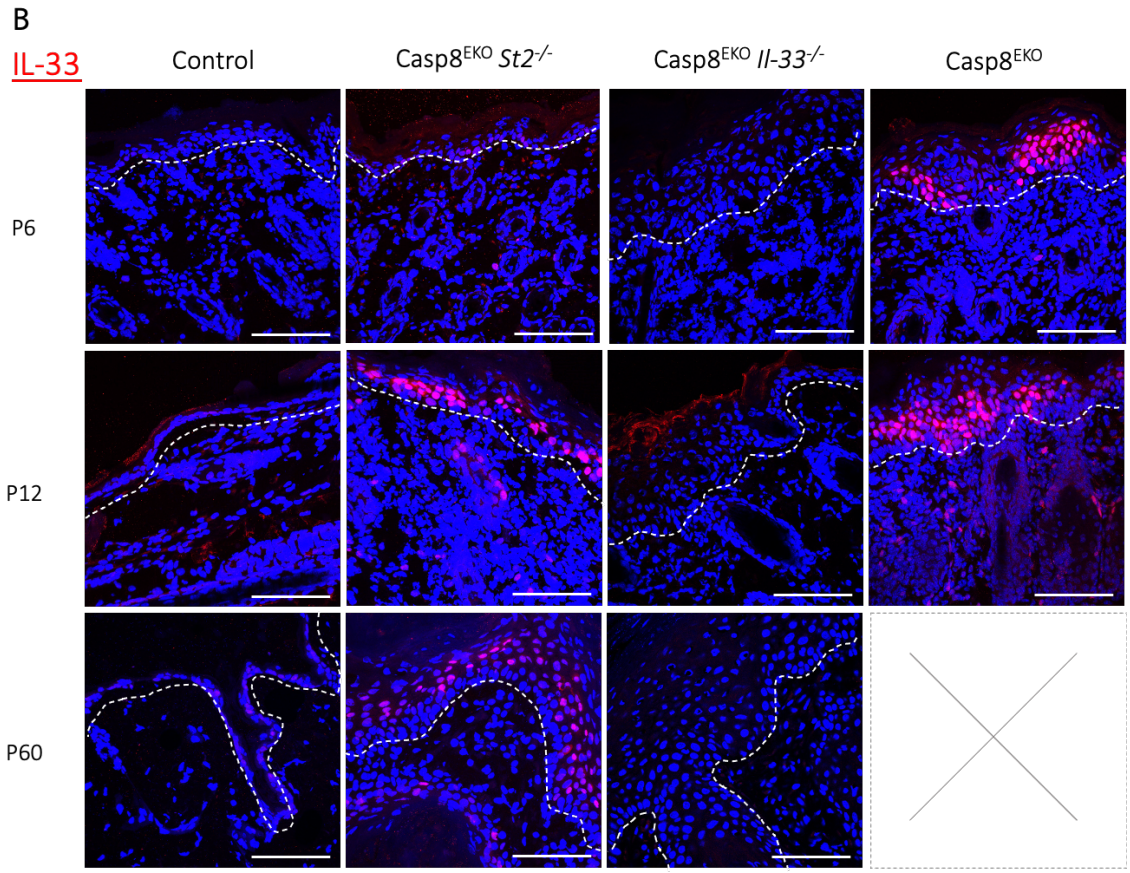
B
IL-33
Control
Casp8EKO St2-/-
Casp8EKO Il-33-/-
Casp8EKO
P6
P12
P60

Figure 5.13: Immunohistological analysis of pro-inflammatory cytokines in Casp-8^{EKO}, Casp-8^{EKO} *Il-33*$^{-/-}$ and Casp-8^{EKO} *St2*$^{-/-}$ skin samples. Skin samples were collected at different timepoints (P6, P12 and P60) from Casp-8^{EKO}, Casp-8^{EKO} *Il-33*$^{-/-}$, Casp-8^{EKO} *St2*$^{-/-}$ and control littermates. Sections were fixed and immunostained (red) for **(A)** TNF and **(B)** IL-33. Nuclei were stained with DAPI (blue). To facilitate lesion to lesion comparison, images of lesional areas have been included whenever possible, even if not representative of the phenotype. Images were obtained using Zeiss LSM 880 scanning confocal microscope using a Z-stack function at magnification 63X. Scale bar represents 50 μm. Mice analysed for each genotype: TNF, C8^{EKO} P6 n=4, P12 n=7; C8^{EKO} *Il-33*$^{-/-}$ P6 n=6, P12 n=5, P60 n=5; C8^{EKO} *St2*$^{-/-}$ P6 n= 7, P12 n=11, P60 n=4; Control P6 n=3, P12 n=4, P60 n=2. IL-33, C8^{EKO} P6 n=4, P12 n=5; C8^{EKO} *Il-33*$^{-/-}$ P6 n=3, P12 & P60 n=6. C8^{EKO} *St2*$^{-/-}$ P6 n= 7, P12 n=5, P60 n=4. Control P6 n=2, P12 n=3, P60 n=2.

5.3 Discussion

IL-33 is a pro-inflammatory cytokine that plays an important role in tissue inflammation and has been found to be upregulated in necroptosis-dependent skin inflammation models (Kovalenko et al., 2009; personal communication, Bonnet MC). This chapter explored the role of IL-33 in the necroptosis-dependent skin inflammation model Casp-8^{EKO} through the knock-out of IL-33 or its receptor ST2. The results presented here show that the deletion of IL-33 or ST2 leads to a major rescue of the Casp-8^{EKO} skin inflammation phenotype. Deletion of IL-33 or ST2 from Casp-8^{EKO} animals leads to a delay in the skin inflammation phenotype and drastically reduced the rate of development of the inflammation. The reduced number and decreased severity of lesions in the skin of Casp-8^{EKO} *Il-33*$^{-/-}$ and Casp-8^{EKO} *St2*$^{-/-}$ animals result in significant increase in survival of double KO animals compared to Casp-8^{EKO} mice. This significant increase in the survival demonstrates that IL-33 is an essential necroptosis-induced inflammatory mediator in the skin. Interestingly, only TNF/TNFR1 signalling has been described to have a similarly significant impact in Casp-8^{EKO} and FADD^{EKO} necroptosis-dependent skin inflammation models (Bonnet et al., 2011; Kovalenko et al., 2009).

Necroptosis, as other forms of programmed necrosis, is a pro-inflammatory form of cell death given that leakage of intracellular DAMPs can propagate inflammatory responses. Necroptosis has been shown to directly release biologically active IL-33 (Shlomovitz et al., 2019). IL-33 plays an important role in various diseases such as asthma (Liew et al., 2010), rheumatoid arthritis (Palmer & Gabay, 2011) or chronic inflammation in the gut (Lopetuso et al., 2013). Similarly, treating mice with IL-33 induces an inflammatory response and leads to epithelial hyperplasia in the skin, pulmonary and GI tract (Han et al., 2017; Axel J. Hueber et al., 2011). Furthermore, and in line with the results reported here, IL-33 has been reported to contribute to disease severity of different inflammation models (Arshad et al., 2013; Y. Duan et al., 2019; Haenuki et al., 2012).

The results reported here show that deletion of IL-33 and ST2 leads to reduced inflammatory lesions in the skin, observed both macroscopically and through histological analysis. Reduced hyperplasia was accompanied by decreased alteration of skin proliferation and differentiation markers. Differences in KRT-10 or LOR expression between Casp-8^{EKO} *Il-33*$^{-/-}$ and Casp-8^{EKO} *St2*$^{-/-}$ animals were not observed, contrasting a proposed nuclear role of IL-33 downregulating or supressing the expression of filaggrin (FIL), LOR and KRT-10 in the skin (X. Dai et al., 2021). Others have attributed this function to the cytokine role of IL-33 (Ryu et al., 2016). In line with this theory, both Casp-8^{EKO} *Il-33*$^{-/-}$ and Casp-8^{EKO} *St2*$^{-/-}$animals showed higher expression of these differentiation markers than Casp-8^{EKO} skin. However, higher expression of differentiation markers is normally observed as a result of the rescue of the epidermal hyperplasia, as seen in the TNFR1 partial rescue of FADD^{EKO} animals (Bonnet et al., 2011).

Staining for ph-MLKL and RIPK3 confirmed ongoing keratinocyte necroptosis in all lesion-presenting animals, caused by Casp-8 deletion. Cleaved Casp-3 could not be found in the skin of any of the animals analysed, confirming apoptosis does not play a role in this model. Furthermore, deletion of IL-33 or ST2 did not affect the initiation of necroptosis, given that necroptotic markers RIPK3 and ph-MLKL could be found in the prelesional skin of all studied lines. Dermal immune cell infiltrates were always associated with lesions. Given that double-KO animals had a reduced number of lesions, it was essential to perform lesion-to lesion comparisons between Casp-8^{EKO} and double-KO skin. Contrasting immune cell stainings with the expression of necroptotic markers was also key to understand the kinetics of the early inflammation in Casp-8^{EKO} *Il-33*$^{-/-}$ and Casp-8^{EKO} *St2*$^{-/-}$animals. Furthermore, the inflammatory lesions were distributed in patches throughout the epidermis, conferring variability within samples of the same genotype. Hence why the representativeness of the skin samples collected was assessed through the quantification of lesions per sample (through H&E) and a minimum of five individual animals were analysed in each experiment.

It is important to take into account that the conclusions stated along this chapter regarding the changes or the absence of these in immunofluorescence experiments are based on visual inspection of the samples by a trained eye and lack the corresponding quantification to support given observations. This is especially relevant when comparing immune cell infiltrate and cytokine expression between the different knock-out lines. The large size of the skin samples collected and the use of the Z-stack function to acquire images made the acquisition of full-size sample images impracticable. For that reason, the acquisition of the images was aimed to record representative positive stainings of each sample. However, a specific criterion was not established prior to image

acquisition, hindering the normalisation of these images to the total number of lesions per sample and subsequent quantification of the stainings produced. Therefore, even though the observed decrease of Gr-1 positive cells infiltration and TNF expression are consistent throughout the samples, formal quantification of these assessments would help confirm and add strength to the data produced here.

Visual analysis of the immune cell infiltrate associated with lesions revealed that IL-33 or ST2 deletion did not affect T-cell recruitment, consistent with previous research that found FADD^{EKO} inflammation is B- and T-cell independent (Bonnet et al., 2011). This data further supports the idea that inflammation is driven by an innate immune response that does not require T- or B-lymphocytes. Macrophages have been widely associated with DAMP recognition (G. Y. Chen & Nuñez, 2010), and subsequent cytokine production, including TNF (Flynn et al., 1995). They have also been suggested to express ST2 receptor (D. Li et al., 2014), which made them potential candidates to respond to IL-33 signalling in the present model. Changes in macrophage recruitment to lesions, however, were not observed after IL-33 or ST2 deletion. This observation supports previous research that showed that pharmacological depletion of macrophages did not affect Casp-8^{EKO} phenotype (Kovalenko et al., 2009). Furthermore, while macrophage recruitment could be found in early skin lesions, TNF expression, in comparison, was delayed and associated with more severe and hyperplastic lesions at later stages, which suggested that macrophages were not a TNF source in the Casp-8EKO model.

Visual inspection of the samples revealed a reduction of the Gr-1+ infiltrate in early lesions found in Casp-8^{EKO} *Il-33*$^{-/-}$ and Casp-8^{EKO} *St2*$^{-/-}$ skin at P6 compared to Casp-8^{EKO}, which indicates that granulocyte recruitment to inflammatory lesions might be delayed by the deletion of IL-33 and ST2. This suggests that granulocytes, through IL-33-induced

recruitment, play an important role in amplifying necroptosis-dependent inflammation. Indeed, IL-33 has been documented to induce granulocyte recruitment in skin inflammation (Axel J. Hueber et al., 2011), sites of infection (Oshio et al., 2017) and a murine model of arthritis (Verri et al., 2010). In line with these reports, forced extracellular IL-33 (through the deletion of the N-terminal nuclear domain of IL-33) led to multi-organ inflammation with dense infiltrates of eosinophils, neutrophils and macrophages (Bessa et al., 2014). In an IMQ-induced model of psoriasiform dermatitis, deletion of IL-33 resulted in marked reduction in absolute number of immune cells with a reduction of neutrophils and mast cells and an increase on DCs and macrophages (Zeng et al., 2021).

IL-33-dependent granulocyte recruitment could be mediated through interaction with resident ST2+ immune cells in the skin. ILC2s, DCs and mast cells have been traditionally proposed as the main primary tissue-resident targets of IL-33, given that they constitutively express high levels of ST2 (Allakhverdi et al., 2007; Enoksson et al., 2011; Moro et al., 2010b; Neill et al., 2010). Indeed, mast cells have been shown to be partially responsible for the IL-33-dependent recruitment of neutrophils in the skin (Axel J. Hueber et al., 2011). This hypothesis is in agreement with a potential local role of IL-33 released from psoriatic keratinocytes, while no circulating IL-33 was reported (Balato et al., 2012). Analysis of circulating IL-33 in the animals is currently in progress. Staining for mast cells, ILC2s and other potential ST2-expressing resident immune cells has not been performed but could be the subject of further investigations.

IL-33 is subject to bio-activity regulation through inflammatory proteases that produce shorter mature forms of the cytokine or through caspase cleavage that inactivate IL-33. Proteases include neutrophil elastase, cathepsin G, and proteinase 3 (PR3), as well as mast cell chymase, tryptase and granzyme B. Some mature forms generated by inflammatory proteases

can increase biological activity compared to IL- 33 precursor (Lefrançais et al., 2012, 2014). IL-33 and ST2 deletion from Casp-8^{EKO} animals, through a decreased recruitment of granulocytes to early skin inflammation sites, could be delaying the release of these proteases and the production of more active forms of IL-33, that would further reinforce inflammation.

Similar to the changes observed in granulocyte recruitment, a decrease in TNF expression was observed through visual inspection in Casp-8^{EKO} *Il-33*$^{-/-}$ and Casp-8^{EKO} *St2*$^{-/-}$ skin at P6, while Casp-8^{EKO} lesions showed strong TNF staining at both timepoints. This indicates that IL-33 and ST2 deletion might lead to a delay in TNF production and suggests a connection between the IL-33/ST2 signalling and TNF production in this model. Considering that TNF is known to play a role in necroptosis-dependent skin inflammation, the delayed inflammation in Casp-8^{EKO} *Il-33*$^{-/-}$ and Casp-8^{EKO} *St2*$^{-/-}$ mice could be, in part, due to a decreased production of TNF by immune cells. The cell type responsible for TNF production, in this case, could be one or more granulocytes, given that recruitment of Gr-1 and TNF-positive cells is similarly delayed in Casp-8^{EKO} *Il-33*$^{-/-}$ and Casp-8^{EKO} *St2*$^{-/-}$ skin. A possible explanation for these observations is that IL-33 acts recruiting one or more types of granulocytes (directly or through immune cells), which, in turn, produce and release TNF at the inflammation site, contributing to its development. Deletion of IL-33 or ST2 would prevent early recruitment of TNF-producing granulocytes and therefore cause a delay in the inflammatory phenotype of double-KO animals. Other signals, however, are likely to be involved in granulocyte recruitment since, eventually, these cells are found to infiltrate both Casp-8^{EKO} *Il-33*$^{-/-}$ and Casp-8^{EKO} *St2*$^{-/-}$ lesions. To elucidate if granulocytes are, in fact, responsible for TNF production, a double staining of TNF and Gr-1 (Ly6g) could be performed. The Ly6g or TNF antibodies used in this

study were raised in the same species (rat), and the mentioned double staining would have required acquiring and optimising a new Ly6g or TNF antibody.

IL-33 was barely expressed in control skin but strongly associated with lesions in Casp-8^{EKO} and Casp-8^{EKO} *St2*$^{-/-}$ skin. This observation seemed contradictory to previous research that had shown IL-33 to be constitutively expressed in murine healthy skin but lost during inflammation (Sundnes et al., 2015). They, however, report the immunostaining of nuclear IL-33, which disappears from this localisation in acute inflammation. Even though the mentioned experiment and the one reported here use the same IL-33 antibody, differences in the immunostaining protocol, such as tissue storage (paraffin-embedded versus frozen) and permeabilization (none versus 0.1% saponin), are likely the reason of different IL-33 detection. In contrast to TNF, which was observed only in the dermis and associated to immune cells, IL-33 was detected strictly in the epidermis of early lesions found in P6 as well as non-hyperplastic and hyperplastic patches found at P12. The epidermal localisation had a similar pattern to that observed in ph-MLKL staining in non-hyperplastic skin, which further supports the idea that IL-33 is released during keratinocyte necroptosis.

In addition to IL-33 recruitment of TNF-producing granulocytes, the idea that IL-33 could be playing a local role inducing inflammation cannot be dismissed. Lee et al. showed that immunosuppressants (dexamethasone/indomethacin) did not abolish the Casp-8^{EKO} inflammatory phenotype completely, suggesting epidermal and immune cell signalling work together for the initiation and development of inflammation. Interestingly, *in vitro* stimulation of keratinocytes with IL-33 leads to the release of pro-inflammatory cytokines (Meephansan et al., 2012; Zeng et al., 2021). Furthermore, ST2 expression has been found to

be increased in the epidermis of patients with several skin pathologies including psoriasis, AD and vitiligo (Balato et al., 2012; P. Li et al., 2015; Savinko et al., 2012), suggesting that an autocrine circuit of IL-33/ST2 in keratinocytes could contribute to skin inflammation. This potential local action of IL-33 propagating inflammation in the epidermis could be contributing to the delay observed in the appearance of lesions upon IL-33 deletion but also could explain the slower growth rate of these lesions in Casp-8^{EKO} *Il-33*$^{-/-}$ and *St2*$^{-/-}$ animals. In conclusion, the role of an IL-33/TNF loop in this phenotype might be a result of crosstalk between keratinocytes and immune cells and IL-33 could also play a more local role in development of inflammation through keratinocyte signalling. Comparison of the phenotypes obtained from Casp-8^{EKO} *St2*$^{-/-}$ and ST2^{EKO} animals could help determine if ST2-expressing keratinocytes play a role in necroptosis-dependent inflammation. A schematic view of the working hypothesis is shown in Figure 5.14.

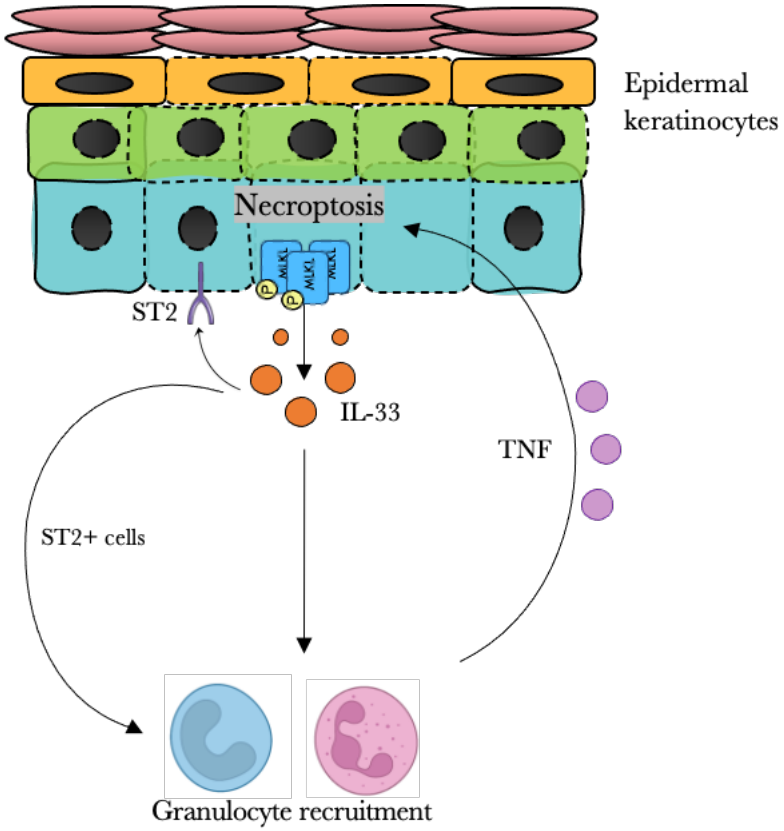

Figure 5.14: Schematic view of proposed working hypothesis of IL-33 in Casp-8^{EKO} skin. Epidermal keratinocytes release IL-33, as well as other cytokines, during necroptosis (as detected through MLKL phosphorylation). IL-33 acts recruiting granulocytes either directly or through immune cell activation. Infiltrating granulocytes produce TNF at the inflammation sites, contributing to keratinocyte necroptosis and inflammation in the skin. IL-33/ST2 signalling in keratinocytes could also contribute to release of pro-inflammatory cytokines.

IL-33 has been extensively described as a type-2 cytokine, as it activates immune cells involved in type-2 immunity such as ICL2s or Th2 cells. Consistently, IL-33 has been widely associated with the pathophysiology of AD. However, several recent studies have described that the action of IL-33 is not limited to the activation of type-2 immune responses. Indeed, they have uncovered important roles of IL-33 in the activation of immune cells involved in type-1 immunity, infection and chronic inflammation such as Th-1 cells, NK cells, CD8+ T cells, neutrophils and macrophages. For example, blocking of ST2 in different arthritis models have led to disease attenuation and reduced Th-17 and Th-1 responses (P. Martin et al., 2013; Palmer et al., 2009).

The initial work on Casp-8^{EKO} mice linked the skin inflammation to AD through upregulation of Casp-1 and NLRP3 expression in keratinocytes, resulting in inflammasome-mediated release of IL-1α (Pedro Lee et al., 2009). However, further studies confirmed that survival of Casp-8^{EKO} or FADD^{EKO} animals was not affected by the deletion of IL-1α and IL-1β or IL-1R, respectively (Bonnet et al., 2011; Kovalenko et al., 2009), demonstrating that IL-1 does not play a role in necroptosis-dependent lesion development. Histopathological analysis of necroptosis-dependent skin lesions reported here and by others (Bonnet et al., 2011; Kovalenko et al., 2009) display several psoriatic hallmarks such as neutrophil abscesses, parakeratosis and diminished granular layer. Furthermore, necroptosis-dependent skin inflammation has been shown to be partially dependent on TNF/TNFR1 signalling, considered as a typical Th-1

signature (Bonnet et al., 2011; Kovalenko et al., 2009). Finally, as described in the previous chapter, necroptosis-dependent skin inflammation has been shown to be more severe in animals with a C57BL/6 background (Bonnet et al., 2011; Kovalenko et al., 2009), typically associated with type-1 responses, than in BALB/c mice (Pedro Lee et al., 2009), which display a prototypical type-2 response. The results reported here indicate that IL-33 plays a role in psoriasis-like inflammation. Indeed, a few recent studies have suggested IL-33 might play a role in psoriasis, as it has been shown to be overexpressed in psoriasis patients (A J Hueber et al., 2010) and can induce ST2-dependent psoriasis-like dermatitis (Zeng et al., 2021). IL-33 has also been shown to be increased in the IMQ-induced psoriasiform model, and IL-33 or ST2 deficiency ameliorate disease severity (Zeng et al., 2021). The mixed genetic background of the animals used in my study, however, do not help elucidate the type of inflammatory response triggered. Backcrossing animals used to a C57BL/6N background is currently in progress. Shifting the background to a obtain a predominant type-1 immune response will provide better understanding of the role of IL-33 in necroptosis-induced skin inflammation.

At early stages of inflammatory phenotype, no differences were found between Casp-8^{EKO} *Il-33*$^{-/-}$ and Casp-8^{EKO} *St2*$^{-/-}$ animals. Small macroscopical and histological differences were observed, leaning towards a slightly more severe phenotype of Casp-8^{EKO} *Il-33*$^{-/-}$ animals, but the statistical analysis revealed these were not significant. This was maintained at least until animals reached P12, the second timepoint studied. As animals grew older, however, the development of the lesions was significantly more severe in Casp-8^{EKO} *Il-33*$^{-/-}$ than Casp-8^{EKO} *St2*$^{-/-}$ animals, which translated in decreased survival. One possible explanation for this could be the previously mentioned fact that *Il-33*$^{-/-}$ and *St2*$^{-/-}$

animals had different genetic background when crossed with Casp-8^{EKO} mice. Necroptosis skin models have shown different severity when different backgrounds have been used (Bonnet et al., 2011; Kovalenko et al., 2009; Pedro Lee et al., 2009). As also mentioned earlier, small changes in the genetic background can slightly shift the type of immune response (Th1/Th2) of the animal during inflammation.

Interestingly, a difference between IL-33 and *St2*$^{-/-}$ has been previously described in an arthritis model (P. Martin et al., 2013). The authors of this study investigated potential factors, including the purity of the genetic background, and found it was not responsible for this observation. It is not uncommon that cytokine knock-outs are compensated by other cytokines cross-signalling. This was the case for FADD^{EKO} TNF and TNFR1, given that lymphotoxin alpha (LT-α) can also bind TNFR1. IL-33 is the only described ligand of ST2. It can interact with either the transmembrane form, ST2L, or soluble form, sST2, of the receptor, both of which are disrupted in the *St2*$^{-/-}$ animals described here (Senn et al., 2000). However, another cytokine, not previously described could be binding to ST2 and be responsible for the differences observed here.

Injection of IL-33 induced ear swelling in *wild type* mice but had no effect in *St2*$^{-/-}$ mice (Axel J. Hueber et al., 2011), which disagrees with the previous mentioned explanation. Another possibility could include a nuclear role of IL-33 as the cause of the observed difference in the skin inflammation phenotype. IL-33 has been reported to play a role in wound healing, although there are several contradictory studies in this field. IL-33 was found to promote wound healing through ST2 signalling (Gause et al., 2013; J. S. Lee et al., 2016), but a later study claimed it was nuclear IL-33 which was involved in this process (Oshio et al., 2017). Other studies have linked an ST2-independent role of IL-33 to tissue fibrosis (Kotsiou et al., 2018), which, if extrapolated to the skin, could explain the more

severe phenotype observed in Casp-8^{EKO} *Il-33*$^{-/-}$. Finally, even though ST2 is the only described receptor for IL-33 to this date, it is also possible that extracellular IL-33 can interact with other binding partners. In this scenario, a protective role of ST2-independent IL-33 signalling could explain the described differences between Casp-8^{EKO} *Il-33*$^{-/-}$ and Casp-8^{EKO} *St2*$^{-/-}$ phenotypes.

In summary, this chapter shows that IL-33, through ST2 signalling, contributes to Casp-8^{EKO} skin inflammation. These are the key findings and achievements:

- Deletion of IL-33 or ST2 from Casp-8^{EKO} animals leads to a partial rescue of the Casp-8^{EKO} skin phenotype by delaying the initiation of lesion development and decreasing the growth rate of the lesions.
- The survival of Casp-8^{EKO} *Il-33*$^{-/-}$ and Casp-8^{EKO} *St2*$^{-/-}$ animals is significantly improved compared to Casp-8^{EKO} animals, which reach adulthood and are able to breed.
- The presence of late differentiation epidermal markers in Casp-8^{EKO} *Il-33*$^{-/-}$ and Casp-8^{EKO} *St2*$^{-/-}$ animals suggests the cornification process is less altered in these animals when compared to Casp-8^{EKO} ones.
- IL-33/ST2 signalling might contribute to granulocyte recruitment, given that a reduction of granulocyte infiltration could be visually detected in Casp-8^{EKO} *Il-33*$^{-/-}$ and Casp-8^{EKO} *St2*$^{-/-}$ skin.
- The observed granulocyte reduction coincides with visually detected decrease in TNF expression, suggesting a connection between IL-33/ST2 signalling, granulocyte recruitment and TNF secretion in Casp-8^{EKO} animals, which should be explored in the future.

- The presence ph-MLKL in Casp-8^{EKO} skin shows, for the first time, active necroptosis in this model. Furthermore, staining of ph-MLKL shows necroptosis is active at very early stages of lesion development, preceding changes in the epidermis, immune cell recruitment and TNF secretion.
- Deletion of IL-33 or ST2 does not affect the initiation of necroptosis, given that necroptotic markers RIPK3 and ph-MLKL could be found in the non-hyperplastic skin of all lesion-presenting animals.
- Significant differences between Casp-8^{EKO} *Il-33*$^{-/-}$ and Casp-8^{EKO} *St2*$^{-/-}$adult mice have been observed regarding phenotype severity and are yet to be investigated.

Chapter 6

RAGE signalling in the Casp-8^{EKO} skin inflammation model

6.1 Background and aims

HMGB1 is a highly conserved, chromatin-associated protein present in all nucleus-containing cells, which has been extensively studied for its prototypical DAMP functions in mediating inflammation. Release of HMGB1, either through active secretion or passive release upon cell death, triggers, and sustains the inflammatory response through immune cell activation and cytokine production (Bertheloot & Latz, 2017). HMGB1 has been described as a late mediator of lethal systemic inflammation during sepsis (Haichao Wang et al., 1999). In contrast, HMGB1 acts as an early mediator of inflammation and organ damage in ischaemia reperfusion injury (Andrassy et al., 2008; Tsung et al., 2005). Indeed, deleting or neutralizing extracellular HMGB1 in sterile and infection-induced inflammation generally ameliorates disease damage (Andersson et al., 2015).

HMGB1 has been also widely associated with the development of arthritis (Kokkola et al., 2002; Pullerits et al., 2003; Taniguchi et al., 2003) and other chronic inflammatory diseases such as systemic and cutaneous lupus erythematosus (SLE, CLE) (Barkauskaite et al., 2007; Ma et al., 2012; Popovic et al., 2005). Lesions found in the skin of patients with CLE show significantly increased expression of HMGB1 in the dermis and epidermis

(Popovic et al., 2005). Similarly, HMGB1 is produced by psoriatic keratinocytes and increased levels of serum HMGB1 correlate with psoriasis severity (Bergmann et al., 2016; T. Chen et al., 2013). Extracellular HMGB1 is found in skin lesions found in the necroptosis-dependent skin inflammation FADD^{EKO} model (Bonnet et al., 2011), Furthermore, results shown in Chapter 3 suggest a role for HMGB1 in the induction of necroptosis in keratinocytes *in vitro.*

RAGE is the first identified and best studied receptor for HMGB1 and mediates many of the described extracellular functions of HMGB1. Increased expression of RAGE has been detected in several inflammatory lesions and inhibition or deletion of RAGE leads to the improvement of inflammation outcome in sepsis, ischemic brain and tumour development and in arthritis, noting its potential role sustaining inflammation (Lutterloh et al., 2007; Muhammad et al., 2008; Taguchi et al., 2000). RAGE has been shown to mediate and modulate skin inflammation in the context of skin carcinogenesis: although not essential for initiation of inflammation, RAGE contributes to the maintenance of inflammatory reaction as deletion of RAGE protects mice from carcinogenic TPA-induced tumour development (Gebhardt et al., 2008; Riehl et al., 2010) and production of pro-inflammatory cytokines MIP-2 and TNF (Wolf et al., 2010).

In order to determine a possible role of HMGB1 in necroptosis-dependent skin inflammation, this chapter will examine the role of RAGE signalling in the previously described skin inflammation model Casp-8^{EKO}. Constitutive deletion of RAGE allows the downregulation of RAGE-dependent signalling, including RAGE-dependent immune cell activation, which has been shown to be essential for TPA-induced inflammation in the skin (Gebhardt et al., 2008). The keratinocyte-specific role of RAGE during necroptosis-dependent inflammation has also been investigated as to better understand the skin compartment responsible for potential RAGE-

mediated inflammation. Interestingly, an immunomodulatory function has been attributed specifically to epidermal RAGE in TPA-induced skin inflammation (Leibold et al., 2013).

Three different mouse lines have been generated to study the role of RAGE signalling in necroptosis-induced skin inflammation: Casp-8^{EKO}, Casp-8^{EKO} *Rage*$^{-/-}$ and Casp-8^{EKO} RAGE^{EKO}. *Rage*$^{-/-}$ and RAGE^{EKO} animals have been described before and are healthy and fertile, although they develop obesity with time (Leuner et al., 2012). The animals have been studied using the methods and following the aims listed in the introduction of Part II and detailed in Chapter 5. Briefly, the obtained animals were monitored to assess their skin inflammatory phenotype macroscopically and determine the experimental endpoint of the different lines. Immunostaining of the skin samples collected at different timepoints allowed the analysis of the expression of different epidermal proliferation and differentiation makers as well as cell death markers including necroptotic markers RIPK3 and ph-MLKL and apoptotic marker cleaved Casp-3. The presence of immune cell infiltrate in lesions developed in each line was also investigated, together with the presence of other necroptosis-related cytokines such as TNF and IL-33.

6.2 Results

6.2.1 Macroscopical observation and phenotype analysis

Casp-8^{EKO}, Casp-8^{EKO} *Rage*$^{-/-}$ and Casp-8^{EKO} RAGE^{EKO} animals born from the breedings described above start showing skin lesions around P3. The inflammatory phenotype observed in Casp-8^{EKO} at this timepoint was drastically more affected than that observed in Casp-8^{EKO} animals described in Chapter 5. This phenotypical difference has been documented and quantified and is described in Appendix III. All lesion-presenting

animals show multiple lesions on the body surface by P4 (Figure 6.1A, left side) which spread and worsen in severity rapidly, affecting over 20% of the body of these animals by P6 (Figure 6.1A, right side). Based on these observations, an early timepoint to study the phenotype was established at P5. Indeed, quantification of the skin lesions at P5 showed that all lesion-presenting animals showed a significantly different phenotype than littermate controls (Figure 6.1B). Interestingly, no significant difference was observed between the lesion score of Casp-8^{EKO}, Casp-8^{EKO} *Rage*$^{-/-}$ and Casp-8^{EKO} RAGE^{EKO} pups at P5 (Figure 6.1B).

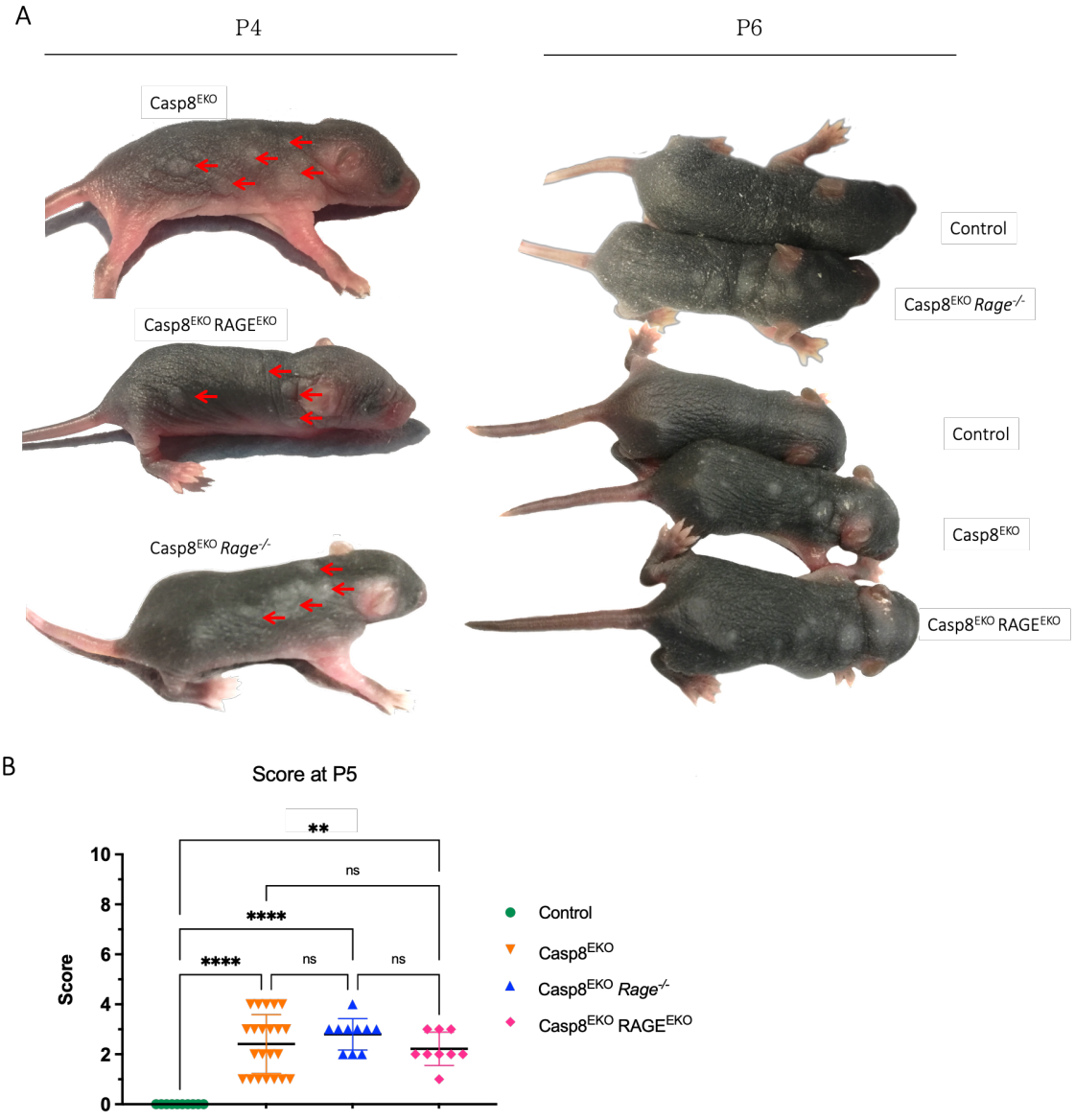

Figure 6.1: Representative images and lesion quantification of the inflammatory phenotypes of Casp-8^{EKO}, Casp-8^{EKO} *Rage*$^{-/-}$ and Casp-8^{EKO} RAGE^{EKO} animals at early stages. (A) Images of Casp-8^{EKO}, Casp-8^{EKO} *Rage*$^{-/-}$, Casp-8^{EKO} RAGE^{EKO} and control littermates at P4 (left side) and P6 (right side). Red arrows point skin lesions. **(B)** The number and severity of the lesions were assessed macroscopically using a scoring system. Graph plots individual values, mean and SD. The statistical analysis performed was Kruskal-Wallis test followed by Dunn's multiple comparison test. ****p<0,0001, **p=0.0046. Number of animals analysed: C8^{EKO} n=22; C8^{EKO} *Rage*$^{-/-}$ n=10; C8^{EKO} RAGE^{EKO} n=9; Control n=10.

Consistent with the initial observations, Casp-8^{EKO}, Casp-8^{EKO} *Rage*$^{-/-}$ and Casp-8^{EKO} RAGE^{EKO} animals reached the maximum lesion score soon after the first timepoint. Some variability was observed between animals, and even though a few survived until P10, most animals reached experimental endpoint at P9. For that reason, animals were culled on P9, which was established as the second timepoint to study the phenotype. Quantification of the lesions at P9 confirmed no significant differences between the three different mouse lines (Figure 6.2B). Lesions affected the abdominal area as well as patches covering the back, neck and face of the animals. As observed in Figure 6.2A, all animals affected by lesions appear runted, with obvious size differences and drastically reduced mobility. These features become obvious after P7, when lesions start covering more than 30% of the total body surface.

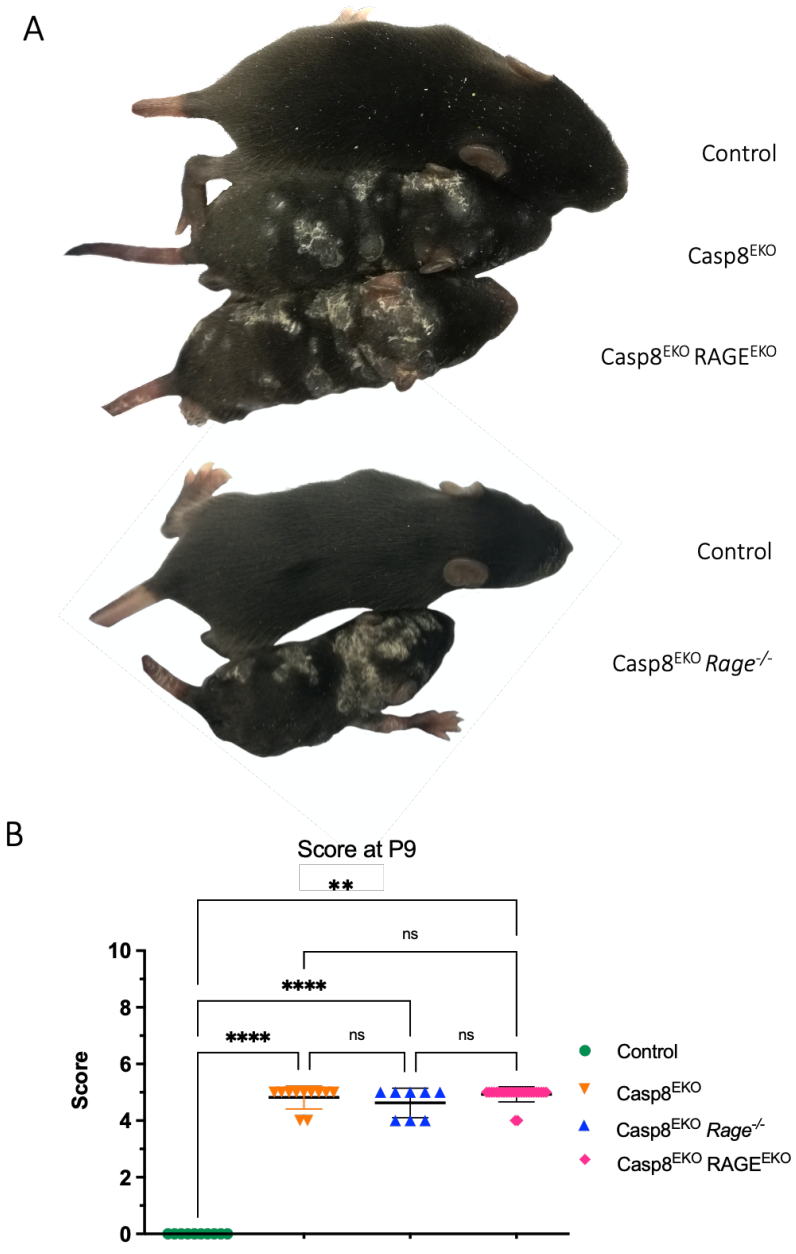

Figure 6.2: Representative images and lesion quantification of the inflammatory phenotypes Casp-8^{EKO}, Casp-8^{EKO} *Rage*$^{-/-}$ and Casp-8^{EKO} RAGE^{EKO} animals at P9. **(A)** Representative images of Casp-8^{EKO}, Casp-8^{EKO} *Rage*$^{-/-}$, Casp-8^{EKO} RAGE^{EKO} and control littermates at P9. **(B)** Graph shows the quantification of lesions through scoring system attending number and severity of these. Graph plots individual values, mean and SD The statistical analysis performed was Kruskal-Wallis test followed by Dunn's multiple comparison test. ****p<0,0001, **p=0.0015. Number of animals analysed: C8^{EKO} n=26; C8^{EKO} *Rage*$^{-/-}$ n=11; C8^{EKO} RAGE^{EKO} n=8; Control n=10

In general, the inflammatory phenotype of all lesion-presenting animals developed at a fast rate. Indeed, the rapid progression of the phenotype was notable as soon as lesions start appearing (Figure 6.1A, left and right panel) and reaches its peak in only 3 to 4 days (Figure 6.2A). To determine if there were any differences in how fast the lesions develop between the different lines, the score of each animal was plotted against their age (in days). Figure 6.3A shows the linear regression analysis of each set of data. Comparison of these models determined that the slope of the lines was not significantly different. In fact, the slope of the lines calculated for Casp-8^{EKO}, Casp-8^{EKO} *Rage*$^{-/-}$ and Casp-8^{EKO} RAGE^{EKO} was almost identical (0,5191, 0,5803 and 0.5428, respectively). Given that skin lesions seemed to affect Casp-8^{EKO} and double KO animals similarly, the survival of the animals was calculated attending to the small variabilities observed in the phenotype. As expected, there was no significant difference between the survival of Casp-8^{EKO}, Casp-8^{EKO} *Rage*$^{-/-}$ and RAGE^{EKO} animals (Figure 6.3B).

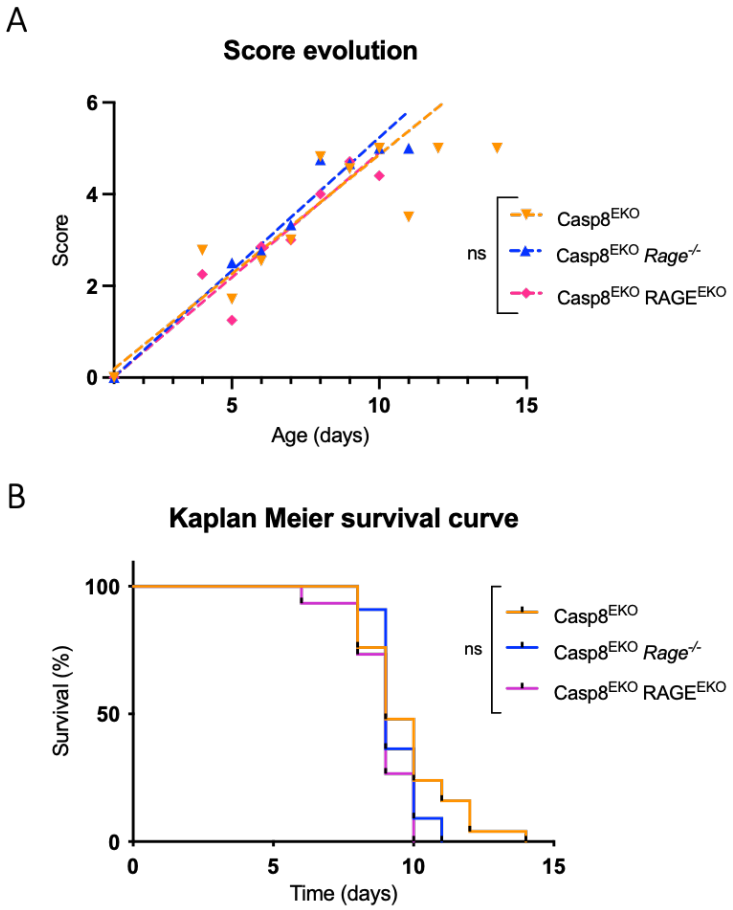

Figure 6.3: Lesion score over time and survival of Casp-8^{EKO}, Casp-8^{EKO} *Rage*$^{-/-}$ and Casp-8^{EKO} RAGE^{EKO} animals. (A) Graph plots lesion score versus time (in days) for the three different lesion-presenting animals. Each set of data is plotted through individual values that represent the mean score of the animals at a determined age. Linear regressions were calculated for each set of data and slope comparison was performed using Graphpad. **(B)** Kaplan Meier survival curve representing the survival of Casp-8^{EKO}, Casp-8^{EKO} *Rage*$^{-/-}$ and Casp-8^{EKO} RAGE^{EKO} animals. The Gehan-Breslow- Wilcoxon test was used for curve comparison statistical analysis. Number of animals analysed: (A) C8^{EKO} n=29, C8^{EKO} *Rage*$^{-/-}$ n=11, C8^{EKO} RAGE^{EKO} n= 24. (B) C8^{EKO} n=25, C8^{EKO} *Rage*$^{-/-}$ n=11, C8^{EKO} RAGE^{EKO} n=15.

6.2.2 Histological analysis of skin samples

Animals were monitored daily soon after birth and skin samples were collected at P5 or P9 and frozen in OCT at -80 °C for further immunohistological analysis. Histological analysis, through H&E staining, of Casp-8^{EKO} and Casp-8^{EKO} RAGE^{EKO} skin samples at P5 showed inflammatory lesions at initial stages. Casp-8^{EKO} *Rage*$^{-/-}$ H&E images and

epidermal thickness analysis at P5 are not available due to accessibility problems to these samples during the COVID-19 pandemic. At this timepoint, Casp-8^{EKO} and Casp-8^{EKO} RAGE^{EKO} samples were mostly non-hyperplastic, but at least one lesion could be observed in all samples analysed. This translated in significantly higher overall epidermal thickness of Casp-8^{EKO} and Casp-8^{EKO} RAGE^{EKO} skin compared to control littermates (Figure 6.4B). The calculated epidermal thickness was not significantly different between Casp-8^{EKO} and Casp-8^{EKO} RAGE^{EKO} skin samples (Figure 6.4B).

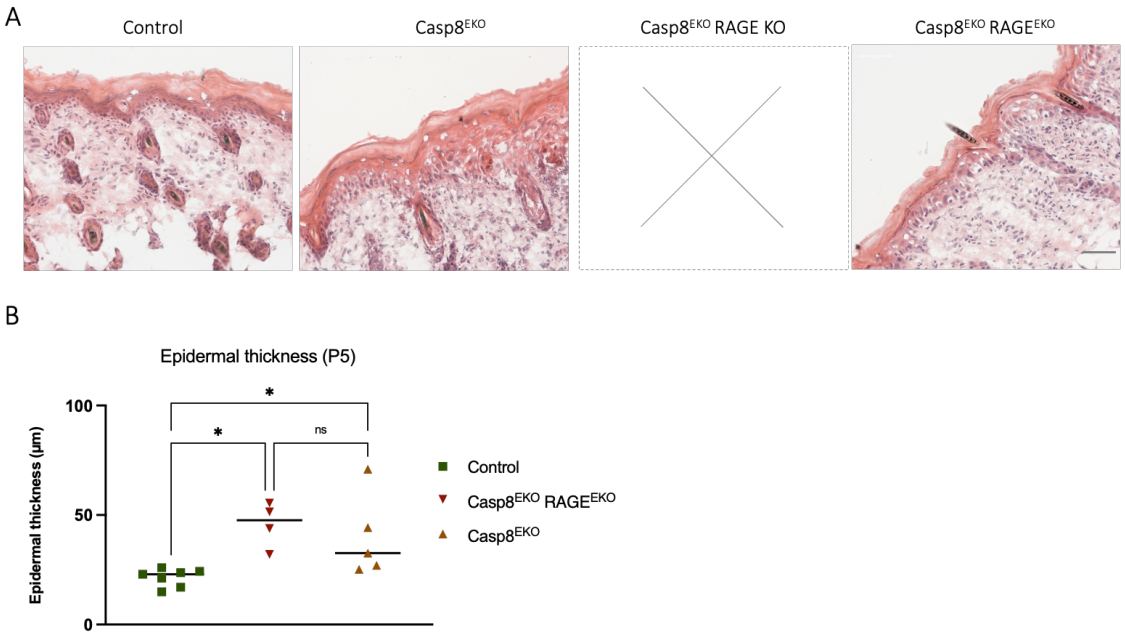

Figure 6.4: Histological analysis and quantification of epidermal thickness of Casp-8^{EKO} and Casp-8^{EKO} RAGE^{EKO} samples at P5. (A) Representative images of the histological samples obtained for each line. Images obtained using Zeiss Apotome Axio Observer microscope, magnification 40X. Scale bar represents 50 µm. **(B)** Epidermal thickness quantification of samples collected from Casp-8^{EKO}, Casp-8^{EKO} RAGE^{EKO} and control littermates. Graph shows individual values and their mean. The statistical analysis performed was Kruskal-Wallis followed by Dunn's multiple comparison test. *p=0.0118 (A-B); *p=0.0341 (A-C). Number of animals analysed: C8^{EKO} n=5; C8 ^{EKO} *Rage*$^{-/-}$ n=0; C8 ^{EKO} RAGE^{EKO} n=4; Control n=7.

H&E staining of Casp-8^{EKO} *Rage*$^{-/-}$ and Casp-8^{EKO} RAGE^{EKO} P9 skin samples revealed an elevated number of inflammatory lesions, showing similar histological features observed in Casp-8^{EKO} littermates (see

Appendix III). These included increased dermal cellularity, marked acanthosis with clear necrotic keratinocytes in the basal layer and marked hyperkeratosis (Figure 6.5A). Almost the totality of the samples analysed were hyperplastic at this stage. Indeed, the quantification of lesions per sample was close to 100% (mean value) and was not significantly different for single and double knock-out animals (Figure 6.5B). The high number of lesions translated in a strong increase of the epidermal thickness. Casp-8^{EKO}, Casp-8^{EKO} *Rage*$^{-/-}$ and Casp-8^{EKO} RAGE^{EKO} skin samples showed significantly higher epidermal thickness than control animals (Figure 6.5C). As expected, no differences in epidermal thickness were found between the three lesion-presenting lines (Figure 6.5C).

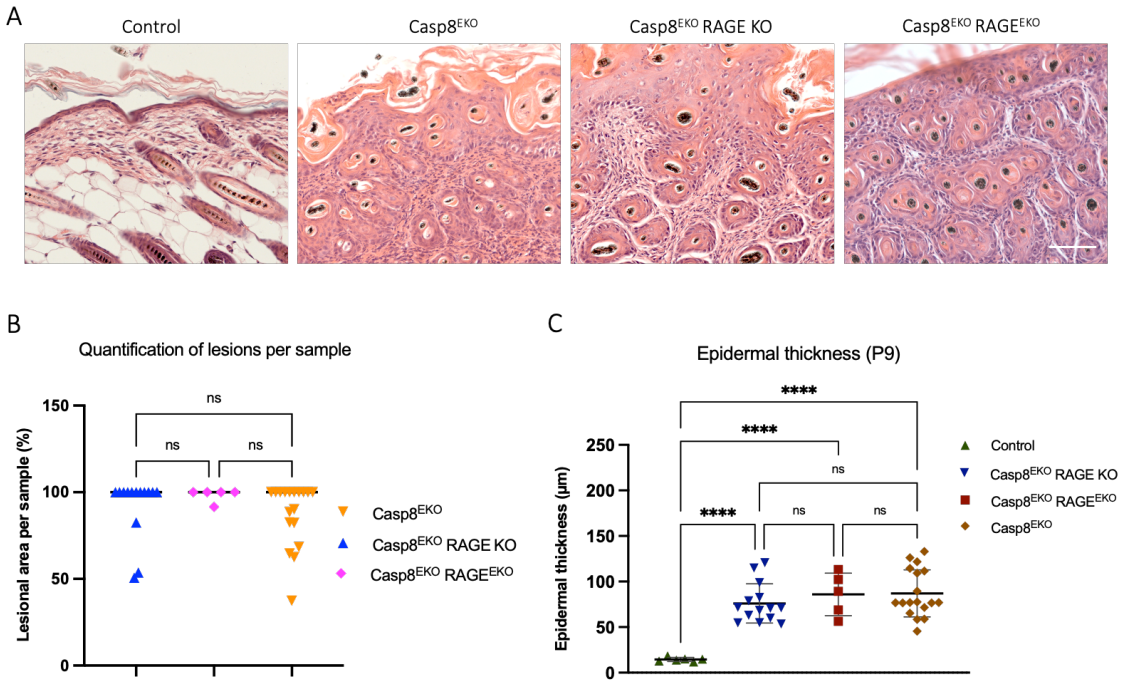

Figure 6.5: Histological analysis, lesion and epidermal thickness quantification of Casp-8^{EKO}, Casp-8^{EKO} *Rage*$^{-/-}$ and Casp-8^{EKO} RAGE^{EKO} samples at P9. (A) Representative images of the histological observations made foreach line. Images obtained using Zeiss Apotome Axio Observer microscope, magnification 40X. Scale bar represents 50 µm. **(B)** Quantification of lesions found in skin sections collected at P9 through histological analysis. Each dot represents the percentage a specific sample affected by lesions; the mean of each set of data is also represented. Statistical analysis performed is one-way ANOVA followed by Turkey multiple comparison test. **(C)** Epidermal thickness quantification of samples collected from

Casp-8^{EKO}, Casp-8^{EKO} *Rage*$^{-/-}$, Casp-8^{EKO} RAGE^{EKO} animals and control littermates. Graph shows individual values and their mean ± SD. The statistical analysis performed for (B) and (C) was Kruskal-Wallis test followed by Dunn's multiple comparison test, ***p=0,0004, *p=0.0170 (Control- C8^{EKO} *Rage*$^{-/-}$), *p=0.0170 (Control- C8^{EKO} RAGE^{EKO}). Number of animals analysed for: C8^{EKO} n=18; C8^{EKO} *Rage*$^{-/-}$ n=14; C8^{EKO} RAGE^{EKO} n=5; Control n=6.

6.2.3 Immunohistological analysis of proliferation and differentiation markers in the skin

In order to assess the lesions found in Casp-8^{EKO}, Casp-8^{EKO} *Rage*$^{-/-}$ and Casp-8^{EKO} RAGE^{EKO} skin, samples were stained for different epidermal proliferation and differentiation markers. Epidermal stem cell marker KRT-6, normally expressed only in hair follicles stem cells, was highly expressed throughout the thickened epidermis of early lesions (Figure 6.6). Similarly, the specific marker of proliferating basal keratinocytes KRT-14 was expressed throughout hyperplastic patches of skin, evidencing a high proliferation state of the epidermal keratinocytes at P5 (Figure 6.6). Indeed, proliferation marker Ki-67 was highly expressed along the basal layer of the epidermis as well as in some cells found in upper layers (Figure 6.6). No differences were found in the proliferation state of Casp-8^{EKO} lesions compared to Casp-8^{EKO} *Rage*$^{-/-}$ and Casp-8^{EKO} RAGE^{EKO} skin at P5 (Figure 6.6). At P9, hyperplastic patches of skin express KRT-6 and KRT-14 throughout all epidermal layers (Figure 6.7). Ki-67 positive cells are found abundantly in the basal layer and intermittently in the upper layers (Figure 6.7). Again, no differences in these markers were found between Casp-8^{EKO}, Casp-8^{EKO} *Rage*$^{-/-}$ and Casp-8^{EKO} RAGE^{EKO} lesions at P9.

Suprabasal differentiation marker KRT-10 was found localised intermittently in hyperplasic patches at P5, mostly restricted to a thickened and slightly altered suprabasal layer (Figure 6.6). Loricrin, a late differentiation marker expressed in the granular layer, was limited to outer

layers of the epidermis, even in very hyperplastic patches (Figure 6.6). Generally, the expression of suprabasal marker KRT-10 was less altered than the expression of late differentiation marker LOR, in lesions affecting Casp-8^{EKO}, Casp-8^{EKO} *Rage*$^{-/-}$ and Casp-8^{EKO} RAGE^{EKO} animals. KRT-10 was expressed inside keratinocytes dispersed around the epidermis, mostly in suprabasal layers, indicating impaired and altered differentiation states of the keratinocytes at P9 (Figure 6.7). The expression of LOR was also altered in P9 lesions. With less intensity than KRT-10, some LOR-expressing keratinocytes were distributed in the outer layers of the epidermis (Figure 6.7). Again, no differences were found between the three different mouse lines (Figure 6.7).

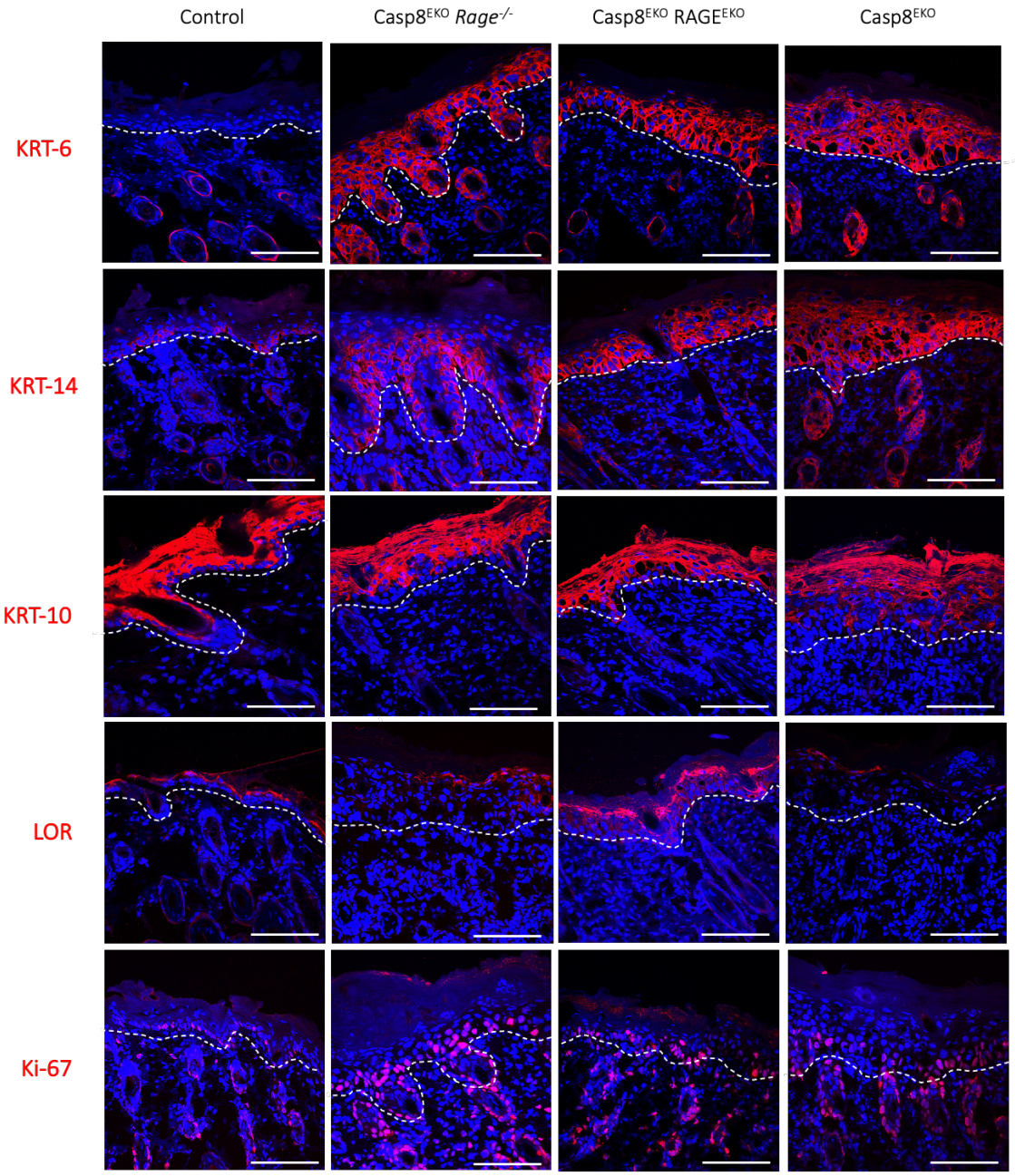

Figure 6.6: Immunohistological analysis of proliferation and differentiation markers in Casp-8^{EKO}, Casp-8^{EKO} *Rage*$^{-/-}$ and Casp-8^{EKO} RAGE^{EKO} skin at P5. Skin samples were collected at P5, fixed and immunostained (red) for stem cell marker KRT-6 and KRT-14, differentiation markers KRT-10 and LOR and proliferation marker Ki-67. Nuclei were stained with DAPI (blue). Representative images have been selected for each line. Images were obtained using Zeiss LSM 880 scanning confocal microscope using a Z-stack function at magnification 63X. Scale bar represents 50 μm. Animals analysed for each genotype: KRT-6: C8^{EKO} n=5, C8^{EKO} *Rage*$^{-/-}$ n=2, C8^{EKO} RAGE^{EKO} n=6, Control n=2. KRT-14: C8^{EKO} n=5 C8^{EKO} *Rage*$^{-/-}$ n=2, C8^{EKO} RAGE^{EKO} n=6, Control n=X. KRT-10: C8^{EKO} n=5, C8^{EKO} *Rage*$^{-/-}$ n=2, C8^{EKO} RAGE^{EKO} n=X6 Control n=3. LOR: C8^{EKO} n=5, C8^{EKO} *Rage*$^{-/-}$ n=2, C8^{EKO} RAGE^{EKO} n=5, Control n=2. Ki-67: C8^{EKO} n=5, C8^{EKO} *Rage*$^{-/-}$ n=2, C8^{EKO} RAGE^{EKO} n=6, Control n=2.

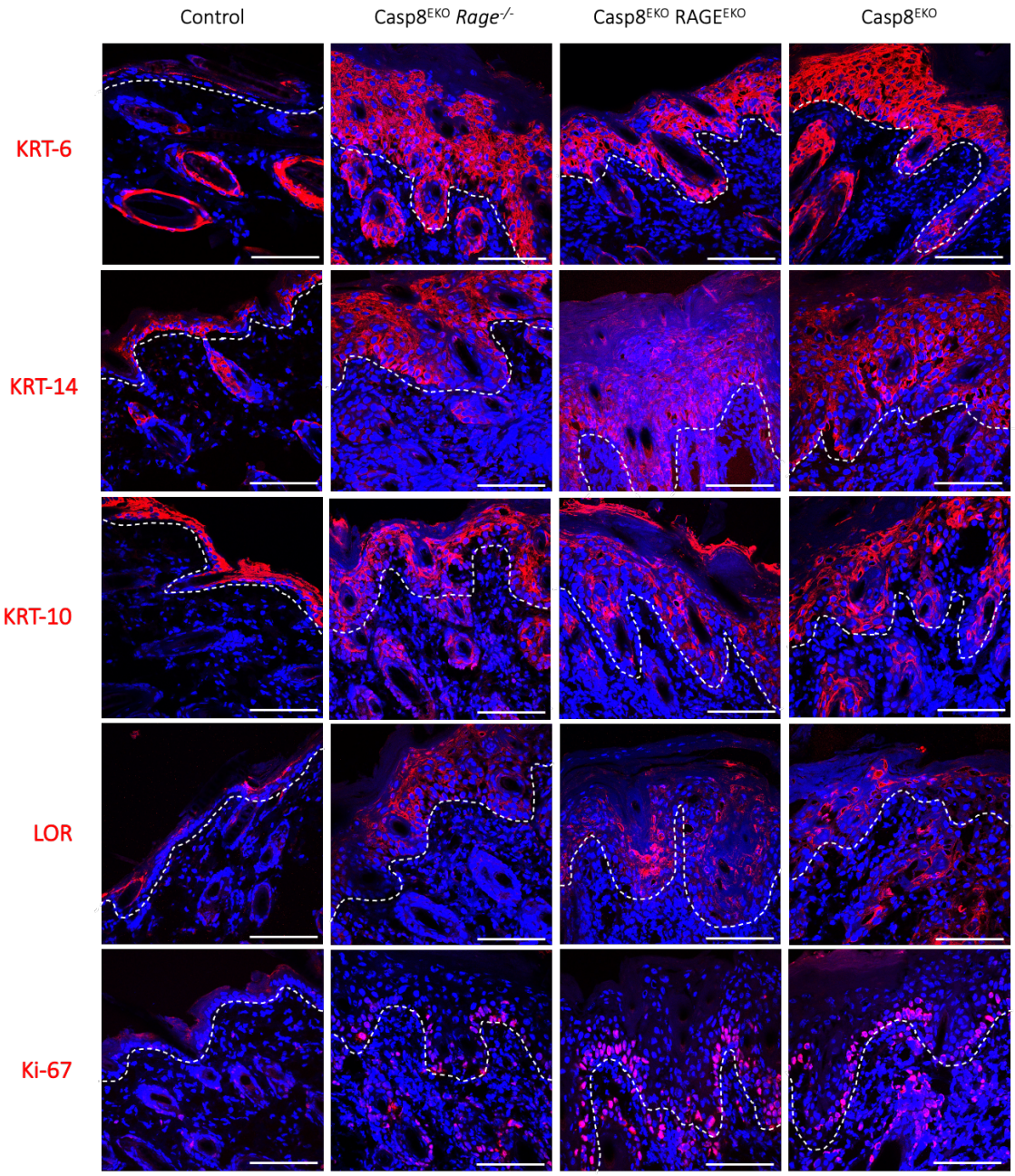

Figure 6.7: Immunohistological analysis of proliferation and differentiation markers in Casp-8^{EKO}, Casp-8^{EKO} *Rage*$^{-/-}$ and Casp-8^{EKO} RAGE^{EKO} skin at P9. Skin samples were collected at P9, fixed and immunostained (red) for stem cell marker KRT-6 and KRT-14, differentiation markers KRT-10 and LOR and proliferation marker Ki-67. Nuclei were stained with DAPI (blue). Representative images have been selected for each line. Images were obtained using Zeiss LSM 880 scanning confocal microscope using a Z-stack function at magnification 63X. Scale bar represents 50 μm. Animals analysed for each genotype: KRT-6: C8^{EKO} n=9, C8^{EKO} *Rage*$^{-/-}$ n=4, C8^{EKO} RAGE^{EKO} n=4, Control n=3. KRT-14: C8^{EKO} n=9, C8^{EKO} *Rage*$^{-/-}$ n=4, C8^{EKO} RAGE^{EKO} n=7, Control n=2. KRT-10: C8^{EKO} n=8, C8^{EKO} *Rage*$^{-/-}$ n=6, C8^{EKO} RAGE^{EKO} n=13, Control n=3. LOR: C8^{EKO} n=6, C8^{EKO} *Rage*$^{-/-}$ n=5, C8^{EKO}

RAGE^{EKO} n=5, Control n=X. Ki-67: C8^{EKO} n=9, C8^{EKO} *Rage*$^{-/-}$ n=4, C8^{EKO} RAGE^{EKO} n=5, Control n=2.

6.2.4 Immunohistological analysis of necroptotic and apoptotic markers

The presence of necroptotic and apoptotic markers in the skin of Casp-8^{EKO} *Rage*$^{-/-}$ and Casp-8^{EKO} RAGE^{EKO} was assessed through immunostainings. Main necroptosis effector molecule, ph-MLKL, was highly expressed in the membrane of keratinocytes throughout the epidermis of hyperplastic patches (Figure 6.8). Necroptotic, ph-MLKL-positive keratinocytes could be found in the skin of the three studied lines (Figure 6.8A). However, a slight decrease in ph-MLKL expression was detected in the skin of Casp-8^{EKO} RAGE^{EKO} animals at P9, when compared to Casp-8^{EKO} *Rage*$^{-/-}$ and Casp-8^{EKO} animals (Figure 6.8B). RIPK3 expression was increased in hyperplastic patches of skin found in Casp-8^{EKO} and double knock-out animals at P5 (Figure 6.8A) and P9 (Figure 6.8B). RIPK3 expression at earlier stages of lesion development (P5) seemed to be slightly more restricted to the basal layer (Figure 6.8A). RIPK3 staining of Casp-8^{EKO} *Rage*$^{-/-}$ skin at P5 was unsuccessful due to technical difficulties.

None or very few scattered cleaved Casp-3 positive cells could be found in the epidermis of Casp-8^{EKO} *Rage*$^{-/-}$ and Casp-8^{EKO} RAGE^{EKO} animals at P5 (Figure 6.8A) and P9 (Figure 6.8B), confirming that apoptosis does not play a role in the development of Casp-8^{EKO} skin inflammatory phenotype. A positive control of the cleaved Casp-3 staining is included in section 6.2.5. In conclusion, we can confirm that necroptosis is active in the skin lesions caused by specific deletion of Casp-8, while apoptosis is generally absent. Furthermore, it is suggested that the deletion of RAGE does not

affect the initiation or propagation of necroptosis in the inflammatory phenotype.

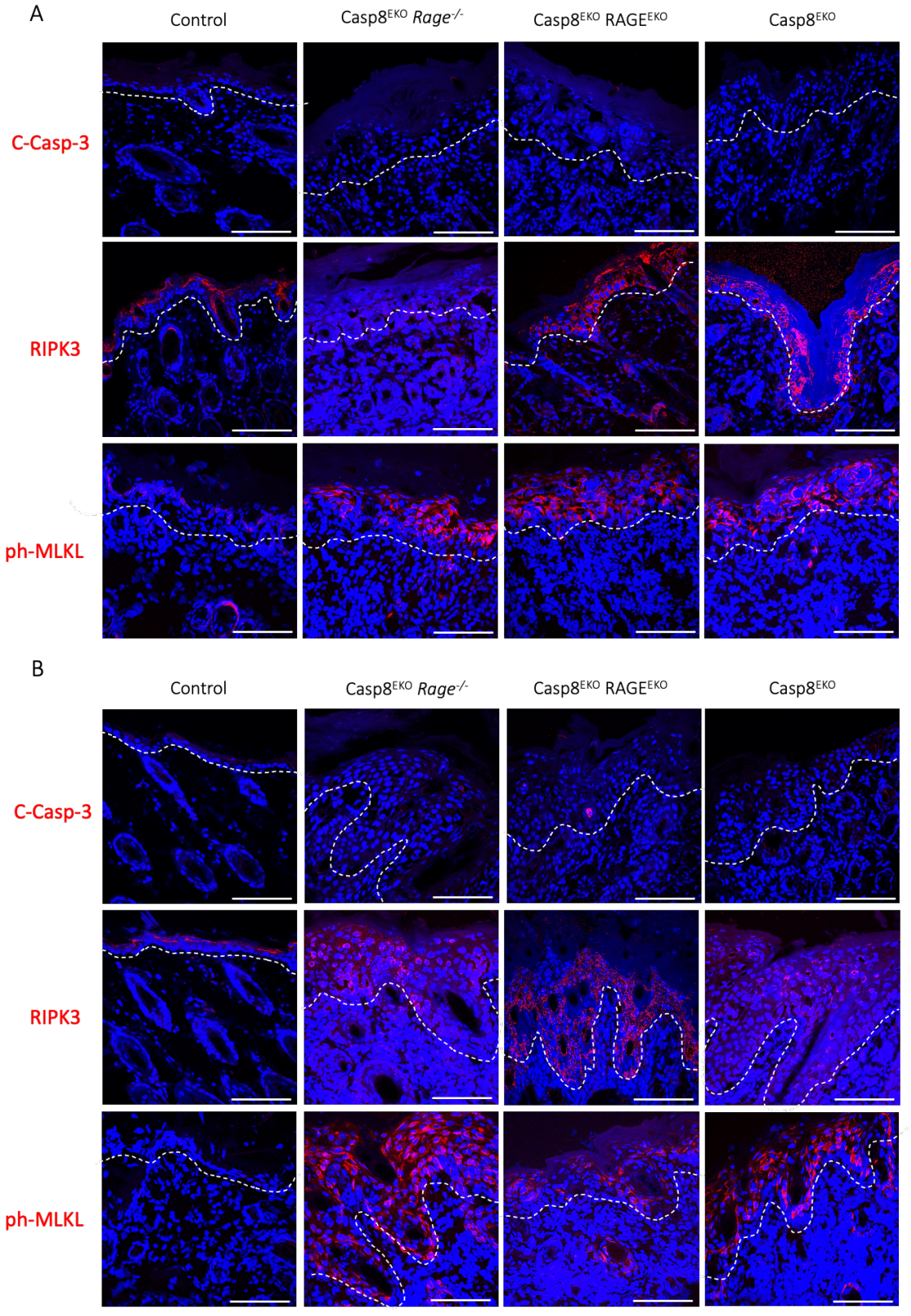

Figure 6.8: Immunohistological analysis of cell death markers in Casp-8^{EKO}, Casp-8^{EKO} *Rage*$^{-/-}$ and Casp-8^{EKO} RAGE^{EKO} skin samples at P5 and P9. Skin samples were collected at **(A)** P5 and **(B)** P9, fixed and immunostained (red) for apoptotic marker, cleaved Casp-3 (C-Casp-3) and necroptosis markers RIPK3 and ph-MLKL. Nuclei were stained with DAPI (blue). Representative images have been selected for each line. Images were obtained using Zeiss LSM 880 scanning confocal microscope using a Z-stack function at magnification 63X. Scale bar represents 50 μm. (A) Animals analysed for each genotype: C-Casp-3: C8^{EKO} P5 n=3, P9 n=6; C8^{EKO} *Rage*$^{-/-}$ P5 n=2, P9 n=4; C8^{EKO} RAGE^{EKO} P5 n=4, P9 n=4; Control P5 n=2, P9 n=2. RIPK3: C8^{EKO} P5 n=4, P9 n=6; C8^{EKO} *Rage*$^{-/-}$ P5 n=2, P9 n=5; C8^{EKO} RAGE^{EKO} P5 n=5, P9 n=4; Control P5 n=X, P9 n=2. Ph-MLKL: C8^{EKO} P5 n=6, P9 n=7; C8^{EKO} *Rage*$^{-/-}$ P5 n=2, P9 n=5; C8^{EKO} RAGE^{EKO} P5 n=5, P9 n=5; Control P5 n=3, P9 n=2.

6.2.5 Immunohistological analysis of inflammatory immune cells

Skin lesions found in Casp-8^{EKO}, Casp-8^{EKO} *Rage*$^{-/-}$ and Casp-8^{EKO} RAGE^{EKO} animals were characterised by the presence of a dense cell infiltrate in the dermis. In order to better understand the infiltrating immune response in the lesions, skin samples were stained for T-cells (CD3), macrophages (F4/80) and granulocytes (Gr-1).

As seen in Chapter 5, CD3+ cells could be found in the epidermis and hair follicles of control skin at both timepoints (Figure 6.9A and B), corresponding to skin resident DETCs. Some of these cells were still present in lesional areas found in single and double knock-out skin at P5 (Figure 6.9A) and P9 (Figure 6.9B). In addition, round CD3-expressing cells start appearing in the dermis of hyperplastic skin patches, indicating T-cell infiltration (Figure 6.9A and B). Epidermal specific or full body knock-out of RAGE did not seem to alter CD3+ cells infiltrate from Casp-8^{EKO} skin.

F4/80-positive cells infiltrate the dermis of Casp-8^{EKO}, Casp-8^{EKO} *Rage*$^{-/-}$ and Casp-8^{EKO} RAGE^{EKO} animals at early stages of lesion development (P5,

Figure 6.9A), which increases at later stages, when animals reach experimental endpoint (Figure 6.9B). No differences in macrophage infiltrate were found between the different mouse lines. Granulocytes were also present in the immune infiltrate associated with hyperplastic skin. Gr-1+ infiltrating cells could be found both in the dermis and epidermis of P5 lesions (Figure 6.9A), corresponding to neutrophil abscesses also observed at this timepoint through histological observation (Figure 6.4B). This infiltrate was abundant in terminal stages of the Casp-8^{EKO}, Casp-8^{EKO} *Rage*$^{-/-}$ and Casp-8^{EKO} RAGE^{EKO} phenotypes and no differences were found between the three lines (Figure 6.9B).

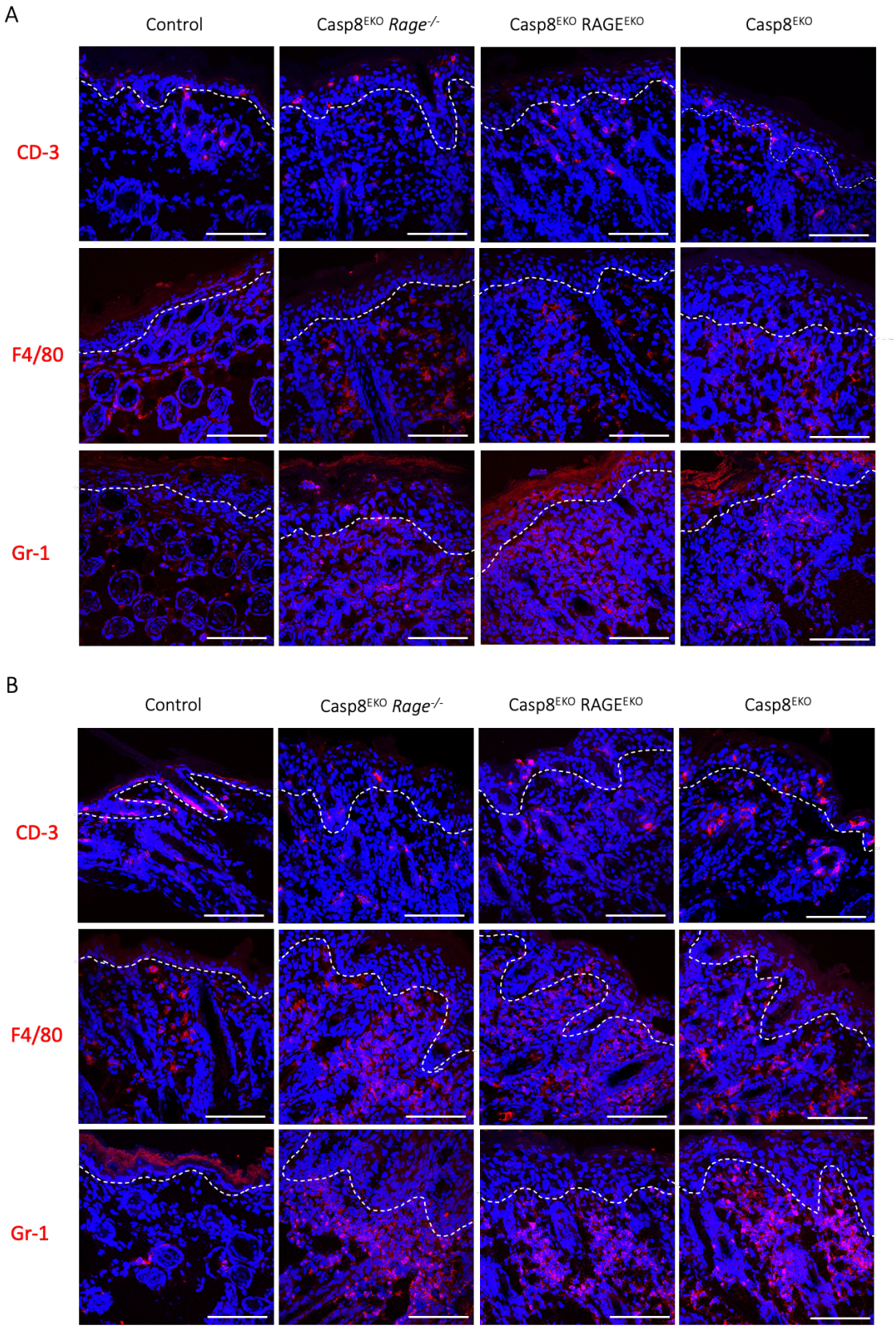

Figure 6.9: Immunohistological analysis of immune cell infiltrate in Casp-8^{EKO}, Casp-8^{EKO} *Rage*$^{-/-}$ and Casp-8^{EKO} RAGE^{EKO} skin samples at P5 and P9. Skin samples were collected at **(A)** P5 and **(B)** P9, fixed and immunostained (red) for

T-cell marker CD3, macrophage marker F4/80 and granulocyte marker Gr-1. Nuclei were stained with DAPI (blue). Representative images have been selected for each line. Images were obtained using Zeiss LSM 880 scanning confocal microscope using a Z-stack function at magnification 63X. Scale bar represents 50 μm. Animals analysed for each genotype: CD3: C8^{EKO} P5 n=5, P9 n=8; C8^{EKO} *Rage*$^{-/-}$ P5 n=2, P9 n=5; C8^{EKO} RAGE^{EKO} P5 n=4, P9 n=6; Control P5 n=2, P9 n=2. F4/80: C8^{EKO} P5 n=5, P9 n=7; C8^{EKO} *Rage*$^{-/-}$ P5 n=2, P9 n=5; C8^{EKO} RAGE^{EKO} P5 n=, 4P9 n=5; Control P5 n=3, P9 n=3. Gr-1: C8^{EKO} P5 n=6, P9 n=6; C8^{EKO} *Rage*$^{-/-}$ P5 n=2, P9 n=6; C8^{EKO} RAGE^{EKO} P5 n=4, P9 n=5; Control P5 n=3, P9 n=3.

6.2.6 Immunohistological analysis of inflammatory cytokines

TNF and IL-33 play important roles in the development of necroptosis-dependent skin inflammation (Bonnet et al., 2011; Kovalenko et al., 2009; Chapter 5 of this thesis). TNF and IL-33 stainings were performed in order to determine what role RAGE signalling plays in the expression of these inflammatory cytokines.

Both TNF and IL-33 were associated with skin lesions at P5 and P9 (Figure 6.10A and B). A strong epidermis-localised staining of IL-33 could be detected in hyperplastic skin patches in Casp-8^{EKO} *Rage*$^{-/-}$ samples at P5 which was slightly weaker in lesions found in Casp-8^{EKO} and Casp-8^{EKO} RAGE^{EKO} skin (Figure 6.10A). IL-33 expression was similar between Casp-8^{EKO} and Casp-8^{EKO} *Rage*$^{-/-}$ skin at P9 but remained weak in Casp-8^{EKO} RAGE^{EKO} samples (Figure 6.10B). TNF was detected around infiltrating cells in the dermis near hyperplastic patches of skin. It could be found in single and double knock-out skin early lesions (Figure 6.10A). At P9, a greater amount of TNF-positive staining was observed, mainly due to an increase in infiltrating cells surrounding lesional areas (Figure 6.10B). No differences in TNF expression were found between Casp-8^{EKO}, Casp-8^{EKO} *Rage*$^{-/-}$ and Casp-8^{EKO} RAGE^{EKO} animals at the studied timepoints.

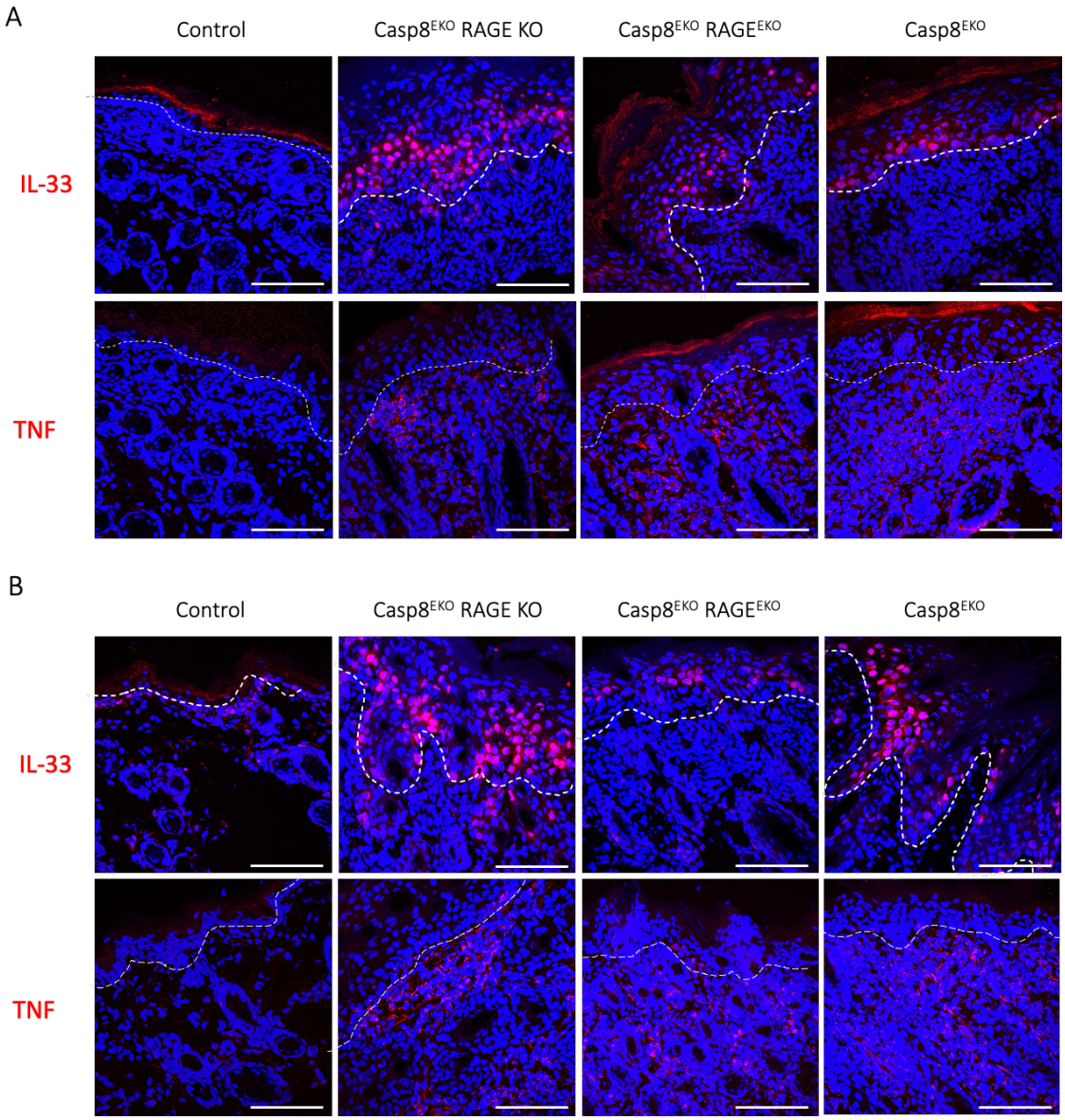

Figure 6.10: Immunohistological analysis of inflammatory cytokines in Casp-8^{EKO}, Casp-8^{EKO} *Rage*$^{-/-}$ and Casp-8^{EKO} RAGE^{EKO} skin samples at P5 and P9. Skin samples were collected at **(A)** P5 and **(B)** P9, fixed and immunostained (red) for TNF and IL-33. Nuclei were stained with DAPI (blue). Representative images have been selected for each line. Images were obtained using Zeiss LSM 880 scanning confocal microscope using a Z-stack function at magnification 63X. Scale bar represents 50 µm. Animals analysed for each genotype: IL-33: C8^{EKO} P5 n=5, P9 n=9; C8^{EKO} *Rage*$^{-/-}$ P5 n=2, P9 n=4; C8^{EKO} RAGE^{EKO} P5 n=5, P9 n=6; Control P5 n=3, P9 n=2. TNF: C8^{EKO} P5 n=4, P9 n=8; C8^{EKO} *Rage*$^{-/-}$ P5 n=2, P9 n=5; C8^{EKO} RAGE^{EKO} P5 n=4, P9 n=5; Control P5 n=3, P9 n=2.

6.3 Discussion

Release of HMGB1 has been shown to occur during necroptotic cell death (Weinlich et al., 2017) and has been found in the epidermis necroptosis-induced skin inflammation model FADD^{EKO} (Bonnet et al., 2011). Interaction of HMGB1 and its receptor RAGE has been reported to activate a range of signalling pathways which promote cytokine production and cell survival (R. Kang et al., 2014). This chapter has studied the potential role of HMGB1/RAGE signalling in Casp-8^{EKO} skin inflammation through the generation and analysis of three mouse lines: Casp-8^{EKO}, Casp-8^{EKO} *Rage*$^{-/-}$ and Casp-8^{EKO} RAGE^{EKO}. No phenotypical differences have been observed between these animals regarding lesion severity and survival, suggesting RAGE signalling does not play a role in necroptosis-dependent skin inflammation.

Deletion of RAGE constitutively or specifically from keratinocytes did not lead to a delay in the development of lesions, as Casp-8^{EKO} *Rage*$^{-/-}$ and Casp-8^{EKO} RAGE^{EKO} start showing pustular skin lesions soon after birth (P4), at a similar time than Casp-8^{EKO} animals. These lesions developed rapidly, and all animals reached the experimental endpoint by P9. Some variability of the inflammatory phenotype was observed between animals with the same genotype, probably due to the mixed genetic background of the animals (see Appendix III). Macroscopical assessment and quantification of the lesions found in the inflammatory phenotypes at P5 and P9 showed no differences between the studied mouse lines which translated in no significantly different phenotype score at these timepoints. These results did not match the initial hypothesis, contrasting the extensively described pro-inflammatory role of HMGB1, which has been found to be key in acute sepsis or sterile inflammation as well as in chronic inflammatory diseases (R. Kang et al., 2014). Signalling through RAGE has

also been found to be a critical component of the deleterious effects of acute inflammation, such as sepsis-related inflammation. Indeed, genetic ablation of RAGE has been found to provide protection from the lethal effect of septic shock caused by cecal ligation and puncture (Liliensiek et al., 2004; Lutterloh et al., 2007). Similarly, inhibition of RAGE expression or activity has been found to reduce inflammatory responses in animal models of diabetic atherosclerosis (Soro-Paavonen et al., 2008) and delayed-type hypersensitivity (Hofmann et al., 1999), as well as to mediate ischemic brain damage (Muhammad et al., 2008), prevent aortic aneurysm (F. Zhang et al., 2010), or confer renoprotection (Hagiwara et al., 2018). In fact, studies claiming that RAGE does not contribute to injury or inflammatory responses are uncommon. RAGE has been found to not contribute to cardiac remodelling induced by pressure overload (H. Lin et al., 2016). In addition, although contradictory, some studies report that the deletion of RAGE has no effect on pulmonary injury during sepsis due to Gram- infection (Achouiti et al., 2016; van Zoelen et al., 2009).

Ubiquitous deletion of RAGE prevents production of inflammatory mediators in vivo (Zhong et al., 2020) and leads to impairment of chronic inflammatory response in the skin, induced by the phorbol ester TPA (Gebhardt et al., 2008; Riehl et al., 2010). Keratinocyte-specific deletion of RAGE has been shown to modulate the kinetics of TPA-induced skin inflammation *in vivo* (Leibold et al., 2013). In this study, TPA-induced hyperplasia was not affected by the keratinocyte-specific deletion of RAGE during the initial phase (up to 24 hours). 48 hours after administration, however, Casp-8^{EKO} RAGE^{EKO} animals exhibited a significant reduction in epidermal thickness when compared to control animals (Leibold et al., 2013). While RAGE might modulate TPA-induced inflammation, my results suggest that RAGE does not contribute to necroptosis-dependent skin inflammation.

It must be considered that the efficiency of the Cre-lox system regarding the deletion of RAGE specifically in keratinocytes has not been investigated. The efficiency of the Cre-lox system can vary between different genes, as some are more easily recombined than others due to accessibility: the chromatin state can prevent Cre from accessing the loxP sites (Turlo et al., 2010; Vooijs et al., 2001). Although no significant differences have been found between Casp8^{EKO} *Rage*$^{-/-}$ and Casp8^{EKO} RAGE^{EKO} animals, it could be arguable that compensatory mechanisms play a role in the outcome of these phenotypes. On the other hand, a previous study has reported efficient deletion of RAGE from epidermal keratinocytes using the KRT-14 promoter, setting precedent on the good accessibility of this gene by the Cre-lox system (Leibold et al., 2013). Nevertheless, isolation of the epidermal tissue from RAGEEKO would help confirm the efficacy of the deletion in the animals investigated in this chapter.

Histological analysis of the skin samples collected from the Casp-8^{EKO} RAGE^{EKO} and Casp-8^{EKO} animals revealed no differences between the lines studied regarding epidermal thickness and immune cell infiltration. Due to technical difficulties, images of H&E stainings from Casp-8^{EKO} *Rage*$^{-/-}$ samples at P5 and epidermal thickness measurements are not available. Nonetheless, no differences were observed between these samples and those collected from Casp-8^{EKO} RAGE^{EKO} and Casp-8^{EKO} when the epidermal thickness was assessed by microscopy using DAPI staining in further immunohistological analysis. Of note, a forced reduction of the animal colony and limited access to the animal facility during the COVID-19 pandemic impeded the collection of sufficient Casp-8^{EKO} *Rage*$^{-/-}$ samples at P5 ($n<5$). Although the analysis of a greater number of samples would be ideal, considering the reproducibility of the phenotype and that

no differences are observed between the different lines at P9, no differences are expected to be observed from additional samples.

It has been shown that RAGE is important for the establishment and maintenance of an innate immune reaction mediated by neutrophils, monocytes and macrophages. Deletion of RAGE reduces dermal immune cell infiltration (Gebhardt et al., 2008), while *Rage*$^{-/-}$ mice can mount a normal adaptative immune response (Liliensiek et al., 2004). Furthermore, HMGB1-mediated recruitment of neutrophils following tissue injury has been shown to be dependent on RAGE, and not on other HMGB1 receptors such as TLR-4 or CXCR4 (Huebener et al., 2015) However, my results show that constitutive or keratinocyte-specific RAGE deficiency did not affect the infiltration of CD3, F4/80 or Gr-1 positive cells in necroptosis-dependent skin inflammation.

Deletion of RAGE has been directly associated with a decrease in necroptotic cell death *in vitro* (Faust, 2020). In fact, direct interaction between RAGE and RIPK3 has been reported (Faust, 2020). However, despite some technical difficulties regarding RIPK3 immunostaining, the expression of necroptotic marker RIPK3 was not affected by constitutive or keratinocyte-specific deletion of RAGE from the Casp-8^{EKO} model at P5 or P9. A slight decrease in the expression of ph-MLKL was observed in the skin collected from Casp-8^{EKO} RAGE^{EKO}. Interestingly, a similar reduction was observed in the expression of IL-33 in these animals. Evidence gathered during the experimental procedures suggests that the quality of some of the skin samples collected from these animals is relatively poor (i.e., some stainings had to be repeated). Hence, stainings using freshly cut samples are needed to confirm these observations. Nevertheless, the obtained results point towards a possible protective role of RAGE, which is dependent on a different compartment than the epidermis, such as infiltrating immune cells.

Even though the deletion of RAGE did not seem to affect the outcome of the Casp-8^{EKO} inflammation model, HMGB1 could still play a role in necroptosis-dependent skin inflammation. In recent years, an increasing number of studies have found TLR-4 as a major receptor for HMGB1 (M. Yu et al., 2006). Oxidation converts HMGB1 into a potent activator of pro-inflammatory production via TLR-4 receptor stimulation. TLR-4 activation of macrophages through HMGB1 treatment leads to the production of TNF in the absence of RAGE (H. Yang et al., 2010). Similarly, production of inflammatory cytokines TNF-α, MIP-2, IL-6, IL-1β, and IL-10 is significantly inhibited in macrophages from HMGB1-stimulated TLR-4-deficient mice (H. Yang et al., 2010). In contrast, these cytokines are produced normally by HMGB1-stimulated TLR2- and RAGE-deficient macrophages (H. Yang et al., 2010), suggesting that TLR4 might be the main receptor for macrophage activation, cytokine release and tissue injury (Apetoh et al., 2007; J. Fan et al., 2007; Tsung, Klune, et al., 2007; Z. Yang et al., 2013).

Regulation of the HMGB1 redox state has been found to be dynamic, tissue and environment-specific (Ferrara et al., 2020), suggesting that the predilection to interact different receptors could also be. In the skin, both RAGE and TLR-4 neutralisation result in enhanced wound healing of InVee mice, a disease model of psoriasis-like dermatitis that constitutively expresses mitogen-activated protein kinase (MEK1) in the epidermis. In fact, the effect of TLR-4 neutralisation was slightly higher than the one observed with RAGE (Hoste et al., 2019). Interestingly, blockade of RAGE, TLR-4 or TLR-2 alone only partly reduces the activation, migration and collagen synthesis of fibroblasts, while blocking of all three receptors had an additive effect and returned activation markers to basal levels, suggesting a compensatory effect of these receptors during hypertrophic scaring (Jingling Zhao et al., 2018). This possible compensatory effect

between TLR-4 and RAGE signalling could explain why the deletion of RAGE did not seem to have an effect in the Casp-8^{EKO} inflammatory phenotype. Another study, however, has reported that the deletion of RAGE decreases TLR-4 expression in macrophages *in vivo* (Zhong et al., 2020), in contrast with the possible compensatory effect. Further work could focus on blocking the interaction between HMGB1 and TLR-4 through the small molecule inhibitor P5779, which acts as an MD-2 antagonist or the deletion of the *Tlr-4* gene. Administration of this inhibitor to Casp-8^{EKO} and Casp-8^{EKO} *Rage*$^{-/-}$ and Casp-8^{EKO} RAGE^{EKO} animals would help to better understand the role these receptors play in necroptosis-dependent skin inflammation.

Other than TLR-4, HMGB1 has also been shown to interact with CXCR4 by forming a complex with CXCL12 (Schiraldi et al., 2012). This interaction is not associated to direct pro-inflammatory effects but exerts chemotactic activity, facilitating the recruitment of immune cells to the site of inflammation (Schiraldi et al., 2012). Considering granulocytes might contribute to necroptosis skin inflammation in the Casp8^{EKO} model (Chapter 5), a role for HMGB1/CXCL12/CXCR4 in granulocyte recruitment is also possible. In fact, CXCL12/CXCR4 has been directly linked to neutrophil recruitment (De Filippo & Rankin, 2018). In disagreement with this hypothesis, inhibition of CXCL12 neutralizing antibodies or specific inhibition of CXCR4 did not affect neutrophil recruitment toward necrotic liver tissue (Huebener et al., 2015)

Given the obtained results, it is possible to hypothesise that HMGB1 does not play a role in necroptosis-dependent skin inflammation. Several pro-inflammatory cytokines have been investigated in this context and very few, so far, have been reported to play a role in this and similar models. Only IL-33/ST2 (as reported in Chapter 5 of this thesis) and TNF/TNFR1 deletion have led to a partial rescue of FADD^{EKO} and Casp-8^{EKO} models

(Bonnet et al., 2011; Kovalenko et al., 2009). On the other hand, and despite its well described pro-inflammatory effect, Casp-8^{EKO} and FADD^{EKO} skin inflammation was shown to be IL-1 signalling independent (Bonnet et al., 2011). Hence, even though HMGB1 can be found in FADD^{EKO} skin samples (Bonnet et al., 2011), it is possible that HMGB1 does not contribute to necroptosis-dependent skin inflammation.

Because HMGB1 interacts with multiple receptors, the use of gene knock-outs to investigate HMGB1-receptor interactions in immune and inflammatory responses *in vivo* becomes more challenging. Targeting HMGB1 directly would allow us to better understand its role in inflammatory responses. HMGB1 deficient mice die shortly after birth due to downregulation of the glucocorticoid receptor and inability to use glycogen stored in the liver (Calogero et al., 1999). Hence, genetic deletion of HMGB1 must be performed specifically in tissues. HMGB1 from different cellular sources, such as dying epithelial cells and HMGB1-secreting inflammatory cells, differentially affects inflammatory response after necrosis (Huebener et al., 2015). In necroptotic skin lesions, it can be passively released by necroptotic keratinocytes (Bonnet et al., 2011). Specific keratinocyte deletion, but not myeloid cell deletion, of HMGB1 has been shown to delay skin wound healing both during normal skin wounding and in InvEE mice (Hoste et al., 2019). Similarly, epithelial, but not bone marrow-derived HMGB1 has been shown to be required for sterile inflammation liver injury (Huebener et al., 2015). If HMGB1 plays a role in the initiation or maintenance of necroptosis-induced skin inflammation, specific keratinocyte of HMGB1 in Casp-8^{EKO} mice could help better understand the dynamic and skin compartment responsible for this contribution.

However, genetic deletion has had little impact in some inflammatory models (Huebener et al., 2015). Targeting HMGB1 through anti-HMGB1

antibodies is an efficient way of inhibiting its activity. There are several polyclonal antibodies available that have been used to antagonise extracellular HMGB1 in sepsis (Suda et al., 2006; H Wang et al., 1999), arthritis (Kokkola et al., 2003), pancreatitis (Sawa et al., 2006) or haemorrhagic shock (R. Yang et al., 2006). Further beneficial effects of anti-HMGB1 antibodies include protective roles in the lung (Hamada et al., 2008), liver (Tsung et al., 2005) and brain infarction (K. Liu et al., 2007). The molecule glycyrrhizin directly binds to HMGB1 inhibiting its chemotactic function (L. Mollica et al., 2007) and has been shown to ameliorate sepsis-induced AKI (H. Zhao et al., 2016), renal ischemic reperfusion (Lau et al., 2014; Sohn et al., 2003) or brain ischemia-perfusion injury (J. Zhang et al., 2014). Other methods of inhibiting HMGB1 activity include the use of HMGB1 competitor BoxA or C-terminally truncated RAGE decoy receptor, sRAGE. BoxA has shown beneficial effects in models of sepsis (Suda et al., 2006; H. Yang et al., 2004), hepatitis (Sitia et al., 2007) and pancreatitis (Yuan et al., 2009), although its mechanism of action has not been elucidated and, as HMGB1 binds to multiple receptors, it might interfere with the activities of other ligands such as S100 proteins. Similarly, sRAGE can block HMGB1/RAGE signalling, mitigating the deleterious effects in several disease models (Bucciarelli et al., 2002; Cataldegirmen et al., 2005; Taguchi et al., 2000) and appears as a promising clinical biomarker for multiple disorders (Pilzweger & Holdenrieder, 2015). However, sRAGE can interact with other receptors (Pullerits et al., 2006), and the use of sRAGE does not exclude interaction of RAGE with its other ligands. In conclusion, there is abundant room for further progress in determining the role of HMGB1 in necroptosis-dependent skin inflammation. Studies using a targeted approach to delete or inhibit HMGB1 signalling, ideally using a pure mice genetic background, are therefore suggested for future work.

In summary, this chapter shows that RAGE signalling does not contribute to necroptosis-dependent skin inflammation, as the deletion of this receptor either constitutively or specifically in keratinocytes does not affect the inflammatory phenotype of Casp-8^{EKO} animals. This observation was confirmed through the analysis of the lesion severity and survival of the animals, as well as immunohistological analysis, which revealed no changes in skin proliferation and differentiation markers or immune cell infiltration. A role for HMGB1 signalling, through TLR-4, in necroptosis-dependent skin inflammation is possible and should be further studied.

Chapter 7

General discussion

The aim of this thesis has been to evaluate the role of DAMPs in necroptosis and inflammation by investigating the effect of HMGB1 in human epidermal keratinocytes *in vitro* and the role of IL-33/ST2 and RAGE signalling in the Casp-8^{EKO} necroptosis-dependent skin inflammation model. This section will briefly state the aims, key findings and achievements described in the present thesis as well as discuss their implications and limitations.

7.1 Key findings and implications

7.1.1 *In vitro* analysis of HMGB1-treated NHEK

The first part of this thesis focuses on *in vitro* studies aimed at investigating the hypothesis that HMGB1 is able to induce MLKL phosphorylation and keratinocyte necroptosis. HMGB1 has been described to have pro-inflammatory functions when released or secreted into the extracellular space. It is, therefore, a DAMP, and used as a marker of cell death or tissue injury, given its ability to activate the innate immune system (Bertheloot & Latz, 2017). The hypothesis underpinning this thesis is based on previous experiments that led to the detection of the necroptosis marker ph-MLKL upon HMGB1 treatment of NHEK *in vitro* and in skin explants *ex vivo* (personal communication, MC Bonnet). My results show that treatment of NHEK with HMGB1 leads to an increase in MLKL phosphorylation, suggesting a new role for HMGB1 potentially inducing keratinocyte necroptosis. Although the role of

HMGB1 has been extensively studied as a pro-inflammatory factor, no other studies have examined HMGB1 as a trigger inducing cell death apart from the work of (J. Xu et al., 2014), who have described a role for HMGB1 inducing pyroptosis in macrophages through RAGE-mediated endocytosis. This was shown both *in vitro* and *in vivo*, using a model of mouse endotoxemia. Results obtained here suggest this mechanism is cell-type dependent, as cleavage of pyroptosis marker Gasdermin D was not affected in HMGB1-treated NHEKs,

As a new potential necroptosis inducer, the molecular cascade induced by HMGB1 treatment of NHEK is unknown. Generally, RIPK3 and its substrate MLKL consistently form the necrosome, independent of the upstream trigger. However, different necrosome compositions have been described depending on the initial trigger, this is particularly the case regarding the presence or absence of RIPK1. In order to investigate the composition of the potential HMGB1-induced necrosome, endogenous RIPK3 and ph-MLKL were immunoprecipitated from NHEK lysates. Chapter 3 shows the successful immunoprecipitation of ph-MLKL from lysates of HT-29 and NHEK cells treated with TSZ or HMGB1 respectively. This protocol has not been described elsewhere and provides a novel and unique method for studying necroptosis-dependent and independent functions of ph-MLKL. My results show that RIPK3 and RIPK1 failed to co-immunoprecipitate with ph-MLKL, suggesting a different kinase might act phosphorylating MLKL upon HMGB1 stimulation of NHEK. Indeed, under certain culture conditions, MLKL can be phosphorylated in a manner that depends on CAMKII but not RIPK3 (Q. Zhan et al., 2021).

Chapter 4 investigated whether HMGB1 induces cell death in NHEKs. Several approaches were used to measure cell death with the aim of determining the most accurate method to study necroptosis in NHEK. Results obtained using PI-based and LDH-based cell death assays, as well as the WST-1 viability assay, showed that HMGB1 was unable to induce necroptosis or affect NHEK

viability *in vitro*. These results were confirmed by microscopic assessment of cell morphology. One possible explanation for this result might be that phosphorylated MLKL has necroptosis-independent functions in NHEK. Activated ph-MLKL has been linked with autophagy and is proposed to disrupt auto-lysosomal functions by translocating to intracellular membranes (Frank et al., 2019; X. Wu et al., 2020; Q. Zhan et al., 2021). Other than inducing cell death, MLKL has been shown to translocate to the nucleus and might be involved in gene regulation in specific contexts (reviewed in C. Zhan et al., 2021).

However, HMGB1 treatment of NHEKs leads to phosphorylation of MLKL at S358 and T357, an event which has been principally linked to the necroptotic cascade (I. Khan et al., 2021; L. Sun et al., 2012; Huayi Wang et al., 2014). An alternative explanation for the fact that HMGB1 does not appear to induce necroptosis in NHEK might be that downstream regulation of ph-MLKL could be preventing NHEK from achieving cell death. Several regulatory checkpoints downstream of ph-MLKL have been described, which modulate events such as MLKL oligomerisation and disengagement from the necrosome (Garnish et al., 2021), membrane translocation and membrane accumulation (Petrie et al., 2020; Samson et al., 2020). These mechanisms are thought to interfere with ph-MLKL-mediated pore formation and plasma permeabilization. Exocytosis through the ESCRT-III system or flotillin-mediated endocytosis of oligomerised ph-MLKL also act to prevent cell death downstream of pore formation at the plasma membrane (Y. N. Gong et al., 2017; Yoon et al., 2017). Immunostaining of ph-MLKL, together with Annexin V, in HMGB1-treated NHEKs would allow us to identify possible extracellular or intracellular vesicles containing ph-MLKL and determine its intracellular localisation. Furthermore, large-scale proteomic analysis of ph-MLKL immunoprecipitates could help elucidate the proteins that ph-MLKL associates with upon HMGB1 treatment of NHEKs.

7.1.2 Role of IL-33/ST2 and RAGE signalling in Casp-8^{EKO} animals

The second part of this thesis focused on exploring the effect of IL-33, ST2 and HMGB1 through RAGE signalling, in the necroptosis-dependent skin inflammation Casp-8^{EKO} model. This analysis was carried out using a genetic approach, by generating four double knock-out lines - Casp-8^{EKO} *Il-33*$^{-/-}$, Casp-8^{EKO} *St2*$^{-/-}$ (Chapter 5), Casp-8^{EKO} *Rage*$^{-/-}$ and Casp-8^{EKO} RAGE^{EKO} (Chapter 6) - which have been compared to Casp-8^{EKO} animals.

In Chapter 5, I have shown that the IL-33/ST2 axis is a major mediator of necroptosis-induced skin inflammation. Deletion of IL-33 or ST2 from Casp-8^{EKO} animals resulted in a major rescue of the skin inflammatory phenotype which led to an increase in the survival of the animals. In line with the reduced severity of the phenotype, immunohistological analysis of the skin of Casp-8^{EKO} *Il-33*$^{-/-}$ and Casp-8^{EKO} *St2*$^{-/-}$ animals showed significant decrease in the epidermal thickness and reduced alterations of keratinocyte proliferation and differentiation markers as well as general proliferation markers.

Skin inflammation induced by the specific deletion of FADD or Casp-8 in epidermal keratinocytes has been confirmed to be necroptosis-dependent by rescue of the phenotype through ablation of RIPK3 (Bonnet et al., 2011; Weinlich et al., 2013). In this thesis, the specific immunostaining of phosphorylated MLKL is shown, for the first time, in a necroptosis-dependent skin inflammation model (Chapters 6 and 7). Plasma membrane-bound ph-MLKL was specifically detected in keratinocytes found in hyperplastic patches of skin as well as in non-hyperplastic skin before detection of hyperplasia and immune cell infiltration of the dermis. The presence of ph-MLKL in non-hyperplastic skin, detected soon after birth (P5 is the first timepoint studied) confirms that necroptosis precedes and initiates inflammation in this model.

The initiation of necroptosis is not affected by the deletion of IL-33 or ST2, as phosphorylation of MLKL is detected at similar timepoints in the epidermis of Casp-8^{EKO}, Casp-8^{EKO} *Il-33*$^{-/-}$ and Casp-8^{EKO} *St2*$^{-/-}$ animals. Hence, the initial trigger of necroptosis in the skin of Casp-8^{EKO} animals remains to be elucidated. However, early detection of MLKL phosphorylation is followed by the expression of IL-33 in the epidermis, in line with reports of increased IL-33 mRNA expression in P3 Casp-8^{EKO} and FADD^{EKO} animals (Bonnet et al., 2011; Kovalenko et al., 2009). Moreover, the expression pattern of IL-33 and ph-MLKL affects similar areas of the epidermis, supporting the idea that keratinocyte necroptosis induces the release of IL-33. Indeed, necroptosis has been shown to directly release biologically active IL-33 *in vitro* and *in vivo* (Shlomovitz et al., 2019).

A reduction in granulocyte recruitment to the sites of inflammation was observed upon deletion of IL-33 or ST2, suggesting that IL-33 recruited granulocytes play an important role in amplifying necroptosis-dependent inflammation. Indeed, IL-33 has been shown to act in recruiting mast cells and neutrophils during inflammation (Artru et al., 2020; Bessa et al., 2014; Zeng et al., 2021). In the skin, IL-33-dependent activation of mast cells are responsible for the recruitment of neutrophils to sites of inflammation (Axel J. Hueber et al., 2011). Identification of the subtypes of granulocytes recruited by the release of IL-33 could be investigated through the specific immunostaining of neutrophils, mast cells and eosinophils in Casp-8^{EKO}, Casp-8^{EKO} *Il-33*$^{-/-}$ and Casp-8^{EKO} *St2*$^{-/-}$ skin. The delay in granulocyte recruitment coincides with an apparent reduction of TNF expression in the dermal compartment. The fact that both the recruitment of granulocytes and TNF expression were observed to be similarly delayed suggested that granulocytes were the main source of TNF in Casp-8^{EKO} skin inflammation. A double immunofluorescence staining would allow confirmation of this hypothesis and the optimisation of this protocol is currently in progress. As necroptosis-dependent skin inflammation is in part

dependent on TNF (Bonnet et al., 2011; Kovalenko et al., 2009), TNF potentially secreted by IL-33-recruited granulocytes, might contribute to the severity of the inflammatory phenotype in Casp-8^{EKO} skin. This would identify IL-33 as regulator of necroptosis-dependent skin inflammation upstream of TNF. This would be a highly relevant finding, not only to understand the molecular pathways implicated in necroptosis-dependent skin inflammation but also for potential therapeutical consideration in skin diseases that have been associated with TNF or necroptosis such as psoriasis and psoriatic arthritis. It is also important to consider that both mast cells and neutrophils can release inflammatory proteases that modulate the biological activity of extracellular IL-33 (Cayrol & Girard, 2018). Hence, decreased recruitment of granulocytes to early skin inflammation sites could also be delaying the release of proteases and the production of more active forms of IL-33, that would further reinforce inflammation.

Necroptosis-dependent skin inflammation models have been associated with a Type 1 immune responses for the following reasons. First, skin lesions found in necroptosis models of skin inflammation have morphological and histological characteristics which resemble pustular psoriasis skin lesions in humans, primarily driven by Th-1/Th17 responses. Second, the inflammatory phenotype is more severe in animals with a C57BL/6 genetic background (Bonnet et al., 2011; Kovalenko et al., 2009), which exhibit a Th1-predominant immune response, than BALB/c mice (Pedro Lee et al., 2009), which mostly shows Th2-predominant immune responses, associated with mild inflammation and no lethality. Finally, inflammation in these models is dependent on TNF signalling, a typical hallmark of Th-1-dependent inflammation. Taking this into consideration and recent supporting studies, neutrophils stand out as possible candidates for the IL-33-recuited granulocyte subtype, although experimental evidence would be needed to support this idea. The results reported here, challenge the traditional notion of IL-33 as a purely type-2 cytokine. This idea

is supported by additional studies that associate IL-33 activity with Th-1/Th-17 immune responses, such as those driving rheumatoid arthritis. In a murine model of rheumatoid arthritis, collagen-induced arthritis, treatment with anti-ST2 antibody or sST2-Fc fusion protein attenuated the disease and decreased production of IFN-γ, TNF and IL-17 (Leung et al., 2004; Palmer et al., 2009). Given its role in Th-2 immune responses, IL-33 has been extensively studied in the context of AD. However, given the identification of IL-33 as a potent amplifier of psoriasis-like inflammation in the Casp-8EKO model, IL-33 might also act as a potential regulator in psoriasis. Indeed, some studies have suggested that IL-33 contributes to psoriasis-like inflammation in murine models and IL-33 is upregulated in human psoriatic skin samples (Balato et al., 2012; Zeng et al., 2021, Di Meglio's lab BSID 2021).

Interestingly, the effect of RAGE signalling in Casp-8^{EKO} animals, described in Chapter 6, does not appear to be determinant for the development of necroptosis-dependent skin inflammation. Full-body deletion of RAGE or cell-specific genetic ablation from epidermal keratinocytes does not contribute to the inflammatory phenotype, as Casp-8^{EKO} *Rage*$^{-/-}$ and Casp-8^{EKO} $RAGE^{EKO}$ show similar lesion development, survival and epidermal thickness than Casp-8^{EKO} animals. Indeed, no changes were observed in skin proliferation and differentiation markers, necroptotic markers, immune cell infiltration or cytokine release between these lines. These results differ from several studies reporting that RAGE contributes to the severity of other models of inflammatory diseases including septic shock or atherosclerosis (Bucciarelli et al., 2002; Liliensiek et al., 2004). A link has been established between keratinocyte derived HMGB1 and psoriasis-like dermatitis (Z. Wang et al., 2021)given that knock-down of HMGB1 by subcutaneous injection of a lentivirus expressing shRNA against HMGB1, or specific deletion of HMGB1 from keratinocytes significantly ameliorates IMQ-induced psoriatic skin lesions (Z. Wang et al., 2021). However, whether RAGE is the receptor responsible for

such HMGB1 functions has not been addressed. RAGE is not required for the initiation of inflammatory process but rather its maintenance in TPA-carcinogenic inflammation (Gebhardt et al., 2008).

Nevertheless, it should be emphasised that HMGB1 is a ligand with multiple receptors and that other receptors, such as TLR-4 and CXCR4, may be involved in HMGB1 signalling in necroptosis-dependent skin inflammation. Both receptors, either through pro-inflammatory signalling or chemotactic functions, respectively, have shown to contribute to the recruitment of immune cells and inflammation (R. Kang et al., 2014; Schiraldi et al., 2012).

7.2 Limitations of the study

The main limitation encountered when working with epidermal keratinocytes *in vitro* is related to the complexity of obtaining, maintaining and handling primary cells, especially when large quantities of cell lysate are needed. Although working with cell lines generally generates more reproducible results, some necroptosis triggers can be cell type specific, and immortalised cell lines, although extensively used to study necroptosis, are not expected to respond in the same manner to different death-inducing stimuli. Consequently, extensive in-depth and time-consuming optimisations of the experimental procedures has been needed to adapt experimental conditions to NHEKs.

The source of NHEKs from different human donors, as well as the progressive differentiation of the keratinocytes in culture, led to variability between experiments. Consequently, inconsistency in the results requires increasing experimental replicates, which further adds to the challenge of working with NHEKs. Although donor differences represent intrinsic variables when working with primary cells, other factors can be more easily controlled. The use of FCS, as well as the Ca^{+2} concentrations in the culture media can induce keratinocyte differentiation (Carolina, 2016) and further enhance variability. Commercially

available keratinocyte culture mediums are serum-free and low on Ca^{+2} and, although briefly tested in Chapter 4, in depth growth rate analysis of NHEKs in these conditions have not been performed. Future studies using NHEKs could focus on investigating this approach to minimise keratinocyte differentiation and variability *in vitro.*

The epidermis has been shown to be particularly sensitive to necroptosis when compared to other tissues (Dannappel et al., 2014; Takahashi et al., 2014). However, difficulties were encountered when attempting to induce keratinocyte death *in vitro.* Crosstalk between epidermal keratinocytes and dermal fibroblasts, together with other cell types, has been shown to be critical for epidermal maturation and the pathophysiological processes *in vivo*. However, and unfortunately, recapitulation of the complex paracrine interactions between keratinocytes and the dermal compartment *in vitro* remains a challenge. The use of skin explants *ex vivo* or commercially available skin equivalents *in vitro* provides a deeper mechanistic analysis of the role HMGB1 plays in the skin. Indeed, stimulation of skin explants with HMGB1 has been performed (Dr. MC Bonnet's lab). However, this approach does not allow the analysis of molecular cascades triggered in HMGB1-treated keratinocytes such as the immunoprecipitation procedures.

Numerous reports identify the genetic background as a major source of phenotypical variation in animal models due to differences in the innate immune response and multiple reported passenger mutations (Eisfeld et al., 2019; S. K. Kang et al., 2018; Thach et al., 2000; Tom Vanden Berghe, Hulpiau, et al., 2015). This issue has been noted by several groups as impact on the severity of necroptosis-dependent skin inflammation models is background-dependent (Bonnet et al., 2011; I.-D. Kim et al., 2010; Kovalenko et al., 2009). The Casp-8^{EKO} animals that I have used throughout this thesis have a mixed genetic background. Thus, it is possible that the mixed background of these mice had

a distinct impact on their immune responses which may in turn have had a knock-on effect in the phenotypical variabilities described in Appendix III. Furthermore, strain-specific differential mutations can affect immune responses in animals, such as mutations in *Nlrp12* that cause defects on neutrophil recruitment (Ulland et al., 2016). Strain differences have also been identified regarding a mutation in serine (or cysteine) peptidase inhibitor, clade A, member 3I (*Serpina3i*), which encodes a protein that normally acts inhibiting IL-33 degradation *in vitro* and *in vivo*. BALB/c mice, specifically, have been shown to produce a truncated version of this protein and are therefore unable to successfully inhibit IL-33 degradation (Teufelberger et al., 2020). Considering the implication of IL-33 in necroptosis-dependent skin inflammation, strain-dependent genetic differences in mice could explain the variability of the severity of inflammation observed in Casp-8^{EKO} models. This strain-dependent variations could be the cause of the phenotypical differences between Casp-8^{EKO} *Il-33*$^{-/-}$ and Casp-8^{EKO} *St2*$^{-/-}$ animals, which were mostly observed in adults and significantly affected the survival of the animals. Future strategies should focus on obtaining animals with a pure genetic background to facilitate the analysis of the results and allow a clear understanding of the models. Furthermore, it would prove informative to identify significant genetic modifiers of the necroptosis-dependent inflammatory response that modulate inflammation in different genetic backgrounds since these variations may play an important part in skin inflammation.

Another clear limitation has been encountered when drawing conclusions from the results obtained from immunofluorescence stainings. Unlike macroscopical or histological observations which were easily quantifiable, the obtention of full-size projections of the immunostained skin samples was unfeasible. The obtention of formal quantification from the stainings produced would have supported the observations made for each condition and would have added strength to the conclusions drawn from these. In hindsight, establishing clear

criteria regarding the acquisition of the images would have allowed the normalisation and quantification of the results. For example, taking images of all lesions in a sample and normalising the positive staining to the total number of lesions or taking a determined number of randomised images per sample. These reflections should be taken into consideration in future studies in order to produce stronger quantifiable data.

7.3 Future directions

The work presented in this thesis rises interesting questions regarding the role of HMGB1 and IL-33 in skin necroptosis. For example, the kinase responsible for MLKL phosphorylation upon HMGB1 treatment of NHEKs remains to be elucidated. Further understanding of the function of HMGB1 in skin necroptosis could be achieved through large-scale proteomic analysis of HMGB1-treated NHEKs or ph-MLKL immunoprecipitate eluates obtained using the novel ph-MLKL immunoprecipitation protocol described here. This approach would additionally shed light on possible necroptosis-independent roles of ph-MLKL in NHEKs, as well as potential regulators of necroptosis execution that are not easily identifiable through targeted approaches using specific antibodies.

The use of different commercially available necroptosis inhibitors that target known necroptotic effector molecules would also help elucidate the molecular signalling involved in HMGB1-dependent MLKL phosphorylation in NHEKs. Considering HMGB1 has been shown to play a role in inducing other forms of programmed necrosis in different cell types, investigating HMGB1-dependent induction of necroptosis in other cell types could be of interest. However, as with other necroptosis triggers, HMGB1-induced MLKL phosphorylation could be specific to keratinocytes.

Other than investigating the role of ph-MLKL in HMGB1-treated NHEKs, further studies could focus on determining the means by which HMGB1 is

recognised and the signalling transduction activated. HMGB1 has been reported to signal through several receptors, of which RAGE and TLR-4 are best described. Considering the deletion of RAGE did not affect necroptosis-dependent inflammation *in vivo* (Chapter 6), it could be hypothesised that HMGB1-induced activation of the necroptotic pathway *in vitro* is mediated by TLR-4. Indeed, TLR-4 has been found to induce RIPK3- and TRIF-dependent necrosis in response to LPS in macrophages (He et al., 2011). To further investigate the role of HMGB1 in skin necroptosis, different blocking antibodies for known receptors of HMGB1 could be used. Specifically, RAGE and TLR-4 receptors would be of special interest. Additional research could focus on the generation of Casp-8^{EKO} *Tlr-4*$^{-/-}$ mice in a pure C57/BL6N genetic background and the obtained phenotype with Casp-8^{EKO} *Rage*$^{-/-}$ animals with the same background. Similarly, the generation Casp-8^{EKO} HMGB1^{EKO} would provide useful information regarding the role of necroptosis-released HMGB1 in skin inflammation.

Finally, the finding that IL-33 is an early mediator of necroptosis-dependent psoriasis-like skin inflammation leaves abundant room for future research in different contexts. This could include investigating whether IL-33 is involved other necroptosis-associated inflammatory diseases in which TNF plays a role such as multiple sclerosis and inflammatory arthritis. Indeed, ST2 blockade was effective in animal models of arthritis. IL-33/ST2 pathway may be a target for disease such as psoriatic arthritis in which skin and joint inflammation occur in the same patient. Future translational research could benefit from some of the procedures described in this thesis. In-depth analysis of the expression of IL-33 and ph-MLKL at different times of lesion development could be an interesting future area of research.

7.4 Concluding remarks

Since its discovery, necroptosis has drawn the attention of numerous studies and is today the best studied form programmed necrosis. The present thesis addresses several questions regarding the relationship between necroptosis and DAMPs, which have been traditionally studied as downstream pro-inflammatory mediators in the context of cell death. However, results obtained by members of my laboratory, together with results obtained by myself and shown in this thesis indicate that HMGB1 leads to MLKL phosphorylation in keratinocytes *in vitro* as well as in *ex vivo* skin explants. These results provide a new understanding of how this DAMP might interact with epidermal keratinocytes The absence of necroptotic cell death when using this stimulus *in vitro*, however, leaves several unanswered interrogations that will need further investigation. Cells have intricate regulatory mechanisms aiming at maintaining cell survival after MLKL phosphorylation, which could be acting in HMGB1-treated NHEKs *in vitro*. Considering that HMGB1/RAGE signalling does not contribute to Casp-8^{EKO} skin inflammation, suggests that either i) HMGB1 could not, in fact, induce necroptosis in keratinocytes (therefore ph-MLKL plays a necroptosis-independent role in this context), or ii) HMGB1 contributes to necroptosis in keratinocytes through a different receptor, such as TLR-4, but regulatory mechanisms prevent necroptosis *in vitro*. These questions remain to be elucidated, leaving abundant room for further work.

Several new strategies for studying necroptosis have been described in this thesis, including the successful immunoprecipitation of ph-MLKL (from HT-29 cell line and NHEK primary cells) and the specific immunostaining of ph-MLKL in mouse-collected skin tissue. These applications of a ph-MLKL antibody make an important contribution to the field as they will facilitate the investigation of necroptotic signalling *in vitro* and *in vivo.* The present thesis also makes a major contribution to understanding necroptosis-dependent skin

inflammation *in vivo* by identifying IL-33/ST2 signalling as a central mediator of the inflammatory response in Casp-8^{EKO} animals (Fernandez-Nasarre et al., in preparation). Improved understanding of the molecular mechanisms driving necroptosis-induced inflammation in the skin could extend our knowledge regarding chronic and acute sterile inflammation diseases in humans, positioning the work presented here as a notable and promising research topic.

Bibliography

Abeyama, K., Stern, D. M., Ito, Y., Kawahara, K., Yoshimoto, Y., Tanaka, M., Uchimura, T., Ida, N., Yamazaki, Y., Yamada, S., Yamamoto, Y., Yamamoto, H., Iino, S., Taniguchi, N., & Maruyama, I. (2005). The N-terminal domain of thrombomodulin sequesters high-mobility group-B1 protein, a novel antiinflammatory mechanism. *The Journal of Clinical Investigation*, *115*(5), 1267–1274. https://doi.org/10.1172/JCI22782

Achouiti, A., de Vos, A. F., van 't Veer, C., Florquin, S., Tanck, M. W., Nawroth, P. P., Bierhaus, A., van der Poll, T., & van Zoelen, M. A. D. (2016). Receptor for Advanced Glycation End Products (RAGE) Serves a Protective Role during Klebsiella pneumoniae - Induced Pneumonia. *PloS One*, *11*(1), e0141000. https://doi.org/10.1371/journal.pone.0141000

Akinduro, O., Sully, K., Patel, A., Robinson, D. J., Chikh, A., McPhail, G., Braun, K. M., Philpott, M. P., Harwood, C. A., Byrne, C., O'Shaughnessy, R. F. L., & Bergamaschi, D. (2016). Constitutive Autophagy and Nucleophagy during Epidermal Differentiation. *Journal of Investigative Dermatology*, *136*(7), 1460–1470. https://doi.org/10.1016/j.jid.2016.03.016

Ali, M., & Mocarski, E. S. (2018). Proteasome inhibition blocks necroptosis by attenuating death complex aggregation article. *Cell Death and Disease*, *9*(3). https://doi.org/10.1038/s41419-018-0371-x

Allakhverdi, Z., Smith, D. E., Comeau, M. R., & Delespesse, G. (2007). Cutting Edge: The ST2 Ligand IL-33 Potently Activates and Drives Maturation of Human Mast Cells. *The Journal of Immunology*, *179*(4), 2051 LP – 2054. https://doi.org/10.4049/jimmunol.179.4.2051

Alvarez-Diaz, S., Dillon, C. P., Lalaoui, N., Tanzer, M. C., Rodriguez, D. A., Lin, A., Lebois, M., Hakem, R., Josefsson, E. C., O'Reilly, L. A., Silke, J., Alexander, W. S., Green, D. R., & Strasser, A. (2016). The Pseudokinase MLKL and the Kinase RIPK3 Have Distinct Roles in Autoimmune Disease Caused by Loss of Death-Receptor-Induced Apoptosis. *Immunity*, *45*(3), 513–526. https://doi.org/10.1016/j.immuni.2016.07.016

Andersson, U., Tracey, K. J., & Health, C. (2015). *HMGB1 Is a Therapeutic Target for Sterile Inflammation and Infection*. 139–162. https://doi.org/10.1146/annurev-immunol-030409-101323.HMGB1

Andrassy, M., Volz, H. C., Igwe, J. C., Funke, B., Eichberger, S. N., Kaya, Z., Buss, S., Autschbach, F., Pleger, S. T., Lukic, I. K., Bea, F., Hardt, S. E., Humpert, P. M., Bianchi, M. E., Mairbäurl, H., Nawroth, P. P., Remppis, A., Katus, H. A., & Bierhaus, A. (2008). High-mobility group box-1 in ischemia-reperfusion injury

of the heart. *Circulation*, *117*(25), 3216–3226. https://doi.org/10.1161/CIRCULATIONAHA.108.769331

Apetoh, L., Ghiringhelli, F., Tesniere, A., Obeid, M., Ortiz, C., Criollo, A., Mignot, G., Maiuri, M. C., Ullrich, E., Saulnier, P., Yang, H., Amigorena, S., Ryffel, B., Barrat, F. J., Saftig, P., Levi, F., Lidereau, R., Nogues, C., Mira, J.-P., … Zitvogel, L. (2007). Toll-like receptor 4-dependent contribution of the immune system to anticancer chemotherapy and radiotherapy. *Nature Medicine*, *13*(9), 1050–1059. https://doi.org/10.1038/nm1622

Armaka, M., Ospelt, C., Pasparakis, M., & Kollias, G. (2018). The p55TNFR-IKK2-Ripk3 axis orchestrates arthritis by regulating death and inflammatory pathways in synovial fibroblasts. *Nature Communications*, *9*(1). https://doi.org/10.1038/s41467-018-02935-4

Arshad, M. I., Patrat-Delon, S., Piquet-Pellorce, C., L'helgoualc'h, A., Rauch, M., Genet, V., Lucas-Clerc, C., Bleau, C., Lamontagne, L., & Samson, M. (2013). Pathogenic mouse hepatitis virus or poly(I:C) induce IL-33 in hepatocytes in murine models of hepatitis. *PloS One*, *8*(9), e74278. https://doi.org/10.1371/journal.pone.0074278

Artru, F., Bou Saleh, M., Maggiotto, F., Lassailly, G., Ningarhari, M., Demaret, J., Ntandja-Wandji, L. C., Pais de Barros, J. P., Labreuche, J., Drumez, E., Helou, D. G., Dharancy, S., Gantier, E., Périanin, A., Chollet-Martin, S., Bataller, R., Mathurin, P., Dubuquoy, L., & Louvet, A. (2020). IL-33/ST2 pathway regulates neutrophil migration and predicts outcome in patients with severe alcoholic hepatitis. *Journal of Hepatology*, *72*(6), 1052–1061. https://doi.org/10.1016/j.jhep.2019.12.017

Athari, S. K., Poirier, E., Biton, J., Semerano, L., Hervé, R., Raffaillac, A., Lemeiter, D., Herbelin, A., Girard, J.-P., Caux, F., Boissier, M.-C., & Bessis, N. (2016). Collagen-induced arthritis and imiquimod-induced psoriasis develop independently of interleukin-33. *Arthritis Research & Therapy*, *18*(1), 143. https://doi.org/10.1186/s13075-016-1042-x

Aziz, M., Brenner, M., & Wang, P. (2019). Extracellular CIRP (eCIRP) and inflammation. *Journal of Leukocyte Biology*, *106*(1), 133–146. https://doi.org/10.1002/JLB.3MIR1118-443R

Baekkevold, E. S., Roussigné, M., Yamanaka, T., Johansen, F.-E., Jahnsen, F. L., Amalric, F., Brandtzaeg, P., Erard, M., Haraldsen, G., & Girard, J.-P. (2003). Molecular characterization of NF-HEV, a nuclear factor preferentially expressed in human high endothelial venules. *The American Journal of Pathology*, *163*(1), 69–79. https://doi.org/10.1016/S0002-9440(10)63631-0

Baker, M. (2015). Blame it on the antibodies. *Nature*, *521*, 274–276. https://doi.org/10.1088/2058-7058/22/08/43

Balato, A., Lembo, S., Mattii, M., Schiattarella, M., Marino, R., De Paulis, A., Balato, N., & Ayala, F. (2012). IL-33 is secreted by psoriatic keratinocytes and induces

pro-inflammatory cytokines via keratinocyte and mast cell activation. *Experimental Dermatology*, *21*(11), 892–894. https://doi.org/10.1111/exd.12027

Barkauskaite, V., Ek, M., Popovic, K., Harris, H. E., Wahren-Herlenius, M., & Nyberg, F. (2007). Translocation of the novel cytokine HMGB1 to the cytoplasm and extracellular space coincides with the peak of clinical activity in experimentally UV-induced lesions of cutaneous lupus erythematosus. *Lupus*, *16*(10), 794–802. https://doi.org/10.1177/0961203307081895

Bäsler, K., & Brandner, J. M. (2017). Tight junctions in skin inflammation. *Pflugers Archiv European Journal of Physiology*, *469*(1), 3–14. https://doi.org/10.1007/s00424-016-1903-9

Bass, J. J., Wilkinson, D. J., Rankin, D., Phillips, B. E., Szewczyk, N. J., Smith, K., & Atherton, P. J. (2017). An overview of technical considerations for Western blotting applications to physiological research. *Scandinavian Journal of Medicine and Science in Sports*, *27*(1), 4–25. https://doi.org/10.1111/sms.12702

Batista, M. D., Tincati, C., Milush, J. M., Ho, E. L., Ndhlovu, L. C., York, V. A., Kallas, E. G., Kalil, J., Keating, S. M., Norris, P. J., Chang, D., Unemori, P., Leslie, K. S., Maurer, T., Liao, W., & Nixon, D. F. (2013). CD57 Expression and Cytokine Production by T Cells in Lesional and Unaffected Skin from Patients with Psoriasis. *PLOS ONE*, *8*(2), e52144. https://doi.org/10.1371/journal.pone.0052144

Beg, A. A., Sha, W. C., Bronson, R. T., & Baltimore, D. (1995). Constitutive NF-kappa B activation, enhanced granulopoiesis, and neonatal lethality in I kappa B alpha-deficient mice. *Genes & Development*, *9*(22), 2736–2746. https://doi.org/10.1101/gad.9.22.2736

Berger, S. B., Kasparcova, V., Hoffman, S., Swift, B., Dare, L., Schaeffer, M., Capriotti, C., Cook, M., Finger, J., Hughes-Earle, A., Harris, P. A., Kaiser, W. J., Mocarski, E. S., Bertin, J., & Gough, P. J. (2014). Cutting Edge: RIP1 Kinase Activity Is Dispensable for Normal Development but Is a Key Regulator of Inflammation in SHARPIN-Deficient Mice. *The Journal of Immunology*, *192*(12), 5476–5480. https://doi.org/10.4049/jimmunol.1400499

Bergers, G., Reikerstorfer, A., Braselmann, S., Graninger, P., & Busslinger, M. (1994). Alternative promoter usage of the Fos-responsive gene Fit-1 generates mRNA isoforms coding for either secreted or membrane-bound proteins related to the IL-1 receptor. *The EMBO Journal*, *13*(5), 1176–1188.

Berghe, T. Vanden, Vanlangenakker, N., Parthoens, E., Deckers, W., Devos, M., Festjens, N., Guerin, C. J., Brunk, U. T., Declercq, W., & Vandenabeele, P. (2010). Necroptosis, necrosis and secondary necrosis converge on similar cellular disintegration features. *Cell Death and Differentiation*, *17*(6), 922–930. https://doi.org/10.1038/cdd.2009.184

Bergmann, C., Strohbuecker, L., Lotfi, R., Sucker, A., Joosten, I., Koenen, H., & Körber, A. (2016). High mobility group box 1 is increased in the sera of psoriatic

patients with disease progression. *Journal of the European Academy of Dermatology and Venereology*, *30*(3), 435–441. https://doi.org/10.1111/jdv.13564

Bertheloot, D., & Latz, E. (2017). HMGB1, IL-1α, IL-33 and S100 proteins: Dual-function alarmins. *Cellular and Molecular Immunology*, *14*(1), 43–64. https://doi.org/10.1038/cmi.2016.34

Bessa, J., Meyer, C. A., de Vera Mudry, M. C., Schlicht, S., Smith, S. H., Iglesias, A., & Cote-Sierra, J. (2014). Altered subcellular localization of IL-33 leads to non-resolving lethal inflammation. *Journal of Autoimmunity*, *55*(1), 33–41. https://doi.org/10.1016/j.jaut.2014.02.012

Bianchi, M. E., Falciola, L., Ferrari, S., & Lilley, D. M. (1992). The DNA binding site of HMG1 protein is composed of two similar segments (HMG boxes), both of which have counterparts in other eukaryotic regulatory proteins. *The EMBO Journal*, *11*(3), 1055–1063.

Bieber, T. (2010). Atopic dermatitis. *Annals of Dermatology*, *22*(2), 125–137. https://doi.org/10.5021/ad.2010.22.2.125

Bikle, D. D., Xie, Z., & Tu, C.-L. (2012). Calcium regulation of keratinocyte differentiation. *Expert Review of Endocrinology & Metabolism*, *7*(4), 461–472. https://doi.org/10.1586/eem.12.34

Boehncke, W. H., & Schön, M. P. (2015). Psoriasis. *The Lancet*, *386*(9997), 983–994. https://doi.org/10.1016/S0140-6736(14)61909-7

Bonaldi, T., Talamo, F., Scaffidi, P., Ferrera, D., Porto, A., Bachi, A., Rubartelli, A., Agresti, A., & Bianchi, M. E. (2003). Monocytic cells hyperacetylate chromatin protein HMGB1 to redirect it towards secretion. *EMBO Journal*, *22*(20), 5551–5560. https://doi.org/10.1093/emboj/cdg516

Bonilla, W. V, Fröhlich, A., Senn, K., Kallert, S., Fernandez, M., Johnson, S., Kreutzfeldt, M., Hegazy, A. N., Schrick, C., Fallon, P. G., Klemenz, R., Nakae, S., Adler, H., Merkler, D., Löhning, M., & Pinschewer, D. D. (2012). The alarmin interleukin-33 drives protective antiviral $CD8^+$ T cell responses. *Science (New York, N.Y.)*, *335*(6071), 984–989. https://doi.org/10.1126/science.1215418

Bonnet, M. C., Preukschat, D., Welz, P. S., Van Loo, G., Ermolaeva, M. A., Bloch, W., Haase, I., & Pasparakis, M. (2011). The Adaptor Protein FADD Protects Epidermal Keratinocytes from Necroptosis In Vivo and Prevents Skin Inflammation. *Immunity*, *35*(4), 572–582. https://doi.org/10.1016/j.immuni.2011.08.014

Bucciarelli, L. G., Wendt, T., Qu, W., Lu, Y., Lalla, E., Rong, L. L., Goova, M. T., Moser, B., Kislinger, T., Lee, D. C., Kashyap, Y., Stern, D. M., & Schmidt, A. M. (2002). RAGE blockade stabilizes established atherosclerosis in diabetic apolipoprotein E-null mice. *Circulation*, *106*(22), 2827–2835. https://doi.org/10.1161/01.cir.0000039325.03698.36

Byers, D. E., Alexander-Brett, J., Patel, A. C., Agapov, E., Dang-Vu, G., Jin, X., Wu, K., You, Y., Alevy, Y., Girard, J.-P., Stappenbeck, T. S., Patterson, G. A., Pierce, R. A., Brody, S. L., & Holtzman, M. J. (2013). Long-term IL-33-producing epithelial progenitor cells in chronic obstructive lung disease. *The Journal of Clinical Investigation*, *123*(9), 3967–3982. https://doi.org/10.1172/JCI65570

Cai, Z., Jitkaew, S., Zhao, J., Chiang, H. C., Choksi, S., Liu, J., Ward, Y., Wu, L. G., & Liu, Z. G. (2014). Plasma membrane translocation of trimerized MLKL protein is required for TNF-induced necroptosis. *Nature Cell Biology*, *16*(1), 55–65. https://doi.org/10.1038/ncb2883

Calogero, S., Grassi, F., Aguzzi, A., Voigtländer, T., Ferrier, P., Ferrari, S., & Bianchi, M. E. (1999). The lack of chromosomal protein Hmg1 does not disrupt cell growth but causes lethal hypoglycaemia in newborn mice. *Nature Genetics*, *22*(3), 276–280. https://doi.org/10.1038/10338

Carolina, N. (2016). Reproducibility : Respect Your Cells ! *Nature*, *537*, 433–435.

Carriere, V., Roussel, L., Ortega, N., Lacorre, D.-A., Americh, L., Aguilar, L., Bouche, G., & Girard, J.-P. (2007). IL-33, the IL-1-like cytokine ligand for ST2 receptor, is a chromatin-associated nuclear factor in vivo. *Proceedings of the National Academy of Sciences of the United States of America*, *104*(1), 282–287. https://doi.org/10.1073/pnas.0606854104

Cataldegirmen, G., Zeng, S., Feirt, N., Ippagunta, N., Dun, H., Qu, W., Lu, Y., Rong, L. L., Hofmann, M. A., Kislinger, T., Pachydaki, S. I., Jenkins, D. G., Weinberg, A., Lefkowitch, J., Rogiers, X., Yan, S. F., Schmidt, A. M., & Emond, J. C. (2005). RAGE limits regeneration after massive liver injury by coordinated suppression of TNF-α and NF-κB . *Journal of Experimental Medicine*, *201*(3), 473–484. https://doi.org/10.1084/jem.20040934

Cayrol, C., & Girard, J. P. (2009). The IL-1-like cytokine IL-33 is inactivated after maturation by caspase-1. *Proceedings of the National Academy of Sciences of the United States of America*, *106*(22), 9021–9026. https://doi.org/10.1073/pnas.0812690106

Cayrol, C., & Girard, J. P. (2018). Interleukin-33 (IL-33): A nuclear cytokine from the IL-1 family. *Immunological Reviews*, *281*(1), 154–168. https://doi.org/10.1111/imr.12619

Cecconi, F., Alvarez-Bolado, G., Meyer, B. I., Roth, K. A., & Gruss, P. (1998). Apaf1 (CED-4 homolog) regulates programmed cell death in mammalian development. *Cell*, *94*(6), 727–737. https://doi.org/10.1016/s0092-8674(00)81732-8

Chackerian, A. A., Oldham, E. R., Murphy, E. E., Schmitz, J., Pflanz, S., & Kastelein, R. A. (2007). IL-1 Receptor Accessory Protein and ST2 Comprise the IL-33 Receptor Complex. *The Journal of Immunology*, *179*(4), 2551–2555. https://doi.org/10.4049/jimmunol.179.4.2551

Chan, F. K., Farias Luz, N., & Moriwaki, K. (2015). *Programmed necrosis in the*

Cross Talk of Cell Death and inflammation (Issue 11). https://doi.org/10.1111/obr.12065.Variation

Chen, G., Li, J., Ochani, M., Rendon-Mitchell, B., Qiang, X., Susarla, S., Ulloa, L., Yang, H., Fan, S., Goyert, S. M., Wang, P., Tracey, K. J., Sama, A. E., & Wang, H. (2004). Bacterial endotoxin stimulates macrophages to release HMGB1 partly through CD14- and TNF-dependent mechanisms. *Journal of Leukocyte Biology*, *76*(5), 994-1001. https://doi.org/10.1189/jlb.0404242

Chen, G. Y., & Nuñez, G. (2010). Sterile inflammation: Sensing and reacting to damage. *Nature Reviews Immunology*, *10*(12), 826-837. https://doi.org/10.1038/nri2873

Chen, T., Guo, Z. P., Li, L., Wang, L., Jia, R. Z., Cao, N., Qin, S., & Li, M. M. (2013). Increased HMGB1 serum levels and altered HMGB1 expression in patients with psoriasis vulgaris. *Archives of Dermatological Research*, *305*(3), 263-267. https://doi.org/10.1007/s00403-013-1330-0

Chen, W.-Y., Hong, J., Gannon, J., Kakkar, R., & Lee, R. T. (2015). Myocardial pressure overload induces systemic inflammation through endothelial cell IL-33. *Proceedings of the National Academy of Sciences of the United States of America*, *112*(23), 7249-7254. https://doi.org/10.1073/pnas.1424236112

Chen, W., Wu, J., Li, L., Zhang, Z., Ren, J., Liang, Y., Chen, F., Yang, C., Zhou, Z., Su, S. S., Zheng, X., Zhang, Z., Zhong, C.-Q., Wan, H., Xiao, M., Lin, X., Feng, X.-H., & Han, J. (2015). Ppm1b negatively regulates necroptosis through dephosphorylating Rip3. *Nature Cell Biology*, *17*(4), 434-444. https://doi.org/10.1038/ncb3120

Chen, Y., Huang, X.-J., Yu, N., Xie, Y., Zhang, K., Wen, F., Liu, H., & Di, Q. (2015). HMGB1 Contributes to the Expression of P-Glycoprotein in Mouse Epileptic Brain through Toll-Like Receptor 4 and Receptor for Advanced Glycation End Products. *PloS One*, *10*(10), e0140918. https://doi.org/10.1371/journal.pone.0140918

Cho, Y. S., Challa, S., Moquin, D., Genga, R., Ray, T. D., Guildford, M., & Chan, F. K. M. (2009). Phosphorylation-Driven Assembly of the RIP1-RIP3 Complex Regulates Programmed Necrosis and Virus-Induced Inflammation. *Cell*, *137*(6), 1112-1123. https://doi.org/10.1016/j.cell.2009.05.037

Choi, M. E., Price, D. R., Ryter, S. W., & Choi, A. M. K. (2019). Necroptosis: A crucial pathogenic mediator of human disease. *JCI Insight*, *4*(15). https://doi.org/10.1172/jci.insight.128834

Choi, S.-W., Park, H.-H., Kim, S., Chung, J. M., Noh, H.-J., Kim, S. K., Song, H. K., Lee, C.-W., Morgan, M. J., Kang, H. C., & Kim, Y.-S. (2018). PELI1 Selectively Targets Kinase-Active RIP3 for Ubiquitylation-Dependent Proteasomal Degradation. *Molecular Cell*, *70*(5), 920-935.e7. https://doi.org/10.1016/j.molcel.2018.05.016

Chu, D. H., & Loomis, C. a. (2017). Structure and Development of the Skin and Cutaneous Appendages. In *Fetal and Neonatal Physiology* (Fifth Edit). Elsevier Inc. https://doi.org/10.1016/b978-0-323-35214-7.00048-2

Cohen, E. S., Scott, I. C., Majithiya, J. B., Rapley, L., Kemp, B. P., England, E., Rees, D. G., Overed-Sayer, C. L., Woods, J., Bond, N. J., Veyssier, C. S., Embrey, K. J., Sims, D. A., Snaith, M. R., Vousden, K. A., Strain, M. D., Chan, D. T. Y., Carmen, S., Huntington, C. E., … Mustelin, T. (2015). Oxidation of the alarmin IL-33 regulates ST2-dependent inflammation. *Nature Communications*, *6*(1), 8327. https://doi.org/10.1038/ncomms9327

Conos, S. a., Chen, K. W., De Nardo, D., Hara, H., Whitehead, L., Núñez, G., Masters, S. L., Murphy, J. M., Schroder, K., Vaux, D. L., Lawlor, K. E., Lindqvist, L. M., & Vince, J. E. (2017). Active MLKL triggers the NLRP3 inflammasome in a cell-intrinsic manner. *Proceedings of the National Academy of Sciences of the United States of America*, *114*(6), E961–E969. https://doi.org/10.1073/pnas.1613305114

Conos, S. A., Chen, K. W., De Nardo, D., Hara, H., Whitehead, L., Núñez, G., Masters, S. L., Murphy, J. M., Schroder, K., Vaux, D. L., Lawlor, K. E., Lindqvist, L. M., & Vince, J. E. (2017). Active MLKL triggers the NLRP3 inflammasome in a cell-intrinsic manner. *Proceedings of the National Academy of Sciences of the United States of America*, *114*(6), E961–E969. https://doi.org/10.1073/pnas.1613305114

Crutchfield, E. C. T., Garnish, S. E., & Hildebrand, J. M. (2021). The role of the key effector of necroptotic cell death, mlkl, in mouse models of disease. *Biomolecules*, *11*(6), 1–22. https://doi.org/10.3390/biom11060803

Cummings, B. S., Wills, L. P., & Schnellmann, R. G. (2004). Measurement of Cell Death in Mammalian Cells. *Curr Protoc Phamacol*, *1*(Lemasters 1999), 1–30. https://doi.org/10.1002/0471141755.ph1208s25.Measurement

Cuppari, C., Manti, S., Salpietro, A., Valenti, S., Capizzi, A., Arrigo, T., Salpietro, C., & Leonardi, S. (2016). HMGB1 levels in children with atopic eczema/dermatitis syndrome (AEDS). In *Pediatric allergy and immunology : official publication of the European Society of Pediatric Allergy and Immunology* (Vol. 27, Issue 1, pp. 99–102). https://doi.org/10.1111/pai.12481

D'Cruz, A. A., Speir, M., Bliss-Moreau, M., Dietrich, S., Wang, S., Chen, A. A., Gavillet, M., Al-Obeidi, A., Lawlor, K. E., Vince, J. E., Kelliher, M. A., Hakem, R., Pasparakis, M., Williams, D. A., Ericsson, M., & Croker, B. A. (2018). The pseudokinase MLKL activates PAD4-dependent NET formation in necroptotic neutrophils. *Science Signaling*, *11*(546), 1–12. https://doi.org/10.1126/scisignal.aao1716

Dai, J., Zhang, C., Guo, L., He, H., Jiang, K., Huang, Y., Zhang, X., Zhang, H., Wei, W., Zhang, Y., Lu, L., & Hu, J. (2020). A necroptotic-independent function of MLKL in regulating endothelial cell adhesion molecule expression. *Cell Death and Disease*, *11*(4). https://doi.org/10.1038/s41419-020-2483-3

Dai, X., Utsunomiya, R., Shiraishi, K., Mori, H., Muto, J., Murakami, M., & Sayama, K. (2021). Nuclear IL-33 Plays an Important Role in the Suppression of FLG, LOR, Keratin 1, and Keratin 10 by IL-4 and IL-13 in Human Keratinocytes. *Journal of Investigative Dermatology*. https://doi.org/10.1016/j.jid.2021.04.002

Dajnoki, Z., Béke, G., Mócsai, G., Kapitány, A., Gáspár, K., Hajdu, K., Emri, G., Nagy, B., Kovács, I., Beke, L., Dezső, B., & Szegedi, A. (2016). Immune-mediated Skin Inflammation is Similar in Severe Atopic Dermatitis Patients With or Without Filaggrin Mutation. *Acta Dermato-Venereologica*, *96*(5), 645–650. https://doi.org/10.2340/00015555-2272

Dannappel, M., Vlantis, K., Kumari, S., Polykratis, A., Kim, C., Wachsmuth, L., Eftychi, C., Lin, J., Corona, T., Hermance, N., Zelic, M., Kirsch, P., Basic, M., Bleich, A., Kelliher, M., & Pasparakis, M. (2014). RIPK1 maintains epithelial homeostasis by inhibiting apoptosis and necroptosis. *Nature*, *513*(7516), 90–94. https://doi.org/10.1038/nature13608

Dara, L. (2018). The Receptor Interacting Protein Kinases in the Liver. *Seminars in Liver Disease*, *38*(1), 73–86. https://doi.org/10.1055/s-0038-1629924

Davies, K. A., Tanzer, M. C., Griffin, M. D. W., Mok, Y. F., Young, S. N., Qin, R., Petrie, E. J., Czabotar, P. E., Silke, J., & Murphy, J. M. (2018). The brace helices of MLKL mediate interdomain communication and oligomerisation to regulate cell death by necroptosis. *Cell Death and Differentiation*, *25*(9), 1567–1580. https://doi.org/10.1038/s41418-018-0061-3

De Filippo, K., & Rankin, S. M. (2018). CXCR4, the master regulator of neutrophil trafficking in homeostasis and disease. *European Journal of Clinical Investigation*, *48 Suppl 2*(Suppl Suppl 2), e12949. https://doi.org/10.1111/eci.12949

Debes, G. F., & McGettigan, S. E. (2019). Skin-associated B cells in health and inflammation Gudrun. *J Immunol*, *202*(6), 1659–1666. https://doi.org/10.4049/jimmunol.1801211.Skin-associated

Degterev, A., Huang, Z., Boyce, M., Li, Y., Jagtap, P., Mizushima, N., Cuny, G. D., Mitchison, T. J., Moskowitz, M. A., & Yuan, J. (2005). Chemical inhibitor of nonapoptotic cell death with therapeutic potential for ischemic brain injury. *Nature Chemical Biology*, *1*, 112. http://dx.doi.org/10.1038/nchembio711

Denning, N. L., Aziz, M., Gurien, S. D., & Wang, P. (2019). Damps and nets in sepsis. *Frontiers in Immunology*, *10*(OCT), 1–15. https://doi.org/10.3389/fimmu.2019.02536

Dillon, C. P., Weinlich, R., Rodriguez, D. A., Cripps, J. G., Quarato, G., Gurung, P., Verbist, K. C., Brewer, T. L., Llambi, F., Gong, Y. N., Janke, L. J., Kelliher, M. A., Kanneganti, T. D., & Green, D. R. (2014). RIPK1 blocks early postnatal lethality mediated by caspase-8 and RIPK3. *Cell*, *157*(5), 1189–1202. https://doi.org/10.1016/j.cell.2014.04.018

Dondelinger, Y., Darding, M., Bertrand, M. J. M., & Walczak, H. (2016). Poly-ubiquitination in TNFR1-mediated necroptosis. *Cellular and Molecular Life Sciences*, *73*(11–12), 2165–2176. https://doi.org/10.1007/s00018-016-2191-4

Dondelinger, Y., Declercq, W., Montessuit, S., Roelandt, R., Goncalves, A., Bruggeman, I., Hulpiau, P., Weber, K., Sehon, C. A., Marquis, R. W., Bertin, J., Gough, P. J., Savvides, S., Martinou, J. C., Bertrand, M. J. M., & Vandenabeele, P. (2014). MLKL Compromises Plasma Membrane Integrity by Binding to Phosphatidylinositol Phosphates. *Cell Reports*, *7*(4), 971–981. https://doi.org/10.1016/j.celrep.2014.04.026

Dondelinger, Y., Delanghe, T., Rojas-Rivera, D., Priem, D., Delvaeye, T., Bruggeman, I., Van Herreweghe, F., Vandenabeele, P., & Bertrand, M. J. M. (2017). MK2 phosphorylation of RIPK1 regulates TNF-mediated cell death. *Nature Cell Biology*, *19*(10), 1237–1247. https://doi.org/10.1038/ncb3608

Dondelinger, Y., Vandenabeele, P., & Bertrand, M. J. M. (2016). Regulation of RIPK1's cell death function by phosphorylation. *Cell Cycle*, *15*(1), 5–6. https://doi.org/10.1080/15384101.2015.1112688

Dong, Y., Sun, Y., Huang, Y., Fang, X., Sun, P., Dwarakanath, B., Kong, L., & Lu, J. J. (2019). Depletion of MLKL inhibits invasion of radioresistant nasopharyngeal carcinoma cells by suppressing epithelial-mesenchymal transition. *Annals of Translational Medicine*, *7*(23), 741–741. https://doi.org/10.21037/atm.2019.11.104

Duan, X., Liu, X., Liu, N., Huang, Y., Jin, Z., Zhang, S., Ming, Z., & Chen, H. (2020). Inhibition of keratinocyte necroptosis mediated by RIPK1/RIPK3/MLKL provides a protective effect against psoriatic inflammation. *Cell Death and Disease*, *11*(2). https://doi.org/10.1038/s41419-020-2328-0

Duan, Y., Dong, Y., Hu, H., Wang, Q., Guo, S., Fu, D., Song, X., Kalvakolanu, D. V., & Tian, Z. (2019). IL-33 contributes to disease severity in Psoriasis-like models of mouse. *Cytokine*, *119*(December 2018), 159–167. https://doi.org/10.1016/j.cyto.2019.02.019

Eckhart, L., Lippens, S., Tschachler, E., & Declercq, W. (2013). Cell death by cornification. *Biochimica et Biophysica Acta - Molecular Cell Research*, *1833*(12), 3471–3480. https://doi.org/10.1016/j.bbamcr.2013.06.010

Einck, L., Soares, N., & Bustin, M. (1984). Localization of HMG chromosomal proteins in the nucleus and cytoplasm by microinjection of functional antibody fragments into living fibroblasts. *Experimental Cell Research*, *152*(2), 287–301. https://doi.org/10.1016/0014-4827(84)90631-1

Eisfeld, A. J., Gasper, D. J., Suresh, M., & Kawaoka, Y. (2019). C57BL/6J and C57BL/6NJ Mice Are Differentially Susceptible to Inflammation-Associated Disease Caused by Influenza A Virus. *Frontiers in Microbiology*, *9*, 3307. https://doi.org/10.3389/fmicb.2018.03307

Ellis, R. E., Yuan, J., & Horvitz, H. R. (1991). Mechanisms and functions of cell death. *Annual Review of Cell Biology*, *7*, 663–698. https://doi.org/10.1146/annurev.cb.07.110191.003311

Eming, S. A., Krieg, T., & Davidson, J. M. (2007). Inflammation in wound repair: Molecular and cellular mechanisms. *Journal of Investigative Dermatology*, *127*(3), 514–525. https://doi.org/10.1038/sj.jid.5700701

Enoksson, M., Lyberg, K., Möller-Westerberg, C., Fallon, P. G., Nilsson, G., & Lunderius-Andersson, C. (2011). Mast cells as sensors of cell injury through IL-33 recognition. *Journal of Immunology (Baltimore, Md. : 1950)*, *186*(4), 2523–2528. https://doi.org/10.4049/jimmunol.1003383

Ermolaeva, M. A., Michallet, M.-C., Papadopoulou, N., Utermöhlen, O., Kranidioti, K., Kollias, G., Tschopp, J., & Pasparakis, M. (2008). Function of TRADD in tumor necrosis factor receptor 1 signaling and in TRIF-dependent inflammatory responses. *Nature Immunology*, *9*(9), 1037–1046. https://doi.org/10.1038/ni.1638

Espinassous, Q., Garcia-de-Paco, E., Garcia-Verdugo, I., Synguelakis, M., von Aulock, S., Sallenave, J.-M., McKenzie, A. N. J., & Kanellopoulos, J. (2009). IL-33 enhances lipopolysaccharide-induced inflammatory cytokine production from mouse macrophages by regulating lipopolysaccharide receptor complex. *Journal of Immunology (Baltimore, Md. : 1950)*, *183*(2), 1446–1455. https://doi.org/10.4049/jimmunol.0803067

Fadok, V. A., Voelker, D. R., Campbell, P. A., Cohen, J. J., Bratton, D. L., & Henson, P. M. (1992). Exposure of phosphatidylserine on the surface of apoptotic lymphocytes triggers specific recognition and removal by macrophages. *Journal of Immunology (Baltimore, Md. : 1950)*, *148*(7), 2207–2216.

Fan, J., Li, Y., Levy, R. M., Fan, J. J., Hackam, D. J., Vodovotz, Y., Yang, H., Tracey, K. J., Billiar, T. R., & Wilson, M. A. (2007). Hemorrhagic shock induces NAD(P)H oxidase activation in neutrophils: role of HMGB1-TLR4 signaling. *Journal of Immunology (Baltimore, Md. : 1950)*, *178*(10), 6573–6580. https://doi.org/10.4049/jimmunol.178.10.6573

Fan, W., Guo, J., Gao, B., Zhang, W., Ling, L., Xu, T., Pan, C., Li, L., Chen, S., Wang, H., Zhang, J., & Wang, X. (2019). Flotillin-mediated endocytosis and ALIX–syntenin-1–mediated exocytosis protect the cell membrane from damage caused by necroptosis. *Science Signaling*, *12*(583). https://doi.org/10.1126/scisignal.aaw3423

Faust, H., Lam, L. M., Hotz, M. J., Qing, D., & Mangalmurti, N. S. (2020). RAGE interacts with the necroptotic protein RIPK3 and mediates transfusion-induced danger signal release. *Vox Sanguinis*, *115*(8), 729–734. https://doi.org/10.1111/vox.12946

Feng, L., Matsumoto, C., Schwartz, A., Schmidt, A. M., Stern, D. M., & Pile-Spellman, J. (2005). Chronic vascular inflammation in patients with type 2 diabetes:

endothelial biopsy and RT-PCR analysis. *Diabetes Care*, *28*(2), 379–384. https://doi.org/10.2337/diacare.28.2.379

Feng, S., Yang, Y., Mei, Y., Ma, L., Zhu, D. e., Hoti, N., Castanares, M., & Wu, M. (2007). Cleavage of RIP3 inactivates its caspase-independent apoptosis pathway by removal of kinase domain. *Cellular Signalling*, *19*(10), 2056–2067. https://doi.org/10.1016/j.cellsig.2007.05.016

Ferrara, M., Chialli, G., Ferreira, L. M., Ruggieri, E., Careccia, G., Preti, A., Piccirillo, R., Bianchi, M. E., Sitia, G., & Venereau, E. (2020). Oxidation of HMGB1 Is a Dynamically Regulated Process in Physiological and Pathological Conditions. *Frontiers in Immunology*, *11*(June), 1–13. https://doi.org/10.3389/fimmu.2020.01122

Ferrari, S., Ronfani, L., Calogero, S., & Bianchi, M. E. (1994). The mouse gene coding for high mobility group 1 protein (HMG1). *The Journal of Biological Chemistry*, *269*(46), 28803–28808.

Flynn, J. L., Goldstein, M. M., Chan, J., Triebold, K. J., Pfeffer, K., Lowenstein, C. J., Schreiber, R., Mak, T. W., & Bloom, B. R. (1995). Tumor necrosis factor-alpha is required in the protective immune response against Mycobacterium tuberculosis in mice. *Immunity*, *2*(6), 561–572. https://doi.org/10.1016/1074-7613(95)90001-2

Frank, D., Vaux, D. L., Murphy, J. M., Vince, J. E., & Lindqvist, L. M. (2019). Activated MLKL attenuates autophagy following its translocation to intracellular membranes. *Journal of Cell Science*, *132*(5). https://doi.org/10.1242/jcs.220996

Fritsch, M., Günther, S. D., Schwarzer, R., Albert, M. C., Schorn, F., Werthenbach, J. P., Schiffmann, L. M., Stair, N., Stocks, H., Seeger, J. M., Lamkanfi, M., Krönke, M., Pasparakis, M., & Kashkar, H. (2019). Caspase-8 is the molecular switch for apoptosis, necroptosis and pyroptosis. *Nature*, *575*(7784), 683–687. https://doi.org/10.1038/s41586-019-1770-6

Galluzzi, L., Maiuri, M. C., Vitale, I., Zischka, H., Castedo, M., Zitvogel, L., & Kroemer, G. (2007). Cell death modalities: classification and pathophysiological implications. *Cell Death & Differentiation*, *14*(7), 1237–1243. https://doi.org/10.1038/sj.cdd.4402148

Galluzzi, L., Vitale, I., Aaronson, S. A., Abrams, J. M., Adam, D., Agostinis, P., Alnemri, E. S., Altucci, L., Amelio, I., Andrews, D. W., Annicchiarico-Petruzzelli, M., Antonov, A. V., Arama, E., Baehrecke, E. H., Barlev, N. A., Bazan, N. G., Bernassola, F., Bertrand, M. J. M., Bianchi, K., … Kroemer, G. (2018). Molecular mechanisms of cell death: Recommendations of the Nomenclature Committee on Cell Death 2018. *Cell Death and Differentiation*, *25*(3), 486–541. https://doi.org/10.1038/s41418-017-0012-4

Gardella, S., Andrei, C., Ferrera, D., Lotti, L. V., Torrisi, M. R., Bianchi, M. E., & Rubartelli, A. (2002). The nuclear protein HMGB1 is secreted by monocytes via a non-classical, vesicle-mediated secretory pathway. *EMBO Reports*, *3*(10),

995–1001. https://doi.org/10.1093/embo-reports/kvf198

Garnish, S. E., Meng, Y., Koide, A., Sandow, J. J., Denbaum, E., Jacobsen, A. V., Yeung, W., Samson, A. L., Horne, C. R., Fitzgibbon, C., Young, S. N., Smith, P. P. C., Webb, A. I., Petrie, E. J., Hildebrand, J. M., Kannan, N., Czabotar, P. E., Koide, S., & Murphy, J. M. (2021). Conformational interconversion of MLKL and disengagement from RIPK3 precede cell death by necroptosis. *Nature Communications*, *12*(1), 1–14. https://doi.org/10.1038/s41467-021-22400-z

Gatti, F., Mia, S., Hammarström, C., Frerker, N., Fosby, B., Wang, J., Pietka, W., Sundnes, O., Hol, J., Kasprzycka, M., & Haraldsen, G. (2021). Nuclear IL-33 restrains the early conversion of fibroblasts to an extracellular matrix-secreting phenotype. *Scientific Reports*, *11*(1), 108. https://doi.org/10.1038/s41598-020-80509-5

Gause, W. C., Wynn, T. A., & Allen, J. E. (2013). Type 2 immunity and wound healing: evolutionary refinement of adaptive immunity by helminths. *Nature Reviews. Immunology*, *13*(8), 607–614. https://doi.org/10.1038/nri3476

Gautier, V., Cayrol, C., Farache, D., Roga, S., Monsarrat, B., Burlet-Schiltz, O., Gonzalez De Peredo, A., & Girard, J. P. (2016). Extracellular IL-33 cytokine, but not endogenous nuclear IL-33, regulates protein expression in endothelial cells. *Scientific Reports*, *6*(October), 1–12. https://doi.org/10.1038/srep34255

Gebhardt, C., Riehl, A., Durchdewald, M., Németh, J., Fürstenberger, G., Müller-Decker, K., Enk, A., Arnold, B., Bierhaus, A., Nawroth, P. P., Hess, J., & Angel, P. (2008). RAGE signaling sustains inflammation and promotes tumor development. *Journal of Experimental Medicine*, *205*(2), 275–285. https://doi.org/10.1084/jem.20070679

Geoghegan, J. A., Irvine, A. D., & Foster, T. J. (2018). Staphylococcus aureus and Atopic Dermatitis: A Complex and Evolving Relationship. *Trends in Microbiology*, *26*(6), 484–497. https://doi.org/10.1016/j.tim.2017.11.008

Gibson, S., Tu, S., Oyer, R., Anderson, S. M., & Johnson, G. L. (1999). Epidermal Growth Factor Protects Epithelial Cells against Fas-induced Apoptosis: REQUIREMENT FOR Akt ACTIVATION*. *Journal of Biological Chemistry*, *274*(25), 17612–17618. https://doi.org/https://doi.org/10.1074/jbc.274.25.17612

Gilda, J. E., Ghosh, R., Cheah, J. X., West, T. M., Bodine, S. C., & Gomes, A. V. (2015). Western blotting inaccuracies with unverified antibodies: Need for a Western Blotting Minimal Reporting Standard (WBMRS). *PLoS ONE*, *10*(8), 1–18. https://doi.org/10.1371/journal.pone.0135392

Gong, T., Liu, L., Jiang, W., & Zhou, R. (2020). DAMP-sensing receptors in sterile inflammation and inflammatory diseases. *Nature Reviews Immunology*, *20*(2), 95–112. https://doi.org/10.1038/s41577-019-0215-7

Gong, Y. N., Guy, C., Olauson, H., Becker, J. U., Yang, M., Fitzgerald, P., Linkermann, A., & Green, D. R. (2017). ESCRT-III Acts Downstream of MLKL to Regulate

Necroptotic Cell Death and Its Consequences. *Cell*, *169*(2), 286–300.e16. https://doi.org/10.1016/j.cell.2017.03.020

Grasl-Kraupp, B., Ruttkay-Nedecky, B., Koudelka, H., Bukowska, K., Bursch, W., & Schulte-Hermann, R. (1995). In situ detection of fragmented DNA (TUNEL assay) fails to discriminate among apoptosis, necrosis, and autolytic cell death: a cautionary note. *Hepatology (Baltimore, Md.)*, *21*(5), 1465–1468. https://doi.org/10.1002/hep.1840210534

Griesenauer, B., & Paczesny, S. (2017). The ST2/IL-33 axis in immune cells during inflammatory diseases. *Frontiers in Immunology*, *8*(APR), 1–17. https://doi.org/10.3389/fimmu.2017.00475

Grinberg-Bleyer, Y., Dainichi, T., Oh, H., Heise, N., Klein, U., Schmid, R. M., Hayden, M. S., & Ghosh, S. (2015). Cutting edge: NF-κB p65 and c-Rel control epidermal development and immune homeostasis in the skin. *Journal of Immunology (Baltimore, Md. : 1950)*, *194*(6), 2472–2476. https://doi.org/10.4049/jimmunol.1402608

Grooten, J., Goossens, V., Vanhaesebroeck, B., & Fiers, W. (1993). Cell membrane permeabilization and cellular collapse, followed by loss of dehydrogenase activity: early events in tumour necrosis factor-induced cytotoxicity. *Cytokine*, *5*(6), 546–555. https://doi.org/10.1016/s1043-4666(05)80003-1

Grootjans, S., Vanden Berghe, T., & Vandenabeele, P. (2017). Initiation and execution mechanisms of necroptosis: An overview. *Cell Death and Differentiation*, *24*(7), 1184–1195. https://doi.org/10.1038/cdd.2017.65

Guillet, F., Tournefier, A., Denoulet, P., Capony, J. P., Kerfourn, F., & Charlemagne, J. (1990). High levels of HMG1-2 protein expression in the cytoplasm and nucleus of hydrocortisone sensitive amphibian thymocytes. *Biology of the Cell*, *69*(3), 153–160. https://doi.org/10.1016/0248-4900(90)90341-y

Guo, L., Wei, G., Zhu, J., Liao, W., Leonard, W. J., Zhao, K., & Paul, W. (2009). IL-1 family members and STAT activators induce cytokine production by Th2, Th17, and Th1 cells. *Proceedings of the National Academy of Sciences*, *106*(32), 13463 LP – 13468. https://doi.org/10.1073/pnas.0906988106

Haenuki, Y., Matsushita, K., Futatsugi-Yumikura, S., Ishii, K. J., Kawagoe, T., Imoto, Y., Fujieda, S., Yasuda, M., Hisa, Y., Akira, S., Nakanishi, K., & Yoshimoto, T. (2012). A critical role of IL-33 in experimental allergic rhinitis. *The Journal of Allergy and Clinical Immunology*, *130*(1), 184–94.e11. https://doi.org/10.1016/j.jaci.2012.02.013

Hagiwara, S., Sourris, K., Ziemann, M., Tieqiao, W., Mohan, M., McClelland, A. D., Brennan, E., Forbes, J., Coughlan, M., Harcourt, B., Penfold, S., Wang, B., Higgins, G., Pickering, R., El-Osta, A., Thomas, M. C., Cooper, M. E., & Kantharidis, P. (2018). RAGE deletion confers renoprotection by reducing responsiveness to transforming growth factor-β and increasing resistance to apoptosis. *Diabetes*, *67*(5), 960–973. https://doi.org/10.2337/db17-0538

Hamada, N., Maeyama, T., Kawaguchi, T., Yoshimi, M., Fukumoto, J., Yamada, M., Yamada, S., Kuwano, K., & Nakanishi, Y. (2008). The role of high mobility group box1 in pulmonary fibrosis. *American Journal of Respiratory Cell and Molecular Biology*, *39*(4), 440–447. https://doi.org/10.1165/rcmb.2007-0330OC

Han, L., Zhang, M., Liang, X., Jia, X., Jia, J., Zhao, M., & Fan, Y. (2017). Interleukin-33 promotes inflammation-induced lymphangiogenesis via ST2/TRAF6-mediated Akt/eNOS/NO signalling pathway. *Scientific Reports*, *7*(1), 1–8. https://doi.org/10.1038/s41598-017-10894-x

Hardman, C. S., Panova, V., & Mckenzie, A. N. J. (2013). IL-33 citrine reporter mice reveal the temporal and spatial expression of IL-33 during allergic lung inflammation. *European Journal of Immunology*, *43*(2), 488–498. https://doi.org/10.1002/eji.201242863

Harris, H. E., Andersson, U., & Pisetsky, D. S. (2012). HMGB1: A multifunctional alarmin driving autoimmune and inflammatory disease. *Nature Reviews Rheumatology*, *8*(4), 195–202. https://doi.org/10.1038/nrrheum.2011.222

Hayakawa, H., Hayakawa, M., Kume, A., & Tominaga, S. (2007). Soluble ST2 blocks interleukin-33 signaling in allergic airway inflammation. *The Journal of Biological Chemistry*, *282*(36), 26369–26380. https://doi.org/10.1074/jbc.M704916200

Hazlett, L. D., McClellan, S. A., Barrett, R. P., Huang, X., Zhang, Y., Wu, M., van Rooijen, N., & Szliter, E. (2010). IL-33 shifts macrophage polarization, promoting resistance against Pseudomonas aeruginosa keratitis. *Investigative Ophthalmology & Visual Science*, *51*(3), 1524–1532. https://doi.org/10.1167/iovs.09-3983

He, S., Huang, S., & Shen, Z. (2016). Biomarkers for the detection of necroptosis. *Cellular and Molecular Life Sciences*, *73*(11–12), 2177–2181. https://doi.org/10.1007/s00018-016-2192-3

He, S., Liang, Y., Shao, F., & Wang, X. (2011). Toll-like receptors activate programmed necrosis in macrophages through a receptor-interacting kinase-3-mediated pathway. *Proceedings of the National Academy of Sciences of the United States of America*, *108*(50), 20054–20059. https://doi.org/10.1073/pnas.1116302108

He, S., Wang, L., Miao, L., Wang, T., Du, F., Zhao, L., & Wang, X. (2009). Receptor Interacting Protein Kinase-3 Determines Cellular Necrotic Response to TNF-α. *Cell*, *137*(6), 1100–1111. https://doi.org/10.1016/j.cell.2009.05.021

He, S., & Wang, X. (2018). RIP kinases as modulators of inflammation and immunity. *Nature Immunology*, *19*(9), 912–922. https://doi.org/10.1038/s41590-018-0188-x

Herrera, M., Sparks, M. A., Alfonso-Pecchio, A. R., Harrison-Bernard, L. M., & Coffman, T. M. (2013). Lack of specificity of commercial antibodies leads to

misidentification of angiotensin type 1 receptor protein. *Hypertension (Dallas, Tex. : 1979)*, *61*(1), 253–258. https://doi.org/10.1161/HYPERTENSIONAHA.112.203679

Hildebrand, J. M., Tanzer, M. C., Lucet, I. S., Young, S. N., Spall, S. K., Sharma, P., Pierotti, C., Garnier, J. M., Dobson, R. C. J., Webb, A. I., Tripaydonis, A., Babon, J. J., Mulcair, M. D., Scanlon, M. J., Alexander, W. S., Wilks, A. F., Czabotar, P. E., Lessene, G., Murphy, J. M., & Silke, J. (2014). Activation of the pseudokinase MLKL unleashes the four-helix bundle domain to induce membrane localization and necroptotic cell death. *Proceedings of the National Academy of Sciences of the United States of America*, *111*(42), 15072–15077. https://doi.org/10.1073/pnas.1408987111

Ho, A. W., & Kupper, T. S. (2019). T cells and the skin: from protective immunity to inflammatory skin disorders. *Nature Reviews Immunology*, *19*(8), 490–502. https://doi.org/10.1038/s41577-019-0162-3

Hofmann, M. A., Drury, S., Fu, C., Qu, W., Taguchi, A., Lu, Y., Avila, C., Kambham, N., Bierhaus, A., Nawroth, P., Neurath, M. F., Slattery, T., Beach, D., McClary, J., Nagashima, M., Morser, J., Stern, D., & Schmidt, A. M. (1999). RAGE mediates a novel proinflammatory axis: A central cell surface receptor for S100/calgranulin polypeptides. *Cell*, *97*(7), 889–901. https://doi.org/10.1016/S0092-8674(00)80801-6

Holler, N., Zaru, R., Micheau, O., Thome, M., Attinger, a, Valitutti, S., Bodmer, J. L., Schneider, P., Seed, B., & Tschopp, J. (2000). Fas triggers an alternative, caspase-8-independent cell death pathway using the kinase RIP as effector molecule. *Nature Immunology*, *1*(6), 489–495. https://doi.org/10.1038/82732

Honda, T., Yamamoto, O., Sawada, Y., Egawa, G., Kitoh, A., Otsuka, A., Dainichi, T., Nakajima, S., Miyachi, Y., & Kabashima, K. (2017). Receptor-interacting protein kinase 3 controls keratinocyte activation in a necroptosis-independent manner and promotes psoriatic dermatitis in mice. *Journal of Allergy and Clinical Immunology*, *140*(2), 619-622.e6. https://doi.org/10.1016/j.jaci.2017.02.027

Hoshino, K., Kashiwamura, S., Kuribayashi, K., Kodama, T., Tsujimura, T., Nakanishi, K., Matsuyama, T., Takeda, K., & Akira, S. (1999). The absence of interleukin 1 receptor-related T1/ST2 does not affect T helper cell type 2 development and its effector function. *The Journal of Experimental Medicine*, *190*(10), 1541–1548. https://doi.org/10.1084/jem.190.10.1541

Hoste, E., Arwert, E. N., Lal, R., South, A. P., Salas-Alanis, J. C., Murrell, D. F., Donati, G., & Watt, F. M. (2015). Innate sensing of microbial products promotes wound-induced skin cancer. *Nature Communications*, *6*. https://doi.org/10.1038/ncomms6932

Hoste, E., Maueröder, C., van Hove, L., Catrysse, L., Vikkula, H. K., Sze, M., Maes, B., Karjosukarso, D., Martens, L., Gonçalves, A., Parthoens, E., Roelandt, R., Declercq, W., Fuentes, I., Palisson, F., Gonzalez, S., Salas-Alanis, J. C., Boon, L., Huebener, P., … van Loo, G. (2019). Epithelial HMGB1 Delays Skin Wound

Healing and Drives Tumor Initiation by Priming Neutrophils for NET Formation. *Cell Reports*, *29*(9), 2689-2701.e4. https://doi.org/10.1016/j.celrep.2019.10.104

Hsu, H., Shu, H. B., Pan, M. G., & Goeddel, D. V. (1996). TRADD-TRAF2 and TRADD-FADD interactions define two distinct TNF receptor 1 signal transduction pathways. *Cell*, *84*(2), 299–308. https://doi.org/10.1016/S0092-8674(00)80984-8

Hsu, H., Xiong, J., & Goeddel, D. V. (1995). The TNF receptor 1-associated protein TRADD signals cell death and NF-kappa B activation. *Cell*, *81*(4), 495–504. https://doi.org/10.1016/0092-8674(95)90070-5

Hu, X. M., Li, Z. X., Lin, R. H., Shan, J. Q., Yu, Q. W., Wang, R. X., Liao, L. S., Yan, W. T., Wang, Z., Shang, L., Huang, Y., Zhang, Q., & Xiong, K. (2021). Guidelines for Regulated Cell Death Assays: A Systematic Summary, A Categorical Comparison, A Prospective. *Frontiers in Cell and Developmental Biology*, *9*(March), 1–28. https://doi.org/10.3389/fcell.2021.634690

Huebener, P., Pradere, J. P., Hernandez, C., Gwak, G. Y., Caviglia, J. M., Mu, X., Loike, J. D., Jenkins, R. E., Antoine, D. J., & Schwabe, R. F. (2015). The HMGB1/RAGE axis triggers neutrophil-mediated injury amplification following necrosis. *Journal of Clinical Investigation*, *125*(2), 539–550. https://doi.org/10.1172/JCI76887

Hueber, A J, Miller, A. M., Asquith, D. L., Millar, N. L., Gilchrist, D., Gracie, A., & McInnes, I. B. (2010). Alarmin interleukin 33 is overexpressed in psoriasis and induces ST2-dependent psoriasis-like dermatitis. *Annals of the Rheumatic Diseases*, *69*(Suppl 2), A40--A41. https://doi.org/10.1136/ard.2010.129627n

Hueber, Axel J., Alves-Filho, J. C., Asquith, D. L., Michels, C., Millar, N. L., Reilly, J. H., Graham, G. J., Liew, F. Y., Miller, A. M., & McInnes, I. B. (2011). IL-33 induces skin inflammation with mast cell and neutrophil activation. *European Journal of Immunology*, *41*(8), 2229–2237. https://doi.org/10.1002/eji.201041360

Humphreys, N. E., Xu, D., Hepworth, M. R., Liew, F. Y., & Grencis, R. K. (2008). IL-33, a potent inducer of adaptive immunity to intestinal nematodes. *Journal of Immunology (Baltimore, Md. : 1950)*, *180*(4), 2443–2449. https://doi.org/10.4049/jimmunol.180.4.2443

Hung, L.-Y., Lewkowich, I. P., Dawson, L. A., Downey, J., Yang, Y., Smith, D. E., & Herbert, D. R. (2013). IL-33 drives biphasic IL-13 production for noncanonical Type 2 immunity against hookworms. *Proceedings of the National Academy of Sciences of the United States of America*, *110*(1), 282–287. https://doi.org/10.1073/pnas.1206587110

Imai, Y., Yasuda, K., Nagai, M., Kusakabe, M., Kubo, M., Nakanishi, K., & Yamanishi, K. (2019). IL-33–Induced Atopic Dermatitis–Like Inflammation in Mice Is Mediated by Group 2 Innate Lymphoid Cells in Concert with Basophils. *Journal of Investigative Dermatology*, *139*(10), 2185-2194.e3. https://doi.org/10.1016/j.jid.2019.04.016

Imai, Y., Yasuda, K., Sakaguchi, Y., Haneda, T., Mizutani, H., Yoshimoto, T., Nakanishi, K., & Yamanishi, K. (2013). Skin-specific expression of IL-33 activates group 2 innate lymphoid cells and elicits atopic dermatitis-like inflammation in mice. *Proceedings of the National Academy of Sciences of the United States of America*, *110*(34), 13921–13926. https://doi.org/10.1073/pnas.1307321110

Irmler, M., Thome, M., Hahne, M., Schneider, P., Hofmann, K., Steiner, V., Bodmer, J. L., Schröter, M., Burns, K., Mattmann, C., Rimoldi, D., French, L. E., & Tschopp, J. (1997). Inhibition of death receptor signals by cellular FLIP. *Nature*, *388*(6638), 190–195. https://doi.org/10.1038/40657

Ivanov, S., Dragoi, A.-M., Wang, X., Dallacosta, C., Louten, J., Musco, G., Sitia, G., Yap, G. S., Wan, Y., Biron, C. A., Bianchi, M. E., Wang, H., & Chu, W.-M. (2007). A novel role for HMGB1 in TLR9-mediated inflammatory responses to CpG-DNA. *Blood*, *110*(6), 1970–1981. https://doi.org/10.1182/blood-2006-09-044776

Jaco, I., Annibaldi, A., Lalaoui, N., Wilson, R., Tenev, T., Laurien, L., Kim, C., Jamal, K., Wicky John, S., Liccardi, G., Chau, D., Murphy, J. M., Brumatti, G., Feltham, R., Pasparakis, M., Silke, J., & Meier, P. (2017). MK2 Phosphorylates RIPK1 to Prevent TNF-Induced Cell Death. *Molecular Cell*, *66*(5), 698–710.e5. https://doi.org/10.1016/j.molcel.2017.05.003

Jacobsen, A. V., Lowes, K. N., Tanzer, M. C., Lucet, I. S., Hildebrand, J. M., Petrie, E. J., Van Delft, M. F., Liu, Z., Conos, S. A., Zhang, J. G., Huang, D. C. S., Silke, J., Lessene, G., & Murphy, J. M. (2016). HSP90 activity is required for MLKL oligomerisation and membrane translocation and the induction of necroptotic cell death. *Cell Death and Disease*, *7*, e2051. https://doi.org/10.1038/cddis.2015.386

Jiang, W., Lian, J., Yue, Y., & Zhang, Y. (2021). IL-33/ST2 as a potential target for tumor immunotherapy. *European Journal of Immunology*, *51*(8), 1943–1955. https://doi.org/10.1002/eji.202149175

Johnston, A. N., Ma, Y., Liu, H., Liu, S., Hanna-Addams, S., Chen, S., Chen, C., & Wang, Z. (2020). Necroptosis-blocking compound NBC1 targets heat shock protein 70 to inhibit MLKL polymerization and necroptosis. *Proceedings of the National Academy of Sciences of the United States of America*, *117*(12), 6521–6530. https://doi.org/10.1073/pnas.1916503117

Julie Henry Eve Toulza, C.-Y. H. L. P. S. B. J. M.-H. C. P. G. S. N. J. M. S. (2012). Update on the epidermal differentiation complex. *Frontiers in Bioscience-Landmark*, *17*(4), 1517–1532. https://doi.org/10.2741/4001

Kabashima, K., Honda, T., Ginhoux, F., & Egawa, G. (2019). The immunological anatomy of the skin. *Nature Reviews Immunology*, *19*(1), 19–30. https://doi.org/10.1038/s41577-018-0084-5

Kaczmarek, A., Vandenabeele, P., & Krysko, D. V. (2013). Necroptosis: The Release of Damage-Associated Molecular Patterns and Its Physiological Relevance.

Immunity, *38*(2), 209–223. https://doi.org/10.1016/j.immuni.2013.02.003

Kaiser, W. J., Daley-Bauer, L. P., Thapa, R. J., Mandal, P., Berger, S. B., Huang, C., Sundararajan, A., Guo, H., Roback, L., Speck, S. H., Bertin, J., Gough, P. J., Balachandran, S., & Mocarski, E. S. (2014). RIP1 suppresses innate immune necrotic as well as apoptotic cell death during mammalian parturition. *Proceedings of the National Academy of Sciences of the United States of America*, *111*(21), 7753–7758. https://doi.org/10.1073/pnas.1401857111

Kaiser, W. J., & Offermann, M. K. (2005). Apoptosis induced by the toll-like receptor adaptor TRIF is dependent on its receptor interacting protein homotypic interaction motif. *Journal of Immunology (Baltimore, Md. : 1950)*, *174*(8), 4942–4952. https://doi.org/10.4049/jimmunol.174.8.4942

Kaiser, W. J., Sridharan, H., Huang, C., Mandal, P., Upton, J. W., Gough, P. J., Sehon, C. A., Marquis, R. W., Bertin, J., & Mocarski, E. S. (2013). Toll-like receptor 3-mediated necrosis via TRIF, RIP3, and MLKL. *The Journal of Biological Chemistry*, *288*(43), 31268–31279. https://doi.org/10.1074/jbc.M113.462341

Kaiser, W. J., Upton, J. W., Long, A. B., Livingston-Rosanoff, D., Daley-Bauer, L. P., Hakem, R., Caspary, T., & Mocarski, E. S. (2011). RIP3 mediates the embryonic lethality of caspase-8-deficient mice. *Nature*, *471*(7338), 368–373. https://doi.org/10.1038/nature09857

Kaiser, W. J., Upton, J. W., & Mocarski, E. S. (2013). Viral modulation of programmed necrosis. *Current Opinion in Virology*, *3*(3), 296–306. https://doi.org/10.1016/j.coviro.2013.05.019

Kakkar, R., Hei, H., Dobner, S., & Lee, R. T. (2012). Interleukin 33 as a mechanically responsive cytokine secreted by living cells. *Journal of Biological Chemistry*, *287*(9), 6941–6948. https://doi.org/10.1074/jbc.M111.298703

Kalinina, N., Agrotis, A., Antropova, Y., DiVitto, G., Kanellakis, P., Kostolias, G., Ilyinskaya, O., Tararak, E., & Bobik, A. (2004). Increased expression of the DNA-binding cytokine HMGB1 in human atherosclerotic lesions: role of activated macrophages and cytokines. *Arteriosclerosis, Thrombosis, and Vascular Biology*, *24*(12), 2320–2325. https://doi.org/10.1161/01.ATV.0000145573.36113.8a

Kamo, N., Ke, B., Ghaffari, A. A., Shen, X., Busuttil, R. W., Cheng, G., & Kupiec-Weglinski, J. W. (2013). ASC/caspase-1/IL-1β signaling triggers inflammatory responses by promoting HMGB1 induction in liver ischemia/reperfusion injury. *Hepatology (Baltimore, Md.)*, *58*(1), 351–362. https://doi.org/10.1002/hep.26320

Kang, R., Chen, R., Zhang, Q., Hou, W., Wu, S., Cao, L., Huang, J., Yu, Y., Fan, X. G., Yan, Z., Sun, X., Wang, H., Wang, Q., Tsung, A., Billiar, T. R., Zeh, H. J., Lotze, M. T., & Tang, D. (2014). HMGB1 in health and disease. *Molecular Aspects of Medicine*, *40*, 1–116. https://doi.org/10.1016/j.mam.2014.05.001

Kang, S. K., Hawkins, N. A., & Kearney, J. A. (2018). C57BL/6J and C57BL/6N

substrains differentially influence phenotype severity in the Scn1a (+/-) mouse model of Dravet syndrome. *Epilepsia Open*, *4*(1), 164–169. https://doi.org/10.1002/epi4.12287

Kang, T.-B., Yang, S.-H., Toth, B., Kovalenko, A., & Wallach, D. (2013). Caspase-8 blocks kinase RIPK3-mediated activation of the NLRP3 inflammasome. *Immunity*, *38*(1), 27–40. https://doi.org/10.1016/j.immuni.2012.09.015

Kearley, J., Silver, J. S., Sanden, C., Liu, Z., Berlin, A. A., White, N., Mori, M., Pham, T.-H., Ward, C. K., Criner, G. J., Marchetti, N., Mustelin, T., Erjefalt, J. S., Kolbeck, R., & Humbles, A. A. (2015). Cigarette smoke silences innate lymphoid cell function and facilitates an exacerbated type I interleukin-33-dependent response to infection. *Immunity*, *42*(3), 566–579. https://doi.org/10.1016/j.immuni.2015.02.011

Kearney, C. J., Cullen, S. P., Clancy, D., & Martin, S. J. (2014). RIPK1 can function as an inhibitor rather than an initiator of RIPK3-dependent necroptosis. *The FEBS Journal*, *281*(21), 4921–4934. https://doi.org/10.1111/febs.13034

Kelliher, M. A., Grimm, S., Ishida, Y., Kuo, F., Stanger, B. Z., & Leder, P. (1998). The death domain kinase RIP mediates the TNF-induced NF-κB signal. *Immunity*, *8*(3), 297–303. https://doi.org/10.1016/S1074-7613(00)80535-X

Kerr, J. F. R., Wyllie, A. H., & Currie, A. R. (1972). Apoptosis: A Basic Biological Phenomenon with Wide-ranging Implications in Tissue Kinetics. *British Journal of Cancer*, *26*(4), 239–257. http://www.ncbi.nlm.nih.gov/pmc/articles/PMC2008650/

Khan, I., Yousif, A., Chesnokov, M., Hong, L., & Chefetz, Ii. I. (2021). A decade of cell death studies: Breathing new life into necroptosis. *Pharmacology and Therapeutics*, *220*, 107717. https://doi.org/10.1016/j.pharmthera.2020.107717

Khan, N., Lawlor, K. E., Murphy, J. M., & Vince, J. E. (2014). More to life than death: molecular determinants of necroptotic and non-necroptotic RIP3 kinase signaling. *Current Opinion in Immunology*, *26*, 76–89. https://doi.org/https://doi.org/10.1016/j.coi.2013.10.017

Khoury, M. K., Gupta, K., Franco, S. R., & Liu, B. (2020). Necroptosis in the Pathophysiology of Disease. *American Journal of Pathology*, *190*(2), 272–285. https://doi.org/10.1016/j.ajpath.2019.10.012

Kim, I.-D., Lim, C.-M., Kim, J.-B., Nam, H. Y., Nam, K., Kim, S.-W., Park, J.-S., & Lee, J.-K. (2010). Neuroprotection by biodegradable PAMAM ester (e-PAM-R)-mediated HMGB1 siRNA delivery in primary cortical cultures and in the postischemic brain. *Journal of Controlled Release*, *142*(3), 422–430. https://doi.org/https://doi.org/10.1016/j.jconrel.2009.11.011

Kim, S. K., Kim, W. J., Yoon, J. H., Ji, J. H., Morgan, M. J., Cho, H., Kim, Y. C., & Kim, Y. S. (2015). Upregulated RIP3 Expression Potentiates MLKL Phosphorylation-Mediated Programmed Necrosis in Toxic Epidermal Necrolysis. *Journal of*

Investigative Dermatology, *135*(8), 2021–2030. https://doi.org/10.1038/jid.2015.90

Klement, J. F., Rice, N. R., Car, B. D., Abbondanzo, S. J., Powers, G. D., Bhatt, P. H., Chen, C. H., Rosen, C. A., & Stewart, C. L. (1996). IkappaBalpha deficiency results in a sustained NF-kappaB response and severe widespread dermatitis in mice. *Molecular and Cellular Biology*, *16*(5), 2341–2349. https://doi.org/10.1128/MCB.16.5.2341

Kobayashi, T., Ricardo-Gonzalez, R. R., & Moro, K. (2020). Skin-Resident Innate Lymphoid Cells – Cutaneous Innate Guardians and Regulators. *Trends in Immunology*, *41*(2), 100–112. https://doi.org/10.1016/j.it.2019.12.004

Kokkola, R., Li, J., Sundberg, E., Aveberger, A. C., Palmblad, K., Yang, H., Tracey, K. J., Andersson, U., & Erlandsson Harris, H. (2003). Successful treatment of collagen-induced arthritis in mice and rats by targeting extracellular high mobility group box chromosomal protein 1 activity. *Arthritis and Rheumatism*, *48*(7), 2052–2058. https://doi.org/10.1002/art.11161

Kokkola, R., Sundberg, E., Ulfgren, A.-K., Palmblad, K., Li, J., Wang, H., Ulloa, L., Yang, H., Yan, X.-J., Furie, R., Chiorazzi, N., Tracey, K. J., Andersson, U., & Harris, H. E. (2002). High mobility group box chromosomal protein 1: a novel proinflammatory mediator in synovitis. *Arthritis and Rheumatism*, *46*(10), 2598–2603. https://doi.org/10.1002/art.10540

Kostura, M. J., Tocci, M. J., Limjuco, G., Chin, J., Cameron, P., Hillman, A. G., Chartrain, N. A., & Schmidt, J. A. (1989). Identification of a monocyte specific pre-interleukin 1 beta convertase activity. *Proceedings of the National Academy of Sciences of the United States of America*, *86*(14), 5227–5231. https://doi.org/10.1073/pnas.86.14.5227

Kotsiou, O. S., Gourgoulianis, K. I., & Zarogiannis, S. G. (2018). IL-33/ST2 Axis in Organ Fibrosis. *Frontiers in Immunology*, *9*, 2432. https://doi.org/10.3389/fimmu.2018.02432

Kovalenko, A., Kim, J.-C., Kang, T.-B., Rajput, A., Bogdanov, K., Dittrich-Breiholz, O., Kracht, M., Brenner, O., & Wallach, D. (2009). Caspase-8 deficiency in epidermal keratinocytes triggers an inflammatory skin disease. *The Journal of Experimental Medicine*, *206*(10), 2161–2177. https://doi.org/10.1084/jem.20090616

Kroemer, G., Dallaporta, B., & Resche-Rigon, M. (1998). THE MITOCHONDRIAL DEATH/LIFE REGULATOR IN APOPTOSIS AND NECROSIS. *Annual Review of Physiology*, *60*(1), 619–642. https://doi.org/10.1146/annurev.physiol.60.1.619

Krysko, O., Løve Aaes, T., Bachert, C., Vandenabeele, P., & Krysko, D. V. (2013). Many faces of DAMPs in cancer therapy. *Cell Death & Disease*, *4*(5), e631. https://doi.org/10.1038/cddis.2013.156

Kuida, K., Haydar, T. F., Kuan, C. Y., Gu, Y., Taya, C., Karasuyama, H., Su, M. S.,

Rakic, P., & Flavell, R. A. (1998). Reduced apoptosis and cytochrome c-mediated caspase activation in mice lacking caspase 9. *Cell*, *94*(3), 325–337. https://doi.org/10.1016/s0092-8674(00)81476-2

Kuida, K., Zheng, T. S., Na, S., Kuan, C., Yang, D., Karasuyama, H., Rakic, P., & Flavell, R. A. (1996). Decreased apoptosis in the brain and premature lethality in CPP32-deficient mice. *Nature*, *384*(6607), 368–372. https://doi.org/10.1038/384368a0

Kumar, S., Tzimas, M. N., Griswold, D. E., & Young, P. R. (1997). Expression of ST2, an interleukin-1 receptor homologue, is induced by proinflammatory stimuli. *Biochemical and Biophysical Research Communications*, *235*(3), 474–478. https://doi.org/10.1006/bbrc.1997.6810

Kumari, S., Bonnet, M. C., Ulvmar, M. H., Wolk, K., Karagianni, N., Witte, E., Uthoff-Hachenberg, C., Renauld, J. C., Kollias, G., Toftgard, R., Sabat, R., Pasparakis, M., & Haase, I. (2013). Tumor necrosis factor receptor signaling in keratinocytes triggers interleukin-24-dependent psoriasis-like skin inflammation in mice. *Immunity*, *39*(5), 899–911. https://doi.org/10.1016/j.immuni.2013.10.009

Kumari, S., & Pasparakis, M. (2015). Epithelial cell death and inflammation in skin. *Current Topics in Microbiology and Immunology*, *6*(4), 23–27. https://doi.org/10.1007/82

Kumari, S., Redouane, Y., Lopez-Mosqueda, J., Shiraishi, R., Romanowska, M., Lutzmayer, S., Kuiper, J., Martinez, C., Dikic, I., Pasparakis, M., & Ikeda, F. (2014). Sharpin prevents skin inflammation by inhibiting TNFR1-induced keratinocyte apoptosis. *ELife*, *3*. https://doi.org/10.7554/eLife.03422

Kumari, S., Van, T. M., Preukschat, D., Schuenke, H., Basic, M., Bleich, A., Klein, U., & Pasparakis, M. (2021). NF-κB inhibition in keratinocytes causes RIPK1-mediated necroptosis and skin inflammation. *Life Science Alliance*, *4*(6), 1–14. https://doi.org/10.26508/LSA.202000956

Kypriotou, M., Huber, M., & Hohl, D. (2012). The human epidermal differentiation complex: cornified envelope precursors, S100 proteins and the “fused genes” family. *Experimental Dermatology*, *21*(9), 643–649. https://doi.org/10.1111/j.1600-0625.2012.01472.x

Lalaoui, N., Boyden, S. E., Oda, H., Wood, G. M., Stone, D. L., Chau, D., Liu, L., Stoffels, M., Kratina, T., Lawlor, K. E., Zaal, K. J. M., Hoffmann, P. M., Etemadi, N., Shield-Artin, K., Biben, C., Tsai, W. L., Blake, M. D., Kuehn, H. S., Yang, D., … Silke, J. (2020). Mutations that prevent caspase cleavage of RIPK1 cause autoinflammatory disease. *Nature*, *577*(7788), 103–108. https://doi.org/10.1038/s41586-019-1828-5

Laster, S. M., Wood, J. G., & Gooding, L. R. (1988). Tumor necrosis factor can induce both apoptic and necrotic forms of cell lysis. *Journal of Immunology (Baltimore, Md. : 1950)*, *141*(8), 2629–2634.

Lau, A., Wang, S., Liu, W., Haig, A., Zhang, Z.-X., & Jevnikar, A. M. (2014). Glycyrrhizic acid ameliorates HMGB1-mediated cell death and inflammation after renal ischemia reperfusion injury. *American Journal of Nephrology*, *40*(1), 84–95. https://doi.org/10.1159/000364908

Lauffer, F., Jargosch, M., Krause, L., Garzorz-Stark, N., Franz, R., Roenneberg, S., Böhner, A., Mueller, N. S., Theis, F. J., Schmidt-Weber, C. B., Biedermann, T., Eyerich, S., & Eyerich, K. (2018). Type I Immune Response Induces Keratinocyte Necroptosis and Is Associated with Interface Dermatitis. *Journal of Investigative Dermatology*, *138*(8), 1785–1794. https://doi.org/10.1016/j.jid.2018.02.034

Laurien, L., Nagata, M., Schünke, H., Delanghe, T., Wiederstein, J. L., Kumari, S., Schwarzer, R., Corona, T., Krüger, M., Bertrand, M. J. M., Kondylis, V., & Pasparakis, M. (2020). Autophosphorylation at serine 166 regulates RIP kinase 1-mediated cell death and inflammation. *Nature Communications*, *11*(1). https://doi.org/10.1038/s41467-020-15466-8

Lawlor, K. E., Khan, N., Mildenhall, A., Gerlic, M., Croker, B. A., D'Cruz, A. A., Hall, C., Kaur Spall, S., Anderton, H., Masters, S. L., Rashidi, M., Wicks, I. P., Alexander, W. S., Mitsuuchi, Y., Benetatos, C. A., Condon, S. M., Wong, W. W. L., Silke, J., Vaux, D. L., & Vince, J. E. (2015). RIPK3 promotes cell death and NLRP3 inflammasome activation in the absence of MLKL. *Nature Communications*, *6*. https://doi.org/10.1038/ncomms7282

Lawton, S. (2019). Structure and Functions of the Skin. *Nursing Times [Online]*, *29*(12), 30–33. https://doi.org/10.1097/00000441-183411000-00032

Le, H. T., Tran, V. G., Kim, W., Kim, J., Cho, H. R., & Kwon, B. (2012). IL-33 priming regulates multiple steps of the neutrophil-mediated anti-Candida albicans response by modulating TLR and dectin-1 signals. *Journal of Immunology (Baltimore, Md. : 1950)*, *189*(1), 287–295. https://doi.org/10.4049/jimmunol.1103564

Lee, E. G., Boone, D. L., Chai, S., Libby, S. L., Chien, M., Lodolce, J. P., & Ma, A. (2000). Failure to regulate TNF-induced NF-kappaB and cell death responses in A20-deficient mice. *Science (New York, N.Y.)*, *289*(5488), 2350–2354. https://doi.org/10.1126/science.289.5488.2350

Lee, H., Shin, N., Song, M., Kang, U.-B., Yeom, J., Lee, C., Ahn, Y. H., Yoo, J. S., Paik, Y.-K., & Kim, H. (2010). Analysis of Nuclear High Mobility Group Box 1 (HMGB1)-Binding Proteins in Colon Cancer Cells: Clustering with Proteins Involved in Secretion and Extranuclear Function. *Journal of Proteome Research*, *9*(9), 4661–4670. https://doi.org/10.1021/pr100386r

Lee, J. S., Seppanen, E., Patel, J., Rodero, M. P., & Khosrotehrani, K. (2016). ST2 receptor invalidation maintains wound inflammation, delays healing and increases fibrosis. *Experimental Dermatology*, *25*(1), 71–74. https://doi.org/10.1111/exd.12833

Lee, P., Lee, D. J., Chan, C., Chen, S. W., Ch'en, I., & Jamora, C. (2009). Dynamic expression of epidermal caspase 8 simulates a wound healing response. *Nature*, *458*(7237), 519–523. https://doi.org/10.1038/nature07687.Dynamic

Lee, Pedro, Lee, D. J., Chan, C., Chen, S. W., Chen, I., & Jamora, C. (2009). Dynamic expression of epidermal caspase 8 simulates a wound healing response. *Nature*, *458*(7237), 519–523. https://doi.org/10.1038/nature07687

Lefrançais, E., Duval, A., Mirey, E., Roga, S., Espinosa, E., Cayrol, C., & Girard, J.-P. (2014). Central domain of IL-33 is cleaved by mast cell proteases for potent activation of group-2 innate lymphoid cells. *Proceedings of the National Academy of Sciences of the United States of America*, *111*(43), 15502–15507. https://doi.org/10.1073/pnas.1410700111

Lefrançais, E., Roga, S., Gautier, V., Gonzalez-de-Peredo, A., Monsarrat, B., Girard, J.-P., & Cayrol, C. (2012). IL-33 is processed into mature bioactive forms by neutrophil elastase and cathepsin G. *Proceedings of the National Academy of Sciences of the United States of America*, *109*(5), 1673–1678. https://doi.org/10.1073/pnas.1115884109

Leibold, J. S., Riehl, A., Hettinger, J., Durben, M., Hess, J., & Angel, P. (2013). Keratinocyte-specific deletion of the receptor rage modulates the kinetics of skin inflammation in vivo. *Journal of Investigative Dermatology*, *133*(10), 2400–2406. https://doi.org/10.1038/jid.2013.185

Leuner, B., Max, M., Thamm, K., Kausler, C., Yakobus, Y., Bierhaus, A., Sel, S., Hofmann, B., Silber, R.-E., Simm, A., & Nass, N. (2012). RAGE influences obesity in mice. *Zeitschrift Für Gerontologie Und Geriatrie*, *45*(2), 102–108. https://doi.org/10.1007/s00391-011-0279-x

Leung, B. P., Xu, D., Culshaw, S., McInnes, I. B., & Liew, F. Y. (2004). A novel therapy of murine collagen-induced arthritis with soluble T1/ST2. *Journal of Immunology (Baltimore, Md. : 1950)*, *173*(1), 145–150. https://doi.org/10.4049/jimmunol.173.1.145

Li, D., Guabiraba, R., Besnard, A.-G., Komai-Koma, M., Jabir, M. S., Zhang, L., Graham, G. J., Kurowska-Stolarska, M., Liew, F. Y., McSharry, C., & Xu, D. (2014). IL-33 promotes ST2-dependent lung fibrosis by the induction of alternatively activated macrophages and innate lymphoid cells in mice. *Journal of Allergy and Clinical Immunology*, *134*(6), 1422–1432.e11. https://doi.org/https://doi.org/10.1016/j.jaci.2014.05.011

Li, J.-X., Feng, J.-M., Wang, Y., Li, X.-H., Chen, X.-X., Su, Y., Shen, Y.-Y., Chen, Y., Xiong, B., Yang, C.-H., Ding, J., & Miao, Z.-H. (2014). The B-Raf(V600E) inhibitor dabrafenib selectively inhibits RIP3 and alleviates acetaminophen-induced liver injury. *Cell Death & Disease*, *5*(6), e1278. https://doi.org/10.1038/cddis.2014.241

Li, Jianfeng, Qu, X., & Schmidt, A. M. (1998). Sp1-binding Elements in the Promoter of RAGE Are Essential for Amphoterin-mediated Gene Expression in Cultured

Neuroblastoma Cells*. *Journal of Biological Chemistry*, *273*(47), 30870–30878. https://doi.org/https://doi.org/10.1074/jbc.273.47.30870

Li, Jixi, McQuade, T., Siemer, A. B., Napetschnig, J., Moriwaki, K., Hsiao, Y.-S., Damko, E., Moquin, D., Walz, T., McDermott, A., Chan, F. K.-M., & Wu, H. (2012). The RIP1/RIP3 Necrosome Forms a Functional Amyloid Signaling Complex Required for Programmed Necrosis. *Cell*, *150*(2), 339–350. https://doi.org/https://doi.org/10.1016/j.cell.2012.06.019

Li, P., Ma, H., Han, D., & Mou, K. (2015). Interleukin-33 affects cytokine production by keratinocytes in vitiligo. *Clinical and Experimental Dermatology*, *40*(2), 163–170. https://doi.org/10.1111/ced.12464

Liew, F. Y., Pitman, N. I., & McInnes, I. B. (2010). Disease-associated functions of IL-33: The new kid in the IL-1 family. *Nature Reviews Immunology*, *10*(2), 103–110. https://doi.org/10.1038/nri2692

Liliensiek, B., Weigand, M. A., Bierhaus, A., Nicklas, W., Kasper, M., Hofer, S., Plachky, J., Gröne, H. J., Kurschus, F. C., Schmidt, A. M., Yan, S. Du, Martin, E., Schleicher, E., Stern, D. M., Hämmerling, G. J., Nawroth, P. P., & Arnold, B. (2004). Receptor for advanced glycation end products (RAGE) regulates sepsis but not the adaptive immune response. *Journal of Clinical Investigation*, *113*(11), 1641–1650. https://doi.org/10.1172/JCI200418704

Lin, H., Shen, L., Zhang, X., Xie, J., Hao, H., Zhang, Y., Chen, Z., Yamamoto, H., Liao, W., Bin, J., Cao, S., Huang, X., & Liao, Y. (2016). HMGB1-RAGE axis makes no contribution to cardiac remodeling induced by pressure-overload. *PLoS ONE*, *11*(6), 1–13. https://doi.org/10.1371/journal.pone.0158514

Lin, J., Kumari, S., Kim, C., Van, T. M., Wachsmuth, L., Polykratis, A., & Pasparakis, M. (2016). RIPK1 counteracts ZBP1-mediated necroptosis to inhibit inflammation. *Nature*, *540*(7631), 124–128. https://doi.org/10.1038/nature20558

Liu, K., Mori, S., Takahashi, H. K., Tomono, Y., Wake, H., Kanke, T., Sato, Y., Hiraga, N., Adachi, N., Yoshino, T., & Nishibori, M. (2007). Anti-high mobility group box 1 monoclonal antibody ameliorates brain infarction induced by transient ischemia in rats. *The FASEB Journal*, *21*(14), 3904–3916. https://doi.org/10.1096/fj.07-8770com

Liu, T., Zhang, L., Joo, D., & Sun, S. C. (2017). NF-κB signaling in inflammation. *Signal Transduction and Targeted Therapy*, *2*(April). https://doi.org/10.1038/sigtrans.2017.23

Liu, X., Shi, F., Li, Y., Yu, X., Peng, S., Li, W., Luo, X., & Cao, Y. (2016). Post-translational modifications as key regulators of TNF-induced necroptosis. *Cell Death & Disease*, *7*(7), e2293. https://doi.org/10.1038/cddis.2016.197

Liu, Yongbo, Fan, C., Zhang, Y., Yu, X., Wu, X., Zhang, X., Zhao, Q., Zhang, H., Xie, Q., Li, M., Li, X., Ding, Q., Ying, H., Li, D., & Zhang, H. (2017). RIP1 kinase activity-dependent roles in embryonic development of Fadd-deficient mice. *Cell*

Death and Differentiation, *24*(8), 1459–1469. https://doi.org/10.1038/cdd.2017.78

Liu, Yuping, Liu, T., Lei, T., Zhang, D., Du, S., Girani, L., Qi, D., Lin, C., Tong, R., & Wang, Y. (2019). RIP1/RIP3-regulated necroptosis as a target for multifaceted disease therapy (Review). *Int J Mol Med*, *44*(3), 771–786. https://doi.org/10.3892/ijmm.2019.4244

Löhning, M., Stroehmann, A., Coyle, A. J., Grogan, J. L., Lin, S., Gutierrez-Ramos, J.-C., Levinson, D., Radbruch, A., & Kamradt, T. (1998). T1/ST2 is preferentially expressed on murine Th2 cells, independent of interleukin 4, interleukin 5, and interleukin 10, and important for Th2 effector function. *Proceedings of the National Academy of Sciences*, *95*(12), 6930 LP – 6935. https://doi.org/10.1073/pnas.95.12.6930

Lopetuso, L. R., Chowdhry, S., & Pizarro, T. T. (2013). Opposing Functions of Classic and Novel IL-1 Family Members in Gut Health and Disease. *Frontiers in Immunology*, *4*, 181. https://doi.org/10.3389/fimmu.2013.00181

Lork, M., Verhelst, K., & Beyaert, R. (2017). CYLD, A20 and OTULIN deubiquitinases in NF-κB signaling and cell death: So similar, yet so different. *Cell Death and Differentiation*, *24*(7), 1172–1183. https://doi.org/10.1038/cdd.2017.46

Lu, B., Nakamura, T., Inouye, K., Li, J., Tang, Y., Lundbäck, P., Valdes-Ferrer, S. I., Olofsson, P. S., Kalb, T., Roth, J., Zou, Y., Erlandsson-Harris, H., Yang, H., Ting, J. P.-Y., Wang, H., Andersson, U., Antoine, D. J., Chavan, S. S., Hotamisligil, G. S., & Tracey, K. J. (2012). Novel role of PKR in inflammasome activation and HMGB1 release. *Nature*, *488*(7413), 670–674. https://doi.org/10.1038/nature11290

Lüthi, A. U., Cullen, S. P., McNeela, E. A., Duriez, P. J., Afonina, I. S., Sheridan, C., Brumatti, G., Taylor, R. C., Kersse, K., Vandenabeele, P., Lavelle, E. C., & Martin, S. J. (2009). Suppression of interleukin-33 bioactivity through proteolysis by apoptotic caspases. *Immunity*, *31*(1), 84–98. https://doi.org/10.1016/j.immuni.2009.05.007

Lutterloh, E. C., Opal, S. M., Pittman, D. D., Keith, J. C., Tan, X. Y., Clancy, B. M., Palmer, H., Milarski, K., Sun, Y., Palardy, J. E., Parejo, N. A., & Kessimian, N. (2007). Inhibition of the RAGE products increases survival in experimental models of severe sepsis and systemic infection. *Critical Care*, *11*(6), 1–9. https://doi.org/10.1186/cc6184

Ma, C., Jiao, Y., Zhang, J., Yang, Q., Zhang, Z., Shen, Y., Chen, Z., & Zhao, Y. (2012). Elevated plasma level of HMGB1 is associated with disease activity and combined alterations with IFN-α and TNF-α in systemic lupus erythematosus. *Rheumatology International*, *32*(2), 395–402. https://doi.org/10.1007/s00296-010-1636-6

Majno, G., & Joris, I. (1995). Apoptosis, oncosis, and necrosis. An overview of cell

death. *The American Journal of Pathology*, *146*(1), 3–15.

Manetti, M., Ibba-Manneschi, L., Liakouli, V., Guiducci, S., Milia, A. F., Benelli, G., Marrelli, A., Conforti, M. L., Romano, E., Giacomelli, R., Matucci-Cerinic, M., & Cipriani, P. (2010). The IL1-like cytokine IL33 and its receptor ST2 are abnormally expressed in the affected skin and visceral organs of patients with systemic sclerosis. *Annals of the Rheumatic Diseases*, *69*(3), 598–605. https://doi.org/10.1136/ard.2009.119321

Martin, N. T., & Martin, M. U. (2016). Interleukin 33 is a guardian of barriers and a local alarmin. *Nature Immunology*, *17*(2), 122–131. https://doi.org/10.1038/ni.3370

Martin, P., Talabot-Ayer, D., Seemayer, C. A., Vigne, S., Lamacchia, C., Rodriguez, E., Finckh, A., Smith, D. E., Gabay, C., & Palmer, G. (2013). Disease severity in K/BxN serum transfer-induced arthritis is not affected by IL-33 deficiency. *Arthritis Research and Therapy*, *15*(1), R13. https://doi.org/10.1186/ar4143

Marvie, P., Lisbonne, M., L'helgoualc'h, A., Rauch, M., Turlin, B., Preisser, L., Bourd-Boittin, K., Théret, N., Gascan, H., Piquet-Pellorce, C., & Samson, M. (2010). Interleukin-33 overexpression is associated with liver fibrosis in mice and humans. *Journal of Cellular and Molecular Medicine*, *14*(6B), 1726–1739. https://doi.org/10.1111/j.1582-4934.2009.00801.x

Matsui, T., & Amagai, M. (2015). Dissecting the formation, structure and barrier function of the stratum corneum. *International Immunology*, *27*(6), 269–280. https://doi.org/10.1093/intimm/dxv013

Matzinger, P. (1994). Tolerance, danger, and the extended family. *Annual Review of Immunology*, *12*, 991–1045. https://doi.org/10.1146/annurev.iy.12.040194.005015

McComb, S., Cessford, E., Alturki, N. A., Joseph, J., Shutinoski, B., Startek, J. B., Gamero, A. M., Mossman, K. L., & Sad, S. (2014). Type-I interferon signaling through ISGF3 complex is required for sustained Rip3 activation and necroptosis in macrophages. *Proceedings of the National Academy of Sciences of the United States of America*, *111*(31), E3206-13. https://doi.org/10.1073/pnas.1407068111

Meephansan, J., Tsuda, H., Komine, M., Tominaga, S. I., & Ohtsuki, M. (2012). Regulation of IL-33 expression by IFN-γ and tumor necrosis factor-α in normal human epidermal keratinocytes. *Journal of Investigative Dermatology*, *132*(11), 2593–2600. https://doi.org/10.1038/jid.2012.185

Menon, M. B., Gropengießer, J., Fischer, J., Novikova, L., Deuretzbacher, A., Lafera, J., Schimmeck, H., Czymmeck, N., Ronkina, N., Kotlyarov, A., Aepfelbacher, M., Gaestel, M., & Ruckdeschel, K. (2017). P38 MAPK /MK2-dependent phosphorylation controls cytotoxic RIPK1 signalling in inflammation and infection. *Nature Cell Biology*, *19*(10), 1248–1259. https://doi.org/10.1038/ncb3614

Merenmies, J., Pihlaskari, R., Laitinen, J., Wartiovaara, J., & Rauvala, H. (1991). 30-kDa heparin-binding protein of brain (amphoterin) involved in neurite outgrowth: Amino acid sequence and localization in the filopodia of the advancing plasma membrane. *Journal of Biological Chemistry*, *266*(25), 16722–16729. https://doi.org/10.1016/s0021-9258(18)55361-8

Milev, P., Chiba, A., Häring, M., Rauvala, H., Schachner, M., Ranscht, B., Margolis, R. K., & Margolis, R. U. (1998). High Affinity Binding and Overlapping Localization of Neurocan and Phosphacan/Protein-tyrosine Phosphatase-ζ/β with Tenascin-R, Amphoterin, and the Heparin-binding Growth-associated Molecule*. *Journal of Biological Chemistry*, *273*(12), 6998–7005. https://doi.org/https://doi.org/10.1074/jbc.273.12.6998

Mitsui, A., Tada, Y., Takahashi, T., Shibata, S., Kamata, M., Miyagaki, T., Fujita, H., Sugaya, M., Kadono, T., Sato, S., & Asano, Y. (2016). Serum IL-33 levels are increased in patients with psoriasis. *Clinical and Experimental Dermatology*, *41*(2), 183–189. https://doi.org/10.1111/ced.12670

Mocarski, E. S., Upton, J. W., & Kaiser, W. J. (2011). Viral infection and the evolution of caspase 8-regulated apoptotic and necrotic death pathways. *Nature Reviews. Immunology*, *12*(2), 79–88. https://doi.org/10.1038/nri3131

Mollica, J. P., Oakhill, J. S., Lamb, G. D., & Murphy, R. M. (2009). Are genuine changes in protein expression being overlooked? Reassessing Western blotting. *Analytical Biochemistry*, *386*(2), 270–275. https://doi.org/10.1016/j.ab.2008.12.029

Mollica, L., De Marchis, F., Spitaleri, A., Dallacosta, C., Pennacchini, D., Zamai, M., Agresti, A., Trisciuoglio, L., Musco, G., & Bianchi, M. E. (2007). Glycyrrhizin Binds to High-Mobility Group Box 1 Protein and Inhibits Its Cytokine Activities. *Chemistry and Biology*, *14*(4), 431–441. https://doi.org/10.1016/j.chembiol.2007.03.007

Molnár, T., Mázló, A., Tslaf, V., Szöllősi, A. G., Emri, G., & Koncz, G. (2019). Current translational potential and underlying molecular mechanisms of necroptosis. *Cell Death and Disease*, *10*(11). https://doi.org/10.1038/s41419-019-2094-z

Montagna, W., & Parakkal, P. F. (1974). *1 - An Introduction to Skin* (W. Montagna & P. F. B. T.-T. S. & F. of S. (Third E. Parakkal (eds.); pp. 1–17). Academic Press. https://doi.org/https://doi.org/10.1016/B978-0-12-505263-4.50006-6

Moro, K., Yamada, T., Tanabe, M., Takeuchi, T., Ikawa, T., Kawamoto, H., Furusawa, J. I., Ohtani, M., Fujii, H., & Koyasu, S. (2010a). Innate production of TH 2 cytokines by adipose tissue-associated c-Kit+ Sca-1+ lymphoid cells. *Nature*, *463*(7280), 540–544. https://doi.org/10.1038/nature08636

Moro, K., Yamada, T., Tanabe, M., Takeuchi, T., Ikawa, T., Kawamoto, H., Furusawa, J., Ohtani, M., Fujii, H., & Koyasu, S. (2010b). Innate production of TH2 cytokines by adipose tissue-associated c-Kit+ Sca-1+ lymphoid cells. *Nature*, *463*(7280), 540–544. https://doi.org/10.1038/nature08636

Mou, K., Liu, W., Han, D., & Li, P. (2017). HMGB1/RAGE axis promotes autophagy and protects keratinocytes from ultraviolet radiation-induced cell death. *Journal of Dermatological Science*, *85*(3), 162–169. https://doi.org/10.1016/j.jdermsci.2016.12.011

Moujalled, D. M., Cook, W. D., Okamoto, T., Murphy, J., Lawlor, K. E., Vince, J. E., & Vaux, D. L. (2013). TNF can activate RIPK3 and cause programmed necrosis in the absence of RIPK1. *Cell Death & Disease*, *4*(1), e465. https://doi.org/10.1038/cddis.2012.201

Moussion, C., Ortega, N., & Girard, J. P. (2008). The IL-1-like cytokine IL-33 is constitutively expressed in the nucleus of endothelial cells and epithelial cells in vivo: A novel "Alarmin"? *PLoS ONE*, *3*(10), 1–8. https://doi.org/10.1371/journal.pone.0003331

Muhammad, S., Barakat, W., Stoyanov, S., Murikinati, S., Yang, H., Tracey, K. J., Bendszus, M., Rossetti, G., Nawroth, P. P., Bierhaus, A., & Schwaninger, M. (2008). The HMGB1 receptor RAGE mediates ischemic brain damage. *The Journal of Neuroscience : The Official Journal of the Society for Neuroscience*, *28*(46), 12023–12031. https://doi.org/10.1523/JNEUROSCI.2435-08.2008

Muñoz-Planillo, R., Franchi, L., Miller, L. S., & Núñez, G. (2009). A critical role for hemolysins and bacterial lipoproteins in Staphylococcus aureus-induced activation of the Nlrp3 inflammasome. *Journal of Immunology (Baltimore, Md. : 1950)*, *183*(6), 3942–3948. https://doi.org/10.4049/jimmunol.0900729

Murai, S., Yamaguchi, Y., Shirasaki, Y., Yamagishi, M., Shindo, R., Hildebrand, J. M., Miura, R., Nakabayashi, O., Totsuka, M., Tomida, T., Adachi-Akahane, S., Uemura, S., Silke, J., Yagita, H., Miura, M., & Nakano, H. (2018). A FRET biosensor for necroptosis uncovers two different modes of the release of DAMPs. *Nature Communications*, *9*(1), 5–21. https://doi.org/10.1038/s41467-018-06985-6

Murao, A., Aziz, M., Wang, H., Brenner, M., & Wang, P. (2021). Release mechanisms of major DAMPs. *Apoptosis*, *26*(3–4), 152–162. https://doi.org/10.1007/s10495-021-01663-3

Murphy, J. M., Czabotar, P. E., Hildebrand, J. M., Lucet, I. S., Zhang, J. G., Alvarez-Diaz, S., Lewis, R., Lalaoui, N., Metcalf, D., Webb, A. I., Young, S. N., Varghese, L. N., Tannahill, G. M., Hatchell, E. C., Majewski, I. J., Okamoto, T., Dobson, R. C. J., Hilton, D. J., Babon, J. J., … Alexander, W. S. (2013). The pseudokinase MLKL mediates necroptosis via a molecular switch mechanism. *Immunity*, *39*(3), 443–453. https://doi.org/10.1016/j.immuni.2013.06.018

Murphy, R. M., & Lamb, G. D. (2013). Important considerations for protein analyses using antibody based techniques: Down-sizing Western blotting up-sizes outcomes. *Journal of Physiology*, *591*(23), 5823–5831. https://doi.org/10.1113/jphysiol.2013.263251

Nagato, M., Okamoto, K., Abe, Y., Higure, A., & Yamaguchi, K. (2009). Recombinant

human soluble thrombomodulin decreases the plasma high-mobility group box-1 protein levels, whereas improving the acute liver injury and survival rates in experimental endotoxemia. *Critical Care Medicine*, *37*(7), 2181–2186. https://doi.org/10.1097/CCM.0b013e3181a55184

Neill, D. R., Wong, S. H., Bellosi, A., Flynn, R. J., Daly, M., Langford, T. K. A., Bucks, C., Kane, C. M., Fallon, P. G., Pannell, R., Jolin, H. E., & McKenzie, A. N. J. (2010). Nuocytes represent a new innate effector leukocyte that mediates type-2 immunity. *Nature*, *464*(7293), 1367–1370. https://doi.org/10.1038/nature08900

Nelson, M. P., Christmann, B. S., Werner, J. L., Metz, A. E., Trevor, J. L., Lowell, C. A., & Steele, C. (2011). IL-33 and M2a alveolar macrophages promote lung defense against the atypical fungal pathogen Pneumocystis murina. *Journal of Immunology (Baltimore, Md. : 1950)*, *186*(4), 2372–2381. https://doi.org/10.4049/jimmunol.1002558

Nenci, A., Huth, M., Funteh, A., Schmidt-Supprian, M., Bloch, W., Metzger, D., Chambon, P., Rajewsky, K., Krieg, T., Haase, I., & Pasparakis, M. (2006). Skin lesion development in a mouse model of incontinentia pigmenti is triggered by NEMO deficiency in epidermal keratinocytes and requires TNF signaling. *Human Molecular Genetics*, *15*(4), 531–542. https://doi.org/10.1093/hmg/ddi470

Nestle, F. O., Di Meglio, P., Qin, J. Z., & Nickoloff, B. J. (2009). Skin immune sentinels in health and disease. *Nature Reviews Immunology*, *9*(10), 679–691. https://doi.org/10.1038/nri2622

Newton, K., Dugger, D. L., Wickliffe, K. E., Kapoor, N., De Almagro, M. C., Vucic, D., Komuves, L., Ferrando, R. E., French, D. M., Webster, J., Roose-Girma, M., Warming, S., & Dixit, V. M. (2014). Activity of protein kinase RIPK3 determines whether cells die by necroptosis or apoptosis. *Science*, *343*(6177), 1357–1360. https://doi.org/10.1126/science.1249361

Newton, K., Sun, X., & Dixit, V. M. (2004). Kinase RIP3 is dispensable for normal NF-kappa Bs, signaling by the B-cell and T-cell receptors, tumor necrosis factor receptor 1, and Toll-like receptors 2 and 4. *Molecular and Cellular Biology*, *24*(4), 1464–1469. https://doi.org/10.1128/MCB.24.4.1464-1469.2004

Newton, K., Wickliffe, K. E., Dugger, D. L., Maltzman, A., Roose-Girma, M., Dohse, M., Kőműves, L., Webster, J. D., & Dixit, V. M. (2019). Cleavage of RIPK1 by caspase-8 is crucial for limiting apoptosis and necroptosis. *Nature*, *574*(7778), 428–431. https://doi.org/10.1038/s41586-019-1548-x

Nguyen, A. V., & Soulika, A. M. (2019). The dynamics of the skin. *International Journal of Molecular Sciences*, *20*(1881).

Nienhuis, H. L., de Leeuw, K., Bijzet, J., Smit, A., Schalkwijk, C. G., Graaff, R., Kallenberg, C. G., & Bijl, M. (2008). Skin autofluorescence is increased in systemic lupus erythematosus but is not reflected by elevated plasma levels of advanced glycation endproducts. *Rheumatology (Oxford, England)*, *47*(10), 1554–1558. https://doi.org/10.1093/rheumatology/ken302

Nogusa, S., Thapa, R. J., Dillon, C. P., Liedmann, S., Oguin, T. H. 3rd, Ingram, J. P., Rodriguez, D. A., Kosoff, R., Sharma, S., Sturm, O., Verbist, K., Gough, P. J., Bertin, J., Hartmann, B. M., Sealfon, S. C., Kaiser, W. J., Mocarski, E. S., López, C. B., Thomas, P. G., … Balachandran, S. (2016). RIPK3 Activates Parallel Pathways of MLKL-Driven Necroptosis and FADD-Mediated Apoptosis to Protect against Influenza A Virus. *Cell Host & Microbe*, *20*(1), 13–24. https://doi.org/10.1016/j.chom.2016.05.011

Nomura, M., Ueno, A., Saga, K., Fukuzawa, M., & Kaneda, Y. (2014). Accumulation of cytosolic calcium induces necroptotic cell death in human neuroblastoma. *Cancer Research*, *74*(4), 1056–1066. https://doi.org/10.1158/0008-5472.CAN-13-1283

Nowak-Terpiłowska, A., Śledziński, P., & Zeyland, J. (2021). Impact of cell harvesting methods on detection of cell surface proteins and apoptotic markers. *Brazilian Journal of Medical and Biological Research = Revista Brasileira de Pesquisas Medicas e Biologicas*, *54*(2), e10197. https://doi.org/10.1590/1414-431X202010197

Nygaard, U., Hvid, M., Johansen, C., Buchner, M., Fölster-Holst, R., Deleuran, M., & Vestergaard, C. (2016). TSLP, IL-31, IL-33 and sST2 are new biomarkers in endophenotypic profiling of adult and childhood atopic dermatitis. *Journal of the European Academy of Dermatology and Venereology*, *30*(11), 1930–1938. https://doi.org/10.1111/jdv.13679

Oberst, A., Dillon, C. P., Weinlich, R., McCormick, L. L., Fitzgerald, P., Pop, C., Hakem, R., Salvesen, G. S., & Green, D. R. (2011). Catalytic activity of the caspase-8-FLIP L complex inhibits RIPK3-dependent necrosis. *Nature*, *471*(7338), 363–368. https://doi.org/10.1038/nature09852

Oboki, K., Ohno, T., Kajiwara, N., Arae, K., Morita, H., Ishii, A., Nambu, A., Abe, T., Kiyonari, H., Matsumoto, K., Sudo, K., Okumura, K., Saito, H., & Nakae, S. (2010). IL-33 is a crucial amplifier of innate rather than acquired immunity. *Proceedings of the National Academy of Sciences of the United States of America*, *107*(43), 18581–18586. https://doi.org/10.1073/pnas.1003059107

Onizawa, M., Oshima, S., Schulze-Topphoff, U., Oses-Prieto, J. A., Lu, T., Tavares, R., Prodhomme, T., Duong, B., Whang, M. I., Advincula, R., Agelidis, A., Barrera, J., Wu, H., Burlingame, A., Malynn, B. A., Zamvil, S. S., & Ma, A. (2015). The ubiquitin-modifying enzyme A20 restricts ubiquitination of the kinase RIPK3 and protects cells from necroptosis. *Nature Immunology*, *16*(6), 618–627. https://doi.org/10.1038/ni.3172

Orlova, V. V, Choi, E. Y., Xie, C., Chavakis, E., Bierhaus, A., Ihanus, E., Ballantyne, C. M., Gahmberg, C. G., Bianchi, M. E., Nawroth, P. P., & Chavakis, T. (2007). A novel pathway of HMGB1-mediated inflammatory cell recruitment that requires Mac-1-integrin. *The EMBO Journal*, *26*(4), 1129–1139. https://doi.org/https://doi.org/10.1038/sj.emboj.7601552

Orozco, S., Yatim, N., Werner, M. R., Tran, H., Gunja, S. Y., Tait, S. W. G., Albert, M.

L., Green, D. R., & Oberst, A. (2014). RIPK1 both positively and negatively regulates RIPK3 oligomerization and necroptosis. *Cell Death and Differentiation*, *21*(10), 1511–1521. https://doi.org/10.1038/cdd.2014.76

Oshikawa, K., Kuroiwa, K., Tago, K., Iwahana, H., Yanagisawa, K., Ohno, S., Tominaga, S. I., & Sugiyama, Y. (2001). Elevated soluble ST2 protein levels in sera of patients with asthma with an acute exacerbation. *American Journal of Respiratory and Critical Care Medicine*, *164*(2), 277–281. https://doi.org/10.1164/ajrccm.164.2.2008120

Oshio, T., Komine, M., Tsuda, H., Tominaga, S. ichi, Saito, H., Nakae, S., & Ohtsuki, M. (2017). Nuclear expression of IL-33 in epidermal keratinocytes promotes wound healing in mice. *Journal of Dermatological Science*, *85*(2), 106–114. https://doi.org/10.1016/j.jdermsci.2016.10.008

Palmer, G., & Gabay, C. (2011). Interleukin-33 biology with potential insights into human diseases. *Nature Reviews Rheumatology*, *7*(6), 321–329. https://doi.org/10.1038/nrrheum.2011.53

Palmer, G., Lipsky, B. P., Smithgall, M. D., Meininger, D., Siu, S., Talabot-Ayer, D., Gabay, C., & Smith, D. E. (2008). The IL-1 receptor accessory protein (AcP) is required for IL-33 signaling and soluble AcP enhances the ability of soluble ST2 to inhibit IL-33. *Cytokine*, *42*(3), 358–364. https://doi.org/10.1016/j.cyto.2008.03.008

Palmer, G., Talabot-Ayer, D., Lamacchia, C., Toy, D., Seemayer, C. A., Viatte, S., Finckh, A., Smith, D. E., & Gabay, C. (2009). Inhibition of interleukin-33 signaling attenuates the severity of experimental arthritis. *Arthritis and Rheumatism*, *60*(3), 738–749. https://doi.org/10.1002/art.24305

Pasparakis, M., Courtois, G., Hafner, M., Schmidt-Supprian, M., Nenci, A., Toksoy, A., Krampert, M., Goebeler, M., Gillitzer, R., Israel, A., Krieg, T., Rajewsky, K., & Haase, I. (2002). TNF-mediated inflammatory skin disease in mice with epidermis-specific deletion of IKK2. *Nature*, *417*(6891), 861–866. https://doi.org/10.1038/nature00820

Pasparakis, M., Haase, I., & Nestle, F. O. (2014). Mechanisms regulating skin immunity and inflammation. *Nature Reviews Immunology*, *14*(5), 289–301. https://doi.org/10.1038/nri3646

Pasparakis, M., & Vandenabeele, P. (2015). Necroptosis and its role in inflammation. *Nature*, *517*(7534), 311–320. https://doi.org/10.1038/nature14191

Pasqualini, J. R., Sterner, R., Mercat, P., & Allfrey, V. G. (1989). Estradiol enhanced acetylation of nuclear high mobility group proteins of the uterus of newborn guinea pigs. *Biochemical and Biophysical Research Communications*, *161*(3), 1260–1266. https://doi.org/10.1016/0006-291x(89)91378-8

Patel, S., Webster, J. D., Varfolomeev, E., Kwon, Y. C., Cheng, J. H., Zhang, J., Dugger, D. L., Wickliffe, K. E., Maltzman, A., Sujatha-Bhaskar, S., Bir Kohli, P.,

Ramaswamy, S., Deshmukh, G., Liederer, B. M., Fong, R., Hamilton, G., Lupardus, P., Caplazi, P., Lee, W. P., … Vucic, D. (2020). RIP1 inhibition blocks inflammatory diseases but not tumor growth or metastases. *Cell Death and Differentiation*, *27*(1), 161–175. https://doi.org/10.1038/s41418-019-0347-0

Peine, M., Marek, R. M., & Löhning, M. (2016). IL-33 in T Cell Differentiation, Function, and Immune Homeostasis. *Trends in Immunology*, *37*(5), 321–333. https://doi.org/10.1016/j.it.2016.03.007

Peltzer, N., Darding, M., Montinaro, A., Draber, P., Draberova, H., Kupka, S., Rieser, E., Fisher, A., Hutchinson, C., Taraborrelli, L., Hartwig, T., Lafont, E., Haas, T. L., Shimizu, Y., Böiers, C., Sarr, A., Rickard, J., Alvarez-Diaz, S., Ashworth, M. T., … Walczak, H. (2018). LUBAC is essential for embryogenesis by preventing cell death and enabling haematopoiesis. *Nature*, *557*(7703), 112–117. https://doi.org/10.1038/s41586-018-0064-8

Peltzer, N., Rieser, E., Taraborrelli, L., Draber, P., Darding, M., Pernaute, B., Shimizu, Y., Sarr, A., Draberova, H., Montinaro, A., Martinez-Barbera, J. P., Silke, J., Rodriguez, T. A., & Walczak, H. (2014). HOIP deficiency causes embryonic lethality by aberrant TNFR1-mediated endothelial cell death. *Cell Reports*, *9*(1), 153–165. https://doi.org/10.1016/j.celrep.2014.08.066

Petrie, E. J., Birkinshaw, R. W., Koide, A., Denbaum, E., Hildebrand, J. M., Garnish, S. E., Davies, K. A., Sandow, J. J., Samson, A. L., Gavin, X., Fitzgibbon, C., Young, S. N., Hennessy, P. J., Smith, P. P. C., Webb, A. I., Czabotar, P. E., Koide, S., & Murphy, J. M. (2020). Identification of MLKL membrane translocation as a checkpoint in necroptotic cell death using Monobodies. *Proceedings of the National Academy of Sciences of the United States of America*, *117*(15), 8468–8475. https://doi.org/10.1073/pnas.1919960117

Petrie, E. J., Czabotar, P. E., & Murphy, J. M. (2019). The Structural Basis of Necroptotic Cell Death Signaling. *Trends in Biochemical Sciences*, *44*(1), 53–63. https://doi.org/10.1016/j.tibs.2018.11.002

Petrie, E. J., Sandow, J. J., Jacobsen, A. V., Smith, B. J., Griffin, M. D. W., Lucet, I. S., Dai, W., Young, S. N., Tanzer, M. C., Wardak, A., Liang, L. Y., Cowan, A. D., Hildebrand, J. M., Kersten, W. J. A., Lessene, G., Silke, J., Czabotar, P. E., Webb, A. I., & Murphy, J. M. (2018). Conformational switching of the pseudokinase domain promotes human MLKL tetramerization and cell death by necroptosis. *Nature Communications*, *9*(1). https://doi.org/10.1038/s41467-018-04714-7

Pichery, M., Mirey, E., Mercier, P., Lefrancais, E., Dujardin, A., Ortega, N., & Girard, J.-P. (2012). Endogenous IL-33 Is Highly Expressed in Mouse Epithelial Barrier Tissues, Lymphoid Organs, Brain, Embryos, and Inflamed Tissues: In Situ Analysis Using a Novel Il-33–LacZ Gene Trap Reporter Strain. *The Journal of Immunology*, *188*(7), 3488–3495. https://doi.org/10.4049/jimmunol.1101977

Pietka, W., Sundnes, O., Hammarström, C., Zucknick, M., Khnykin, D., & Haraldsen, G. (2020). Lack of interleukin-33 and its receptor does not prevent calcipotriol-induced atopic dermatitis-like inflammation in mice. *Scientific Reports*, *10*(1), 1–

8. https://doi.org/10.1038/s41598-020-63410-z

Pietkiewicz, S., Schmidt, J. H., & Lavrik, I. N. (2015). Quantification of apoptosis and necroptosis at the single cell level by a combination of Imaging Flow Cytometry with classical Annexin V/propidium iodide staining. *Journal of Immunological Methods*, *423*, 99–103. https://doi.org/10.1016/j.jim.2015.04.025

Pilzweger, C., & Holdenrieder, S. (2015). Circulating HMGB1 and RAGE as Clinical Biomarkers in Malignant and Autoimmune Diseases. *Diagnostics*, *5*(2), 219–253. https://doi.org/10.3390/diagnostics5020219

Polykratis, A., Hermance, N., Zelic, M., Roderick, J., Kim, C., Van, T.-M., Lee, T. H., Chan, F. K. M., Pasparakis, M., & Kelliher, M. A. (2014). Cutting Edge: RIPK1 Kinase Inactive Mice Are Viable and Protected from TNF-Induced Necroptosis In Vivo. *The Journal of Immunology*, *193*(4), 1539–1543. https://doi.org/10.4049/jimmunol.1400590

Popovic, K., Ek, M., Espinosa, A., Padyukov, L., Harris, H. E., Wahren-Herlenius, M., & Nyberg, F. (2005). Increased expression of the novel proinflammatory cytokine high mobility group box chromosomal protein 1 in skin lesions of patients with lupus erythematosus. *Arthritis and Rheumatism*, *52*(11), 3639–3645. https://doi.org/10.1002/art.21398

Prendergast, P., Oñate, S., Christense, K., & Edwards, D. (1994). Nuclear accessory factors enhance the binding of progesterone receptor to specific target DNA. *The Journal of Steroid Biochemistry and Molecular Biology*, *48*, 1–13.

Pullerits, R., Brisslert, M., Jonsson, I. M., & Tarkowski, A. (2006). Soluble receptor for advanced glycation end products triggers a proinflammatory cytokine cascade via β2 integrin Mac-1. *Arthritis and Rheumatism*, *54*(12), 3898–3907. https://doi.org/10.1002/art.22217

Pullerits, R., Jonsson, I. M., Verdrengh, M., Bokarewa, M., Andersson, U., Erlandsson-Harris, H., & Tarkowski, A. (2003). High mobility group box chromosomal protein 1, a DNA binding cytokine, induces arthritis. *Arthritis and Rheumatism*, *48*(6), 1693–1700. https://doi.org/10.1002/art.11028

Raju, S., Whalen, D. M., Mengistu, M., Swanson, C., Quinn, J. G., Taylor, S. S., Webster, J. D., Newton, K., & Shaw, A. S. (2018). Kinase domain dimerization drives RIPK3-dependent necroptosis. *Science Signaling*, *11*(544). https://doi.org/10.1126/scisignal.aar2188

Rak, G. D., Osborne, L. C., Siracusa, M. C., Kim, B. S., Wang, K., Bayat, A., Artis, D., & Volk, S. W. (2016). IL-33-Dependent Group 2 Innate Lymphoid Cells Promote Cutaneous Wound Healing. *Journal of Investigative Dermatology*, *136*(2), 487–496. https://doi.org/10.1038/JID.2015.406

Rankin, A. L., Mumm, J. B., Murphy, E., Turner, S., Yu, N., McClanahan, T. K., Bourne, P. A., Pierce, R. H., Kastelein, R., & Pflanz, S. (2010). IL-33 Induces IL-13–Dependent Cutaneous Fibrosis. *The Journal of Immunology*, *184*(3), 1526–

1535. https://doi.org/10.4049/jimmunol.0903306

Rebholz, B., Haase, I., Eckelt, B., Paxian, S., Flaig, M. J., Ghoreschi, K., Nedospasov, S. A., Mailhammer, R., Debey-Pascher, S., Schultze, J. L., Weindl, G., Förster, I., Huss, R., Stratis, A., Ruzicka, T., Röcken, M., Pfeffer, K., Schmid, R. M., & Rupec, R. A. (2007). Crosstalk between Keratinocytes and Adaptive Immune Cells in an IκBα Protein-Mediated Inflammatory Disease of the Skin. *Immunity*, *27*(2), 296–307. https://doi.org/10.1016/j.immuni.2007.05.024

Rebsamen, M., Heinz, L. X., Meylan, E., Michallet, M.-C., Schroder, K., Hofmann, K., Vazquez, J., Benedict, C. A., & Tschopp, J. (2009). DAI/ZBP1 recruits RIP1 and RIP3 through RIP homotypic interaction motifs to activate NF-kappaB. *EMBO Reports*, *10*(8), 916–922. https://doi.org/10.1038/embor.2009.109

Reichenbach, D. K., Schwarze, V., Matta, B. M., Tkachev, V., Lieberknecht, E., Liu, Q., Koehn, B. H., Pfeifer, D., Taylor, P. A., Prinz, G., Dierbach, H., Stickel, N., Beck, Y., Warncke, M., Junt, T., Schmitt-Graeff, A., Nakae, S., Follo, M., Wertheimer, T., … Blazar, B. R. (2015). The IL-33/ST2 axis augments effector T-cell responses during acute GVHD. *Blood*, *125*(20), 3183–3192. https://doi.org/10.1182/blood-2014-10-606830

Rheinwald, J. (1989). Methods for clonal growth and serial cultivation of normal human epidermal keratinocytes and mesothelial cells. In *Cell Growth and Division: A Practical Approach*.

Rheinwald, J. G., & Green, H. (1975). Serial Cultivation of Strains of Human Epidermal Keratinocytes: the Formation of Keratinizing Colonies from Single Cells. *Cell*, *6*, 331–344. https://doi.org/10.1016/S0092-8674(75)80001-8

Rickard, J. A., Anderton, H., Etemadi, N., Nachbur, U., Darding, M., Peltzer, N., Lalaoui, N., Lawlor, K. E., Vanyai, H., Hall, C., Bankovacki, A., Gangoda, L., Wong, W. W.-L., Corbin, J., Huang, C., Mocarski, E. S., Murphy, J. M., Alexander, W. S., Voss, A. K., … Silke, J. (2014). TNFR1-dependent cell death drives inflammation in Sharpin-deficient mice. *ELife*, *3*. https://doi.org/10.7554/eLife.03464

Rickard, J. A., O'Donnell, J. A., Evans, J. M., Lalaoui, N., Poh, A. R., Rogers, T., Vince, J. E., Lawlor, K. E., Ninnis, R. L., Anderton, H., Hall, C., Spall, S. K., Phesse, T. J., Abud, H. E., Cengia, L. H., Corbin, J., Mifsud, S., Di Rago, L., Metcalf, D., … Silke, J. (2014). RIPK1 regulates RIPK3-MLKL-driven systemic inflammation and emergency hematopoiesis. *Cell*, *157*(5), 1175–1188. https://doi.org/10.1016/j.cell.2014.04.019

Riehl, A., Bauer, T., Brors, B., Busch, H., Mark, R., Németh, J., Gebhardt, C., Bierhaus, A., Nawroth, P., Eils, R., König, R., Angel, P., & Hess, J. (2010). Identification of the Rage-dependent gene regulatory network in a mouse model of skin inflammation. *BMC Genomics*, *11*(1). https://doi.org/10.1186/1471-2164-11-537

Rodriguez, D. A., Weinlich, R., Brown, S., Guy, C., Fitzgerald, P., Dillon, C. P., Oberst,

A., Quarato, G., Low, J., Cripps, J. G., Chen, T., & Green, D. R. (2016). Characterization of RIPK3-mediated phosphorylation of the activation loop of MLKL during necroptosis. *Cell Death and Differentiation*, *23*(1), 76–88. https://doi.org/10.1038/cdd.2015.70

Romani, N., Koide, S., Crowley, M., Witmer-Pack, M., Livingstone, A. M., Fathman, C. G., Inaba, K., & Steinman, R. M. (1989). Presentation of exogenous protein antigens by dendritic cells to T cell clones. Intact protein is presented best by immature, epidermal Langerhans cells. *The Journal of Experimental Medicine*, *169*(3), 1169–1178. https://doi.org/10.1084/jem.169.3.1169

Romani, N., Lenz, A., Glassel, H., Stössel, H., Stanzl, U., Majdic, O., Fritsch, P., & Schuler, G. (1989). Cultured human Langerhans cells resemble lymphoid dendritic cells in phenotype and function. *The Journal of Investigative Dermatology*, *93*(5), 600–609. https://doi.org/10.1111/1523-1747.ep12319727

Ros, U., Peña-Blanco, A., Hänggi, K., Kunzendorf, U., Krautwald, S., Wong, W. W. L., & García-Sáez, A. J. (2017). Necroptosis Execution Is Mediated by Plasma Membrane Nanopores Independent of Calcium. *Cell Reports*, *19*(1), 175–187. https://doi.org/10.1016/j.celrep.2017.03.024

Rouhiainen, A., Tumova, S., Valmu, L., Kalkkinen, N., & Rauvala, H. (2007). Pivotal advance: analysis of proinflammatory activity of highly purified eukaryotic recombinant HMGB1 (amphoterin). *Journal of Leukocyte Biology*, *81*(1), 49–58. https://doi.org/10.1189/jlb.0306200

Roussel, L., Erard, M., Cayrol, C., & Girard, J.-P. (2008). Molecular mimicry between IL-33 and KSHV for attachment to chromatin through the H2A–H2B acidic pocket. *EMBO Reports*, *9*(10), 1006–1012. https://doi.org/10.1038/embor.2008.145

Roy, A., Ganesh, G., Sippola, H., Bolin, S., Sawesi, O., Dagälv, A., Schlenner, S. M., Feyerabend, T., Rodewald, H.-R., Kjellén, L., Hellman, L., & Åbrink, M. (2014). Mast cell chymase degrades the alarmins heat shock protein 70, biglycan, HMGB1, and interleukin-33 (IL-33) and limits danger-induced inflammation. *The Journal of Biological Chemistry*, *289*(1), 237–250. https://doi.org/10.1074/jbc.M112.435156

Ryu, W. I., Lee, H., Bae, H. C., Ryu, H. J., & Son, S. W. (2016). IL-33 down-regulates filaggrin expression by inducing STAT3 and ERK phosphorylation in human keratinocytes. *Journal of Dermatological Science*, *82*(2), 131–134. https://doi.org/10.1016/j.jdermsci.2016.01.011

Sabatino, G., Nicoletti, M., Neri, G., Saggini, A., Rosati, M., Conti, F., Cianchetti, E., Toniato, E., Fulcheri, M., Caraffa, A., Antinolfi, P., Frydas, S., Pandolfi, F., Potalivo, G., Galzio, R., Conti, P., & Theoharides, T. C. (2012). Impact of IL -9 and IL-33 in mast cells. *Journal of Biological Regulators and Homeostatic Agents*, *26*(4), 577–586.

Sai, K., Parsons, C., House, J. S., Kathariou, S., & Ninomiya-Tsuji, J. (2019).

Necroptosis mediators RIPK3 and MLKL suppress intracellular Listeria replication independently of host cell killing. *Journal of Cell Biology*, *218*(6), 1994–2005. https://doi.org/10.1083/JCB.201810014

Saito, N., Qiao, H., Yanagi, T., Shinkuma, S., Nishimura, K., Suto, A., Fujita, Y., Suzuki, S., Nomura, T., Nakamura, H., Nagao, K., Obuse, C., Shimizu, H., & Abe, R. (2014). An annexin A1–FPR1 interaction contributes to necroptosis of keratinocytes in severe cutaneous adverse drug reactions. *Science Translational Medicine*, *6*(245), 245ra95. https://doi.org/10.1126/scitranslmed.3008227

Salimi, M., Barlow, J. L., Saunders, S. P., Xue, L., Gutowska-Owsiak, D., Wang, X., Huang, L. C., Johnson, D., Scanlon, S. T., McKenzie, A. N. J., Fallon, P. G., & Ogg, G. S. (2013). A role for IL-25 and IL-33-driven type-2 innate lymphoid cells in atopic dermatitis. *Journal of Experimental Medicine*, *210*(13), 2939–2950. https://doi.org/10.1084/jem.20130351

Saluja, R., Khan, M., Church, M. K., & Maurer, M. (2015). The role of IL-33 and mast cells in allergy and inflammation. *Clinical and Translational Allergy*, *5*, 33. https://doi.org/10.1186/s13601-015-0076-5

Samson, A. L., Zhang, Y., Geoghegan, N. D., Gavin, X. J., Davies, K. A., Mlodzianoski, M. J., Whitehead, L. W., Frank, D., Garnish, S. E., Fitzgibbon, C., Hempel, A., Young, S. N., Jacobsen, A. V., Cawthorne, W., Petrie, E. J., Faux, M. C., Shield-Artin, K., Lalaoui, N., Hildebrand, J. M., … Murphy, J. M. (2020). MLKL trafficking and accumulation at the plasma membrane control the kinetics and threshold for necroptosis. *Nature Communications*, *11*(1), 1–17. https://doi.org/10.1038/s41467-020-16887-1

Sanada, S., Hakuno, D., Higgins, L. J., Schreiter, E. R., McKenzie, A. N. J., & Lee, R. T. (2007). IL-33 and ST2 comprise a critical biomechanically induced and cardioprotective signaling system. *The Journal of Clinical Investigation*, *117*(6), 1538–1549. https://doi.org/10.1172/JCI30634

Sarhan, M., Land, W. G., Tonnus, W., Hugo, C. P., & Linkermann, A. (2018). Origin and Consequences of Necroinflammation. *Physiological Reviews*, *98*(2), 727–780. https://doi.org/10.1152/physrev.00041.2016

Savinko, T., Matikainen, S., Saarialho-Kere, U., Lehto, M., Wang, G., Lehtimäki, S., Karisola, P., Reunala, T., Wolff, H., Lauerma, A., & Alenius, H. (2012). IL-33 and ST2 in atopic dermatitis: Expression profiles and modulation by triggering factors. *Journal of Investigative Dermatology*, *132*(5), 1392–1400. https://doi.org/10.1038/jid.2011.446

Sawa, H., Ueda, T., Takeyama, Y., Yasuda, T., Shinzeki, M., Nakajima, T., & Kuroda, Y. (2006). Blockade of high mobility group box-1 protein attenuates experimental severe acute pancreatitis. *World Journal of Gastroenterology*, *12*(47), 7666–7670. https://doi.org/10.3748/wjg.v12.i47.7666

Scaffidi, C., Schmitz, I., Krammer, P. H., & Peter, M. E. (1999). The role of c-FLIP in

modulation of CD95-induced apoptosis. *The Journal of Biological Chemistry*, *274*(3), 1541–1548. https://doi.org/10.1074/jbc.274.3.1541

Scaffidi, P., Misteli, T., & Bianchi, M. E. (2002). Release of chromatin protein HMGB1 by necrotic cells triggers inflammation. *Nature*, *418*(6894), 191–195. https://doi.org/10.1038/nature00858

Schiering, C., Krausgruber, T., Chomka, A., Fröhlich, A., Adelmann, K., Wohlfert, E. A., Pott, J., Griseri, T., Bollrath, J., Hegazy, A. N., Harrison, O. J., Owens, B. M. J., Löhning, M., Belkaid, Y., Fallon, P. G., & Powrie, F. (2014). The alarmin IL-33 promotes regulatory T-cell function in the intestine. *Nature*, *513*(7519), 564–568. https://doi.org/10.1038/nature13577

Schiraldi, M., Raucci, A., Muñoz, L. M., Livoti, E., Celona, B., Venereau, E., Apuzzo, T., De Marchis, F., Pedotti, M., Bachi, A., Thelen, M., Varani, L., Mellado, M., Proudfoot, A., Bianchi, M. E., & Uguccioni, M. (2012). HMGB1 promotes recruitment of inflammatory cells to damaged tissues by forming a complex with CXCL12 and signaling via CXCR4. *Journal of Experimental Medicine*, *209*(3), 551–563. https://doi.org/10.1084/jem.20111739

Schmidt, A. M., Yan, S. Du, Yan, S. F., & Stern, D. M. (2001). The multiligand receptor RAGE as a progression factor amplifying immune and inflammatory responses. *Journal of Clinical Investigation*, *108*(7), 949–955. https://doi.org/10.1172/JCI200114002

Schmitz, J., Owyang, A., Oldham, E., Song, Y., Murphy, E., McClanahan, T. K., Zurawski, G., Moshrefi, M., Qin, J., Li, X., Gorman, D. M., Bazan, J. F., & Kastelein, R. A. (2005). IL-33, an Interleukin-1-like Cytokine that Signals via the IL-1 Receptor-Related Protein ST2 and Induces T Helper Type 2-Associated Cytokines. *Immunity*, *23*(5), 479–490. https://doi.org/https://doi.org/10.1016/j.immuni.2005.09.015

Schreiber, A., Rousselle, A., Becker, J. U., von Mässenhausen, A., Linkermann, A., & Kettritz, R. (2017). Necroptosis controls NET generation and mediates complement activation, endothelial damage, and autoimmune vasculitis. *Proceedings of the National Academy of Sciences of the United States of America*, *114*(45), E9618–E9625. https://doi.org/10.1073/pnas.1708247114

Schweichel, J. U., & Merker, H. J. (1973). The morphology of various types of cell death in prenatal tissues. *Teratology*, *7*(3), 253–266. https://doi.org/10.1002/tera.1420070306

Senn, K. A., McCoy, K. D., Maloy, K. J., Stark, G., Fröhli, E., Rülicke, T., & Klemenz, R. (2000). T1-deficient and T1-Fc-transgenic mice develop a normal protective Th2-type immune response following infection with Nippostrongylus brasiliensis. *European Journal of Immunology*, *30*(7), 1929–1938. https://doi.org/10.1002/1521-4141(200007)30:7<1929::AID-IMMU1929>3.0.CO;2-1

Seo, J., Lee, E. W., Sung, H., Seong, D., Dondelinger, Y., Shin, J., Jeong, M., Lee, H.

K., Kim, J. H., Han, S. Y., Lee, C., Seong, J. K., Vandenabeele, P., & Song, J. (2016). CHIP controls necroptosis through ubiquitylation-and lysosome-dependent degradation of RIPK3. *Nature Cell Biology*, *18*(3), 291–302. https://doi.org/10.1038/ncb3314

Seymour, R. E., Hasham, M. G., Cox, G. A., Shultz, L. D., Hogenesch, H., Roopenian, D. C., & Sundberg, J. P. (2007). Spontaneous mutations in the mouse Sharpin gene result in multiorgan inflammation, immune system dysregulation and dermatitis. *Genes and Immunity*, *8*(5), 416–421. https://doi.org/10.1038/sj.gene.6364403

Sha, Y., Zmijewski, J., Xu, Z., & Abraham, E. (2008). HMGB1 Develops Enhanced Proinflammatory Activity by Binding to Cytokines. *The Journal of Immunology*, *180*(4), 2531–2537. https://doi.org/10.4049/jimmunol.180.4.2531

Sharma, S. K., & Carew, T. J. (2002). Inclusion of phosphatase inhibitors during Western blotting enhances signal detection with phospho-specific antibodies. *Analytical Biochemistry*, *307*(1), 187–189. https://doi.org/10.1016/S0003-2697(02)00008-8

Shetty, S., & Gokul, S. (2012). Keratinization and its disorders. *Oman Medical Journal*, *27*(5), 348–357. https://doi.org/10.5001/omj.2012.90

Shimazu, R., Akashi, S., Ogata, H., Nagai, Y., Fukudome, K., Miyake, K., & Kimoto, M. (1999). MD-2, a molecule that confers lipopolysaccharide responsiveness on Toll-like receptor 4. *The Journal of Experimental Medicine*, *189*(11), 1777–1782. https://doi.org/10.1084/jem.189.11.1777

Shimizu, M., Matsuda, A., Yanagisawa, K., Hirota, T., Akahoshi, M., Inomata, N., Ebe, K., Tanaka, K., Sugiura, H., Nakashima, K., Tamari, M., Takahashi, N., Obara, K., Enomoto, T., Okayama, Y., Gao, P.-S., Huang, S.-K., Tominaga, S.-I., Ikezawa, Z., & Shirakawa, T. (2005). Functional SNPs in the distal promoter of the ST2 gene are associated with atopic dermatitis. *Human Molecular Genetics*, *14*(19), 2919–2927. https://doi.org/10.1093/hmg/ddi323

Shimpo, M., Morrow, D. A., Weinberg, E. O., Sabatine, M. S., Murphy, S. A., Antman, E. M., & Lee, R. T. (2004). Serum levels of the interleukin-1 receptor family member ST2 predict mortality and clinical outcome in acute myocardial infarction. *Circulation*, *109*(18), 2186–2190. https://doi.org/10.1161/01.CIR.0000127958.21003.5A

Shlomovitz, I., Erlich, Z., Speir, M., Zargarian, S., Baram, N., Engler, M., Edry-Botzer, L., Munitz, A., Croker, B. A., & Gerlic, M. (2019). Necroptosis directly induces the release of full-length biologically active IL-33 in vitro and in an inflammatory disease model. *FEBS Journal*, *286*(3), 507–522. https://doi.org/10.1111/febs.14738

Shutinoski, B., Alturki, N. A., Rijal, D., Bertin, J., Gough, P. J., Schlossmacher, M. G., & Sad, S. (2016). K45A mutation of RIPK1 results in poor necroptosis and cytokine signaling in macrophages, which impacts inflammatory responses in

vivo. *Cell Death and Differentiation*, *23*(10), 1628–1637. https://doi.org/10.1038/cdd.2016.51

Silke, J., Rickard, J. A., & Gerlic, M. (2015). The diverse role of RIP kinases in necroptosis and inflammation. *Nature Immunology*, *16*(7), 689–697. https://doi.org/10.1038/ni.3206

Simoes Eugénio, M., Faurez, F., Kara-Ali, G. H., Lagarrigue, M., Uhart, P., Bonnet, M. C., Gallais, I., Com, E., Pineau, C., Samson, M., Le Seyec, J., & Dimanche-Boitrel, M. T. (2021). TRIM21, a New Component of the TRAIL-Induced Endogenous Necrosome Complex. *Frontiers in Molecular Biosciences*, *8*(April), 1–11. https://doi.org/10.3389/fmolb.2021.645134

Simon, M. M., Greenaway, S., White, J. K., Fuchs, H., Gailus-Durner, V., Wells, S., Sorg, T., Wong, K., Bedu, E., Cartwright, E. J., Dacquin, R., Djebali, S., Estabel, J., Graw, J., Ingham, N. J., Jackson, I. J., Lengeling, A., Mandillo, S., Marvel, J., … Brown, S. D. M. (2013). A comparative phenotypic and genomic analysis of C57BL/6J and C57BL/6N mouse strains. *Genome Biology*, *14*(7), R82–R82. https://doi.org/10.1186/gb-2013-14-7-r82

Simpson, K., & Browning, M. (2017). Antibodies That Work Again and Again and Again. In A. E. Kalyuzhny (Ed.), *Signal Transduction Immunohistochemistry: Methods and Protocols* (pp. 41–59). Springer New York. https://doi.org/10.1007/978-1-4939-6759-9_2

Sitia, G., Iannacone, M., Müller, S., Bianchi, M. E., & Guidotti, L. G. (2007). Treatment with HMGB1 inhibitors diminishes CTL-induced liver disease in HBV transgenic mice. *Journal of Leukocyte Biology*, *81*(1), 100–107. https://doi.org/https://doi.org/10.1189/jlb.0306173

Sohn, E.-J., Kang, D.-G., & Lee, H.-S. (2003). Protective effects of glycyrrhizin on gentamicin-induced acute renal failure in rats. *Pharmacology & Toxicology*, *93*(3), 116–122. https://doi.org/10.1034/j.1600-0773.2003.930302.x

Soro-Paavonen, A., Watson, A. M. D., Li, J., Paavonen, K., Koitka, A., Calkin, A. C., Barit, D., Coughlan, M. T., Drew, B. G., Lancaster, G. I., Thomas, M., Forbes, J. M., Nawroth, P. P., Bierhaus, A., Cooper, M. E., & Jandeleit-Dahm, K. A. (2008). Receptor for advanced glycation end products (RAGE) deficiency attenuates the development of atherosclerosis in diabetes. *Diabetes*, *57*(9), 2461–2469. https://doi.org/10.2337/db07-1808

Stehle, C., Saikali, P., & Romagnani, C. (2016). Putting the brakes on ILC2 cells. *Nature Immunology*, *17*(1), 43–44. https://doi.org/10.1038/ni.3353

Straino, S., Di Carlo, A., Mangoni, A., De Mori, R., Guerra, L., Maurelli, R., Panacchia, L., Di Giacomo, F., Palumbo, R., Di Campli, C., Uccioli, L., Biglioli, P., Bianchi, M. E., Capogrossi, M. C., & Germani, A. (2008). High-mobility group box 1 protein in human and murine skin: Involvement in wound healing. *Journal of Investigative Dermatology*, *128*(6), 1545–1553. https://doi.org/10.1038/sj.jid.5701212

Stros, M., Muselíková-Polanská, E., Pospísilová, S., & Strauss, F. (2004). High-affinity binding of tumor-suppressor protein p53 and HMGB1 to hemicatenated DNA loops. *Biochemistry*, *43*(22), 7215–7225. https://doi.org/10.1021/bi049928k

Suda, K., Kitagawa, Y., Ozawa, S., Saikawa, Y., Ueda, M., Ebina, M., Yamada, S., Hashimoto, S., Fukata, S., Abraham, E., Maruyama, I., Kitajima, M., & Ishizaka, A. (2006). Anti-High-Mobility Group Box Chromosomal Protein 1 Antibodies Improve Survival of Rats with Sepsis. *World Journal of Surgery*, *30*(9), 1755–1762. https://doi.org/10.1007/s00268-005-0369-2

Sun, L., Wang, H., Wang, Z., He, S., Chen, S., Liao, D., Wang, L., Yan, J., Liu, W., Lei, X., & Wang, X. (2012). Mixed Lineage Kinase Domain-like Protein Mediates Necrosis Signaling Downstream of RIP3 Kinase. *Cell*, *148*(1–2), 213–227. https://doi.org/https://doi.org/10.1016/j.cell.2011.11.031

Sun, X., Yin, J., Starovasnik, M. A., Fairbrother, W. J., & Dixit, V. M. (2002). Identification of a novel homotypic interaction motif required for the phosphorylation of receptor-interacting protein (RIP) by RIP3. *The Journal of Biological Chemistry*, *277*(11), 9505–9511. https://doi.org/10.1074/jbc.M109488200

Sundberg, J. P., Herbert Pratt, C., Goodwin, L. P., Silva, K. A., Kennedy, V. E., Potter, C. S., Dunham, A., Sundberg, B. A., & HogenEsch, H. (2020). Keratinocyte-specific deletion of SHARPIN induces atopic dermatitis-like inflammation in mice. *PLoS ONE*, *15*(7 July), 1–28. https://doi.org/10.1371/journal.pone.0235295

Sundnes, O., Pietka, W., Loos, T., Sponheim, J., Rankin, A. L., Pflanz, S., Bertelsen, V., Sitek, J. C., Hol, J., Haraldsen, G., & Khnykin, D. (2015). Epidermal expression and regulation of interleukin-33 during homeostasis and inflammation: Strong species differences. *Journal of Investigative Dermatology*, *135*(7), 1771–1780. https://doi.org/10.1038/jid.2015.85

Taguchi, A., Blood, D. C., del Toro, G., Canet, A., Lee, D. C., Qu, W., Tanji, N., Lu, Y., Lalla, E., Fu, C., Hofmann, M. A., Kislinger, T., Ingram, M., Lu, A., Tanaka, H., Hori, O., Ogawa, S., Stern, D. M., & Schmidt, A. M. (2000). Blockade of RAGE-amphoterin signalling suppresses tumour growth and metastases. *Nature*, *405*(6784), 354–360. https://doi.org/10.1038/35012626

Takahashi, N., Vereecke, L., Bertrand, M. J. M., Duprez, L., Berger, S. B., Divert, T., Gonçalves, A., Sze, M., Gilbert, B., Kourula, S., Goossens, V., Lefebvre, S., Günther, C., Becker, C., Bertin, J., Gough, P. J., Declercq, W., van Loo, G., & Vandenabeele, P. (2014). RIPK1 ensures intestinal homeostasis by protecting the epithelium against apoptosis. *Nature*, *513*, 95. http://dx.doi.org/10.1038/nature13706

Talabot-Ayer, D., Lamacchia, C., Gabay, C., & Palmer, G. (2009). Interleukin-33 is biologically active independently of caspase-1 cleavage. *Journal of Biological Chemistry*, *284*(29), 19420–19426. https://doi.org/10.1074/jbc.M901744200

Tamagawa-Mineoka, R., Okuzawa, Y., Masuda, K., & Katoh, N. (2014). Increased serum levels of interleukin 33 in patients with atopic dermatitis. *Journal of the American Academy of Dermatology*, *70*(5), 882–888. https://doi.org/https://doi.org/10.1016/j.jaad.2014.01.867

Tanaka, N., Yonekura, H., Yamagishi, S., Fujimori, H., Yamamoto, Y., & Yamamoto, H. (2000). The receptor for advanced glycation end products is induced by the glycation products themselves and tumor necrosis factor-alpha through nuclear factor-kappa B, and by 17beta-estradiol through Sp-1 in human vascular endothelial cells. *The Journal of Biological Chemistry*, *275*(33), 25781–25790. https://doi.org/10.1074/jbc.M001235200

Tang, D., Kang, R., Livesey, K. M., Cheh, C.-W., Farkas, A., Loughran, P., Hoppe, G., Bianchi, M. E., Tracey, K. J., Zeh III, H. J., & Lotze, M. T. (2010). Endogenous HMGB1 regulates autophagy. *Journal of Cell Biology*, *190*(5), 881–892. https://doi.org/10.1083/jcb.200911078

Tang, Yiting, Zhao, X., Antoine, D., Xiao, X., Wang, H., Andersson, U., Billiar, T. R., Tracey, K. J., & Lu, B. (2016). Regulation of Posttranslational Modifications of HMGB1 During Immune Responses. *Antioxidants and Redox Signaling*, *24*(12), 620–634. https://doi.org/10.1089/ars.2015.6409

Tang, Yong, Tu, H., Zhang, J., Zhao, X., Wang, Y., Qin, J., & Lin, X. (2019). K63-linked ubiquitination regulates RIPK1 kinase activity to prevent cell death during embryogenesis and inflammation. *Nature Communications*, *10*(1), 4157. https://doi.org/10.1038/s41467-019-12033-8

Taniguchi, N., Kawahara, K. ichi, Yone, K., Hashiguchi, T., Yamakuchi, M., Goto, M., Inoue, K., Yamada, S., Ijiri, K., Matsunaga, S., Nakajima, T., Komiya, S., & Maruyama, I. (2003). High mobility group box chromosomal protein 1 plays a role in the pathogenesis of rheumatoid arthritis as a novel cytokine. *Arthritis and Rheumatism*, *48*(4), 971–981. https://doi.org/10.1002/art.10859

Tanzer, M. C., Matti, I., Hildebrand, J. M., Young, S. N., Wardak, A., Tripaydonis, A., Petrie, E. J., Mildenhall, A. L., Vaux, D. L., Vince, J. E., Czabotar, P. E., Silke, J., & Murphy, J. M. (2016). Evolutionary divergence of the necroptosis effector MLKL. *Cell Death and Differentiation*, *23*(7), 1185–1197. https://doi.org/10.1038/cdd.2015.169

Taraborrelli, L., Peltzer, N., Montinaro, A., Kupka, S., Rieser, E., Hartwig, T., Sarr, A., Darding, M., Draber, P., Haas, T. L., Akarca, A., Marafioti, T., Pasparakis, M., Bertin, J., Gough, P. J., Bouillet, P., Strasser, A., Leverkus, M., Silke, J., & Walczak, H. (2018). LUBAC prevents lethal dermatitis by inhibiting cell death induced by TNF, TRAIL and CD95L. *Nature Communications*, *9*(1), 1–12. https://doi.org/10.1038/s41467-018-06155-8

Taylor, S. C., Berkelman, T., Yadav, G., & Hammond, M. (2013). A defined methodology for reliable quantification of western blot data. *Molecular Biotechnology*, *55*(3), 217–226. https://doi.org/10.1007/s12033-013-9672-6

Teufelberger, A. R., Van Nevel, S., Hulpiau, P., Nordengrün, M., Savvides, S. N., De Graeve, S., Akula, S., Holtappels, G., De Ruyck, N., Declercq, W., Vandenabeele, P., Hellman, L., Bröker, B. M., Krysko, D. V., Bachert, C., & Krysko, O. (2020). Mouse Strain-Dependent Difference Toward the Staphylococcus aureus Allergen Serine Protease-Like Protein D Reveals a Novel Regulator of IL-33. *Frontiers in Immunology*, *11*(September), 1–13. https://doi.org/10.3389/fimmu.2020.582044

Thach, D. C., Kimura, T., & Griffin, D. E. (2000). Differences between C57BL/6 and BALB/cBy mice in mortality and virus replication after intranasal infection with neuroadapted Sindbis virus. *Journal of Virology*, *74*(13), 6156–6161. https://doi.org/10.1128/jvi.74.13.6156-6161.2000

Thapa, R. J., Nogusa, S., Chen, P., Maki, J. L., Lerro, A., Andrake, M., Rall, G. F., Degterev, A., & Balachandran, S. (2013). Interferon-induced RIP1/RIP3-mediated necrosis requires PKR and is licensed by FADD and caspases. *Proceedings of the National Academy of Sciences of the United States of America*, *110*(33), E3109–18. https://doi.org/10.1073/pnas.1301218110

Tian, J., Avalos, A. M., Mao, S.-Y., Chen, B., Senthil, K., Wu, H., Parroche, P., Drabic, S., Golenbock, D., Sirois, C., Hua, J., An, L. L., Audoly, L., La Rosa, G., Bierhaus, A., Naworth, P., Marshak-Rothstein, A., Crow, M. K., Fitzgerald, K. A., … Coyle, A. J. (2007). Toll-like receptor 9-dependent activation by DNA-containing immune complexes is mediated by HMGB1 and RAGE. *Nature Immunology*, *8*(5), 487–496. https://doi.org/10.1038/ni1457

Tominaga, S. (1989). A putative protein of a growth specific cDNA from BALB/c-3T3 cells is highly similar to the extracellular portion of mouse interleukin 1 receptor. *FEBS Letters*, *258*(2), 301–304. https://doi.org/10.1016/0014-5793(89)81679-5

Tonnus, W., & Linkermann, A. (2017). The in vivo evidence for regulated necrosis. *Immunological Reviews*, *277*(1), 128–149. https://doi.org/10.1111/imr.12551

Townsend, M. J., Fallon, P. G., Matthews, D. J., Jolin, H. E., & McKenzie, A. N. (2000). T1/ST2-deficient mice demonstrate the importance of T1/ST2 in developing primary T helper cell type 2 responses. *The Journal of Experimental Medicine*, *191*(6), 1069–1076. https://doi.org/10.1084/jem.191.6.1069

Tsung, A., Klune, J. R., Zhang, X., Jeyabalan, G., Cao, Z., Peng, X., Stolz, D. B., Geller, D. A., Rosengart, M. R., & Billiar, T. R. (2007). HMGB1 release induced by liver ischemia involves Toll-like receptor 4 dependent reactive oxygen species production and calcium-mediated signaling. *The Journal of Experimental Medicine*, *204*(12), 2913–2923. https://doi.org/10.1084/jem.20070247

Tsung, A., Sahai, R., Tanaka, H., Nakao, A., Fink, M. P., Lotze, M. T., Yang, H., Li, J., Tracey, K. J., Geller, D. A., & Billiar, T. R. (2005). The nuclear factor HMGB1 mediates hepatic injury after murine liver ischemia-reperfusion. *The Journal of Experimental Medicine*, *201*(7), 1135–1143. https://doi.org/10.1084/jem.20042614

Tsung, A., Zheng, N., Jeyabalan, G., Izuishi, K., Klune, J. R., Geller, D. A., Lotze, M. T., Lu, L., & Billiar, T. R. (2007). Increasing numbers of hepatic dendritic cells promote HMGB1-mediated ischemia-reperfusion injury. *Journal of Leukocyte Biology*, *81*(1), 119–128. https://doi.org/10.1189/jlb.0706468

Turin, S. Y., Ledwon, J. K., Bae, H., Buganza-Tepole, A., Topczewska, J., & Gosain, A. K. (2018). Digital analysis yields more reliable and accurate measures of dermal and epidermal thickness in histologically processed specimens compared to traditional methods. *Experimental Dermatology*, *27*(6), 687–690. https://doi.org/10.1111/exd.13534

Turlo, K. A., Gallaher, S. D., Vora, R., Laski, F. A., & Iruela-Arispe, M. L. (2010). When Cre-mediated recombination in mice does not result in protein loss. *Genetics*, *186*(3), 959–967. https://doi.org/10.1534/genetics.110.121608

Ulland, T. K., Jain, N., Hornick, E. E., Elliott, E. I., Clay, G. M., Sadler, J. J., Mills, K. A. M., Janowski, A. M., Volk, A. P. D., Wang, K., Legge, K. L., Gakhar, L., Bourdi, M., Ferguson, P. J., Wilson, M. E., Cassel, S. L., & Sutterwala, F. S. (2016). Nlrp12 mutation causes C57BL/6J strain-specific defect in neutrophil recruitment. *Nature Communications*, *7*, 13180. https://doi.org/10.1038/ncomms13180

Upton, J. W., Kaiser, W. J., & Mocarski, E. S. (2012). DAI/ZBP1/DLM-1 complexes with RIP3 to mediate virus-induced programmed necrosis that is targeted by murine cytomegalovirus vIRA. *Cell Host & Microbe*, *11*(3), 290–297. https://doi.org/10.1016/j.chom.2012.01.016

van Hogerlinden, M., Rozell, B. L., Ahrlund-Richter, L., & Toftgård, R. (1999). Squamous cell carcinomas and increased apoptosis in skin with inhibited Rel/nuclear factor-kappaB signaling. *Cancer Research*, *59*(14), 3299–3303.

van Zoelen, M. A. D., Schmidt, A.-M., Florquin, S., Meijers, J. C., de Beer, R., de Vos, A. F., Nawroth, P. P., Bierhaus, A., & van der Poll, T. (2009). Receptor for advanced glycation end products facilitates host defense during Escherichia coli-induced abdominal sepsis in mice. *The Journal of Infectious Diseases*, *200*(5), 765–773. https://doi.org/10.1086/604730

Vanden Berghe, Tom, Grootjans, S., Goossens, V., Dondelinger, Y., Krysko, D. V., Takahashi, N., & Vandenabeele, P. (2013). Determination of apoptotic and necrotic cell death in vitro and in vivo. *Methods*, *61*(2), 117–129. https://doi.org/10.1016/j.ymeth.2013.02.011

Vanden Berghe, Tom, Hassannia, B., & Vandenabeele, P. (2016). An outline of necrosome triggers. *Cellular and Molecular Life Sciences*, *73*(11–12), 2137–2152. https://doi.org/10.1007/s00018-016-2189-y

Vanden Berghe, Tom, Hulpiau, P., Martens, L., Vandenbroucke, R. E., Van Wonterghem, E., Perry, S. W., Bruggeman, I., Divert, T., Choi, S. M., Vuylsteke, M., Shestopalov, V. I., Libert, C., & Vandenabeele, P. (2015). PasSenger Mutations Confound Interpretation Of All Genetically Modified Congenic Mice.

Immunity, *43*(1), 200–209. https://doi.org/10.1016/j.immuni.2015.06.011

Vanden Berghe, Tom, Kaiser, W. J., Bertrand, M. J., & Vandenabeele, P. (2015). Molecular crosstalk between apoptosis, necroptosis, and survival signaling. *Molecular & Cellular Oncology*, *2*(4), e975093. https://doi.org/10.4161/23723556.2014.975093

Vanden Berghe, Tom, Linkermann, A., Jouan-Lanhouet, S., Walczak, H., & Vandenabeele, P. (2014). Regulated necrosis: The expanding network of non-apoptotic cell death pathways. *Nature Reviews Molecular Cell Biology*, *15*(2), 135–147. https://doi.org/10.1038/nrm3737

Vaux, D. L., & Korsmeyer, S. J. (1999). Cell Death in Development. *Cell*, *96*(2), 245–254. https://doi.org/https://doi.org/10.1016/S0092-8674(00)80564-4

Vénéreau, E., Ceriotti, C., & Bianchi, M. E. (2015). DAMPs from Cell Death to New Life. *Frontiers in Immunology*, *6*, 422. https://doi.org/10.3389/fimmu.2015.00422

Venereau, E., De Leo, F., Mezzapelle, R., Careccia, G., Musco, G., & Bianchi, M. E. (2016). HMGB1 as biomarker and drug target. *Pharmacological Research*, *111*, 534–544. https://doi.org/10.1016/j.phrs.2016.06.031

Vercammen, D., Beyaert, R., Denecker, G., Goossens, V., Van Loo, G., Declercq, W., Grooten, J., Fiers, W., & Vandenabeele, P. (1998). Inhibition of Caspases Increases the Sensitivity of L929 Cells to Necrosis Mediated by Tumor Necrosis Factor . *The Journal of Experimental Medicine*, *187*(9), 1477–1485. http://www.ncbi.nlm.nih.gov/pmc/articles/PMC2212268/

Verri, W. A., Souto, F. O., Vieira, S. M., Almeida, S. C. L., Fukada, S. Y., Xu, D., Alves-Filho, J. C., Cunha, T. M., Guerrero, A. T. G., Mattos-Guimaraes, R. B., Oliveira, F. R., Teixeira, M. M., Silva, J. S., McInnes, I. B., Ferreira, S. H., Louzada-Junior, P., Liew, F. Y., & Cunha, F. Q. (2010). IL-33 induces neutrophil migration in rheumatoid arthritis and is a target of anti-TNF therapy. *Annals of the Rheumatic Diseases*, *69*(9), 1697–1703. https://doi.org/10.1136/ard.2009.122655

Vince, J. E., Wong, W. W.-L., Gentle, I., Lawlor, K. E., Allam, R., O'Reilly, L., Mason, K., Gross, O., Ma, S., Guarda, G., Anderton, H., Castillo, R., Hacker, G., Silke, J., & Tschopp, J. (2012). Inhibitor of apoptosis proteins limit RIP3 kinase-dependent interleukin-1 activation. *Immunity*, *36*(2), 215–227. https://doi.org/10.1016/j.immuni.2012.01.012

Vocca, L., Di Sano, C., Uasuf, C. G., Sala, A., Riccobono, L., Gangemi, S., Albano, G. D., Bonanno, A., Gagliardo, R., & Profita, M. (2015). IL-33/ST2 axis controls Th2/IL-31 and Th17 immune response in allergic airway diseases. *Immunobiology*, *220*(8), 954–963. https://doi.org/10.1016/j.imbio.2015.02.005

Vooijs, M., Jonkers, J., & Berns, A. (2001). A highly efficient ligand-regulated Cre recombinase mouse line shows that LoxP recombination is position dependent. *EMBO Reports*, *2*(4), 292–297. https://doi.org/10.1093/embo-reports/kve064

Wallach, D., Kang, T. B., Yang, S. H., & Kovalenko, A. (2014). The in vivo significance of necroptosis: Lessons from exploration of caspase-8 function. *Cytokine and Growth Factor Reviews*, *25*(2), 157–165. https://doi.org/10.1016/j.cytogfr.2013.12.001

Wang, H, Bloom, O., Zhang, M., Vishnubhakat, J. M., Ombrellino, M., Che, J., Frazier, A., Yang, H., Ivanova, S., Borovikova, L., Manogue, K. R., Faist, E., Abraham, E., Andersson, J., Andersson, U., Molina, P. E., Abumrad, N. N., Sama, A., & Tracey, K. J. (1999). HMG-1 as a late mediator of endotoxin lethality in mice. *Science (New York, N.Y.)*, *285*(5425), 248–251. https://doi.org/10.1126/science.285.5425.248

Wang, Haichao, Bloom, O., Zhang, M., Vishnubhakat, J. M., Ombreliino, M., Che, J., Frazier, A., Yang, H., & Ivanova, S. (1999). *HMG-1 as a Late Mediator of Endotoxin Lethality in Mice*. *285*(July), 248–251.

Wang, Huayi, Sun, L., Su, L., Rizo, J., Liu, L., Wang, L. F., Wang, F. S., & Wang, X. (2014). Mixed Lineage Kinase Domain-like Protein MLKL Causes Necrotic Membrane Disruption upon Phosphorylation by RIP3. *Molecular Cell*, *54*(1), 133–146. https://doi.org/10.1016/j.molcel.2014.03.003

Wang, Z., Zhou, H., Zheng, H., Zhou, X., Shen, G., Teng, X., Liu, X., Zhang, J., Wei, X., Hu, Z., Zeng, F., Hu, Y., Hu, J., Wang, X., Chen, S., Cheng, J., Zhang, C., Gui, Y., Zou, S., … Li, J. (2021). Autophagy-based unconventional secretion of HMGB1 by keratinocytes plays a pivotal role in psoriatic skin inflammation. *Autophagy*, *17*(2), 529–552. https://doi.org/10.1080/15548627.2020.1725381

Wautier, J. L., Zoukourian, C., Chappey, O., Wautier, M. P., Guillausseau, P. J., Cao, R., Hori, O., Stern, D., & Schmidt, A. M. (1996). Receptor-mediated endothelial cell dysfunction in diabetic vasculopathy. Soluble receptor for advanced glycation end products blocks hyperpermeability in diabetic rats. *The Journal of Clinical Investigation*, *97*(1), 238–243. https://doi.org/10.1172/JCI118397

Weber, K., Roelandt, R., Bruggeman, I., Estornes, Y., & Vandenabeele, P. (2018). Nuclear RIPK3 and MLKL contribute to cytosolic necrosome formation and necroptosis. *Communications Biology*, *1*(1), 1–13. https://doi.org/10.1038/s42003-017-0007-1

Weidinger, S., Beck, L. A., Bieber, T., Kabashima, K., & Irvine, A. D. (2018). Atopic dermatitis. *Nature Reviews Disease Primers*, *4*(1), 1. https://doi.org/10.1038/s41572-018-0001-z

Weinlich, R., Oberst, A., Beere, H. M., & Green, D. R. (2017). Necroptosis in development, inflammation and disease. *Nature Reviews Molecular Cell Biology*, *18*(2), 127–136. https://doi.org/10.1038/nrm.2016.149

Weinlich, R., Oberst, A., Dillon, C. P., Janke, L. J., Milasta, S., Lukens, J. R., Rodriguez, D. A., Gurung, P., Savage, C., Kanneganti, T. D., & Green, D. R. (2013). Protective Roles for Caspase-8 and cFLIP in Adult Homeostasis. *Cell Reports*, *5*(2), 340–348. https://doi.org/10.1016/j.celrep.2013.08.045

Wen, S., Ling, Y., Yang, W., Shen, J., Li, C., Deng, W., Liu, W., & Liu, K. (2017). Necroptosis is a key mediator of enterocytes loss in intestinal ischaemia/reperfusion injury. *Journal of Cellular and Molecular Medicine*, *21*(3), 432–443. https://doi.org/10.1111/jcmm.12987

Weng, D., Marty-Roix, R., Ganesan, S., Proulx, M. K., Vladimer, G. I., Kaiser, W. J., Mocarski, E. S., Pouliot, K., Chan, F. K.-M., Kelliher, M. A., Harris, P. A., Bertin, J., Gough, P. J., Shayakhmetov, D. M., Goguen, J. D., Fitzgerald, K. A., Silverman, N., & Lien, E. (2014). Caspase-8 and RIP kinases regulate bacteria-induced innate immune responses and cell death. *Proceedings of the National Academy of Sciences of the United States of America*, *111*(20), 7391–7396. https://doi.org/10.1073/pnas.1403477111

Wertz, I. E., Rourke, K. M. O., Zhou, H., Eby, M., Aravind, L., Seshagiri, S., Wu, P., Wiesmann, C., & Dixit, V. M. (2004). ligase domains of A20 downregulate NF- k B signalling. *Nature*, *430*(August), 1–6.

Wolf, R., Mascia, F., Dharamsi, A., Howard, O. M. Z., Cataisson, C., Bliskovski, V., Winston, J., Feigenbaum, L., Lichti, U., Ruzicka, T., Chavakis, T., & Yuspa, S. H. (2010). Gene from a psoriasis susceptibility locus primes the skin for inflammation. *Science Translational Medicine*, *2*(61). https://doi.org/10.1126/scitranslmed.3001108

Wong, R., Geyer, S., Weninger, W., Guimberteau, J. C., & Wong, J. K. (2016). The dynamic anatomy and patterning of skin. *Experimental Dermatology*, *25*(2), 92–98. https://doi.org/10.1111/exd.12832

Wright Muelas, M., Ortega, F., Breitling, R., Bendtsen, C., & Westerhoff, H. V. (2018). Rational cell culture optimization enhances experimental reproducibility in cancer cells. *Scientific Reports*, *8*(1), 3029. https://doi.org/10.1038/s41598-018-21050-4

Wu, J., Huang, Z., Ren, J., Zhang, Z., He, P., Li, Y., Ma, J., Chen, W., Zhang, Y., Zhou, X., Yang, Z., Wu, S.-Q., Chen, L., & Han, J. (2013). Mlkl knockout mice demonstrate the indispensable role of Mlkl in necroptosis. *Cell Research*, *23*(8), 994–1006. https://doi.org/10.1038/cr.2013.91

Wu, X.-N., Yang, Z.-H., Wang, X.-K., Zhang, Y., Wan, H., Song, Y., Chen, X., Shao, J., & Han, J. (2014). Distinct roles of RIP1–RIP3 hetero- and RIP3–RIP3 homo-interaction in mediating necroptosis. *Cell Death & Differentiation*, *21*(11), 1709–1720. https://doi.org/10.1038/cdd.2014.77

Wu, X., Poulsen, K. L., Sanz-Garcia, C., Huang, E., McMullen, M. R., Roychowdhury, S., Dasarathy, S., & Nagy, L. E. (2020). MLKL-dependent signaling regulates autophagic flux in a murine model of non-alcohol-associated fatty liver and steatohepatitis. *Journal of Hepatology*, *73*(3), 616–627. https://doi.org/10.1016/j.jhep.2020.03.023

Wullaert, A., Bonnet, M. C., & Pasparakis, M. (2011). NF-κB in the regulation of epithelial homeostasis and inflammation. *Cell Research*, *21*(1), 146–158.

https://doi.org/10.1038/cr.2010.175

Xia, B., Fang, S., Chen, X., Hu, H., Chen, P., Wang, H., & Gao, Z. (2016). MLKL forms cation channels. *Cell Research*, *26*(5), 517–528. https://doi.org/10.1038/cr.2016.26

Xu, D, Chan, W. L., Leung, B. P., Huang, F. p, Wheeler, R., Piedrafita, D., Robinson, J. H., & Liew, F. Y. (1998). Selective expression of a stable cell surface molecule on type 2 but not type 1 helper T cells. *The Journal of Experimental Medicine*, *187*(5), 787–794. https://doi.org/10.1084/jem.187.5.787

Xu, Daichao, Jin, T., Zhu, H., Chen, H., Ofengeim, D., Zou, C., Mifflin, L., Pan, L., Amin, P., Li, W., Shan, B., Naito, M. G., Meng, H., Li, Y., Pan, H., Aron, L., Adiconis, X., Levin, J. Z., Yankner, B. A., & Yuan, J. (2018). TBK1 Suppresses RIPK1-Driven Apoptosis and Inflammation during Development and in Aging. *Cell*, *174*(6), 1477–1491.e19. https://doi.org/10.1016/j.cell.2018.07.041

Xu, Ding, Young, J., Song, D., & Esko, J. D. (2011). Heparan sulfate is essential for high mobility group protein 1 (HMGB1) signaling by the receptor for advanced glycation end products (RAGE). *The Journal of Biological Chemistry*, *286*(48), 41736–41744. https://doi.org/10.1074/jbc.M111.299685

Xu, H., Du, X., Liu, G., Huang, S., Du, W., Zou, S., Tang, D., Fan, C., Xie, Y., Wei, Y., Tian, Y., & Fu, X. (2019). The pseudokinase MLKL regulates hepatic insulin sensitivity independently of inflammation. *Molecular Metabolism*, *23*(February), 14–23. https://doi.org/10.1016/j.molmet.2019.02.003

Xu, J., Jiang, Y., Wang, J., Shi, X., Liu, Q., Liu, Z., Li, Y., Scott, M. J., Xiao, G., Li, S., Fan, L., Billiar, T. R., Wilson, M. A., & Fan, J. (2014). Macrophage endocytosis of high-mobility group box 1 triggers pyroptosis. *Cell Death and Differentiation*, *21*(8), 1229–1239. https://doi.org/10.1038/cdd.2014.40

Yamada, S. S. (2004). Preparation of human epidermal keratinocyte cultures. *Current Protocols in Cell Biology / Editorial Board, Juan S. Bonifacino ... [et Al.]*, *Chapter 2*, Unit 2.6. https://doi.org/10.1002/0471143030.cb0206s21

Yan, S. F., Ramasamy, R., Naka, Y., & Schmidt, A. M. (2003). Glycation, Inflammation, and RAGE: A Scaffold for the Macrovascular Complications of Diabetes and Beyond. *Circulation Research*, *93*(12), 1159–1169. https://doi.org/10.1161/01.RES.0000103862.26506.3D

Yanagisawa, K., Takagi, T., Tsukamoto, T., Tetsuka, T., & Tominaga, S. (1993). Presence of a novel primary response gene ST2L, encoding a product highly similar to the interleukin 1 receptor type 1. *FEBS Letters*, *318*(1), 83–87. https://doi.org/10.1016/0014-5793(93)81333-u

Yang, D., Liang, Y., Zhao, S., Ding, Y., Zhuang, Q., Shi, Q., Ai, T., Wu, S. Q., & Han, J. (2020). ZBP1 mediates interferon-induced necroptosis. *Cellular and Molecular Immunology*, *17*(4), 356–368. https://doi.org/10.1038/s41423-019-0237-x

Yang, H., Hreggvidsdottir, H. S., Palmblad, K., Wang, H., Ochani, M., Li, J., Lu, B., Chavan, S., Rosas-Ballina, M., Al-Abed, Y., Akira, S., Bierhaus, A., Erlandsson-Harris, H., Andersson, U., & Tracey, K. J. (2010). A critical cysteine is required for HMGB1 binding to toll-like receptor 4 and activation of macrophage cytokine release. *Proceedings of the National Academy of Sciences of the United States of America*, *107*(26), 11942–11947. https://doi.org/10.1073/pnas.1003893107

Yang, H., Lundbäck, P., Ottosson, L., Erlandsson-Harris, H., Venereau, E., Bianchi, M. E., Al-Abed, Y., Andersson, U., Tracey, K. J., & Antoine, D. J. (2012). Redox modification of cysteine residues regulates the cytokine activity of high mobility group box-1 (HMGB1). *Molecular Medicine (Cambridge, Mass.)*, *18*(1), 250–259. https://doi.org/10.2119/molmed.2011.00389

Yang, H., Ochani, M., Li, J., Qiang, X., Tanovic, M., Harris, H. E., Susarla, S. M., Ulloa, L., Wang, H., DiRaimo, R., Czura, C. J., Wang, H., Roth, J., Warren, H. S., Fink, M. P., Fenton, M. J., Andersson, U., & Tracey, K. J. (2004). Reversing established sepsis with antagonists of endogenous high-mobility group box 1. *Proceedings of the National Academy of Sciences of the United States of America*, *101*(1), 296–301. https://doi.org/10.1073/pnas.2434651100

Yang, H., Wang, H., & Andersson, U. (2020). Targeting Inflammation Driven by HMGB1. *Frontiers in Immunology*, *11*(March), 1–9. https://doi.org/10.3389/fimmu.2020.00484

Yang, H., Wang, H., Ju, Z., Ragab, A. A., Lundbäck, P., Long, W., Valdes-Ferrer, S. I., He, M., Pribis, J. P., Li, J., Lu, B., Gero, D., Szabo, C., Antoine, D. J., Harris, H. E., Golenbock, D. T., Meng, J., Roth, J., Chavan, S. S., … Al-Abed, Y. (2015). MD-2 is required for disulfide HMGB1-dependent TLR4 signaling. *The Journal of Experimental Medicine*, *212*(1), 5–14. https://doi.org/10.1084/jem.20141318

Yang, R., Harada, T., Mollen, K. P., Prince, J. M., Levy, R. M., Englert, J. A., Gallowitsch-Puerta, M., Yang, L., Yang, H., Tracey, K. J., Harbrecht, B. G., Billiar, T. R., & Fink, M. P. (2006). Anti-HMGB1 Neutralizing Antibody Ameliorates Gut Barrier Dysfunction and Improves Survival after Hemorrhagic Shock. *Molecular Medicine*, *12*(4), 105–114. https://doi.org/10.2119/2006-00010.Yang

Yang, Y., Jiang, K., Liu, X., Qin, M., & Xiang, Y. (2021). CaMKII in Regulation of Cell Death During Myocardial Reperfusion Injury. *Frontiers in Molecular Biosciences*, *8*(June), 1–15. https://doi.org/10.3389/fmolb.2021.668129

Yang, Z., Deng, Y., Su, D., Tian, J., Gao, Y., He, Z., & Wang, X. (2013). TLR4 as receptor for HMGB1-mediated acute lung injury after liver ischemia/reperfusion injury. *Laboratory Investigation*, *93*(7), 792–800. https://doi.org/10.1038/labinvest.2013.66

Yasuda, K., Muto, T., Kawagoe, T., Matsumoto, M., Sasaki, Y., Matsushita, K., Taki, Y., Futatsugi-Yumikura, S., Tsutsui, H., Ishii, K. J., Yoshimoto, T., Akira, S., & Nakanishi, K. (2012). Contribution of IL-33-activated type II innate lymphoid

cells to pulmonary eosinophilia in intestinal nematode-infected mice. *Proceedings of the National Academy of Sciences of the United States of America*, *109*(9), 3451–3456. https://doi.org/10.1073/pnas.1201042109

Yin, H., Li, X., Hu, S., Liu, T., Yuan, B., Gu, H., Ni, Q., Zhang, X., & Zheng, F. (2013). IL-33 accelerates cutaneous wound healing involved in upregulation of alternatively activated macrophages. *Molecular Immunology*, *56*(4), 347–353. https://doi.org/10.1016/j.molimm.2013.05.225

Ying, Z., Pan, C., Shao, T., Liu, L., Li, L., Guo, D., Zhang, S., Yuan, T., Cao, R., Jiang, Z., Chen, S., Wang, F., & Wang, X. (2018). Mixed Lineage Kinase Domain-like Protein MLKL Breaks Down Myelin following Nerve Injury. *Molecular Cell*, *72*(3), 457–468.e5. https://doi.org/10.1016/j.molcel.2018.09.011

Yoo, H., Im, Y., Ko, R. E., Lee, J. Y., Park, J., & Jeon, K. (2021). Association of plasma level of high-mobility group box-1 with necroptosis and sepsis outcomes. *Scientific Reports*, *11*(1), 1–9. https://doi.org/10.1038/s41598-021-88970-6

Yoon, S., Kovalenko, A., Bogdanov, K., & Wallach, D. (2017). MLKL, the Protein that Mediates Necroptosis, Also Regulates Endosomal Trafficking and Extracellular Vesicle Generation. *Immunity*, *47*(1), 51–65.e7. https://doi.org/10.1016/j.immuni.2017.06.001

Youn, J. H., Oh, Y. J., Kim, E. S., Choi, J. E., & Shin, J.-S. (2008). High mobility group box 1 protein binding to lipopolysaccharide facilitates transfer of lipopolysaccharide to CD14 and enhances lipopolysaccharide-mediated TNF-alpha production in human monocytes. *Journal of Immunology (Baltimore, Md. : 1950)*, *180*(7), 5067–5074. https://doi.org/10.4049/jimmunol.180.7.5067

Yu, M., Wang, H., Ding, A., Golenbock, D. T., Latz, E., Czura, C. J., Fenton, M. J., Tracey, K. J., & Yang, H. (2006). HMGB1 signals through toll-like receptor (TLR) 4 and TLR2. *Shock (Augusta, Ga.)*, *26*(2), 174–179. https://doi.org/10.1097/01.shk.0000225404.51320.82

Yu, S. S., Li, H. J., Goodwin, G. H., & Johns, E. W. (1977). Interaction of non-histone chromosomal proteins HMG1 and HMG2 with DNA. *European Journal of Biochemistry*, *78*(2), 497–502. https://doi.org/10.1111/j.1432-1033.1977.tb11762.x

Yu, W., & Hill, W. G. (2013). Lack of specificity shown by P2Y6 receptor antibodies. *Naunyn-Schmiedeberg's Archives of Pharmacology*, *386*(10), 885–891. https://doi.org/10.1007/s00210-013-0894-8

Yuan, H., Jin, X., Sun, J., Li, F., Feng, Q., Zhang, C., Cao, Y., & Wang, Y. (2009). Protective effect of HMGB1 a box on organ injury of acute pancreatitis in mice. *Pancreas*, *38*(2), 143–148. https://doi.org/10.1097/MPA.0b013e31818166b4

Zargarian, S., Shlomovitz, I., Erlich, Z., Hourizadeh, A., Ofir-Birin, Y., Croker, B. A., Regev-Rudzki, N., Edry-Botzer, L., & Gerlic, M. (2017). Phosphatidylserine

externalization, “necroptotic bodies” release, and phagocytosis during necroptosis. *PLoS Biology*, *15*(6), 1–23. https://doi.org/10.1371/journal.pbio.2002711

Zemskova, M., McClain, N., Niihori, M., Varghese, M. V, James, J., Rafikov, R., & Rafikova, O. (2020). Necrosis-Released HMGB1 (High Mobility Group Box 1) in the Progressive Pulmonary Arterial Hypertension Associated With Male Sex. *Hypertension*, *76*(6), 1787–1799. https://doi.org/10.1161/HYPERTENSIONAHA.120.16118

Zeng, F., Chen, H., Chen, L., Mao, J., Cai, S., Xiao, Y., Li, J., Shi, J., Li, B., Xu, Y., Tan, Z., Gong, F., Li, B., Qian, Y., Dong, L., & Zheng, F. (2021). An Autocrine Circuit of IL-33 in Keratinocytes Is Involved in the Progression of Psoriasis. *Journal of Investigative Dermatology*, *141*(3), 596-606.e7. https://doi.org/10.1016/j.jid.2020.07.027

Zhan, C., Huang, M., Yang, X., & Hou, J. (2021). MLKL: Functions beyond serving as the Executioner of Necroptosis. *Theranostics*, *11*(10), 4759–4769. https://doi.org/10.7150/thno.54072

Zhan, Q., Jeon, J., Li, Y., Huang, Y., Xiong, J., Wang, Q., Xu, T. Le, Li, Y., Ji, F. H., Du, G., & Zhu, M. X. (2021). CAMK2/CaMKII activates MLKL in short-term starvation to facilitate autophagic flux. *Autophagy*, *00*(00), 1–19. https://doi.org/10.1080/15548627.2021.1954348

Zhang, C. C., Krieg, S., & Shapiro, D. J. (1999). HMG-1 stimulates estrogen response element binding by estrogen receptor from stably transfected HeLa cells. *Molecular Endocrinology (Baltimore, Md.)*, *13*(4), 632–643. https://doi.org/10.1210/mend.13.4.0264

Zhang, D.-W., Shao, J., Lin, J., Zhang, N., Lu, B.-J., Lin, S.-C., Dong, M.-Q., & Han, J. (2009). RIP3, an Energy Metabolism Regulator That Switches TNF-Induced Cell Death from Apoptosis to Necrosis. *Science*, *325*(5938), 332 LP – 336. http://science.sciencemag.org/content/325/5938/332.abstract

Zhang, D. W., Shao, J., Lin, J., Zhang, N., Lu, B. J., Lin, S. C., Dong, M. Q., & Han, J. (2009). RIP3, an energy metabolism regulator that switches TNF-induced cell death from apoptosis to necrosis. *Science*, *325*(5938), 332–336. https://doi.org/10.1126/science.1172308

Zhang, F., Kent, K. C., Yamanouchi, D., Zhang, Y., Kato, K., Tsai, S., Nowygrod, R., Schmidt, A. M., & Liu, B. (2010). *Anti-receptor for advanced glycation end products therapies as novel treatment for abdominal aortic aneurysm*. *250*(3), 416–423. https://doi.org/10.1097/SLA.0b013e3181b41a18.Anti-receptor

Zhang, J., Wu, Y., Weng, Z., Zhou, T., Feng, T., & Lin, Y. (2014). Glycyrrhizin protects brain against ischemia-reperfusion injury in mice through HMGB1-TLR4-IL-17A signaling pathway. *Brain Research*, *1582*, 176–186. https://doi.org/10.1016/j.brainres.2014.07.002

Zhang, S., Su, Y., Ying, Z., Guo, D., Pan, C., Guo, J., Zou, Z., Wang, L., Zhang, Z., Jiang, Z., Zhang, Z., & Wang, X. (2019). RIP1 kinase inhibitor halts the progression of an immune-induced demyelination disease at the stage of monocyte elevation. *Proceedings of the National Academy of Sciences of the United States of America*, *116*(12), 5675–5680. https://doi.org/10.1073/pnas.1819917116

Zhang, T., Zhang, Y., Cui, M., Jin, L., Wang, Y., Lv, F., Liu, Y., Zheng, W., Shang, H., Zhang, J., Zhang, M., Wu, H., Guo, J., Zhang, X., Hu, X., Cao, C. M., & Xiao, R. P. (2016). CaMKII is a RIP3 substrate mediating ischemia- and oxidative stress-induced myocardial necroptosis. *Nature Medicine*, *22*(2), 175–182. https://doi.org/10.1038/nm.4017

Zhang, W., Guo, S., Li, B., Liu, L., Ge, R., Cao, T., Wang, H., Gao, T., Wang, G., & Li, C. (2017). Proinflammatory effect of high-mobility group protein B1 on keratinocytes: an autocrine mechanism underlying psoriasis development. *Journal of Pathology*, *241*(3), 392–404. https://doi.org/10.1002/path.4848

Zhang, Xixi, Zhang, H., Xu, C., Li, X., Li, M., Wu, X., Pu, W., Zhou, B., Wang, H., Li, D., Ding, Q., Ying, H., Wang, H., & Zhang, H. (2019). Ubiquitination of RIPK1 suppresses programmed cell death by regulating RIPK1 kinase activation during embryogenesis. *Nature Communications*, *10*(1), 4158. https://doi.org/10.1038/s41467-019-11839-w

Zhang, Xuhua, Dowling, J. P., & Zhang, J. (2019). RIPK1 can mediate apoptosis in addition to necroptosis during embryonic development. *Cell Death and Disease*, *10*(3). https://doi.org/10.1038/s41419-019-1490-8

Zhao, H., Liu, Z., Shen, H., Jin, S., & Zhang, S. (2016). Glycyrrhizic acid pretreatment prevents sepsis-induced acute kidney injury via suppressing inflammation, apoptosis and oxidative stress. *European Journal of Pharmacology*, *781*, 92–99. https://doi.org/10.1016/j.ejphar.2016.04.006

Zhao, Jie, Jitkaew, S., Cai, Z., Choksi, S., Li, Q., Luo, J., & Liu, Z. G. (2012). Mixed lineage kinase domain-like is a key receptor interacting protein 3 downstream component of TNF-induced necrosis. *Proceedings of the National Academy of Sciences of the United States of America*, *109*(14), 5322–5327. https://doi.org/10.1073/pnas.1200012109

Zhao, Jingling, Yu, J., Xu, Y., Chen, L., Zhou, F., Zhai, Q., Wu, J., Shu, B., & Qi, S. (2018). Epidermal HMGB1 Activates Dermal Fibroblasts and Causes Hypertrophic Scar Formation in Reduced Hydration. *Journal of Investigative Dermatology*, *138*(11), 2322–2332. https://doi.org/10.1016/j.jid.2018.04.036

Zhao, X. M., Chen, Z., Zhao, J. B., Zhang, P. P., Pu, Y. F., Jiang, S. H., Hou, J. J., Cui, Y. M., Jia, X. L., & Zhang, S. Q. (2016). Hsp90 modulates the stability of MLKL and is required for TNF-induced necroptosis. *Cell Death and Disease*, *7*(2), 1–9. https://doi.org/10.1038/cddis.2015.390

Zhong, H., Li, X., Zhou, S., Jiang, P., Liu, X., Ouyang, M., Nie, Y., Chen, X., Zhang, L.,

Liu, Y., Tao, T., & Tang, J. (2020). Interplay between RAGE and TLR4 Regulates HMGB1-Induced Inflammation by Promoting Cell Surface Expression of RAGE and TLR4. *The Journal of Immunology*, *205*(3), 767–775. https://doi.org/10.4049/jimmunol.1900860

Zhou, T., DeRoo, E., Yang, H., Stranz, A., Wang, Q., Ginnan, R., Singer, H. A., & Liu, B. (2021). MLKL and CaMKII Are Involved in RIPK3-Mediated Smooth Muscle Cell Necroptosis. *Cells*, *10*(9). https://doi.org/10.3390/cells10092397

Zhou, W., & Yuan, J. (2014). Necroptosis in health and diseases. *Seminars in Cell and Developmental Biology*, *35*, 14–23. https://doi.org/10.1016/j.semcdb.2014.07.013

Zhuang, C., & Chen, F. (2020). Small-Molecule Inhibitors of Necroptosis: Current Status and Perspectives. *Journal of Medicinal Chemistry*, *63*(4), 1490–1510. https://doi.org/10.1021/acs.jmedchem.9b01317

Supplementary material

Appendix I – Reagents

Reagent	Working concentration	Provider
DMEM, high glucose GlutaMAX Supplement	1X	Gibco
Foetal calf serum (FCS)	10% (v/v)	Gibco
Penicillin (5000 U) – Streptomycin (5 mg)	1X	Sigma Aldrich
Dubecco's Phosphate-Buffered Saline (PBS)	1X	Gibco
Tween-20	0.05% (v/v)	Sigma Aldrich
Trypsin-EDTA (0.05%) phenol red	1X	Gibco
DMSO	1X	Sigma Aldrich
PureCol	0.1 mg/mL (dH_20)	Advanced Biomatrix
Antibiotic/Antimycotic (100X)	1X	Gibco
Trypsin-EDTA (2.5%), no phenol red	1X	Gibco
Ham's F12 Nutrient Mix, GlutaMAX Supplement	1X	Gibco
Hydrocortisone (HC)	0.4 μg/mL	Sigma Aldrich
Cholera Toxin (CT)	8.4 ng/mL	Sigma Aldrich
Insulin	5 μg/mL	Sigma Aldrich
Adenine	24 μg/mL	Sigma Aldrich
Human EGF	10 ng/mL	R&D Systems
Recombinant human TNF	20 ng/mL	PeproTech
Birinapant	1 μM	SelleckChem

Z-VAD-fmk	20 μM	SelleckChem
Disulfide HMGB1, LPS free	50 μM	HMGBiotech
Nec-1s	20 μM	SelleckChem
Necrosulfamide (NSA)	1 μM	Gift M-T Dimanche-Boitrel
GSK872	1 μM	SelleckChem
GW806742X	5 μM	SYNkinase
Propidium Iodide (PI)	10 μg/mL	Sigma Aldrich
Triton X-100	10% (v/v)	ThermoFisher
LDH-Glo TM Cytotoxicity Assay	MI	Promega
Cell proliferation reagent WST-1	MI	Roche
cOmplete ULTRA tablets, Mini, EASYpack	1X (MI)	Roche
PhosSTOP EASYpack (ROCHE). Phosphatase inhibitor cocktail tablets	1X (MI)	Roche
Bio-Rad Protein Assay	MI	Bio-Rad
Standard 0.3 mg/ml HAS	-	Sigma Aldrich
Pierce BCA Protein Assay Kit	MI	ThermoFisher
β-Mercaptoethanol	20% (v/v)	Sigma Aldrich
NuPAGE™ LDS Sample Buffer (4X)	1X	ThermoFisher
Bolt 4-12% (w/v) acrylamide gels	MI	ThermoFisher
30% (w/v) Acrylamide/Bis Solution	-	Bio-Rad
TEMED	-	Sigma Aldrich
Bolt MOPS SDS running buffer (20X)	1X	ThermoFisher
Non-Fat Dried Milk (NFDM)	5% (w/v)	Sigma Aldrich
Bovine serum albumin (BSA)	5% (w/v)	Sigma Aldrich
Amersham ECL Rainbow Marker	5 μL	Sigma Aldrich
Spectra Multicolor Broad Range Protein Ladder	5 μL	Thermo Fisher

SuperSignal West Pico Luminescent Solution	MI	Thermo Fisher
Supersignal West Femto Maximum Sensitivity assay	MI	Thermo Fisher
Sepharose Protein A/G beads	MI	Rockland
Protein A/G PLUS-Agarose	MI	Santa Cruz
Proteinase K, recombinant PCR grade	3% (v/v)	Roche
Nuclease free distilled water	1X	Qiagen
KAPA Mouse Genotyping kit	MI	KAPA Biosystems
Agarose	1,5% (w/v)	Appleton
Ethidium bromide 1% solution	20 μM	Fisher Scientific
100 bp DNA ladder	-	Invitrogen
Paraformaldehyde (PFA)	4% (w/v)	Sigma Aldrich
OCT Embedding Matrix	1X	CellPath
Trypsin from porcine pancreas tablet	1:100	Sigma Aldrich
Goat serum	10% (v/v)	Sigma Aldrich
Gelatine from cold water fish skin	0.02% (v/v)	Sigma Aldrich
Vectashield Antifade Mounting Media	1X	Vector Laboratories

Table A1: List of reagents, general working concentration and provider. Stated concentration is always used unless stated otherwise. MI: manufacturer's instructions.

Appendix II – Primers

Genotype	Target gene	Sequence (5'-3')	Annealing T°	Amplicon size (bp)
KRT-14	KRT-14 *wt*	GTAGGTGGAAATTCTAGCATCATCC	60 °C	600 bp
	KRT-14-cre	TTCCTCAGGAGTGTCTTCGC	60 °C	350 bp
		GTCCATGTCCTTCCTGAAGC		
Casp-8	Casp-8 *wt-fl*	ATAATTCCCCCAAATCCTCGCATC	60 °C	200 bp (*wt*) 300 bp (*fl*)
		GGCTCACTCCCAGGGCTTCCT		
IL-33	IL-33 *wt*	CCAGATGAACTTGTGATTGTTGCTCCCTC	61 °C	1000 bp
		CTTGGAGTTGGAATACTTCATTCTAGG		
	Citrine	AGGAGCGCACCATCTTCTTCAAG	61 °C	370
		CATGTGATCGCGCTTCTCGTTG		
ST2	ST2 *wt*	TCGTCCTGGGGTCTGGAAAATGA	58 °C	500 bp
		CCTGAACAGTACCTTCTGATAACA		
	ST2 KO	TCTCTTCTGGACCCTACCTCA	54 °C	1300 bp
		CTCTTCGCGCTATTACGCCAGC		
RAGE	RAGE exon 5/7	AGCTGGCACTTAGATGGGAAACTT	60 °C	500 bp
		TGGGCAGAGATGGCACAGGT		
	eGFP	AGTGCTTCAGCCGCTACC	60 °C	99 bp
		GAAGATGGTGCGCTCCTG		
	RAGE exon 6/8	CCCCACCCAAGGAGGAAC	60 °C	950 bp
		TCAGGGAGGAGCAGCACAG		

Table A2: List of primer sequences, annealing temperature and expected amplicon size.

Appendix III – Characterisation of Casp-8^{EKO} skin inflammation model

The Casp-8^{EKO} skin inflammation model was first described over ten years ago. However, differences in the genetic background of these animals led to strong differences in the severity of the phenotype as well as the animal survival (Kovalenko et al., 2009; Pedro Lee et al., 2009). Indeed, genetic background accounts for many of the differences reported in studies based in animals (S. K. Kang et al., 2018; Simon et al., 2013; Teufelberger et al., 2020; Tom Vanden Berghe, Hulpiau, et al., 2015).

This supplementary information includes a characterisation of the Casp-8EKO skin inflammatory lesions obtained during the breedings of the different double knock-out lines. It reports the phenotype variability observed between Casp-8EKO animals obtained from different breedings, as well as their phenotype evolution. Furthermore, it details the characteristic skin histology observed in the Casp-8EKO animals, which coincides with previous reports of necroptotic skin inflammation (Bonnet et al., 2011; Kovalenko et al., 2009; P. Lee et al., 2009).

Casp-8^{EKO} phenotype variability

The obtained Casp-8EKO animals showed skin inflammation distributed in patches around the body, but the distribution and severity of the lesions was not the same in all animals. This phenotype variability was most obvious when comparing Casp-8EKO animals obtained by crossing K14Cre+ Casp-8fl/+ with Il-33$^{-/-}$ or *St2*$^{-/-}$ animals and their offspring and those obtained when crossing K14Cre+ *Casp-8*$^{fl/+}$ mice with Rage$^{-/-}$ with *Rage*$^{fl/fl}$ animals and their offspring (Figure A3.1). Specifically, Casp-8^{EKO} *IL-33*$^{+/-}$ or Casp-8^{EKO}, *IL-33*$^{+/+}$ littermates and Casp-8^{EKO} *St2*$^{+/-}$ or Casp-

8^{EKO} *St2*$^{+/+}$ littermates displayed a much less severe skin inflammation phenotype than Casp-8^{EKO} *Rage*$^{+/-}$ or Casp-8^{EKO} *Rage*$^{+/+}$ littermates and Casp-8^{EKO} *Rage*$^{fl/+}$ or Casp-8^{EKO} *Rage*$^{+/+}$ littermates.

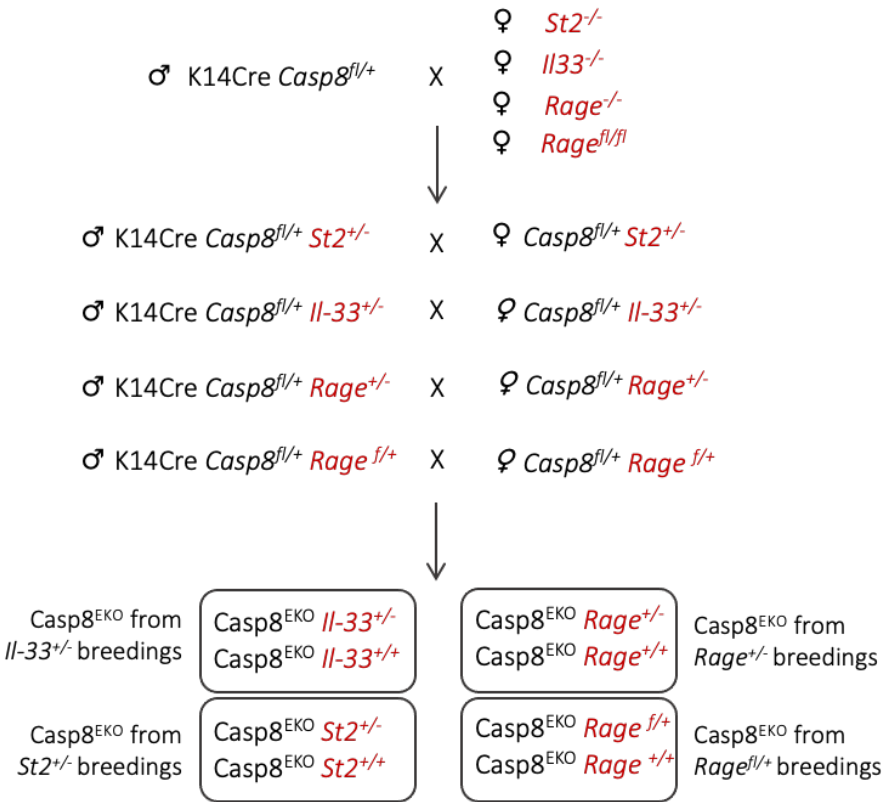

Figure A3.1: Breeding strategy leads to the obtention of Casp-8^{EKO} animals from different crosses. The different Casp-8^{EKO} animals (in boxes) obtained from different breeding crosses are referred to in the text as: Casp-8^{EKO} animals obtained from *Il-33*$^{+/-}$, *St2*$^{+/-}$, *Rage*$^{+/-}$ or *Rage*$^{fl/+}$ breedings.

Figure A3.2 shows images of Casp-8^{EKO} at P10 obtained from the four different breeding colonies. Casp-8^{EKO} animals obtained from *IL-33*$^{+/-}$ or *St2*$^{+/-}$ breedings show small, scattered lesions around the back and neck area (Figure A3.2A, top left and right panels) while patches of skin inflammation in Casp-8^{EKO} animals obtained from *Rage*$^{+/-}$ or *Rage*$^{fl/+}$ animals are considerably larger and cover a greater portion of the body (Figure A3.1A, bottom left and right panels). The severity of the phenotype was assessed through the scoring system during the first 10-11 days after birth (see section 2.8.1). Figure A3.2B shows the lesion

score of the animals over time in a scattered plot on which simple linear regression has been performed.

The data for lesion scores obtained from Casp-8^{EKO} IL-33$^{+/-}$, Casp-8^{EKO} St2$^{+/-}$Casp-8^{EKO} Rage$^{+/-}$ and Casp-8^{EKO} Rage$^{fl/+}$ breedings were analysed and regression lines were calculated for each set of data. The slopes of the lines were obtained and compared using Graphpad. This analysis showed that the slopes obtained from Casp-8^{EKO} *Rage*$^{+/-}$ and Casp-8^{EKO} *Rage*$^{fl/+}$ data are significantly higher than those from Casp-8^{EKO} *IL-33*$^{+/-}$ and Casp-8^{EKO} *St2*$^{+/-}$ sets of data (Figure A3.2B). This indicates that the phenotype of Casp-8 ^{EKO} animals born on *Rage*$^{+/-}$ and *Rage*$^{fl/+}$ breedings was more severe and developed at a faster rate than Casp-8 ^{EKO} animals born from *IL-33*$^{+/-}$or *St2*$^{+/-}$ breedings.

Furthermore, this analysis showed, as observed macroscopically, that the phenotype score was not significantly different between Casp-8^{EKO} animals obtained from *IL-33*$^{+/-}$or *St2*$^{+/-}$ breedings (Figure A3.2B, pink and yellow lines) or between Casp-8^{EKO} animals obtained from *Rage*$^{+/-}$ and *Rage*$^{fl/+}$ breedings (Figure A3.2B, green and blue lines). Due to the lack of phenotypical differences seen between Casp-8^{EKO} *IL-33*$^{+/-}$ and Casp-8^{EKO} *St2*$^{+/-}$ mice, data from these animals have been grouped together for analysis, as were animals obtained from Casp-8^{EKO} *Rage*$^{+/-}$ and Casp-8^{EKO} *Rage*$^{fl/+}$ breedings. Most importantly, all double knock-out animals obtained from these breedings have been compared to their Casp-8^{EKO} littermates, in order to eliminate any bias from the effect of the genetic background.

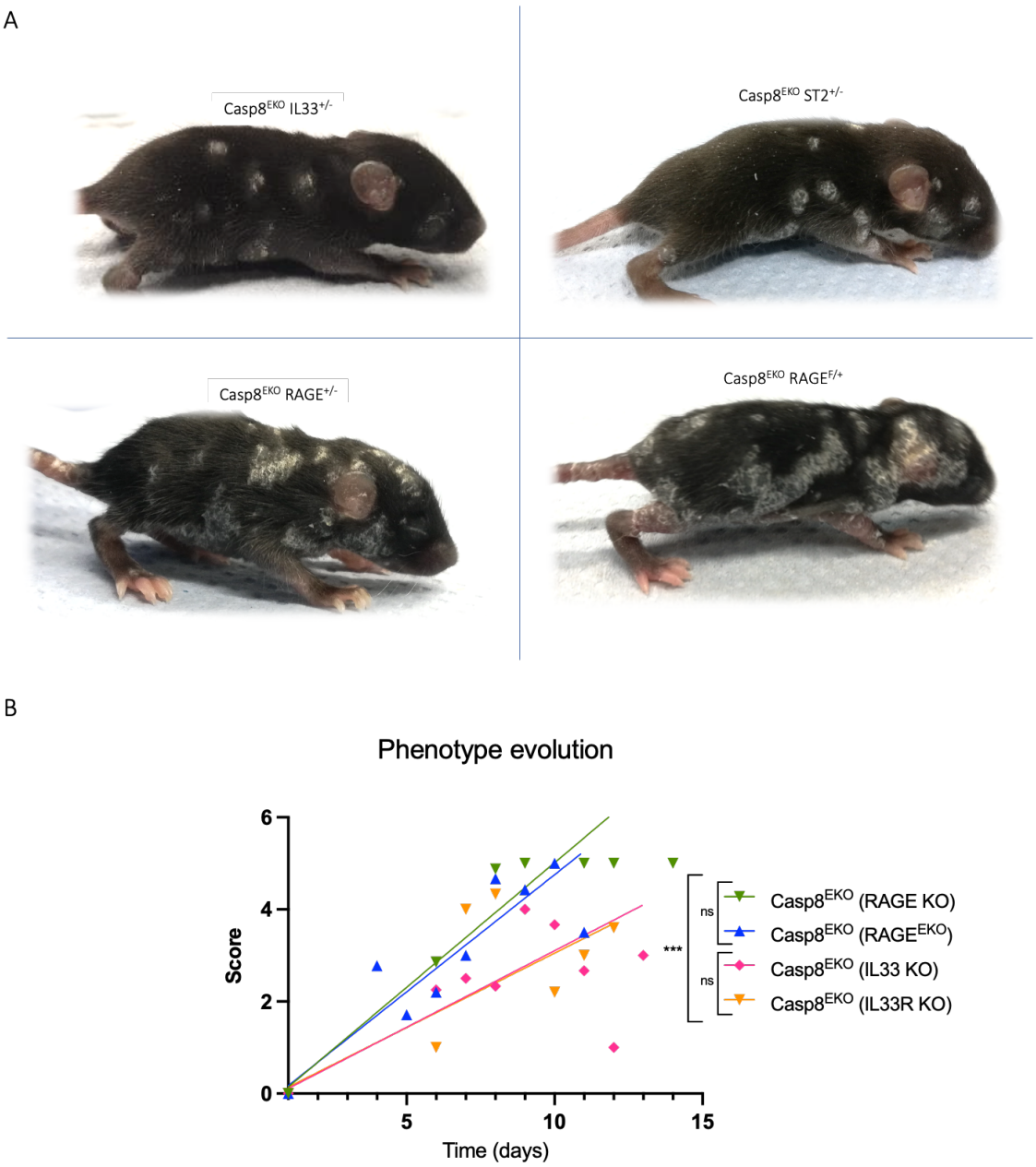

Figure A3.2: Casp-8 ^{EKO} animals with obtained from *Il-33*$^{+/-}$ and *St2*$^{+/-}$ breedings show a less severe skin inflammation phenotype than Casp-8^{EKO} animals from *Rage*$^{+/-}$ and *Rage*$^{fl/+}$ breedings. (A) Representative images of Casp-8^{EKO} animals at P10 obtained from the four different breeding lines established for study. **(B)** Graph plots of lesion score versus time (in days) for Casp-8^{EKO} animals obtained from the four different breeding lines. Each set of data is plotted through individual values that represent the mean score of the animals at a determined age. Linear regressions were calculated for each set of data and slope comparison was performed using Graphpad.

The differences in the skin inflammation phenotype were also obvious when assessing other general wellbeing features of the animals. Casp-

8^{EKO} animals from *Rage*$^{+/-}$ and *Rage*$^{fl/fl}$ breedings were significantly smaller and appeared runted when compared to Casp-8^{EKO} animals from *Il-33*$^{-/-}$ and *St2*$^{-/-}$ breedings (Figure A3.3). Given this variability, and to preserve the wellbeing of the animals, the experimental endpoint (lesions affecting 50% of body surface) was reached earlier, hence study timepoints for these genotypes were adjusted.

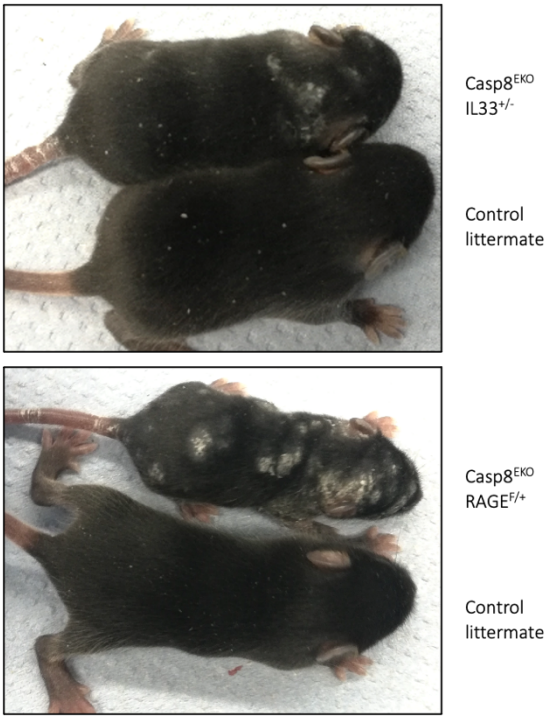

Figure A3.3: Casp-8^{EKO} animals from *Rage*$^{fl/+}$ breedings are smaller than Casp-8^{EKO} animals from *Il-33*$^{+/-}$ breedings and littermate controls. Images of Casp-8^{EKO} *Il-33*$^{+/-}$ animals and littermate controls (top panel) and Casp-8^{EKO} *RAGE*$^{fl/+}$ and littermate control (bottom panel) at P9.

Differences in the necroptosis-dependent skin inflammation phenotype have been described before. Both $FADD^{EKO}$ and Casp-8^{EKO} animals described by Bonnet et al. and Kovalenko et al. from epidermal keratinocytes resulted in mice displaying macroscopic lesions from postnatal day 3 (P3) and death at postnatal day 8 (P8) while the Casp-8^{EKO} inflammatory phenotype described by Lee et al. was drastically less severe, with mild skin lesions developing at P10 (Pedro Lee et al., 2009). The main difference between these studies is that animals used by Bonnet et al. and Kovalenko et al. were on C57BL/6 genetic background

(C57BL/6N in the first case, undefined in the latter) while the Casp-8^{EKO} mice described by Lee et al. were on BALB/c background. This highlights the importance of the animal's genetic background on the development of the necroptotic-dependent inflammation, suggesting that mutations carried by different mouse strains affect the development of necroptosis. Animals used in the present study had a mixed genetic background. As described in section 2.6.2 of this thesis, both Casp-8$^{fl/fl}$ animals and *Il-33*$^{-/-}$ animals were a backcross on C57BL/6J background mice while *St2*$^{-/-}$, *Rage*$^{-/-}$ and *Rage*$^{fl/fl}$ animals were on a mixed 129sv x C57BL/6J background (I Liliensek et al., 2004; Senn et al., 2000). This fact has been considered throughout the analysis of the results, especially when making direct comparisons to previous research. For this reason, quantification of the lesions has been systematically performed for all animals, not only macroscopically but also through histological analysis. The observations made here further highlights the importance of maintaining the genetic background a constant when studying necroptosis in animal models and points out the importance of using the appropriate controls in each experiment.

Casp-8EKO skin histology

The inflammatory lesions found in Casp-8^{EKO} animals are characterised by increased dermal cellularity, epidermal hyperplasia (acanthosis) and thickening of the cornified layer (hyperkeratosis) (Figure A3.3A and B). Widened intercellular spaces in the basal layer of the epidermis were observed throughout the lesions, showing loss of cell-to-cell contact (Figure A3.3A) due to plasma membrane rupture caused by keratinocyte necroptosis. Neutrophil abscesses (Figure A3.3A) could also be seen in the inflammatory skin lesions. Necroptotic keratinocytes were observed throughout the lesions, characterised by irregular shape and eosinophilic

cytoplasm together with hyperchromatic, condensed and partly fragmented nuclei (Figure A3.3B).

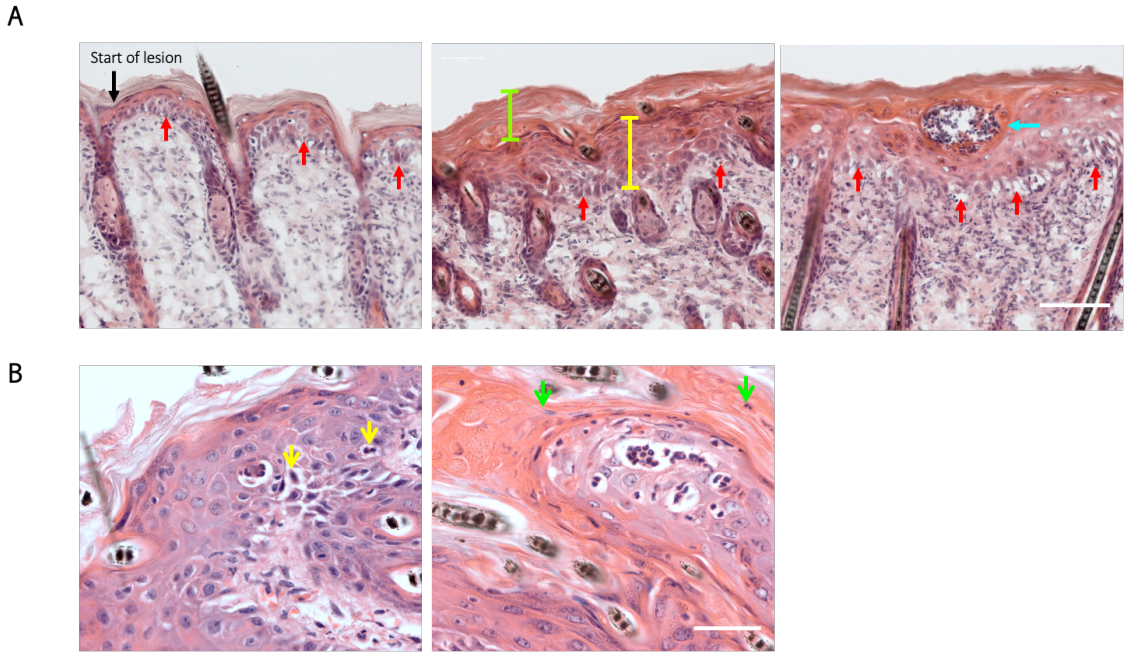

Figure A3.4: Histological features found in Casp-8^{EKO} lesional skin. (A) Casp-8^{EKO} skin samples were fixed and stained for haematoxylin and eosin. Black arrow indicates the start of a small lesion. Read arrows indicate widened intercellular spaces between keratinocytes. Blue arrow points out a neutrophil abscess. Acanthosis and hyperkeratosis are indicated by yellow and green lines respectively. **(B)** Casp-8^{EKO} skin samples were fixed and stained for haematoxylin and eosin. Yellow arrows indicate necroptotic keratinocytes. Green arrows indicate retained nuclei in the cornified layer (parakeratosis). Images obtained using Zeiss Apotome Axio Observer microscope: (A) magnification 40X, (B) magnification 40X. Scale bars represents (A) 25 μm, (B) 50 μm.

The histological features found in Casp-8^{EKO} born from *Il-33*$^{-/-}$ and *St2*$^{-/-}$ breedings and *Rage*$^{+/-}$ and *Rage*$^{fl/fl}$ breedings were similar, with the only difference being that inflammatory lesions started appearing earlier in Casp-8^{EKO} animals obtained from *Rage*$^{+/-}$ and *Rage*$^{fl/fl}$ breedings (as shown in phenotype evolution, Figure A3.2B). As the phenotype developed faster, the skin of Casp-8^{EKO} animals obtained from *Rage*$^{+/-}$ and *Rage*$^{fl/fl}$ breedings displayed a characteristic histology around hair follicles (Figure A3.5) that was not observed in Casp-8^{EKO} animals born from *Il-33*$^{-/-}$ and *St2*$^{-/-}$ breedings at the same age. The skin displayed a marked increase in the

number of hair follicles which appeared to fuse with each other and have inside keratinous layers (Figure 5.5).

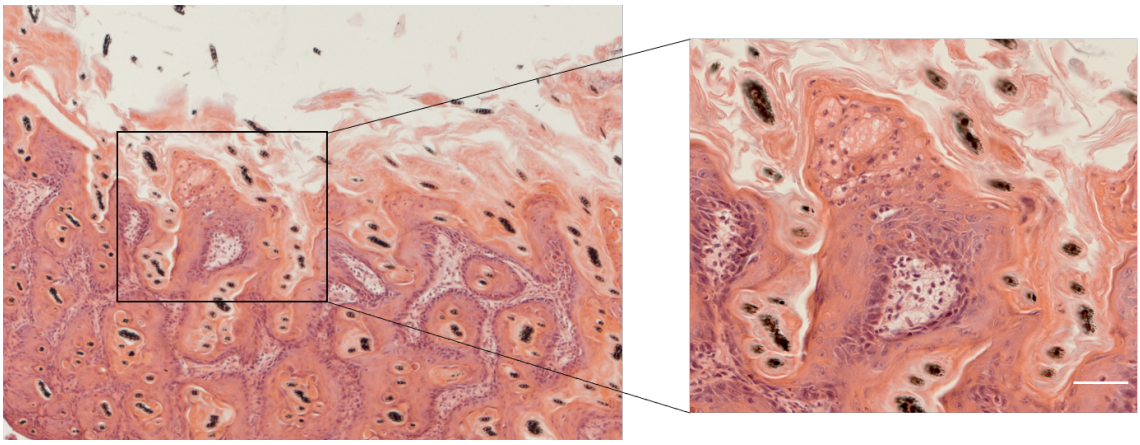

Figure A3.5: Characteristic histology found in the skin of Casp-8^{EKO} animals obtained from *Rage*$^{+/-}$ and *Rage*$^{fl/+}$ breedings. Image of epidermis morphology and hair follicle histology found in the skin of a Casp-8^{EKO} *Rage*$^{fl/+}$ animal at P9. Images obtained using Zeiss Apotome Axio Observer microscope: left panel, magnification 5X; right panel, magnification 40X. Scale bars represents 50 μm.

Appendix IV – Uncropped images from Western blots

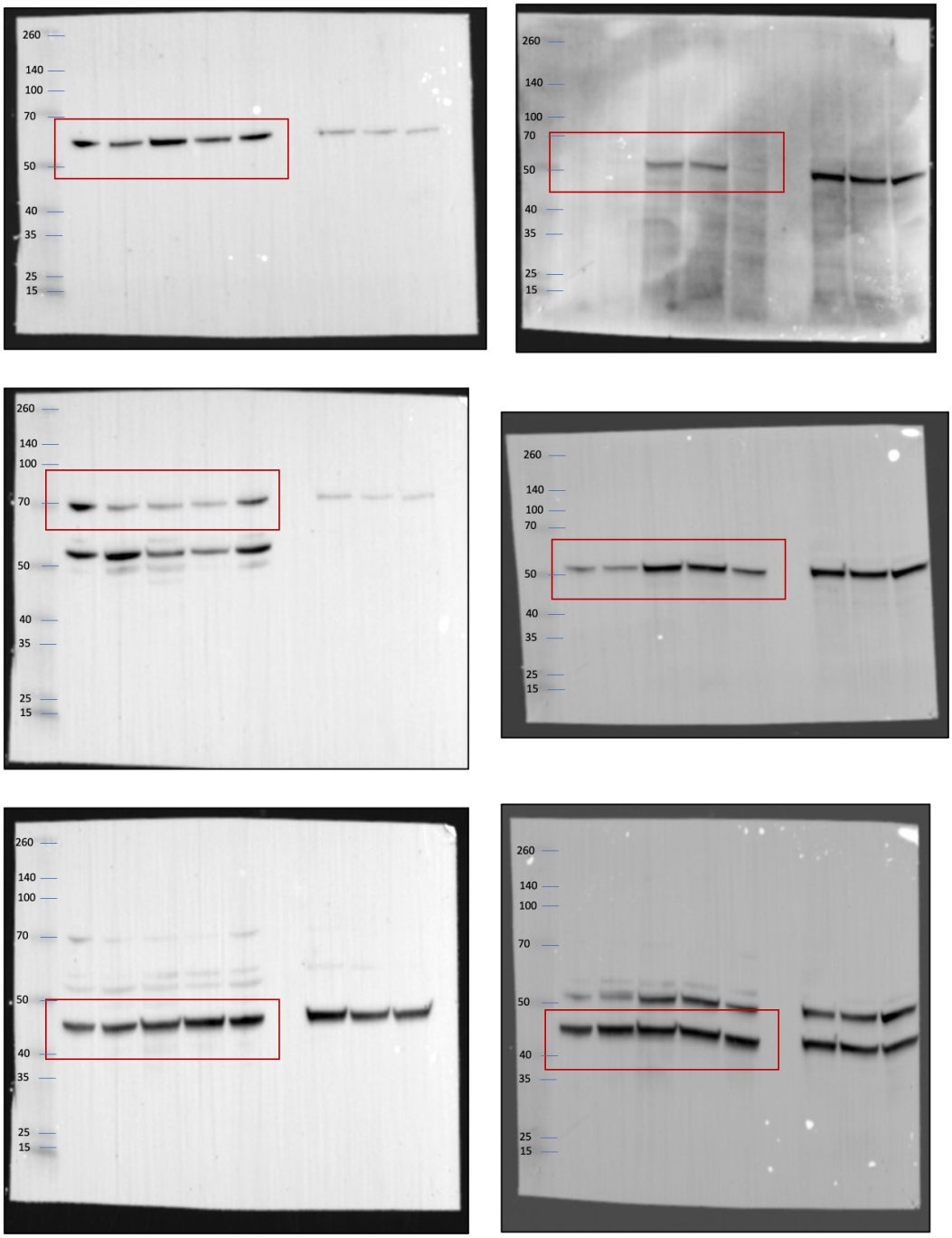

Figure A4.1: Uncropped Western blots used in Figure 3.1.

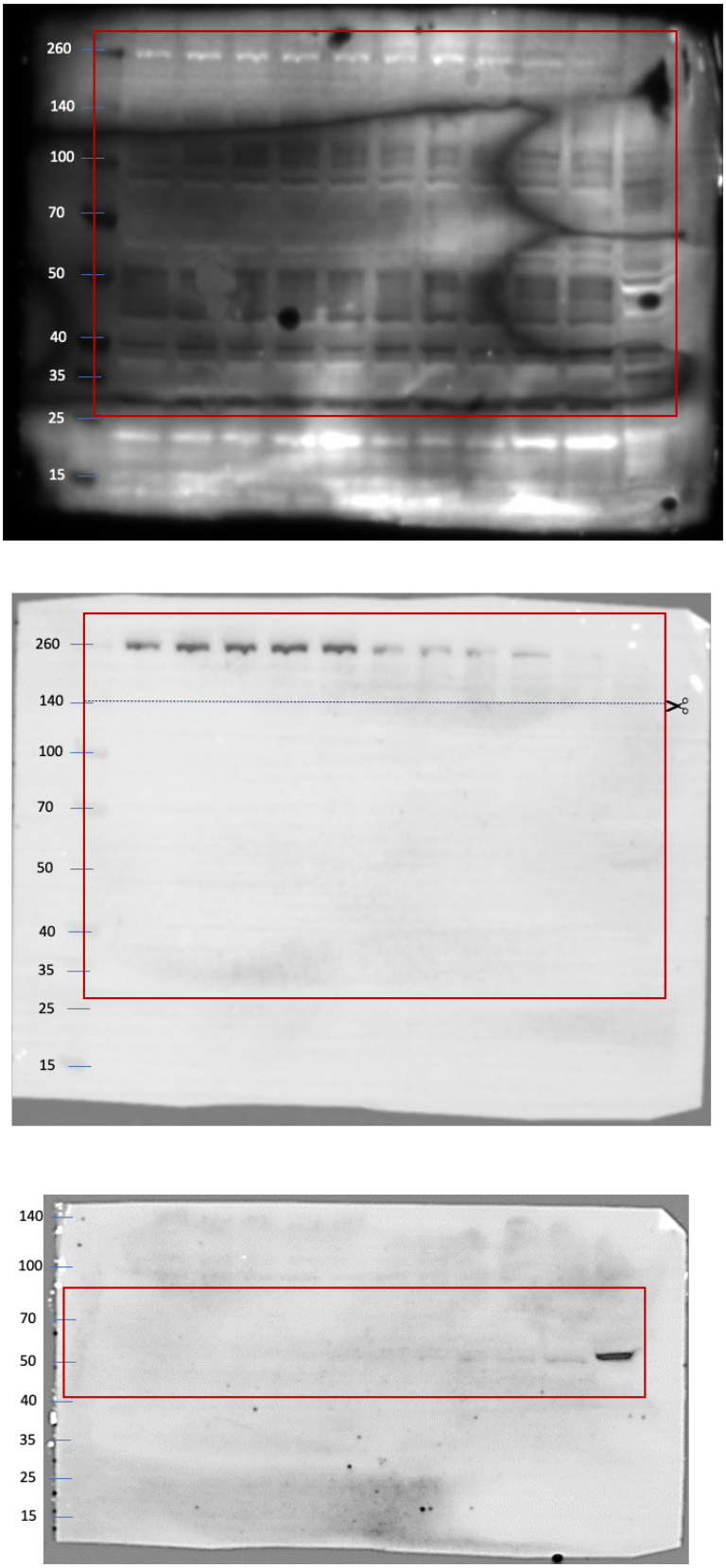

Figure 8.2: Uncropped Western blots used in Figure 3.2A, B and C.

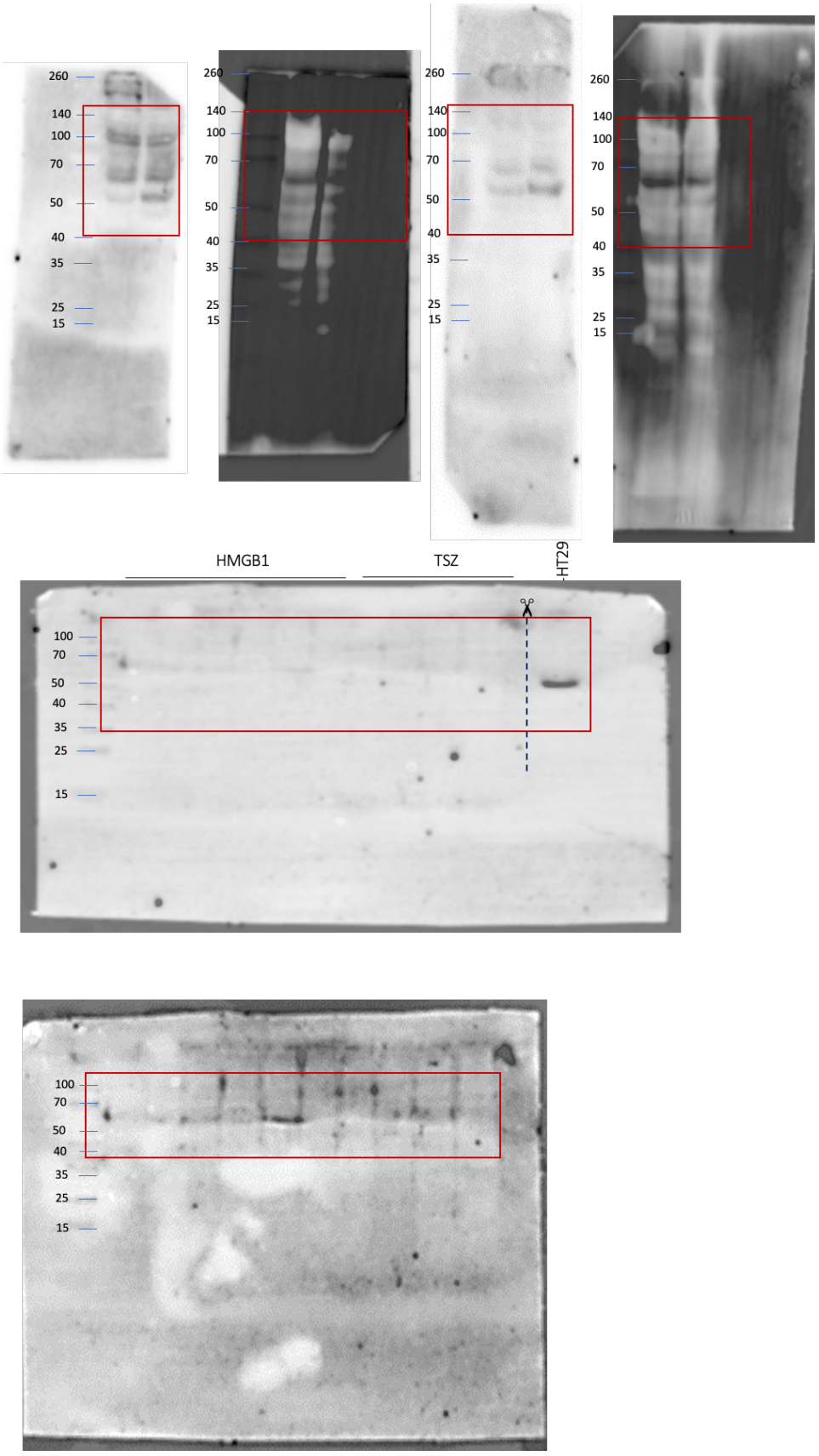

Figure A4.3: Uncropped Western blots used in Figure 3.3A and B.

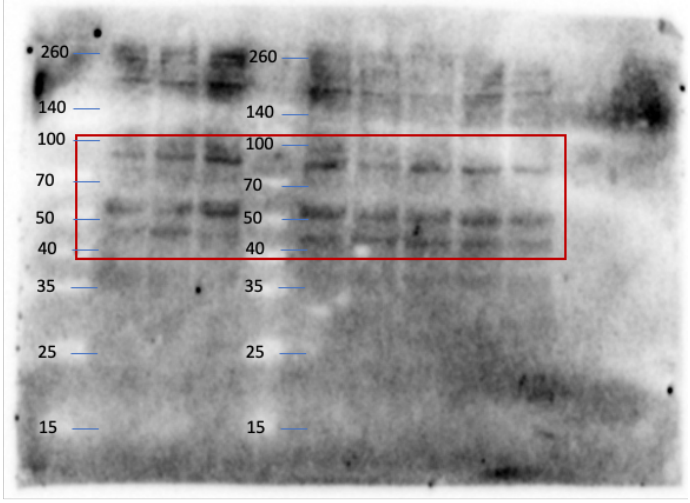

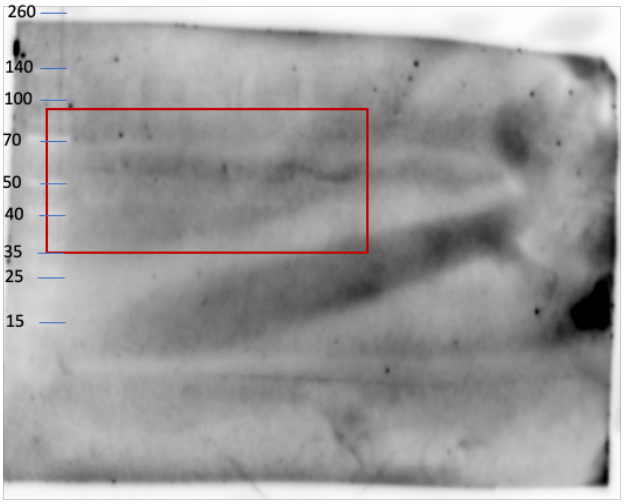

Figure A4.4: Uncropped Western blots used in Figure 3.4A and B.

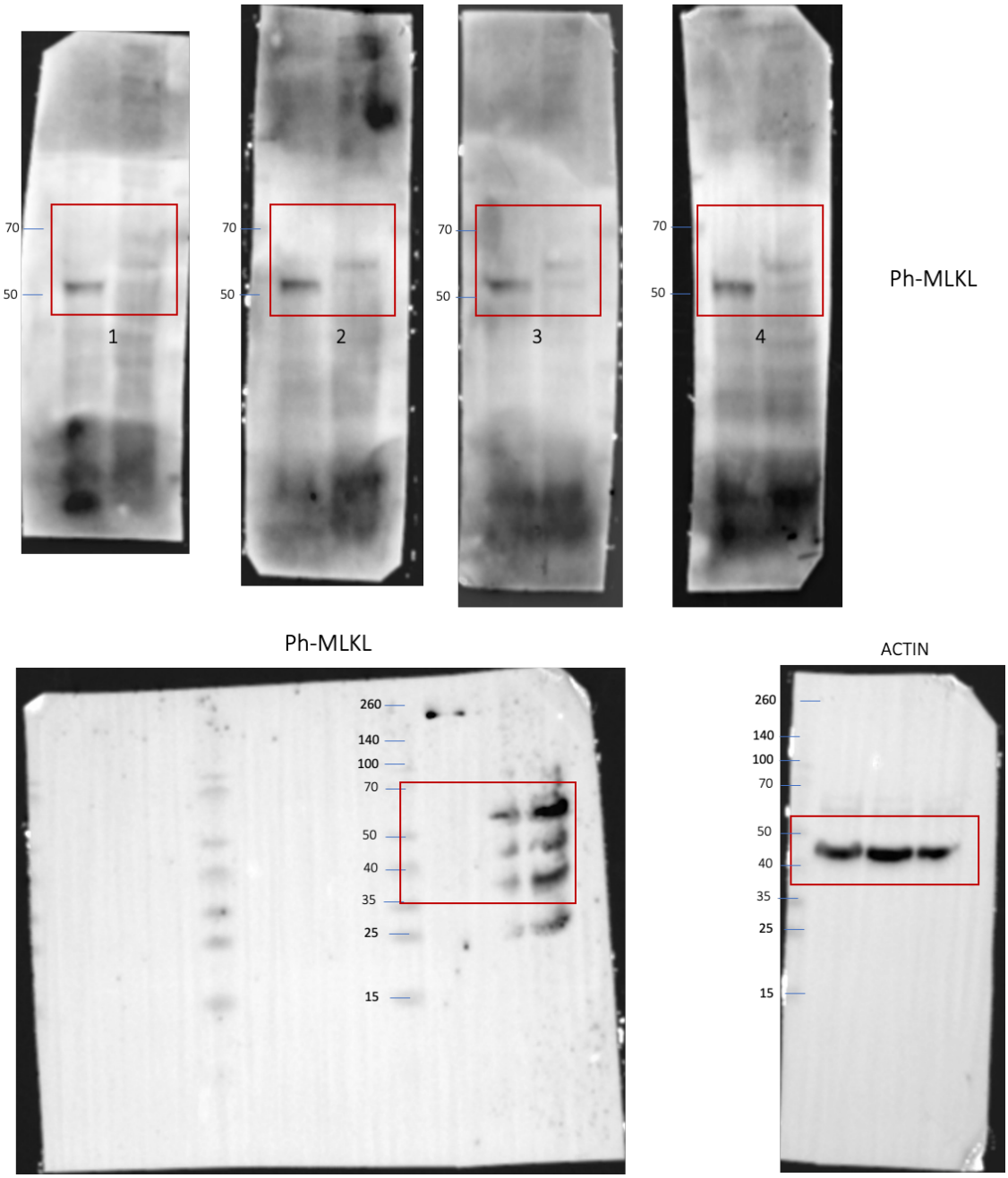

Figure A4.5: Uncropped Western blots used in Figure 3.5A and B.

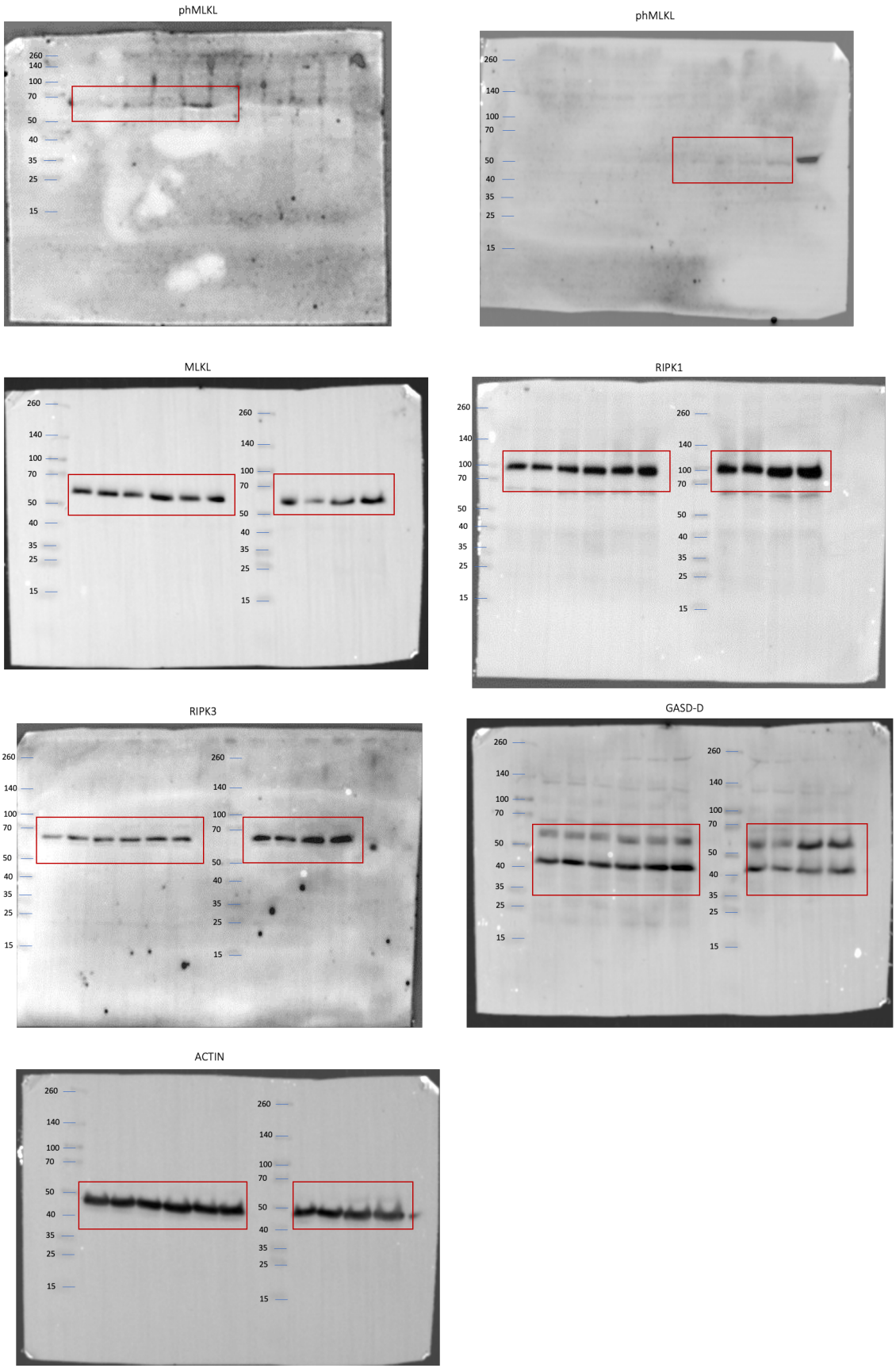

Figure A4.6: Uncropped Western blots used in Figure 3.6.

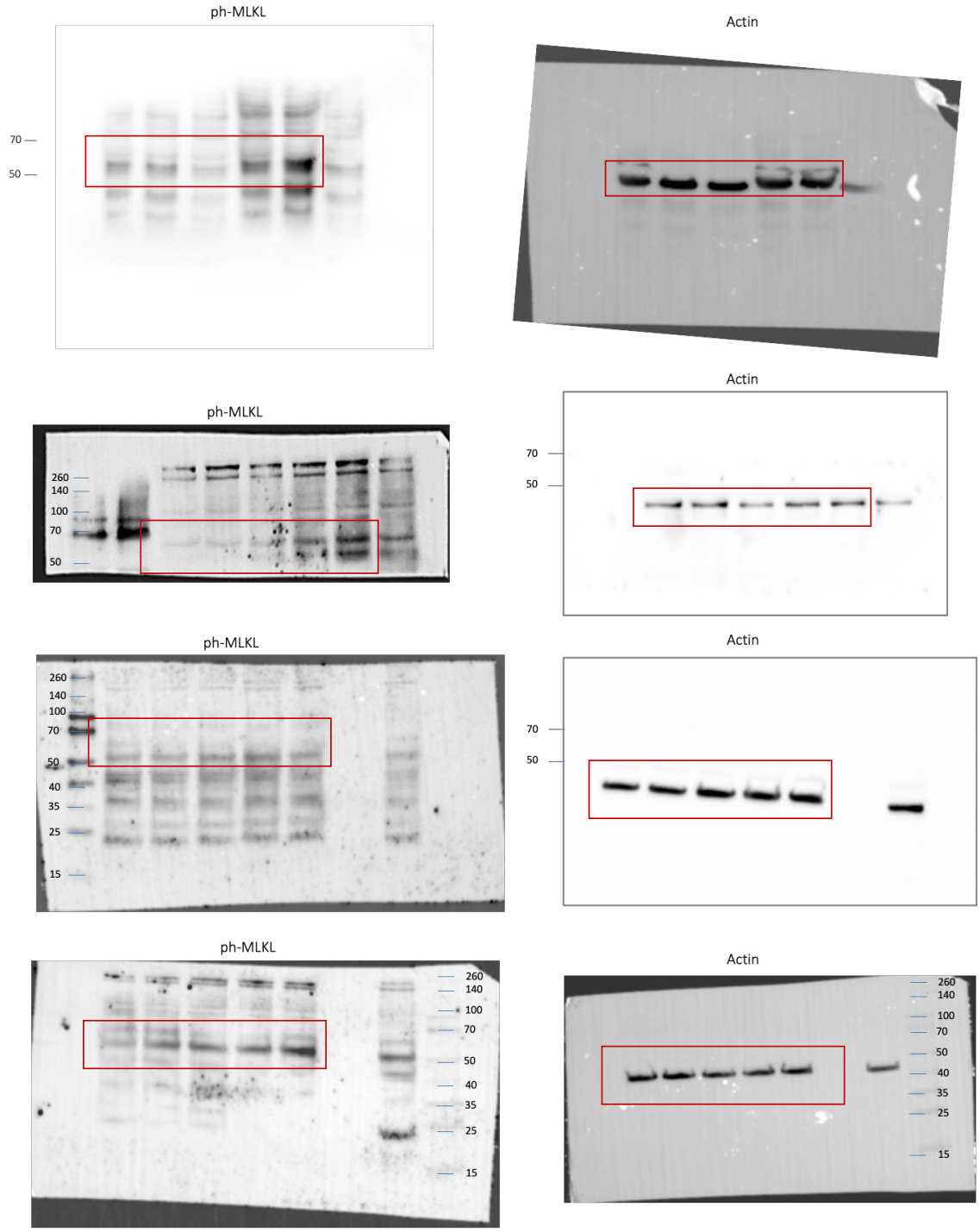

Figure A4.7: Uncropped Western blots used in Figure 3.7.

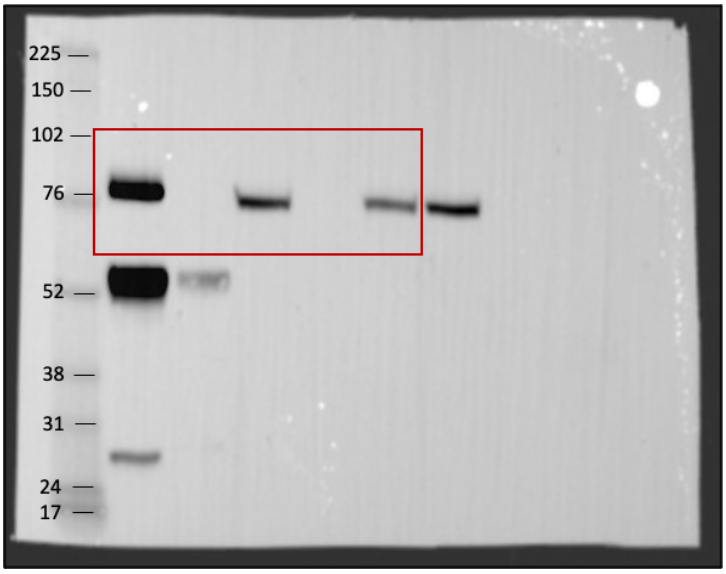

Figure A4.8: Uncropped Western blots used in Figure 3.8.

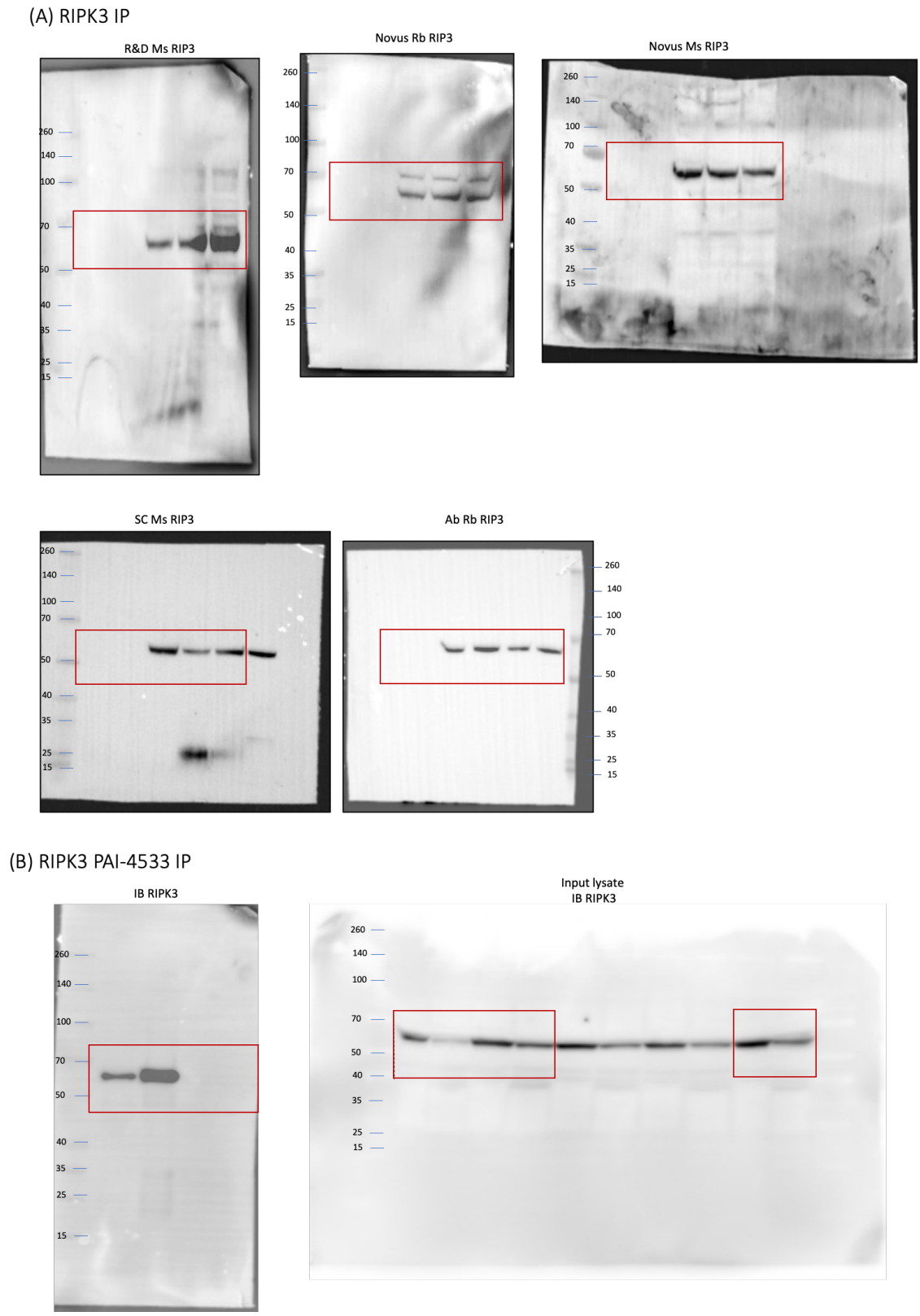

Figure A4.9: Uncropped Western blots used in Figure 3.9A and B.

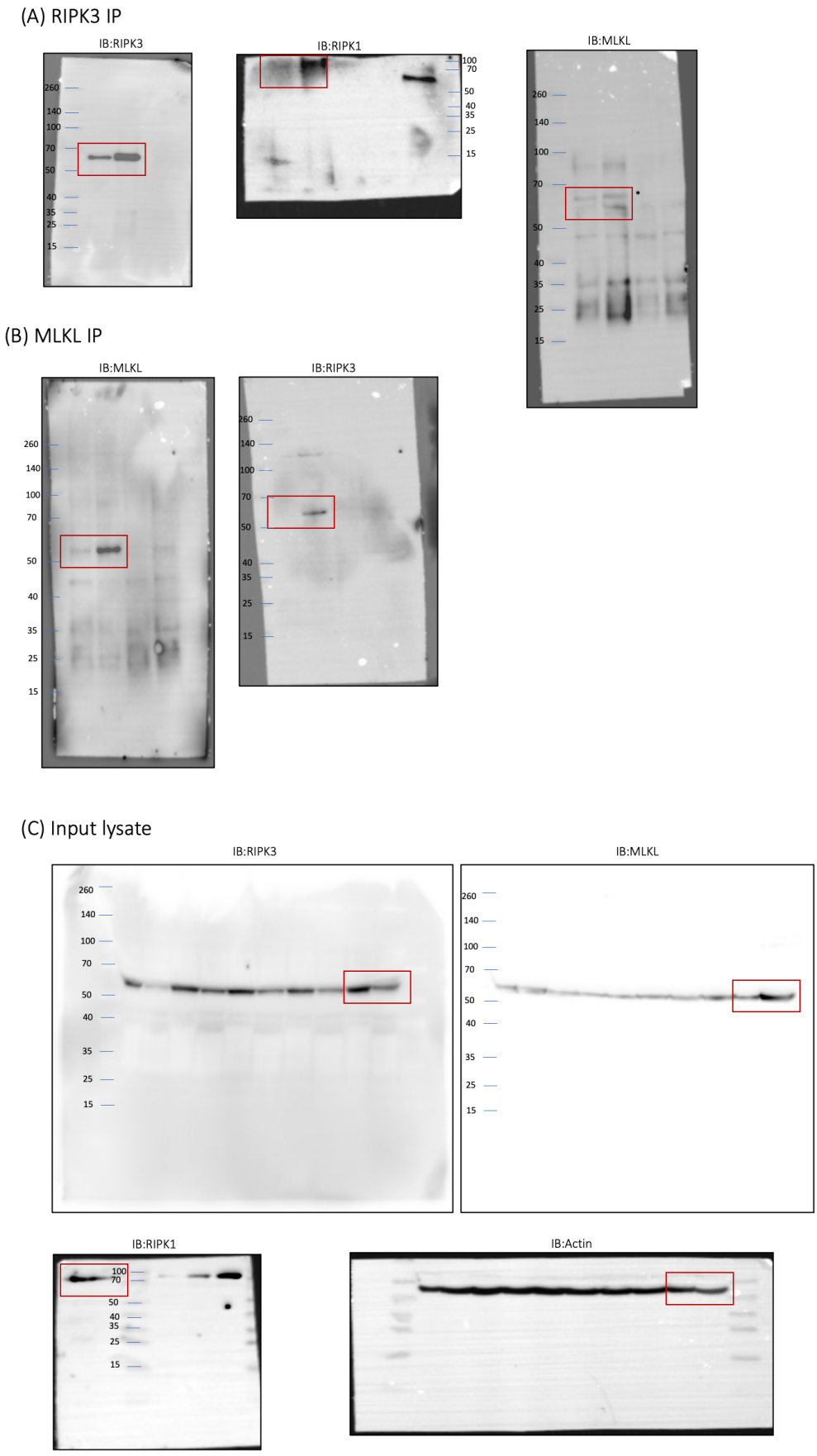

Figure A4.10: Uncropped Western blots used in Figure 3.10A, B and C.

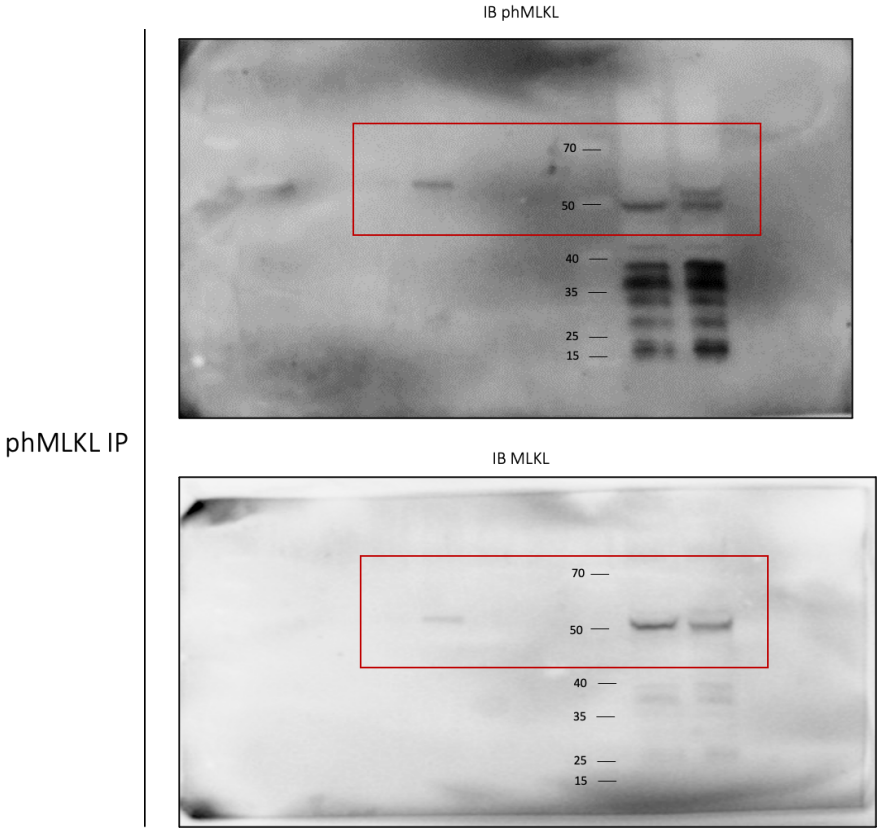

Figure A4.11: Uncropped Western blots used in Figure 3.11.

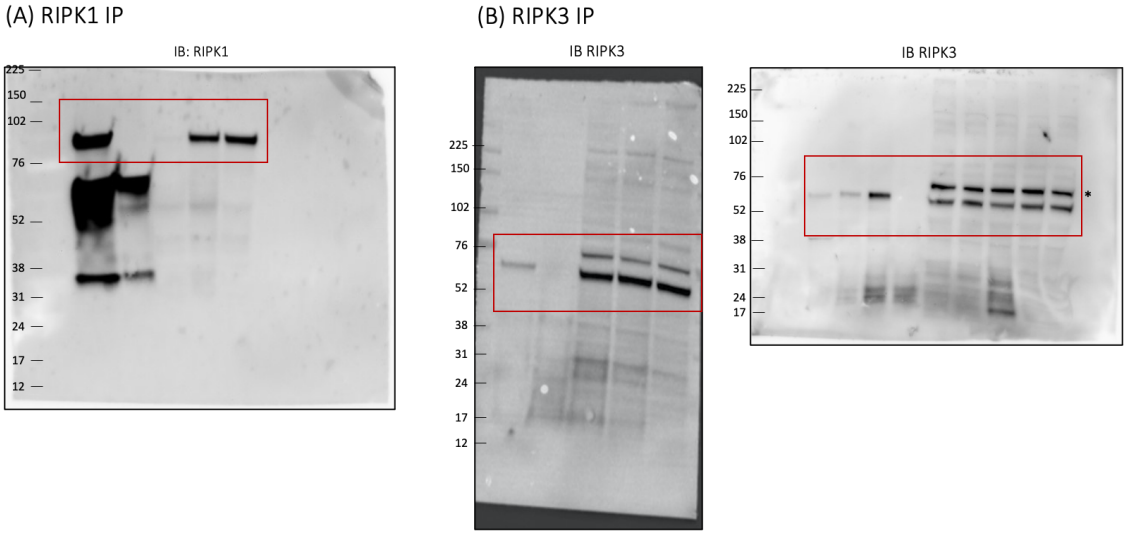

Figure A4.12: Uncropped Western blots used in Figure 3.12A and B.

(A) RIPK3 IP

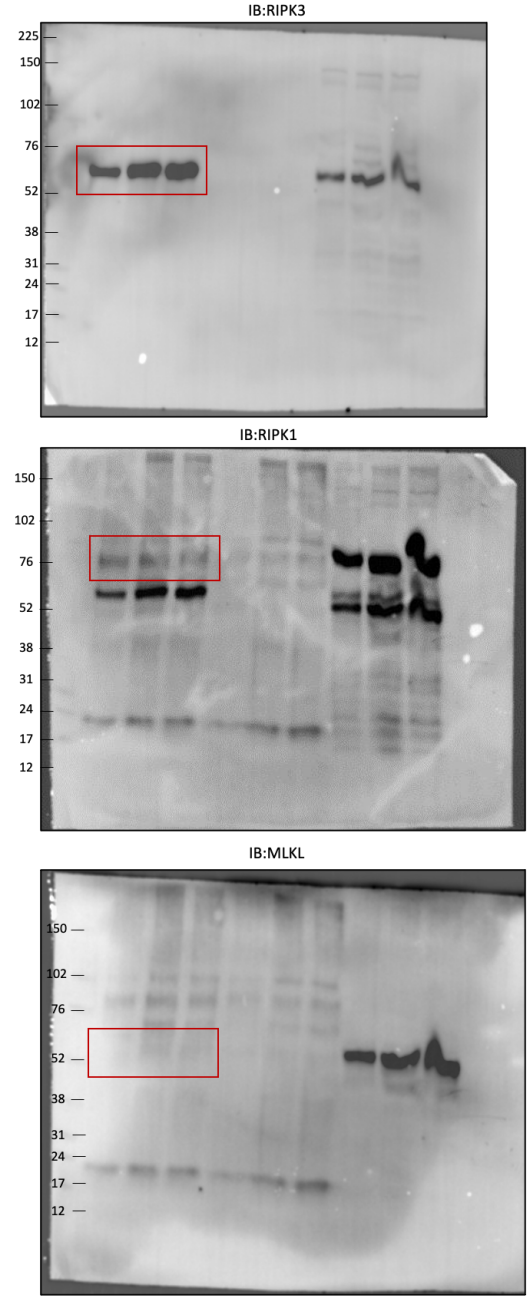

(B) phMLKL IP

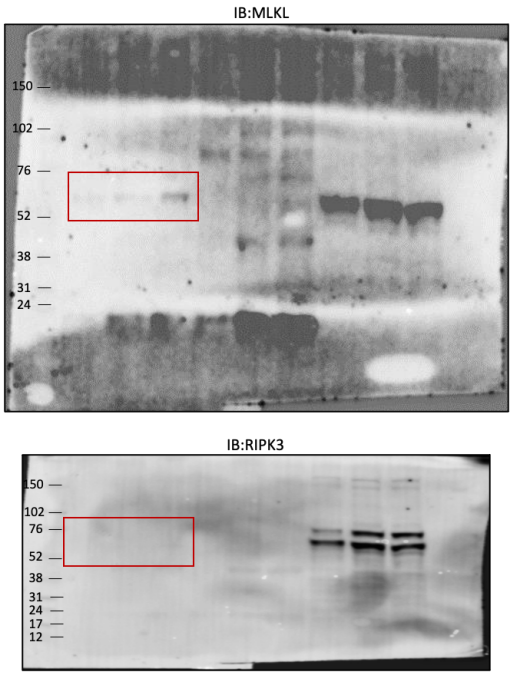

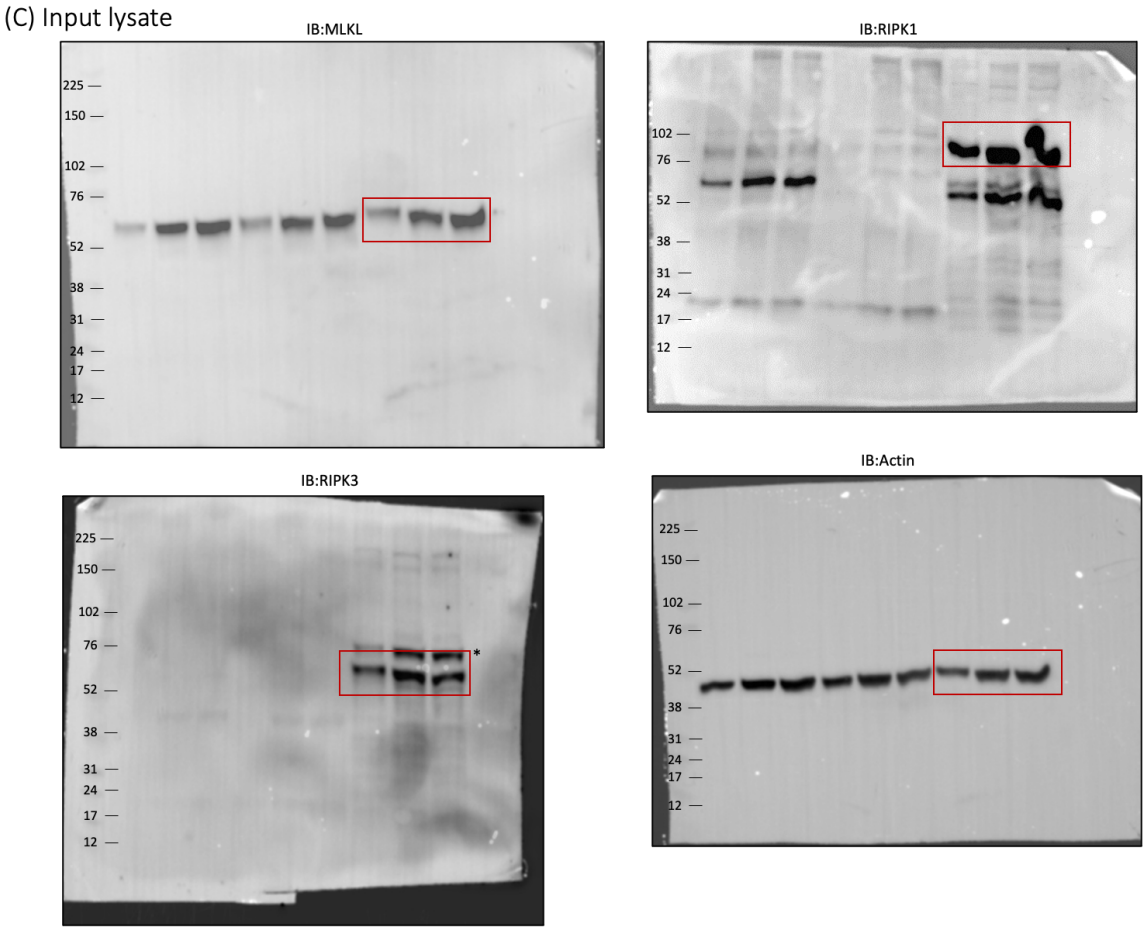

Figure A4.13: Uncropped Western blots used in Figure 3.14A, B and C.